Application of Quantum Mechanics to Fundamental Interactions in Chemical Physics:

Studies of Atom-Molecule and Ion-Molecule Interactions Under Single-Collision Conditions: Crossed Molecular Beams;

Single-Crystal Mössbauer Spectroscopy: Microscopic Tensor Properties of ^{57}Fe Sites in Inorganic Ferrous High-Spin Compounds

James N. Bull

a thesis presented in partial fulfilment of the degree of Doctor of Philosophy in Chemistry at the University of Canterbury

February 2007 - January 2010

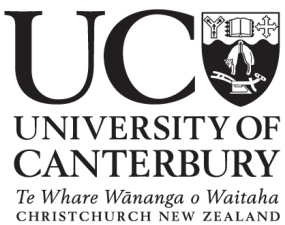

"The fundamental laws necessary for the mathematical treatment of a large part of physics and the whole of chemistry are thus completely known, and the difficulty lies only in the fact that application of these laws leads to equations that are too complex to be solved." - *Paul Dirac, 1933 Nobel Prize in Physics.*

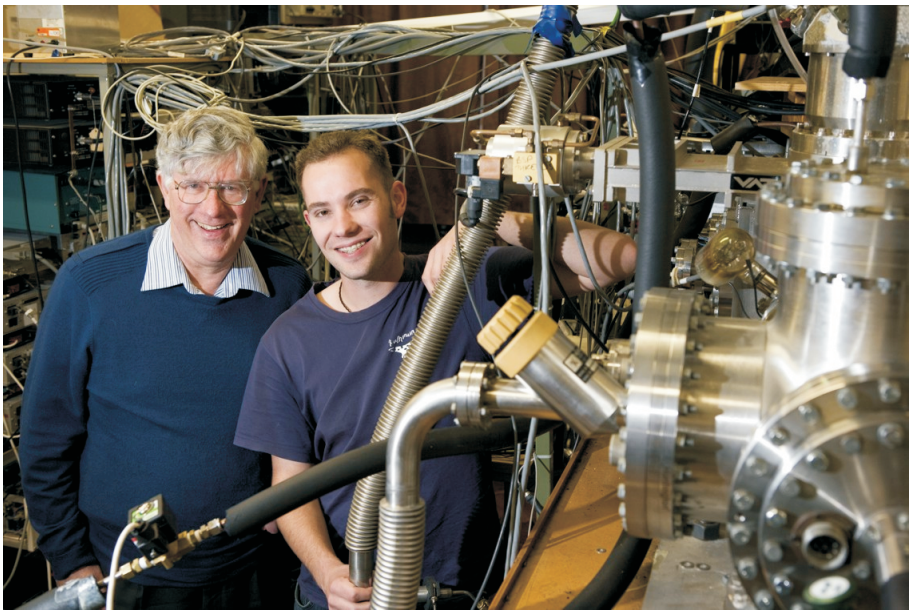

Assoc. Prof. Robert Maclagan (left) and thesis author James Bull (right) in front of Prof. Peter Harland's molecular beam machine laboratory. This photo was taken for one of the examples in: BlueFern - A Case Study and Vision for Collaborative High-Performance Computing and E-Research in New Zealand. This case study has been submitted to New Zealand Parliament as the first steps towards developing a centralized nationwide supercomputing facility for commerce, industry and research.

Abstract

As part of this project and in preparation for future experimental studies of gas-phase ion-molecule reactions, extensive modification and characterization of the crossed molecular beam machine in the Department of Chemistry, University of Canterbury has been carried out. This instrument has been configured and some preliminary testing completed to enable the future study of gas-phase ion-molecule collisions of H_3^+ and Y^- (Y = F, Cl, Br) with dipole-oriented CZ_3X (Z = H, F and X = F, Cl, Br). Theoretical calculations (*ab initio* and density functional theory) are reported on previously experimentally characterized Na + CH_3NO_2, Na + CH_3NC, and K + CH_3NC systems, and several other systems of relevance. All gas-phase experimental and theoretical studies have the common theme of studying collision orientation dependence of reaction under single-collision conditions. Experimental measurements, theoretical simulations and calculations are also reported on some selected ferrous (Fe^{2+}) high-spin (S=2) crystals, in an attempt to resolve microscopic contributions of two fundamental macroscopic tensor properties: the electric-field gradient (efg); and the mean square displacement (msd) in the case when more than one symmetry related site of low local point-group symmetry contributes to the same quadrupole doublet. These determinations have been made using the nuclear spectroscopic technique of Mössbauer spectroscopy, and complemented with X-ray crystallographic measurements.

Acknowledgements

This Ph.D. thesis, like the majority of others, cannot solely be attributed to the work of the author, rather, also to the collective support of many supervisors, co-workers, technical staff members and students. These acknowledgements represent an attempt to mention all the sources of assistance.

Firstly, my formal supervisors Prof. Peter Harland and Assoc. Prof. Robert Maclagan are thanked for encouragement, advice, friendship, and refined skills in the abundant administration in reports, applications and manuscript writing. I also wish to thank Dr. Craig Tennant who developed into an informal supervisor and provided the opportunity to undertake the Mössbauer work described in this thesis - I hope that I can undertake similar studies in my retirement. Dr. Craig Tennant throughout the course of this research spent months modifying and refining the source code of the program MOSREF which was used to simulate and refine our single crystal Mössbauer data. Without this program, and also several others: MOSPOW - powder spectrum averaging from single-crystal derived microscopic data; THICKMOD - for thickness and polarization corrections to observed quadrupole doublet intensities for non-infinitely thin absorbers, the studies outlined in several chapters in this thesis would not have been able to be undertaken.

The Department of Chemistry has provided an excellent research environment, and many other academic and technical staff need to be acknowledged. The expertise and aid of the mechanical and electronic workshops kept the experimental molecular beam research together. This was through the assistance and advice of Russell Gillard, Danny Leonard, Nick Oliver, Wayne MacKay, Sandy Ferguson, Steven Graham, Roger Merryweather and Robert MacGregor. Danny and Nick turned many drawings into machinery components of outstanding quality, while Sandy, Steven and Roger repaired, built and modified much electronic instrumentation, and were always available for advice and assistance. Prof. Ward Robinson and Dr. Chris Fitchett are acknowledged for assistance with X-ray crystal structure determinations, and Prof. Hartmut Speiring and Dr. Catherine McCammon for discussions and organization of crystal cutting facilities. Rob Spiers (Geology) is thanked for assistance with crystal mounting, cutting and polishing, in addition to use of their digital micrometer. Despite the neighbouring physics department administration always trying to inflate prices for our largest consumable, liquid nitrogen, thanks is extended to Bob Flygenring for keeping a supply of liquid nitrogen, and fixing the cryogenerator upon his return. Julian from facilities management is thanked for the many days spent implementing and assistance in repairing the new closed-loop coolant system for the molecular beam machine. Tony Dale and Colin McMurtry from the University of Canterbury Supercomputer (UCSC) facility are thanked for compiling and implementing the GAMESS-US and NWChem packages on the p575 and Blue

Gene/L supercomputers.

Thanks is also extended to family, friends and flatmates for support, and the occupants (or inhabitants) of room 732 (Michelle Hamilton, Ben Perston, Brett Davis, Louise Crawley, Daniel Packwood, Rachel Hanover-Conner, Lisa Graham, and Omar El-Hadad) throughout my time in the department for motivation, friendship, and the circulating juicy gossip. Thanks to Philipp Kitschke (exchange student) for choosing to undertake a 400-level research project for a four month period on *ab initio* calculations in relation to some of my research objectives, and providing an opportunity for some supervising experience.

Finally, financial support was initially provided by a Canterbury Scholarship (top eight graduates from University of Canterbury eligible for a University of Canterbury Doctoral Scholarship), which was then superseded by a Tertiary Education Commission (TEC) Top Achiever Doctoral Scholarship (top New Zealand Government scholarship scheme at the time). As well as a generous stipend and payment of fees, this scholarship also provided a travel allowance each year for attendance at conferences. The New Zealand Institute of Chemistry (NZIC), University of Canterbury Evans Fund, Royal Society of New Zealand, Japanese Society for the Promotion of Science, and United States Air Force in conjunction with Ohio State University must also be acknowledged for giving financial contributions for conference attendance. The Royal Society of New Zealand is acknowledged for the offer of the prestigious R. H. T. Bates scholarship for 2010, which was declined owing to the shortening of this Ph.D. from the anticipated four years to three.

Preface

This thesis in the field of chemical physics is in partial completion of the requirements for the degree of Doctor of Philosophy (Ph.D.) in Chemistry at the University of Canterbury, under the formal supervision of Professor Peter W. Harland and Associate Professor Robert G. A. R. Maclagan, and informal supervision of Dr. Craig Tennant in the slightly less than three year period between February 2007 and January 2010.

The presentation style herein is non-traditional for a New Zealand thesis in several ways. Firstly, this thesis is made up from three quite different parts. The first, experimental gas-phase reaction dynamics and the second part, on theoretical gas-phase reaction dynamics was originally the anticipated Ph.D. research. The experimental and theoretical fields of understanding are often distinct and not well interfaced. The original objective was to have Ph.D. research experience that merged these two fields in some complementary manner. The third thesis part is an entirely different project, concerned with condensed matter chemical physics. While extensive literature reviews were performed for all studies, these are not reproduced as chapters in this thesis, rather in the condensed introductions to respective chapters. The motivation in each study was to provide an emphasis on fundamentals and the development of physical pictures; in line with the author's interest in a fundamental understanding of the elusive nature of processes at the atomic and molecular level. The incomplete portions of research started here are only very briefly outlined and will be part of ongoing future studies.

The approach to this research was to publish work as it was completed, ideally before thesis submission, so thesis chapter preparation required the conversion of each paper into chapters. In this way, with the peer-review process, assurance is gained as to the validity of work as it is completed. This thesis therefore consists of results chapters in modified manuscript or draft manuscript form, that intentionally may to some extent appear discrete in content. The author's first publication (see list of publications), was submitted and accepted during the first Ph.D. year, and contained the results of the University of Canterbury B.Sc. (Hons.) degree research project, and therefore is not discussed further in this thesis.

It was unfortunate that during the first year of Ph.D. studies, it was discovered that the ion-imaging micro-channel plates (MCPs) were cracked, and replacements took several months to arrive. Further, there was a period of more than six months in total where the quantities of liquid nitrogen required were unavailable due to the self destruction of both the physics department cyrogenerators. While small quantities were obtainable on some days, the amounts required for diffusion pump operation ($\approx$ 75 L per day) were not available. These setbacks meant that experimental work had not progressed as expected, and theoretical work was undertaken

during these periods.

Several honours and distinctions achieved during the course of this thesis are also listed below:

- Offer of the 2010 R. H. T. Bates Scholarship, 2009
- Attendance by invitation - 2^{nd} HOPE Meeting with the Nobel Laureates, 2009
- Attendance by invitation - 59^{th} Meeting of the Nobel Laureates in Lindau, Germany, 2009
- Ralph H. Earle Jnr. Seminar Prize, 2008 (best second year review seminar in chemistry)

One other major time component of this thesis was preparation, attendance and travel to several conferences. Conference attendance was financially possible by the award of the Tertiary Education Commission Top Achiever Doctoral Scholarship, that contained a generous travel allowance. In summation, conference preparation, attendance and travel consumed approximately five months. These conferences are listed below:

- World Association of Computational and Theoretical Chemistry (WATOC), Sept 2008, Sydney, Australia, with poster presentation: *Ab Initio* Calculations on the Orientation Dependence of the Na + CH_3NO_2 and CH_3NC Electron Transfer Reactions
- University of Canterbury Postgraduate Showcase, Sept 2008, Christchurch, New Zealand, with oral communication: Ion-Molecule Reactions Under Single-Collision Conditions
- New Zealand Institute of Chemistry (NZIC) 2008: Chemistry and the Biosphere, Dunedin, New Zealand, Nov/Dec 2008, with oral communication: *Ab Initio* Calculations on the Orientation Dependence of Some Simple Bimolecular Reactions
- Inorganic Chemistry 2008 (IC08), Christchurch, New Zealand, Dec 2008, with poster presentation: Mössbauer and X-ray Single Crystal Determination of Microscopic EFG and MSD Tensors in Ferrous High Spin Salts
- Presentation of a one hour review seminar on the Mössbauer effect and Mössbauer spectroscopy to the Department of Chemistry, University of Canterbury, with review article published in ChemEd NZ, Aug 2008
- The 59^{th} Meeting of the Nobel Laureates in Chemistry, Lindau, Germany, June 2009 - two candidates competitively selected from New Zealand
- Dynamics of Molecular Collisions (DMC) 2009, Snowbird (Utah), USA, July 2009, with poster presentation: Experimental and theoretical studies of positive and negative ion collisions with spatially oriented molecules
- HOPE 2009 Meeting - Art in Science, with Nobel Laureates in Chemistry, Hakone, Japan, Sept 2009 - three candidates competitively selected from New Zealand, with poster presentation: Orientation dependence of ion-molecule reactions using crossed molecular beams under single-collision conditions, and group presentation: What is needed to make new discoveries and to do creative research?

Finally, during the course of this thesis at least one or two afternoons each week during the semester teaching periods was devoted to teaching, demonstrating and the grading of undergraduate course laboratory experiments. This provided teaching experience in the courses listed below:

- 100-level (first year) general chemistry laboratory supervisor (2007)
- 200-level (second year) physical and analytical chemistry laboratory demonstrator (2007-2009)
- 300-level (third year) physical and analytical chemistry laboratory demonstrator (2007-2008)

List of Abbreviations and Acronyms

Abbreviation/Acronym	Definition
AC	alternating current
ADP	atomic displacement parameter
BDE	bond dissociation energy
BSSE	basis set superposition error
CEMS	conversion electron Mössbauer spectroscopy
CP	counterpoise
DC	direct current
DSIR	Division of Scientific and Industrial Research
EA	electron affinity
efg	electric field gradient
EPR	electron paramagnetic (spin) resonance
DFT	density functional theory
FAS	ferrous ammonium sulphate hexahydrate
FCL	ferrous chloride tetrahydrate
FWHM	full width at half maximum
HF	Hartree-Fock
HOMO	highest occupied molecular orbital
HV	high voltage
HWHM	half width at half maximum
IE	ion energy
IP	ionization energy
LUMO	lowest occupied molecular orbital
MCA	multi-channel analyser
MCP	micro-channel plates
msd	mean square displacement
MPG	multi-pulse generator
NBO	natural bond order
OD	outer diameter
RMSD	root mean square displacement
SNP	sodium nitroprusside
TDDFT	time-dependent density functional theory
TOF	time-of-flight
ZPE/ZPV	zero point energy/valence

Contents

List of Figures

List of Tables

List of Publications

Listed in order of journal appearance.

Absolute electron impact ionization cross-sections and polarizability volumes for C_2 to C_4 aldehydes, C_4 and C_6 symmetric ethers and C_3 to C_6 ketones, James N. Bull and Peter W. Harland, *Int. J. Mass Spectrom.*, 273 (2008) 53-57

Orientation Dependence of the Na + CH_3NO_2 Reaction, James. N. Bull, Robert G. A. R. Maclagan, and Peter W. Harland, *Mol. Phys.*, 107(8) (2009) 1123-1137

Ferrous ammonium sulphate hexahydrate Mössbauer revised: a combined ^{57}Fe Mössbauer X-ray single crystal study, James. N. Bull, Ward T. Robinson, and W. Craighead Tennant, *Hyperfine Interact.*, 104 (2009) 347-366

From a child's toy to a Nobel prize: Mössbauer Spectroscopy, James N. Bull, *ChemEd NZ*, 116 (2009) 11-19

On the electron affinity of nitromethane (CH_3NO_2), James N. Bull, Robert G. A. R. Maclagan, Peter W. Harland, *J. Phys. Chem. A*, 114 (2010) 3622-3629

Isomorphism of ferrous chloride tetrahydrate: X-ray and Mössbauer, James N. Bull, Christopher M. Fitchett, Robert G. A. R. Maclagan, Ward T. Robinson, W. Craighead Tennant, *J. Phys. Chem. Sol.*, in submission

Mössbauer and X-ray single crystal study of ferrous chloride tetrahydrate, James N. Bull, Christopher M. Fitchett, W. Craighead Tennant, in preparation

Isocyanide orientation dependence: the Na and K + CH_3NC rebound reactions, James N. Bull, Robert G. A. R. Maclagan, in preparation

Part I.

Experimental Studies of Atom-Molecule and Ion-Molecule Interactions Under Single-Collision Conditions: Crossed Molecular Beams

1. General introduction

The majority of chemical reactions occur in solution or high-particle density gas-phase, where each particle experiences millions of collisions each second. In solution phase, these collisions alter the energy distributions and may even change the final products before measurement is possible. In addition, non-spherical reactants may exhibit orientation dependence; for example, collisions at one end of the molecule may have a different efficiency and possibly a different product than collisions at the other end. There is no way to pre-define collision orientations or sites in high-particle density phases to study such fundamental orientation dependence. These experimental limitations may be overcome by the study of bimolecular reactions in the gas phase under single-collision conditions at ultra-high vacuum ($\leq 10^{-7}$ Torr) where the distance travelled between collisions exceeds the distance to the product detector. Under these conditions, the products are examined before they are able to be modified by further collisions. To undertake such studies, a pulsed crossed molecular beam machine has been modified and characterized. Experimental studies are presently being undertaken to study fundamental proton transfer (H_3^+) and the S_N2 Walden inversion process (Y^-, where Y=F, Cl or Br) with some classic halocarbons, CZ_3X (Z=H or F, X=F, Cl or Br). In such experiments, as an example, a H_3^+ ion will be directed to the CH_3-end of a molecule such as CH_3Cl and then to the Cl-end by reversing the direction of an orienting electric field on a beam of upper Stark state selected molecules.

Briefly, the molecular beam machine consists of a series of stainless-steel chambers, with two intersecting beams at right angles. The pulsed molecular beam, containing CZ_3X species that may be neat (pure) or seeded (in a carrier gas), is generated with a piezoelectric source, with a skimmer selecting the central core of the beam which has essentially only one velocity component. From jet expansion, the beam is internally cold, in that molecules are in their lowest internal energy states. A high-voltage hexapole rod assembly provides an inhomogeneous field ($\approx$ 10 kV) that facilitates the focusing of upper Stark rotational states, which in turn can be oriented with a pulsed homogeneous field at $\approx$ 300 V. The instrument had not been used in some time before commencement of these studies, and required essentially complete reconfiguration of mechanical and electrical components, in addition to the modification and construction of new hardware.

The molecular beam source was overhauled and the piezoelectric crystal ring was replaced so that the source would function correctly with a new skimmer featuring a smaller glancing angle for better molecular beam profiles. In addition, the quadrupole mass spectrometers were stripped down and the electron impact ion-source on the molecular beam line quadrupole was changed. The hexapole rods that had previously been removed where reinserted, and a new laser mounting system allowing beam alignment constructed. Hexapole

focusing enhancements of up to four to five fold were obtained for the halocarbons of interest.

An existing H_3^+ ion source that produced ions by electron impact ionization of relatively high-pressure H_2 ($\approx 10^{-3}$ Torr) was stripped down and rebuilt with some modifications to lens elements and gas reservoir. Two ion-source controllers allow iterative manual control over lens elements for a continuous ion beam. The reimplementation of a new fibre-optic triggering system with up to 3 *n*s resolution, and modification of an old element pulsing unit employed in previous electron impact ionization orientation experiments that only boasted microsecond resolution allowed modulation of a shutter lens yielding H_3^+ ion-beam pulses with less that ≈ 300 *n*s rise times. In situations involving pulsed electrode elements, care and testing was required to avoid current-sagging recovery effects when *RC* type circuits were employed with fast switching with residual element currents. Such considerations are intuitive for high-speed switching electronics. It was further shown that the H_2^+:H_3^+ ratio can be well controlled by changing the pressure of the H_2 gas in the electron impact collision source. A new gas inlet system was constructed, replacing the existing line that only allowed minimal control.

The ion-imaging detection assembly essentially generates molecular photographic snapshots at selected times after the beams cross, and yields information on scattering angular dynamics and energy-momentum dynamics with mathematical interpretation and application of physical conservation laws. The previously broken ion-imaging flight tube was repaired and cracked MCP plates were replaced and reconnected to high-voltage power supplies. The extraction and repeller electrostatic plates and flight tube were reconnected and new high-voltage power supplies implemented. Preliminary testing showed the ion-imaging apparatus to yield excellent ≈ 200 ns temporal resolution on the camera gate allowing selection of individual time-of-flight ions, and a photomultiplier tube to show excellent resolution between ions ranging from 14 amu to > 100 amu.

2. The Molecular Beam Machine

The term "molecular beam machine" is the common reference given to the scientific apparatus in room 733 of the Chemistry Department, University of Canterbury that is used to perform studies with crossed molecular/ion beams. Molecular dynamics or reaction dynamics is the study of the dynamics, energetics (inter- and intra-molecular) and mechanisms of elementary physical and chemical collision processes. This chapter provides a brief overview of some of the modifications made to the molecular beam machine in order to facilitate future studies. The implementation philosophy was to allow control over all possible reaction condition variables, in order to remove any ambiguity in results. One of the major changes considered in this work was the requirement of ultra-fast pulsing sequences, which are practically difficult to obtained with charged particle beams. Since these studies involve charged particles, the instrumentation makes heavy use of electrostatic focusing, deflection and retarding lens elements. Emphasis has not been placed on including this as major portion of this thesis, since this only contributed as a small part of the thesis research and the author will be undertaking subsequent research on this instrument following submission of this thesis. A recent photograph during the course of this thesis is shown in figure 2.1. Several images in this chapter have been modified from Bart [1] and Vallance citemb-vallance.

Figure 2.1.: Photograph of the molecular beam machine during the course of this thesis.

2.1. Historical account

The molecular beam machine (in its current form) can be dated back to the construction of the first vacuum chambers started in June 1991 and completed in October 1992 by the Chemistry Department Mechanical Workshop [2]. The custom design requirements, complex shape, and the need for ultra-high vacuum capabilities meant that manufacture was beyond the capabilities of any other New Zealand based firm at the time. The chambers were constructed from high grade stainless steel, ranging from 1.0 cm to 2.5 cm thick, with several 1.6 cm thick glass windows for interior inspection and illumination. The original machine contained two high vacuum chambers, with a supersonic nozzle source mounted in the first, and a quadrupole mass spectrometer detector mounted in the second. These two chambers were separated by a skimmer that allowed selection of a portion of the supersonic beam leading into a flight tube, and facilitated study of the application of supersonic molecular beam expansion with subsequent mathematical modelling. The initial research objectives focused around time-of-flight mass spectrometry (TOF-MS) for the analysis of modulated (pulsed) and continuous molecular beam distribution parameters, including beam velocities, beam temperatures, and non-equilibrium velocity and temperature slips for mixtures of gases.

In the 18 years following construction, the molecular beam machine has seen redevelopment by Honours, numerous Ph.D. and Post Doctoral Fellows, targeting a variety of molecular beam research objectives. A brief overview of the contributions from several individuals will be outlined.

Cameron [3] (Ph.D.) modified the original instrument for investigations on atomic and molecular van der Waals clusters produced from supersonic molecular beam sources. Construction of a supersonic source allowed characterization of supersonic beam intensities as a function of reservoir pressure, nozzle-skimmer distance, supersonic beam speed distributions for various monoatomic and diatomic gases, and speed distributions for binary monoatomic mixtures by TOF-MS. Further modifications also allowed size distribution measurements for cluster complexes formed by Ar and He seeded gases containing SO_2, N_2O, H_2O, NO and NO_2 with NH_3. The appearance potentials of several cluster species formed in the supersonic expansion and cluster ion fragments were determined by electron impact ionization.

Movement of the general research field from clusters to spatial orientation of polar molecules resulted in modification of the molecular beam machine to allow insertion of hexapole field rods, that provided hexapole rotational Stark state filtering (outlined later) by Aitken [4] (Ph.D.). The hexapole rods and associated electronics were constructed and required two additional vacuum chambers to be constructed, to house the 833 mm length rods. Characterization of the hexapole field led to investigations on the focusing effects for various C_{3V} symmetric molecules, performed by measuring beam intensities as a function of hexapole potentials. Initial asymmetry experiments involving measurement of ion formation by electron impact were undertaken for the methyl halide series, and resulting experiments showed an affinity for ionization from positive end collisions. Further investigations were started that involved measuring electron impact ionization cross-sections

as a function of electron energy and hexapole voltage, however a mechanical pump oil back-flow contamination prevented completion of this work.

Further developments were undertaken to facilitate the study of oriented ion-molecule collision, and again required construction and insertion of a new buffer vacuum chamber, as well as an overhaul and increase in vacuum pumping capabilities. In addition, the most important modification was the design and construction of a new scattering chamber allowing crossed molecular beams studies. This scattering chamber had a considerably larger volume than any of the other chambers, and housed a rotatable mass spectrometer. An increase in the nozzle chamber size also allowed higher source stagnation pressures providing higher quality molecular beams.

Blunt [5] (Ph.D.) continued the work of Aitken, by undertaking investigations of rotational quantum state selected spatially orientated C_{3V} molecules. Upper Stark state relaxation cross-sections for molecular beams of CH_3Cl and 20% CCl_3H seeded in Ar were measured with several different quencher species. Interpretation of quenching lifetime with van der Waals potential coupling provided an explanation of observations. It was shown for the first time (in conjunction with the work being carried out by Aitken) that electron impact ionization cross-section magnitude is dependent upon molecular orientation with four different methyl halides. Efficiencies are highest, or the cross-section is largest, at the positive end of the dipole of a polar molecule. Following, it was demonstrated that the product mass spectra are also orientation dependent.

Harris [6] (Ph.D.) investigated rotationally inelastic collisional attenuation of hexapole focused upper Stark state C_{3V} molecules as a function of scattering gas density. He found that such defocusing interactions are long range, occurring at intermolecular distances of upto 15 Å.

Vallance and Hu [7, 8] (Ph.D.) undertook several modifications. Two new vacuum chambers were added allowing insertion of a resonance cell between hexapole chambers for resonance beam spectroscopy, and also a housing for an ion/electron crossed beam source located off the main scattering chamber, allowing ion-molecule crossed beam experiments. Following from Harris, both investigated Stark state collisional relaxation cross-sections for single quantum rotational states of methyl halides, followed by characterization of Stark state selected spatial deorientation lifetimes of methyl halides initially oriented in an electric field. A new scattering chamber lid was designed for a state of the art ion imaging system to be implemented. Construction and partial characterization was started, however not finished and Vallance carried out a series of calculations for ion-molecule product energies. Such an assembly represented the future for this type of crossed molecular beam research, and was globally in early stages of development.

Bart [1] (Ph.D.) continued development of the machine, further modifying the ion imaging assembly and generating ion-images for electron impact ionization of oxygen. This was the first time an ion imaging assembly had been applied to electron impact ionization in order to measure angular scattering and energy disposal. Bart was assisted by Honours student Michelle Hamilton in the latter part of his studies.

Following Bart, Dr. Todd Clements wrote several programs for computer control and automated acquisition and interpretation of ion imaging data, known as Image and WinAbel. Clements removed alot of the internal molecular beam components and disconnected racked electronics.

2.2. Molecular beam machine components

One of the fundamental requirements in order to undertake orientation dependence studies of isolated chemical reactions is the state known as single collision conditions. Under single collision conditions, the outcomes from reagent collisions are detected before any subsequent collisions can occur that cause the nascent non-statistical quantum state occupation or non-thermodynamic outcomes to become thermodynamic or collisionally relaxed. Single collision conditions require low background pressures and rapid detection times, where spatial isolation can be defined by considering the mean free path, λ, which is the expectation path length between collisions. Spatial isolation experiments require that λ is much greater than the distance between the location of product species formation and product detection. In the simple collision theory picture, this condition is summarised in equation 2.1.

$$\lambda = \frac{1}{\sigma n} \tag{2.1}$$

where σ is a typical collision cross-section at ≈ 10 Å^2 for general background species or ≈ 200 Å^2 for rotation state relaxation, and $n = \frac{P}{kT}$ is the particle number density, in terms of total background (assuming a non-interacting beam) pressure, P, and temperature, T. The unperturbed flux at a separation, x, from preparation to detection can calculated by equation 2.2.

$$I(x) = I_\circ e^{-x\sigma n} \tag{2.2}$$

where $I_\circ$ is the flux at the reaction centre. In the molecular beam apparatus used in this work, the separation between beam crossing region and detection by mass spectrometers or ion imaging is between 5 cm and 20 cm, meaning that background pressures of $< 5 \times 10^{-7}$ Torr in the machine are required to achieve the single collision condition $\frac{I(x)}{I_0} \approx 1$.[1] In contrast to vibrational excitation that can survive $\approx 10^5$ collisions before vibrational relaxation, rotational excitation is rapidly quenched within a few collisions since coupling periods (vibrational frequency and rotational period compared with collision interaction period) are more ideal in the latter case.

The construct of the molecular beam machine apparatus consists of six stainless steel high vacuum chambers that are all interconnected by means of 10" OD, 8" OD or 6" OD Conflat flanges with high-grade copper gaskets. A general schematic of the instrument and connectivity of each of the chambers is outlined in figure 2.2. A schematic showing all of the internal components considered in the modifications here is given in figure 2.3.

[1] λ at 1×10^{-6} Torr is ≈ 30 m for $\sigma = 10$ Å^2 and $n = 3 \times 10^{10}$ cm^{-3}.

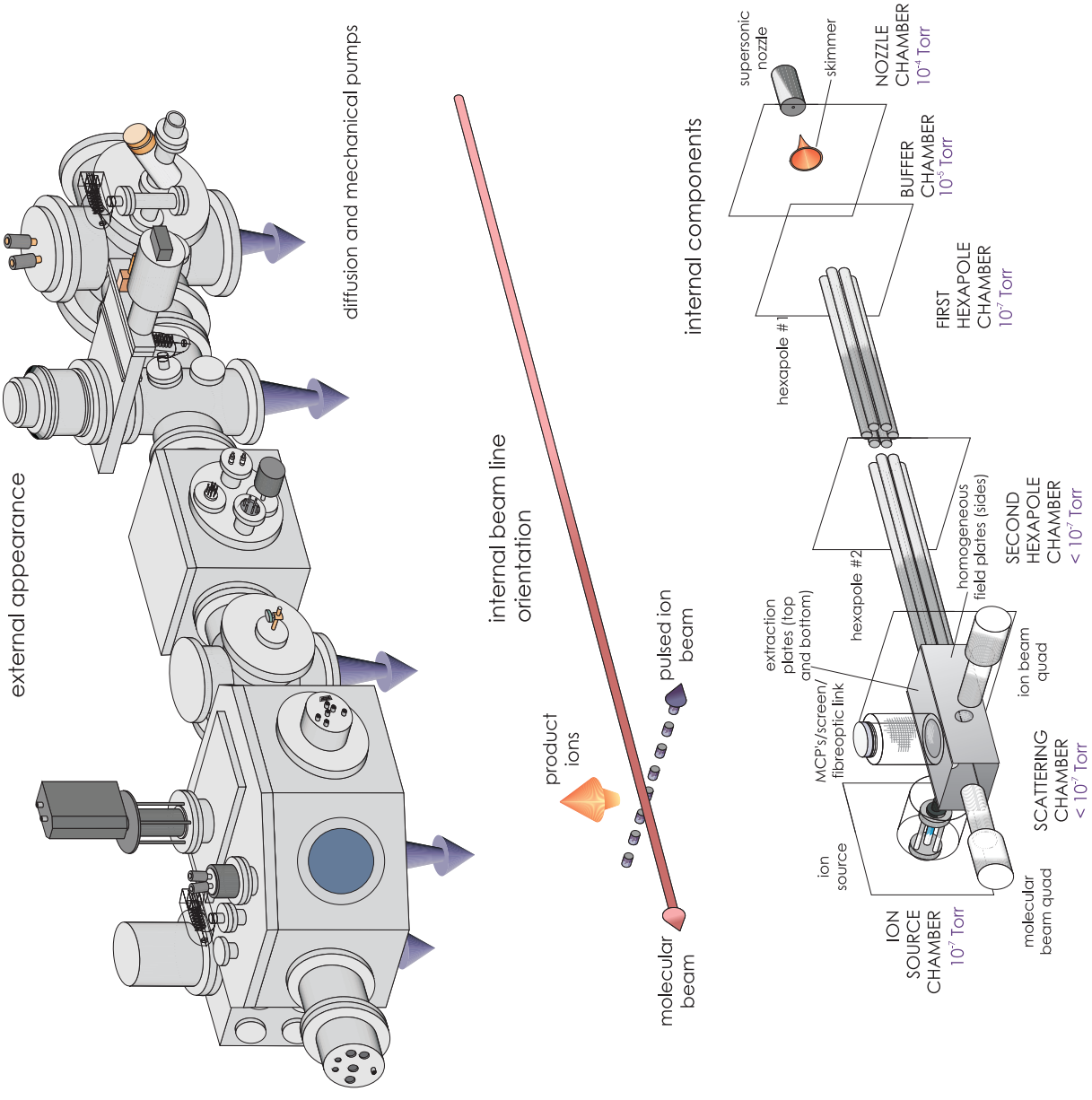

Figure 2.2.: The crossed molecular beam machine at the University of Canterbury, Department of Chemistry, which consists of a series of ultra-high vacuum chambers. The top section shows the outside appearance, the central section the supersonic and ion-beam crossings, and the lower section shows the various internal instrumentation required for state-selection and product detection. The flight tube and ion imaging assembly sits vertically above the beam crossing region. All these components will be briefly outlined. Figure modified from Vallance [7].

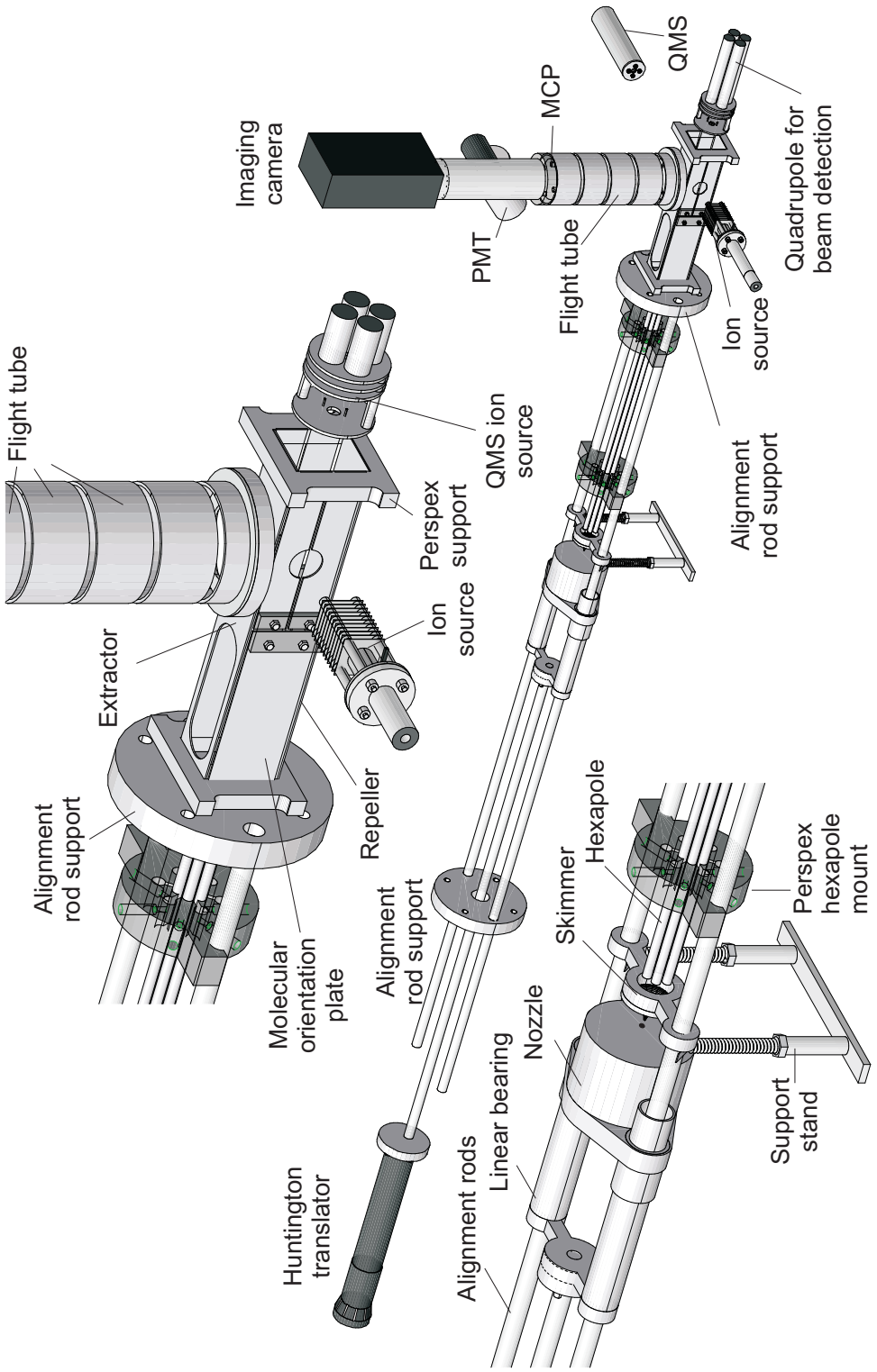

Figure 2.3.: The internal configuration of the components in the 'molecular beam machine' at the University of Canterbury, Department of Chemistry. QMS = quadrupole mass spectrometer. Figure modified from bart [1].

The box-shaped first hexapole and scattering chambers both have removable lids using an overhead chain block, and each lid is sealed with a large Viton O-ring. All chambers are mounted on a common frame that runs the full length of the instrument, and each chamber is held in place on a roller-bearing platform that allows horizontal movement along frame rails when modification is required. All of the six chambers are differentially vacuum pumped by either a silicon-oil pot-belly Varian diffusion pump, an Acatel turbomolecular pump and/or a liquid nitrogen cryogenic trap. Each chamber has common name that denotes its respective function, with their pump configurations outlined below:

1. nozzle - 8" diffusion pump
2. buffer - CFF450 turbomolecular pump and 4" diffusion pump
3. hexapole 1 - 6" diffusion pump
4. hexapole 2 - 4" diffusion pump
5. scattering - CFV900 turbomolecular pump and 6" diffusion pump
6. quadrupole - CFF450 turbomolecular pump

Each of the turbomolecular and diffusion pumps can be isolated from the connected vacuum chambers by an electromechanical pneumatic valve or hand operated gate valve. In turn, each turbomolecular and diffusion pump can be isolated from its backing mechanical pump. In several instances owing to the age of mechanical pumps, these had to be disassembled and internally overhauled. In the worst case, teflon valves on the scattering chamber mechanical pump had to be hand manufactured since replacement parts were not available. In addition, a two stage Alcatel mechanical pump capable of pumping 300 L/min failed several times and was replaced with (older) Edwards three-phase mechanical pump capable of 450 L/min pumping rate, also requiring reconstruction of the inlet line connecting to the diffusion pump exhaust line. Implementation of this new pump facilitated a better achievable vacuum in the hexapole 2 chamber that was required in order to achieve good hexapole focusing characteristics. Diffusion pump exhaust lines (mechanical pump fore lines) all have pressures monitored with MKS 531 thermocouple gauge heads connected to MKS 286 thermocouple readouts, allowing determination of differential pumping conditions and the ability to monitor the onset of vacuum failure. All diffusion pumps and cryogenic traps are liquid nitrogen cooled through $\frac{3}{8}$" OD copper pipe from two 75 L reservoirs back pressured with nitrogen gas from a cylinder. Reconstruction of two existing refilling controllers allowed automated filling at predefined intervals utilizing the principle of power diode intrinsic semi-condition potential change upon cooling when liquid nitrogen had filled the diffusion and cryotraps. The diffusion and turbomolecular pumps also require water cooling by a new closed loop coolant system that will be outlined later, with coolant water temperature monitored by several thermocouples. The vacuum pumping and coolant configuration yields typical scattering chamber background pressures of 5×10^{-8} Torr, meeting the background pressure requirements for single-collision conditions.

Background chamber pressures are monitored by Duniway Stockroom Corporation T-100K tungsten filament ion gauges with MKS 290 ion-gauge controllers and readouts, allowing pressure measurement between $\approx 1\times10^{-5}$ Torr to $\approx 1 \times 10^{-9}$ Torr. Four ion-gauges can be operated at one time. All sensitive electronic instrumentation susceptible to damage by vacuum failure (e.g. quadrupole mass spectrometers, ion imaging assembly and filaments), is protected by an in-house vacuum protection system that connects to the (selectable) ion-gauge located on the quadrupole chamber. When this ion-gauge exceeds a (selectable) pressure of $\approx 1 \times 10^{-5}$ Torr, the vacuum system, turbomolecular, diffusion pumps and sensitive electronics are shut down to avoid damage. A MKS 662 absolute Baratron head was installed on the first hexapole chamber that is driven by a custom 15 V power supply and analogue pressure meter readout allows venting pressures to be measured.

The modifications and reconfigurations considered in this thesis, can be grouped into six major categories:

- general operation
- molecular beam source and skimmer
- hexapole rotational state filtering
- component triggering and synchronization
- ion beam source
- beam and reaction product detection

One of the crucial requirements for the proposed studies is the synchronization of all molecular beam machine components and electronics, which was achieved by the implementation of a relatively new fibre-optic multi-pulse generator. The connectivity of the major instrumental components is outlined with respect to the triggering and synchronization scheme that is given in figure 2.4. The major modifications to each will be briefly outlined.

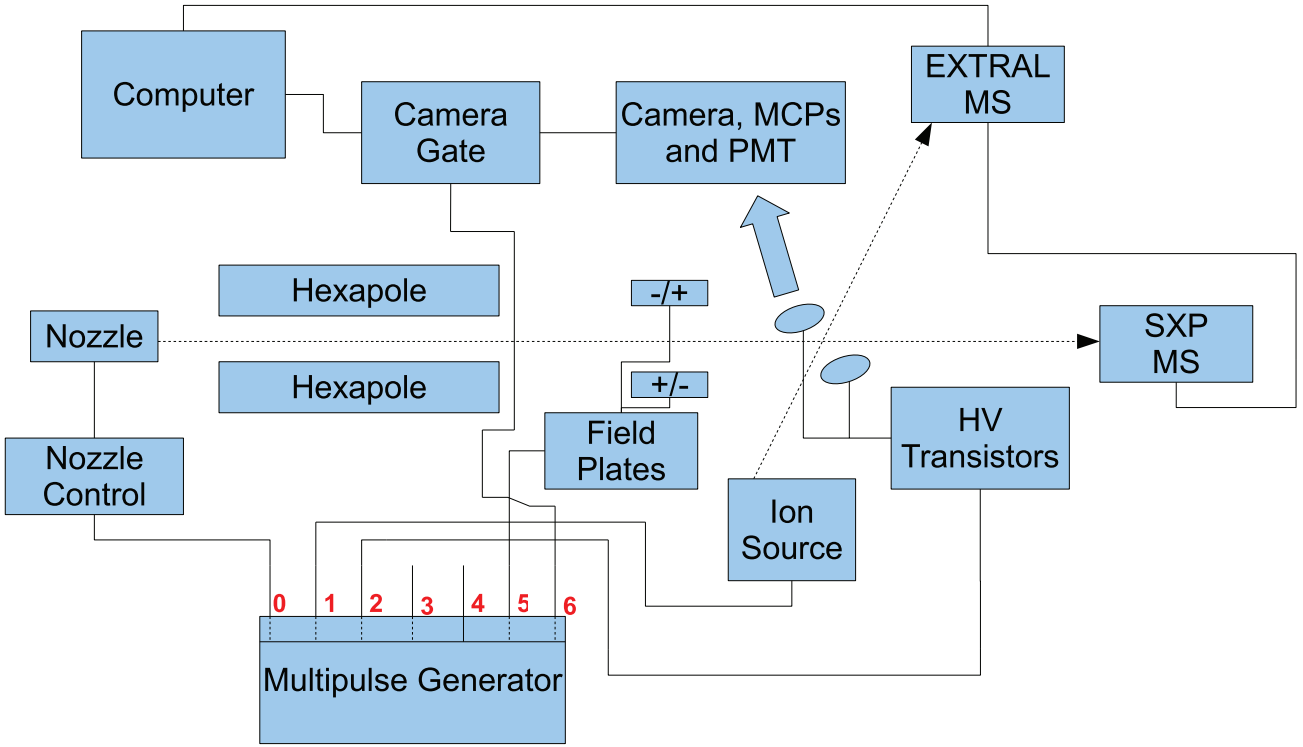

Figure 2.4.: Schematic outline of the major components in the modified molecular beam machine configuration, connectivity indicates the implemented fibre-optic triggering system synchronizing for pulsed operation. MS = mass spectrometer.

2.3. Molecular beam alignment

Following the disassembly of several of the molecular beam chambers, it was discovered that several sections of the molecular beam alignment rods had been removed, and those present in the instrument had been milled down (!) by 0.25 mm as part of Dr. Clements modifications. This modification resulted in the misalignment of the molecular beam source, hexapole rods and quadrupole mass spectrometer detector. Alignment is crucial for several reasons: very narrow beams with large separation from respective sources need to cross; the molecular beam has to pass through one or several skimmers to select the transversely cold core; termination of beams must occur into the narrow mass spectrometer sampling aperture in order to monitor beam signals for characterization; and the beam traversing the hexapole rod assembly must be centralized in order to be symmetrical, where a non-C_3 longitudinal symmetrical electric field does not provide correct rotational state focusing. The original alignment rods were constructed from centerless-ground $\frac{3}{4}$" stainless steel that was used specifically for its high-tolerance straightness properties. These rods extend from the nozzle chamber to the entrance of the scattering chamber, and provide a common location railing for all internal components along the molecular beam line.

As a solution to the misalignment problem, a standard diameter alignment rod section was installed on a mounting plate with a newly designed skimmer bracket on the nozzle-buffer chamber interface, and the milled section was installed half way down the instruments molecular beam line, requiring new joiners. The thinner alignment rod section then needed to locate only one of the perspex mounting brackets of the hexapole rod assembly, and the rods were then aligned by insertion of a 0.25 mm copper shim under the mount.

The fine alignment adjustments of the source, skimmer, hexapole rods and quadrupole mass spectrometer was achieved using a red diode laser that was situated directly in front of the beam source on the alignment rods. Unfortunately, the previous laser alignment assembly consisted of a 5 mW red laser operated from a 9 V battery located in an aluminium carriage mount. This assembly possessed two short falls. Firstly, the mount did not perfectly sit on the alignment rods since the rod separation was slightly different to the mount guides, which was shown to be very significant when the laser beam was projected down the beam line of $\approx$ 2 m. The molecular beam of $\approx$ 2.5 mm diameter must cross an ion-beam of also $\approx$ 2.5 mm diameter at $\approx$ 1.8 m separation from the source. Secondly, the laser was pressed in to a drilled cavity that was shown for long projections to be not quite centralized and in addition, the grub screw allowing alteration of the laser diode angle could not be hand adjusted since it was enclosed in the cavity. This laser alignment assembly was considered inadequate and prompted manufacture of a new laser mount in conjunction with the Department of Chemistry Mechanical Workshop, which is shown in figure 2.5. Six accessible grub screws fix the laser into a slightly larger cavity than the laser casing diameter, and systematic adjustment allowed calibration on a laboratory target. Coarse calibration was performed with a lathe by rotation with a paper target, and fine calibration was achieved by locating the assembly on alignment rods that mimicked those in the machine, which were in turn placed on a polished flat granite slab and the laser beam was projected at a target also located on the rods that was systematically moved to further separation from the laser. Finally, sliding the assembly along the alignment

rods showed no change in projection occurred, indicating alignment of laser with respect to the alignment rods. The new alignment system then allowed molecular beam line components to be iteratively adjusted, with the laser beam finally showing perfect termination in the entrance aperture of the quadrupole mass spectrometer.

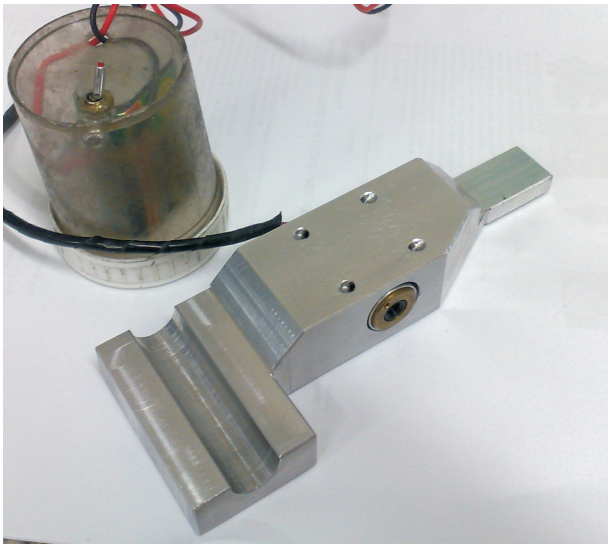

Figure 2.5.: Molecular beam line laser alignment assembly that allows alignment calibration of molecular beam gas pulses and internal components. This apparatus may sit anywhere along the unmilled sections of the alignment rods.

In order to align the ion beam, a vertical high-precision vernier with a flat-weighted bottom was placed on the floor of the scattering chamber, and adjusted to touch the center of the alignment laser beam. The ion source aperture and the quadrupole mass spectrometer were ensured to match this height.

2.4. Quadrupole mass spectrometers

The molecular beam machine houses two quadrupole mass spectrometers that terminate each of the beam lines and allow characterization of beam pulses by measurement of arrival time distributions, and also potentially characterization of any reaction product that remains in the beam line. For example, when reacting a heavy halogenated species such as CF_3Br with H_3^+ it could be anticipated from a direct proton transfer type migration that formation of a CF_3BrH^+ species would involve only very slight momentum change, and therefore could reside in the beam line. The first modifications involved the removal of both quadrupoles and reimplementation in a switched configuration. The Extranuclear Laboratories (EXTRAL) 4-270-9 quadrupole mass spectrometer that was originally characterizing the molecular beam line was switched for detection of the crossed ion-beam source since this mass spectrometer had better performance characteristics that would be ideally required for trace detection of ion-signal from the newly implemented ion source (outlined later). The factory electron impact ionization source was removed, and a new stainless steel top-hat lens element and mount were constructed to

provide an earthed (field-free) region for any incident ion-beam before experiencing the quadrupole field. That is, since H_3^+ is very reactive and the ion-beam is very weak and easily attenuated by background species, the quadrupole detector is required to be as close as possible to the crossing region. However, the crossing region must not be electronically perturbed by the high fields associated with the quadrupole internal operation. The physical dimensions of the Extranuclear Laboratories quadrupole required a new chamber extension of total length 75 mm with standard 8" Conflat flanges to be constructed in-house by the Department of Chemistry Mechanical Workshop. This extension provided a 10 mm separation between the parallel field alignment plates (outlined later) which encloses the beam crossing region, and the quadrupole top-hat. An external photograph of the quadrupole on the extension mount is given in figure 2.6.

Figure 2.6.: Photograph of quadrupole mounting extension for crossed ion-beam beam detection and characterization.

The Extranuclear Laboratories factory electron impact source was modified with a new stainless steel mounting bracket allowing this source to be installed on the SXP300 quadrupole mass spectrometer, which was then installed for detection and characterization of the molecular beam line. The electron impact source was connected to a workshop built six-channel 0-200 V power supply unit, with the filament potential floating with respect to the current ($\approx$ 3.3 A) provided by a Dick Smith Q1760 DC 5 A power supply. Each quadrupole mass spectrometer signal output is initially amplified with a Stanford Research Systems SR570 low-noise current amplifier that in turn connected to a four-channel Fluke PM3394B 200 MHz Combiscope oscilloscope with a RS-232 serial port allowing computer connection and 1024 channel resolution screen captures. Later in this research a four-channel colour Tektronic TDS 3054B oscilloscope was also employed, allowing higher resolution and 10,000 channel screen captures with transfer to computer by floppy disk. Unfortunately, it was discovered that determination of the very weak ion-signals using the high gain (nA / V) setting on these SR670 amplifiers resulted in considerable *RC* time-constant integration (smoothing and tail elongation) of time of flight distributions.

These high amplifications were required when the ion source was operated at low ion-energies. As a solution, a Stanford Research Systems PA-100 fast current pre-amplifier with a fixed 500× gain that was powered by a reconstructed 12 V lead-acid battery so as to reduce AC frequency pickup, in conjunction with a SRS560 low-noise voltage amplifier operating at a significantly lower gain, facilitated measurement of correct beam profiles.

2.5. Instrumental earth

The earth (ground) arrangement for the molecular beam machine is outlined in figure 2.7. In previous years earth floating problems had been encountered when using sensitive electronics to measure small signals that were earthed with respect to the Department's earth. As a solution, an independent ground spike was installed exclusively for the molecular beam machine laboratory. This ground spike directly connects to a 530×75×7 mm brass plate located on the molecular beam machine instrumentation rack, and all important electrical instrumentation was connected to multi-way mains adapters that where earthed to this plate. The original earth implementation by Vallance [7] had an arrangement that approximately conformed to an idealized star topology. However, due to changes made to the instrument since that time and a change in the wring at the main circuit box for the room (see below) new problems had arisen.

Briefly, earth or ground loops arise in a conductor such as a coaxial cable that necessarily has a very small resistance, when two points that are supposed to be at the same potential vary with respect to each other. Therefore, in an earth loop, there exists more than one reference earth with a small potential difference between the two which results in noise and interference. When such a loop exists in conjunction with AC equipment, a mains (50 Hz) potential difference hum can occur. Such potentials may arise when earth cables are located physically close to high current cables, the earth cable "feels" the AC field generated by the mains cable, and the small resistance in the cables results in an induced current thus yielding a potential drop relative to the earth at another point. Higher frequencies may be obtained from harmonics of the 50 Hz AC. During the course of this research, it was noticed that the diffusion pump on/off switching which is automated so that the oil in the pumps does not boil, yielded a significant 50 Hz AC hum on the signal lines from both mass spectrometers. The source of this problem took a long time to identify, and testing revealed this signal to originate from the superposition of the noise from each of the diffusion pumps when in operation. Initially all cables near the high-current molecular beam were isolated, however no improvement resulted and it was unrealistic that a static heating element would be leaking AC to the molecular beam infrastructure. It was then discovered that New Zealand building law requires that the neutral and earth (departmental) lines are tied together at the main corridor switchboard. Circuit diagrams showed that within the molecular beam control unit, the neutral was also tied to the departmental earth which created the large earth loop shown in figure 2.7. Since the large diffusion pumps operate with currents of > 50 A, there operation induced a potential difference between department and independent earth of up to 100 mV peak-to-peak. When measuring molecular beam time-of-flight signals, the DC amplitudes are typically on the order of 2 mV to 20 mV under the normal amplification regime, that is,

much smaller than the 50 Hz noise! Of course the period of molecular beam measurements relative to the period of the 50 Hz hum are orders of magnitude different, however this problem still needed to be addressed. As a solution, the internal connection between neutral and earth was disconnected (X in figure 2.7) and instantly eliminated the problem. It should also be noted that the diffusion pumps do not switch from phase to earth, rather phase to neutral, that may be floating above earth - the molecular beam laboratory was probably also picking up other noise from the department!

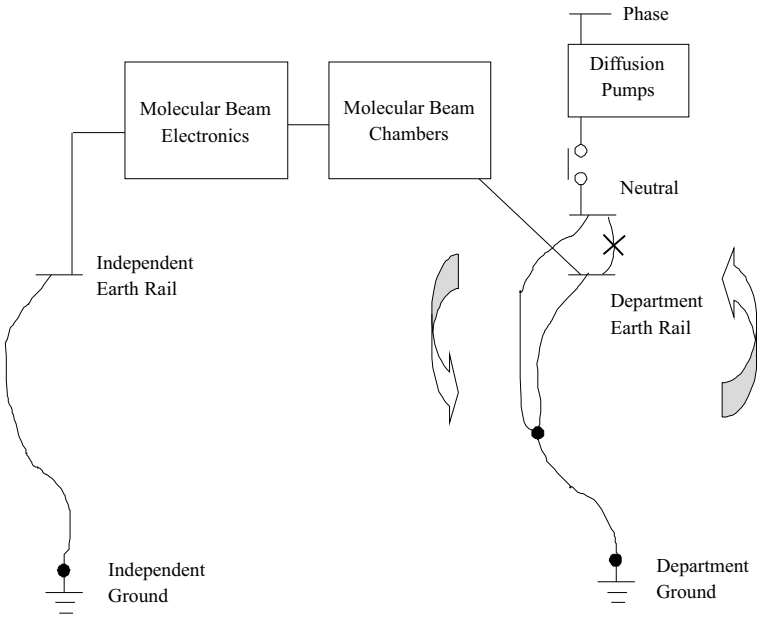

Figure 2.7.: Earth (ground) arrangement for the molecular beam laboratory. Originally two separate earth's existed: the laboratory independent earth; and the departmental earth. The X represents the internal connection of neutral and earth forming an earth loop, that resulted in 50 Hz AC hum when diffusion pumps were operating.

Another caveat should also be identified in the original implementation. Firstly, the departmental earth is *necessarily* connected to the independent earth, and perhaps not realised in original implementation of the star topology system. The mechanical pumps (and diffusion pumps) have earthed casings that are physically connected by conducting material to the respective molecular beam chambers. The molecular beam chambers have copper gaskets, which results in an entirely electrically continuous loop to the independent earth through all feed-through connections. This caveat could, in major part, be overcome by disconnection of the dual three phase earth powering the entire room, and connection to the independent earth which would completely remove the departmental earth from the system. After correcting for the diffusion pump pickup, further hum problems were not observed, and such measures were not required.

Several other possible solutions exist to minimize earth loop problems, such as using shielded coaxial cables that are only earthed at the source. Isolation transformers and opto-isolators also provide a means to eliminate mains hum. The star topology grounding system appeared to be an attempt at the former; however the coaxial

cables from rack instrumentation to respective molecular beam feed-throughs have both ends connected to earth. The machine is then earthed to the brass plate. All rack instrumentation is operated through an isolating transformer and vacuum protection unit, with most instrumentation using further opto-isolators. Several of the trace signal (mass spectrometer) cables have been replaced with disconnection of their coaxial earth loops at the instrumentation, which resulted in a very slight reduction in operating background.

2.6. Coolant manifold system

On commencement of this research, the coolant manifold system for the molecular beam machine consisted of two 150 mm OD PVC reservoirs of $\approx$ 60 L total volume, with diffusion pumps and turbomolecular pumps connected in parallel. The flow reservoir was connected to mains cold water, and the return to vent in the laboratory drain, providing a nominal mains water temperature of approximately 15°C. This implementation suffered from corrosion/thinning of the copper piping, which would eventually require very labour intensive replacement of all the ageing diffusion pump copper cooling pipe. Pre-existing designs had been developed for a closed loop coolant system incorporating a M25-20LL EcoFlex heat exchanger which had in previous times to this research been trialled with ethylene glycol coolant, and found to fall-over several times a week and vent the expensive charge into the drain. With aid of the University of Canterbury Facilities Management and Departmental Mechanical Workshop, the modified scheme outlined in figure 2.8 was installed. This coolant system consists of two isolated counter-current water loops. The first loop contains coolant from the recently implemented Departmental chilled water supply, which is piped throughout the building for such coolant systems, and exhibits nominal mains temperature of a few degrees above zero. The second loop encompasses the molecular beam machine components, where water is circulated through 50 mm outer-diameter PVC pipe by a Lowara 0.67 kW impeller type water pump. The pump flow line first passes water through the heat exchanger, into a ballast tank which then connects into the flow reservoir. The 6 L ballast tank minimizes flow bumps/pulses that could otherwise cause stress on weak points. The flow reservoir is then connected in parallel with Dunlop 10 mm Pressureflex hose to the diffusion and turbomolecular pumps. The buffer turbomolecular pump is located at the highest point of the system and an attached ballcock air release valve vents any air that may build up in the system during operation. All vacuum pump return lines connect to the return reservoir, which in turn connects to the return side of the water pump. The overall capacity of the reservoirs is estimated to not exceed 60 L (under pressure), which must cool all six diffusion pumps and the three turbomolecular pumps. Three solenoid type valves connected to the coolant system control box stop water flow through the heat exchanger from both loops when the pump is not operating. Vent valves on the return reservoir allows the system to be emptied, and the mains pressure connection on the flow reservoir allows recharging when the internal pressure becomes low, which may otherwise result in system shutdown. A water pressure gauge allows determination of line pressure, and a LED panel on the main instrument rack provides notice of operation.

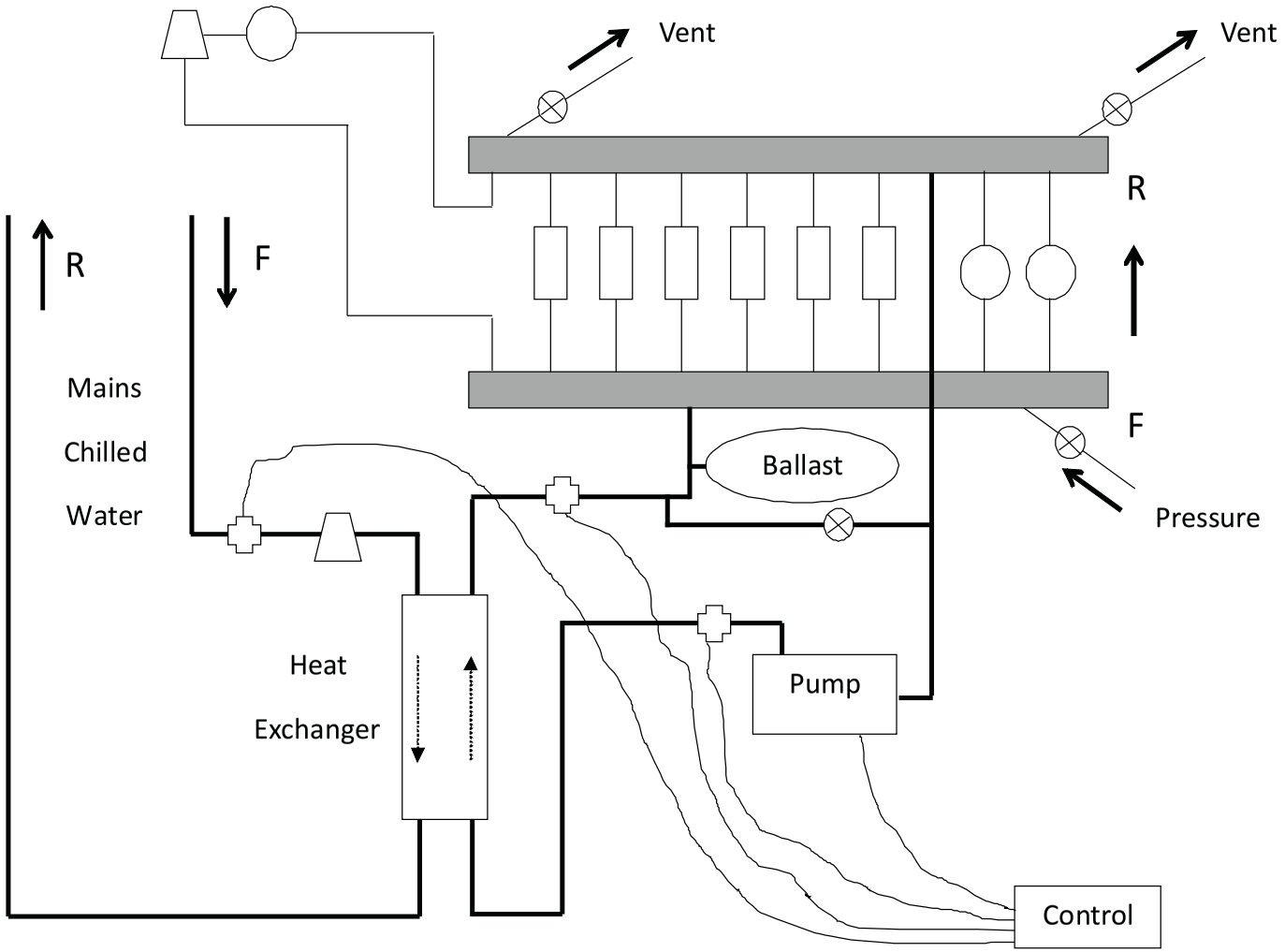

Figure 2.8.: New closed loop molecular beam laboratory coolant manifold system. F = Flow, R = Return, circles = turbomolecular pumps, rectangles = diffusion pumps, trapezoids = ballcock air vent valves, solid crosses = solenoid shut-off valves.

This new coolant system has two distinct advantages over the original mains water coolant system. Firstly, a temperature decrease of $\approx 10°C$ is obtained under normal operation, which is beneficial to diffusion pump cooling and thus attainable vacuum by a very small extent ($\approx 5\%$ improvement). Secondly, when coolant is charged in the closed loop, addition of a commercially secretive complexation agent provides some protection against copper pipe thinning. The new closed loop system has unfortunately caused several moments of despair, requiring extensive removal of pipe work to establish that air-locks may form between the pump and heat exchanger at a high point, which eventually requires the coolant system to be emptied and recharged in a six-month cycle.

2.7. Cross-beam gas inlet system

The cross-beam gas inlet system at the start of this research was poorly designed and did not allow fine control of inlet gas pressure or the gas sample to be easily changed. This situation was not ideal for implementation of a pressure-controlled H_3^+ ion-source, therefore the gas inlet system was redesigned and constructed according to the schematic given in figure 2.9.

The gas inlet system is evacuated by an Edwards EDM12 two stage mechanical pump that connects through a custom $1\frac{1}{8}$" OD brass tube of 145 mm length to a Saunders-Edwards Speedivalve gate valve. A second 270 mm extension terminates at a T intersection, that divides the vacuum line forming a loop configuration. The vertical junction connects to a stainless steel bellows of $\frac{7}{10}$" OD and 190 mm length that absorbs mechanical pump vibration. This bellows then connects through $\frac{1}{2}$" OD stainless steel pipe to a MKS 221D differential Baratron head providing the vacuum/low pressure reference side. This Baratron spans the 0-1500 Torr range, allowing reservoir pressure determination. The second T junction branch connects a Varian type 0531 thermocouple gauge head, the gas cylinder line, and two isolating Nupro style vacuum valves with $\frac{1}{4}$" OD copper piping. In turn, this branch connects to the high pressure side of the differential Baratron, and also tees to a Granville-Phillips Corporation series 203 leak valve that allows fine control of ion source gas pressure. A standard Swagelock needle valve was unable to provide sufficiently fine pressure control. This line then branches through a Nupro valve to a MKS 690A absolute Baratron, providing a 0.1 Torr full-scale range for measurement of the cross-beam source pressure. The main line connects to the scattering vacuum chamber through a $2\frac{1}{2}$" stainless steel high-vacuum vacuum feed-through. The internal side of the feed-through connects to the ion source using a Cajon $\frac{3}{8}$" high-vacuum bellows section, which has excess length to allow for ion source translator movement. Unfortunately, the MKS 690A absolute Baratron died during this research, requiring shipping overseas for repair which took several months.

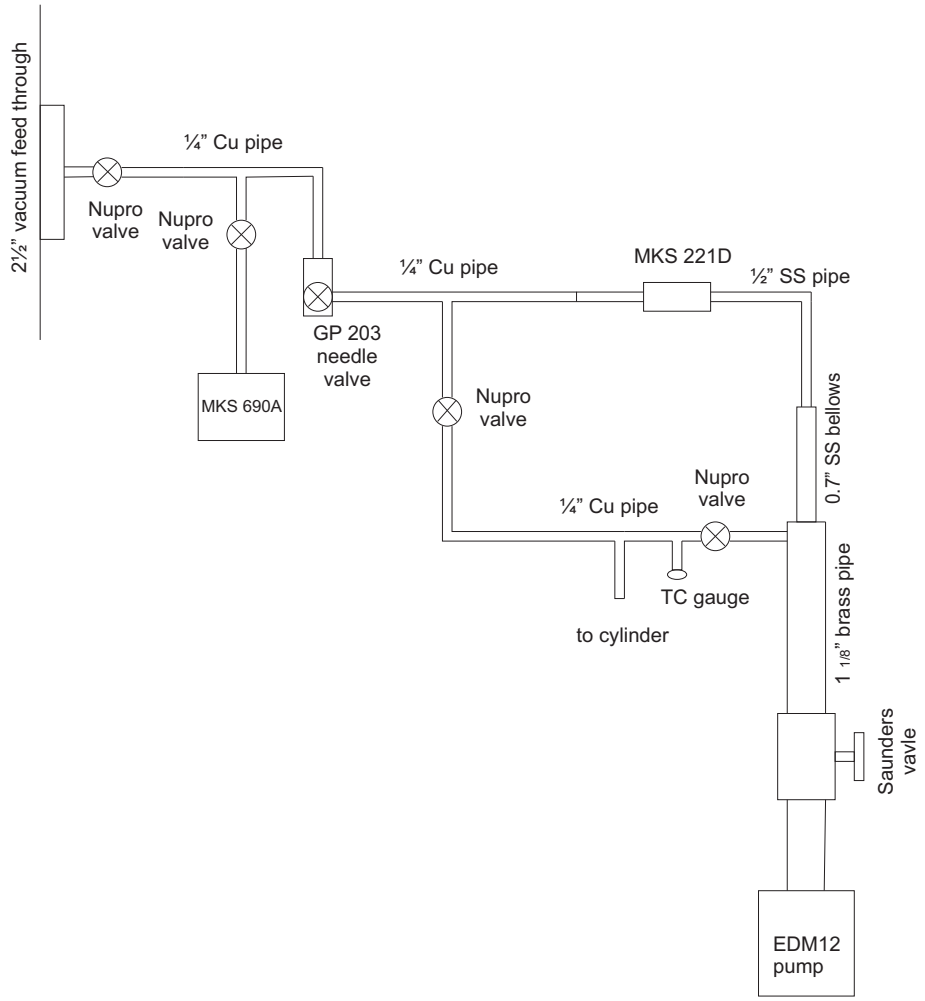

Figure 2.9.: The new cross-beam gas inlet system, allowing fine-tuned pressure control that is required for the H_3^+ high-pressure ion source.

2.8. Molecular beam nozzle (source)

A molecular beam consists of a thin beam of molecules in a high vacuum chamber. There are two common types of molecular beams, effusive and supersonic. These are differentiated by the mean free path, λ, in the source reservoir relative to the diameter of the exit orifice, d, where the ratio is known as the Knudsen number, K, and is given in equation 2.3.

$$K = \frac{\lambda}{d} \tag{2.3}$$

When $K > 1$, the source is effusive in nature with a low beam flux and a Maxwell-Boltzmann temperature profile similar to that in the source reservoir resulting in thermal equilibration in the beam. Such sources can provide limited control of internal quantum states, e.g. vibrational by varying the temperature of the source. The advantage of such sources is that the effusive beams can be described by the kinetic theory of gases, however in practice, narrow velocity distributions are difficult to obtain and traditionally required series of rotating cogs

in the beam line with different wedge cuts allowing systematic selection of a narrow beam velocity. In addition, several skimmers over a long distance can be required to obtain suitable collimation.

In contrast, when $K < 1$, beams are supersonic and have a highly directional velocity vector and very narrow temperature distribution. In supersonic beams the source gas experiences many collisions as leaving through the orifice, resulting in a jet-cooling effect where any internal energy (or temperature) of the beam is converted into directional translational motion in the direction of expansion, yielding an internally cold and essentially non-interacting beam. These conditions are employed for the proposed experiments in this work. There are three temperatures (velocity components) characterizing a supersonic molecular beam: the supersonic expansion temperature T_a; the parallel temperature, T_p, which is the internal beam temperature profile in the direction of beam propagation; and the radial temperature, T_r, which is the temperature orthogonal to the direction of propagation yielding beam dispersion. A typical molecular beam profile is given in figure 2.10. The zone of silence is a non-interacting region, while the barrel shock wave is a turbulent region, and the jet boundary prevents background gas from perturbing the zone of silence. The skimmer selects the core portion of the beam, where T_r is small, which is transmitted to the hexapole assembly in these experiments. Also shown in figure 2.10 are the typical velocity distribution profiles in the source, in the zone of silence before the skimmer, and the typical narrow profile after the skimmer. A full description of supersonic molecular beam characteristics and properties can be found elsewhere [9, 10].

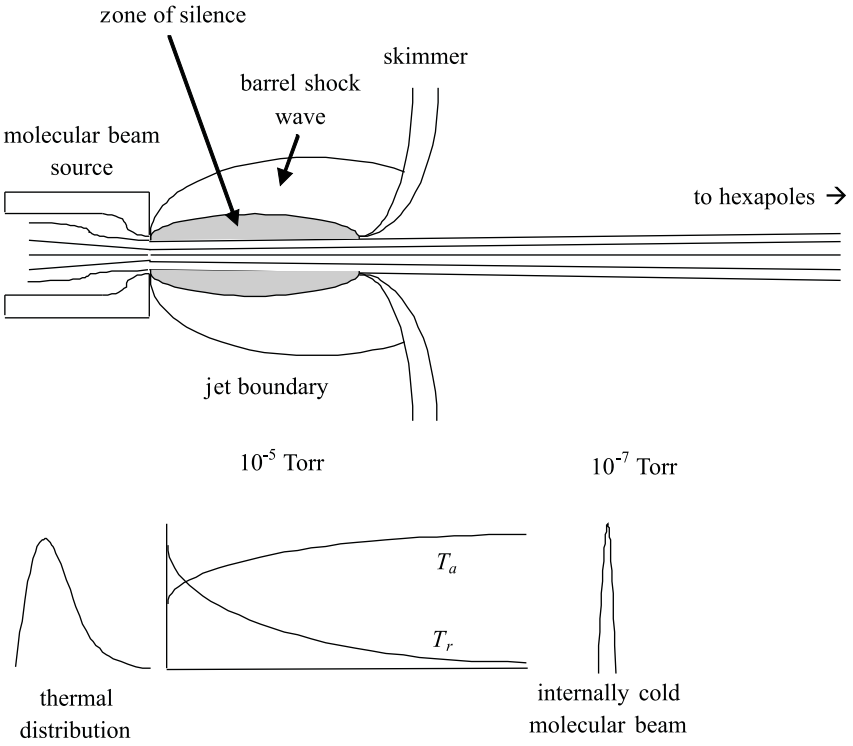

Figure 2.10.: Schematic representation of a supersonic molecular beam source. The lower diagram shows the thermal velocity distribution in the source, the middle figure shows the different beam temperatures as the beam passes through the orifice

Unfortunately there is no formal (from first principles) analytical expression to accurately describing supersonic molecular beams, however it has been well empirically observed that a Maxwell-Boltzmann type distribution provides a good fit, and is given in equation 2.4, allowing determination of the beam characteristics such as T_p.

$$f(v)dv = Av^2 e^{\frac{-m(v-u)^2}{2k_B T_p}} dv \tag{2.4}$$

where A is a normalization factor, v is an instantaneous velocity magnitude, u is the flow velocity (proportional to T_a), m is the average beam mass, and k_B is Boltzmann's constant. A neat molecular beam contains just the molecular reactant of interest and gives a known velocity and beam profile under given source reservoir conditions. A seeded molecular beam contains the species of interest in a carrier gas and the average mass of reagent and carrier allows velocity and energy characteristics of the beam to be modified. Arrival time distributions are the pulsed molecular beam profiles reaching the quadrupole and in principle approximately conform to equation 2.4 as long as the pulse width is small compared to the half line width at half maximum height of the final molecular beam pulse (from parallel temperature of the molecular beam). Four such arrival time distributions measured in this work are presented in figure 2.11, with neat and seeded beams showing the effect of carrier gas on flight time. The condition for supersonic expansion to occur is outlined in equation 2.5, with respect to reservoir source pressure, P_s, and beam pressure, P_b.

$$\frac{P_s}{P_b} = \left(\frac{\gamma+1}{2}\right)^{\left(\frac{\gamma}{\gamma-1}\right)} \tag{2.5}$$

where $\gamma = \frac{C_p}{C_v}$, is the ratio of thermodynamic constant pressure and volume heat capacities for the molecular beam species. When $\frac{P_s}{P_b}$, which is hard to experimentally measure, is greater than unity then shock wave formation occurs and supersonic expansion occurs since the so-called Mach number, M, or ratio of the velocity of the beam compared to the local speed of sound (c.f. information transfer) is also greater than unity. A final supersonic beam velocity depends not only on the mass of the molecular beam species, but also the ratio of heat capacities since jet cooling of internal energy occurs from a thermodynamic source reservoir of known conditions through a small orifice of known volume to a non-thermodynamic beam in near-vacuum surroundings.

The molecular beam source used in this research consists of a piezoelectric Physik Instrumente P-286.20 nozzle and control electronics, with nozzle and carriage shown in the photograph in figure 2.12. Internally, the nozzle operates by applying a high-voltage pulse to a piezoelectric crystal that causes a physical distortion, and allows high pressure gas to flow between the crystal and a small vacuum O-ring exiting through a 70 μm aperture. The pulse width is controlled by the multi-pulse generator, and typically operated at a pulsed width of several hundred microseconds where excellent linear agreement of molecular beam pulse width was established with driver pulse width. The use of short pulse widths minimizes background pressure. The source is mounted on a movable carriage that runs along the alignment rods with ball bearing rollers, and is in turn attached to

a Huntington Laboratories VF-156 linear translator that allows calibrated separation of nozzle from skimmer between ≈ 5 mm to ≈ 25mm. Several sleeve extensions were manufactured in order to connect the carriage and translator for suitable separations to the skimmer. The source reservoir is connected to a gas manifold system that contains six cylinders with isolating valves that allows seeded beam mixtures to be prepared, and the source reservoir pressure is determined by a MKS 122 5000 Torr Baratron. Originally this line was pumped with an Edwards Speedivac ES-100 mechanical pump that was replaced with an Edwards EDM20 pump owing to failure of the former. In several instances after using CH_3Cl molecular beams the rubber O-ring would swell and not permit the release of gas pulses under normal operating conditions. The use of higher voltages is unfavourable since it provides a considerably more stressful environment for the piezoelectric crystal, thus shortening its life. The usual method required removing the source each time and iteratively adjusting with bench testing until suitable pulses were produced. The design and construction of a small socket-type tool with a $\frac{1}{4}$" drive allowed the nozzle O-ring pressure to be adjusted in situ. The nozzle-skimmer separation was iteratively adjusted until molecular beam time-of-flight distribution signal was maximized, and reservoir pressure beam profile characteristics were determined in order to minimize the subsonic molecular beam components. The newly installed skimmer boasted an internal angle of less than half of that previously implemented in order to reduce scattering from the skimmer surface, and the current implementation appears to provide very high quality molecular beams.

In this instrument, typical flight times from the piezoelectric source to the SXP300 quadrupole detector at ≈ 2.0 m separation are several milliseconds. The non-instantaneous nozzle opening and closing time results in a non-square type molecular beam pulse and therefore does not yield ideal distributions to determine beam parameters from, and typically fittings have to make assumptions or take ratios to eliminate machine dependent parameters. Measured beam profile parameters for species of interest in this work correspond very closely to those previously established [1]. From fits of arrival time distributions, beam temperatures, expectation rotational state populations and expectation precession cone angles for a modelled homogeneous spatial alignment field can all be obtained. The distance to the crossing region is ≈ $\frac{7}{8}$ that of the source-quadrupole separation, therefore measurement of the arrival time distributions allows temporal tuning of beam maximum flux in the crossing region for crossed-beam experiments.

2.9. Hexapole rods

The two pre-existing hexapole rod assemblies were installed into the buffer, hexapole 1 and hexapole 2 chambers, and are shown in the photograph in figure 2.13. Each hexapole rod is made from $\frac{1}{4}$" centerless-ground stainless steel, of total length l=530 mm, with a ≈ 3 mm separation between the two sets of rods. As will be outlined, these hexapole rod assemblies, upon application of high voltage electric fields, allow focusing of particular MK rotational quantum states that in turn permits spatial orientation of the molecular beam. These hexapole rod are held with respect to each other by 20 mm thick perspex mounts which sit on the internal alignment rods.

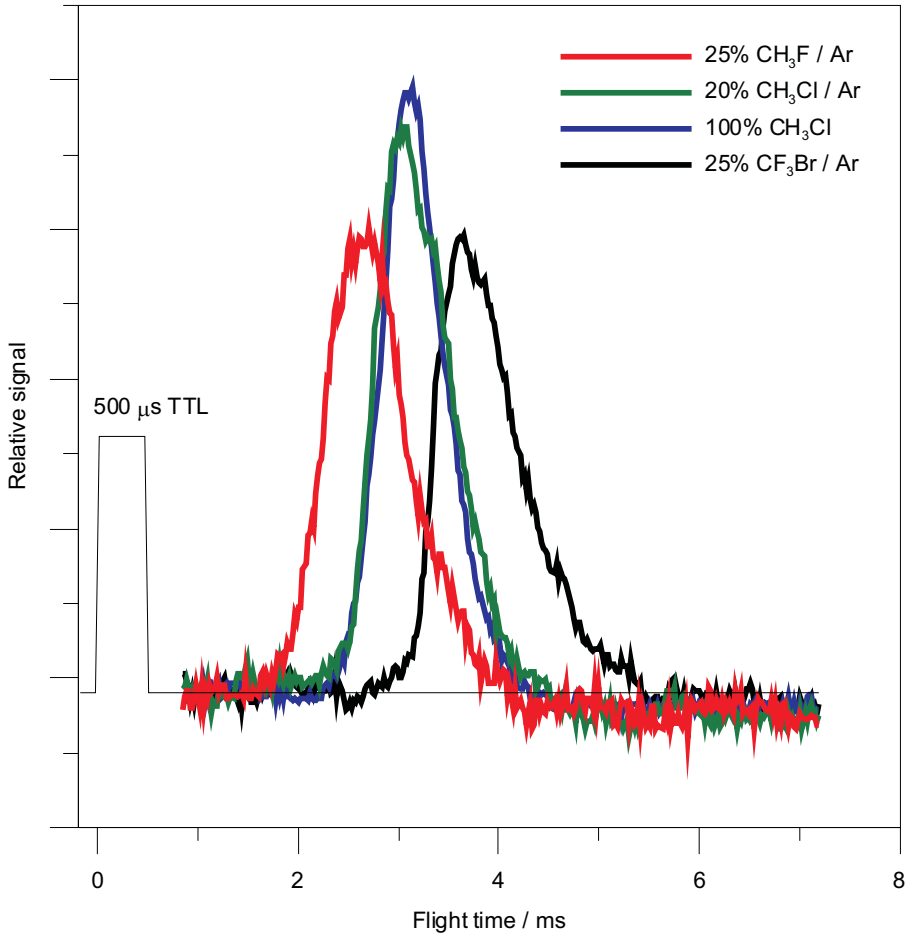

Figure 2.11.: Several arrival time distributions for experimentally relevant pulsed molecular beams in this work. Although the pulse TTL pulse width is approximately equal to the half line width at half maximum height in these distributions, experiments varying the pulse width in this vicinity revealed under the reservoir conditions ($>$ 2000 Torr) that the distribution dispersion was minimal.

Each rod is connected to a high voltage feed-through with braided copper mesh that was enclosed in glass sleeves in order to prevent the possibility of contact with the machine casing or other rods of opposite polarity. Both sets of rods are energised by dual Glassman EH.0 $\pm$ 30 kV power supplies, and a schematic of the resultant hexapole field is given in figure 2.14. Formally, an ideal hexapole rod has hyperbolic shaped elements to best match the shape of the hexapole field lines. Since the radius of each rod is several times smaller than the radius of the hexapole assembly, that the elements are circular has no significant effect on the induced hexapole field. Originally this was achieved by consideration of an ideal ratio between each rods circular diameter and hexapole assembly diameter, that gives closest approximation to an idealized hyperbolic field.

The molecular beam machine has two tandem hexapole rod assemblies with a total length in order to achieve focusing with realistic voltages, V_f, according to equation 2.6. This equation can be obtained by considering the trajectories from the Stark field discussion following.

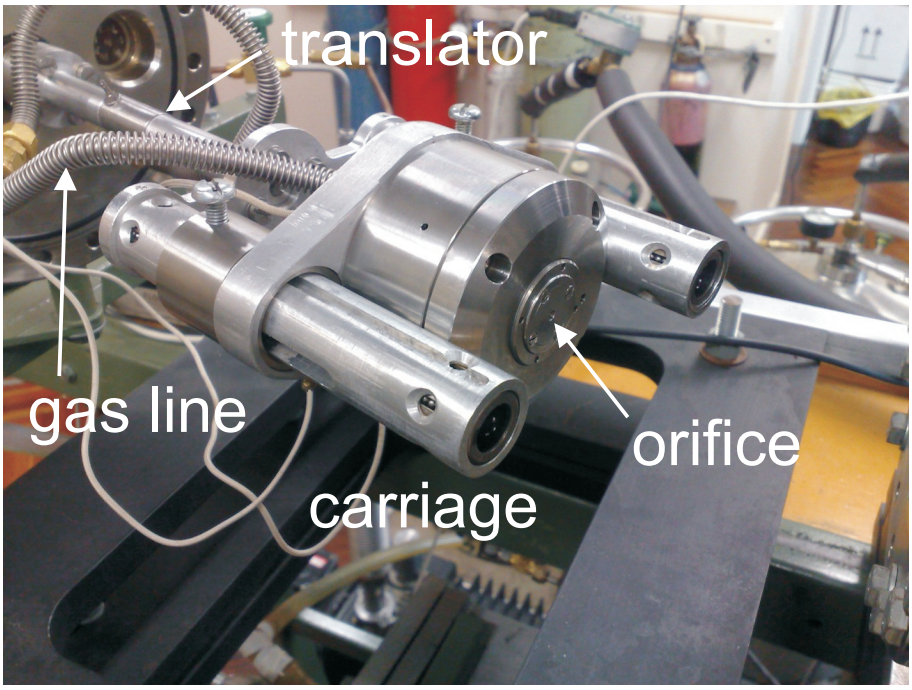

Figure 2.12.: Photograph of the piezoelectric supersonic molecular beam source mounted on the carriage assembly, which is in turn has one-dimension translation controlled with a Huntington Laboratories VF-156 linear translator.

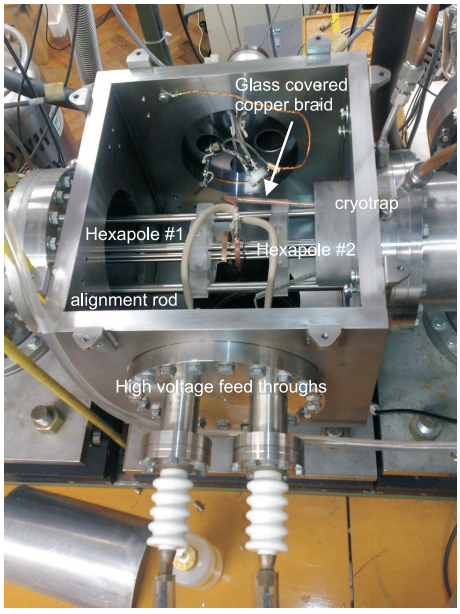

Figure 2.13.: Photograph of the installed hexapoles with connection to the high voltage vacuum feed-throughs, with the photograph looking into the so-called hexapole 1 chamber.

$$V_f = \frac{\pi^2 r_\circ^3}{6l^2}\frac{mv^2}{\mu} \tag{2.6}$$

where v is the molecular velocity for a particle of mass m, μ is the molecular dipole moment, and $r_\circ$ is the

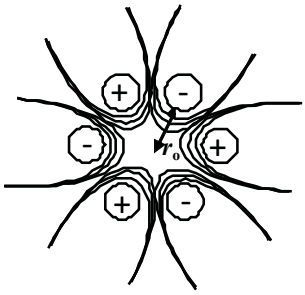

Figure 2.14.: Schematic cross-section of the hexapole electric field showing the ± polarity changing on adjacent rods. Regions where equipotential lines are close are high field gradient regions.

radius of the hexapole rod assembly cross-section. Clearly, V_f decreases as $r_\circ$ decreases and l increases. For the halocarbons of interest, in order to focus $MK < 0$ rotational states near the crossing beam region, voltages of $\approx \pm$ 8 kV are required. This voltage corresponds to a focal length in near co-incidence with the molecular beam crossing region. If only one of the hexapole assemblies was implemented rather than two in tandem, the one would require significantly higher voltages that would pose problems with dangerous discharges. In operation, voltages do not exceed ± 10 kV. Further, it is practically easier to install two half length hexapole rod assemblies than one full length assembly. Some elements of rotational state filtering and focusing will now be briefly outlined.

In this work, all molecular beam reagent species, CH_3X, exhibit C_{3V} point group symmetry and are classified as prolate symmetric top rotors in rotational spectroscopy nomenclature. Molecules conforming to average point group symmetries that preclude an improper axis of rotation necessarily have permanent dipole moments, μ, as a results of asymmetric charge distributions. Application of an external electric field acts as a perturbation to the electrical properties of a molecule and coupling of the dipole moment can occur relative to the applied field, and as a result, a lowering of quantum state degeneracy by the Stark effect occurs. For hexapoles, the symmetry of the electric field perturbation, ε, plays an important role. A given prolate rotor has rotational angular momentum quantized in terms of J, the total angular momentum, with $2J+1$ components with respect to the dipolar axis, denoted $K = \pm\ 0,\ \pm 1,\ \ldots\ ,\ \pm J$. Quantum number M is the projection of J on the perturbation (field) axis, also giving $M = \pm\ 0, \pm 1, \ldots\ , \pm J$ components. The first-order Stark effect interaction energy is given by equation 2.7, where θ is the angle between the molecular dipole and the axis of rotation as shown in figure 2.15.

$$W = -\mu\varepsilon\frac{MK}{J(J+1)} = -\mu\varepsilon\langle\cos\theta\rangle \tag{2.7}$$

where magnitude $\mu = |\mu|$, and $\langle\cos\theta\rangle = \cos\theta$ is the expectation value of the precession cone angle of J.

For the perturbation symmetry of a hexapole field, when $MK > 0$ (lower Stark state), the perturbing field decreases the energy of the system, as compared to when $MK < 0$ (upper Stark state), the perturbing field increases the energy of the system, and when $MK = 0$, symmetry forbids a change in energy of the system.

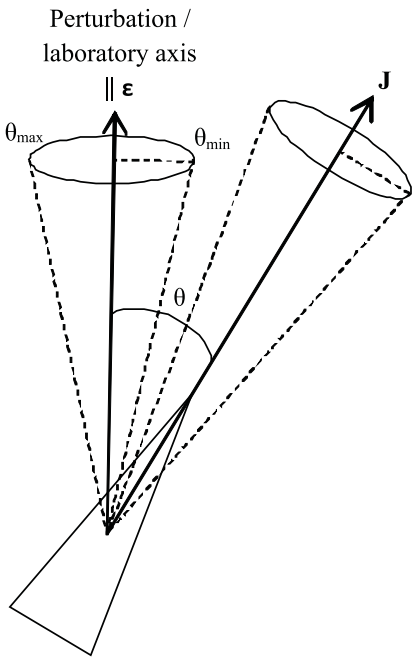

Figure 2.15.: Schematic representation of a prolate (C_{3V}) rotor, and quantization with respect to dipolar orbital angular momentum rotation axis, **J**, and electric field perturbation axis ε.

As a response to the Stark effect, sub-level energies change, where $MK > 0$ states are attracted to high field regions (defocused) in exponential trajectories away from the centre of the hexapole assembly and either escape the hexapole enclosure or hit the rods, and $MK < 0$ are attracted to low field regions (focused) in sinusoidal trajectories where the symmetry gives the lowest field region at the centre of the hexapole, while $MK = 0$ states have unaffected trajectories. The first two situations are schematically outlined in figure 2.16, and provide the basis for dipole orientation since the $MK < 0$ have a net non-zero intrinsic field projection on the dipole moment. The $MK = 0$ provides a constant low level background to focused beams and is less intense than the $MK < 0$ focused beam as a result of radial dispersion. The molecular beams of interest in these studies have been previously shown to typically have a Boltzmann distribution of MK states allowing characterization of expectation precession cone θ [7, 8, 11].

The transmitted $MK < 0$ states can be oriented by the DC homogeneous parallel field plates that enclose the beam crossing region, and are shown in the photograph given in figure 2.22 (later). This orientation procedure is well outlined elsewhere [12], although the crucial requirement is that a state selected molecule must pass between the end of the hexapole and into the orienting field before a state change occurs, that is, adiabatically. Under single-collision conditions, spatial isolation prevents a state change and background pressures are typically required to be $< 1 \times 10^{-6}$ Torr, since collisional relaxation of quantum selected rotation states is very rapid with extraordinary large cross-sections of 200 Å^2 to 670 Å^2 for CH_3Cl [13]. For this reason, very high resolution and fine control over pulsing fields is required. The separation between the end of the hexapole and field plates is ≈ 1.5 cm, with a grounded 1.5 cm diameter adjustable camera lens aperture between the end of the hexapole and the orienting field plates to ensure the hexapole field does not perturb the homogeneous orienting field

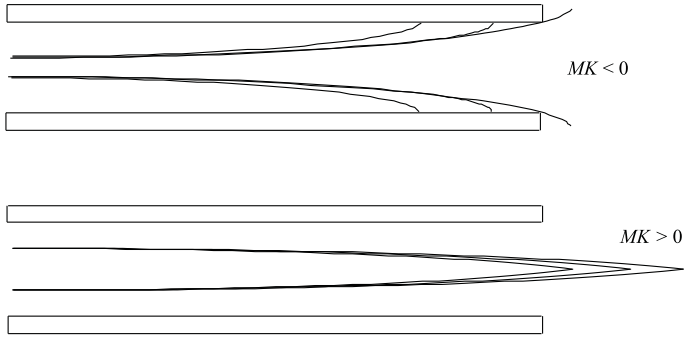

Figure 2.16.: Schematic representation of the response of prolate rotor molecules in a hexapole field. $MK > 0$ states are defocused and $MK < 0$ are focused. The exact JK states show slightly different trajectory tracks and focusing due to slightly differing extents/magnitudes of interaction with the Stark field.

and crossing region. The results of hexapole focusing with neat CH_3Cl molecular beam are shown in figure 2.17. Operation at a typical hexapole voltage of ± 8 kV indicates a 4.5-fold increase in intensity upon focusing, which would indicate excellent configuration for spatial orientation experiments. The other halocarbon species CH_3F, CH_3Br and CF_3Br all show similar hexapole enhancement, as do seeded beams of 5%, 10% and 20% CH_3Cl. The structure shown in the right plot in figure 2.17 presumably arises due to different JK state focusing conditions as the high voltage is changed.

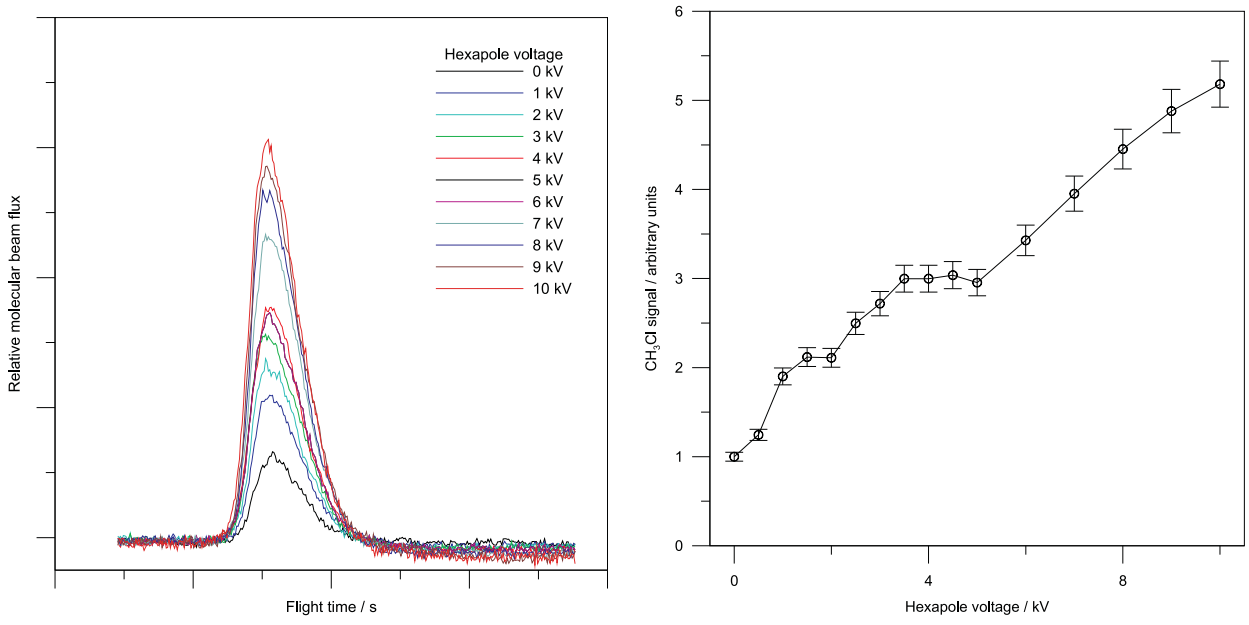

Figure 2.17.: Left: Hexapole focusing of a neat CH_3Cl molecular beam with a scattering chamber pressure of $\approx 1 \times 10^{-7}$ Torr, and molecular beam reservoir source pressure of ≈ 2100 Torr. Right: Neat CH_3Cl flux as a function of hexapole from fitted integration of time-of-flight profiles.

2.10. Triggering and synchronization

Another fundamental requirement of the ion-molecule studies proposed in this research is a pulsed operation mode of the molecular beam machine. Firstly, the molecular beam cannot be operated in continuous mode since this will result in higher background pressures ($>10^{-5}$ Torr) that would be dangerous with the high voltage hexapole rods, since arcing between rods may occur, as well as destroying spatial orientation. Secondly, the ion imaging assembly (outlined later) requires the ion source to be pulsed in order to resolve reaction ion product and not saturate the detector from a continuous beam. Thirdly, the ion imaging assembly is required to take images at various short intervals after the two beams cross (i.e. with several hundred nanosecond resolution), and therefore requires well defined ion-beam pulses and synchronization.

The multi-pulse generator (MPG) used in these studies was originally designed and assembled in-house by the Department of Chemistry, Electronics Workshop, with the first application in the study of electron impact ionization of oxygen by Harland *et al.* [14]. This unit contains a total of seven independent pulse cards providing seven optical channels, although in operation six output channels are available since one is employed as the system clock. Each card is located in a 24-bit slot on a custom motherboard, and an RS-232 interface allows computer control, although control by a keypad and LCD on the front panel is often quicker. Each output channel is connected through a fibre-optic cable of 10 m length to an opto-coupler that converts the optical pulse into a 5 V TTL electrical pulse with a Schmidt trigger boasting a 3 ns rise time. The use of optical pulses is advantageous for best possible signal, by minimizing electrical pickup and pulse distortion which would otherwise be present in copper wiring. Each fibre-optic cable has a length of 10 m, and all cables are the same length in order to keep timing in synchronization by any differences in other cabling lengths negligible relative to the fibre optic cable. Cables over 200 m could be employed for the same results. The fibre cables contain 62.5/125 μm core and clading, with pulses generated at a wavelength of 820 nm (near infra-red). Unfortunately, it was found that several of the fibre-optic cables were dead and had to be replaced. Each opto-coupler is powered by a 5 V DC power supply, and generates a standard 5 V TTL pulse that connects into other pulse generating units through a standard coaxial connector. The MPG system clock operates at 50 MHz, providing pulse resolution of 20 ns, and pulse widths up to ≈ 0.3 s length. In application in this work, an overall molecular beam machine frequency of between 20-30 Hz is employed that is limited by the decay time of the HTS high-voltage extractor/repeller transistor switches (outlined later).

As schematically shown in figure 2.4, a typical experiment requires at least four different pulses. The pulsing sequence uses the MPG internal clock to initially trigger the molecular beam nozzle, with all other timing parameters referenced with respect to the nozzle pulse. The general pulsing scheme follows:

1. MPG triggers molecular beam nozzle yielding molecular beam gas pulse that passes through the energized DC hexapole rods

2. MPG triggers the parallel field alignment plates

3. MPG triggers the ion-source shutter to release a pulse of H_3^+ ions and almost simultaneously turns the parallel field alignment plates off

4. MPG triggers the extraction electrostatic plates, photomultiplier time-of-flight measurement, and camera gate for the ion imaging assembly following a variable delay after the ion-beam leaves the crossing region

This pulsing sequence appears relatively simple when outlined, however in practice other electronic limitations need to be considered. Each pulsing unit has a characteristic turn on and rise time that needed to be determined for typical experimental conditions. This pulsing configuration has the advantage that once the characteristic electronic delay times are known, only three or four MPG channel timings need to be changed for a change in molecular beam or ion-beam, that requires only entering the new delay times for each channel with a digital keypad.

2.11. Parallel field spatial orientation plates

Spatial orientation experiments require the orienting electrostatic elements to be controlled with high voltage pulses. Previous studies on spatial deorientation lifetimes of the halocarbons of interest in this work have shown lifetimes of 100 to 300 μs, and requiring homogeneous orienting field strengths of > 3 V cm^{-1} [15]. Two existing high voltage pulsing units existed that provided ground to +HV and ground to -HV pulses. Two additional units were constructed in-house in conjunction with the Department of Chemistry Electronics Workshop, allowing +HV to ground and -HV to ground pulses. These pulse units take 5 V TTL triggers and output a variable pulse of up to $\pm$ 1000 V, with the general configuration for the different pulse sequences given in figure 2.18. The latter two types of pulses were anticipated for application in ion source pulsing, however as will be outlined later, performance was not ideal. These units are driven by a LM311 voltage comparator with the factory specification of 200 ns resolution. In an experiment, these parallel field plates provide dipole based alignment of the $MK < 0$ states from the hexapole and are required to turn off very quickly so that the ion-beam pulse is not perturbed by these elements acting as electrostatic lenses. The plates have a separation of 30.5 mm, and are shown in the photograph in figure 2.22 (later). At the typical 100 V to 300 V operations, the fall-off time can be calculated from the pulse circuit feedback regulator RC combination at $t = RC = (47\Omega)(470\mu F) = 22.1\mu s$. By definition, the time constant is the time for the capacitor to change between $\frac{1}{e} \approx 62.5\%$ of asymptotic operating values. This time constant is an order of magnitude less than the typical deorientation lifetimes, and therefore these pulsing units should be sufficient to provide molecular beam spatial alignment. Typical H_3^+ flight times to the crossing region are 5 μs, therefore the ion-beam pulse will have to be delayed relative to the switching off of the parallel field plates by approximately two time constants.

Since the time constant is on the same order of magnitude as a typical operation 10 μs pulse, the unit will not be able to provide a steady-state current, resulting in a distorted peak, i.e. with an unfavourable tail. This distortion feature becomes minimized as HV pulse magnitude increases. Unfortunately when considering low

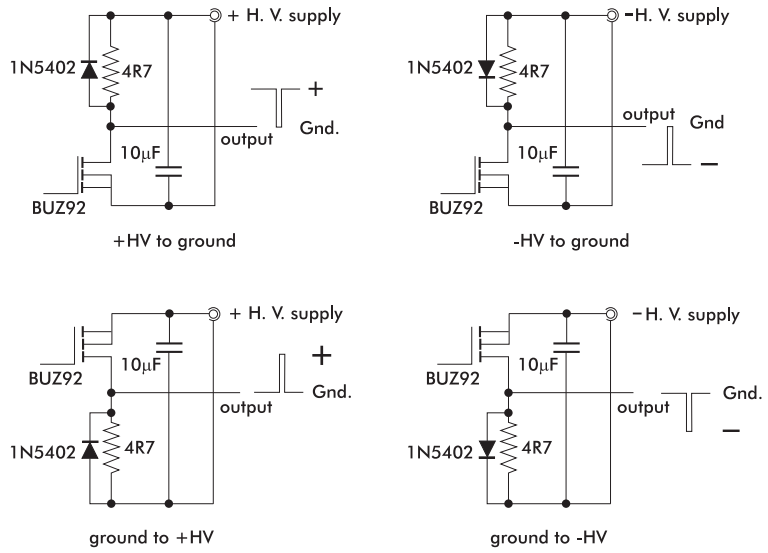

Figure 2.18.: Circuit diagrams for the four different configuration high voltage pulsing units, as recommended from the original National Semiconductor LM311 data sheets.

voltage pulses for the H_3^+ ion-source (outlined later) requiring $\approx$ 200 ns resolution, trials showed these units were unable to produce pulses of sufficient resolution or quality to be employed. The solution is discussed next.

2.12. H_3^+ ion source

In order to study reactions of oriented molecules with H_3^+, a suitable ion source was required, involving the modification and reconstruction of a pre-existing high pressure positive ion source. The pre-existing source was initially stripped down, cleaned and several ceramic insulators were replaced, and a new pulsed shutter lens was incorporated as the last element of the lens assembly. The final ion source is shown in figure 2.19. This source is not restricted to H_3^+, and small optimization of lens conditions yielded excellent Ar^+, N_2^+, He^+, CH_3X (X=Cl, Br) and in principle, any other positive ion species. Ions are generated by electron impact ionization where thermionic electrons emitted from a rhenium filament are constrained to a narrow electron beam by an electron shield, two parallel electron lenses of 2 mm separation and an electron trap. The electron beam traverses the ionization cell and results in electron impact ionization of the reagent gas that is present at $\approx 10^{-3}$ Torr. A negatively charged DC extractor plate that is orthogonal to the original electron beam extracts the ions from the collision cell, and the ions are then focused by a series of electrostatic lens elements. A final pulsed shutter lens (outlined later) modulates the otherwise continuous ion beam. The newly fabricated stainless steel shutter lens has a 0.3 mm thickness, and an aperture diameter of 1.3 mm matching the extractor aperture size. The two top-hat shaped lens are 7.70 mm in length, with an aperture diameter of 10 mm allowing increased flexibility in ion-beam focusing. Lens L1 and L4 (see figure 2.19) also have a 0.3 mm thickness, with all lens elements and ionization cell housing originally fabricated from high quality stainless steel. The electron beam filament (two in parallel) were fabricated from 0.002" rhenium wire, and are held in place with respect to the electron lens

elements by molybdenum posts of 1 mm diameter that are fixed into a ceramic support. The electron beam shield, lens elements, and trap are all separated from the ionization cell casing by 0.2 mm thick teflon insulator sheets. Four 10 BA thread posts that are fixed into the ionization cell and insulated with thin ceramic circular section, align all ion beam lens elements. The gas reservoir is ceramic and connects through a high vacuum bellows to a scatting chamber vacuum feed-through, which in turn connects to the new crossed-beam gas line. The shutter lens is located approximately 10 mm away from the first parallel field plate to achieve maximum ion-beam signal. The H_3^+ ion has a very low mass and it was experimentally observed that a beam is very easily attenuated by distance and background H_2O species.

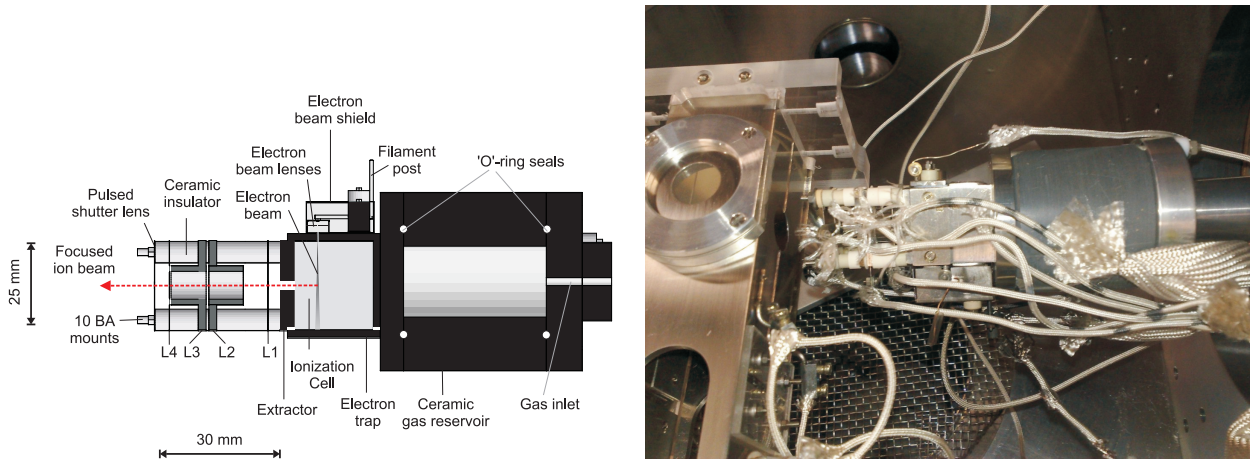

Figure 2.19.: Left: Schematic of the H_3^+ ion source that is approximately to scale with respect to the two given dimensions. Right: Photograph of the ion source in the scattering chamber.

All internal wiring utilized pure silver wire of 0.5 mm diameter that was coated with fine fibreglass sheathing, which in turn was initially baked in a high temperature oven to remove any silicon coating. All ion source elements are controlled with in-house 0-200 V power supplies, and the filament current is produced by a floating Topward 33010D DC power supply typically operating at $\approx$ 4.2 A, with the electron trap current measured with a Keithley 160B digital multimeter. The ion-current on the shutter lens is measured with a Keithley 486 picoammeter, and varies between 10 nA to 12 nA under normal operation. The electrostatic lens potentials were iteratively optimized for H_3^+ (and several other species) to achieve maximum signal and narrow energy spread and are given in table 2.1. These operating parameters had to also be carefully selected in order to minimize electron and ion leakage from the source that was detected as background with the ion imaging assembly.[2] Simulations using the Simion 6.0 electrostatics package support production of a focused ion beam using these lens potentials in the beam crossing region. The thermionic electron filament potential at -78 V referenced with respect to ground is close to the general electron impaction ionization maximum cross-section at $\approx$ 75 eV.

In application, the collision cell ion energy, IE, is referenced with respect to ground, and the extractor, L1,

[2]In hindsight, ideal pulsed operation should probably switch the extractor to a suitable potential when the ion beam pulse is not being generated, in order to minimize leakage of charged ion source species.

Table 2.1.: Optimized ion source element potentials

Ion source element	Applied potential[a] (V)
filament (electron energy)	-79.4
electron shield	-89.4
electron lens	+20.0
electron trap	+44.1
ionization cell reference ('ion energy' or IE)[b]	+41.0 in this configuration
extractor	+25.7
lens 1	-127.1
lens 2	+33.4
lens 3	-79.2
lens 4	earthed
shutter	≈ 30 V 'off', ≈ 0 V 'pulsed on'

[a]all values given with respect to ground reference
[b]ion energy applies to the ionization cell casing potential

L2, L3, and the electron energy all float with respect to IE. The electron shield, electron lens and electron trap all float with respect to the electron energy (filament). An ion beam energy change therefore requires only a change in the IE since all other elements are floating.

The H_3^+ source operates by high pressure H_2 gas at $\approx 10^{-3}$ Torr that is subject to electron impact ionization, and is summarised in the elementary reaction scheme:

$$H_2 + e^- \longrightarrow H^+ + H + 2e^- \text{ (ionization and dissociation)}$$
$$H_2 + e^- \longrightarrow H_2^+ + 2e^- \text{ (ionization)}$$
$$H^+ + H_2 \longrightarrow H_3^+ \text{ (ion-molecule reaction to form } H_3^+\text{)}$$

In accord with this reaction scheme, ionization and dissociation yields the H^+ precursor, and by changing the source H_2 pressure, the required ion-molecule reaction forming H_3^+ can be promoted and therefore the H_3^+ signal increased [16, 17]. Experimentally, this was undertaken for a series of ion-source pressures between 0.5×10^{-3} Torr and 3.0×10^{-3} Torr and found to change the normalized ratio of H_2^+:H_3^+ from unity to approximately 0.2 respectively as shown in figure 2.20. Previously reported kinetic flow tube experiments considering a large range of species revel that proton transfer rates for reactions involving H_3^+ are typically several orders of magnitude larger than those for H_2^+ [18], therefore not requiring *complete* removal of H_2^+ from the ion-beam in this work. These source operating conditions result in external scattering chamber background pressures that are measured by an ion-gauge located approximately 200 mm directly above the ion source to be below 10^{-6} Torr, indicating single collision conditions exist with ion source operation. Each measured H_2^+:H_3^+ pressure-dependent mass spectrum was fitted with two Gaussian-Lorentzian convolutions in order to determine relative areas, with all showing non-linear least squares fittings of $R^2 > 0.97$ indicating good fits with the mass spectral lines showing slightly overlapping tails. This procedure assumes that both the H_2^+ and H_3^+ species have equal detector sensitivities under the measurement parameters. Small H^+ signal was observed at the low end of the ion source pressure scale in figure 2.20 that rapidly disappeared as the H_2^+:H_3^+ ratio was decreased from unity.

The addition of a stainless steel barrier around the ion source that would direct the escaping source gas towards one of the pumps could potentially allow background pressures in the crossing beam region to be reduced when ion source is in operation. One caveat that should be acknowledged is that the current experiments are unable to ascertain the vibrational state populations of the generated H_3^+ ions. H_3^+ has several weakly bound excited electronic states that have been shown to rapidly quench after only a couple of de-excitation collisions [19]. If the ion source extractor was operated in pulsed operation, the average residence time of a given H_3^+ ion would be longer than if operated in continuous mode, and adjustment to the ion source could potentially assist in collisional de-excitation. A literature review of calculations and dynamics on the H_3^+ formation reactions could potentially provide information on relative vibrational state occupancies. Comparisons of our source ion ratios with the claimed ground vibrational state source of Yousif *et al.* [20] reveals our source should perform similarly. Vibrational relaxation is usually a collisionally inefficient process, where excited vibrational states can last typically 10^5 collisions. If source pressures are required to be increased in order to facilitate vibrational state relaxation, a shielding in the scattering chamber around the ion source that directs gas into a pump could allow higher source pressures without destroying single collision conditions in the crossing region. Before experiments are performed, the vibrational state occupancy of the source needs to be assessed.

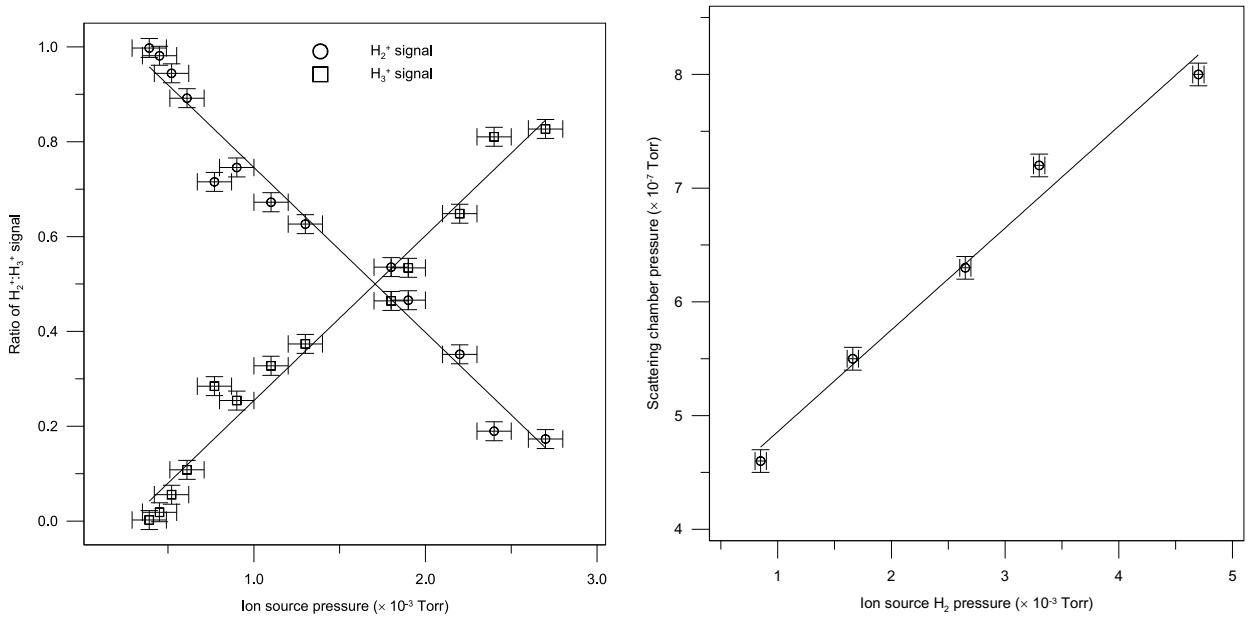

Figure 2.20.: Left: Ratio of H_2^+:H_3^+ ion-beam species as a function of ion source H_2 pressure. Right: Correlation between ion source pressure and background pressure in the present scattering chamber implementation.

A requirement for the study of the energy dependence of proton-transfer is that the ion-beam must have a well defined velocity with minimal energy spread. By applying a systematically increasing positive DC retarding potential to the shutter lens or the two DC parallel field plates (both give the same results), signal intensity decay curves were obtained for several species including H_3^+ and Ar^+. One such example is given in 2.21, where all ion-energies between $\approx$ 2 eV to $\approx$ 20 eV yield a H_3^+ half-maximum-height line width of $\approx$ 1 V. A linear

calibration determined that the beam kinetic IE is ≈ 18 V below that programmed as the IE in the table of electrostatic potentials. In principle, since the last shutter lens elements is earthed, the programmed IE should be equal to the final kinetic energy, however in application this is not always true. This is not problematic since it will be shown that the beams can be controlled with narrow energy spreads over the required range. These data would indicate that the H_3^+ source yields energetically well defined ion pulses suitable for low energy experiments, where typical proton affinities are 6-8 eV (6.71 eV for CH_3Cl [21]).

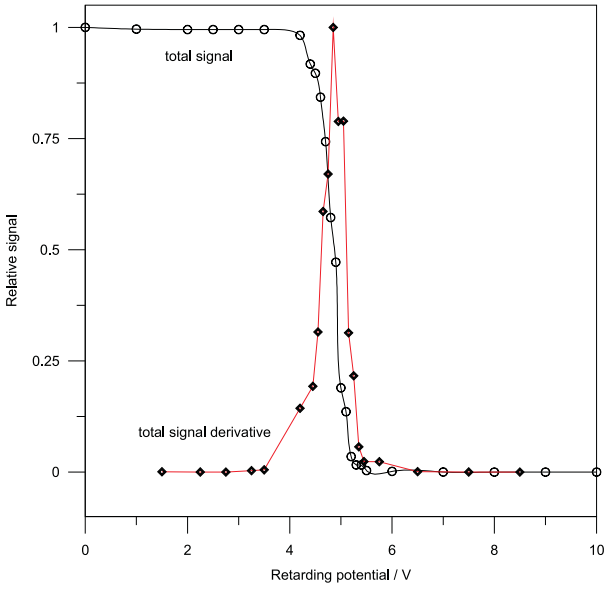

Figure 2.21.: The effect of applying a retarding potential to the H_3^+ ion beam of programmed ion energy. The total signal derivative yields the energy spread of the ion-beam pulse that all show ≈ 1 V spread over the 20 V ion energy range.

A photograph showing the final arrangement of the ion source, parallel field alignment plates, quadrupole mass spectrometer and ion imaging aperture is given in figure 2.22.

2.13. Low voltage pulsing units

Implementation of the above ion source required a well defined pulsing of a suitable lens element in order to obtain a pulsed ion-beam. The expected flight time of H_3^+ from source generation to detector is on the order of microseconds and summarised in figure 2.23 for four different energies in the ideal 0 V to 20 eV energy regime where reaction is expected to occur. Implementation of suitable pulsing units took considerably more time than originally anticipated. The anticipated studies require ion energies between ≈ 0 V to 20 V, and such low energy pulses are usually very difficult to obtain. The high voltage pulsing units used to control the field plates gave large ringing effects when used at low voltages, even with very short and impedance terminated cables, and also yielded very poorly shaped pulses with broad tails that would not go below ≈ 15 V. Neither pulsing of the electron beam lens, nor cathode (filament) elements resulted in usable pulses. In principle, simple operational

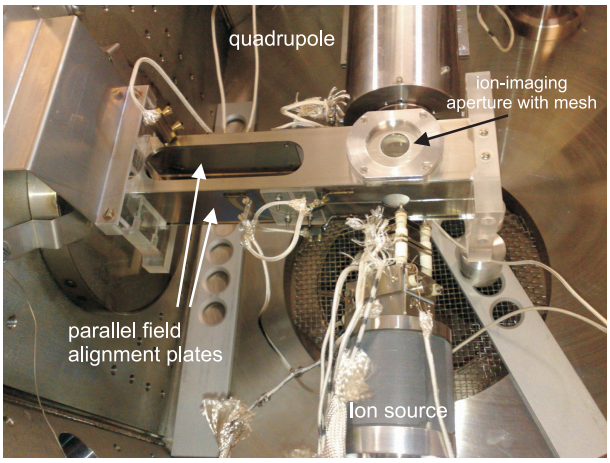

Figure 2.22.: Photograph looking inside the scattering chamber showing the ion source, parallel field alignment plates, ion beam quadrupole mass spectrometer and ion imaging aperture relative to each other.

amplifier circuits can provide low voltage pulses, and are well known to often show faster rise and fall times than factory specifications. A ± 15 V operational amplifier circuit was designed and built, as photographed in figure 2.24, using a TL072CP JFET low-noise operational amplifier. This provided better performance than the high voltage pulsing units, however was still unable to generate appropriate pulses due to rise time limitations, and was therefore abandoned.

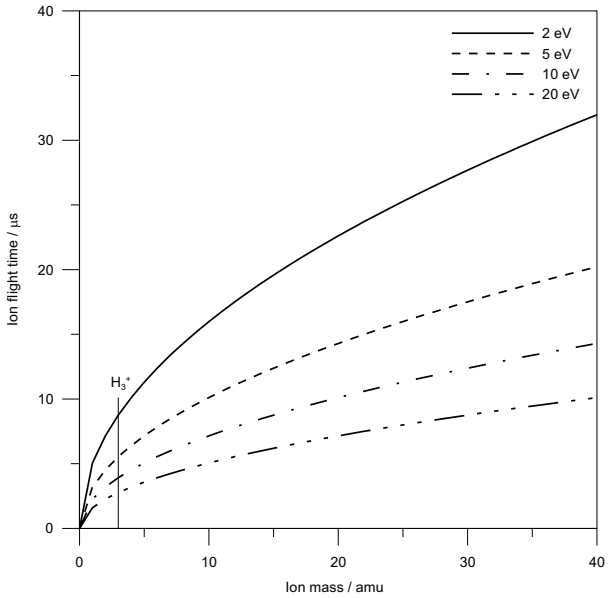

Figure 2.23.: Calculated ion source flight time from generation to detection over the distance of 85 mm, assuming the path in within the quadrupole rods is rapid compared to the crossing beam region, as a function of mass for four different energies. The flight time to the crossing region is approximately half any value determined from this figure.

Searching through old instrumentation resulted in discovery of an original millisecond resolution low voltage

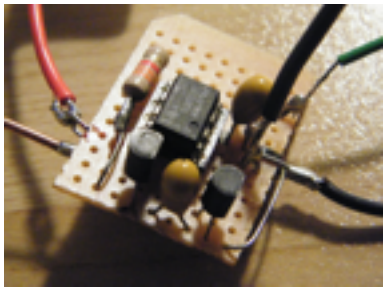

Figure 2.24.: Photograph of the attempt at a low voltage operational amplifier pulsing circuit for ion source shutter control. This was designed to connect directly to an electrical feed-through to minimize slight high frequency cable impedance ringing that cannot be completely removed by terminating resistors for low voltage pulses.

pulsing unit capable of 0 V to 100 V pulses. This unit was originally built in-house by Steven Graham from the Department of Chemistry Electronics Workshop and modified for implementation here. Briefly, it was designed to use TTL (5 V) logic, with six output channels, each with its own floating $\approx$ 6 V to 100 V power supply and optically isolated gated transistor pulsing circuit. Each pulsing channel contained a 74HC14A parallel OR gate integrated circuit with factory rise/fall time of typically $>$ 11 ns at 6 V or $>$ 12 ns at 4.5 V. The original unit had its own internal 5 V TTL drive that was coarsely adjustable from several microseconds to 10 ms. This unit was rewired so each IC is directly triggered by the 5 V TTL MPG pulses which allowed high-precision tuning of output pulse widths than for the original configuration. Several, apparently redundant, optical isolation integrated circuits were bypassed in the original circuits which gave slightly poorer output waveforms. The power transistor amplifier in each circuit is a general fast TIP32C (non-limiting) and provides 0.2 mA peak current, and is easily able to handle the experimental 10 pA ion current when switching low or high for positive and negative ions. All four pulsing schemes shown in figure 2.18 were possible, with the +V to ground configuration adopted for the ion shutter lens. Characterization shows this implementation to yield a rise time of $>$ 15 ns and $\approx$ 90 ns decay time, irrespective of output pulse amplitude or input trigger width. In the experimentally relevant trigger width range between 250 ns and 1 μs, a linear correlation exists between half-width-at-half-maximum-amplitude and programmed trigger width as shown in figure 2.25 along with the time of flight distributions for Ar^+ at three different programmable ion velocities. The same trends are obtained for H_3^+ with faster flight times, and in all instances the ion-beam pulse half-width-at-half-maximum-amplitude reproduced the ion shutter width closely, including pulses at $\approx$ 2 eV energy. Ion-beam pulses are detectable down to 500 ns pulse width with a linear trend in pulse width, with reasonable signal at 800 ns.

Each unit contains a 2.2 pF capacitor across the signal output to earth in order to remove oscillation, which results in a small pulse tail, which is however experimentally irrelevant over time scales considered. The potential on the ion shutter is controlled by a high-precision ten turn potentiometer and potential displayed on a Fluke 45 multimeter. These outlined characteristics are considered suitable for studying ion-beam reactions in pulsed operation.

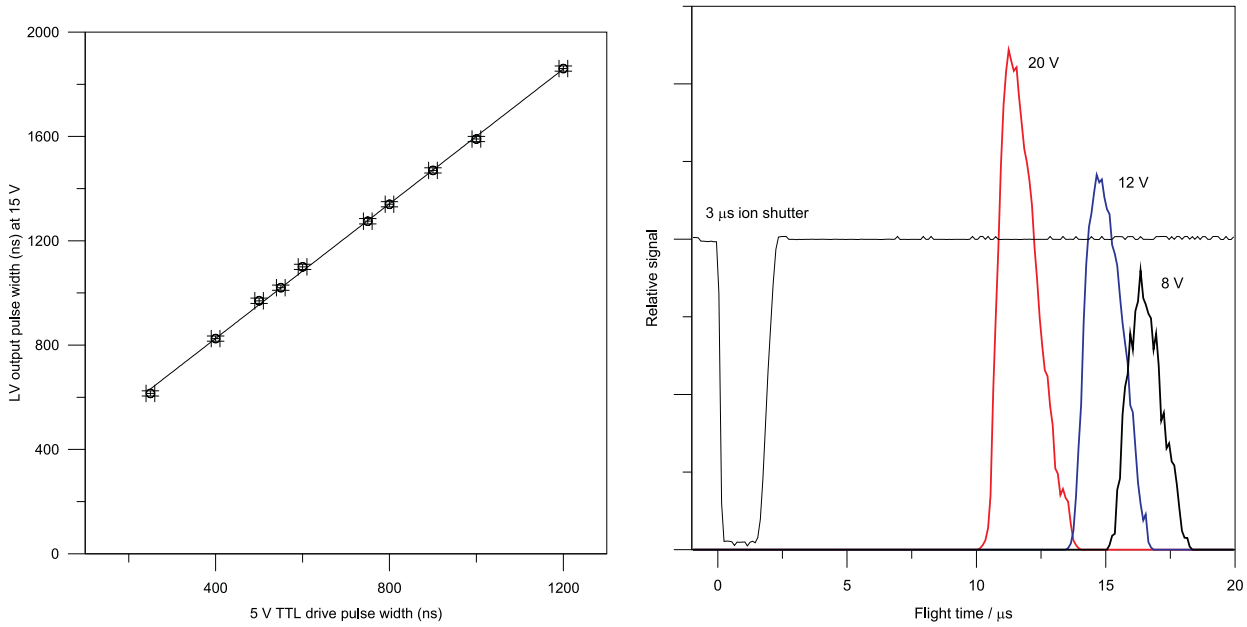

Figure 2.25.: Left: Linear correlation between the low voltage (LV) ion beam shutter pulses and 5 V TTL. Right: Application of the shutter pulsing to a beam of Ar^+ ions of well defined energies, showing excellent pulse responses. Flight time peaks appear well defined with half-height turn off times of $\approx$ 500 ns, and turn on times of $\approx$ 200 ns. Similar characterizations were produced for H_3^+ - not shown here since the rapid flight time superimposes peaks.

2.14. Ion imaging

Ion imaging usually involves a two step procedure, where after a reaction is initiated, e.g. by a laser pulse or occurs by crossed molecular beams, some form of ionizing pulse (e.g. laser) ionizes reaction product. This product is then extracted by electric field plate(s), known as the extractor and repeller here, through an aperture (12.25 mm in this work) that are mounted above and/or below the crossing region in a molecular beam experiment, as shown in figure 2.26. The ion product is extracted as a two-dimensional projected pancake, and after a known flight time strikes a position sensitive imaging detector. Since the pancake ion-cloud retains the spatial integrity of reaction product, a calibrated image allows determination of angular scattering and internal energy disposal by application of a Fourier-transform type domain transformation known as an Abel transformation in cylindrical coordinates. Note that the resolution of traditional ion imaging can be improved by addition of a third earthed field plate mounted above the extractor and with an identical aperture, in order to improve spatial resolution by providing a more uniform extraction field. Such a assembly is known as velocity-map ion imaging [22]. In the ion imaging assembly in this work, an ionizing probe is not required since the products are already ionized and any neutral product can be inferred from mass balances, or even potentially quadrupole mass spectrometry. The pancake ion beam hits a microchannel plate (MCP) that is coplanar with the extraction plates, and by an electron cascade through a second MCP the signal is amplified by many orders of magnitude before projection onto a phosphor screen. A fibre optic vacuum feed-through transmits the light into a light pipe of $\approx$ 120 mm length, where a camera observes the image with charged couple device (ccd) connected to a digital computer. In the final image, the intensity in a given location is proportional to

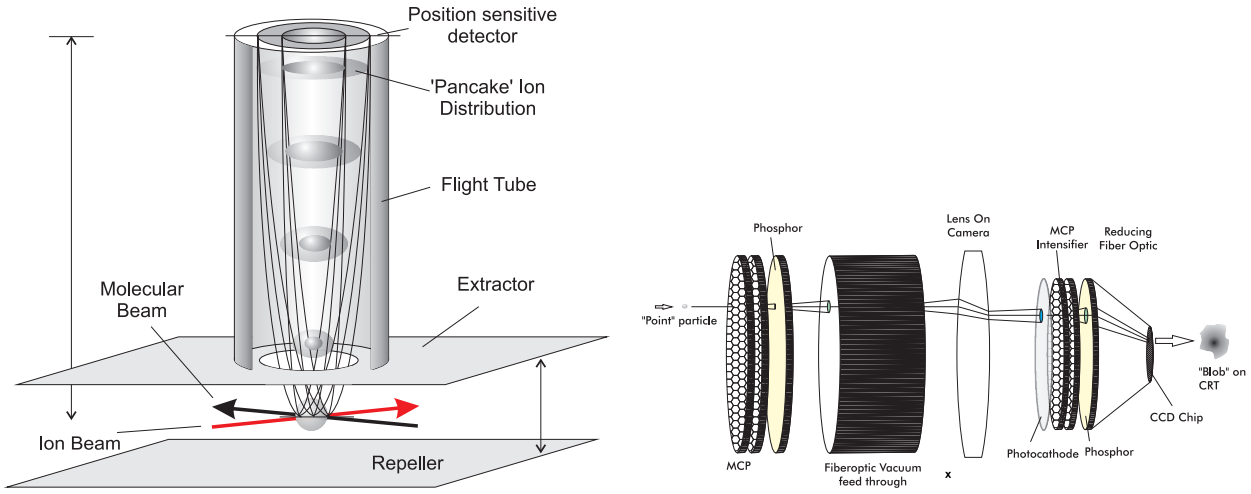

Figure 2.26.: Velocity map ion imaging operation. After reaction, electrostatic extractor and repeller plates vertically project ion product in a pancake like distribution (left-hand figure) to a dual microchannel plate (MCP), which acts as an image magnifier (right hand figure) by electron cascade. In this work, the first MCP has been configured to run at -1.8 kV, the second MCP is earthed, and the phosphor at +2.0 kV. The electron cascade is projected onto a phosphor screen (analogously to a cathode-ray television), where a focused Photonic Science analogue camera with a Cosmicar Pentax lens captures the image using a charge-couple device (ccd). This is then recorded on a digital computer. Synchronization with MPG pulses facilitates "photographs" of chemical reactions.

the ion-count. Individual ion-products can be separated based on their mass in the flight tube by recording photographic snapshots for different time intervals after pulse crossing. The use of the laboratory reference frame for orthogonal intersecting beams is difficult to interpret in images and by the use of Newtonian reference frame transformations, the centre of mass frame is constructed by considering relative velocity vectors in order to visualize and interpret images. Images can sometimes be fuzzy, which is in part due to large amplification by the MCPs, however software enabling centroid-extrapolation methods on the images taken by the assembly at the University of Canterbury have been written by a former Post Doctoral Fellow, Dr. Todd Clements, in order to improve resolution. The objective of this research was first to employ the pre-existing ion imaging apparatus to acquire rough images, and then modify the ion imaging assembly to a velocity map type configuration by addition of an additional electrostatic lens as at the base of the flight tube.

The ion imaging apparatus was pre-existing although characterization was required for the current systems under study. In an experiment, the extractor and repeller plates simultaneously pulse to high voltage to extract both ion-product and non-reacted ions into the flight tube, all species having the same extraction kinetic energy. The extractor and repeller ion extraction plates of separation 30.5 mm are switched by two Eurotek HTS-81 fast high voltage transistor switches, triggered from the MPG. Depending on the high voltage transistor collector phase, these can independently operate in either positive or negative mode. These units have factory specifications summarised in table 2.2.

Table 2.2.: Factory specifications for the Eurotek HTS-81 fast high voltage transistor switches used to control the extractor and repeller plates for the ion imaging instrumentation.

Parameter	**Specification**
Turn-on delay time	50 ns
Turn-on rise time	< 1 ns
Turn-on time	120 ns
Recovery time	300 ns
Operating voltage range	0-8000 V

Testing revealed that application of 1000 V applied to the transistor collector, gives a turn-on time of $<$ 20 ns for pulse widths from 400 ns to 40 μs. The minimum to maximum turn-on times were measured at 115-120 ns for pulse widths between 500 ns and 50 μs, indicating suitable performance for extraction in accord with the factory specifications. That the turn off decay reveals a slow RC type tail extending several hundred microseconds is not serious since the typical molecular beam frequency can be operated at a period that is several orders of magnitude longer. The flight tube originally contained a six-element einzel lens assembly that was removed, and all elements wired together to allow a constant DC potential between 0-200 V. Initial testing on the MCP operation revealed that there was no signal output. The ion imaging assembly was dismantled and unfortunately it was found that the MCP plates were cracked. It is assumed that this had occurred at some stage before this project started, most likely by inadequate storage over the period of years with exposure to atmospheric moisture. New MCP plates were ordered, taking five months to arrive, and replaced as shown in the photograph in figure 2.27. In addition it was found that the original flight tube assembly that contained a perspex housing was broken in two, requiring extensive repair.

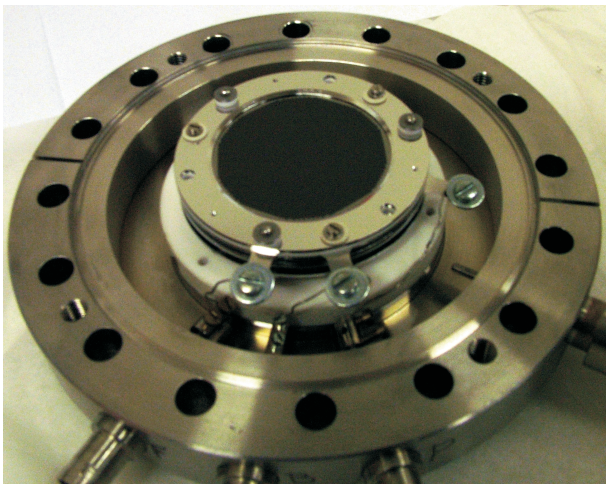

Figure 2.27.: Newly installed micro-channel plates, which constitute the major component of the ion imaging assembly.

ion imaging is designed to obtain short snapshots of reaction progress at a known time after beam crossing. A photograph has boundaries calibrated by a detection of a well characterized reaction with a large cross-section

and well established reaction energetics, such as $Ar^+ + CH_3Cl$ charge transfer. A glass slide mounted at 45° in the external light pipe transmits 2% of the image into a Hamamatsu model R5984 photomultiplier tube with a theoretical amplification factor of 1×10^7 yielding an ion time-of-flight spectrum. The original tube was non-operational and required replacement. Such a spectrum is shown in figure 2.28 for a mixture of different species using a 1 μs ion-beam pulse. Stepping the camera gate in 500 ns flight time intervals allowed images of individual ions to be resolved.

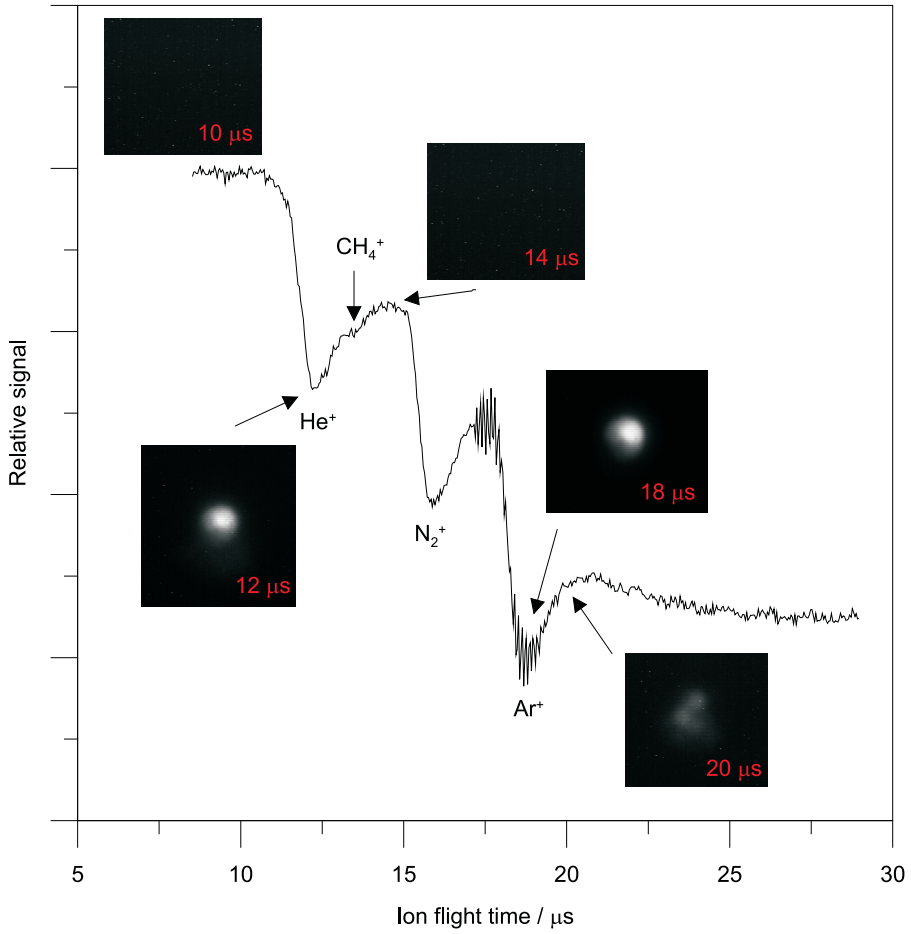

Figure 2.28.: ion imaging time of flight distribution for mixture of ion-beam species (signal is negative going). The broad underlying baseline has subsequently been eliminated with the use of very short and doubly shielded coaxial cables from the photomultiplier tube to the oscilloscope. Each ion-image was collected with a 500 ns gate width.

In accord with the simulations performed by Bart [1], an extractor-repeller ratio of 0.7 (extractor $\approx$ 1300 V and repeller $\approx$ 900 V) achieved best resolution, and allowed observation of the H_3^+ beam-track with the flight tube potential varied between 0 V and $\approx$ 100 V. Preliminary testing on ion source gas mixtures that contained several species of similar atomic masses with a 10,000 channel digital oscilloscope revealed the assembly should be able to discriminate ion-products differing by one atomic mass unit, as required for proton-transfer studies. By systematically adjusting the delay of the extractor and repeller with respect to firing of the ion beam pulse, a sharp cut-off of ion-signal was observed over the range of $\approx$ 200 ns, confirming generation of well defined ion-

beam pulses. This performance was in part attributed to the modification of the ion imaging extraction plate with the instalment of an ultra-fine 5 μm gold mesh over the ion imaging aperture fixed in place by compression with a Viton high-vacuum O-ring. This is shown in the photograph in figure 2.22 (earlier). A final schematic of the scattering chamber showing the orientation of the ion imaging apparatus to the molecular beam crossing region is given in figure 2.29.

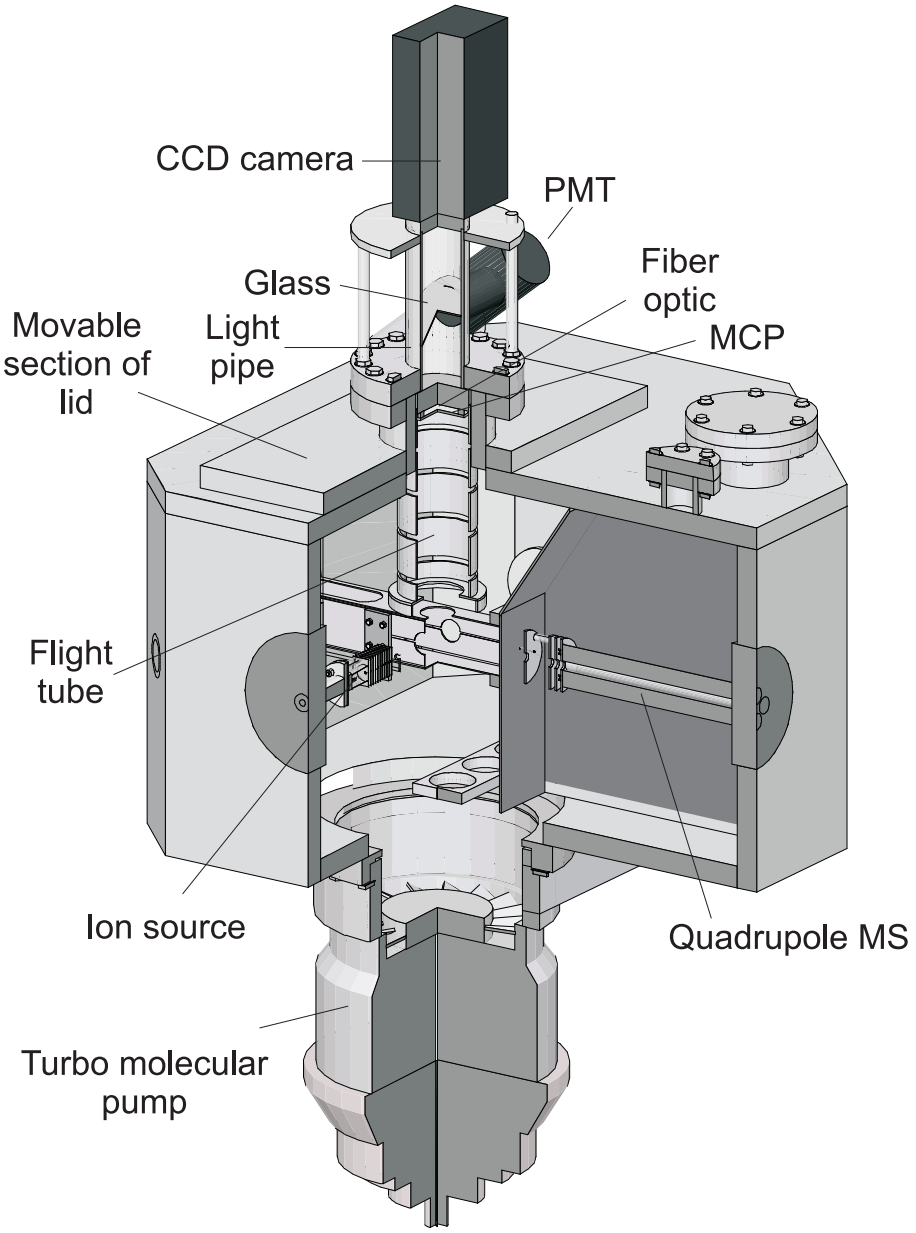

Figure 2.29.: The molecular beam machine scattering chamber, showing the arrangement of the ion source, beam crossing region, and ion imaging assembly.

2.15. Final comments

Another unfortunate consequence of detection of ultra-trace H_3^+ and reaction product ions is the presence of H_3O^+ clusters. H_2O is present as a background species in the scattering chamber and has an exceptionally high cross-section for proton transfer from H_3^+, and as a consequence, all combinations of $H_3O^+ \cdot (H_2O)_n$ were observed in mass spectra, past $n = 10$ even at 1×10^{-7} Torr background pressures. Unfortunately, the CH_3X species have almost identical masses to some of these clusters and therefore contaminate the mass spectra. In several instances after venting of the instrument, the chambers would have to be pumped by turbo-molecular pumps for periods of up to a week in order to reduce this background signal to an acceptable level. Preliminary experiments on crossing neutral molecular beams of CH_4 and CH_3Cl reveals very small signals of positive ion product on the ion imaging. These species were not detected by the quadrupole mass spectrometers at this stage, and experimental parameters need to be iteratively optimized in order to maximize signal. In addition, some preliminary testing of the positive ion source with CH_3Cl indicates formation of Cl^- that could potentially act as a halide source. If not suitable, the thermal source developed by Vallance [7] could be employed. It is anticipated following the successful modifications outlined here and the characterizations also undertaken, and since the Department of Physics now has a new liquid nitrogen cryogenerator that produces abundant supplies of liquid nitrogen, the originally anticipated studies can be performed in a six month research position following thesis submission.

Lastly, in general, experiments and characterizations such as those outlined above can have a tendency to show low reproducibility on the same instrument after shut down. In all the characteristics outlined above, it was ensured that all measurements were reproducible within error under the same experimental conditions on different days.

References

[1] M. Bart. *Electron Impact Ionization: Measurements of Absolute Cross-Sections and Crossed-Beam Studies.* PhD thesis, University of Canterbury, Department of Chemistry, 2003.

[2] Chronicle: University of canterbury. volume 27. September 1992.

[3] B. R. Cameron. *Investigations of the Flow Dynamics of Supersonic Molecular Beams and the Ionization of Molecular Clusters by Electron Impact.* PhD thesis, University of Canterbury, Department of Chemistry, 1993.

[4] C. G. Aitken. *Electron Impact Ionization of Molecular Clusters and Spatially Oriented Molecules.* PhD thesis, University of Canterbury, Department of Chemistry, 1995.

[5] D. A. Blunt. *Studies of State-Elected and Spatially Oriented Molecules.* PhD thesis, University of Canterbury, Department of Chemistry, 1995.

[6] S. A. Harris. *Studies of Ion-Molecule Reactive Processes, Electron Impact Ionization and Inelastic Collisions in State Elected Molecular Beams.* PhD thesis, University of Canterbury, Department of Chemistry, 1997.

[7] C. Vallance. *Studies of Elementary Collision Processes Under Single Collision Conditions.* PhD thesis, University of Canterbury, Department of Chemistry, 1999.

[8] S. Hu. *Non-reactive Scattering of Rotational Quantum State Selected Molecular Beams.* PhD thesis, University of Canterbury, Department of Chemistry, 1999.

[9] R. B. Bernstein. *Chemical Dynamics via Molecular Beam and Laser Techniques.* Oxford University Press: Oxford, 1982.

[10] M. A. D. Fluendy and K. P. Lawley. *Chemical Applications of Molecular Beam Scattering.* Chapman and Hall: London, 1973.

[11] S. D. Wiediger, P. W. Harland, J. R. Holt, and P. R. Brooks. *J. Phys. Chem. A*, 102:1112, 1998.

[12] P. R. Brooks, E. M. Jones, and K. Smith. *J. Chem. Phys.*, 51:3073, 1969.

[13] D. A. Blunt, S. A. Harris, W. Hu, and P. W. Harland. *J. Phys. Chem. A*, 102:1482, 1998.

[14] P. W. Harland, B. R. Cameron, M. Bart, and M. O. Pearce. *Rev. Sci. Instrum.*, 73:2398, 2002.

[15] P. W. Harland, W. Hu, and C. Vallance. *Phys. Rev. A*, 60:3138, 1999.

[16] A. J. Dempster. *Philos. Mag.*, 31:438, 1916.

[17] T. R. Hogness and E. G. Lunn. *Phys. Rev.*, 26:44, 1925.

[18] V. G. Anicich. *J. Phys. Chem. Ref. Data*, 22:1469, 1993.

[19] J. J. Leventhal and L. Friedman. *J. Chem. Phys.*, 50:2928, 1969.

[20] F. B. Yousif, G. Hinojosa, J. de Urquijo, C. Cisneros, and I. Alvarez. *Int. J. Mass Spectrom. Ion Proc.*, 171:127, 1997.

[21] E. P. Hunter and S. G. Lias. *J. Phys. Chem. Ref. Data*, 27:413, 1998.

[22] A. T. J. B. Eppink and D. H. Parker. *Rev. Sci. Instrum.*, 68:3476, 1997.

Part II.

Theoretical Studies of Atom-Molecule and Ion-Molecule Interactions Under Single-Collision Conditions: Crossed Molecular Beams

3. General introduction

Molecular beam experiments are often technically difficult and time-consuming. While such experiments provide fundamental observation, they do not provide complete microscopic or theoretical understanding. High-level quantum chemistry calculations can reproduce the internally cold molecular beam gas-phase conditions, and provide an accurate orbital description of all of the interactions by constructing a reaction potential energy surface. Such calculations are not merely complementary to experiment, but can provide details not experimentally accessible. Once an appropriate level of theory has been established, other related systems can be explored that may not be experimentally accessible.

In this section, some results of *ab initio* and density functional theory calculations are reported. Firstly, the charge-transfer (electron) Na + CH_3NO_2 system was studied, and the previously reported experimental stereodynamics were rationalized. This study also noted that an ambiguity existed in the literature on an accurate electron affinity for CH_3NO_2. Following publication of the Na + CH_3NO_2 study, a new high resolution experimental determination on the electron affinity of CH_3NO_2 was reported in the literature, which was again significantly different to those previously reported. This prompted a series of high-level systematic calculations to be performed in order to find convergence with a suitable level of theory. This study required days of CPU time on the UCSC Blue Fern supercomputer, and it was concluded that the most recent determination was correct. The approach taken could be used as a model for best practice in calculating the electron affinity or a related property of a molecule similar to CH_3NO_2.

Some brief comments are also included on the construction of potential energy surfaces to model H_3^+ and X^- collisions with spatially oriented CH_3X reactions that were originally planned experimental research. Also outlined are some steps towards an *ab intio* model for calculating small harpoon charge-transfer cross sections and stereodynamics (orientation dependence). In addition, a tentative introduction, level of theory testing, and discussion is provided for two studies on the orientation dependence of the Na and K + CH_3NC rebound charge-transfer type reactions. These studies had been fully interpreted with good accord found with experiment, however the discovery that the multi-reference wave function computation package internally incorrectly calculated (slightly) potential energy surfaces required these calculations to be repeated. This study will be completed in the near future, and anticipated to be submitted for publication.

Any calculation will produce an answer, but is this answer correct? The general approach in any theoretical calculations carried out in this thesis was that the level of theory first needed to reproduce relevant (and well-

known) experimental parameters of the system or interaction of interest. This initially involves a level of theory (basis set and electron correlation) assessment. For practicality reasons, very high levels of theory and methods that are highly computationally expensive cannot be employed, as often hundreds of calculations need to be performed for a given study.

Since the work in this thesis involved the use of computational packages both commercial and open-source, and since the field of quantum computational chemistry is rapidly evolving, it can unfortunately take years before new methods are incorporated into usable packages. This is especially true for density functionals that in general have seen huge developments over the last decade. This thesis was started in 2007, and at first made extensive use of the Gaussian 03 package that was released in the year 2003. While some minor functionality updates have been applied, this package mainly provided density functionals pre-2004. It was then during the latter half of the third year of studies that Gaussian 2009 became available, incorporating a wide range of new functionals. DFT functionals need to be very carefully selected for the system of interest through considerable literature review since different functionals can give varying results. Often it is very difficult to identify exactly why a given functional can perform better than another since functional construction involves optimization of many parameters in order to give overall best performance for a given test set of molecules and properties. Individual functional references almost always give a description of supposed strengths and (sometimes) weaknesses, although for a computational system involving several species or different types of interactions the performance across the system may vary. Some functionals are designed for main group chemistry, some for transition metal chemistry, some for improvement of long-range or highly specific interactions, and most available in usable packages attempt to be a jack-of-all-trades. Similar availability arguments are also true for ab intio methods that are much more computationally expensive. Commencement of this research involved the use of only several desktop computers with limited system resources, then, near the end of my first year of studies, the p575 supercomputer at the University of Canterbury became available. Unfortunately, the (free) code employed, GAMESS-US, did not allow for the range of main-stream functionality available in Gaussian, although it had the advantage of multi-reference and highly-tunable configuration interaction methods. Implementation of the BlueFern supercomputer midway through the authors second year of Ph.D. studies was a huge performance advancement, allowing up to 1024 CPUs to be assigned to one process. Unfortunately, the architecture of the Blue Gene system at this time resulted in even more restrictive execution of GAMESS-US, namely, coupled-cluster calculations were not possible and DFT calculations did not scale over many CPUs. Finally, it was during the last quarter of the authors third year when NWChem was implemented by the BlueFern technicians, however was not available in time for the work described herein.

Calculations involved with main group elements have used either Pople or Dunning basis sets. Both of these are by far, and in fact almost exclusively, those employed in modern calculations. In contrast, calculations involving transition metal species have selected basis sets of so-called triple-zeta or higher quality, apart from those utilized in dipole-bound studies that have been rationalized both in this work and in other references. Triple-zeta quality is commonly referred to as “experimental accuracy”. Pople basis sets allow finer tuning

of diffuse and polarization functions for smaller to medium size triple-zeta basis sets, while Dunning basis sets provide systematic correlation consistent (allowing extrapolation procedures to infinity basis set limits, and reasonable comparisons between basis sets) to higher zeta (orbital exponent) degrees although precluding easy finer tuning. In all calculations, choice of electron correlation/functional and basis set were balanced and rationalized with performance of molecular properties within the overall constraint of computational feasibility.

4. Orientation Dependence of the Na + CH_3NO_2 Charge-Transfer Reaction

The reaction of Na + CH_3NO_2 was one of the first investigations started at the commencement of this thesis. This reaction was selected for initial study since previous experimental orientation dependence data had been published, and the molecular beam machine required extensive modifications before experimental data could be obtained.

This chapter is an amended reproduction of a previously published article:

James N. Bull, Robert G. A. R. Maclagan, Peter W. Harland, *Molecular Physics*, 107 (2009) 1123

In the work described in this chapter, Assoc. Prof. Robert Maclagan provided discussions on the computational methods and Prof. Peter Harland provided discussions on his previously published experimental study of the collisions of Na atoms with oriented CH_3NO_2, and on various literature experimental techniques. The majority of the calculations were carried out on a 64-bit dual core personal computer.

Overview

The reaction of atomic sodium with nitromethane, CH_3NO_2, was studied using the B3LYP// 6-311++G(3df,3pd) level of theory to investigate the orientation dependence of the charge-transfer (electron) type reaction. Excellent agreement was found between ground state interaction potentials and recent molecular beam orientation experimental data for free $CH_3NO_2^-$ and NO_2^-. CH_3NO_2 shows slight steric asymmetry for the approach geometry of Na, with reaction favouring attack from the NO_2-end at relatively low (few eV) energies. Increasing reaction energy allows CH_3-end orientations to become accessible and new fragmentation processes to occur. Results indicate that an interpretation involving charge-transfer at relatively large separation, where the positive metal core plays little role in the dynamics following charge-transfer, would not be correct. Coulombic interactions through ion-pair formation facilitate these reactions and, in part, explain some of the previously reported experimental steric asymmetry of this system. Dipole-bound states appear not to play a major role in the reaction dynamics.

4.1. Introduction

The nitromethane molecule, CH_3NO_2, has been extensively investigated over the last few decades because of its interesting properties, which may be divided into several categories: photodynamics and photodissociation [1–3] (and references therein); isomerization to methyl nitrite (CH_3ONO) [4–10]; -NO_2 (nitro) group dipole binding [10–16]; and molecular beam studies [17–22]. Apart from being one of the simplest nitrogen-containing organic compounds, it represents the limiting -NO_2 group containing alkyl compound. It is commonly used in synthesis and as a solvent, it is a component in racing fuels and exhibits prototype explosive properties. More recently, it has been shown to be of atmospheric importance in production of highly reactive CH_3 and NO_x radicals, which are well-known to be ozone destructive and contribute to photochemical smog [23]. CH_3NO_2 shows charge-transfer (electron) type dynamics with alkali earth atoms (Na, K, Rb, Cs) [17–22], and has been previously proposed to show similar dynamics to methyl iodide, CH_3I [20]. It is now accepted to show different dynamics due to significant differences in electronic structure of the NO_2 and I functional groups [18, 21, 22]. One fundamental reaction difference is the formation of the stable parent anion, $CH_3NO_2^-$, and the absence of the molecular ion, CH_3I^-, following alkali metal charge-transfer, which relates to the difference in sign and magnitude of respective electron affinities.

There are two well-known limiting cases of simple bimolecular charge-transfer type reactions, the harpoon mechanism (e.g. Rb + I_2) and the rebound mechanism (e.g. Rb + CH_3I) [24]. Both mechanisms show fundamentally different reaction dynamics due to differences in electronic structure and resulting properties such as molecular electron affinity. The former mechanism is driven by a large positive electron affinity, which may yield the parent anion and fragmentation processes, whereas the latter mechanism shows exclusively product fragmentation, and a negative molecular electron affinity. CH_3NO_2 shows reaction features of both mechanisms, but tends towards the harpoon limit, with a small positive electron affinity and the parent anion detected in abundance for reaction at low reaction energies [21, 22].

Although the concept of a reaction exhibiting orientation dependence is fundamental to chemistry, it is difficult to observe experimentally. Observation may be achieved by use of molecular beam type experiments incorporating inhomogeneous and homogeneous electric fields to facilitate the orientation of dipolar symmetric top molecules in a narrow distribution of rotational states. Brooks *et al.* [21, 22] have recently reported experiments on the CH_3NO_2 system under such conditions using both Na and K atom projectiles. This chapter provides a computational exploration of the reaction potential energy surface orientation dependence, and comparisons are made with the experimental results reported by Brooks *et al.* [21, 22]. Briefly, these experiments involved reactive collisions of crossed molecular beams under ultra-high vacuum or single-collision conditions. CH_3NO_2 was seeded in He carrier gas and injected as an internally cold supersonic beam, which passes through a hexapole electric field filter providing rotational Stark state selection. A thermal oven source produced a beam of Na atoms, which crosses the molecular beam at right angles, with each beam line terminated with a TOF mass spectrometer providing characterization. Detection of reaction product requires separation

of any formed ion-pair species. In the collision region, molecules experience a weak inhomogeneous electric field which provides the required dipole orientation. Experiments on other true C_{3V} symmetric top molecules, under the same hexapole conditions reveals an average distribution of rotational states of approximately ± 25° for t-C_4H_9Br or CH_3Br with respect to the dipole for the two experimental orientations of 'frontside' and 'backside' attack [25]. Other attack orientations are not experimentally achievable.

4.2. Computational details

All calculations have been performed using the Gaussian 03 computational package [26] with the Pople split-valence 6-311++G(3df,3pd) basis set used unless otherwise stated. Levels of theory including electron correlation were selected to reproduce the electron affinity of the CH_3NO_2 species, of which the B3LYP//6-311++G(3df,3pd) level of theory performed the best in reasonable time. The ground state potential energy surface was probed by systematically investigating the optimized interaction potential for several selected approach angles with respect to the C-N internuclear axis with a fixed R(Na-N) separation, and optimizing all other geometrical parameters. This procedure has previously been applied to the lowest energy pathway *ab initio* studies on the K + CH_3CN and CH_3Cl reactions by Maclagan [27, 28]. To monitor charge-transfer, two atomic population schemes were implemented, being Mulliken populations and the Natural Bond Order (NBO) scheme. The charge-transfer separation is defined to be the separation when the NBO charge on the Na atom reaches a threshold of +0.5, selected for best agreement with experiment.

Fourteen different approaches were investigated as shown in figure 4.1, with angles referenced with respect to the CH_3-end at 0°. These are generally divided into three types: axial or direct dipole-ended approaches (1) and (2); sideways eclipsed with H_1 (4), (7), (8), (11), (12), (13); and sideways staggered between the H_2 atoms (3), (5), (6), (9), (10). Approaches (1) and (2) with anticipated ± 25° angular distribution cones are those experimentally investigated by Brooks *et al.* [21].

These orientation calculations are interpreted in terms of: point of charge-transfer and interaction potential; interaction potential minima and their nature; and geometrical changes before, at and after charge-transfer.

4.3. Results and discussion

4.3.1. Geometrical optimizations

Neutral CH_3NO_2 shows an electronic ground state symmetry of ^{1}A' and the parent anion, $CH_3NO_2^-$ of ^{2}A'. Both species formally exhibit C_S point symmetry, however the small barrier to CN rotation of ≈ 0.0061 kcal/mol [29], results in C_{3V} behaviour which fulfils the criterion for producing oriented beams in the experiments carried out by Brooks *et al.* [21, 22]. The lowest energy conformation, where the N-O bonds do not eclipse the C-H bonds is

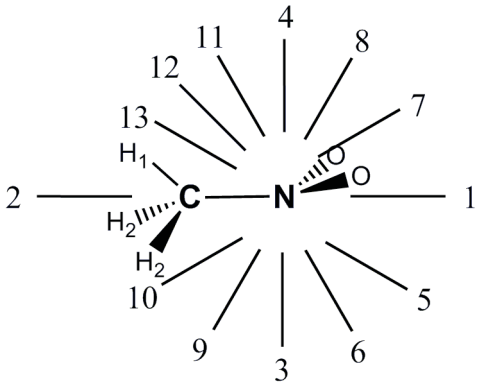

Approach	Description
(1)	NO_2-end axial, 180°
(2)	CH_3-end axial, 0°
(3)	perpendicular staggered, 90°
(4)	perpendicular eclipsed, 90°
(5)	staggered, 135°
(6)	staggered, 120°
(7)	eclipsed, 135°
(8)	eclipsed, 120°
(9)	staggered, 60°
(10)	staggered, 45°
(11)	eclipsed, 60°
(12)	eclipsed, 45°
(13)	eclipsed, 30°
(14)	*oxygen eclipsed, 90°

Figure 4.1.: Thirteen of the fourteen investigated approach orientations for the Na + CH_3NO_2 reaction. Angles are referenced with respect to the C-N axis CH_3-end at 0°. The NO_2 group plane lies perpendicular to the page and H_1 exists in the page plane. Approach orientations from the page top or the H_1 side represent eclipsed approaches, and those from below or the H_2 side are staggered approaches. *Orientation (14) corresponds to approach perpendicular to the plane of the page.

considered in these calculations. Optimized geometric parameters from this work and other reported calculations are given in tables 4.1 and 4.2.

The neutral geometry determined at both the B3LYP//6-311++G(3df,3pd) and B3LYP//aug-cc-pVTZ levels of theory are in excellent agreement with reported experimental parameters, with reported bond lengths within 0.010 Å and angles within 0.3°. Gutsev and Bartlett [30] provide the most recent and detailed theoretical study on CH_3NO_2, and found essentially no difference between geometrical parameters with CCSD(T) and HF(B3LYP) methods for moderate basis sets, but report that the selection of a sufficiently large basis set (including diffuse functions) is important for appropriate (∠CNO) and NO_2 tilt angles of the anion. The most distinct features of the valence anion geometry compared to the neutral is the contraction and weakening of the C-N bond, and the NO_2 tilt angle increasing by ≈ 32°, giving slight elongation of the N-O bond. The NO_2 tilt angle is determined here to be 1.57° and 33.6° for the neutral and anion respectively, both in excellent agreement with previous determinations.

Thirteen of the fundamental vibrational frequencies for both neutral and anion are given in tables 4.3 and 4.4. Those for neutral CH_3NO_2 are in such excellent agreement with experimental values, that only the small gradient correction factors of 0.96 and 1.00 are needed, respectively, to align harmonic and anharmonic calculated values to experimental in a least squares regression. The performance of DFT over *ab initio* methods for CH_3NO_2 has been studied by Jursic [31], who reported that the B3LYP functional performs better than B3PW91 and SVWM (LDSA) in the determination of geometries and frequencies. The B3LYP//6-311++G(3df,3pd) level of theory reproduces the experimental frequencies for CH_3NO_2 considerably better than the Gutsev and Bartlett [30] MP2//6-311++G(d,p) determination. It is concluded that the B3LYP//6-311++G(3df,3pd) level of theory should be sufficient to produce accurate structures.

Table 4.1.: Summary of CH_3NO_2 ground state optimized geometries. All bond lengths in Å, angles in degrees and energies in a.u..

Method	Energy	R(C-N)	R(N-O)	R(C-H_2)	R(C-H_1)	∠(ONO)	∠(CNO)	∠(NCH_2)	∠(NCH_1)	NO_2 tilt
calc[a]	-243.81539	1.508	1.197	1.075	1.080	125.5	117.3	107.6	106.6	-
calc[b]	-243.87878	1.498	1.241	1.078	1.081	124.7	117.7	110.2	108.0	-
calc[c]	-244.65931	1.493	1.229	1.082	1.086	-	117.1	107.9	106.8	1.53
calc[d]	-244.94967	1.504	1.230	1.087	1.091	-	117.3	108.2	106.7	1.51
calc[e]	-245.10968	1.498	1.218	1.081	1.087	125.7	117.1	108.1	106.5	1.57
calc[f]	-245.11521	1.499	1.219	1.084	1.088	125.6	117.2	108.1	106.5	1.51
expt IR/Raman [32]	-	1.489	1.224	1.088	1.088	125.3	117.4	-	-	-
expt Raman [31]	-	1.489	1.224	1.089	1.089	125.3	117.4	-	-	-
expt microwave [29]	-	1.489	1.224	-	-	125.3	-	107.2	-	-

[a]CASSCF(5,6)//6-311++G(2d,2p) [4]
[b]CASSCF(5,6)//6-311++G(2d,2p) [33]
[c]CCSD(T)//6-311++G(2d,2p) [30]
[d]HF(B3LYP)//6-311++G(2d,2p) [30]
[e]B3LYP//6-311++G(3df,3pd) [this work]
[f]B3LYP//aug-cc-pVTZ [this work]

Table 4.2.: Summary of $CH_3NO_2^-$ ground state optimized geometries. All bond lengths are in Å, angles in degrees and energies in a.u.. A diagram can be found in the first figure in the following chapter.

Method	Energy	R(C-N)	R(N-O)	R(C-H_2)	R(C-H_1)	∠(ONO)	∠(CNO)	∠(NCH_2)	∠(NCH_1)	NO_2 tilt
calc[a]	-244.65931	1.462	1.314	1.088	1.099	-	113.6	109.1	108.9	33.7
calc[b]	-244.94967	1.479	1.314	1.093	1.103	-	113.7	109.0	110.1	34.5
calc[c]	-245.12230	1.462	1.301	1.088	1.140	122.3	114.6	109.2	109.6	33.6
calc[d]	-245.12230	1.462	1.301	1.089	1.105	122.4	114.9	109.2	109.6	32.2

[a]CCSD(T)//6-311++G(2d,2p) [30]
[b]HF(B3LYP)//6-311++G(2d,2p) [30]
[c]B3LYP//6-311++G(3df,3pd) [30]
[d]B3LYP//aug-cc-pVTZ [30]

Table 4.3.: Thirteen of the fundamental vibrational frequencies for the CH_3NO_2 ^{1}A' ground state at the B3LYP//6-311++G(3df,3pd) level of theory. Frequencies are in cm^{-1}, and ZPE in kcal/mol (italics).

Experimental		Calculated		
IR/Raman [34]	Raman [32]	harmonic[a]	harmonic[b]	anharmonic[b]
476	475	483	482	474
599	603	604	617	619
647	657	671	663	642
921	918	936	928	906
1097	1096	1135	1113	1092
1153	1131	1157	1137	1106
1384	1380	1405	1403	1363
1413	1397	1445	1433	1401
1449	1410	1496	1466	1425
1488	1434	1506	1478	1431
1582	1583	1730	1623	1590
2965	2974	3126	3079	2967
3048	3080	3404	3168	3027
-	*30.28*	*32.23*	*31.20*	*30.72*

[a]MP2//6-311++G(2d,2p) [30]
[b]B3LYP//6-311++G(3df,3pd) [this work]

Table 4.4.: Thirteen fundamental calculated vibrational frequencies for the $CH_3NO_2^-$ ^{2}A' ground state valence anion at the B3LYP//6-311++G(3df, 3pd) level of theory. Frequencies are in cm^{-1}, and ZPE in kcal/mol (italics).

harmonic[a]	harmonic[b]	harmonic[b]
448	447	442
591	586	573
889	846	836
1092	1061	1036
1126	1091	1036
1282	1024	1159
1349	1283	1251
1408	1390	1354
1491	1459	1409
1501	1470	1431
3016	2884	2699
3125	3053	2906
3175	3108	2946
30.28	*29.30*	*28.85*

[a]MP2//6-311++G(2d,2p) [30]
[a]B3LYP//6-311++G(3df,3pd) [this work]

4.3.2. Electron affinities

A critical requirement for selection of the level of theory is excellent agreement of electron affinities for the valence-bound anion. Consistent with Gutsev and Bartlett [30], MP2 and MP4 electron-correlation treatments

failed to yield a positive electron affinity, even here with more comprehensive triple-zeta basis sets. CCSD(T) theory with the larger basis sets employed here, and for the number of potential energy points required in this study, was not feasible. Table 4.5 summarizes the calculated and previously reported valence-bound anion adiabatic electron affinities. These data show there is a degree of inconsistency in the literature on the experimental electron affinity, with values reported between 0.26 eV and in the range 0.44-0.50 eV, all claiming to be adiabatic. The B3LYP//6-311++G(3df,3pd) ΔZPE corrected value of 0.43 eV is in excellent agreement and within experimental uncertainty of this latter group. These data would indicate that the B3LYP//6-311++G(3df,3pd) level of theory appears to perform considerably better than Gutsev and Bartlett [34] calculations employing smaller basis sets, where they compare to the lower (and single) experimental electron affinity.

Table 4.5.: Adiabatic experimental and calculated valence-bound electron affinities for CH_3NO_2. All values are in eV, and the calculated adiabatic values in this work corrected for the B3LYP//6-311++G(3df,3pd) ΔZPE = 0.082 eV.

Method	Electron affinity
Experimental	
Rydberg exchange [11]	0.26 ± 0.08
Steady-state electron capture [35]	0.45 ± 0.05
Crossed molecular beam thresholds [36]	0.44 ± 0.20
Pulsed high-pressure EI-MS [37]	0.49 ± 0.11
Steady-state electron capture [38]	0.50 ± 0.10
Calculated	
MP2//6-311++G(2d,2p) [34]	-0.25
CCSD//6-311++G(2d,2p) [34]	0.13
CCSD(T)//6-311++G(2d,2p) [34]	0.03
B3LYP//6-311++G(2d,2p) [34]	0.22
BLYP//6-311++G(2d,2p) [34]	0.08
MP2//6-311++G(2df,2pd) [this work]	-0.21
B3LYP//6-311++G(3df,3pd) [this work]	0.43
B3LYP//aug-cc-pVTZ [this work]	0.45
M06-HF//6-311++G(3df,3pd) [this work]	0.59

The C-N bond dissociation energy, BDE(CH_3NO_2), is calculated to be 2.61 eV and 0.70 eV respectively for the neutral and anion. Both of these calculated values are in excellent agreement with the reported experimental values of 2.67 ± 0.10 eV and 0.56 ± 0.20 eV, respectively [31,35]. Calculated Na and K ionization potentials are 4.94 eV and 4.50 eV, in good accord with the accepted values of 5.14 and 4.34 eV [39]. Basis set superposition errors (BSSE) for both CH_3 + NO_2 and Na + CH_3NO_2 fragments, are on average ± 0.03 eV, which should play a minor role in affecting reported energies.

4.3.3. Reaction channels

The optimized and relative energies of several asymptotic and ion-pair reaction channels of experimental relevance referenced with respect to the Na + CH_3NO_2 reactants are given in table 4.6. Channel (i) represents the reactants, which on thermodynamic grounds, represent the asymptotic lowest energy channel, with all other ionic channels endoergic since IP(Na) >EA(CH_3NO_2). The reactive channel (iv) represents reaction resulting in C-N heterolytic cleavage to neutral fragments, which asymptotically would be the most energetically accessible reaction channel. The experiments of Brooks *et al.* [21, 22] are blind to this channel, and these calculations do not reveal this to play any major role. The second most accessible asymptotic channel (ii) involves formation of the parent anion by charge-transfer, where 5.08 eV is the endoergicity required for charge-transfer and the infinite separation of products. Parent anion dissociation yields channel (iii), by addition of an extra 0.75 eV to channel (ii). Channel (v), involving CH_3^- formation, is higher energy and has not been reported to be experimentally important at the collision energies studied. O^- formation reaction channels are expected to open at higher energies, and they are not considered here.

Ion-pair adduct formation and their associated reaction channels may also occur, where the Coulombic interaction in ion-pair formation in part facilitates reaction charge-transfer. Such ion-paired species have been the subject of many molecular beam charge-transfer studies with well documented products, and traditionally characterized by magnetic deflection [17, 18]. Several experimentally relevant ion-pair adducts of the $CH_3NO_2^-$ and NO_2^- anions are included in table 4.6, with their geometries summarized in table 4.7. Formation of ion-pair species lowers or even removes the barrier to reaction. A parent ion-pair from direct CH_3-end attack is not bound, however formation of the $CH_3NO_2^-Na^+$ parent ion-pair from the NO_2-end provides an exoergic channel to reaction.

Generalizing to all approach orientations, the formation of a conformation of a parent ion-pair species shows a broad angular range, and as shown in figure 4.2, a cone-of-acceptance binding channel (described later) of parent ion-pair adduct geometries is defined that is centred about the NO_2-end. The global minimum is not direct axial NO_2-end attack, rather the eclipsing (H_1) approach angle of 25.28°, which has a slightly larger NO_2 tilt angle at 33.26°, but is only ≈ 0.06 eV lower in energy. Reaction channel (iii), involving C-N cleavage, may exist as the product ion-pair channel (a), where the Na^+ species bridges the two O atoms, due to the strong ion-pair binding energy of -6.15 eV for this species, with an exoergic reaction channel of -0.32 eV existing. This is characteristic of a harpoon dissociation process [17]. Channel (b) provides a slightly less stable ion-pair geometry, and now slightly endoergic channel, with the Na^+ species above the NO_2^- C_{2V} rotation axis at its positive end. Other NO_2 ion-pair minimum geometries exist, for example pyramidal, however (a) and (b) are anticipated as the two most likely adducts from CH_3-end and NO_2-end attacks respectively. Such ion-pair species and reaction channels show energetics which would intuitively be expected to be important for collision energies on the order of their binding magnitude. Experimentally, Brooks *et al.* [21] detect the onset of abundant NO_2^- formation at ≈ 5.7 eV, which is close to the channel (iii) 5.83 eV asymptotic limit, and where NO_2^- steric asymmetry averages to zero. They also report detection of some small signal below this asymptotic threshold,

which may be due to some loosely bound and separated ion-pair in the mass spectrometer from channel (a) or (b).

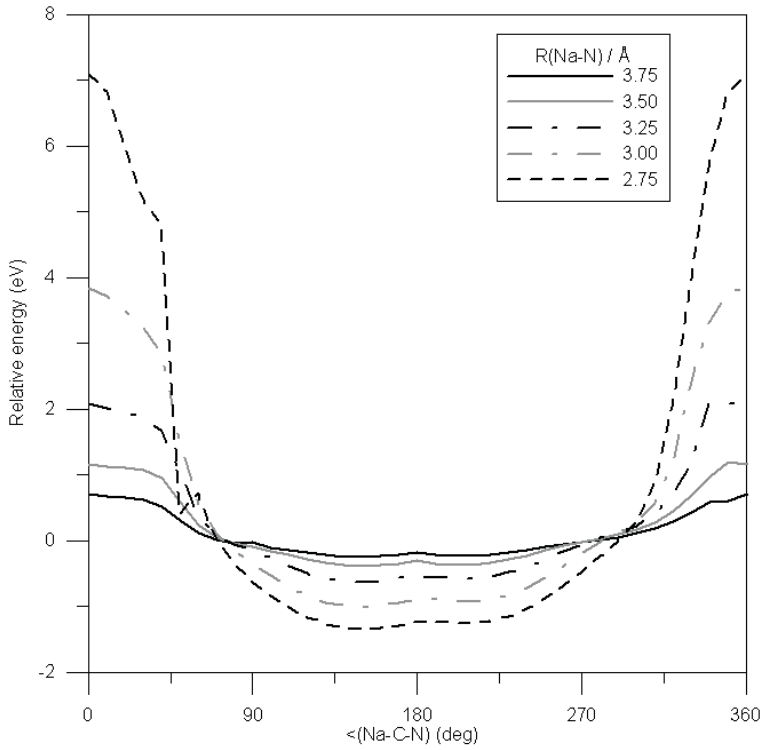

Figure 4.2.: Relative interaction potentials around a circle centred on the nitrogen atom for five R(Na-N) separations, corresponding to complete charge-transfer (2.75 Å (black dashed)) to no charge-transfer (3.75 Å) with some intermediate cases: 3.00 Å; 3.25 Å; 3.50 Å. ∠(NaCN) referenced to CH_3-end axial attack at 0°, and rotating clockwise first through eclipsed conformations for increasing angle.

Table 4.6.: Ground state optimized energies in a.u. of relevant species, and relative reaction channel and ion-pair energies in eV with respect to reaction channel (1)[a] at the B3LYP//6-311++G(3df,3pd) level of theory.

Species	Energy	Reaction Channels	Relative energy
CH_3NO_2	-245.10968	(i) Na + CH_3NO_2	0.00
$CH_3NO_2^-$	-245.12230	(ii) Na^+ + $CH_3NO_2^-$	5.08
Na	-162.28678	(iii)Na^+ + CH_3 + NO_2^-	5.83
Na^+	-162.08757	(iv) Na + CH_3 + NO_2	2.61
CH_3	-39.85836	(v) Na^+ + CH_3^- + NO_2	7.98
NO_2^-	-205.23626		
CH_3^-	-39.86017		
NO_2	-205.15530		
$Na^+CH_3NO_2^-$	N/A		
$CH_3NO_2^-Na^+$	-1.40		
$CH_3NO_2^-Na^+$ (25.58 °)	-1.46		
$NO_2^-Na^+$[b]	-6.15	(a) $NO_2^-Na^+$ + CH_3	-0.32
$Na^+NO_2^-$[b]	-5.29	(b) $Na^+NO_2^-$ + CH_3	0.53

[a]A negative energy corresponds to a bound system with respect to asymptotic reactants.
[b]Binding energy relative to Na^+ + NO_2^-.

Table 4.7.: Ion-pair geometries at the B3LYP//6-311++G(3df,3pd) level of theory. Bond lengths in Å, angles in degrees and energies in a.u..

Species	Energy	R(Na-N)	R(C-N)	R(N-O)	R(C-H_2)	R(C-H_1)	∠(ONO)	∠(CNO)	∠(NCH_2)	∠(NCH_2)	NO_2 tilt
$CH_3NO_2^-Na^+$[a]	-407.44788	2.48	1.45	1.32	1.09	1.10	119.8	118.6	109.1	110.5	19.74
$CH_3NO_2^-Na^+$[b]	-407.45037	2.53	1.46	1.32	1.09	1.10	118.7	116.3	108.5	109.6	33.46
$CH_3NO_2^-K^+$	-845.09112	2.81	1.45	1.31	1.09	1.10	119.9	117.4	108.6	110.1	26.26
$Na^+NO_2^-$	-367.51854	2.20	N/A	1.24	N/A	N/A	120.6	N/A	N/A	N/A	N/A
$NO_2^-Na^+$	-367.54969	2.61	N/A	1.29	N/A	N/A	115.6	N/A	N/A	N/A	N/A
Diabatic dipole	-407.37764	4.50	1.49	1.22	1.08	1.09	125.2	117.4	108.2	106.6	2.30
Adiabatic dipole	-407.39743	4.50	1.49	1.22	1.08	1.09	125.2	117.4	108.2	106.6	0.98
CH_3NO_2	N/A	1.498	1.498	1.218	1.081	1.087	125.7	117.1	108.1	106.5	1.57
NO_2^-	N/A	N/A	N/A	1.254	N/A	N/A	116.8N/A	N/A	N/A	N/A	N/A

[a]NO_2-end.
[b](25.58°) - described in the text.

4.3.4. Steric asymmetry

The molecular beam experimental data reported by Brooks *et al.* [21] for the Na + CH_3NO_2 shows some small steric asymmetry for low energy formation of $CH_3NO_2^-$ and NO_2^-. At their lowest reported collision energies of ≈ 5.1 eV, $CH_3NO_2^-$ formation, albeit with large error bars, is favoured from the 'negative' NO_2-end and then rapidly switches to the 'positive' CH_3-end at ≈ 5.3 eV. As reaction energy was further increased, steric asymmetry became averaged out at ≈ 7 eV. They also observed some smaller steric asymmetry for NO_2^- formation below their thermodynamic threshold of ≈ 5.5 eV, which shows preferential formation from the NO_2-end, however with weak signal and large error this may not be real. The lack of asymmetry for NO_2^- formation indicates sideways or isotropic type formation. In contrast, reaction with K shows a strong low energy (<6.3 eV) asymmetry to NO_2^- formation for CH_3-end attack [22]. The reported interaction potential calculations do not probe O^- formation, or the formation of Na^+ and free electrons (e^-) at low energy, where Brooks *et al.* [21] observed a large free electron signal which extends below the Na ionization potential. Assuming highly monochromatic beams, this signal could result from the ion-dipole $CH_3NO_2Na^+ + e^-$ channel calculated at 4.14 eV with respect to reactants. For this ion-dipole species, the Na^+ ion is weakly bound by the negative dipole at R(Na-N) = 2.75 Å. Brooks *et al.* interpret their experimental signal in terms of an asymmetry factor, G, defined in terms of reaction cross-section, σ, for collisions at the CH_3-end (+) and NO_2-end (-) of the CH_3NO_2 molecule:

$$G = \frac{\sigma(-) - \sigma(+)}{\sigma(-) + \sigma(+)} \tag{4.1}$$

It is proposed that their experimental asymmetry observations for $CH_3NO_2^-$ and NO_2^- may be explained in terms of a combination of the calculated interaction potentials, ion-pair formation processes, and interaction barriers.

For each orientation in figure 4.1, the first three diabatic or excited state energies at the ground state geometry were calculated within the TDDFT framework, since the charge-transfer mechanism involves crossing of a reactant covalent surface with a product ionic surface. This analysis concerns the lowest (minimum) energy or ground state pathway(s) to reaction. It is well-known that TDDFT is erroneous when determining excitation energies of charge-transfer excited states with traditional exchange-correlation functionals such as B3LYP [40,41]. Charge-transfer characterization involving 'long-range' [41] excited states requires incorporation of non-local Hartree-Fock exchange. Several calculations are performed with the recent meta-GGA M06-HF functional of Truhlar *et al.* [42, 43] which incorporates full Hartree-Fock exchange, for NO_2-end approach at geometries before, at, and after B3LYP charge-transfer using the GAMESS-US package [44]. Na Mulliken populations show little difference, however show charge-transfer occurs at ≈ 0.3 Å larger separation. The M06-HF//6-311++G(3df,3pd) level of theory yields a larger adiabatic electron affinity of 0.59 eV, in slightly worse agreement with experimental values in table 4.5, which may explain the larger charge-transfer separation. The charge-transfer (electron affinity) dynamics here appear not to be significantly affected by this TDDFT shortfall.

These calculations reveal that the underlying electronic potential energy surfaces exhibit some steric asymmetry

for $CH_3NO_2^-$ and NO_2^-, both with ion-pair formation, interaction potentials and surface crossing separations, which relate to cross-section. As a starting point from table 4.6, low energy collisions, from ≈ 0-5 eV, of appropriate approach orientation yield parent $CH_3NO_2^-Na^+$ and $NO_2^-Na^+$ ion-pair species, which may separate at higher energy to yield channel (iii). Higher energy collisions, from ≈ 3-6+ eV, open further asymptotic channels which may involve C-N dissociation. All orientations in figure 4.1 yield slightly different approach interaction potentials, however, all show the feature that charge-transfer occurs at relatively large separation (>2.8 Å), resulting in the formation of the $CH_3NO_2^-$ parent anion. As mentioned several times above, one crucial parent anion asymmetry feature of these interaction potentials is that various approach orientations may or may not yield a bound parent ion-pair species. Calculations at the MP2//6-311++G(2df,2pd) level of theory as compared to DFT, gives interaction potential curves different in energy and shape for both CH_3-end and NO_2-end approach, and show different charge-transfer characteristics, due to the poor (negative) electron affinity at this level of theory. These have poor agreement with experiment.

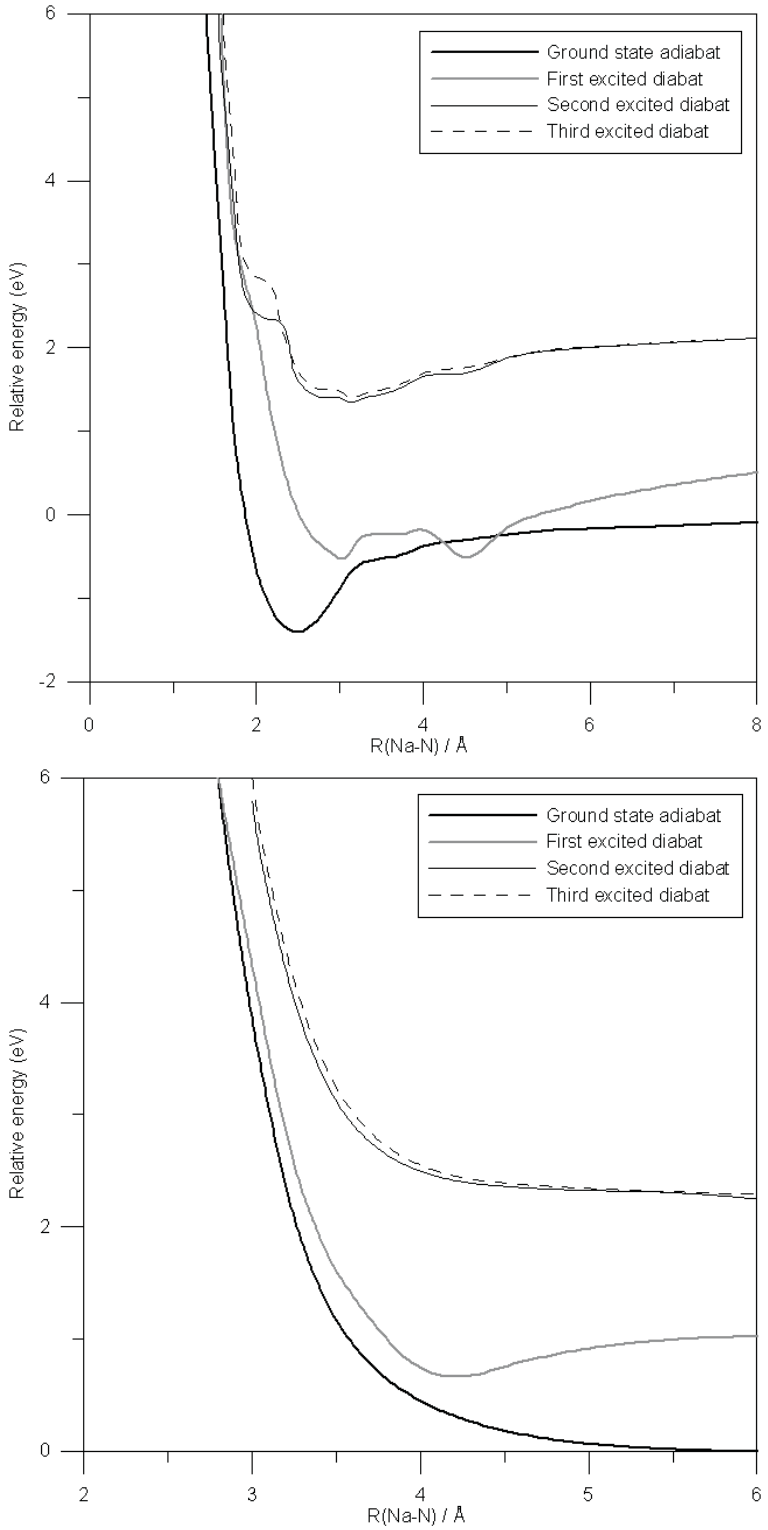

Figure 4.3.: Approach interaction potentials for NO_2-end (top) and CH_3-end (bottom) axial attacks. The ground state curves represent the minimum energy pathway, other curves represent respective diabatic states. In general, for large separations the ground state curve is covalent (neutral), and short separations ionic; vice versa for the first excited state.

The approach interaction potentials for the two experimental orientations, NO_2-end and CH_3-end, are shown in figure 4.3. Although experimentally the molecules precess in a distribution of discrete rotational states, on average they should show characteristics of direct axial approach. The NO_2-end approach interaction potential curve reveals no barrier to reaction, with charge-transfer occurring at R(Na-N) = 3.40 Å, forming the $CH_3NO_2^-Na^+$ ion-pair with a potential energy minimum at R(Na-N) = 2.48 Å. At the point of charge-transfer the adduct geometry is not too different from the reactant, which is characteristic of a harpoon process. The charge-transfer geometries for each approach are summarized in table 4.8. Population analysis for this approach, and indeed all approaches show that charge-transfer, interpreted as a probability, occurs over some small finite separation. Figure 4.4 shows for the NO_2-end and CH_3-end, this occurs from zero to maximum between R(Na-N) = 4.50 Å to 3.00 Å and 4.00 Å to 2.50 Å, respectively. After charge-transfer, the ion-pair further relaxes into a tighter geometry, with parameters summarized in table 4.9 for all approach geometries. For reaction energy less than 6.5 eV, which is the minimum energy required to separate parent ion-pair to products, then free $CH_3NO_2^-$ is not expected. This is in good agreement with Brooks *et al.* [21] experiments where NO_2-end and CH_3-end steric asymmetry is observed to average out to zero at ≈ 7 eV.

Table 4.8.: Summary of geometries at the charge-transfer threshold for each orientation, the isolated neutral an valence anions are also listed for comparison, with bond lengths in Å and angles in degrees. A negative NO_2 tilt angle corresponds to a tilt angle opposite to that of the isolated neutral or the valence anion, namely with oxygen atoms partially eclipsing with the H_2 atoms.

Orientation	R(C-N)	R(N-O)	NO_2 tilt
(1)	1.46	1.26	12.64
(2)	1.46	1.28	9.89
(3)	1.47	1.27	34.48
(4)	1.49	1.29	-43.73
(5)	1.47	1.27	24.29
(6)	1.48	1.23	27.57
(7)	1.48	1.26	25.91
(8)	1.44	1.26	32.68
(9)	1.47	1.27	-21.41
(10)	1.48	1.27	-28.24
(11)	1.49	1.26	-30.44
(12)	1.45	1.26	-22.39
(13)	1.49	1.26	18.37
K NO_2-end	1.46	1.26	6.85
CH_3NO_2	1.50	1.22	1.54
$CH_3NO_2^-$	1.46	1.30	33.39

The experimental detection of a small NO_2^- signal from NO_2-end collisions could be due to the formation of an ion-pair or signal from a sideways geometry with a more weakly bound ion-pair where CH_3-end attack does not yield a correct geometry to form an ion-pair. For separations closer than R(Na-N) = 1.5 Å (4.4 eV), the NO_2 tilt angle rapidly increases yielding a sideways $NO_2^-Na^+$ ion-pair. Decreasing R(Na-N) further yields C-N dissociation, with rearrangement to the bridging $NO_2^-Na^+$ ion-pair. The interaction potential at the start of C-N elongation corresponds reasonably well to the experimental threshold of NO_2^- product detection at ≈ 5.5 eV.

Table 4.9.: Charge-transfer properties and ion-pair potential energy minima for each approach orientation, with separations in Å, and relative energies with respect to reactants in eV. Charge-transfer is considered to occur when the Na NBO charge exceeds +0.5. Separations reported to the nearest 0.05 Å.

Approach	Charge-transfer separation	Relative energy at charge-transfer	Ion-pair separation[a]	Ion-pair binding energy
(1)	3.40	-0.38	2.48	-1.40
(2)	3.10	3.00	N/A	N/A
(3)	3.15	-0.22	2.37	-0.86
(4)	3.10	-0.11	2.35	-0.73
(5)	3.40	-0.44	2.53	-1.42
(6)	3.40	-0.35	2.49	-1.30
(7)	3.00	0.59	N/A	N/A
(8)	2.85	3.51	N/A	N/A
(9)	3.35	-0.42	2.52	-1.31
(10)	3.30	-0.27	2.49	-1.18
(11)	2.85	0.30	N/A	N/A
(12)	2.80	1.24	N/A	N/A
(13)	2.70	6.25	N/A	N/A
K NO_2-end	4.05	-0.37	2.81	-1.50

[a]N/A corresponds to no bound ion-pair.

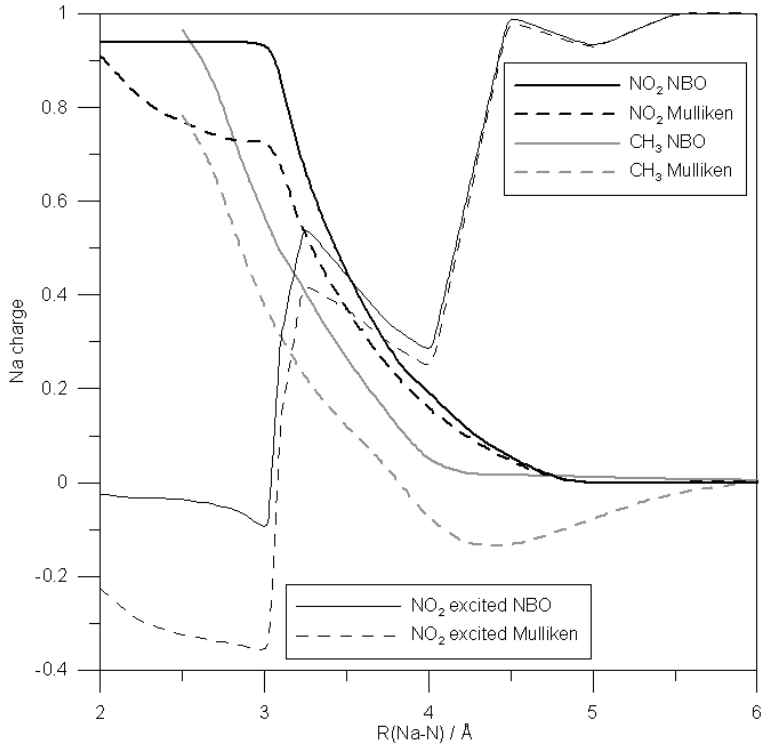

Figure 4.4.: Na charge for the minimum energy NO_2-end and CH_3-end axial attack, and first excited diabat for NO_2-end axial attack in the NBO and Mulliken population schemes.

For CH_3-end attack which is shown in figure 4.3, the approach is optimized with respect to R(Na-C) fixed, and the interaction potential curve is entirely repulsive in nature with no bound parent ion-pair, providing free

$CH_3NO_2^-$. The charge-transfer threshold is reached at an interaction potential of 3.00 eV (on repulsive section of the curve), corresponding to a separation of R(Na-N) = 3.10 Å. Thus, in contrast to NO_2-end approach, direct CH_3-end approach requires a small barrier to charge-transfer. For direct collisions at the CH_3-end, which are not energetic enough to surmount the barrier, elastic scattering may occur or the trajectories may be guided into a more favourable reaction orientation by the potential energy surface. The cone-of-acceptance in figure 4.2 (described later) does show a ± 25° cone about the CH_3-end that on average would reproduce axial CH_3-end approach. In general, reaction is expected to show some steric asymmetry for free $CH_3NO_2^-$ from the CH_3-end for energies above the reaction barrier but below 6.5 eV, as most of the product from the NO_2-end is bound as the ion-pair. This was experimentally observed by Brooks *et al.* [21]. This range of interaction potentials encompasses the Na ionization potential and indicates ion-pair interactions play a less significant role in the CH_3-end dynamics.

The calculated threshold to asymptotic reaction at 5.08 eV corresponds well to the upper limit, albeit with large error bars, of the switch from experimental NO_2-end (loose parent ion-pair) for CH_3-end $CH_3NO_2^-$ asymmetry at ≈ 5.3 eV. Thus, the lowest energy $CH_3NO_2^-$ experimental data favouring the NO_2-end is consistent with formation of an ion-pair adduct from this approach, and the detection of a portion of this separated adduct. These data indicate that the presence of the CH_3 group lowers the charge-transfer probability or cross-section for CH_3-end attack at low energies by providing an energetically higher interaction approach through the absence of ion-pair interactions. Further, from the CH_3-end, dissociation is observed for R(Na-C) separations closer than ≈ 1.5 Å, or interaction potentials of ≈ 7.1 eV. This corresponds well to where the observed NO_2^- experimental steric asymmetry averages to zero. That is, when reaction energies are higher than the ion-pair binding energy and barrier to dissociation channel (iii), then ion-pair separation occurs and the channels product asymmetry tends to zero.

The other approach orientations outlined in figure 4.1 also show similar to intermediate steric asymmetry to $CH_3NO_2^-$ and NO_2^- formation. Approaches (9), (10), (11), (12) and (13) are 'CH_3-sided', and like axial CH_3-end attack, show repulsive type interaction potential curves shown in figure 4.5. These orientations show the features that: charge-transfer separation slowly decreases (i.e. becomes shorter-ranged) with increasing angle from NO_2-end attack; and interaction potentials increase for a given R(Na-N) separation. As reaction becomes more sideways in nature, crossing with the dissociative NO_2^- curve occurs at a smaller interaction potential and slightly closer separation. This trend occurs since the Na^+ is in a better orientation to ion-pair with NO_2^-, lowering the barrier to dissociation for sideways orientations. The 60° approaches show the lowest energy dissociation crossing which would be in an ideal geometry to form the $Na^+NO_2^-$ ion-pair. Nearing the dissociation channel, the CH_3 group tends to trigonal planar geometry with R(C-N) elongation. Generally, eclipsed approach curves exhibit slightly higher interaction potentials than corresponding staggered approaches, becoming more prominent with decreasing angle to CH_3-end axial due to steric hindrance. The low barrier to free C-N rotation almost certainly averages out any conformation effects. Staggered approaches are characterized by the feature shown in figure 4.6 and table 4.8, that at a characteristic separation before charge-transfer, a

NO_2 tilt angle inversion occurs where the group becomes eclipsed with the H_2-hydrogen atoms. This inversion process occurs to better orient the positive Na and negatively charged O atoms through the strong ion-pair Coulombic interactions.

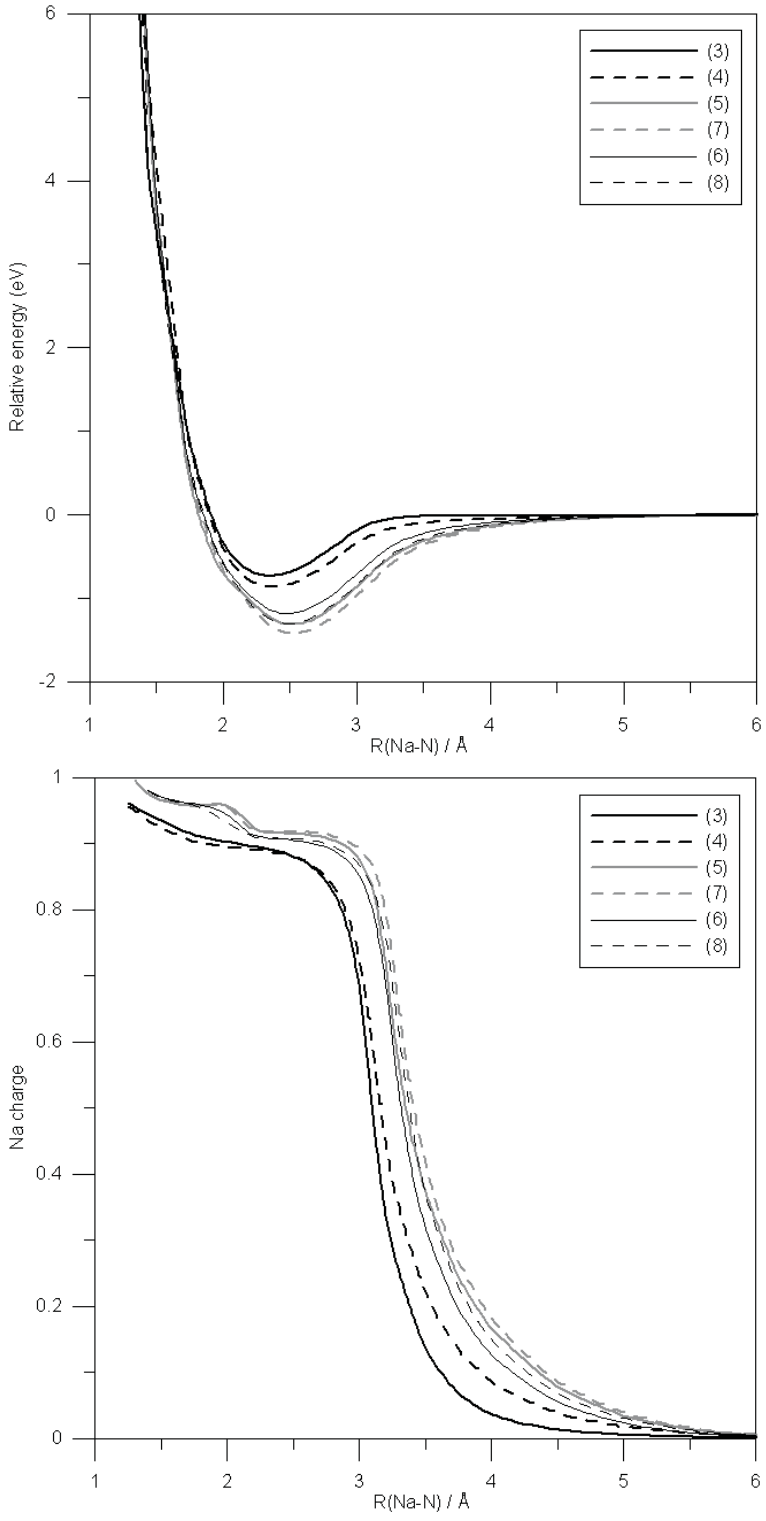

Figure 4.5.: Approach interaction potentials for attack orientations on the NO_2-side and perpendicular (top) and the corresponding Na NBO charge (bottom). Numbers in each legend indicate approach orientations.

Approaches (5), (6), (7), (8), (3) and (4) are 'NO_2-ended' and include direct sideways or perpendicular orientations, respectively, shown in figure 4.7. For all these approaches, parent ion-pair potential energy minima

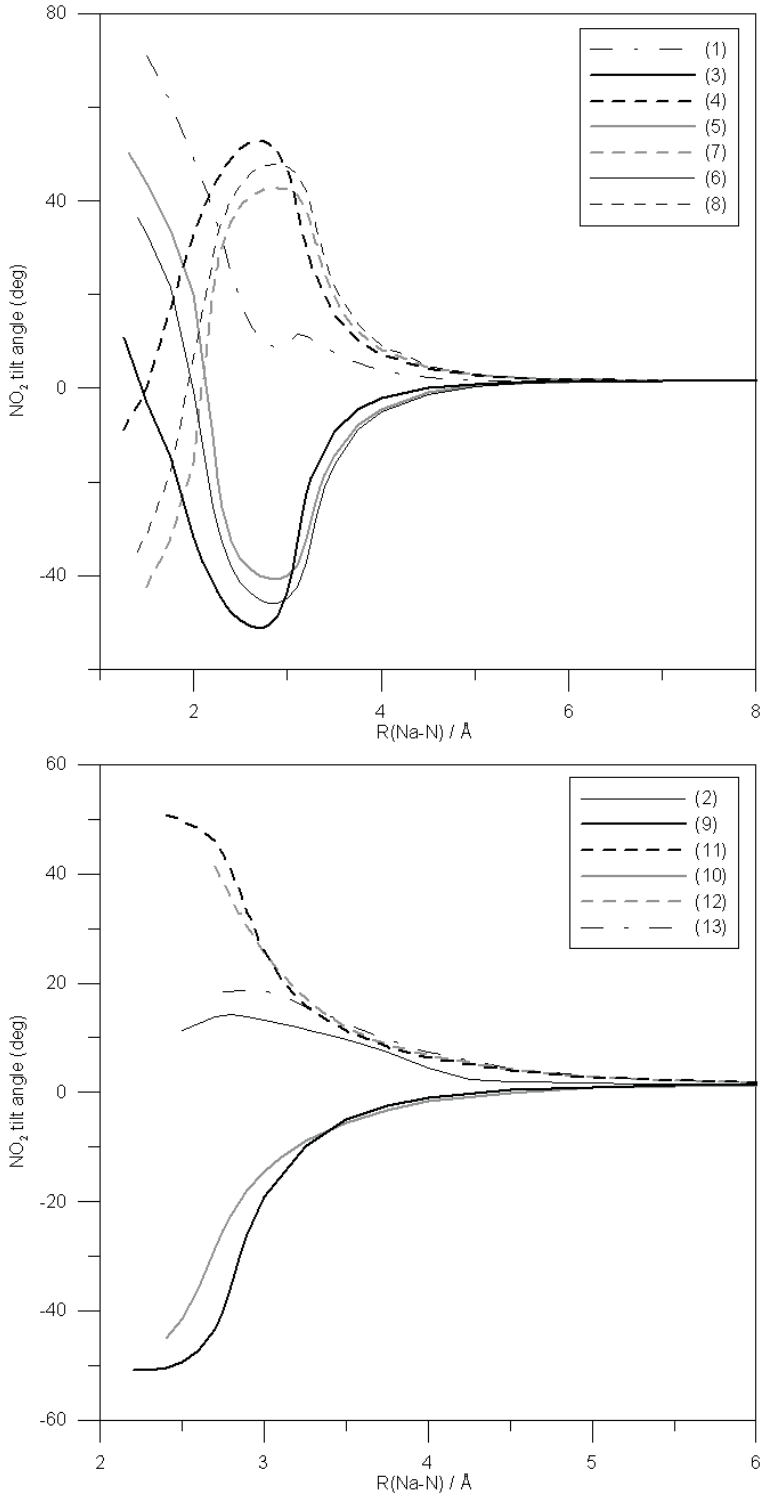

Figure 4.6.: Effect of NO_2 tilt angle with Na approach. A negative NO_2 tilt angle corresponds to that of opposite direction to isolated neutral or valence anion, namely with oxygen atoms eclipsing with the H_2 hydrogen atoms. Numbers in each legend indicate approach orientations.

are exhibited, as for direct NO_2-end attack, and charge-transfer occurs before the minimum. As the approach angle is increased from NO_2-end axial attack, the ion-pair minimum binding becomes slightly weaker, and

charge-transfer occurs at slightly shorter separations, as seen in table 4.9. Staggered approaches are again characterized by an NO_2 tilt angle inversion. Orientations (5), (6), (7) and (8) show little NO_2 tilt angle deviation from direct NO_2-end attack in figure 4.7, indicating an isotropic ion-pair formation geometry about NO_2-ended attack. For perpendicular approaches (3) and (4), the interaction potential minima are ≈ 0.8 eV less binding than the global minimum, with the eclipsed orientation now slightly more favourable. Orientation (5) shows the lowest energy ion-pair geometry, which is the closest geometry to the optimized parent ion-pair at 22.58°.

Approach (14) shows charge-transfer, however with one N-O bond becoming elongated and an NO_2 bending distortion giving breaking of C_S symmetry. This approach is most likely a source of O^- formation, which may also result from unimolecular dissociation of excited NO_2^- [2, 45].

To better visualize angular orientation dependence, the interaction potentials and Na charges at R(Na-N) = 2.75, 3.00, 3.25, 3.50 and 3.75 Å at 10° increments around a circle centred on the nitrogen atom were computed. The shortest R(Na-N) separation corresponds to complete charge-transfer for all angles, and the largest to no charge-transfer for any angle. These constant-separation curves are shown in figure 4.2 and NBO populations in figure 4.8, with an anticlockwise rotation, referenced with respect to the CH_3-end, proceeding first through eclipsed (0° to 180°) and staggered (180° to 360°) orientations. Each of the orientation interaction potentials in figures 4.3, 4.5 and 4.6 is effectively a slice through appropriate angles in figure 4.2.

Figure 4.2 shows two distinct features: the step like shape at close separation; and broad binding interaction between $\approx 70°$ and 290°. This broad well is in effect a large cone-of-acceptance (ranging $\approx 210°$) favouring charge-transfer reaction centred from the NO_2-end, including sideways approaches, and is slightly exoergic to parent ion-pair formation. For separations as close as 2.75 Å, the figure exemplifies the diffuse isotropic nature of the charge-transfer to the NO_2-end, which shows very little effect from eclipsed or staggered and NO_2 tilt inverted conformations. It would then be expected that in an experimental study, low energy (0 eV to 2 eV) collisions would show a strong preference to attack centred about the NO_2-end, yielding the parent ion-pair or channels (a) and (b). Approaches from the CH_3-end with energies below the threshold to reach charge-transfer may elastically rebound or the potential energy surface may guide the trajectory into a more optimum approach inducing vibrational and rotational energy in the products. It is emphasized that since the interaction potential in the cone-of-acceptance for all separations is (well) below that of any asymptotic channel, the Na species through ion-pair interactions plays a crucial role in both the energetics and dynamics *before and after* charge-transfer. The Na Mulliken and NBO charges for each angle and separation, shown in figure 4.8, reproduce each other's shape well and yield an inverse step interaction potential well shape. The Mulliken charge is systematically slightly below that given by the NBO scheme, by up to 0.2 e^-. Further, the less comprehensive Mulliken scheme shows some negative charge contribution on the Na atom for some orientations which is not present in the always-positive NBO scheme.

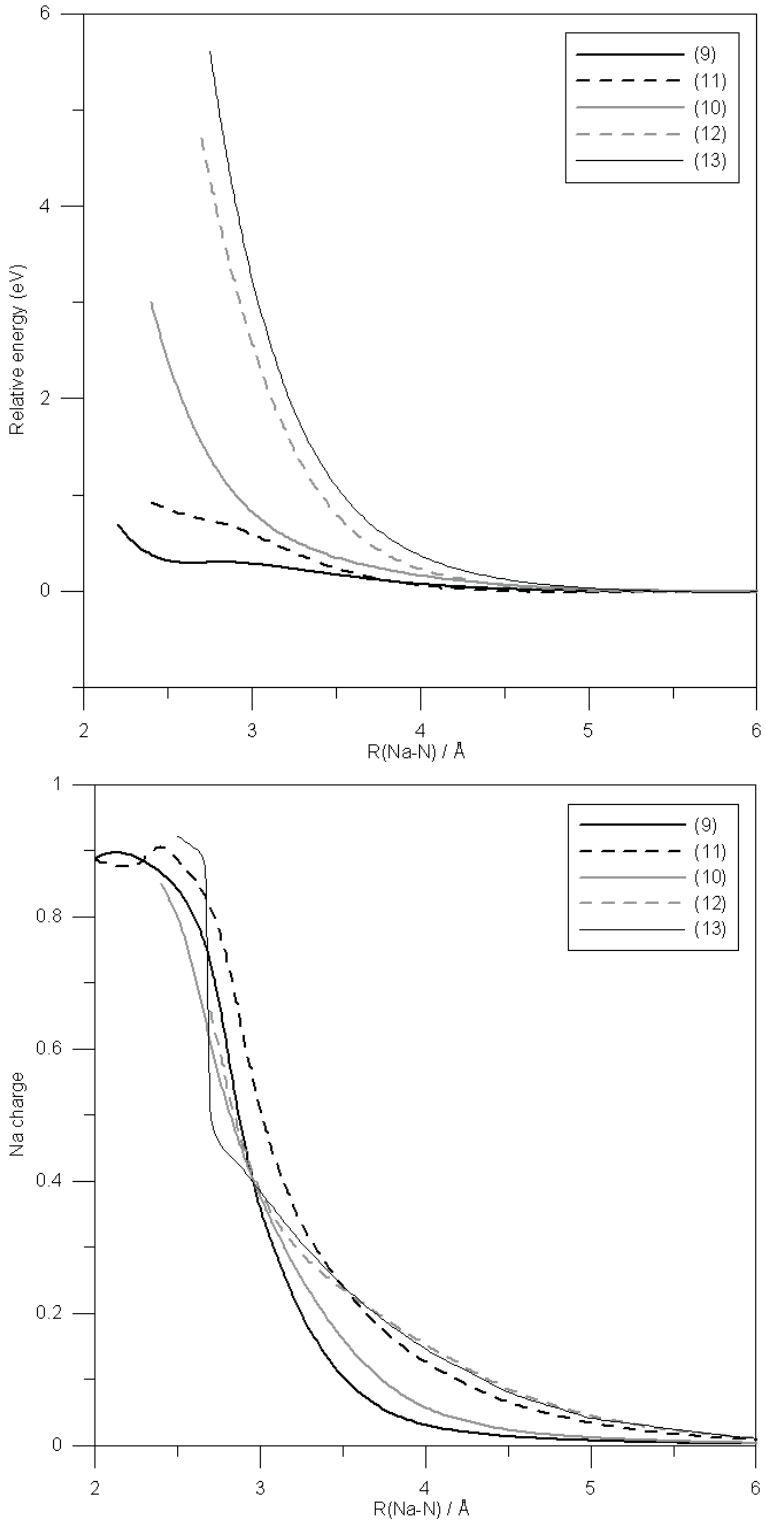

Figure 4.7.: Approach interaction potentials for attack orientations on the CH_3-side (top) and corresponding Na NBO charge (bottom). Numbers in each legend indicate approach orientations.

The Na + CH_3NO_2 reaction has generally been interpreted in terms of a crossing of the R(C-N) dissociative neutral covalent curve with the parent anion curve, providing the surface crossing in the absence of any

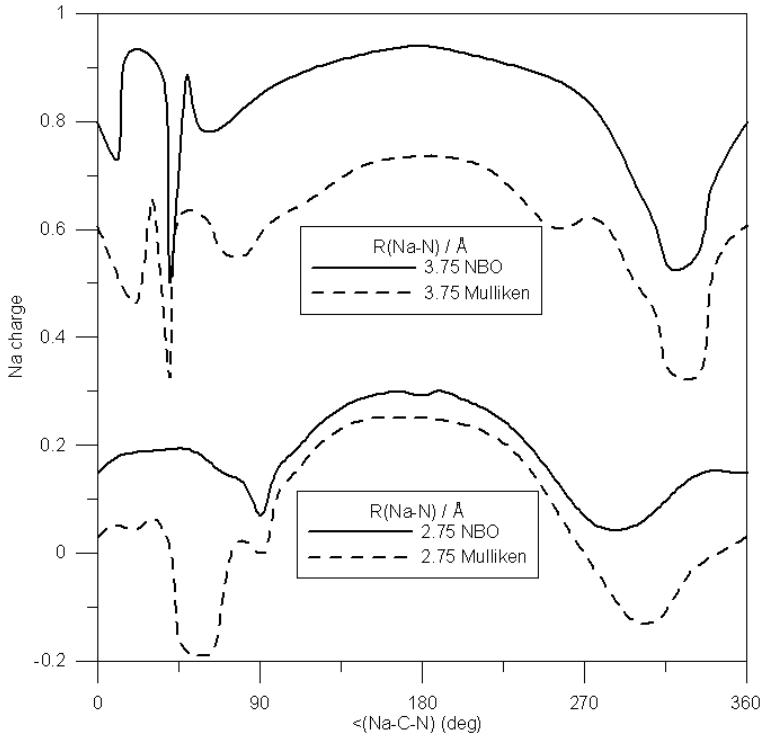

Figure 4.8.: R(Na-N) = 2.75 Å and R(Na-N) = 3.75 Å Mulliken and NBO atomic Na charges for the circular angular approaches in figure 4.2.

interaction with the Na species [3, 19]. These calculations indicate that these previous interpretations are incorrect. The Na species has a strong influence on the dynamics at the point of charge-transfer, thus facilitating reaction. This is intuitive for a reaction showing intermediate harpoon and rebound dynamics, and is also consistent with differing products observed in electron-impact negative ion mass spectra in comparison to the ion species observed in Brooks *et al.* [21] experimental charge-transfer processes [22, 46]. Gutsev *et al.* [9] also reports that direct dissociation requires a consideration of more than just R(C-N) elongation, with R(N-O), R(C-H) lengths and ∠(HCH) angles showing significant change on dissociation, and with the CH_3 hydrogen umbrella inverting before becoming planar at larger separation.

In general, these results support the theory that the electron withdrawing nature of the NO_2 group is crucial for charge-transfer. The process is relatively spherical in nature around the N atom, and the 'steric' CH_3 group plays a charge-transfer minor role, but plays an ion-pair formation significant role [45]. One feature of the present calculations which further confirms some intermediate harpoon-rebound type dynamics, is the formation of the parent anion or ion-pair, yet the reaction exoergicity is significantly less than the interaction potential required for C-N bond dissociation.

Calculations were performed at the B3LYP optimized geometries with the CCSD(T)/6-311++G(2d,p) level of theory to visualize the molecular orbitals. These orbitals show the same ordering as the lesser correlated MP2//aug-cc-pVTZ orbitals reported by Brooks *et al.* [21], or for the isolated neutral, a LUMO Rydberg type

orbital from the CH_3-end. Tilting the neutral NO_2 group to the optimized anion geometry yields a frontier orbital energy swapping to give a predominantly anti-bonding π^*_{NO} LUMO, which then becomes the singly occupied HOMO of the isolated anion. Calculations on the NO_2-end optimized parent ion-pair revels this also to be the case for the smaller tilt angle of 19.74° both in the field and absence of the Na^+ core. The Kohn-Sham orbitals for each orientation show charge-transfer to occur from the Na 3s orbital to the π^*_{NO} orbital at each respective orientation charge-transfer threshold.

4.4. Dipole-bound states

Isolated CH_3NO_2 exhibits a large experimental dipole moment of 3.46 D [39], due to the electron withdrawing NO_2 group with internal charge-separation. This is calculated to be 3.60 D at the B3LYP//6-311++G(3df,3pd) level of theory, in good agreement in good agreement with experiment, whereas MP2 theory overestimates this by 22%. Molecules with large dipole moments may form dipole-bound anion states, where the electron is weakly captured at relatively large separation with little rearrangement from the neutral geometry [47,48]. This process has been considered to act as a possible 'doorway' state to formation of the valence-bound anion [11,15,15,30] although Brooks *et al.* [21] find no evidence that the dipole-bound state played any major role in the title reaction. Intuitively it would be expected that a large asymmetry to the 'positive' or CH_3-end of the dipole would result if the dipole-bound state played a dominant role. Such a species could arise from occupation of the neutral CH_3-ended Rydberg type LUMO. However, in the presence of the Na^+ core, and as seen in figure 4.3, this appears to play no major role. The existence of the small potential well centred at R(Na-N) = 4.5 Å for only the NO_2-end approach in figure 4.3 is attributed to the presence of an ion-dipole bound state. This yields a small diabatic (vertical) binding interaction in the first excited state curve of 0.21 eV with respect to the valence curve. This species was optimized, with parameters in table 4.7, to yield an adiabatic binding energy of 26 meV. Gutsev and Bartlett [30] report calculations on the interaction of the valence and dipole anions in the absence of any metal species, proposing that in the absence of the Na^+ core, the $CH_3NO_2^-$ dipole-bound state may develop into the valence-bound state for tilt angles >|20°|. The diabatic and adiabatic dipole-bound states calculated in this work show a NO_2 tilt angle of 2.50° and 0.98° respectively, which is a ≈ 0.7° increase and ≈ 0.6° decrease relative to the neutral. From figure 4.7, the tilt angle does not reach |20°| until after charge-transfer forming the valence-bound anion, which is well after this ion-dipole state, and the valence-bound anion is formed with an NO_2 tilt angle increase of ≈ 11°. In the region of the dipole minimum, the ground state Na Mulliken and NBO populations begin to show the onset of a positive charge from zero charge. In contrast, as shown in figure 4.3, this first excited state well Na NBO charge decreases rapidly from a charge of 0.99 to 0.29 or 0.22 adiabatic, and then as the separation is further decreased the charges start to become more reactant in nature until the expected valence charge-transfer occurs. Compton *et al.* [11] experimentally determined the vertical electron binding energy to be 12 ± 3 meV, and Gutsev and Bartlett [30] determine this to be 13 meV at the EA-EOM-CCSD//6-311++G(d,p) (and EA-EOM-CCSD//6-311++G(d,p)+6*sp* where 6*sp* denotes augmentation of additional diffuse functions) level of theory in accordance

with Koopmans' theorem. The calculated vertical electron affinity of -0.73 eV here is in excellent agreement with the experimental value of -0.72 eV reported by Walker and Fluendy [3]. Further, the ion-dipole calculated binding energies are considerably larger than the experimental value of 12 ± 3 meV, due to the presence of the positive Na core, which is emphasized, occurs from the 'negative' or NO_2-end rather than the 'positive' or CH_3-end. The performance of TDDFT with insufficient non-local Hartree-Fock exchange for charge-transfer should not rigidly interpret this binding/excitation energy. Suess *et al.* [15] state that the presence and nature of the alkali ion core after charge-transfer to form a dipole-bound state may account for the n-dependence of $CH_3NO_2^-$ formation, where n is the principle quantum number for excited alkali earth atoms. As n increases, electron capture occurs at large separation and Coulombic interactions are decreased. With the existence of the ion-dipole bound state, it is anticipated that as n is increased to an ionization energy of approximately equal to the ion-dipole state binding energy, then reaction will start to show such effects for glancing collisions. Suess *et al.* [15] also state that if dipole-bound states are to act as doorway states to valence-bound states, that the time scale for coupling with the valence-bound state must be less than the duration of their K^+ and $CH_3NO_2^-$ ion interaction, typically 10-50 ps, which is longer than a typical vibrational period. For the low energy gas-phase single-collision conditions considered here, this requirement would not be met.

It is therefore proposed that such a dipole-bound state may act as a doorway state to charge-transfer perhaps for free electrons, with its extent depending on translational energy, and probably with lower energy collisions utilizing this channel. However, in the presence of the metal core, such a dipole-bound doorway state would not play a role in overall charge-transfer reaction. The presence of the metal core both promotes and for NO_2-end attack holds the charge-transfer NO_2 tilt angle at less than that of the isolated valence anion, and therefore would alter the coupling between dipole and valence-bound states compared to free electron capture.

4.5. Cross-sections

The parent anion interaction potential asymmetry arguments relate to cross-section. Charge-transfer occurs at larger separation in general from an NO_2-end approach than from a CH_3-end approach. For low energy collisions, this would perhaps increase steric asymmetry to reaction to the NO_2-end further. This was earlier tentatively proposed to play a role in the two lowest energy collision measurements of Brooks *et al.* [21], where experimentally some separated ion-pairs may be detected. A basic model has been constructed in this work, with no energy dependence, to determine an approximate reaction cross-section to charge-transfer, similar to the polarizability cross-section model for electron-impact ionization by Vallance *et al.* [49]. This model involves constructing a series of circles incorporating the charge-transfer region as the boundary surface for each orientation, and by averaging over all orientations in figure 4.1, an average area or cross-section is calculated at 30 $Å^2$. Lowering the Na NBO charge-transfer threshold to +0.25 increases this cross-section estimate to 40 $Å^2$. These can be interpreted with knowledge of the interaction potential to obtain estimates of orientation dependent cross-sections. The two principally of interest are NO_2-end and CH_3-end approaches; achieved by

averaging the contributions for the cross-section determination at each end (i.e. 90° cones), yielding values of 34 and 27 Å^2, respectively, or 41 and 36 Å^2 for the +0.25 NBO charge-transfer threshold. These both give an asymmetry factor G ≈ 0.1, which is close to the lowest energy (5.14 eV) steric asymmetry factors reported by Brooks *et al.* [21] for CH_3NO_2. Such an energy would be more than sufficient to surmount the barrier to CH_3-ended reaction. The cross-section arguments from this model are only relevant for channel (ii) at asymptotic reaction energies, or ≈ 5 eV. Herm and Hershbach [17] experimentally *estimated* the charge-transfer reaction cross-section to be on the order of ≈ 100 Å^2. Although disagreement exists, both the Herm and Hershbach [17] and calculated estimate here do show that reaction charge-transfer, and bond formation, occurs at separations typically on the order of 1.5 to 2.5 times normal covalent C-C separations.

4.6. Potassium attack

Calculations on the interaction potential between K atoms and NO_2-end axial attack, closely parallel those for Na, and experimentally, K and Cs reaction collision data closely parallels that of Na [17, 18, 21, 22]. The calculated K + NO_2-end interaction potentials are summarized in tables 4.7, 4.8, and 4.9, and reveal that charge-transfer occurs at a 0.65 Å larger separation than with Na. Further, for a given R(K-N) separation close to the the charge-transfer separation, interaction energies are approximately 0.50 eV more binding, and the K parent ion-pair minimum is 0.10 eV more stable than that for Na. The more diffuse nature of K atoms and lower ionization potential results in slightly higher exoergic parent ion-pair reaction; however the relative difference between Na and K energy minima is not reflected by just the difference between ionization potentials. K attack yields a larger R(K-N) parent ion-pair separation by 0.33 Å at 2.81 Å for K vs. 2.48 Å for Na. Rough correlation with appearance potentials for NO_2^- formation from the experiments of Brooks *et al.* [21, 22] show that the difference between Na and K is ≈ 0.15 eV, in reasonable agreement with the calculated parent ion-pair binding energy difference of 0.10 eV, assuming a constant reaction BDE(CH_3-NO_2). Brooks *et al.* [22] observe a strong steric asymmetry (G ≈ 0.5) to formation of NO_2^- from the CH_3-end. It is therefore tentatively predicted that free NO_2^- asymmetry, as for Na, will preferentially result from the CH_3-end (positive) at low energies since that formed at the NO_2-end is bound as the ion-pair. This NO_2^- asymmetry is expected to be more pronounced at low energies due to a lower interaction potential (barrier) at the charge-transfer separation for CH_3-end attack, and the stronger NO_2-end ion-pair formation. The K + NO_2-end calculations also reveal that the NO_2 tilt angle is half that for the analogous Na reaction at the charge-transfer threshold, indicating the geometry is more neutral (harpoon) in nature, which is intuitively expected for a more electropositive alkali earth metal.

4.7. Conclusions

Overall, the charge-transfer reaction dynamics can be summarized in the scheme, for M = Na:

$M + CH_3NO_2 \longrightarrow M^+CH_3NO_2^- \longrightarrow M^+ + CH_3NO_2^- \longrightarrow NO_2^- M^+ + CH_3$ (0-5 eV collisions)

$\longrightarrow M^+ + NO_2^- + CH_3$ (>5 eV collisions)

Other higher energy channels may open which include O^- formation. The results from these calculations on the orientation dependence of the charge-transfer dynamics for $Na + CH_3NO_2$ can be summarized into five key points:

(1) The B3LYP//6-311++G(3df,3pd) level of theory reproduces the adiabatic electron affinity of CH_3NO_2 well, and gives geometries and frequencies in excellent agreement with experimental values.

(2) Interaction potential analysis shows the reaction to exhibit steric or orientation dependence to $CH_3NO_2^-$ formation and to a lesser extent NO_2^- formation, which are both more important at lower reaction energies. The NO_2-end approaches show interaction potentials to be binding and exoergic in nature, and larger charge-transfer separations are more favourable for low energy reaction. These orientations form exoergic $CH_3NO_2^-Na^+$ and $NO_2^-Na^+$ ion-pairs, that crucially facilitate reaction. The cone-of-acceptance for the NO_2-end reaction is large, with an internal angle of up to 200°, and shows a sharp cut-off.

(3) The CH_3 group acts as a steric blocking group, preventing some ion-pair formation with the charge-transfer active NO_2 group, and providing a barrier to reaction for CH_3-end approaches. Since no bound ion-pair exists from direct CH_3-attack, then free $CH_3NO_2^-$ may be detected for energies below asymptotic ion-pair separation, since Coulombic interactions are much weaker.

(4) A weak Na^+ ion-dipole-bound anion state exists from direct axial attack at the NO_2-end, however is not expected to play a role in the orientation dynamics or overall reaction cross-section.

(5) Reaction generally occurs at large separations for all orientations, of 1.5-2.5× larger than typical covalent bonding separations, and the Na core plays a crucial role in reaction dynamics. $K + NO_2$-end attack is slightly longer ranged but apparently parallels the reaction of Na.

Future studies of this type should ideally incorporate, with BSSE corrections, further diffuse basis functions when charge-transfer is expected to occur at large separation.

4.8. Post-publication comments

This study was started and in major part completed and interpreted before a version of GAMESS-US was released that incorporated some DFT functionals that allowed better description of Hartree-Fock exchange.

Several months after this work was published an article appeared [50] that again experimentally determined an electron affinity for nitromethane that was smaller than all previous determinations. In the following chapter this value has been reproduced with accurate multi-reference calculations. Some tentative calculations reveal that there are no serious ramifications for the above Na + CH_3NO_2 study. This may be argued by the fact that the difference would be less that 0.2 eV, which is small compared to the overall energetics considered. Secondly, the fact that if the above DFT calculations do have an incorrect electron affinity, this is a positive overestimate rather than underestimate, or much worse, negative. A slightly more positive result for the harpoon process will still reproduce harpoon type dynamics. The UCSC supercomputer had not been installed at the time of this study, and the calculations reported took approximately six months of continuous processing time on a personal dual core 2.8 GHz Pentium D system.

References

[1] J. F. Arenas, J. C. Otero, D. Peláez, and J. Soto. *J. Chem. Phys.*, 122:084324, 2005.

[2] F. Sun, G. P. Glass, and R. F. Curl. *Chem. Phys. Lett.*, 337:72, 2001.

[3] I. C. Walker and M. A. D. Fluendy. *Int. J. Mass Spectrom.*, 205:171, 2001.

[4] M. R. Manna and L. E. Fried. *J. Phys. Chem. A*, 102:9884, 1998.

[5] J. F. Arenas, J. C. Otero, D. Peláez, J. Soto, and L. Serrano-Andrés. *J. Chem. Phys.*, 121:4127, 2004.

[6] J. F. Arenas, J. C. Otero, D. Peláez, and J. Soto. *J. Chem. Phys.*, 119:7814, 2003.

[7] W. F. Hu, T. J. He, D. M. Chen, and F. C. Liu. *J. Phys. Chem. A*, 106:7294, 2002.

[8] M. T. Nguyen, H. T. Le, B. Hajgató T. Veszprémi, and M. C. Lin. *J. Phys. Chem. A*, 106:4286, 2003.

[9] G. L. Gutsev, P. Jena, and R. J. Bartlett. *J. Chem. Phys.*, 110:3549, 1999.

[10] A. M. Wodtke, E. J. Hintsa, and Y. T. Lee. *J. Phys. Chem.*, 90:3549, 1986.

[11] R. N. Compton, H. S. Carman Jr., C. Desfrancois, H. Abdoul-Carmine, J. P. Schermann, J. H. Hendricks, S. A. Lyapustina, and K. H. Bowen. *J. Chem. Phys.*, 105:3472, 1996.

[12] J. A. Stockdale, F. J. Davis, R. N. Compton, and C. E. Klots. *J. Chem. Phys.*, 60:4279, 1974.

[13] F. Lecomte, S. Carles, and C. Desfrancois. *J. Chem. Phys.*, 113:10973, 2000.

[14] T. Somerfield. *Phys. Chem. Chem. Phys.*, 4:2511, 2002.

[15] L. Suess, R. Parthasarathy, and F. B. Dunning. *Chem. Phys. Lett.*, 119:9532, 2003.

[16] Y. Liu, M. Cannon, L. Suess, F. B. Dunning, V. E. Chernov, and D. A. Zon. *Chem. Phys. Lett.*, 433:1, 2006.

[17] R. R. Herm and D. R. Herschbach. *J. Chem. Phys.*, 52:5783, 1970.

[18] C. M. Sholeen and R. R. Herm. *J. Chem. Phys.*, 65:5398, 1976.

[19] R. F. M. Lobo, A. M. C. Moutinho, K. Lacmann, and J. Los. *J. Chem. Phys.*, 95:166, 1991.

[20] M. A. D. Fluendy and S. Lunt. *Mol. Phys.*, 16:1007, 1983.

[21] P. R. Brooks, P. W. Harland, and C. E. Redden. *J. Am. Chem. Soc.*, 128:4773, 2006.

[22] P. R. Brooks, P. W. Harland, and C. E. Redden. *J. Phys. Chem. A*, 110:4697, 2006.

[23] W. D. Taylor, T. D. Allston, M. J. Moscato, G. B. Fazekas, R. Kozlowski, and G. A. Takacs. *Int. J. Chem. Kinetics*, 12:231, 1980.

[24] D. R. Herschbach. *Ad. Chem. Phys.*, 10:319, 1966.

[25] P. R. Brooks and S. A. Harris. *J. Chem. Phys.*, 117:4220, 2002.

[26] M. J. Frisch, G. W. Trucks, H. B. Schlegel, G. E. Scuseria, M. A. Robb, J. R. Cheeseman, J. A. Montgomery, Jr., T. Vreven, K. N. Kudin, J. C. Burant, J. M. Millam, S. S. Iyengar, J. Tomasi, V. Barone, B. Mennucci, M. Cossi, G. Scalmani, N. Rega, G. A. Petersson, H. Nakatsuji, M. Hada, M. Ehara, K. Toyota, R. Fukuda, J. Hasegawa, M. Ishida, T. Nakajima, Y. Honda, O. Kitao, H. Nakai, M. Klene, X. Li, J. E. Knox, H. P. Hratchian, J. B. Cross, V. Bakken, C. Adamo, J. Jaramillo, R. Gomperts, R. E. Stratmann, O. Yazyev, A. J. Austin, R. Cammi, C. Pomelli, J. W. Ochterski, P. Y. Ayala, K. Morokuma, G. A. Voth, P. Salvador, J. J. Dannenberg, V. G. Zakrzewski, S. Dapprich, A. D. Daniels, M. C. Strain, O. Farkas, D. K. Malick, A. D. Rabuck, K. Raghavachari, J. B. Foresman, J. V. Ortiz, Q. Cui, A. G. Baboul, S. Clifford, J. Cioslowski, B. B. Stefanov, G. Liu, A. Liashenko, P. Piskorz, I. Komaromi, R. L. Martin, D. J. Fox, T. Keith, M. A. Al-Laham, C. Y. Peng, A. Nanayakkara, M. Challacombe, P. M. W. Gill, B. Johnson, W. Chen, M. W. Wong, C. Gonzalez, and J. A. Pople. Gaussian 03, Revision C.02. Gaussian, Inc., Wallingford, CT, 2004.

[27] R. G. A. R. Maclagan. *Chem. Phys. Lett.*, 373:586, 2003.

[28] R. G. A. R. Maclagan. *J. Phys. Chem. A*, 108:11779, 2004.

[29] A. P. Cox and S. J. Waring. *J. Chem. Soc. Faraday Trans.*, 68:1060, 1972.

[30] G. L. Gutsev and R. J. Bartlett. *J. Chem. Phys.*, 105:8785, 1996.

[31] B. S. Jursic. *Int. J. Quant. Chem.*, 64:263, 1997.

[32] D. Gorse, D. Cavagnat, M. Pesquer, and C. Lapouge. *J. Phys. Chem.*, 97:4262, 1993.

[33] M. R. Manna and L. E. Fried. *J. Phys. Chem. A*, 130:9349, 1999.

[34] A. J. Wells and Jr. E. Bright Wilson. *J. Chem. Phys.*, 9:314, 1941.

[35] E. C. M. Chen and W. E. Wentworth. *J. Phys. Chem.*, 87:45, 1983.

[36] R. N. Compton, P. W. Rienhardt, and C. D. Cooper. *J. Chem. Phys.*, 68:4360, 1978.

[37] E. P. Grimsrud, G. Caldwell, S. Chowdhury, and P. Kebarle. *J. Am. Chem. Soc.*, 107:4627, 1985.

[38] E. C. M. Chen, N. Welk, E. S. Chen, and W. E. Wentworth. *J. Phys. Chem. A*, 103:9072, 1999.

[39] D. R. Lide, editor. *CRC Handbook of Chemistry and Physics*, volume 77, chapter 10, page 214. CRC Press, Cleveland, OH, 1996.

[40] A. Dreuw, J. L. Weisman, and M. Head-Gordon. *J. Chem. Phys.*, 119:2943, 2003.

[41] M. J. G. Peach, P. Benfield, T. Helgaker, and D. J. Tozer. *J. Chem. Phys.*, 128:044118, 2008.

[42] Y. Zhao and D. G. Truhlar. *J. Phys. Chem. A*, 110:13130, 2006.

[43] Y. Zhao and D. G. Truhlar. *Acc. Chem. Res.*, 41:157, 2008.

[44] M. W. Schmidt, K. K. Baldridge, J. A. Boatz, S. T. Elbert, M. S. Gordon, J. H. Jensen, S. Kosecki, N. Matsunaga, K. A. Nguyen, S. J. Su, T. L. Windus, M. Dupuis, and J. A. Montgomery. *J, Comput. Chem.*, 14:1347, 1993.

[45] D. A. Kleier and M. A. Lipton. *J. Mol. Struct. (THEOCHEM)*, 109:39, 1984.

[46] A. Di Domenico and J. L. Franklin. *Int. J. Mass Spectrom. Ion Phys.*, 9:171, 1972.

[47] O. H. Crawford. *Mol. Phys.*, 20:585, 1971.

[48] O. H. Crawford and W. R. Garrett. *J. Chem. Phys.*, 66:4968, 1977.

[49] C. Vallence, P. W. Harland, and R. G. A. R. Maclagan. *J. Phys. Chem.*, 110:15021, 1996.

[50] C. L. Adams, H. Schneider, K. M. Ervin, and J. M. Weber. *J. Chem. Phys.*, 130:074307, 2009.

5. On the Electron Affinity of Nitromethane (CH_3NO_2)

This chapter provides a high-level systematic computational-based determination of the adiabatic valence electron affinity of nitromethane to resolve apparent ambiguity on an accepted literature value, that was first noted in the foregoing chapter. This chapter is a reproduction of an accepted article:

James N. Bull, Robert G. A. R. Maclagan, Peter W. Harland, *Journal of Physical Chemistry A*, 114 (2010) 3622

In the work described in this chapter, Assoc. Prof. Robert Maclagan provided discussions in the computational chemistry and methods, and Prof. Peter Harland provided discussions on various literature experimental techniques. Computing facilities for GAMESS-US calculations were provided by the UCSC BlueFern (Blue Gene/L) facility.

Overview

A high-level systematic computational study is presented on an accurate value for the adiabatic valence electron affinity of nitromethane, CH_3NO_2, to resolve literature disagreements in theoretical and experimental reported values. Density functional methods with triple-zeta quality basis sets gave good fortuitous agreement with early experimental determinations, while single-reference wave function based methods employing up to CCSD(T) gave poor or fortuitous agreement depending on the experimental reference value. Density functional theory methods in general cannot accurately describe electron attachment from the result of unphysical electron self-interaction. It was found that multi-reference methods with aug-cc-pVTZ or similar basis sets are required to converge to an experimental value. The highest level of theory 3S-MCQDPT2 and 7S-MCQDPT2 calculations with an aug-cc-pVTZ quality basis description yield values of 0.188 eV and 0.176 eV (0.170 eV with polynomial extrapolation), in excellent agreement with the most recent experimental value of 0.172 ± 0.006 eV. CCSD(T)//aug-cc-pVTZ provides a fortuitously reasonable description. The isolated dipole-bound anion binding energy is calculated to be 7-8 meV.

5.1. Introduction

Nitromethane, CH_3NO_2, is the simplest alkyl species containing the nitro (-NO_2) functional group. It is known to possess a small positive adiabatic valence electron affinity, EA_{ad}, and form a dipole-bound anion where an electron is captured at the positive end of the dipole field with little geometrical rearrangement from the neutral. [1,2] In the gas phase, formation of the valence anion, $CH_3NO_2^-$, was first observed and characterized through collisions of Rydberg-excited Ar and Kr atoms. [3] There have subsequently been six experimental attempts to determine the electron affinity, albeit one a redetermination of existing data. [1,4–8] The new data have resulted in disagreements in the literature on a definitive experimental value, as outlined in table 5.1.

Table 5.1.: Summary of experimental adiabatic valence electron affinity determinations, in eV, for CH_3NO_2, existing in two discrete groupings.

Experimental technique	$\boldsymbol{EA_{ad}}$
Crossed molecular beam thresholds[a] [4]	0.44/0.35 ± 0.20
Steady-state electron capture [5]	0.45 ± 0.08
Pulsed high-pressure EI-MS [6]	0.49 ± 0.11
Steady-state electron capture redetermination [7]	0.50 ± 0.10
Laser photodetachment photoelectron spectroscopy[b] [1]	0.26 ± 0.08
Velocity map photoelectron imaging[b] [8]	0.172 ± 0.006

[a]Two experimental values correspond to the use of different alkali metal charge-transfer reagents, with the larger error incorporating both values.
[b]Performed under collision geometry relaxation conditions.

The experimental data for the electron affinity of CH_3NO_2 can be arranged into two groups, four averaging 0.47 eV, all within respective experimental errors, and two at 0.26 ± 0.08 eV and 0.172 ± 0.006 eV, the latter being the most recent determination. The former of these two involved extrapolation of a photoelectron vibrational progression to the last resolvable spectral peak, with this value appearing to be that most widely cited and employed in subsequent calculation at this time. The uncertainty, ranging the value between 180-340 meV, was assigned to allow for one further nonresolvable spectral peak. This value has been suggested to possibly represent an excited state of the anion. [7] The most recent value of 0.172 ± 0.006 eV involved low-energy (higher resolution) photoelectron imaging spectroscopy in an attempt to resolve congestion at the band head. Photoelectron methods are in general not ideally suited to adiabatic measurements but are very well suited to measurement of vertical electron processes, which are the most intense spectral peaks in a full progression. All reported experimental values include errors that in major part do not overlap the two groups. In this chapter, a series of high level single-reference and multi-reference calculations in order to resolve this inconsistency and the apparent lack of convergence of supporting *ab initio* calculations.

From a theoretical viewpoint, assuming the Born-Oppenheimer approximation, the adiabatic valence electron affinity, EA_{ad}, for a molecular species, where ΔZPV is the molecular zero point energy correction, is given as:

$$\begin{aligned} EA_{ad} &= E(neutral) - E(anion) - \Delta ZPV \\ \Delta ZPV &= ZPV(anion) - ZPV(neutral) \end{aligned} \tag{5.1}$$

The most comprehensive previous theoretical investigation of the electron affinity for CH_3NO_2 was carried out by Gutsev *et al.* [2, 9], where experimental comparison was made *only* to the Compton *et al.* [1] value of 0.26 ± 0.08. This study was performed using coupled-cluster, and HFDFT methods. Their DFT-type calculation, denoted HFDFT, is a Hartree-Fock density functional theory providing self-interaction density corrections in an attempt to improve anion description. [10] Their findings showed that CCSD (0.055 eV) and CCSD(T) (-0.058 eV) methods with the 6-311++G(d,p) basis set gave very poor agreement, with the latter being negative. Extension to the 6-311++G(2d,2p) basis set improved these values by ≈ 50-60%, yet they were still in poor agreement with the CCSD value at 0.131 eV. A hybrid basis set designed for identification of dipole-bound states, containing the addition of seven *sp* diffuse functions to a 6-311++G(d,p) valence, gave agreement within the lower bound of experimental error with the CCSD (0.192 eV) method, and would apparently be in reasonable agreement with the most recent Adams *et al.* [8] measurement at 0.172 ± 0.006 eV. Of the basis sets employed, CCSD(T) electron correlation always yielded values smaller that CCSD counterparts. The HFDFT(B3LYP)//6-311++G(2d,2p) level of theory yielded reasonable (0.223 eV) but still lower-bound agreement, and MP2 (≤ -0.215 eV) methods always performed exceptionally poorly. Surprisingly, their basis set designed to describe the dipole-bound anion provides the apparent closest agreement, yet is not designed to provide a valence description - this may be fortuitous. For a species with a high degree of electron delocalization, one would expect that polarization functions would be important for an accurate description. Further, it must be noted that without ΔZPV corrections, many of these calculations yield negative electron affinities. Three concerns arise: an inadequate valence basis set, shown by the lack of apparent convergence on addition of extra polarization functions; failure of a single-reference wave function to accurately describe the species; comparison with an individual and perhaps incorrect experimental value.

It is useful to first consider nitrogen dioxide, NO_2, which is known to require multi-configurational wave functions, [11, 12] and references therein, since the -NO_2 group orbitals play the dominant role in CH_3NO_2 electron capture, with associated geometrical changes. [2, 11–15] A Lewis-type interpretation of NO_2 shows resonant charge-separation in order to preclude each atom from exceeding the octet rule. Acceptance of one electron forms a closed-shell NO_2^- state, completing each atoms octet and yielding a positive valence electron affinity. Alternatively, NO_2 may σ-bond with a methyl radical, $\cdot CH_3$, forming closed-shell CH_3NO_2. Methyl nitrite, or CH_3ONO, is also a stable species and has been calculated to be only ≈ 2 kcal mol^{-1} higher in energy, and in addition a $HOCH_2NO$ species may exist that has tentatively been calculated to be ≈ 2 kcal mol^{-1} *lower* in energy than CH_3NO_2. [15] Neither of these two latter species are considered here since experimental gas phase vibrational frequencies for CH_3NO_2 are in excellent agreement with calculations reported herein. Hartree-Fock NO_2 and NO_3 descriptions suffer from symmetry breaking in the wave function where a lower or nearly degenerate energy can be obtained by breaking a higher symmetry. [11,12,16–18] UHF or ROHF [19] wave functions tend to yield orbital localization over resonance, and multi-configurational wave functions with high levels of static (i.e. large active space) and dynamic electron correlation overcome spatial symmetry breaking and yield a correct description. [18] For NO_2, the nonsymmetry breaking active space has been established to be CASSCF(13,10). [11] Of interest, DFT methods are usually resistant to symmetry breaking, and it has

been shown by Sherrill *et al.* [20] that an increase in the extent of HF exchange (from functional) may promote symmetry breaking. Symmetry breaking considerations for CH_3NO_2 are most likely small, nevertheless, they are ideally considered for the -NO_2 group on electron attachment since the anion geometry is significantly different from the neutral, and the O-N-O (Walsh type) bond angle may change with electron detachment. [11]

There have been several previous studies indicating the importance of multi-configurational wave functions in the accurate description of the -NO_2 group in CH_3NO_2 dynamics. [15, 20–25] Curve crossings owing to near degeneracy with slight C-N bond stretching on dissociation indicate that π to π^* configurations become more important on electron capture, [20–22] to give reasonable description of $CH_3NO_2 \rightarrow CH_3ONO$ rearrangements, [15] photodynamics and intersystem crossings, [23–25] and anion dissociation dynamics. [14] Calculations have also shown dynamic electron correlation to be important for a description of the neutral, [22] and in accord with NO_2, a CASSCF(14,11) space to be important for wave functions free of symmetry breaking for dissociation. This large active space includes the σ_{CN*} orbital, which is important for dissociation. The importance of multi-configurational and dynamical electron correlation has also been shown to be important for CH_3ONO which readily interconverts with CH_3NO_2. [26] MS-CASPT2 calculations indicate that the closely related anionic CH_3ONO^- species is not stable (negative EA_{ad}), [14] in contrast to the single-reference (inappropriate) MP2 and CC results of Gutsev *et al.* [9], which yielded a substantially positive EA_{ad} well above CH_3NO_2 at 0.60 eV HFDFT, 0.27 eV MP2, 0.26 eV CCSD, and 0.30 eV CCSD(T). Arenas *et al.* [14] also report the highest literature level of theory electron affinity calculation with the MS-CASPT2//ANO-L method using a CASSCF(15,11) reference to be 0.18 eV with ΔZPV correction. Unfortunately, as discussed below, this ΔZPV correction is incorrect. They also state that removal of f-type polarization reduces the value by $\approx$ 0.02 eV, indicating importance of high-order angular momentum functions in the -NO_2 group description. MS-CASPT2 provides systematic improvement of CASPT2 by addition of further CASSCF reference states. [27] All literature calculations mentioned above indicate electron capture to involve a π^* orbital.

Any wave function calculation providing an accurate electron affinity for CH_3NO_2 should therefore be of multi-configurational nature. Such calculations are very computationally expensive. However, density functional theory (DFT) methods are computationally inexpensive and inherently include some multi-configurational character. Unfortunately, traditional Kohn-Sham DFT (KSDFT) for anions exhibits unphysical electron self-interaction, altering the energy. [28] In addition, KSDFT employing traditional functionals are known to be less accurate when describing π electrons than for σ electrons. [29] Nevertheless, DFT performance for several common functionals will be evaluated.

5.2. Computational method

All DFT, Moller-Plesset perturbation theory, and coupled cluster calculations have been performed using the Gaussian computational package. [30] All multi-configurational and multi-reference calculations were performed

using the GAMESS-US package, [31] as were MP2//aug-cc-pVQZ optimization calculations.[1] Geometrical optimizations and single-point energy calculations at B3LYP geometries were performed for most DFT functional and single-reference wave function methods, and all multi-configurational calculations were performed at the B3LYP geometry as outlined later.

The DFT functionals trialed here are of hybrid or meta-GGA type, which include portions of exact HF exchange to minimize self-interaction. The functionals employed, with the extent of exact HF exchange in parentheses, are: B3LYP (20%); X3LYP (21.8%); TPSS (0%); TPSSh (10%); from the M06 suite of functionals by Truhlar *et al.* [32,33], M06-L (0%), M06 (27%), M06-2X (54%), and M06-HF (100%); and BMK (42%). The BMK functional has been shown to on average perform better than B3LYP and TPSSh. [34] Of the M06 suite, based on average performance, the M06 and M06-2X functionals would be expected to be the most applicable here by consideration of performance in reported test sets. In addition, the recent and more comprehensive double-hybrid B2PLYP [34] and MPW2PLYP [35] functions were trialed that include exact HF exchange with MP2 type correlation, and in general outperform B3LYP.

Construction of the CASSCF space follows Schaefer *et al.* [11] and the detailed description by Arenas *et al.* [14]. Briefly, this involves: C_{1s}, N_{1s}, O_{1s}, O_{2s}, and σ_{CH} as core orbitals, with all remaining occupied orbitals active. The final active space is denoted (14/15,11), where 14/15 denotes the number of neutral/anion electrons, and 11 the number of active orbitals. Wave functions were calculated with C_S point group symmetry. Dynamical electron correlation is included using multi-configurational quasi-degenerate perturbation theory of second order, NS-MCQDPT2 [36] (analogous to MS-CASPT2) method, and when applied to one CASSCF reference state is known as the second-order multi-reference Moller-Plesset perturbation theory approach (MRMP2). [37] N denotes the number of equally weighted CASSCF configurations, with polynomial extrapolation using $\frac{1}{N}$. MRMP2 intruder states arising from quasi-degeneracy are small (and nearly negligible) and removed by denominator level shifting of 0.1 for neutral and anion ground states. [38][2] High-level MRCI calculations are too expensive for CASSCF references and species of this size.

Four composite basis sets, denoted GEN1 to GEN4 are also constructed in order to estimate the relative importance of CH_3 and NO_2 groups, by providing different but systematically better descriptions of both groups. These basis sets are summarized in table 5.2.

For dipole-bound calculations, the procedure outlined by Simons *et al.* [39, 40] is followed in calculating the dipole binding energy at the CCSD(T)/aug-cc-pVDZ+6$sp7d$ level of theory. This basis has an aug-cc-pVDZ valence augmented with six additional sp and seven d-type diffuse functions (+6$sp7d$) centred on the

[1] Levels of theory are denoted SP/OPT/BS, where SP denotes the single-point electron correlation method, OPT denotes the optimization electron correlation method (omitted with // if identical to the energy calculation), and BS denotes the basis set used throughout.

[2] Intruder states arise in multireference perturbation theory due to quasi-degeneracies resulting from a limited CASSCF active space as the Hamiltonian is perturbed before diagonaliztion. Such intruder states yield correlation energy denominators to cancel to zero, resulting in energy singularities (loose convergence criteria my recognize as incorrect minima) in a potential energy function. Denominator (or imaginary) level shifting adds a small number, typically 0.1, to the energy denominator so cancellation does not occur - this can be subtracted later. This procedure can effectively eliminate weak intruder states that have small coefficients.

Table 5.2.: Custom basis sets for CH_3NO_2 electron affinity determinations.

Basis set	CH_3 description	NO_2 description
GEN1	aug-cc-pVDZ	aug-cc-pVTZ
GEN2	6-311++G(d,p)	aug-cc-pVTZ
GEN3	aug-cc-pVDZ	aug-cc-pVQZ
GEN4	aug-cc-pVDZ[a]	aug-cc-pVQZ

[a]Carbon atom is treated with aug-cc-pVQZ basis set.

methyl carbon atom. The additional diffuse function orbital exponents start at 7.239×10^{-3} for *sp* functions and 2.316×10^{-2} for *d* functions, and decrease with an even-tempered geometric progression factor of 3.2. These exponents range the same orders of magnitude as the Gutsev and Bartlett [2] dipole-bound anion study and minimize linear dependence effects. This additional augmentation is critical in order to obtain a bound state, where default valence basis sets have an incomplete long-range description. The B3LYP//aug-cc-pVTZ geometry of the neutral is assumed. Simons *et al.* [39,40] show additional *f*-type diffuse functions in general are nonbeneficial for similar species, and that treating the dipole-bound state with an aug-cc-pVTZ valence yields no gain over the aug-cc-pVDZ valence.

5.3. Results and discussion

5.3.1. Geometries

An initial requirement for electron affinity calculations is accurate geometries for CH_3NO_2 ($^1A'$ ground state) and $CH_3NO_2^-$ ($^2A'$ ground state); however, for the latter there exists no experimental comparison. As a preliminary, it is useful to consider NO_2 and NO_2^- optimizations at the B3LYP//aug-cc-pVTZ level of theory, and its ability to reproduce experimental gas phase anharmonic fundamental vibration frequencies, as summarized in table 5.3. These data show that the dominant vibrational change upon electron capture is a decrease in the

Table 5.3.: Experimental and calculated gas phase infrared anharmonic vibrational frequencies, in cm^{-1}, for NO_2 and NO_2^- in parentheses. Root-mean-square-displacement (RMSD) for B3LYP//aug-cc-pVTZ values are 25 cm^{-1} and 16 cm^{-1} for NO_2 and NO_2^- respectively, with the individual errors on experimental data for the anion exceeding respective RMSD.

Description	NO_2^a $(NO_2^-)^{b,c}$	B3LYP
A_1 NO_2 stretch	1318 (1284 ± 30)[b]	1360 (1302)
A_1 NO_2 bend	750 (766 ± 30)[b]	757 (787)
B_2 NO_2 stretch	1618 (1244)[c]	1643 (1252)

[a]Ref [41].
[b]Ref [42].
[c]Ref [43] - measured in argon.

NO_2 stretching frequency, corresponding to a bond weakening in support of π^*-type orbital involvement in electron capture. Calculated values are in excellent agreement for both the neutral (open-shell) and anion (closed-shell), indicating the B3LYP//aug-cc-pVTZ level of theory yields accurate geometries for both the

neutral and anion. For CH_3NO_2, geometrical bonding parameters at the B3LYP//aug-cc-pVTZ level of theory are shown in figure 5.1, and have been previously shown to be in excellent agreement with experiment. [13] The calculated anion geometry has also been shown to be in excellent agreement (third decimal place) with wave function methods. [2,13] Figure 5.1 shows the dominant geometric change upon electron capture to be an increase of the NO_2 tilt angle, θ. These calculated geometries are also in excellent accord with the B3LYP//6-311++G(2d,p) and CCSD(T)//aug-cc-pVTZ optimizations of Adams *et al.* [8], noting they report the NO_2 tilt angles at half their actual value (14.0° and 15.6°, respectively), and in slightly better agreement than at the CASSCF(14,11)//ANO-L level of theory (tilt angle neglected for the neutral, 36.8° anion) with their NO bond length in 0.08 Å poorer agreement to experiment. [24] The CASSCF(14,11)//ANO-L calculation presumably lacks dynamical electron correlation correction to geometries. Calculated gas phase anharmonic vibrational frequencies for CH_3NO_2 with experimental comparison are reported in table 5.4. These data are in excellent agreement with experiment, and also those calculated at the B3LYP//6-311++G(3df,3pd) level of theory, [13] with a root-mean-square displacement of 14 cm^{-1}.

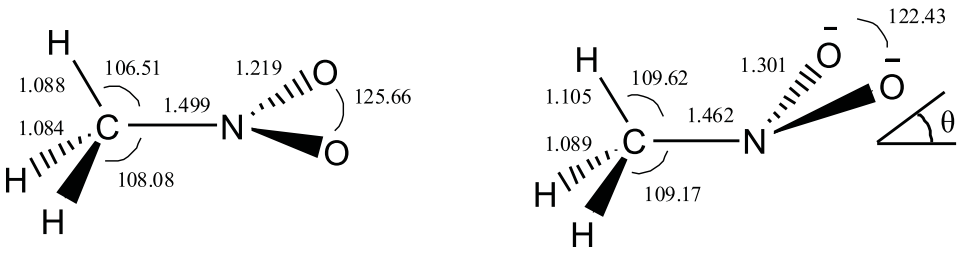

Figure 5.1.: CH_3NO_2 and $CH_3NO_2^-$ B3LYP//aug-cc-pVTZ optimized geometries. $CH_3NO_2^-$ -NO_2 tilt angle $\theta = 32.31°$ and 31.55° at the B3LYP//aug-cc-pVTZ and B3LYP//aug-cc-pVQZ levels of theory respectively. For CH_3NO_2, these are $\theta = 1.64°$ and 1.54°. Bond lengths reported in Å, and angles in degrees.

When a species has a small (< 1 eV) adiabatic valence electron affinity, and both neutral and anion show different geometries, an accurate ΔZPE correction is required since this may constitute a significant portion of the final value. For CH_3NO_2 this correction is found to be ≈ 45% of the final value. The anharmonic ΔZPV is calculated to be 0.078 eV at the B3LYP//aug-cc-pVTZ and B3LYP//6-311++G(3df,3pd) levels of theory. [13] This correction is slightly larger than the Gutsev and Bartlett [2] MP2/6-311+G(2d,2p) harmonic value at ΔZPV = 0.064 eV. The experimentally determined zero point energy for CH_3NO_2 is 30.28 ± 0.01 kcal/mol, [41] in good agreement with the calculated anharmonic value of 30.72 kcal/mol, and in significantly better agreement than with the value of 31.78 kcal/mol by Gutsev and Bartlett [2]. Adams *et al.* [8] obtain a harmonic B3LYP//6-311++G(2d,p) ΔZPV = 0.081 eV. These calculations indicate that the Gutsev and Bartlett [2] ΔZPV correction is a therefore a slight underestimate.

5.3.2. Adiabatic electron affinity

To address the concern regarding the basis set in the Gutsev and Bartlett [2] study, a series of electron affinity calculations are performed with increasing basis set description using B3LYP, MP2, MP4SDQ, CCSD and

Table 5.4.: Experimental and calculated gas phase infrared anharmonic fundamental vibrational frequencies, in cm^{-1}, for CH_3NO_2 at the B3LYP//aug-cc-pVTZ level of theory. Zero point energy (ZPV) in units of kcal/mol. Description of modes follows Gutsev and Bartlett [2].

Description	Experimental[a]	Calculated
A'' NO_2 rock	475	474
A' NO_2 wag	603	611
A' NO_2 scissor	657	645
A' CN stretch	936	918
A' CH_3 rock	1096	1088
A' CH_3 rock	1131	1108
A' CH_3 deform	1380	1364
A' NO_2	1397	1397
A'' CH_3 deform	1410	1421
A' CH_3 deform	1434	1438
A'' CH_3 stretch	1583	1588
A' CH_3 stretch	2974	2969
A' CH_3 stretch	3045	3030
A'' CH_3 stretch	3080	3049
ZPV	30.28 ± 0.01	30.72[b]

[a]Ref [44] - it is believed the claimed ZPV accuracy is tentative.
[b]Anion ZPV = 28.92 kcal/mol.

CCSD(T) methods. Each basis set is assigned an ascending arbitrary description number, ranging 0-7.5, representing performance for plotting purposes only. The basis sets employed, with number of Cartesian basis functions in parentheses indicating computational complexity are: 0, 6-311G (61); 1, 6-311++G (80); 2, 6-311++G(d,p) (113); 2.5, 6-311++G(df,pd) (171); 3, 6-311++G(2d,2p) (146); 3.5, 6-311++G(2df,2pd) (204); 4, 6-311++G(3p,3d) (179); 4.5, 6-311++G(3df,3pd) (237); 5, GEN2 (209); 5.5, GEN1 (217); 6, aug-cc-pVTZ (295); 6.5, GEN3 (367); 7, GEN4 (447); 7.5, aug-cc-pVQZ (585). These data are shown in figure 5.2, and all assume the B3LYP//aug-cc-pVTZ geometry and ΔZPV correction.

Each electron correlation treatment shown in figure 5.2 reveals a sharp positive increase for all correlation methods on initial addition of valence diffuse type (++) basis functions. Such basis functions are known to be important for anion states, with these highly positive erroneous EA_{ad} resulting from an overall inadequate valence description. Further diffuse augmentation shows a converging decreasing trend for B3LYP, and a converging increasing trend for wave function based methods. This slow convergence can be assumed to arise with increasing variational freedom as the basis set size increases. The B3LYP calculations show early convergence to a value in agreement with the first set of experimental data, and no significant change as the basis set is increased beyond 6-311++G(3d,3p). In all instances, MP2 yields a negative electron affinity, whereas MP4SDQ yields positive values in good accord with CCSD(T). CCSD values apparently show slow convergence to between the Adams *et al.* [8] (0.172 ± 0.006 eV) and Compton *et al.* [1] (0.026 ± 0.08 eV) values, whereas the CCSD(T) value are systematically smaller and appear to converge slowly to approximately the Adams *et al.* [8] electron affinity. That the CCSD(T) values are systematically smaller in magnitude than the CCSD

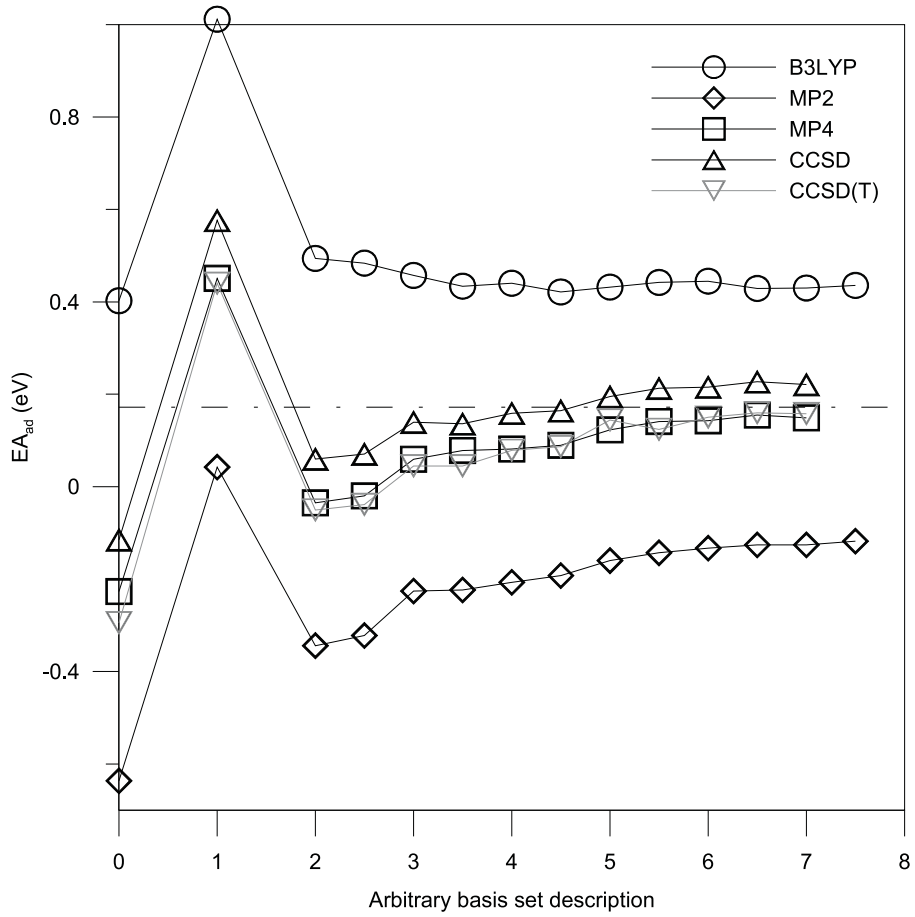

Figure 5.2.: Convergence of basis set to an adiabatic electron affinity (EA_{ad}) in eV for B3LYP, MP2, MP4SDQ, CCSD and CCSD(T) electron correlation methods. All calculations were performed at the B3LYP//aug-cc-pVTZ geometries with the ΔZPV=0.078 eV correction. The arbitrary assignment of basis set to a numerical value is described in the text.

values may indicate a better description of neutral and not anion for CCSD, or the fortuitous agreement of CCSD to the Compton *et al.* [1] value if correct. Assuming the CCSD(T) method to be more reliable, this data convergence would indicate the Adams *et al.* [8] value to be correct. Higher-order CCSDT or CCSDTQ would allow much more comprehensive single-reference determinations. That the Gutsev and Bartlett [2] study stated their 'best' valence electron affinity determination at 0.192 eV (CCSD) to be with their 6-311++G(d,p)+7*sp* basis set is most likely reflective of the initial low basis set EA_{ad} jump shown here, where the anion is treated considerably better than the neutral in the absence of adequate polarization type basis functions. That is, their agreement is most likely fortuitous - their additional diffuse functions are designed (without basis set superposition error correction) to describe dipole-bound states off the CH_3-end, not a valence description of the NO_2-end. These data all indicate lack of convergence. Of interest, the GEN1 or GEN3 and aug-cc-pVTZ or GEN4 basis sets yield almost identical values, again indicating that is is the NO_2-group that is important in electron capture. The GEN1 basis set may therefore provide aug-cc-pVTZ quality description at a significantly lower computational cost for higher electron correlation treatments. Electron affinity determinations on similar species containing the -NO_2 group have found that CCSD(T) methods in general underestimate the electron

affinity relative to HFDFT methods. The comparative statement has been made as to the "relative insensitivity of density functional theory approaches to augmentations of *spd* basis sets by functions with higher angular momentum, whereas the convergence of the correlation energy in coupled cluster methods is proportional to $1/L^4$, ... harmonics up to L=5 are required to reach 0.03 eV accuracy". [9] L represents the highest order angular momentum basis function. This same trend has been observed for species employing pentuple-zeta quality bases with iterative triplet coupled cluster corrections. [45] The results of the largest-basis-set calculations of adiabatic electron affinities are reported in table 5.5.

The DFT functionals trialed yield a wide range of values spanning all experimental determinations. As expected, B3LYP and X3LYP reproduce each other well, and are apparently in excellent agreement with the higher set of experimental values. The TPSS and M06 suite of functionals show the general trend that as the extent of HF exchange is increased, electron affinities move from being a poor underestimate (0%), to in reasonable agreement with the Compton *et al.* [1] value (27%), to a poor overestimate (100%). The TPSS, TPSSh and BMK functionals all yield values between the two groupings of experimental data. The two double hybrid methods yield values between the Compton *et al.* [1] and Adams *et al.* [8] values but do perform considerably better than other functionals employing some high degree of HF exchange. Although DFT calculations are inherently multi-configurational, [28] the large variance for electron affinity calculations here gives rise to some skepticism on their use for accurate CH_3NO_2 electron attachment or relative anion energetics. These calculations reveal that none of the DFT methods trialed here give reliable agreement to the Adams *et al.* [8] value. Single-reference wave function calculations all underestimate the Compton *et al.* [1] value, although as noted above, CCSD(T) shows reasonable agreement with the Adams *et al.* [8] value. The GEN4 basis set does appear to slightly improve the triple-zeta quality description. These single-reference wave function methods would again indicate the higher of the two experimental electron affinity groupings to be incorrect.

Multi-configurational *ab initio* methods show systematic improvement with an increasing the degree of dynamic electron correlation. The most comprehensive multi-configurational literature calculated value is that of Arenas *et al.* [14] at 0.18 eV, with the MS-CASPT2/CASSCF(15,11)/ANO-L level of theory (CASSCF ΔZPV) which appears to be in good agreement with the Adams *et al.* [8] value. This value is erroneous, as their tabulated zero-point energies, presumably from application of an incorrect conversion factor in interpretation of computational output, are systematically an order of magnitude less than values calculated here, or reported experimental values. As a result, their ΔZPV is incorrect at ≈ 0.01 eV. Application of the calculated anharmonic ΔZPV correction to the tabulated MS-CASPT2 energies then yields 0.246 eV, which is now in closer agreement with the Compton *et al.* [1] value. These calculations indicated the GEN1 basis set to provide a slightly better description of this system. The inherent multi-configurational nature of CH_3NO_2 and $CH_3NO_2^-$ can be seen by considering RHF and ROHF weights in the CASSCF wave function given in table 5.6. The GEN1 basis set again reproduces the aug-cc-pVTZ description at a lower cost. CASSCF data yield a negative electron affinity, which is significantly improved with MP2 dynamic electron correlation with the MCQDPT2 wave functions that show weights similar to the MS-CASPT2 calculations of Arenas *et al.* [14].

Table 5.5.: Summary of calculated adiabatic electron affinities, in eV, for CH_3NO_2. The values in parentheses are calculated using the at B3LYP//aug-cc-pVTZ optimized geometry. All calculated values corrected using the B3LYP//aug-cc-pVTZ zero point energy correction, ΔZPV = 0.078 eV.

Level of theory	EA_{ad}
HFDFT(B3LYP)//6-311++G(2d,2p)[a]	0.223
B3LYP//6-311++G(2d,2p)	0.459
B3LYP//aug-cc-pVTZ	0.445
B3LYP//aug-cc-pVQZ	0.436
X3LYP//aug-cc-pVTZ	0.411 (0.411)
TPSS//aug-cc-pVTZ	0.315 (0.317)
TPSSh//aug-cc-pVTZ	0.271 (0.295)
M06-L//aug-cc-pVTZ	(0.024)
M06//aug-cc-pVTZ	(0.211)
M06-2X//aug-cc-pVTZ	0.304 (0.345)
M06-HF//aug-cc-pVTZ	0.595 (0.616)
BMK//aug-cc-pVTZ	0.351 (0.346)
B2PLYP//aug-cc-pVTZ	(0.200)
mPW2PLYP//aug-cc-pVTZ	(0.241)
mPW2PLYP//aug-cc-pVQZ	(0.236)
MP2//aug-cc-pVTZ	-0.126 (-0.133)
MP2//aug-cc-pVQZ	-0.109 (-0.118)
MP4SDQ//aug-cc-pVTZ	(0.143)
CCSD//GEN2	(0.195)
CCSD(T)//GEN2	(0.144)
CCSD//GEN1	(0.213)
CCSD(T)//GEN1	(0.124)
CCSD//aug-cc-pVTZ	(0.216)
CCSD(T)//aug-cc-pVTZ[b]	0.160 (0.150)
CCSD//GEN3	(0.227)
CCSD(T)//GEN3	(0.160)
CCSD//GEN4	(0.221)
CCSD(T)//GEN4	(0.158)
SS-MCQDPT2//aug-cc-pVTZ[c]	(0.286)
SS-MCQDPT2//aug-cc-pVTZ	(0.266)
SS-MCQDPT2//GEN1	(0.266)
2S-MCQDPT2//GEN1	(0.204)
3S-MCQDPT2//GEN1	(0.188)
7S-MCQDPT2//GEN1	(0.178)
MS-CASPT2//ANO-L[d]	0.18 / 0.24

[a]Ref [2] with MP2//6-311+G(2d,2p) harmonic ΔZPV correction.
[b]Ref [8] gives an optimized value at 0.162 eV with a B3LYP//6-311++G(2df,2p) harmonic ΔZPV correction.
[c]Using a CASSCF(14,10) and CASSCF(15,10) reference wave function for neutral and anion respectively.
[d]Ref 14 with an erroneous ΔZPV $\approx$ 0.01 eV correction, the EA_{ad} becomes 0.24 eV with the anharmonic ΔZPV correction determined here.

SS-MCQDPT2 calculations with the smaller 10 orbital CASSCF active space yields an electron affinity 0.02 eV larger than that with 11 orbitals which represents the feasible limit at this time. Again, the GEN1 basis set reproduces the aug-cc-pVTZ value, which is in good agreement with the Compton *et al.* [1] value. A SS-MCQDPT2 reoptimization with 2×10^{-5} gradient threshold for the anion yields essentially no change to the reference geometry and nonoptimized energy, indicating the anion B3LYP reference geometry to be reasonable.

Table 5.6.: CH_3NO_2 RHF / ($CH_3NO_2^-$ ROHF in parentheses) wave function weights in CASSCF wave functions.

Active space	HF weight
CASSCF(14/15,10)/aug-cc-pVTZ	0.91 (0.96)
CASSCF(14/15,10)/GEN1	0.91 (0.95)
CASSCF(14/15,11)/aug-cc-pVTZ	0.90 (0.93)
CASSCF(14/15,11)/GEN1	0.90 (0.93)

Addition of two, three, and seven further CASSCF reference configurations then show convergence to the Adams *et al.* [8] value, with the 7S-MCQDPT2 calculation within the limits of the small experimental error. A four-point third-order polynomial extrapolation of these data then yields a limiting value of 0.170 eV, which is again within the small experimental error. These MCQDPT2 data represent very comprehensive wave functions, and with multi-configurational character properly treated, the convergence on further dynamic electron correlation is most likely real. In summary, for the adiabatic electron affinity, the Adams *et al.* [8] value appears to represent an accurate experimental determination for the adiabatic electron affinity, and the higher experimental set of electron affinities do not appear to be correct in the limit of accurate *ab initio* multi-reference wave functions.

5.3.3. Vertical electron affinity

As a cross-check, the vertical electron processes are also calculated. Photoelectron techniques generally involve formation of the neutral species by photoinduced electron detachment of the anion and are ideally suited to observation of vertical processes. The recent Adams *et al.* [8] study for resolution purposes did not employ a photo-detachment wavelength that would yield a full photoelectron spectrum scan. However, the Compton *et al.* [1] and recent Goebbert *et al.* [46] studies did employ appropriate wavelengths and determined the vertical detachment energy at the anion geometry to be 0.96 ± 0.01 eV. The experimental vertical electron affinity at the neutral geometry has also been reported at 0.72 eV (uncertainty predicted to be ≈ ± 0.1 eV) by dissociative electron detachment methods. [47] The vertical neutral electron affinity, EA_v, and vertical anion electron detachment energy, DE_v, are reported in table 5.7.

Vertical valence electron affinities (at the neutral geometry) are all negative or unfavourable, indicating that a valence-bound anion is not formed at the neutral geometry, and the vertical detachment energies (at the anion geometry) are positive or unfavourable. The vertical detachment energy of the anion is alternatively known as the first vertical ionization potential of the anion at its optimized geometry. These two properties are significantly different (≈ 0.25 eV) owing to the large tilt angle difference of the NO_2 group in optimized neutral and anion geometries; that is, these two vertical processes consider two quite different geometries. For the vertical electron affinity, mPW2PLYP and CCSD methods underestimate the value by ≈ 50%. MP2 overestimates the value, while MP4SDQ and CCSD(T) yield almost identical underestimations of ≈ 25%. As expected for a vertical process, single-reference wave functions appear inappropriate. MCQDPT values are in excellent agreement with experiment. The vertical anion electron detachment energies show trends similar to those of the adiabatic electron affinity calculations. MP2 and MP4SDQ underestimate, CCSD fortuitously

Table 5.7.: Calculated vertical electron affinities, EA_v, at the CH_3NO_2 geometry, and vertical anion detachment energies (first vertical ionization potential), DE_v, at the $CH_3NO_2^-$ geometry. All calculations assume the B3LYP//aug-cc-pVTZ geometry, and energies in eV.

Level of theory	EA_v	DE_v
HFDFT(B3LYP)//6-311++G(2d,2p)[a]	N/A	1.214
B3LYP//aug-cc-pVTZ	-0.79[b]	1.152
mPW2PLYP//aug-cc-pVTZ	-0.353	0.878
mPW2PLYP//aug-cc-pVQZ	-0.324	0.849
MP2//aug-cc-pVTZ	-0.822	0.403
MP4SDQ//aug-cc-pVTZ	-0.516	0.842
CCSD//aug-cc-pVTZ	-0.375	0.950
CCSD(T)//aug-cc-pVTZ	-0.519	0.718
SS-MCQDPT2//GEN1	-0.733	0.780
3S-MCQDPT2//GEN1	-0.764	0.875
MS-CASPT2//ANO-L[c]	-0.40	N/A

[a]Ref [2] EA_v not reported.
[b]Ref [13] with 6-311++G(3df,3pd) basis set, aug-cc-pVTZ optimizes to the dipole-bound anion.
[c]Ref [14] - DE_v not reported.

calculates close to the experimental value, and CCSD(T) underestimates by ≈ 25%. The MCQDPT2 data, as for the adiabatic data above, shows convergence to the experimental value, with a three-point extrapolation yielding a value of ≈ 0.96 eV. These data further confirm the requirement for multi-configurational wave functions and the apparent convergence of the highest level of theory employed here. A summary of the experimental data consistent with these calculations is given in figure 5.3.

5.3.4. Dipole-bound anion

The first reported experimental dipole-bound state binding energy, BE_D, of $CH_3NO_2^-$ was by Compton *et al.* [1] at 12 ± 3 meV, which also has been tentatively observed at 8 ± 8 meV by Adams *et al.* [8]. The resonant electron transfer experiments of Compton *et al.* [1] do generally show larger binding energies than other experimental methods and respective calculations. [48] Gutsev and Bartlett [2], employing the EA-EOM-CCSD/MP2/6-311++G(d,p)+7*sp* level of theory determined this to be 13 meV, [49] in apparent excellent agreement with experiment. Their additional diffuse functions were only of *sp* type with a geometric progression ratio of 2 that would promote basis set linear dependence problems. This same calculated binding energy was also earlier reported with ΔCCSD theory involving three additional *sp* diffuse functions augmented to a double-zeta quality valence basis set, and with Koopmans' theorem overestimating by ≈ 40% attributed to a poor dipole moment. [50] For dipole-bound anion determinations, description of molecular valence is less important than the dipole-bonding region since these two electronic configurations have little interaction. The Gutsev and Bartlett [2] dipole-binding study showed trends similar to the adiabatic electron affinity (figure 5.2), that initial diffuse function (++) augmentation yielded a ≈ 60% (6.1 meV to 14.4 meV) increase, with further polarization (2d,2p) yielding a slight decrease to apparent excellent agreement (12.7 meV) with experiment. Application of

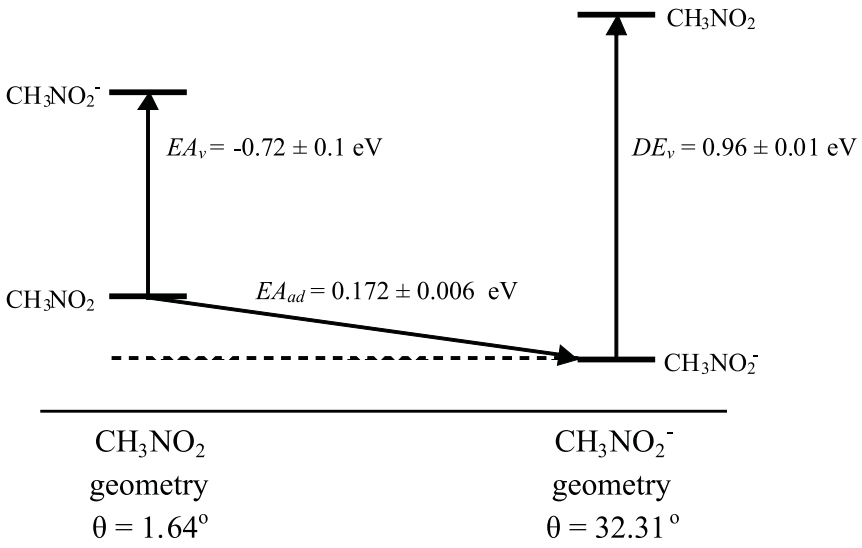

Figure 5.3.: Summary of suggested experimental valence electron binding and detachment energies consistent with the reported MCQDPT2/B3LYP/GEN1 calculations.

the 6-311++G(d,p)+7*sp* basis set yielded a slight increase to 13.3 meV, and still with the Compton *et al.* [1] experimental error. Such additional diffuse functions for other species with similar magnitude dipole moments are crucial for dipole-bound anions [39,40], yet appeared to show intolerance in the EA-EOM-CCSD calculations. EA-EOM-CCSD ($\approx$ ΔCCSD level of theory) has been shown for O_3, which is isoelectronic to NO_2^-, to yield larger vertical valence electron affinities than EA-EOM-CCSDT with iterative triplets. [49] For valence effects, EA-EOM-CC methods do have the advantage of including some multi-configurational character for an intensive type determination. [51] It has also been previously shown for a range of dipole-bound anions that ΔCCSD typically overestimates, while ΔCCSD(T) yields reasonable agreement. [39] All dipole-bound anion calculations here are again performed at the B3LYP//aug-cc-pVTZ geometry with any ΔZPV correction negligible. These calculations are summarized in table 5.8. The experimental dipole moment of 3.46 D [52] is in good agreement with reported B3LYP//aug-cc-pVTZ or GEN1 calculation, both at 3.60 D, and CASSCF(14,11)/B3LYP/aug-cc-pVTZ or GEN1, both at 3.43 D, and the CCD density at 3.63 D with the aug-cc-pVDZ+6*sp*7*d* basis set.

Table 5.8.: Calculated $CH_3NO_2^-$ dipole-bound anion binding energies, BE_D, in meV. ACCD = aug-cc-pVDZ+6*sp*7*d*, with calculations assuming the B3LYP//aug-cc-pVTZ neutral geometry.

Level of theory	BE_D
MP2/ACCD	4.8
CCSD/ACCD	7.9
CCSD(T)/ACCD	7.4
3S-MCQDPT/GEN1	8.9
Resonant charge transfer[a]	12±3
Velocity map imaging[b]	8±8

[a]Ref [1]
[b]Ref [8]

These calculations reproduce the literature trend that ΔCCSD values appear to be slightly larger than ΔCCSD(T). The CCSD(T)/aug-cc-pVDZ+6*sp*7*d* calculation is smaller than the Compton *et al.* [1] value at 12 ± 3 meV, but in excellent accord with the value of Adams *et al.* [8] at 8 ± 8 meV, albeit larger error that includes the Compton *et al.* [1] value. These calculations indicate the Gutsev and Bartlett [2] value of 13 meV warrants reinvestigation with a higher level of theory in basis set and electron correlation, as their agreement to the Compton *et al.* [1] value may again be fortuitous. Similar to EA-EOM-CCSD, analysis of 3S-MCQDPT2/B3LYP/GEN1 (without diffuse function augmentation) states yields a dipole binding energy of 8.9 meV.

The Adams *et al.* [8] study, consistent with a previous study by Lecomte *et al.* [53], observed the dipole-bound state to disappear with argon solvation of the anion. To briefly qualitatively investigate this observation, calculations for the Ar·$CH_3NO_2^-$ cluster at the MP2//aug-cc-pVDZ+6*sp*7*d* level of theory with a single Ar atom fixed at each end of the dipole, at a 3.5 Å separation with respect to the carbon or nitrogen are performed. Counterpoise basis set superposition error corrections to the energies are included for Ar and CH_3NO_2 monomers. These binding energies are all strongly negative, on the order of ≈ -900 meV and would indicate the dipole-bound state to disappear in the presence of single axial (3.5 Å) dipole solvation by argon. In accordance, the dipole-bound state appears to be an isolated phenomenon.

5.4. Conclusions

The reported calculations on the electron affinity of nitromethane demonstrate the difficulty of obtaining agreement between theory and experiment on a fundamental chemical molecular property, where both may be erroneous. It is believed that progress has been made on an accurate electron affinity determination for this species, and it has been demonstrated that ideally multi-configurational wave functions are required to accurately describe the neutral and anion. Single-reference wave function calculations show some fortuitous or Pauling-point agreement, where cancellation of errors from inadequate descriptions in basis set and/or electron correlation treatment may yield accidental agreement with a reported experimental value. The level of theory must be very carefully selected to accurately describe the system before any theoretical statements can be made on the accuracy of experimental data. By providing a systematic single and multi-reference study, convergence of the reported calculations supports the experimental value of 0.172 ± 0.006 eV to be consistent with theory, and the earlier and larger experimental determinations an overestimate. Are these calculations again in some fortuitous agreement? This is believed not to be the case. However, as a check, MRCC or large scale MRCI calculations could be employed but at this time are considered far too expensive for the benefit. Present density functional theory (DFT) methods on first comparisons to some reported experimental electron affinities apparently appear to perform well but should be avoided for accurate energetic calculations involving anions from unphysical self-interaction. The double-hybrid mPW2PLYP and B2PLYP methods do appear to make a step toward an accurate description, where other methods incorporating full Hartree-Fock exchange significantly overestimate the adiabatic electron binding. B3LYP does provide very fast and accurate geometries. The highest

level of theory, 3S-MCQDPT2 and 7S-MCQDPT2 with an aug-cc-pVTZ quality basis, yields adiabatic values of 0.188 eV and 0.176 eV (0.170 eV extrapolated) respectively, and are assumed to the best reported theoretical calculation so far, and it appears that the CCSD(T)/B3LYP/aug-cc-pVDZ+6$sp7d$ dipole-bound state binding energy of 7-8 meV is an improvement on previous EA-EOM-CCSD calculations employing poorer diffuse basis set description. The results of this study recommend use of the Adams *et al.* [8] value of 0.172 ± 0.006 eV as the molecular adiabatic valence electron affinity for nitromethane.

5.5. Final comments

Several calculations were performed in order to assess MR-CISD electron affinities for CH_3NO_2. Briefly, the virtual space was curtailed to 40 virtual orbitals by an initial single-reference CIS calculation which showed no orbital beyond this virtual space to have any coefficient larger than 0.001 weighting for the neutral or anion. Using the CASSCF reference wave functions, the MR-CISD/B3LYP/aug-cc-pVTZ and MR-CISD/B3LYP/GEN1 adiabatic electron affinity was calculated at ≈ 0.04 eV. The single-reference CISD value was more negative than the respective MP2 values. Clearly, the CI wave functions require higher order excitations, however were not computationally feasible at this time. Inclusion of Davidson (Q) corrections may provide a slight improvement to MR-CI wave functions, however the combination of a curtailed virtual space, highly truncated excitation level, and only single state MR-CI (GAMESS cannot perform multi-configurational-MRCI type calculations) would not be suitable. In addition, computational packages to perform CI excitations higher than second-order are not common, and GAMESS-US only allows such calculations to be perform in serial (single CPU) execution mode, and therefore not on a supercomputer employing parallel processing.

References

[1] J. A. Stockdale, F. J. Davis, R. N. Compton, and C. E. Klots. *J. Chem. Phys.*, 60:4279, 1974.

[2] G. L. Gutsev and R. J. Bartlett. *J. Chem. Phys.*, 105:8785, 1996.

[3] J. A. Stockdale, F. J. Davis, R. N. Compton, and C. E. Klots. *J. Chem. Phys.*, 60:4279, 1974.

[4] R. N. Compton, P. W. Rienhardt, and C. D. Cooper. *J. Chem. Phys.*, 68:4360, 1978.

[5] E. C. M. Chen and W. E. Wentworth. *J. Phys. Chem.*, 87:45, 1983.

[6] E. P. Grimsrud, G. Caldwell, S. Chowdhury, and P. Kebarle. *J. Am. Chem. Soc.*, 107:4627, 1985.

[7] E. C. M. Chen, N. Welk, E. S. Chen, and W. E. Wentworth. *J. Phys. Chem. A*, 103:9072, 1999.

[8] K. M. Ervin C. L. Adams, H. Schneider and J. M. Weber. *J. Chem. Phys.*, 130:074307, 2009.

[9] G. L. Gutsev, P. Jena, and R. J. Bartlett. *J. Chem. Phys.*, 110:403, 1999.

[10] N. Oliphant and R. J. Bartlett. *J. Chem. Phys.*, 100:6550, 1994.

[11] C. P. Blahous, B. F. Yates, Y. Xie, and H. F. Schaefer III. *J. Chem. Phys.*, 93:8105, 1990.

[12] P. Lykos and G. W. Pratt. *Rev. Mod. Phys.*, 35:496, 1963.

[13] J. N. Bull, Robert G. A. R. Maclagan, and P. W. Harland. *Mol. Phys.*, 107:1123, 2009.

[14] J. F. Arenas, J. C. Otero, D. Peláez, J. Soto, and L. Serrano-Andrés. *J. Chem. Phys.*, 121:4127, 2004.

[15] M. T. Nguyen, H. T. Le, B. Hajgató T. Veszprémi, and M. C. Lin. *J. Phys. Chem. A*, 106:4286, 2003.

[16] P. P. Bera, Y. Yamaguchi, H. F. Schaefer III, and T. D. Crawford. *J. Phys. Chem. A*, 112:2669, 2008.

[17] E. R. Davidson and W. T. Borden. *J. Phys. Chem.*, 87:4783, 1983.

[18] W. Eisfield and K. Morokuma. *J. Chem. Phys.*, 113:5587, 2000.

[19] X. Li and J. Paldus. *Int. J. Quant. Chem.*, 109:1756, 2009.

[20] C. D. Sherrill, M. S. Lee, and M. Head-Gordon. *Chem. Phys. Lett.*, 302:425, 1999.

[21] M. R. Manna and L. E. Fried. *J. Phys. Chem. A*, 102:9884, 1998.

[22] J. F. Arenas, S. P. Centeno, I. López-Tocón, D. Pleáz, and J. Soto. *J. Mol. Struct. (Theochem)*, 630:17, 2003.

[23] M. R. Manna and L. E. Fried. *J. Phys. Chem. A*, 130:9349, 1999.

[24] J. F. Arenas, J. C. Otero, D. Peláez, and J. Soto. *J. Chem. Phys.*, 119:7814, 2003.

[25] J. F. Arenas, J. C. Otero, D. Peláez, and J. Soto. *J. Chem. Phys.*, 122:084324, 2005.

[26] R. S. Zhu and M. C. Lin. *Chem. Phys. Lett.*, 478:11, 2009.

[27] J. Finley, P. Malmqvist, B. O. Roos, and L. Serrano-Andrés. *Chem. Phys. Lett.*, 1998:299, 288.

[28] J. Gräfenstein and D. Cremer. *Theor. Chem. Acc.*, 123:171, 2009.

[29] Y. Zhao and D. G. Truhlar. *J. Phys. Chem. A*, 110:10478, 2006.

[30] M. J. Frisch, G. W. Trucks, H. B. Schlegel, G. E. Scuseria, M. A. Robb, J. R. Cheeseman, J. A. Montgomery, Jr., T. Vreven, K. N. Kudin, J. C. Burant, J. M. Millam, S. S. Iyengar, J. Tomasi, V. Barone, B. Mennucci, M. Cossi, G. Scalmani, N. Rega, G. A. Petersson, H. Nakatsuji, M. Hada, M. Ehara, K. Toyota, R. Fukuda, J. Hasegawa, M. Ishida, T. Nakajima, Y. Honda, O. Kitao, H. Nakai, M. Klene, X. Li, J. E. Knox, H. P. Hratchian, J. B. Cross, V. Bakken, C. Adamo, J. Jaramillo, R. Gomperts, R. E. Stratmann, O. Yazyev, A. J. Austin, R. Cammi, C. Pomelli, J. W. Ochterski, P. Y. Ayala, K. Morokuma, G. A. Voth, P. Salvador, J. J. Dannenberg, V. G. Zakrzewski, S. Dapprich, A. D. Daniels, M. C. Strain, O. Farkas, D. K. Malick, A. D. Rabuck, K. Raghavachari, J. B. Foresman, J. V. Ortiz, Q. Cui, A. G. Baboul, S. Clifford, J. Cioslowski, B. B. Stefanov, G. Liu, A. Liashenko, P. Piskorz, I. Komaromi, R. L. Martin, D. J. Fox, T. Keith, M. A. Al-Laham, C. Y. Peng, A. Nanayakkara, M. Challacombe, P. M. W. Gill, B. Johnson, W. Chen, M. W. Wong, C. Gonzalez, and J. A. Pople. Gaussian 03, Revision C.02. Gaussian, Inc., Wallingford, CT, 2004.

[31] M. W. Schmidt, K. K. Baldridge, J. A. Boatz, S. T. Elbert, M. S. Gordon, J. H. Jensen, S. Kosecki, N. Matsunaga, K. A. Nguyen, S. J. Su, T. L. Windus, M. Dupuis, and J. A. Montgomery. *J, Comput. Chem.*, 14:1347, 1993.

[32] Y. Zhao and D. G. Truhlar. *Theor. Chem. Acc.*, 120:215, 2008.

[33] Y. Zhao and D. G. Truhlar. *Acc. Chem. Res.*, 41:157, 2008.

[34] S. Grimme. *J. Chem. Phys.*, 124:034108, 2006.

[35] T. Schwabe and G. Grimme. *Phys. Chem. Chem. Phys.*, 8:4398, 2006.

[36] H. Nakano. *Chem. Phys. Lett.*, 201:59, 1993.

[37] K. Hirao. *Chem. Phys. Lett.*, 201:59, 1993.

[38] Y. Choe, H. A. Witek, J. P. Finley, and K. Hirao. *J. Chem. Phys.*, 114:3914, 2001.

[39] M. Gutowski, P. Skurski, K. D. Jordan, and J. Simons. *Int. J. Quant. Chem.*, 64:183, 1997.

[40] P. Skurski, M. Gutowski, and J. Simons. *Int. J. Quant. Chem.*, 80:1024, 2000.

[41] T. Shimanouchi. *J. Chem. Phys. Ref. Data*, 6:993, 1972.

[42] K. M. Ervin, J. Ho, and W. C. Lineberger. *J. Phys. Chem.*, 92:5405, 1988.

[43] D. E. Milligan and M. E. Jacox. *J. Chem. Phys.*, 55:3404, 1971.

[44] D. Gorse, D. Cavagnat, M. Pesquer, and C. Lapouge. *J. Phys. Chem.*, 97:4262, 1993.

[45] G. L. Gutsev, P. Jena, and R. J. Bartlett. *Chem. Phys. Lett.*, 291:547, 1988.

[46] D. J. Goebbert, K. Pichugin, and A. Sanov. *J. Chem. Phys.*, 131:164308, 2009.

[47] I. C. Walker and M. A. D. Fluendy. *Int. J. Mass Spectrom.*, 205:171, 2001.

[48] N. I. Hammer, K. Diri, K. D. Jordan, C. Desfrancois, and R. N. Compton. *J. Chem. Phys.*, 119:3650, 2003.

[49] M. Nooijen and R. J. Bartlett. *J. Chem. Phys.*, 102:3629, 1995.

[50] L. Adamowicz. *J. Chem. Phys.*, 91:7787, 1989.

[51] M. Musial and R. J. Bartlett. *J. Chem. Phys.*, 119:1901, 2003.

[52] D. R. Lide, editor. *CRC Handbook of Chemistry and Physics*, volume 77, chapter 10. CRC Press: Cleveland, OH, 1996.

[53] F. Lecomte, S. Carles, D. Desfrancois, and M. A. Johnson. *J. Chem. Phys.*, 113:10973, 2000.

6. Several additional ab initio investigations

This chapter outlines some preliminary studies that have been started during the course of this research, and are anticipated for completion in the near future. All of these studies have progressed significantly further than outlined here, however have not been fully completed or written up into manuscript form appropriate for inclusion in this thesis. This chapter should therefore be considered as some preliminary notes for future studies.

6.1. H_3^+ potential energy surfaces

In parallel with the experimental studies on the reaction between H_3^+ and oriented CH_3X molecules, *ab initio* calculations on the minimum energy pathway potential energy surfaces have been started. These calculations and interpretations will be completed after experimental data becomes available. Analogous to the charge-transfer reactions in the previous chapters that require an accurate description of the electron affinity, an accurate description of the proton affinity is required for any of the H_3^+ potential energy surfaces [1–3]. Calculations on the proton affinities for CH_3X for X = F, Cl or Br show formation of CH_3XH^+ species, where the proton forms an ion-dipole type bond in accord with experiment [4]. The results indicate that MP2//aug-cc-pVTZ and CCSD(T)/MP2/aug-cc-pVTZ levels of theory appear to be appropriate to describe these reactions.

The H_3^+ ion is a very reactive species due to the resonant two-electron three-center bonding configuration and can exist in two possible isomeric forms, that are linear or triangular. It is well-known and reproduced by *ab initio* calculations that the triangular form is more stable and is therefore this form that is considered in the calculations here. As a preliminary, calculations on the simple H_3^+ + NH_3 system at the CCSD(T)//aug-cc-pVTZ level of theory are considered, since this reaction has been previously studied [5,6]. The NH_3 species can also exhibit the Walden inversion process (inversion of umbrella conformation or configuration), except without loss of a leaving group, and can therefore act as test case to assess which initial conformations of triangular H_3^+ are important. The conformations considered are shown in figure 6.1 and summarised in the same order in table 6.1.

In an experiment, the H_3^+ species would have rotational motion that mean collisions were averaged over all orientations. However, in the calculations performed here, the orientations need to be considered, since some combinations from symmetry considerations may not yield reaction as expected. The zero-point-energy-corrected proton affinity for NH_3 is 860 kJ/mol at the CCSD(T)//aug-cc-pVTZ level of theory, in excellent

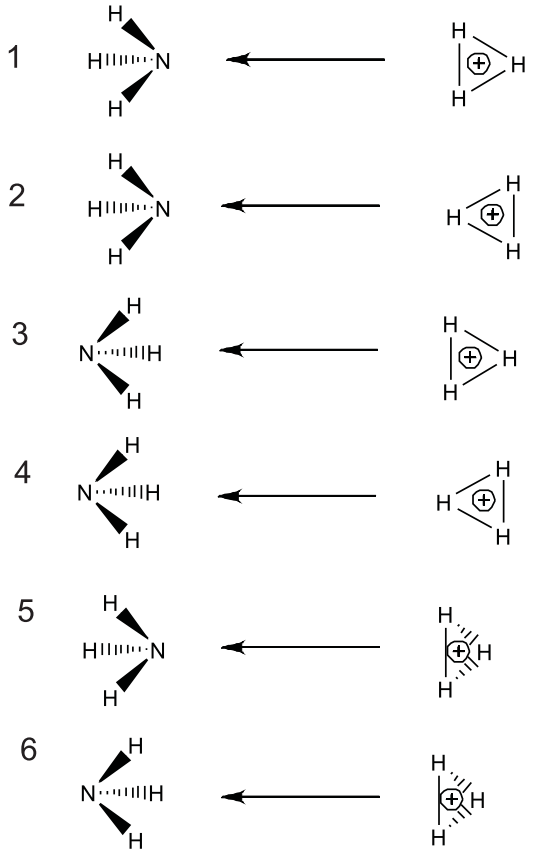

Figure 6.1.: Several different relative orientations (conformations) of the H_3^+ + NH_3 reaction, with numerical orientation assignment from 1 to 6.

accord with the experimental value at 854 kJ/mol [7]. Proton affinities for CH_3Z with ZPV corrections at the same level of theory are also in excellent agreement with experiment. Several optimized H_3^+ + NH_3 potential energy curves are given figure 6.2.

From figure 6.2, it can be seen that in orientation 4, or indeed any inverted orientation, Walden inversion occurs at R(N-H_3^+) $\approx$ 3.3 Å. These preliminary calculations indicate that the apex orientations 2 and 4 are those appropriate for describing proton transfer to C_{3V} target molecules. That the minimum interaction potential for orientation 2 is significantly less than the proton affinity indicates the presence of the H_2 species plays an influential role after proton transfer. Orientation 5 precludes single-atom charge transfer from symmetry.

For for CH_3Z species, H_3^+ potential energy surfaces have also been calculated for reaction with CH_3X (X=F, Cl, Br) in apex approach orientations at angles of: 0°; 45°; and 90° with respect to each end of the dipole. These potential energy surfaces await future interpretation.

Table 6.1.: Description of H_3^+ + NH_3 orientations. A/B corresponds to H_3^+ and NH_3 orientation parameters respectively, as shown in figure 6.1.

orientation	description
1	edge/regular
2	apex/regular
3	edge/staggered
4	apex/inverted
5	face/regular
6	face/inverted

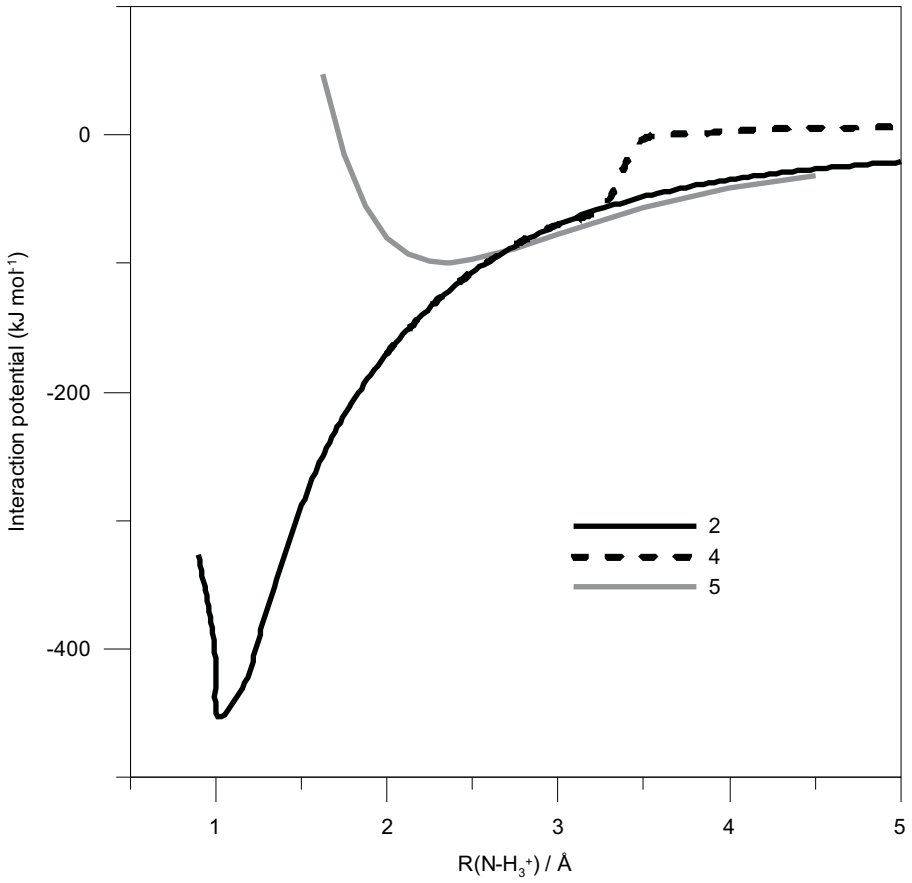

Figure 6.2.: Several different potential energy curves for different approach orientations of the H_3^+ + NH_3 reaction. The numbers in the legend refer to the different approach orientations. Orientation 4 shows Walden inversion, to become identical to orientation 2.

6.2. S_N2 potential energy surfaces

Similar to the proposed H_3^+ reactions, potential energy surfaces have been calculated for the reaction between Y^- + CH_3X, where Y=F,Cl,Br. The S_N2 reaction, or second-order nucleophilic substitution reaction, is probably the most common and well-studied reaction in organic chemistry [8]. This reaction is well-known to exhibit entrance (pre-transition state) and exit (post-transition state) ion-dipole complexes, as shown in figure 6.3, where the molecular dipole at long range forms a weak bonding interaction with the nucelophilic anion [9].

These species are weakly bound, at typically 400 meV to 500 meV, and exist in the gas-phase only. In solution phase, cage effects and surrounding solvent destroys the long-range bonding interaction. Such interactions need to be suitably described when constructing orientation-dependent potential energy surfaces. As a starting point, systematic calculations were performed in order to assess the suitability of the aug-cc-pVTZ basis set to describe the ion-dipole interaction. The effects of basis set superposition error (BSSE) are important when considering long-range complexes [10, 11], and can be incorporated using the Counterpoise (CP) method of Boys and Bernardi [12]. Since the ion-dipole species are described by a shallow and broad minimum, BSSE corrections may need to be applied in the geometrical optimization gradient, as well as the final energy.

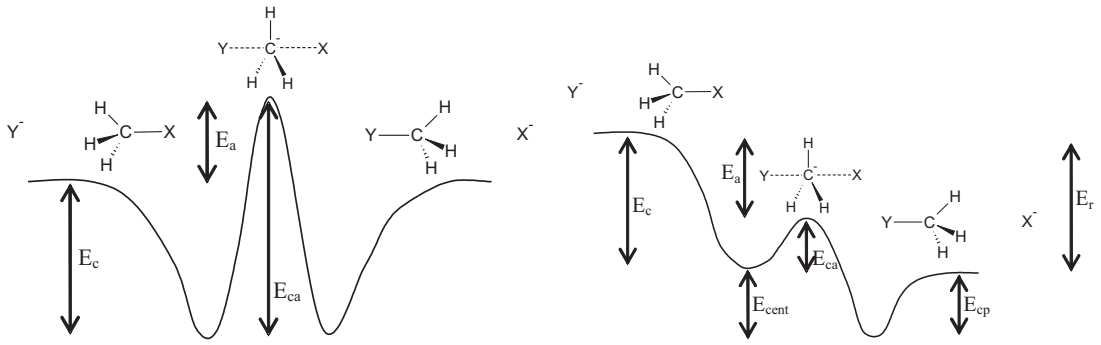

Figure 6.3.: Schematic representation of the traditional S_N2 Walden inversion by backside attack, for the case of the identity or symmetrical reaction (X=Y) (left), and the non-identity or unsymmetrical reaction (right). The identity reaction proceeds with a D_{3H} transitions state, whereas the non-identity proceeds with a C_{3V} transition state. E_a is the asymptotic activation energy, E_c and E_{cp} are the entrance and exit ion-dipole complex binding energies, E_{ca} is the gas-phase transition state destabilization, E_{cent} is the energy difference between the non-identity ion-dipole complex species, and E_r is the reaction (in the non-identity instance) exoergicity.

The default Dunnings' aug-cc-pVNZ basis sets implemented in Gaussian [13–16], for N = 2 to 5, have similar orbital exponents in the addition of the augmented functions with the "aug-" prefix. These augmentation diffuse functions only become slightly more diffuse (i.e. less than a factor of two) on increase of basis set cardinal number (zeta-quality). This makes these bases, without further augmentation, susceptible to error in complete basis set extrapolations involving long-range complexes, i.e. > 2.5 Å, with N = 2 to 5 basis sets. Complexes were first optimized at the MP2//aug-cc-pVTZ level of theory with and without CP BSSE corrections to the gradient. The effect of diffuse function augmentation is considered by systematic addition of *spd* functions and re-optimization, with counterpoise corrections at the same level of theory, and tight convergence criteria. After convergence of binding energy, complexes are re-optimized at the MP2//aug-cc-pVQZ level of theory, again with and without counterpoise and 6*sp*6*d* diffuse corrections. The complexes also had counterpoise corrected properties calculated at the CCSD(T)/MP2/aug-cc-pVNZ(+6sp6d) level of theory, where N=T,Q. The additional diffuse functions have orbital exponents starting at 7.239×10^{-3} and 2.315×10^{-2} respectively for *sp*-type and *d*-type orbitals, with an even-tempered geometric progression factor of 3.2. This minimizes linear dependence effects. Initial exponents were selected following consideration of the most diffuse orbitals in the aug-cc-pVTZ basis set. Note that for any additional augmentation, the additional most diffuse *sp*-type and *d*-type orbitals do not have equal

exponents. CP corrections consider a dimer species, with the first monomer being CH_3X with a closed-shell singlet spin-state and no charge. The second monomer, Y^-, is in a closed-shell singlet spin-state with one negative charge. Mulliken populations on non-counterpoise optimized ion-dipole complex geometries reproduce these asymptotic cases. That CP corrections do not include asymptotic relaxation terms is warranted as the ion-dipole haloalkane shows almost identical geometry to the isolated species.

Since the S_N2 reaction involves the interaction of a halide anion with a haloalkane, any calculation requires a good description of halide electron affinity, which in turn indicates a good relative description of the anion. Calculations on the electron affinity with zero point energy corrections showed the MP2//aug-cc-pVTZ level of theory to give good (Pauling-point) agreement with experimental electron affinities and ion-dipole binding energies, in accord with previous high-level benchmark calculations [17]. In addition, these calculations determine dipole moments in excellent accord with experimental values.

The results from the MP2//aug-cc-pVTZ(+M*spd*) optimizations, where M is the extent of diffuse augmentation, are shown in figures 6.4 and 6.5 for the identity and non-identity S_N2 ion-dipole complexes respectively. For all complexes, binding energy convergence to $\approx 1\times10^{-5}$ eV is reached with M = 4, and $< 10^{-6}$ for M = 6. For the $[Cl..CH_3Cl]^-$ ion-dipole species, the diffuse augmentation improves binding energy by only 1.6 meV, and the complex BSSE is $\approx 5\%$ of the total complex binding energy. These data indicate that consideration of BSSE correction is crucial to obtaining correct geometries and binding energies. The optimized complex bond-length (with MP2//aug-cc-pVQZ in parentheses) changes from 3.128 Å (3.128 Å) to 3.163 Å (3.143 Å) with BSSE gradient corrections, and then to 3.160 Å (3.146 Å) with 6*spd* augmentation. The non-BSSE corrected MP2//aug-cc-pVNZ(+M*spd*) for N = 3, 4; and M = 0, 6, bond lengths for all complexes are in agreement. Thus, addition of additional diffuse functions to a standard triple-zeta valence basis appears not to be required for an accurate description of the S_N2 ion-dipole complexes. However, BSSE corrections should be employed. It is not computationally feasible to increase the basis set description beyond aug-cc-pVTZ for the number of potential energy surface points required to describe the gas-phase reaction.

The same conclusions were found when employing the less expensive 6-311++G(2df,2pd) basis set when considering approach interaction potential over a circle of geometries referenced with respect to the C-X internuclear axis analogous to the Na + CH_3NO_2 study. The MP2//6-311++G(2df,2p) angular S_N2 entrance potential energy surface for the F^- + CH_3F reaction is given in figure 6.6. The entrance and exit surfaces for Cl^- + CH_3F are given in figures 6.7 and 6.8 respectively.

Briefly, these orientation potential energy surfaces all show an interesting characteristic that the ion-dipole complexes show a broad "bowl" or cone of acceptance, spanning $\approx 280°$, to formation centred at the methyl end of the halocarbon, with the boundary at apparent equipotential points at zero interaction potential. These calculations have atom type referencing that allows study of the prototypical S_N2 halide exchange reaction, and other channels are under investigation. Other possible (ground state) asymptotic reaction channel energies for

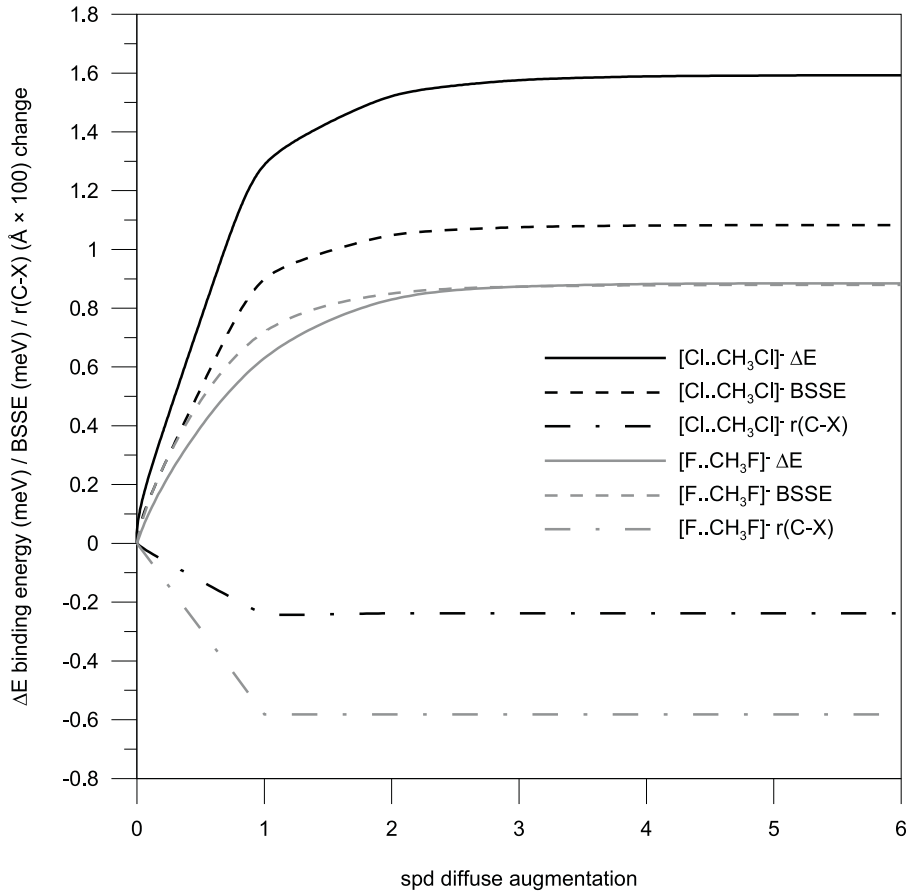

Figure 6.4.: Change in ion-dipole binding energy (meV), basis set superposition error (BSSE) (meV) and complex bond length (× 100 Å) for identity S_N2 $[Cl..CH_3Cl]^-$ and $[F..CH_3F]^-$ ion-dipole complexes at the counterpoise gradient-corrected MP2//aug-cc-pVTZ(+*spd*) level of theory.

for the Cl^- + CH_3Cl reaction are given in table 6.2. These data indicate that HX and X_2^- channels also compete with the S_N2 reaction at low energies. While these interaction potential curves indicate a cone of acceptance to prototypical S_N2 reaction that broadly centres about the methyl end of the molecule, attack on the average methyl hydrogen cone would most likely result in HX formation, and attack on the halogen end could result in X_2^-. Such observations should be able to be made when the molecular beam experiments are undertaken.

Both the MP2 and CCSD(T) electron correlation treatments appear to describe this system well, with the reaction coordinate for backside (180°) attack of the Cl^- + CH_3Cl reaction shown in figure 6.9. As expected, the MP2 and CCSD(T) calculations yield different descriptions of the transition state, which in the gas phase is on the same order of energy as the ion-dipole complex binding energies. Fortunately, the kinetics of these reactions have been well studied in the gas-phase and there are abundant theoretical studies of transition state geometries and energetics. Tentative CASSCF and CASPT2 calculations for the transition state region have been calculated that allow scaling of this region of the potential energy surface to find accord with experimental studies. No accurate experimental measurement of the ion-dipole binding energies exists for F^- or Cl^- S_N2 reaction.

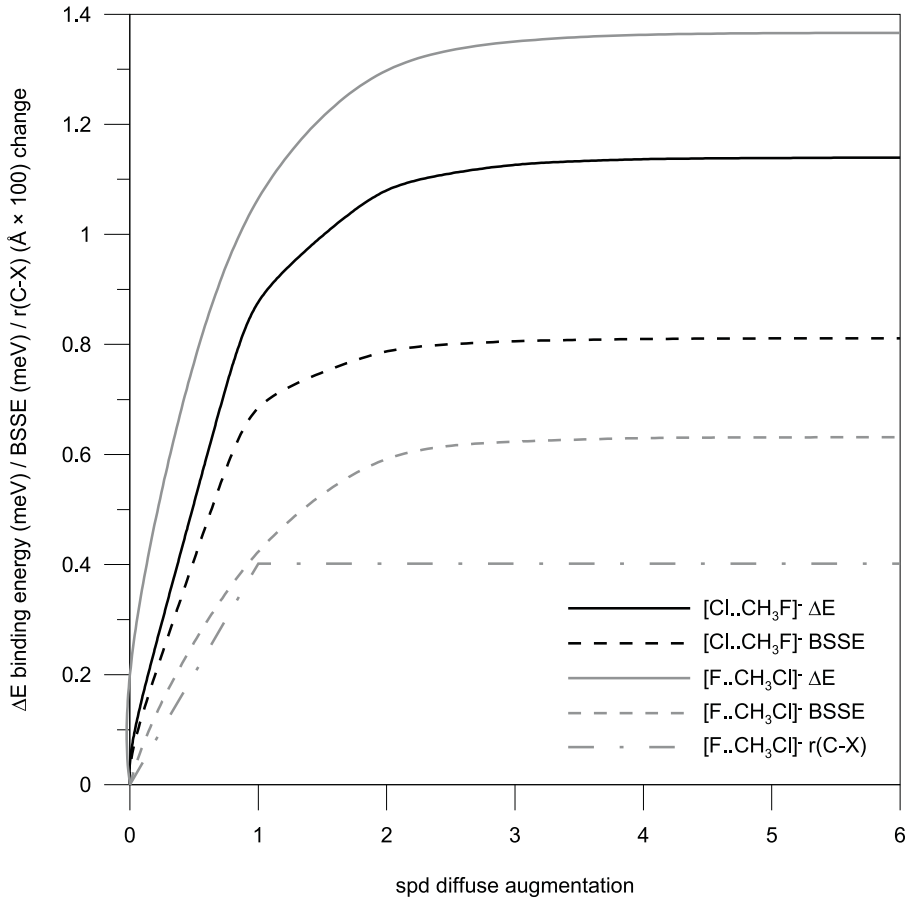

Figure 6.5.: Change in ion-dipole binding energy (meV), basis set superposition error (BSSE) (meV) and complex bond length (× 100 Å) for non-identity S_N2 $[Cl..CH_3F]^-$ and $[F..CH_3Cl]^-$ at the counterpoise gradient-corrected MP2//aug-cc-pVTZ(+*sp*d). [Cl..CH_3F]- shows no change in complex bond length.

Table 6.2.: Relative zero-point corrected energies of possible reaction product channels for Cl^- + CH_3Cl at the MP2//aug-cc-pVTZ and CCSD(T)/MP2/aug-cc-pVTZ in parentheses levels of theory. All channels show endoergic nature relative to the reactants.

Reaction channel	Relative energy (eV)
Cl^- + CH_3Cl	0.00 (0.00)
HCl + CH_2Cl^-	2.79 (2.69)
Cl_2^- + CH_3	2.71 (2.96)
CH_2Cl_2 + H^-	3.83 (3.69)
Cl^- + Cl + CH_3	3.98 (3.76)
Cl + CH_3Cl^-[a]	4.22 (4.06)
HCl^- + CH_2Cl[a]	4.18 (4.05)
Cl^- +H +CH_2Cl	4.37 (4.38)
Cl_2 + CH_3^-	4.78 (4.70)
Cl + H + CH_2Cl^-	7.17 (7.05)
Cl^- + H^+ + CH_2Cl^-	17.14 (17.15)

[a]the CH_3Cl^- and HCl^- species are not stable to electron detachment and/or dissociation, owing to a negative adiabatic electron affinity.

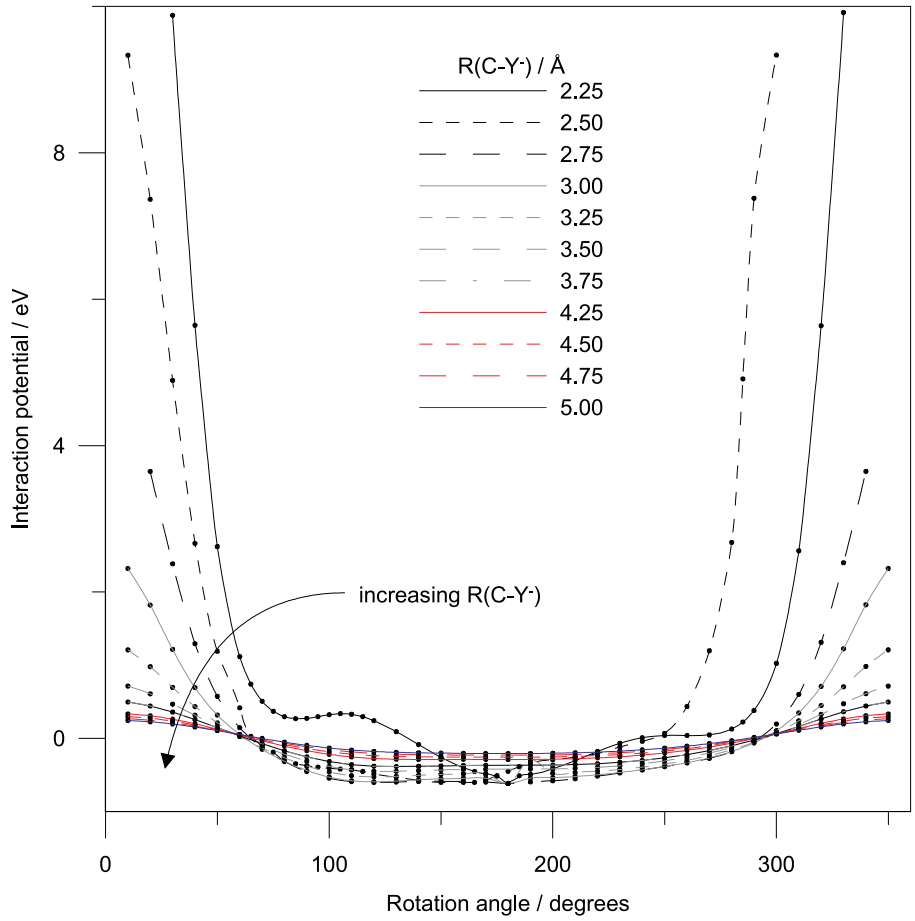

Figure 6.6.: Entrance potential energy surface for the F^- + CH_3F reaction at the MP2//6-311++G(2df,2pd) level of theory. Angles are referenced with respect to the C-F internuclear axis at the halogen end of the molecule with rotation first proceeding through an eclipsing conformation with a methyl hydrogen.

A four month part-time study involving the orientation dependence of some calculations for the Cl^- + CH_3Cl reaction was performed by an exchange Honours student, Philipp Kitschke, as part of his fourth year research project in conjunction with the author of this thesis. This study has been reported elsewhere [18].

Similar to the H_3^+ calculations outlined above, a full interpretation and furthering of the S_N2 potential energy surfaces can be undertaken when experimental results become available for comparisons.

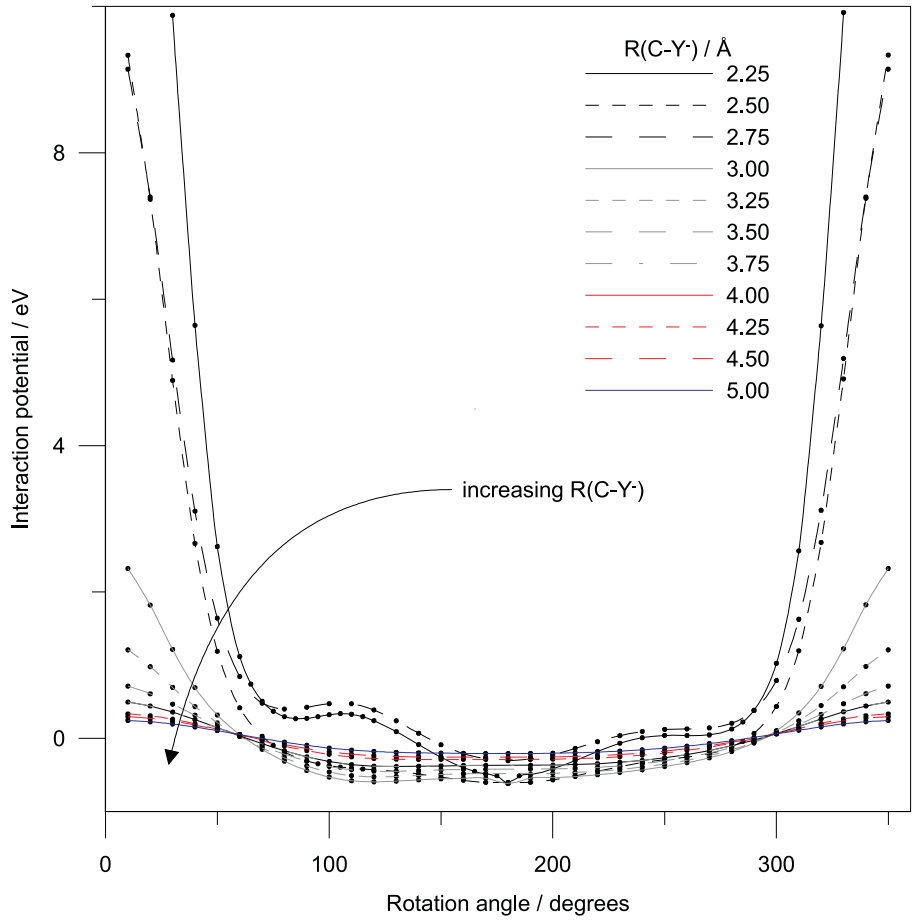

Figure 6.7.: Entrance potential energy surface for the Cl^- + CH_3F reaction at the MP2//6-311++G(2df,2pd) level of theory. Angles are referenced with respect to the C-F internuclear axis at the halogen end of the molecule with rotation first proceeding through an eclipsing conformation with a methyl hydrogen.

6.3. Charge-transfer surfaces for small molecule harpoon stereodynamics

Following the development of a basic *ab initio* method to calculate maximum electron impact ionization $(e, 2e)$ cross-sections and ionization surfaces for small molecules [19], this methodology has been generalized to allow approximate calculation of maximum cross-section and charge-transfer surfaces for classic Harpoon type electron-transfer reactions. Calculations over many angles construct the spatial three-dimensional potential energy surface, and can potentially provide a better cross-section approximation than other methods. Experimental based determinations are difficult and can show considerable variation. This model also allows generalization to calculate asymmetry parameters and can approximate energy dependence in the absence of vibrational and rotational excitation.

6.3.1. Introduction

That a molecular collision exhibits orientation dependence in reaction product nature and energetics for non-spherical reactants is intuitively obvious. Direct experimental evidence is difficult and requires experiments to be

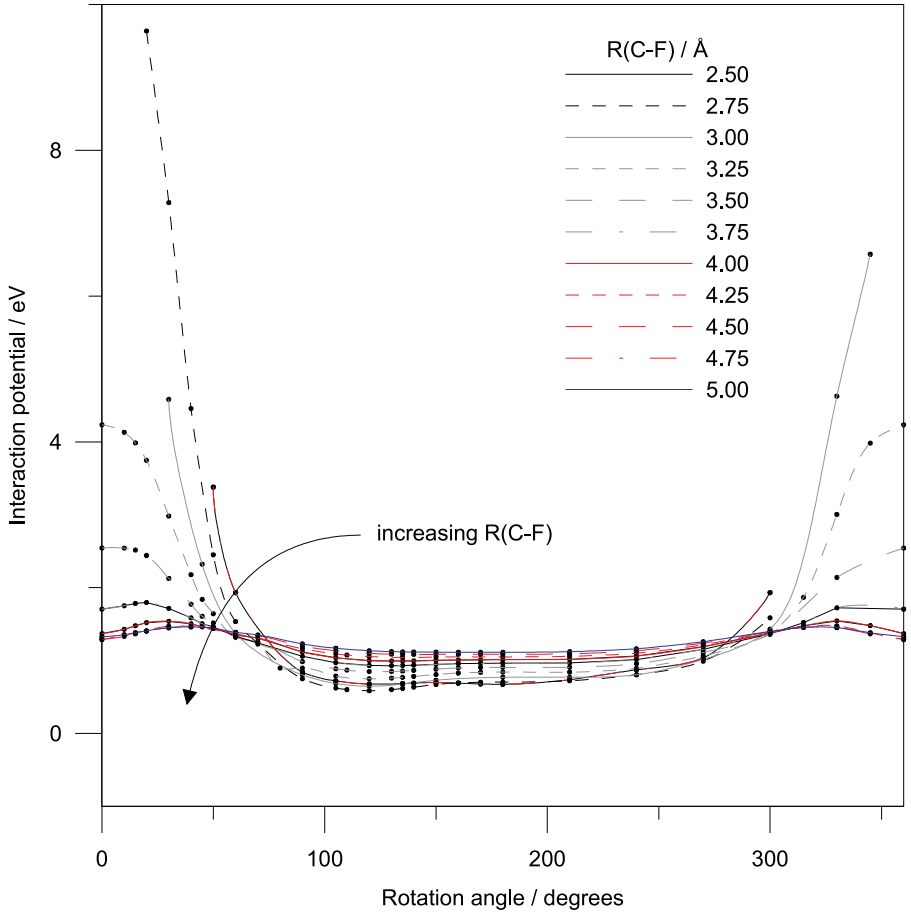

Figure 6.8.: Exit potential energy surface for the Cl^- + CH_3..F reaction at the MP2//6-311++G(2df,2pd) level of theory. Angles are referenced with respect to the C-F internuclear axis at the halogen end of the molecule with rotation first proceeding through an eclipsing conformation with a methyl hydrogen.

performed under single-collision conditions where solvent or 'spectator' species do not perturb the fundamental interactions. Electron impact ionization, herein denoted $(e, 2e)$, by a free electron could be considered as one of the most fundamental interactions in chemistry, yet paradoxically it is only recently that experiments have proven that $(e, 2e)$ exhibits ionization efficiency and fragment orientation dependence [20–22]. Vallance *et al.* [19] developed a basic *ab initio* method to calculate maximum $(e, 2e)$ cross-section, σ, and ionization volume based on systematic HF/6-31G* calculations over several orientation angles, with a systematically decreasing molecule-charge separation until the interaction potential equals the ionization potential where ionization is assumed with unit probability. This method was applied to several small molecules with known experimental σ, where calculated values were in good accord with experiment, and as would be expected, performed similar to the Binary-encounter-Bethe model [23,24], and performed better than the Deutsch-Märk model [25,26]. It is not too surprising that of the small molecules considered, this methodology performed worst for CO, CO_2, NO and NO_2, all of which are inherently multi-configurational owing to the π configurations, and are well-known to require large basis sets with high degrees of electron correlation.

The harpoon reaction involves the transfer of an electron from an electropositive alkali earth metal, at

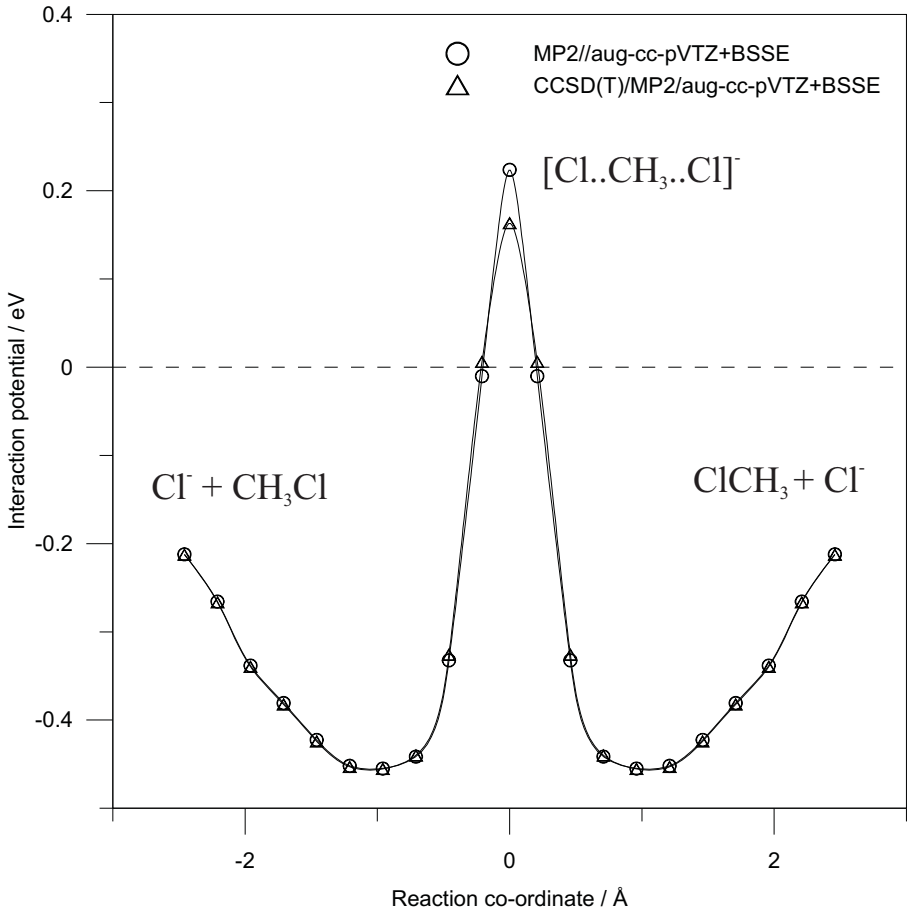

Figure 6.9.: Reaction coordinate along the Cl..C..Cl vector for the identity Cl^- + CH_3Cl backside attack reaction.

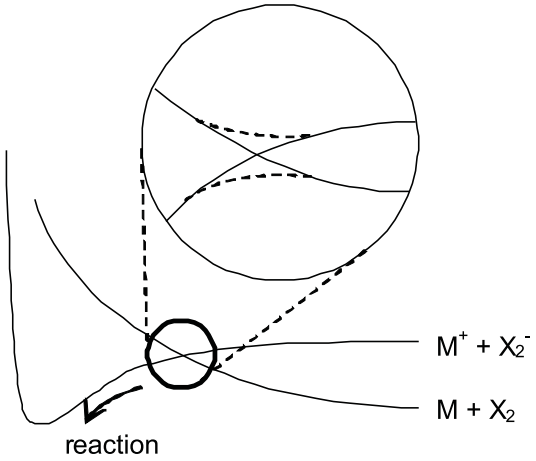

Figure 6.10.: Representation of the harpoon covalent-ionic surface crossing mechanism.

relatively large intermolecular separation ($\approx$ 5 Å) to a molecular target with a positive adiabatic electron affinity, EA $>$ 0. Following electron transfer, the separation between donor and acceptor rapidly decreases owing to ion-pair electrostatic attraction. The classic prototypical examples of such reactions are the group one alkali metals, M, where M = Li, Na, K, Rb, Cs, with the diatomic halogens X_2, where X = F, Cl, Br, I. Unfortunately, molecular beam electrostatic orientation dependence experiments cannot be performed on these simple prototypical Harpoon systems, since molecular orientation cannot be achieved in the absence of a permanent dipole moment. Although alignment are potentially possible with laser pulses, such a procedure causes electronic state changes [27]. Any model should first be able to reproduce the simplest case, and then be generalized to larger and more complicated systems.

The traditional harpoon model assumes a Born-Oppenheimer approach, where rapid changes in electronic wave function for a small change of nuclear configuration occurs, and is summarized in the reaction scheme:

$$M + X_2 \longrightarrow M^+ + {}^-X\text{-}X \longrightarrow M^+X^- + X$$

The first step involves the crossing of a covalent surface with an ionic surface at separation r_c, where charge-transfer of an electron (harpoon) is assumed with unit probability since this is effectively the bond-length of an ion-pair intermediate. The newly formed ion-pair is described by an ionic surface, and the separated ions are strongly pulled together by the inter-atomic Coulombic attraction, yielding dissociation of the X-X^- bond. Figure 6.10 shows the entrance channel involving the crossing of the covalent and ionic surfaces. A similar crossing exists in the exit channel, where the harpoon RX ion-pair product may dissociate to ionic or neutral (covalent) atoms.

The classical ion-pair formation separation at the surface-crossing, r_c, is usually approximated by equality between the Coulombic interaction potential (traditionally assumed at unity electron charge on each ion), e^2, and the electron affinity of X_2, EA(X_2), and the ionization potential of M, IP(M), as given in equation 6.1.

Table 6.3.: Application of the tradition point-Coulombic harpoon model to calculation of charge-transfer cross-section. In parentheses is extension to an ellipsoid model allowing for the equilibrium X-X bond length.

reaction	experimental estimate[a]	Coulombic point model
Li + F_2	82	55 (75)
Na + F_2	85	69 (91)
K + F_2	103	145 (209)

[a]Ref [28]

$$\frac{e^2}{r_c} = IP(M) - EA(X_2) \tag{6.1}$$

The isotropic charge-transfer cross-section, σ, is then assumed to be given by equation 6.2.

$$\sigma = \pi r_c^2 \tag{6.2}$$

Ansiotropy in the charge-transfer cross-section can be accounted for with incorporation of an opacity function, $P(b)$ which represents the probability of charge-transfer as a function of b, the impact parameter which is the M-X_2 separation for a general trajectory. The reaction cross-section can then be expressed in equation 6.3.

$$\sigma = 2\pi \int_0^\infty P(b) \cdot db \tag{6.3}$$

Traditionally, $P(b)$ has been assumed as a unit step function in simple collision theory.

When equation 6.1 is applied to the M + F_2 system (or in fact any X_2), relatively poor agreement that is well beyond the well-established and experimental error of the EA and IP is obtained with respect to experiment as seen in table 6.3. Molecular dynamics simulations can produce cross-sections that invoke certain assumptions, and also require potential energy surfaces.

An *ab initio* model would provide a much improved description of the surface crossing region, and could potentially improve on the simple collision theory step like opacity function by employing a probability type function.

Two limiting curve-crossing models can be applied, known as the diabatic and adiabatic approximations. These two approximations require consideration of the relative time between the charge-transfer interaction, T_c, and the molecular vibrational period, T_v, of the target molecule and corresponds to the response characteristics for the non-perturbed molecular species. Traditionally, the so-called adiabaticity parameter, ξ, is defined in equation 6.4.

$$\xi = \frac{T_c}{T_v} \tag{6.4}$$

where $0 < \xi < \infty$. When $\xi < 0$, then $T_c < T_v$, and the reaction may be assumed to occur through a diabatic surface crossing, which makes the basis of Landau-Zener theory [29]. When $\xi > 1$, then $T_c > T_v$, and the reaction would proceed through an adiabatic pathway. When $T_c \approx T_v$, both dynamics should be considered, but a tuned resonance would take an adiabatic pathway. For thermal (equilibrium) mono-atomic gaseous metal atoms with center-of-mass (translational) experimental energies 1 to 10 eV, T_c and T_v may be on the same order of magnitude depending on the exact M + X_2 system, therefore both approximations should be considered. In the adiabatic model, cross-sections are expected to be slightly larger since the long-range interaction between M and X_2 causes slight X-X bond stretching, which in effect increases EA(X_2).

6.3.2. Proposed computational method

Calculations involving surface crossings in both the diabatic and adiabatic approximations follow the general scheme shown in figure 6.11. Approach of the alkali metal atom, M, is referenced with respect to the mid-point of the isolated halogen molecule, R, such that $R_M > R_X$. In the diabatic model, R_D =R(X_2) = 2× R(X_2/2), whereas for the adiabatic model, R(X_2/2) is fixed and R_D is free to optimize for a given R_M. The potential energy surfaces in both approximations were then calculated using the Gaussian 03 computational package [13], by systematically varying R_M in increments of 0.2 Å over the range from 7.0 Å to 2.0 Å for θ in 15° increments between 0° and 90°. Mulliken and NBO atomic populations were calculated at each point. Neutral X_2 are treated in the $^1\sum_g^+$ ground state, while the anion was treated in the $^2\sum_u^+$ ground state. Calculations on Rb, Cs or I_2 have not been considered owing to requiring core potential type basis sets and consideration of spin-orbit and relativistic corrections [30]. Intuitively, the 90° approach in the diabatic approximation has higher super molecule nuclear point symmetry, and charge-transfer is symmetry-forbidden between the M(^{2}S) and $X_2(\sigma^*)$ orbitals.

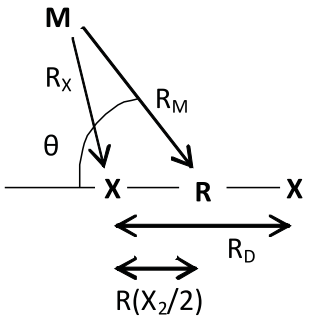

Figure 6.11.: Geometrical arrangement and parameter assignments for orientation dependence calculations. **M** is the alkali metal; **X** is the halogen atom; and **R** is the mid-point for isolated X_2.

6.3.3. Preliminary discussion

The first requirement is to determine an appropriate level of theory to treat the charge-transfer system. The relevant molecular parameters that require accurate description are: alkali metal ionization potential (IP); atomic and adiabatic molecular electron affinities (EA); and halogen bond dissociation energy (BDE). The

Table 6.4.: Experimental (literature) and calculated properties of the harpoon charge-transfer system in units of eV and Å. All calculations were treated with the Pople 6-311++G(3df) basis set. IP - ionization potential, EA - adiabatic electron affinity, BDE - adiabatic bond dissociation energy. All EA and BDE calculated values include the small anharmonic ΔZPV correction at the B3LYP//6-311++G(3df) level of theory.

Property	Species	Experimental	Calculated MP2	CCSD(T)
IP	Li	5.392[a]	5.338[e]	-
	Na	5.139[a]	4.944[e]	-
	K	4.341[a]	4.259[e]	4.265
EA	F	3.401[a]	3.538	3.216
	Cl	3.613[a]	3.594	3.467
	Br	3.364[a]	3.409	3.337
	F_2	3.00 ± 0.07[b]	3.020	3.000
	Cl_2	2.33 ± 0.1[c,d]	2.389	2.408
	Br_2	2.55 ± 0.1[d]	2.539	2.557
BDE	F_2	1.646[a]	1.654	1.412
	Cl_2	2.514[a]	2.450	2.261
	Br_2	1.998[a]	2.140	2.018
	F_2^-	1.21 ± 0.07[b]	1.136	1.196
	Cl_2^-	-	1.246	1.202
	Br_2^-	-	1.204	1.164
$R(X_2)$	F_2	1.4119	1.397	1.415
	Cl_2	1.9878	1.985	2.006
	Br_2	2.2811	2.281	2.304
	F_2^-	-	1.909	1.934
	Cl_2^-	-	2.586	2.618
	Br_2^-	-	2.836	2.870

[a]Experimental uncertainties are smaller than the last decimal figure, [31]
[b]Ref [32]
[c]Ref [33]
[d]Ref [34]
[e]MP2 calculation with additional diffuse functions yields no change to IP

experimental and calculated data are reported in table 6.4.

Calculated IPs are all in excellent agreement with $< 4\%$ difference to experimental values. Atomic halogen electron affinities show the well-known fortuitous Pauling-point agreement at the MP2//6-311++G(3df) level of theory, where the error cancellation arises from a combination of spin-orbit coupling and scalar relativistic effects [17]. MP2 electron correlation shows the largest deviation of $\approx 4\%$ for F. Adiabatic electron affinities for the molecular halogens are in excellent agreement with experiment. Second- and fourth-order Douglas-Kroll-Hess scalar relativistic corrections to EA(Br_2) were calculated to be ≈ -0.01 eV and are negligible. Calculated bond lengths are also in excellent accord with experiment. MP2 calculated vertical electron affinities are in accord with Morse potentials fits [35]. Stretching of the X-X bond increases the electron affinity to the atomic halogen value at infinite separation. Calculated anion equilibrium bond lengths and bond dissociation energies are in good accord with reported Morse parameter fits [36]. These data would indicate that MP2//6-

311++G(3df) level of theory provides sufficiently accurate potential energy surfaces.

While the diffuse nature of the 6-311++G(3df) basis set can treat localized anions satisfactorily, its suitability for a description of long-range interactions ($r_c \approx 4$ Å or greater) needs to be ascertained. This was achieved by addition of three *sp* and three *d* type functions with exponents determined by a decreasing geometric ratio of factor 3.2 from the default basis set's most diffuse orbital. In effect, this provided a set of orbitals an order of magnitude more diffuse than the default valence. Calculations on the Li + Br_2 and K + Br_2 surfaces showed no significant differences in r_c to those without the addition of diffuse augmentation, indicating the 6-311++G(3df) default valence parameterization to be sufficient. In all cases, basis set superposition error corrections are negligible.

The adiabaticity parameter, ξ, is initially considered for two different cases. Firstly (1), for time T_c to correspond to the time for a reaction displacement of $\Delta r_c \approx 1$ Å, corresponding to the separation for the charge on the metal atom, Q(M), to change from ≈ 0 to $\approx +50\%$ of the final ion-pair charge, as determined from Mulliken [37], NBO [38] and CHelpG [39] population schemes reported later. Secondly (2), when the charge gradient, ∇Q(M), is maximum. These two cases are known as the charge-transfer threshold and gradient charge-transfer threshold respectively. The parameter ξ for case (1) is summarised in figure 6.12 for typical experimental energies, and the tabulated diatomic constants (frequencies) of: $\nu = 917$ cm^{-1} (F_2); 560 cm^{-1} (Cl_2); 325 cm^{-1} (Br_2) are assumed [31].

It is obvious from figure 6.12 that for case (1), the lightest Li + F_2 system at high energies could be treated in a diabatic picture, and the heavier K + Br_2 and slower systems would require an adiabatic approximation. In contrast, when $\Delta r_c \approx 0.2$ Å, all reactions would assume the diabatic approximation. It is therefore required that *ab initio* calculations are performed on both cases to see if any significant differences exist in charge-transfer cross-sections and/or energies. Experimentally, that the harpoon reactions show considerably forward peaked reaction product in the center-of-mass reference frame, would intuitively indicate an impulsive diabatic charge-transfer nature [40]. In the electron impact ionization model of Vallance *et al.* [19], any calculation would rigidly assume the nuclear diabatic approximation since for E = 75 eV that corresponds to the typical maximum $(e, 2e)$ cross-section, then T_c would be three orders of magnitude smaller than T_v.

Both Mulliken and NBO population schemes in a probabilistic interpretation indicate that charge-transfer is not instantaneous on curve-crossing, rather the charge on the metal atom changes from zero to maximum over several angstroms, where the point of inflection is intuitively in close agreement with the ionic-covalent surface crossing separation. This feature was also observed in charge-transfer calculations of CH_3NO_2 [41], CH_3CN [42] and CH_3Cl [43]. These data may then be fitted with a three-parameter symmetrical sigmoid as a function of separation, r, as given in equation 6.5.

$$Q = \frac{a}{2}\left(\frac{-(r-b)}{\sqrt{c+(r-b)^2}}\right) + \frac{a}{2} \tag{6.5}$$

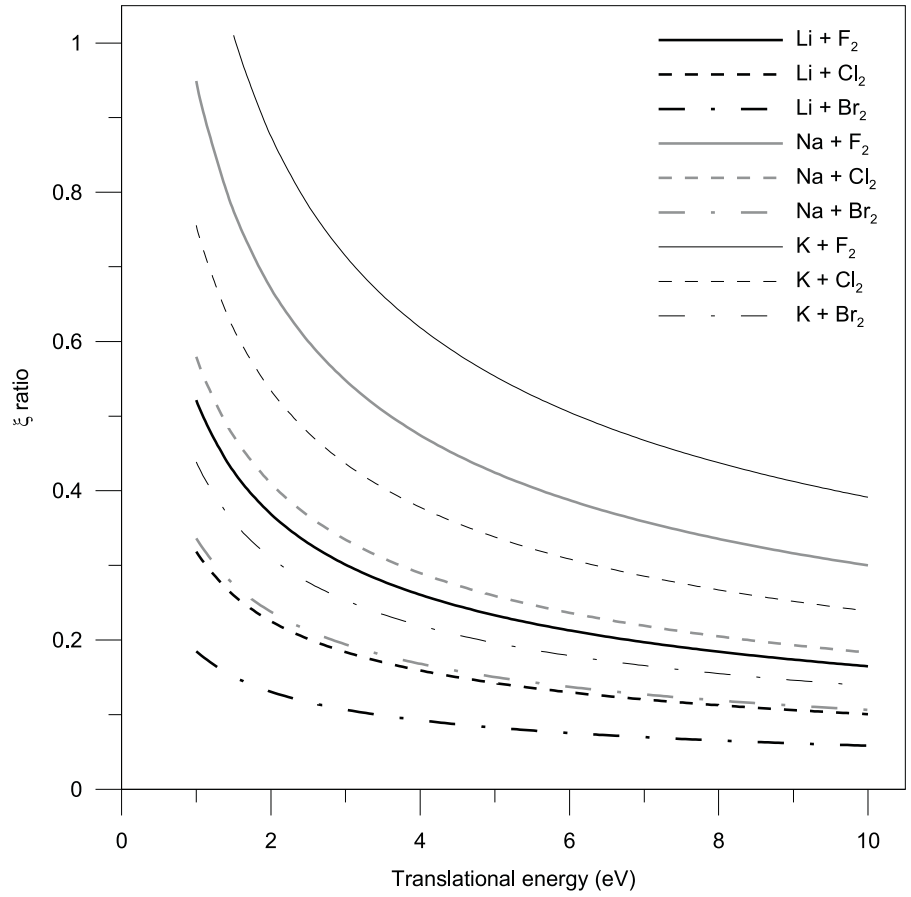

Figure 6.12.: Adiabaticity parameter, ξ, for all M + X_2 considered in this study, and for two different coupling periods, T_c, with parameters for case (1) - $\Delta r_c \approx 1$ Å.

where a corresponds to the maximum "amount" of charge-transfer (i.e. ion-pair Q(M)), $b = r_c$ is the surface crossing separation, and c is a S-like symmetrical tension factor. One such fit is shown in figure 6.13.

An important question is how accurate, or even "physically correct" are such atomic populations? Calculations on Na + CH_3NO_2 that use both these population schemes, with a near point-of inflection threshold, have revealed excellent accord with experimental data [41]. Szefczyk *et al.* [44] have shown that Mulliken and NBO populations yield approximate correlation with extent of charge-transfer for a series of Lewis base neutral-neutral (RHF) interactions. What was not outlined in this study was comparison of the theoretical methods ability to reproduce the experimental EA and IP for each neutral. Their results were consistent with the conclusions of Zou *et al.* [45], where the CHelpG (electrostatic potential-fitted method) approach performed the best. Results from the CHelpG methods appears to be reasonably different from those obtained with Mulliken and NBO here, and are not very physically meaningful at very long separation. Nevertheless, the gradient reproduces the same charge-transfer separations (maximum ∇Q) as Mulliken and NBO schemes for all M and X_2 considered in this study. Assuming that the charges can be interpreted in terms of probability, then equation 6.5 can be adapted into an opacity function for each given angle. Comparison of calculated cross-sections with experiment would need to be performed in order to assess its suitability.

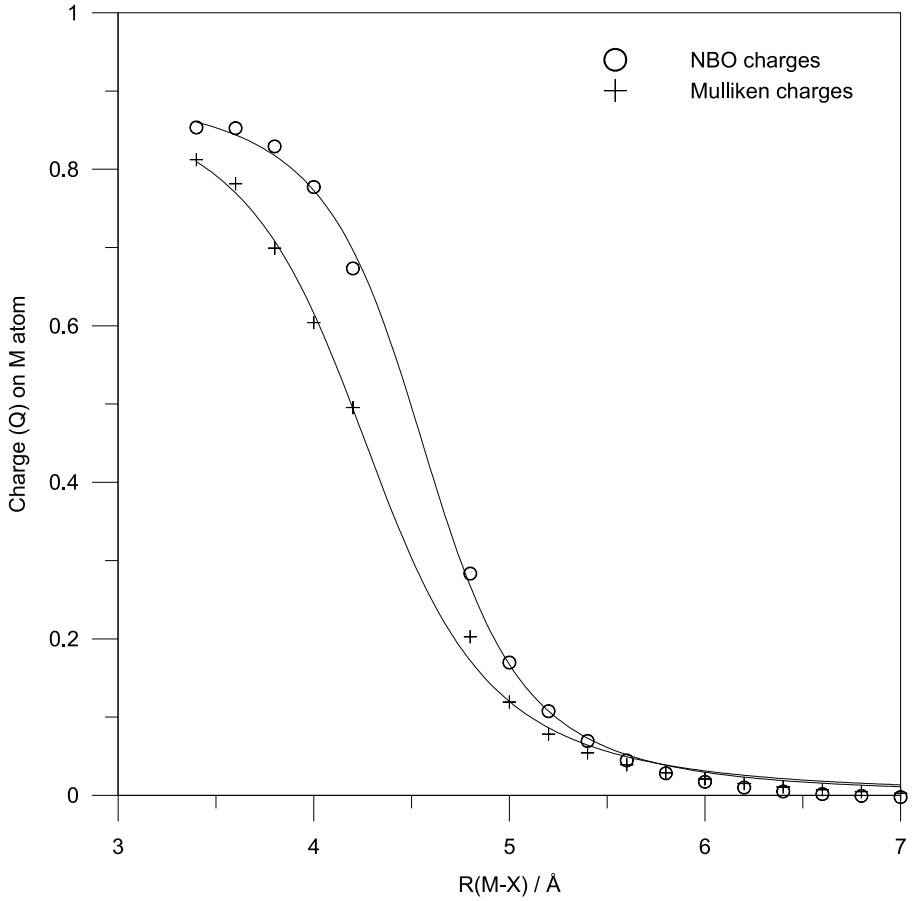

Figure 6.13.: Example of the sigmoidal opacity function fit to the K + Cl_2 diabatic surface for direct axial (0°) approach. Some data near the point of inflection have been omitted in this plot since computational convergence is difficult and the Hartree-Fock single reference wave function treatment breaks down.

One example of the diabatic charge-transfer surface for K + Cl_2 assuming the charge-transfer and gradient charge-transfer approximations is given as a two dimensional projection in figure 6.14. The 15° angular increments appear to yield a suitability smooth charge-transfer surface, which, perhaps not surprisingly, appears to resemble the σ^* anti-bonding orbital. Assuming this model is correct, the anisotropy in charge transfer as a function of approach angle θ indicates that the traditional point-charge isotropic approximation would be incorrect. For the diabatic system considered in figure 6.14, the orientation-averaged total charge-transfer cross-sections are calculated at 82 $Å^2$ and 99 $Å^2$ for the two charge-transfer threshold approximations. The experimental value has been estimated at $\approx$ 100 to 110 $Å^2$, in good accord with the latter value. The point-charge model calculates this cross-section at 78 $Å^2$, which is in poorer agreement. All potential energy surfaces for a given angular orientation show, as expected, no barrier to charge-transfer. The approach potential energy surfaces for K + Cl_2 are shown in figure 6.15. Of course, as soon as charge-transfer has occurred, the value of ξ fundamentally changes with ion-pair formation and X-X bond weakening.

Clearly this model shows potential and will be completed in the near future. All calculations for M=Li,Na,K,

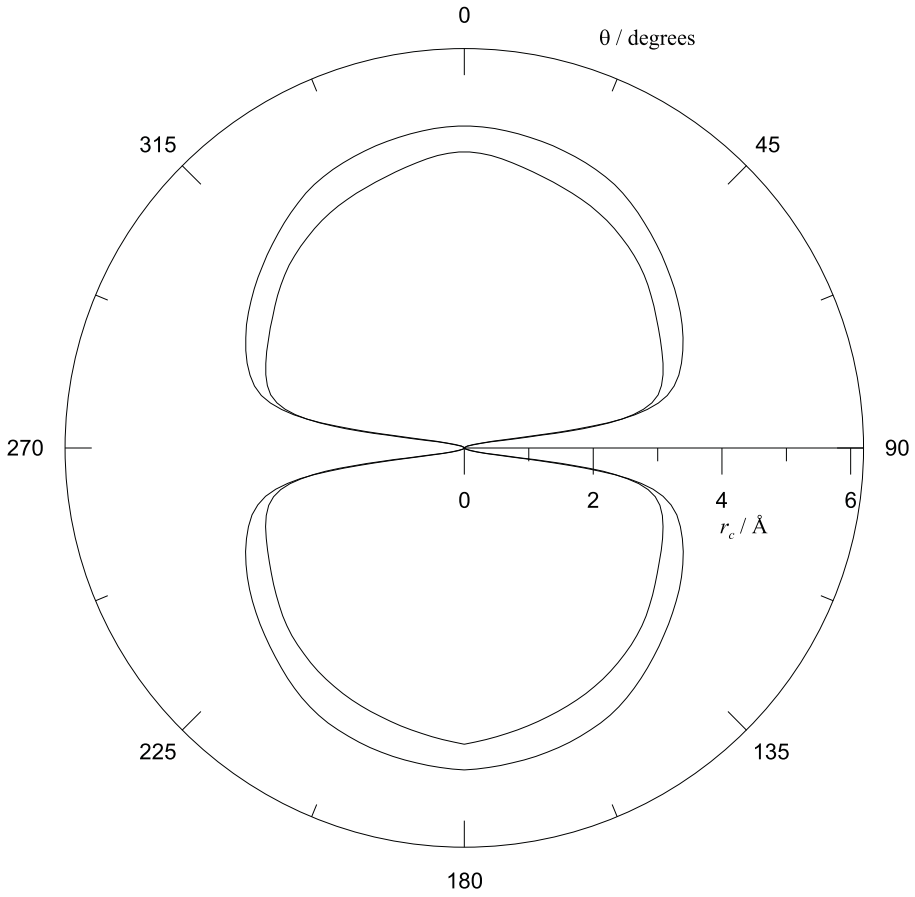

Figure 6.14.: Two-dimensional projection of the charge-transfer surface for the K + Cl_2 reaction in the diabatic approximation. The inner surface represents the charge-transfer threshold, and the outer surface represents the gradient charge-transfer threshold.

and X=F,Cl,Br, in both the diabatic and adiabatic approximations have been performed. These calculations took ≈ 1 month of continuous processing time on a dual core 2.8 GHz Pentium D system.

6.4. Isocyanide orientation dependence: the isolated Na + CH_3NC rebound reaction

Following the successful computational study on the Na + CH_3NO_2 charge-transfer reaction, calculations were performed on both the Na + CH_3NC and K + CH_3NC reactions to describe the potential energy surfaces to find accord with and theoretically explain the experimental results of Brooks *et al.* [46, 47] for the K reaction. Maclagan [48] has previously reported some *ab intio* calculations on the K + CH_3CN reaction, and found no classical harpoon nature, as expected for a species with a negative valence electron affinity. These calculations did not consider the various ion-pair species. In the work briefly introduced in this section, the Na + CH_3NC system was initially chosen for study since many different ion-pair adducts of Na and CN species have been reported previously in the literature. A follow up study calculated for the K + CH_3NC potential energy surfaces

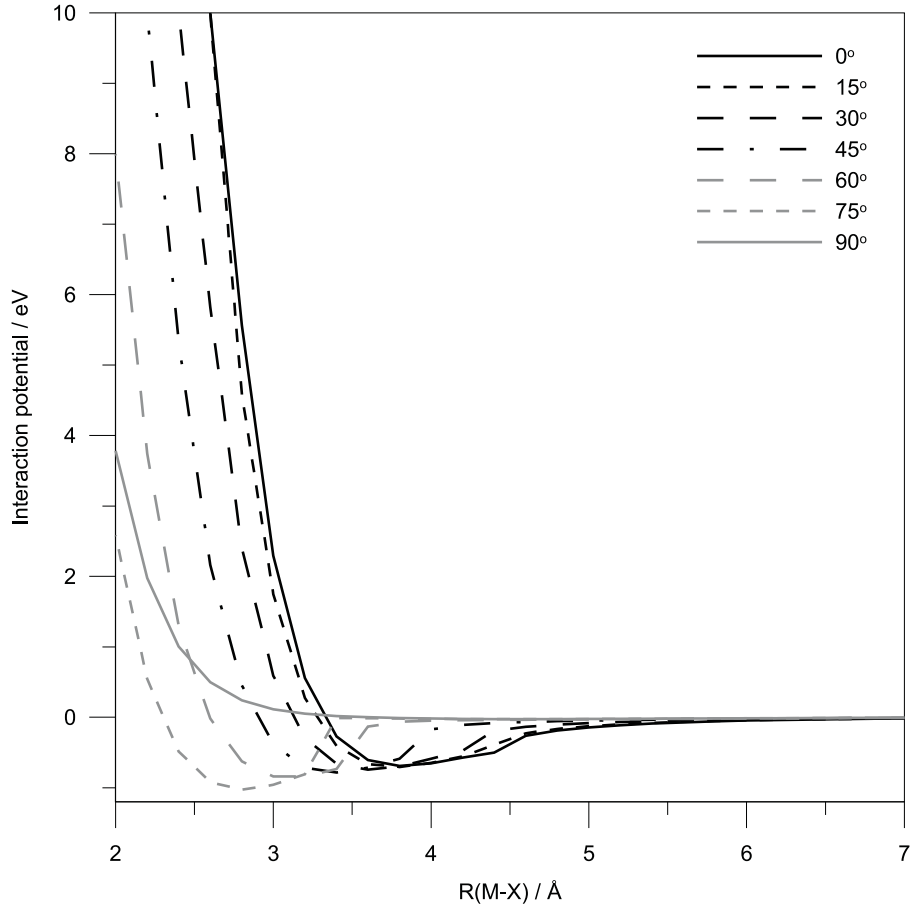

Figure 6.15.: Approach potential energy surface for the K + Cl_2 reaction in the diabatic approximation.

would allow a direct comparison with experiment. Both of these studies employed multi-reference methods that are ideally required to treat cyanide type systems. These studies have, in major part, been completed, and a manuscript is currently being drafted for future publication. One unfortunate set-back in these studies was the discovery that the MRMP2 (multi-reference second-order perturbation theory) procedure in GAMESS-US when using the ALDET (Ames Laboratory full configuration interaction determinant wave function) subroutine yielded incorrect results when computed under the C_S symmetry framework. These calculations have been repeated (on the BlueFern Blue Gene/L supercomputer) and the previous interpretations require updating. There are plans to finish these interpretations in the next month. The following section provides a tentative introduction, and some preliminary discussions adapted from the draft (in shorter form) manuscript.

6.4.1. Preliminary overview

Minimum energy pathway orientation dependence calculations were calculated at the UMP2//6-311++G(2df,2p) and MRMP2/MP2/6-311++G(2df,2p) levels of theory for the charge-transfer reaction of atomic sodium and potassium with methyl isocyanide (CH_3NC). Two distinct types of complexes exist, axial σ-type van der Waals, and sideways π-type charge-transfer type complexes. The dipole-bound state binding energy of CH_3NC^- is calculated at 108 cm^{-1}, and appears to play no role in reaction orientation dependence. This reaction shows

characteristics of a rebound type mechanism, and the presence of the positive alkali metal core through ion-pair formation plays a dominant role after charge-transfer. In accord with previously reported experimental determinations, reaction preferentially occurs through sideways attack to the π-system, and shows fragment orientation dependence for CN^- (NC-end collisions), and CH_2NC^- (CH_3-end collisions).

6.4.2. Introduction

It is intuitive that a gas-phase bimolecular reaction, with at least one non-spherically symmetric reactant, has collision outcomes that depend upon relative orientation [49]. Direct experimental evidence is difficult, where studies must be performed under ultra-high vacuum conditions so background species do not perturb the reactant collisions or product species before detection. Methyl isocyanide, CH_3NC, is the simplest alkyl containing isocyanide species which is known to spontaneously isomerise to methyl cyanide, CH_3CN [50–56]. Both CH_3CN and CH_3NC, and dissociation products are known to be of atmospheric/astrophysical importance [57]. Recently, the effect of molecular orientation on the charge-transfer (electron) reaction of K with the π-bonded CH_3CN and CH_3NC species has been experimentally studied by Brooks *et al.* [46, 47]. Briefly, these experiments involve crossing a beam of hyperthermal K atoms with He seeded molecular beams of CH_3CN or CH_3NC. Use of homogeneous and inhomogeneous electric fields provides rotational state selection and dipole orientation relative to the K beam. The experiments showed that CH_3NC had a full precession cone angle of $\approx 71°$ [47], indicating the majority of molecules are oriented for near-end collision. Coincidence time-of-flight (TOF) mass spectrometers that terminated the beam lines provided characterization, and required any ion-pair products to be separated before detection. Both CH_3CN and CH_3NC show the major free ion products to be CN^-, H^- and CH_2CN^- or CH_2NC^- respectively, with no observation of the negative parent anion, CH_3CN^- or CH_3NC^-. Orientation dependence for a given reaction product is characterized in terms of a so-called G asymmetry parameter at a given energy, where $-1 > G > 1$, which is in turn defined in terms of cross-section, σ, for each dipole end ($\pm$) approach as given in equation 6.6.

$$G = \frac{\sigma(-) - \sigma(+)}{\sigma(-) + \sigma(+)} \tag{6.6}$$

A negative G indicates that reaction favours positive end (CH_3-end) collisions, while a positive G indicates that reaction favours negative end (NC-end) collisions, and when $G \approx 0$, there is no apparent reaction asymmetry. Both CH_3CN and CH_3NC species showed almost identical reaction orientation dependence for all reaction channels. Reaction forming free CH_2NC^- revealed a strong asymmetry for charge-transfer from the CH_3-end, with threshold at ≈ 7.1 eV. CN^- and K^+ were the dominant ion products (by almost two orders of magnitude), and the threshold for CN^- formation was $\approx 5.6 \pm 0.2$ eV, and showed a very slight and energy independent asymmetry favouring collisions from the NC-end. A very weak H^- signal was observed with formation threshold at ≈ 8 eV, and showed slight asymmetry to preferentially form at the NC-end. These experiments concluded that reaction preferentially occurs through sideways attack with the π system, giving charge-transfer into a π^*_{CN} orbital. Recent experiments on CH_3COOH (acetic acid) have shown similar trends to those for CH_3CN and CH_3NC, where charge-transfer appears to be dominated by a π^*_{CO} orbital [58]. In principle, *ab inito*

calculations could provide a theoretical understanding of the experimental observations. Such calculations have previously shown for Na + CH_3NO_2 reaction [59], that ion-pairs can play critical roles in experimental asymmetry parameters and can potentially characterize the reaction interactions.

Theoretical calculations by Maclagan [48] attempted to reproduce and rationalize the minimum energy pathway orbital interaction for the CH_3CN case, where axial approaches were constrained to C_{3V} point symmetry. It was concluded that "approach along a minimum energy pathway does not involve a simple harpoon mechanism". Calculations on the CN-end approach, required stretching of the CH_3-CN bond to achieve charge-transfer, inducing a barrier to reaction. The stretch magnitude, on the order of 0.55 Å, yields barriers of ≈ 2 eV that increase with decreasing alkali metal separation. Similar calculations on the K + CH_3Cl "rebound" system [60], showed stretching of the C-Cl bond facilitated charge-transfer and ion-pair formation by effectively increasing the electron affinity. This observation was not new, and has been previously observed for CH_3I giving charge-transfer barriers [61, 62], and is required for the harpoon-type I_2 reaction [63] to explain experimental dissociation product results. Bond stretching of CH_3CN or CH_3NC in effect would increase electron affinity.

Studies on the interactions of alkali metal atoms and other electronically similar π-bonded (triple) systems show trends of preferential orientation dependence to ion-pair formation. The most well studied system is that containing the C_2H_2 species, existing as acetylene and vinylidene isomers. Experiment and theory are both in agreement that in the gas-phase, two types of complexes can exist [64–71], known as van der Waals complexes and charge transfer complexes. Briefly, van der Waals complexes are weak ($\approx$ 200 meV) long-ranged (London) axial or sideways complexes where essentially no geometrical rearrangement from the isolated species occurs, and the metal atom gains a slight negative charge from σ-density acceptance. Charge-transfer complexes occur from sideways orientations to the π-system, where as a result of charge-transfer, the metal atom gains a positive charge and groups attached to the π-bond bend away from the metal ion with bond weakening. Theoretical calculations indicate synergistic interactions where $\pi^* \leftarrow \mathrm{M}(p)$ donation, and $\mathrm{M}(s/p) \leftarrow \sigma$ acceptance with respect to the metal yields a strong ground-state ion-pair. Ground state ^{2}S alkali metals require ^{2}P curve crossing or excitation to yield correct π symmetry for such an interaction. These trends have also been characterized for CO and CS species that are isoelectronic to CN^- [72–75]. In addition, the absence of axial hydrogen atoms can yield π-complexes from axial orientations. More importantly, argon matrix isolation electron spin resonance (ESR) studies have experimentally characterized these complexes for Li atoms reacted with HCN and CH_3CN [76], with near infra-red irradiation inter-converting the σ and π complexes. ESR results indicate that the doublet electron in the σ complex is located in an *sp*-hybrid orbital on the Li atom that is pointed away from the CN functional group, whereas the electron resides on the in-plane π^* orbital for the π complex. *Ab initio* calculations at the MP2//6-311++G(2df,2p)+ZPV and QCISD(T)/MP2/6-311++G(2df,2p)+ZPV levels of theory support the HCN complexes for Li and Na, and predict similar complexes for HNC [77, 78]. Cationic alkali metal reactants do not show π complexes, since electron transfer cannot occur [77, 79].

There are two limiting cases of charge-transfer type reactions involving electropositive alkali metal atoms with

molecular targets, known as the harpoon (e.g. K + I_2) and rebound (e.g. K + CH_3I) mechanisms [80]. These are distinguished by sign of the molecular adiabatic electron affinity (EA_{ad}), where $EA_{ad} > 0$ for the harpoon mechanism, and $EA_{ad} < 0$ for the rebound mechanism. Traditionally these reactions have been interpreted in the essence of Landau-Zener theory [61, 81], where angular dependence can be approximated with a smooth function. For CH_3CN or CH_3NC with a negative EA_{ad} (not stable to neutral and free electron), reaction is expected to be of the rebound type, with extensive product fragmentation and ion-pair formation which is in agreement with experiment. Rebound reactions typically show cones of no reaction where functional groups block charge-transfer, for example, the CH_3-group [61]. The open-shell CN species is expected to behave analogously to I, where the free halide has a positive EA_{ad}, the hydride (closed-shell) has this slightly negative, and the methylated species (closed-shell) has this strongly negative. With these considerations, it is not surprising that Brooks *et al.* [46, 47] experiments showed reaction to occur preferentially through sideways attack, similar to CH_3I [82]. Any accurate potential energy surface needs to reproduce the possible π-type interactions (i.e. multi-reference), and consider the strong asymmetry type nature of the rebound reaction.

Apart from a valence-bound anion, a molecular species that possesses a large dipole moment (> 2.5 D) may capture an electron at the positive end of the dipole field forming a dipole-bound anion [83, 84]. Such an anion generally exists in the ground vibrational state [85], and shows little geometric rearrangement from the neutral geometry, where the electron typically occupies a very diffuse σ^*-type hybrid orbital localized at the positive end of the dipole. Dipole-binding energies are small (several meV) and therefore difficult to measure experimentally. Despite the valence-bound anion, no evidence for a dipole-bound form was evident in Brooks *et al.* [47] experiments. There have been several experimental characterizations of such a dipole-bound species for CH_3CN. This species was first observed by Stockdale *et al.* [86] with Rydberg excited Ar*, with experiments indicating that decomposition to CH_2CN^- is rapid. There have subsequently been many experiments showing formation of the isolated dipole-bound species using crossed molecular beams with excited state atoms (in a restricted Rydberg range) [85, 87–93], or cluster methods [94–96]. Ground state projectiles (e.g. Ar) show no dipole-bound anion formation, presumably since the close separations required to yield a sufficiently large interaction potential to give charge-transfer would result in very different electronic structure and dynamics. *Ab initio* calculations on the dipole-bound state are in excellent agreement with experiment for CH_3CN [97–102] and CH_2CN [103]. Whether a dipole-bound anion plays a role in the Na + CH_3NC charge-transfer dynamics nevertheless needs to be assessed. Such anions have not been observed to have any influence in Brooks *et al.* [46, 47, 104, 105] experiments, nor other calculations [59].

In this section, some preliminary parts of a computational study are presented on the orientation dependence of the Na and K + CH_3NC reaction, with comparisons to the K + CH_3NC experiments of Brooks *et al.* [46, 47] in order to characterize the interaction potential energy surface, and gain a theoretical understanding of the rebound process when π bonding exists.

6.4.3. Computational details

All reported calculations have been performed using the GAMESS-US [106] and Gaussian 03 [13] computational packages. Molecular orbital visualization was performed with the MacMolPlot program [107]. Inbuilt spin-annihilation procedures were employed for single-reference wave functions, where cyanide species are known to be notorious for spin contamination owing to near degeneracies [55,108]. Further, the Hartree-Fock approach does not correctly describe chemical reactions with curve crossings, or systems with inherent multi-configurational character (e.g. cyanide). Multi-configurational wave functions overcome these limitations, and ideally need to be employed for cyanide/isocyanide and derivative species. Geometrical optimization calculations were initially performed using the UMP2//6-311++G(2df,2p) level of theory, followed by MRMP2/MP2/6-311++G(2df,2p) single-point energy calculations.

Ten different approach orientations were investigated as shown in figure 6.16. These can be divided into three categories: direct axial (1) and (2); sideways methyl (3e) and (3s); and sideways isocyanide (4e), (4s), (5e), (5s), (6e) and (6s). All calculations have been performed under C_S point symmetry, which allows the out of C_3 axis bending of the -CH_3 group, since the analogous bend is known to be important for the Na + HCN/HNC systems [77]. Axial orientations have the Na atom fixed with respect to carbon atoms (or nitrogen atom for orientation (1)) from each respective end. Sideways orientations (3e/s) and (4e/s) have approaches referenced to respective carbon atoms, whereas (5e/s) and 6(e/s) optimize to the minimum energy pathway perpendicular to the triple bond. Charge-transfer is monitored using the Mulliken population scheme by determining atomic charge on the metal atom, which has previously shown to yield good agreement with experiment [41].

Counterpoise basis set superposition error (BSSE) corrections (ΔE_{CP}) [12] were determined using a modified method that takes into account monomer relaxation at the asymptotic limit as given in equation 6.7.

$$\Delta E_{CP} = E_{AB}^{AB} + E_{A}^{A} - E_{A}^{AB} + E_{B}^{B} - E_{B}^{AB} - E_{A}^{'A} - E_{B}^{'B} \tag{6.7}$$

The Counterpoise corrected energy of the dimer, E_{AB}^{CP}, is given in equation 6.8.

$$E_{AB}^{CP} = E_{AB}^{AB} + E_{A}^{CP} + E_{B}^{CP} = E_{AB}^{AB} + E_{A}^{A} - E_{A}^{AB} + E_{B}^{B} - E_{B}^{AB} \tag{6.8}$$

In these expressions, the superscripts refer to basis sets, and subscripts to identify monomer or dimer fragments. Unprimed energies are at the dimer geometry, whereas primed are at asymptotic monomer optimized geometries. These corrections were applied to all optimized complexes.

The active space used for multi-reference calculations consists of 9 electrons in 12 orbitals, with the ground-state configuration: $(\sigma_{C-NC})^2(\sigma_{CH})^2(\pi_{NC})^2(\pi_{NC})^2 Na(3s)^1 Na(3p_x)^0 Na(3p_y)^0 Na(3p_z)^0 (\sigma^*_{CH})^0 (\sigma^*_{C-NC})^0 (\pi^*_{NC})^0 (\pi^*_{NC})^0$. This is the largest practical active space, which includes Na 3p (or K 4p) orbitals and vacant anti-bonding orbitals for σ and π bonds which are expected to play a role in charge-transfer and bond dissociation. MP2 calculations

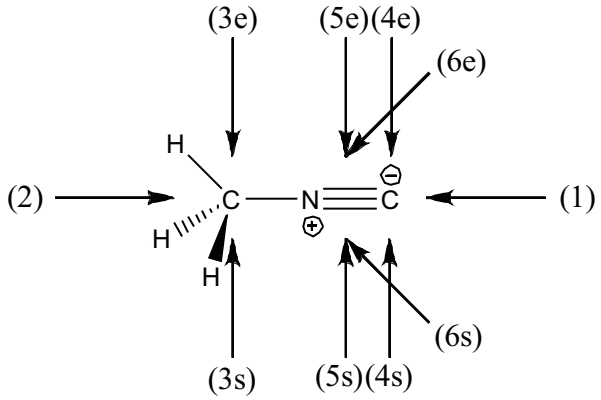

Orientation	Description
(1)	N**C**-end (0°)
(2)	**C**H_3-end (180°)
(3s) and (3e)	90° and 270° **C**H_3
(4s) and (4e)	90° and 270° N**C**
(5s) and (5e)	90° and 270° π
(6s) and (6e)	45° and 315° π

Figure 6.16.: The approach orientations investigated for Na + CH_3NC reaction. Suffixes 's' and 'e' denote staggered and eclipsed conformations respectively. Angles referenced with respect to the NC-end at 0° proceeding in an anticlockwise rotation through eclipsed then staggered orientations.

showed under the C_S symmetry framework, that only one C-H bond stretch appears to be important for the CH_2NC^- reaction channel, allowing two $(\sigma_{CH})^2$ orbitals to be omitted from the active space. Similarly, the bonding $(\sigma_{NC})^2$ and anti-bonding $(\sigma^*_{NC})^2$ orbitals are omitted since both are doubly occupied. To further rationalize the choice of active space, MP2 natural orbital populations were analysed for orientations before and after charge-transfer to ensure the active space did not preclude any orbital with a significant perturbation coefficient (> 0.02) [109]. The initial CASSCF guess wave functions for each orientation were generated from an ROHF calculation at the largest separation where molecular orbitals ordered identically to isolated fragments. The ground state CASSCF wave functions were dominated by one configuration, of typically $> 90\%$ weight, indicating that multi-reference configuration interaction (MRCI) methods were not required. For fragment species, Na is treated with a (1,4) active space, CH_3NC and CH_3NC^- with (8,8) and (9,8) active spaces respectively, NC and NC^- with (5,5) and (5,6) active spaces respectively, and CH_3 with a (3,3) active space. The CH_2NC and CH_2NC^- species have the (7,7) and (8,7) active spaces respectively. Na^+ (0,4) and H (1,1) are RHF fragments, and H^- is treated with the (2,1) active space. Na is treated with the (1,4) active space and is calculated with a full CI wave function. The addition of fragment spaces for the various reaction channels necessarily yields the overall system (9,12) space. A CI space is not size consistent if truncated to a maximum excitation level, however, a full CI within the active space (CASSCF) is size consistent permitting this procedure.

Dipole-bound anion calculations followed the procedure of Simons *et al.* [101, 102] to reproduce the CH_3CN binding energy at the CCSD(T)//aug-cc-pVDZ+6$sp7d$+ZPV level of theory. This involves a aug-cc-pVDZ valence description augmented with six additional *sp* and seven *d* functions centred on the methyl carbon atom.

Table 6.5.: Summary of geometrical parameters for C_{3V} ground-state CH_3NC. All bond lengths in Å, and angles in degrees. Experimental errors are typically smaller than the last figure.

Method	r(CH_3-N)	<(NCH)	r(N-C)	r(CH)
expt[a]	1.426	109.5	1.168	1.095
expt[b]	1.426	109.5	1.167	1.090
MP2//6-311++G(2df,2p)	1.420	109.5	1.178	1.085
MP2//aug-cc-pVTZ	1.421	109.4	1.179	1.086
MP2(full)//6-311++G(2df,2p)	1.416	109.5	1.175	1.083
CCSD(T)//6-311++G(2df,2p)	1.425	109.4	1.175	1.088

[a]Ref [110] [b]Ref [111]

This additional augmentation crucial in order to obtain a bound state, where default valence basis functions have incomplete long-range description. These additional diffuse function orbital exponents start at 7.239×10^{-3} for *sp* functions and 2.316×10^{-2} for *d* functions, and are even-tempered with the geometric progression factor of 3.2. Such factors need to be carefully selected to minimize linear dependence effects. Additional *f*-type diffuse polarization functions have been shown not to be important for description of the CH_3CN dipole-bound anion [102].

6.4.4. Results and discussion

Molecule parameters

The first requirement of any potential energy surface study is to confirm that the chosen level(s) of theory reproduce known relevant (experimental) molecular properties. The title study is concerned with electron attachment and bonding energetics, and calculated electron affinities all need to be assessed. Geometrical optimizations for CH_3NC, CH_2NC and CH_2NC^- at the MP2//6-311++G(2df,2p) level of theory retrieves ≈ 92% and ≈ 93% of the CCSD(T) electron correlation energy for the CH_3NC and CH_2NC^- species. Calculated geometrical parameters for these species are summarized in tables 6.5 and 6.6. For CH_3NC, both the MP2//6-311++G(2df,2p) (or all-electron) and CCSD(T)//6-311++G(2df,2p) optimizations reproduce experimental bonding parameters to within 0.01 Å for all bond lengths, and an increase in basis set to aug-cc-pVTZ giving essentially no change in geometry. For CH_2NC and CH_2NC^-, there exist no experimental bonding parameters, however amongst the levels of theory tested, the same result is obtained that calculated MP2//6-311++G(2df,2p) bond lengths are all within 0.01 Å.

CH_2NC compared to CH_3NC shows an ≈ 0.1 Å shortening of the CH_3-N bond and increase in <(NCH) by ≈ 9°, with the NC bond remaining relatively unchanged. The CH_2NC^- anion relative to CH_2NC shows an ≈ 4° <(CNC) tilt of the NC group away from the hydrogen atoms, and an ≈ 8° decrease in <(NCH) bond angle to close agreement with that for CH_3NC. These data are in accord with molecular orbital analysis indicating electron capture into a CH_3 non-bonding hybridized orbital.

Table 6.6.: Summary of calculated geometrical parameters for CH_2NC and CH_2NC^- with C_{2V} and C_S point symmetry respectively. All bond lengths in Å, and angles in degrees.

Method	r(CH_2-N)	<(CNC)	<(NCH)	r(N-C)	r(CH)
CH_2NC					
MP2//6-311++G(2df,2p)	1.340	-	118.5	1.189	1.075
MP2//aug-cc-pVTZ	1.356	-	118.2	1.175	1.074
MP2(full)//6-311++G(2df,2p)	1.337	-	118.6	1.187	1.074
CCSD(T)//6-311++G(2df,2p)	1.346	-	118.5	1.188	1.078
CH2NC-					
MP2//6-311++G(2df,2p)	1.395	175.6	110.1	1.190	1.089
MP2//aug-cc-pVTZ					
MP2(full)//6-311++G(2df,2p)	1.391	175.8	110.4	1.188	1.088
CCSD(T)//6-311++G(2df,2p)	1.414	175.3	108.7	1.183	1.095

Fundamental harmonic and anharmonic frequencies were calculated at the MP2//6-311++G(2df,2p) level of theory for CH_3NC, and are summarised in table 6.6. For CH_3NC, the small linear scaling coefficient of 1.05 and 1.01 aligns calculated (non-scaled) harmonic and anharmonic frequencies with experiment. Anharmonic frequencies show a root-mean-square deviation (RMSD) of 31 cm^{-1} to experimental, which is only slightly improved with the aug-cc-pVTZ basis set. A B3LYP//6-311++G(3df,3p) optimization (inherently some multi-configurational wave function character) and frequency calculation yields this harmonic scaling factor at 1.03, which is hardly an improvement. These data indicate that the MP2//6-311++G(2df,2p) optimizations, although lacking multi-reference character in optimizations, do yield good geometrical parameters for the isocyanide species. Further, the experimental isomerisation energy for $CH_3NC \rightarrow CH_3CN$ at -23.70 ± 0.14 kcal/mol [56] is in good agreement with the MP2//6-311++G(2df,2p) calculated value at -26.88 kcal/mol, indicating good relative energies between isomers or conformers. A geometric optimization and anharmonic frequency calculation at the MP2//aug-cc-pVTZ level of theory yields an RMSD of 27 cm^{-1} from experimental, which for many potential energy surface points, is hardly an improvement over the faster MP2//6-311++G(2df,2p) level of theory. The Na (K in parentheses) ionization potential is calculated at 4.94 (4.26) eV, in good agreement with the experimental value of 5.14 (4.34) eV [31].

The adiabatic electron affinity (EA_{ad}), given in equation 6.9, within the Born-Oppenheimer (BO) framework is given as the difference in energy between neutral and anion at their optimized geometries including the small zero-point energy (ΔZPV) correction.

$$EA_{ad} = E_{BO}(neutral) - E_{BO}(anion) - (ZPV(anion) - ZPV(neutral)) \tag{6.9}$$

CH_3NC, like CH_3CN, has a negative EA_{ad} calculated at -0.64 eV and -0.46 eV for the MP2//6-311++G(2df,2p) and MRMP2/MP2/6-311++G(2df,2p) levels of theory respectively. For CN, EA_{ad} is calculated at 4.6 eV for the MP2//6-311++G(2df,2p) level of theory, which is at ≈ 20% variance with the experimental value at ≈ 3.8 ± 0.1 eV [113–115]. CASSCF(5,5)//6-311++G(2df,2p) underestimates at 3.0 eV, and MRMP2//6-311++G(2df,2p) gives an improvement at 3.6 eV.

Table 6.7.: Summary of experimental and calculated fundamental harmonic and anharmonic frequencies for C_{3V} point symmetry CH_3NC, with frequencies tabulated in units cm^{-1}, and zero-point energy (ZPV) in kcal/mol.

symmetry	expt[a]	calc[b]	calc[c]	calc[d]
E CNC deform	263	283	283	277
E CNC deform	263	283	283	277
A_1 H_3CN stretch	945	971	954	948
E CNC deform	1130	1165	1139	1134
E CNC deform	1130	1165	1139	1134
A_1 CH_3 deform	1427	1475	1438	1430
E CH_3 deform	1464	1517	1478	1476
E CH_3 deform	1464	1517	1478	1476
A_1 CN stretch	2166	2168	2124	2112
A_1 CH_3 stretch	2965	3101	3010	3004
E CH_3 stretch	3015	3202	3069	3059
E CH_3 stretch	3015	3202	3069	3059
RMSD	-	91	31	27
ZPV	-	28.7	28.3	28.2

[a]Ref [112] gas-phase frequencies
[b]MP2//6-311++G(2df,2p) harmonic
[c]MP2//6-311++G(2df,2p) anharmonic
[d]MP2//aug-cc-pVTZ anharmonic

The dipole-bound state for CH_3CN has been well studied computationally, with excellent agreement between theory and experiment [100–102]. There exists no experimental characterization of a similar dipole-bound species for CH_3NC, which could potentially act as a doorway state to charge-transfer in an approach from the CH_3-end. Calculated dipole moments for CH_3CN and CH_3NC are in excellent agreement with experiment and are reported in table 6.8. It is well-known that a proper description of the dipole-bound state requires a high degree electron correlation treatment, since a large fraction of the binding energy arises from dispersion type interactions of the loosely bound electron and neutral molecule [99–101]. Previously reported experimental and calculated dipole binding energies for CH_3CN^- are summarised in table 6.9. The experimental binding energy of 93 cm^{-1} or 11.5 meV by Desfrancois *et al.* [87] is considered to be the experimental reference. Calculated values using the CCSD(T)//aug-cc-pVDZ(+6*sp*7*d*+ZPV) level of theory are in good agreement at 111 cm^{-1} or 13.8 meV, reproducing those previously calculated [100–102]. Optimized harmonic frequency calculations for dipole-bound anions give ΔZPV to be -4.17 cm^{-1} and -1.32 cm^{-1} for CH_3CN and CH_3NC respectively. Dipole binding energies determined in accordance with Koopmans' theorem as the negative energy of the LUMO for the neutral, always underestimate owing to neglect of both electron correlation effects and orbital relaxation on dipole-binding.

The dipole-bound binding energy for CH_3NC is calculated to be 46 cm^{-1} (5.7 meV) at the MP2//aug-cc-pVDZ(+6*sp*7*d*+ZPV) level of theory, and 108 cm^{-1} (13.5 meV) at the CCSD(T)//aug-cc-pVDZ(+6*sp*7*d*+ZPV) level of theory. As expected, this value is essentially the same as that for CH_3CN. Molecular orbital analysis

Table 6.8.: Dipole moments, μ, in units of Debye, for neutral CH_3CN and CH_3NC in parentheses.

Method	Dipole moment, μ
MP2//6-311++G(2df,2p)	3.95 (3.60)
MP2//aug-cc-pVDZ	3.94 (4.12)
MP2//aug-cc-pVDZ(+6sp7d)	3.93 (4.12)
CCD//aug-cc-pVDZ(+6sp7d)	3.95 (3.87)
CASSCF(8,8)/MP2/6-311++G(2df,2p)	3.93 (4.11)
expt[a]	3.92 ± 0.06 (3.83 ± 0.06)

[a]Ref. [116]

Table 6.9.: Binding energies for the CH_3CN^- dipole-bound anion, reported in cm^{-1} and meV in parentheses, and KT = Koopmans' theorem calculated as the negative energy of the LUMO.

Experimental	Binding energy	KT
$I^-{\cdot}CH_3CN$ photoelectron spectroscopy[a]	≈ 24 (≈ 3)	-
Cluster free electron capture[b]	69 ± 1 (8.5 ± 0.1)	-
K(np) collisions[c]	≈ 89 (≈ 11)	-
Xe(nf) collisions[d]	93 (11.5)	-
Xe(nf,np) collisions[e]	137 ± 24 (17 ± 3)	-
Rydberg Electron Transfer (RET)[f]	-18.7	-
Calculated		
MP2//6-31+G(d,p)(+7$sp4d$)[g,h]	54 (6.7)	39 (4.8)
MP2//6-311++G(2d,2p)(+7sp)[h]	62 (7.7)	46 (5.7)
MP2//aug-cc-pVDZ(+7$sp8d8f$)[i,j,k]	75 (9.3)	53 (6.5)
CCSD(T)//aug-cc-pVTZ(+7$sp8d$+ZPV)[i,j,k]	112 (13.9)	53 (6.5)
MP2//aug-cc-pVDZ(+6$sp7d$+ZPV)[l]	78 (9.7)	53 (6.5)[m]
CCSD(T)//aug-cc-pVDZ(+6$sp7d$+ZPV)[l]	111 (13.8)	53 (6.5)[m]

[a]Ref [92] no error given.
[b]Ref [95].
[c]Ref [88, 89] no error given.
[d]Ref [87] no error given.
[e]Ref [96].
[f]Ref [93] - RET experiments generally yield larger binding energies for a series of species than other determinations that in general are in excellent agreement with CCSD(T)/aug-cc-pVDZ(+diffuse) calculations [101, 102].
[g]Ref [97].
[h]Ref [98].
[i]Ref [99].
[j]Ref [100] addition of the 8f functions does not change the binding energy.
[k]Ref [101, 102].
[l]this work.
[m]calculated from the CCD density.

reveals that the most diffuse orbital does not have a large coefficient in the molecular orbital describing the dipole-bound orbital, indicating convergence with diffuse functions is reached. The dipole-bound geometric optimization shows geometrical parameters to be almost identical to that of the neutral, with the largest change being a decrease in the angle <(H-C-N) by $\approx 0.01°$. Calculation at the MP2//6-311++G(2df,2p) level of theory, without additional diffuse functions, yields a negative dipole-binding energy, therefore the calculations by Maclagan [48] on reaction of K + CH_3CN would not reveal the effects of any isolated dipole-bound state if present.

In order to test for any role of the dipole-bound anion in CH_3-end reaction, CCSD(T)//aug-cc-pVDZ(+6$sp7d$) calculations varying R(Na-CH_3) between 2.0 Å to 4.0 Å were performed with and without (+6$sp7d$) diffuse function augmentation. The valence basis set is suitable to describe interactions closer than 2.0 Å. Relative interaction energies (ΔE), Mulliken charges (ΔMulliken) and dipole moment (Δdipole) are shown in figure 6.17. BSSE corrections are incorporated since the basis set is only of double zeta quality, although the BSSE correction is larger than the difference in diffuse function augmentation energy of the neutral, but less than the dipole-bound state binding energy.

These data confirm that for a basis set capable of reproducing the isolated dipole-bound state, the dipole-bound state plays no role in charge-transfer reaction from the CH_3-end. Under single-collision conditions, and for calculations to characterize an interaction, this interaction must lower the energy of the system. For this to occur, the binding interaction of the electron (where valence is non-favourable) in the Coulombic field of the ion-pair must be larger than the ionization potential of the alkali earth metal. The concept of an 'ion-molecule-dipole-bound' species [74], where a positive sodium ion close to the CH_3-end significantly increases the dipole moment, allowing for a stronger ion-dipole-bound state, is far-fetched [117]. Similar to Na + CH_3NO_2 [41], the presence of the positive alkali metal core in the reaction of Na + CH_3NC appears to fundamentally change the interaction relative to a free electron.

The CH_2CN $^2B_1$ ground state species also exhibits a relatively large dipole moment of 3.7 D to 4.0 D [118], calculated here at 3.51 D with the MP2//6-311++G(2df,2p) level of theory, and has a positive adiabatic valence electron affinity: 1.55 ± 0.01 eV [119]; 1.560 ± 0.006 [120]; and 1.543 ± 0.014 [121]. This species is also known to form a dipole-bound anion [103, 119–123, 123] of experimental binding energy 20 ± 6 meV [120] and <8.2 meV [119]. The CH_2NC $^2B_1$ ground state, with a calculated MP2//6-311++G(2df,2p) dipole moment of 3.50 D here is expected to show a similar species. Such species could potentially be produced as reaction product, but again are unlikely to play any role in the presence of the sodium species when a valence electron affinity of 1.06 ± 0.02 eV [124] exists. The valence electron affinity of this species is calculated to be 1.22 eV at the MP2//6-311++G(2df,2p) level of theory, in good agreement, and the MRMP2/MP2/6-311++G(2df,2p) value of 1.01 eV is in excellent agreement. Consistent with all studies mentioned, the CH_2CN and CH_2NC radicals have C_{2V} ground-state point symmetry; where upon valence electron attachment, the pyramidal CH_2CN^- and CH_2NC^- anions of $^1A\prime$ ground state symmetry, have C_S point symmetry. This distortion of the C-H bonds out

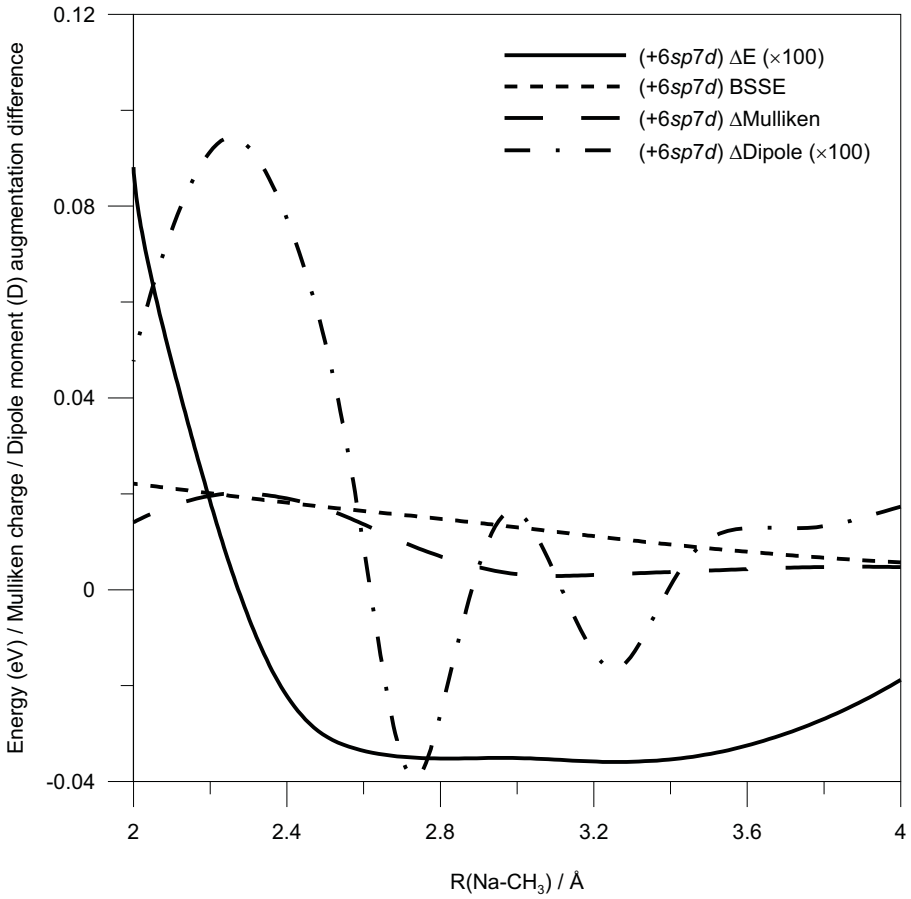

Figure 6.17.: CH_3-end energy and property differences for the CCSD(T)//aug-cc-pVDZ and CCSD(T)//aug-cc-pVDZ(+6*sp*7*d*) levels of theory for R(Na-CH_3) = 2 Å to 4 Å. ΔE difference and ΔDipole difference multiplied by 100-fold to fit on scale - and completely negligible.

of plane and rotation axis results from a change in hybridization of the CH_2 carbon, where Mulliken populations show an increase in negative charge following anion formation. The experimental CH_2 inversion barrier is very small for CH_2CN^- and CH_2NC^- at 81 ± 6 meV [123, 124], and calculated here in good agreement at 104 meV. The calculated ZPV corrected H-CH_2NC bond dissociation energy (BDE) of 4.05 eV and 3.85 eV at MP2//6-311++G(2df,2p) and MRMP2/MP2/6-311++G(2df,2p) levels of theory respectively, are in excellent accord with the experimental value of 3.7 ± 0.2 eV [124].

Electron energy loss and low energy electron impact studies [125, 126] have reported the π^* orbital to be the valence LUMO in CH_3CN. These studies outline that the substitution of H with CH_3 for cyanide and isocyanide species destabilizes both the π and π^* orbitals, which would be expected to yield differences in charge-transfer and complexes between the CH_3NC and HNC systems. In agreement with the calculations in this work, the LUMO for isolated CH_3NC has swapped to the σ^* CH_3-NC orbital. Extended Koopmans' theorem ionization potentials, which do not allow for orbital relaxation, were calculated with the CH_3NC CASSCF(8,8)/MP2/6-311++G(2df,2p) wave function, yielding ionization potentials at 12.5 eV (A_1) and 13.2 eV (E), in good accord with the experimental values of 11.3 eV (A_1) and 12.2 eV (E), and reproduces the correct isocyanide orbital

ordering. These same experimental ionization potentials have also been determined by Penning trap ^{3}S He collisions [85]. The vertical attachment energy of CH_3CN (and CH_3NC) has been determined to be ± -2.84 eV, corresponding to a shape-resonance with the extra electron trapped in a π^* orbital [92, 126, 127]. The corresponding experimental stabilization energy of ≈ 8.5 eV is in good accord with the MP2//6-311++G(2df,2p) Koopmans' binding energy calculated value at ≈ 8.9 eV. The experimental vertical attachment energy for the σ^*_{CH} orbital of CH_3NC is slightly higher at ≈ 5.5 eV [126]. These data would also indicate any charge-transfer association to preferentially occur though the π^* orbital corresponding to sideways orientations.

These calculations indicate that the MRMP2(9,12)/MP2/6-311++G(2df,2p) level of theory should be suitable to treat the potential energy surface. Calculations were also undertaken using aug-cc-pVNZ (N=2 to 6) on the Na + HCN van der Waals complexes in order to assess a suitable level of theory to characterize the σ-type complexes. The 6-311++G(2df,2p) level of theory yields a fortuitously reasonable description with complete basis set extrapolations. Further summarised discussion, potential energy surfaces, interpretation, and comparison with experimental data are anticipated to be completed in the next month.

References

[1] C. A. Deakyne. *Int. J. Mass Spectrom.*, 227:601, 2003.

[2] M. N. Glukhovtsev, J. E. Szulejko, T. B. McMahon, J. W. Gauld, A. P. Scott, B. J. Smith, A. Pross, and L. Radom. *J. Phys. Chem.*, 98:13099, 1994.

[3] J. M. L. Martin and T. J. Lee. *Chem. Phys. Lett.*, 258:136, 1996.

[4] III C. A. Clausen, R. A. Prados, and M. L. Good. *J. Am. Chem. Soc.*, 92:7484, 1970.

[5] U. Kaldor, S. Roszak, P. C. Hariharan, and J. J. Kaufman. *J. Chem. Phys.*, 90:6359, 1989.

[6] H. C. Bei, P. K. Bhowmik, and T. Su. *J. Phys. Chem.*, 90:7046, 1989.

[7] E. P. Hunter and S. G. Lias. *J. Phys. Chem. Ref. Data*, 27:413, 1998.

[8] P. Walden. *Ber.*, 28:1287, 1895.

[9] J. K. Laerdahl and E. Uggerud. *Int. J. Mass Spectrom.*, 214:277, 2002.

[10] S. Simon, M. Duran, and J. J. Dannenberg. *J. Chem. Phys.*, 105:11024, 1996.

[11] N. R. Kestner and J. E. Combariza. *Rev. Comp. Chem.*, 13:99, 1999.

[12] S. F. Boys and F. Bernardi. *Mol. Phys.*, 19:553, 1970.

[13] M. J. Frisch, G. W. Trucks, H. B. Schlegel, G. E. Scuseria, M. A. Robb, J. R. Cheeseman, J. A. Montgomery, Jr., T. Vreven, K. N. Kudin, J. C. Burant, J. M. Millam, S. S. Iyengar, J. Tomasi, V. Barone, B. Mennucci, M. Cossi, G. Scalmani, N. Rega, G. A. Petersson, H. Nakatsuji, M. Hada, M. Ehara, K. Toyota, R. Fukuda, J. Hasegawa, M. Ishida, T. Nakajima, Y. Honda, O. Kitao, H. Nakai, M. Klene, X. Li, J. E. Knox, H. P. Hratchian, J. B. Cross, V. Bakken, C. Adamo, J. Jaramillo, R. Gomperts, R. E. Stratmann, O. Yazyev, A. J. Austin, R. Cammi, C. Pomelli, J. W. Ochterski, P. Y. Ayala, K. Morokuma, G. A. Voth, P. Salvador, J. J. Dannenberg, V. G. Zakrzewski, S. Dapprich, A. D. Daniels, M. C. Strain, O. Farkas, D. K. Malick, A. D. Rabuck, K. Raghavachari, J. B. Foresman, J. V. Ortiz, Q. Cui, A. G. Baboul, S. Clifford, J. Cioslowski, B. B. Stefanov, G. Liu, A. Liashenko, P. Piskorz, I. Komaromi, R. L. Martin, D. J. Fox, T. Keith, M. A. Al-Laham, C. Y. Peng, A. Nanayakkara, M. Challacombe, P. M. W. Gill, B. Johnson, W. Chen, M. W. Wong, C. Gonzalez, and J. A. Pople. Gaussian 03, Revision C.02. Gaussian, Inc., Wallingford, CT, 2004.

[14] Jr. T. H. Dunning. *J. Chem. Phys.*, 90:1007, 1989.

[15] R. A. Kendall, Jr. T. H. Dunning, and R. J. Harrison. *J. Chem. Phys.*, 96:6796, 1992.

[16] D. E. Woon and Jr. T. H. Dunning. *J Chem. Phys.*, 92:1358, 1993.

[17] S. Parthiban, G. de Oliveira, and J. M. L. Martin. 105:895, 2001.

[18] P. Kitschke. *Ab Initio* Calculations on the Orientation Dependence of the Gas-Phase Cl^- + CH_3Cl S_N2 Reaction. Technical report, University of Canterbury, 2009.

[19] C. Vallance, P. W. Harland, and Robert G. A. R. Maclagan. *J. Phys. Chem.*, 100:15021, 1996.

[20] C. G. Aitken, D. A. Blunt, and P. W. Harland. *J. Chem. Phys.*, 101:11074, 1994.

[21] P. W. Harland C. G. Aitken, D. A. Blunt. *Int. J. Mass Spectrom. Ion Proc.*, 149/150:279, 1995.

[22] P. R. Brooks and P. W. Harland. Effects of molecular orientation on electron transfer and electron impact ionization. in advances in gas phase ion chemistry. volume 2. JAI Press Inc.: London, 1996.

[23] Y. K. Kim and M. E. Rudd. *Phys. Rev. A*, 50:3954, 1994.

[24] W. Hwang, Y. K. Kim, and M. E. Rudd. *J. Chem. Phys.*, 104:2956, 1996.

[25] D. Margreiter, H. Deutsch, M. Schmidt, and T. D. Märk. *Int. J. Mass Spectrom. Ion Processes*, 100:157, 1990.

[26] D. Margreiter, H. Deutsch, and T. D. Märk. *Int. J. Mass Spectrom. Ion Processes*, 139:127, 1994.

[27] H. Stapelfeldt and T. Seideman. *Rev. Mod. Phys.*, 75:543, 2003.

[28] B. A. Kuznetsov. *Khimicheskaya Fizika*, 15:82, 1996.

[29] M. S. Child. *Molecular Collision Theory*. Academic Press: London, 1974.

[30] W. Nowak, J. Karwowski, and M. Ktobukowski. *Theoret. Chim. Acta (Berl.)*, 63:13, 1983.

[31] D. R. Lide, editor. *CRC Handbook of Chemistry and Physics*, volume 77, chapter 10, page 214. CRC Press, Cleveland, OH, 1996.

[32] P. G. Wenthold and R. R. Squires. *J. Phys. Chem.*, 99:2002, 1995.

[33] H. Dispert and K. Lacmann. *Chem. Phys. Lett.*, 47:533, 1977.

[34] A. P. M. Baeda. *Physica*, 59:541, 1972.

[35] J. A. Ayala, W. E. Wentworth, and E. C. M. Chen. *J. Phys. Chem.*, 85:768, 1981.

[36] J. G. Dojahn, E. C. M. Chen, and W. E. Wentworth. *J. Phys. Chem.*, 100:9649, 1996.

[37] R. S. Mulliken. *J. Chem. Phys.*, 23:1833, 1955.

[38] A. E. Reed, L. A. Curtiss, , and F. Weinhold. *Chem. Rev.*, 88:899, 1988.

[39] C. M. Breneman and K. B. Wiberg. *J. Comp. Chem.*, 11:361, 1990.

[40] R. B. Bernstein. *Chemical Dynamics via Molecular Beam and Laser Techniques*. Clarendon Press: Oxford, 1982.

[41] J. N. Bull, Robert G. A. R. Maclagan, and Peter W. Harland. *Mol. Phys.*, 107:1123, 2009.

[42] R. G. A. R. Maclagan. *Chem. Phys. Lett.*, 373:586, 2003.

[43] R. G. A. R. Maclagan. *J. Phys. Chem. A*, 108:11779, 2004.

[44] B. Szefczyk, W. A. Sokalski, and J. Leszczynski. *J. Chem. Phys.*, 117:6952, 2002.

[45] J. W. Zou, Y. J. Jiang, M. Guo, G. X. Hu, B. Zhang, H. Liu, and Q. S. Yu. *Chem. Eur. J.*, 11:740, 2005.

[46] S. A. Harris, P. W. Harland, and P. R. Brooks. *Phys. Chem. Chem. Phys.*, 2:787, 2000.

[47] P. R. Brooks, P. W. Harland, S. A. Harris, T. Kennair, C. Redden, and J. F. Tate. *J. Am. Chem. Soc.*, 129:15572, 2007.

[48] R. G. A. R. Maclagan. *Chem. Phys. Lett.*, 373:586, 2003.

[49] R. D. Levine. *J. Phys. Chem.*, 94:8872, 1990.

[50] S. C. Chan, B. S. Rabinovitch, J. T. Byrant, L. D. Spicer, T. Fujimoto, Y. N. Lin, and S. P. Pavlou. *J. Phys. Chem.*, 74:3160, 1970.

[51] W. Dianxun, Q. Ximei, and J. Peng. *Chem. Phys. Lett.*, 258:149, 1996.

[52] P. Saxe, Y. Yamaguchi, P. Pulay, and H. F. Schaefer III. *J. Am. Chem. Soc.*, 102:3718, 1980.

[53] L. Fan and T. Zigler. *J. Am. Chem. Soc.*, 114:10890, 1992.

[54] B. S. Jursic. *Chem. Phys. Lett.*, 256:213, 1996.

[55] P. M. Mayer, M. S. Taylor, M. W. Wong, and L. Radom. *J. Phys. Chem. A*, 102:7074, 1998.

[56] J. L. Collister and H. O. Pritchard. *Can. J. Chem.*, 54:2380, 1976.

[57] J. Cernicharo, K. Kahane, M. Guelin, and J. Gomez-Gonalez. *Astron. Astrophys.*, 198:L1, 1988.

[58] P. R. Brooks. *J. Chem. Phys.*, 130:151102, 2009.

[59] J. N. Bull, R. G. A. R. Maclagan, and P. W. Harland. *Mol. Phys.*, 107:1123, 2009.

[60] R. G. A. R. Maclagan. *J. Phys. Chem. A*, 108:11779, 2004.

[61] A. E. Wiskerke, S. Stolte, H. J. Loesch, and R. D. Levine. *Phys. Chem. Chem. Phys.*, 2:757, 2000.

[62] K. T. Wu. *J. Phys. Chem.*, 83:1043, 1979.

[63] J. A. Aten and J. Los. *J. Chem. Phys.*, 25:7, 1977.

[64] L. Manceron and L. Andrews. *J. Am. Chem. Soc.*, 107:63, 1985.

[65] K. Morokuma S. Sakai. *J. Phys. Chem.*, 91:3661, 1987.

[66] M. T. Nguyen. *J. Phys. Chem.*, 92:1426, 1988.

[67] M. Yoshimine M. T. Nguyen, T. Ha. *Mol. Phys.*, 77:921, 1992.

[68] L. A. Eriksson, J. Wang, and R. J. Boyd. *Chem. Phys. Lett.*, 235:422, 1995.

[69] M. E. Alikhani, Y. Bouteiller, and B. Silvi. *J. Phys. Chem.*, 100:16092, 1996.

[70] P. H. Kasai. *J. Am. Chem. Soc.*, 114:3299, 1992.

[71] M. Jungen. *Helv. Chem. Acta*, 84:1459, 2001.

[72] W. B. Person B. Silvi, O. Ayed. *J. Am. Chem. Soc.*, 108:8148, 1986.

[73] O. Ayed, A. Loutellier, L. Manceron, and J. P. Perchard. *J. Am. Chem. Soc.*, 108:8138, 1986.

[74] P. Pullumbi, Y. Bouteiller, and J. P. Perchard. *J. Chem. Phys.*, 102:5719, 1995.

[75] A. Mavridis A. Kalemos, A. Papakondylis. *Chem. Phys. Lett.*, 259:185, 1996.

[76] P. H. Kasai. *J. Am. Chem. Soc.*, 120:7884, 1998.

[77] N. J. Fitzpatrick and J. P. Deignan. *J. Mol. Struct. (Theochem)*, 505:133, 2000.

[78] G. E. Douberly and R. E. Miller. *J. Phys. Chem. A*, 111:7292, 2007.

[79] A. M. Ferrari, P. Ugliengo, and E. Garrone. *J. Chem. Phys.*, 105:4129, 1996.

[80] D. R. Herschbach. *Adv. Chem. Phys.*, 10:319, 1966.

[81] R. Grice and D. R. Herschbach. *Mol. Phys.*, 27:159, 1974.

[82] Jr. R. J. Beuhler and R. B. Bernstein. *J. Chem. Phys.*, 51:5305, 1969.

[83] E. Fermi and E. Teller. *Phys. Rev.*, 72:406, 1947.

[84] M. Gutowski and P. Skurski. *Recent Res. Devel. Physical Chem.*, 3:245, 1999.

[85] M. Cannon, Y. Liu, L. Suess, and F. B. Dunning. *J. Chem. Phys.*, 128:244307, 2008.

[86] J. A. Stockdale, F. J. Davis, R. N. Compton, and C. E. Klots. *J. Chem. Phys.*, 60:4279, 1974.

[87] D. Desfrancois, H. Abdoul-Carime, N. Khelifa, and J. P. Schermann. *Phys. Rev. Lett.*, 73:2436, 1994.

[88] R. A. Popple, C. D. Finch, and F. B. Dunning. *Chem. Phys. Lett.*, 234:172, 1995.

[89] L. Suess, Y. Liu, R. Parthasarathy, and F. B. Dunning. *J. Chem. Phys.*, 119:12890, 2003.

[90] Y. Liu, L. Suess, and F. B. Dunning. *Chem. Phys. Lett.*, 415:234, 2005.

[91] Y. Liu, M. Cannon, L. Suess, F. B. Dunning, V. E. Chernov, and B. A. Zon. *Chem. Phys. Lett.*, 433:1, 2006.

[92] C. G. Bailey, C. E. H. Dessent, and M. A. Johnson. *J. Chem. Phys.*, 104:6976, 1996.

[93] N. I. Hammer, K. Diri, K. D. Jordan, C. Desfrancois, and R. N. Compton. *J. Chem. Phys.*, 119:3650, 2003.

[94] K. Mitsuke, T. Kondow, and K. Kuchitsu. *J. Phys. Chem.*, 90:1505, 1986.

[95] R. Hashemi and E. Illenberger. *J. Phys. Chem.*, 95:6402, 1991.

[96] D. Desfrancois, H. Abdoul-Carime, C. Adjouri, N. Khelifa, and J. P. Schermann. *Europhys. Lett.*, 26:25, 1994.

[97] G. L. Gutsev, A. L. Sobolewski, and L. Adamowicz. *Chem. Phys.*, 196:1, 1995.

[98] L. Adamowicz G. L. Gutsev. *J. Phys. Chem.*, 99:13412, 1995.

[99] M. Gutowski, P. Skurski, A. Boldyrev, J. Simons, and K. Jordan. *Phys. Rev. A*, 54:1906, 1996.

[100] M. Gutowski, K. D. Jordan, and P. Skurski. *J. Phys. Chem. A*, 108:2624, 1998.

[101] M. Gutowski, P. Skurski, K. D. Jordan, and J. Simons. *Int. J. Quan. Chem.*, 64:183, 197.

[102] J. Simons P. Skurski, M. Gutowski. *Int. J. Quan. Chem.*, 80:1024, 2000.

[103] D. C. Clary. *J. Phys. Chem.*, 92:3173, 1988.

[104] P. R. Brooks, P. W. Harland, and C. E. Redden. *J. Am. Chem. Soc.*, 128:4773, 2006.

[105] P. R. Brooks, P. W. Harland, and C. E. Redden. *J. Phys. Chem. A*, 110:4697, 2006.

[106] M. W. Schmidt, K. K. Baldridge, J. A. Boatz, S. T. Elbert, M. S. Gordon, J. H. Jensen, S. Kosecki, N. Matsunaga, K. A. Nguyen, S. J. Su, T. L. Windus, M. Dupuis, and J. A. Montgomery. *J, Comput. Chem.*, 14:1347, 1993.

[107] B. M. Bode and M. S. Gordon. *J. Mol. Graphics Mod.*, 16:133, 1998.

[108] P. M. W. Gill, J. A. Pople, L. Radom, and R. H. Nobes. *J. Chem. Phys.*, 89:7307, 1988.

[109] D. M. Rogers, C. Wells, M. Joseph, V. J. Boddington, and J. J. W. McDouall. *J. Mol. Struct. (Theochem)*, 434:239, 1998.

[110] M. W. Mackenzie and J. L. Duncan. *J. Mol. Struct.*, 95:245, 1982.

[111] L. Margulés, J. Demaison, and H. D. Ruldolph. *J. Mol. Struct.*, 599:23, 2001.

[112] J. L. Duncan, D. C. Mckean, M. W. Mackenzie, and J. P. Pena. *J. Mol. Spectosc.*, 76:55, 1979.

[113] S. E. Bradforth, E. H. Kim, D. W. Arnold, and D. M. Neumark. *J. Chem. Phys.*, 98:800, 1993.

[114] J. E. Bartmess, J. A. Scott, and Jr. R. T. McIver. *J. Am. Chem. Soc.*, 101:6047, 1979.

[115] J. Berkowitz, W. A. Chupka, and T. A. Walter. *J. Chem. Phys.*, 50:1497, 1969.

[116] S. N. Ghosh, R. Trambarulo, and W. Gordy. *J. Chem. Phys.*, 21:308, 1953.

[117] Q. K. Timerghazin and G. H. Peslherbe. *J. Phys. Chem. B*, 112:520, 2008.

[118] H. Ozeki, T. Hirao, S. Saito, and S. Yamamoto. *Astrophys. J.*, 617:680, 2004.

[119] K. R. Lykke, D. M. Neumark, T. Andersen, V. J. Trapa, and W. C. Lineberger. *J. Chem. Phys.*, 87:6842, 1987.

[120] J. Marks, D. M. Wetsel, P. B. Comita, and J. I Brauman. *J. Chem. Phys.*, 84:5284, 1986.

[121] S. Moran, Jr. H. B. Ellis, D. J. DeFrees, A. D. McLean, and G. B. Ellison. *J. Am. Chem. Soc.*, 109:5996, 1987.

[122] J. Simons. *J. Chem. Phys.*, 91:11, 1989.

[123] G. L. Gutsev and L. Adamowicz. *Chem. Phys. Lett.*, 246:245, 1995.

[124] S. Moran, Jr. H. B. Ellis, D. J. DeFrees, A. D. McLean, S. E. Paulson, and G. B. Ellison. *J. Am. Chem. Soc.*, 109:6004, 1987.

[125] M. Gochel-Dupuis, J. Delwiche, M. J. Hubin-Franskin, J. E. Collin, F. Edard, and M. Tronc. *J. Am. Chem. Soc.*, 112:5425, 1990.

[126] F. Edard, A. P. Hitchcock, and M. Tronc. *J. Phys. Chem.*, 94:2768, 1990.

[127] P. D. Burrows K. D. Jordan. *Acc. Chem. Res.*, 11:342, 1978.

Part III.

Single-Crystal Mössbauer Spectroscopy: Determination of Microscopic Physical Tensor Properties of ^{57}Fe Sites in Inorganic Ferrous High-spin Compounds

7. General introduction

A nucleus embedded in a site (other than cubic) in a crystalline lattice typically experiences a non-uniform electric field whose symmetry reflects that of the site. Mathematically, the interaction between the field gradient generated by the spatial localization of electrons and the nucleus is described by a second-rank tensor (equivalent to a 3×3 matrix) known as the electric-field gradient (efg) tensor. Mössbauer spectroscopy is a nuclear magnetic resonant spectroscopic technique that is almost exclusively restricted to ^{57}Fe. In the absence of an internal or external magnetic field, the Mössbauer spectrum of such a nucleus is a simple two-line quadrupole doublet. In a single crystal, where the Mössbauer γ-beam has an orientation, which is initially unknown with respect to the efg tensor principal directions, the efg interaction is detected as an anisotropy in the Lorentzian line areas of the efg-induced quadrupole doublet. Anisotropy in the total areas are related to mean square displacement (msd) parameters (i.e. *nuclear* vibrational displacements) that can be initially approximated by X-ray crystallography as *atomic* displacements. In the situation when there is more than one symmetry-related Mössbauer nucleus in the unit cell, and this site has lower symmetry than the host crystal, then measurement yields the principal values and principal directions of the expectation, or macroscopic efg and msd tensor from all the contributing sites to the quadrupole doublet rather than individual site or microscopic efg or msd tensors. Both ferrous ammonium sulphate (FAS) and ferrous chloride tetrahydrate (FCL) are monoclinic, space group $P2_1/c$, with two Fe^{2+} ions occupying 1 (Laue class $\bar{1}$) point symmetry sites which would meet these conditions. An implication of the site being lower symmetry than the host crystal is that two elements of microscopic efg tensors could traditionally, at best be represented by a manifold of possible solutions. In the following chapters, application of a previously proposed method has resulted in a unique solution for the ambiguous monoclinic case where the two Fe^{2+} ions do not sit on a two-fold rotation axis. A two-fold rotation axis would be the minimal additional symmetry to raise the site symmetry to a situation where determination would not be ambiguous. This method involves simultaneous determination of total area anisotropy and the use of a quantum mechanical Mössbauer simulation and angular dependence refinement package MOSREF, developed over the last two decades by Dr. Craig Tennant, University of Canterbury.

The thesis chapters devoted to Mössbauer studies begins by providing a low-level historical overview, description of the Mössbauer effect, and mentions some broad interdisciplinary applications. Following, a chapter outlines some of the fundamental principles and instrumentation used in the study of FAS and FCL. The serendipitous discovery and characterization of a previously unreported and unstable isomorph of FCL is also reported. The FAS and FCL single crystal studies then follow, with both studies converging to physically sensible microscopic efg and msd tensors. A final chapter outlines some preliminary *ab initio* and density functional

theory calculations to determine efg tensors (at 0 K), and to explain the development of a method allowing the fitting of total intensities (proportional to anisotropy in the so-called recoilless fraction) in order to smooth data allowing for tighter convergence criteria in microscopic tensor refinements. This chapter also outlines some experimental work towards generalization of the FAS and FCL method to a species with six symmetry-related sites, and the remeasurement of FAS data with a new γ-beam source to decrease error, with planned application of a new simultaneous fitting and refinement procedure.

8. Mössbauer Spectroscopy

This chapter provides a general introduction to some of the material required to understand the following Mössbauer-related chapters. A low-level introductory type discussion can be found in an appendix at the end of this thesis. A description of the Mössbauer spectrometer and the goniometer assembly that was constructed for this work is also included.

8.1. The Mössbauer effect

Recoilless nuclear resonant absorption and emission is probably the most thoroughly investigated nuclear process in solid-state physics, with its major application as a chemical probe providing electronic structure characterization.

Consider the energy spectrum of γ-rays emitted from a nucleus that are initially at rest, and undergo an emission transition from an exited to a ground nuclear state, with transition energy E_t. The energy of the emitted γ-ray, E_γ, is different to E_t for three reasons:

1. The emitting nucleus must recoil with a momentum equal and opposite to the γ-ray, and conservation of energy (and momentum) requires the the recoil energy, E_r, to be taken from E_γ. The magnitude of E_r depends upon the the square of the transition energy and the quotient of the mass as given in equation 8.1.

$$E_r = \frac{E_t^2}{2mc^2} \tag{8.1}$$

where m is the mass of the nucleus. The energy conservation equation is therefore $E_t = E_\gamma + E_r$.

2. The emitting nucleus is part of a chemical system and has thermal motion, e.g. vibration or translation. This thermal motion results in a moving source, and the emitted γ-ray is altered by the Doppler Effect to E_D, as given in equation 8.2.

$$E_D = E_\gamma(1 \pm \frac{v}{c}) \cos\vartheta \tag{8.2}$$

where v the source vibrational velocity magnitude, c is the speed of light, and ϑ is the angle between the motion of the emitting nucleus and the emitted γ-ray. E_γ may therefore be increased or decreased ($\pm$) depending

on the relative motion. In an equilibrium bulk assembly of free thermal nuclei, a distribution of energies will result, which is centred about $E_t - E_r$.

3. any spectroscopic non-perturbed magnetic resonance line has a small natural line width, Γ_0, in accord with the Heisenberg Uncertainty Principle that exists between the the natural half-line width, Γ_0, and the finite lifetime $t_{\frac{1}{2}}$ of the excited state, as given in equation 8.3.

$$\Gamma_0 \geq \frac{\hbar \cdot \ln 2}{t_{\frac{1}{2}}} \tag{8.3}$$

where $\hbar$ is Plank's constant divided by 2π. These three effects also apply to the resonance absorption process, where the nucleus in its ground nuclear state absorbs a γ-photon and is excited to a state lying at energy E_t above the ground state. Recoil requires the energy to be larger than the transition energy by E_r, and the presence of Doppler broadening and the natural line width yields a small distribution about this value. Therefore, by providing Doppler motion to the source or absorber nuclei, resonant conditions can be achieved when γ-ray energy changes caused by the Doppler Effect offset the recoil energy associated with the transition. It is convention in Mössbauer spectroscopy that the measurable changes in resonant energy relative to a calibrate are expressed in terms if a Doppler velocity shift in conventional units of mm sec^{-1}.

The recoil energy in the absence of line broadening mechanisms in the gas-phase prevents any γ-ray source giving a direct transition, since $E_r >>> \Gamma_0$. When the nuclei are bound in a macroscopic solid crystallite, where on the nuclear scale, $m \sim \infty$, there is a probability that the recoil energy can be taken up by the crystalline lattice as a whole rather than by the individual nucleus. In this case, $E_r \sim 0$, allowing resonant absorption and emission processes to occur. Extranuclear electrons interacting with the nuclear state can result in so-called hyperfine interactions that adjust E_t slightly. Therefore, by application of the Doppler effect to the source, these resonance lines can potentially be observed. The probability that recoil is taken up by the lattice as a whole is known as the Lamb-Mössbauer recoilless fraction, f, and is related to the nuclear displacement, which can be described in terms of a mean-square-displacement (msd) tensor. This tensor represents the average thermal nuclear displacement along three orthogonal axes.

A further consideration is the excitation of quantized crystal lattice vibrations or phonons following a nuclear transition, which would also result in slight E_γ energy loss as recoil. Fortunately, for macroscopic crystallites, the transitions are zero-phonon events since the lattice E_r is smaller than the phonon excitation/creation energy and the process is completely recoil-free. In the Einstein model of the crystal these conditions are outlined in equation 8.4.

$$\begin{aligned} E_R &> \hbar\omega \\ E_R &< \hbar\omega \end{aligned} \tag{8.4}$$

where ω is the Einstein frequency of the crystal. These two cases describe the recoil energy either large or small respectively in comparison with the transition energy of the Einstein oscillator. In the former case, many oscillator transitions may occur with the recoil energy, resulting in no resonant absorption and emission. The latter case represents a truly recoilless or zero-phonon process. More commonly, the Mössbauer effect is expressed in terms of a characteristic (phonon) temperature, T_E, given in equation 8.5 that can be related to heat capacity and mass.

$$T_E = \frac{\hbar\omega}{k} \tag{8.5}$$

where k is the Boltzmann constant. Thus, the condition for recoilless nuclear resonance is $E_R < kT_E$. The Lamb-Mössbauer factor can then be expressed in terms of the Einstein model of the crystal and is given in equation 8.6. References to derivations are given in chapter 12.

$$f = e^{-4\pi^2 \frac{\langle U^2 \rangle}{\lambda^2}} \tag{8.6}$$

where $\langle U^2 \rangle$ is the dimensioned mean square displacement tensor or $\langle r^2 \rangle$ for one-dimension along the wave-vector of the γ-beam (in typical units of Å^2), and λ is the γ-beam wavelength. The expression $\langle U^2 \rangle$ may take several functional forms, such as an isotropic-harmonic function or an anisotropic-harmonic function. The Lamb-Mössbauer factor can also be expressed in terms of the Debye model of the crystal with a surroundings temperature, T, and a characteristic Debye temperature, T_D, as given in equation 8.7.

$$f = e^{-\frac{3E_R}{2kT_D}\left[1+4\left(\frac{T}{T_D}\right)^2 \int_0^{\frac{T}{T_D}} \frac{ydy}{e^y-1}\right]} \tag{8.7}$$

where y is a temperature function. In the ideal zero-phonon case, when $T << T_D$, then equation 8.7 simplifies to equation 8.8.

$$f_{T<<T_D} = e^{-\left(\frac{6E_R T}{kT_D^2}\right)} \tag{8.8}$$

Differences between these two models are usually negligible (beyond experimental error) even at low temperatures. Note that they both have the same exponential form, and the exponent in both cases are different expressions for the displacements. These expressions clearly outline the limits on appropriate Mössbauer isotopes. In order to have sufficiently large values of f, m should not be too small i.e. greater than 40 amu, E_t not too large, i.e. less than 150 keV, and T_D not too small, which corresponds to strong chemical bonds and T not too high. A hard, high melting point crystal, such as a polar or refractory compound, meets these conditions. A whole set of new restrictive conditions also apply when appropriate source parent isotopes are considered. Rudolf Mössbauer hit the grand nuclear physics lottery when he serendipitously used one of the only radiocouples that shows slight nuclear recoilless resonant absorption and emission at room temperature, which was then confirmed at low temperatures.

The resonant absorption and emission spectral line shape of a Mössbauer transition arises from the energy

dependence of the maximum nuclear cross-section (Breit-Wigner expression [1]), $\sigma_0(E_\gamma)$, for absorption, which is given in equation 8.9.

$$\sigma_0(E_\gamma) = \frac{(hc)^2(2I_e+1)}{2\pi E_\gamma^2(2I_g+1)}\frac{1}{1+\alpha} \tag{8.9}$$

where $I_e = \frac{3}{2}$ is the excited state nuclear spin, $I_g = \frac{1}{2}$ is the ground state nuclear spin, and α is a nuclear isotope constant known as the internal conversion coefficient.[1] For a non-perturbed natural line, the cross-section energy dependence is given in the Lorentzian expression in equation 8.10.

$$\sigma(E) = \sigma_0\frac{(\frac{\Gamma_0}{2})^2}{(E-E_\gamma)^2+(\frac{\Gamma_0}{2})^2} \tag{8.10}$$

where Γ_0 is the natural line width. In general, in order to observe the Mössbauer effect in a given isotope, E_γ needs to be between 5 keV and 150 keV, and typically below 50 keV as both f (more severely) and σ_0 decrease as E_γ increases. At energies below 5 keV, the high degree of self absorption and interaction with electrons preclude useful application. In the absence of line-broadening effects, a Mössbauer spectrum will show resonance lines very close to the natural line width limit. For ^{57}Fe the (isolated) natural full line width is 0.194 mm sec^{-1}, and the disc source used in the studies in this thesis exhibits a manufacturer tested line width of 0.204 mm sec^{-1}.

8.2. Hyperfine interactions

There are three hyperfine parameters resulting from electron-nucleus interactions, known as the isomer shift, quadrupole splitting, and nuclear Zeeman Effect, that are measurable by Mössbauer spectroscopy and characterize a Mössbauer spectrum. Their effects on the ^{57}Fe Mössbauer nuclear states is summarised in figure 8.1. A brief description of each follows, and the so-called efg and msd tensors are further outlined in chapter 12.

8.2.1. The isomer shift

The isomer shift is analogous to the effect of the chemical shift in NMR spectroscopy. The volume of an excited state nucleus is slightly different than the ground state, hence the non-zero (nodeless) s orbitals' or relativistic p orbitals electron density penetration in each state will be different. This density difference manifests as a slight difference in total binding energy of the electrons to the transition energy, E_t, in the two nuclear states, as summarised in equation 8.11. Since this is a monopole interaction

$$E_t = \Delta E_{nuclear} + \Delta E_{electronic} \tag{8.11}$$

where the first term represents the change in nuclear binding energy, and the second term represents the change in electronic binding energy (of atomic electrons). If the absorbing and emitting nuclei are in different

[1] α represents the number of conversion electrons for each resonantly emitted γ-photon from the absorber, which is 8.2 for ^{57}Fe. Internal conversion is a process that competes with γ-ray emission, in which the nuclear excitation energy is transferred to a core-shell electron (or from a electron-electron knock-out cascade). The electron is emitted from the atom with a kinetic energy equal to the nuclear transition energy minus the electron binding energy.

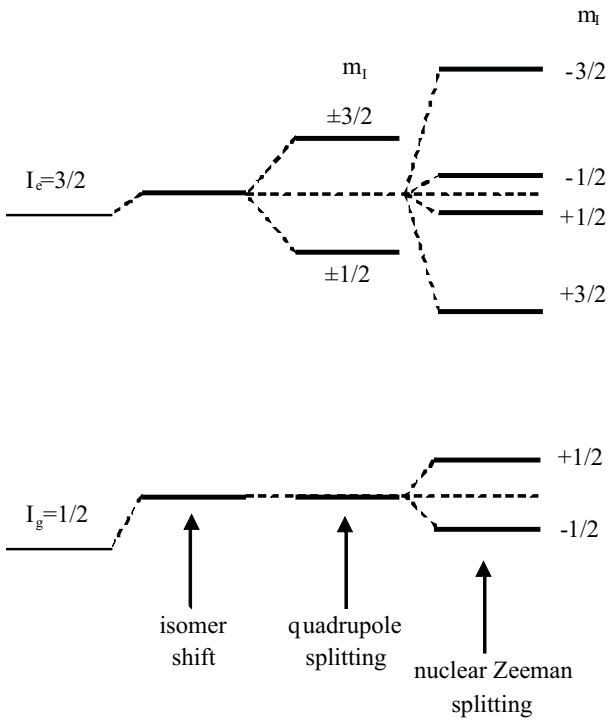

Figure 8.1.: Summary of the effects of isomer shift, quadrupole splitting, and nuclear Zeeman effect on the ^{57}Fe Mössbauer nuclear states.

chemical compounds, the spatial distributions of atomic electrons will be different, resulting in differences in $\Delta E_{electronic}$, and thus E_t. This change is known the isomer shift, δ, and is given approximately in equation 8.12.

$$\delta = \frac{2}{5}\pi e^2(\langle r_e^2\rangle - \langle r_g^2\rangle)[|\psi_e(0)|^2 - |\psi_a(0)|^2] \tag{8.12}$$

where $\langle r_e^2\rangle$ and $\langle r_g^2\rangle$ are the mean square nuclear radii in the excited state and in the ground state respectively, and $|\psi_e(0)|^2$ and $|\psi_a(0)|^2$ are the electrons densities at the nucleus for the emitter and absorber respectively. Another small relativistic contribution to $\Delta E_{electronic}$ arises from the change in rest mass of the nucleus during the emission process, which in turn changes the zero-point vibrational energy. However, this contribution is negligible. Further, the sign of $\langle r_e^2\rangle - \langle r_g^2\rangle$ is the same as the sign of the quadrupole splitting, which is outlined next.

8.2.2. The quadrupole splitting

The electrons surrounding a nucleus form an electric field, and when asymmetric, for example due to low point group symmetry bonding, there exists a non-zero electric-field gradient, efg, at the nucleus. The nucleus is tiny compared to the separation of electrons, therefore any slight change in bonding parameters changes the efg at the nucleus. The efg is a tensor quantity, and can only be non-zero for a non-spherical symmetrical charge distribution of p, d or f orbital electrons. The efg can normally be described by two quantities, the

largest principal value, V_{zz}, where by convention $|V_{zz}| > |V_{yy}| \geq |V_{xx}|$, and the asymmetry parameter, η, where $\eta = \frac{V_{xx}-V_{yy}}{V_{zz}}$. The asymmetry parameter ranges from 0 to 1. If the nucleus has spin $I > \frac{1}{2}$, then it possesses an electric quadrupole moment, Q, resulting from a non-spherically symmetric nuclear charge distribution. This nuclear quadrupole moment may interact with a non-zero efg yielding a hyperfine coupling, or lowering of degeneracy and therefore spectral splitting. The Hamiltonian for the axial nuclear hyperfine quadrupole interaction is given in equation 8.13.

$$\hat{H}_Q = \frac{eV_{zz}Q}{4I(2I-1)}\left[3\hat{I}_z^2 - I(I+1) + \eta(\hat{I}_x^2 - \hat{I}_y^2)\right] \tag{8.13}$$

where I is the spin of the nuclear state, and $\hat{I}_p$ for $p = x, y, z$ are respective nuclear spin projection operators. That the $\hat{I}_z$ operator is a squared function means that $\pm m_I$ will be degenerate, which is commonly known as a Kramers doublet. The eigenvalues of this Hamiltonian are given in equation 8.14.

$$\hat{E}_Q = \frac{e^2 q_{zz} Q}{4I(2I-1)}\left[3I_z^2 - I(I+1)\right]\left(1 + \frac{\eta^2}{3}\right)^{\frac{1}{2}} \tag{8.14}$$

The hyperfine quadrupole splitting is the energy difference between the eigenvalues of the Hamiltonian, and given in equation 8.15.

$$\Delta E_Q = \frac{eQ}{2}V_{zz}\left(1 + \frac{\eta^2}{3}\right)^{\frac{1}{2}} \tag{8.15}$$

The efg has two different contributions in from each charge q_i, as outlined in equation 8.16.

$$q = \sum_i \left((1-R)q_{i,val} + (1-\gamma_{\text{inf}})q_{i,lat}\right) \tag{8.16}$$

where q_{val} is the largest valence term that reflects the asymmetry of the charge distribution arising from valence and bonding electrons, and q_{lat} is the lattice term, which measures the deviation from cubic symmetry of neighbouring atoms in the crystalline lattice. This second term arises from more distant charges in the lattice present in molecular orbitals, and is zero in a pure cubic environment. The constants R (positive and small) and γ_{inf} (negative and large) are known as Sternheimer antishielding factors, and describe the screening effects between charges.

The sign of V_{zz} is known as the sign of the quadrupole splitting, which is usually difficult to determine and varies between compounds. This sign corresponds to the m_I ordering in the spectrum, i.e. whether nuclear component spin states are described by a regular or inverted multiplet, and difficult low temperature magnetically perturbed experiments are usually required to determine this sign for a given species. A detailed review of the quadrupole splitting and electric field gradient in Mössbauber spectroscopy is given by Spiering [2], and further details relevant to the studies in this thesis are given in later chapters. The relative intensities of the two lines in a quadrupole doublet single crystal spectrum depend on the relative orientation of efg and msd tensors. A change in the efg tensor projection for a given single crystal measurement results in changes of

the quadrupole doublet line intensity ratio, whereas changes in the msd tensor (or alternatively the recoilless fraction) results in an angular dependence of the absolute intensity. An isotropic recoilless fraction assumes that two symmetry-related sites contribute equally in any observation orientation.

The Gol'danskii-Karyagin effect

A polycrystalline sample with completely randomized crystallite orientations may also exhibit anisotropy in the recoilless fraction of the two lines of a quadrupole doublet (or magnetic hyperfine intensities), known as the Gol'danskii-Karyagin effect [3]. In the absence of differential relaxation or texture (preferred crystallite orientation packing) effects, the concept of this phenomenon is non-intuitive - but very convincing in the mathematics and well observed experimentally.[2] In short, if the major symmetry axis for a randomly oriented crystallite is at an angle θ to the γ-beam direction, then the nuclear magnetic dipole transition line has an intensity given by $I_0 = \frac{3}{2}f(\theta)\sin^2\theta$ for $\Delta m_I = 0$ and $I_1 = \frac{3}{4}f(\theta)(1+\cos^2\theta)$ for the $\Delta m_I = \pm 1$ transitions. A randomly oriented sample has θ over all possible angles, and the ratio of the absorption intensities is given in equation 8.17.

$$\frac{I_0}{I_1} = \left(\frac{1}{2}\int_0^\pi \frac{3}{2}f(\theta)\sin^3\theta d\theta\right) / \left(\frac{1}{2}\int_0^\pi \frac{3}{4}f(\theta)(1+\cos^2\theta)\sin\theta d\theta\right) \tag{8.17}$$

where $f(\theta)$ is a term describing the angular dependence of the recoilless fraction. This ratio is unity if the recoilless fraction and msd are isotropic. When $f(\theta)$ is anisotropic, then this ratio does not equal unity, yielding a *quadrupole doublet asymmetry in a completely randomly oriented polycrystalline sample.*

Texture effects may give incorrect anisotropy in the recoilless fraction, where crystallites have a common morphology and therefore show some single-crystal type anisotropy. Such effects can be minimized by suitable orientation with respect to the γ-beam [4], or potentially by diluting the analyte in a cubic matrix (e.g. glucose) or preparation in a viscous oil. Spiering [5] provides a detailed mathematical description of the Gol'danskii-Karyagin effect and Pfannes and Gonser [6] outlines the various texture effects that can occur to change the powder quadrupole doublet ratios.

8.2.3. The nuclear magnetic Zeeman Effect

The third type of hyperfine interaction is a magnetic one. The presence of an electronically induced magnetic field (most commonly separated by magnetic ordering or a spin imbalance) completely removes the spin degeneracy and splits a given I level into $2I+1$ nuclear levels, in a phenomenon known as the nuclear Zeeman Effect (strong-field case). The magnitude of the hyperfine magnetic field is related to the magnetic exchange or interaction between adjacent iron atoms, with this effect again depending on valence electronic configuration, electronic spin state, and co-ordination geometry. The magnetic hyperfine interaction couples the magnetic moment of the nucleus, μ_N, that is present for $I > 0$, to the paramagnetic hyperfine magnetic field, $\mathbf{B}_{hf}$, acting at the nuclear site. The interaction Hamiltonian takes the form given in equation 8.18.

[2] This effect was first observed in tin oxide compounds where it is more prominent, and is difficult to observe for ^{57}Fe compounds.

$$\hat{H}_M = -\hat{\mu}_N \bullet \hat{B}_{hf} = -g_N \mu_N \hat{B}_{hf} \bullet \hat{I} \tag{8.18}$$

The eigenvalues of this Hamiltonian are given in equation 8.19.

$$E_M = -g_N \mu_N m_I B_{hf} \tag{8.19}$$

In these expressions, g_N is known as the nuclear Landé factor or the magnetogyric ratio, and is a characteristic of the nucleus; $m_I = I, I-1, .., -I$; and $\hat{I}$ is the total nuclear spin operator. The splitting between each level is $2\mu_B B_{hf}$. For ^{57}Fe, the ground state, with $I = \frac{1}{2}$, splits into two levels, and the excited state with $I = \frac{3}{2}$ splits into four. Overall, there are eight possible transitions, with only six (a sextet) observed by magnetic dipole selection rules ($\Delta m_I = 0, \pm 1$).[3] In order for nuclear magnetic splitting to be well defined, it is necessary that the nuclear magnetic moment remains precessing in a given orientation longer than the Larmor precession period, τ_L, which corresponds to the time required for precession of the magnetic moment vector once around the direction of the magnetic field, and is given in equation 8.20.

$$\tau_L = \frac{4\pi m_p c}{g_N e I_z B_{hf}} \tag{8.20}$$

Most paramagnetic compounds at ambient temperatures have magnetic fields at the nucleus relaxing and fluctuating too rapidly to observe, therefore the hyperfine magnetic field averages to zero. Spin-flip can be slowed down to allow observation of magnetic hyperfine spectra by cooling the absorber to low temperatures. An external magnetic field may also be applied to promote splitting in paramagnetic species which show no magnetic structure at the given temperature. Magnetic dipole and electric quadrupole interactions are usually simultaneous, therefore Hamiltonian operators are combined and referenced (spherical polar (θ, ϕ)) with respect to the principal efg tensor axes. The Hamiltonians and eigenvalues that have been outlined apply only for the axial case, and for the general non-axial case the expressions are much more complex and require numerical Hamiltonian diagonalization methods.

8.3. The University of Canterbury Mössbauer spectrometer

The spectrometer used in the studies in this thesis is arranged in a transmission configuration as outlined in figure 8.2, with its electronic operation outlined in figure 8.3. The spectrometer was originally implemented at the DSIR (Division of Scientific and Industrial Research) Gracefield laboratories, and once decommissioned, was acquired by the Department of Chemistry, University of Canterbury. Briefly, the spectrometer is enclosed in a lead box that is mounted on a large concrete slab with rubber tyre feet. The lead box prevents radiation exchange with surroundings, and the concrete slab mounting eliminates surrounding and building vibrations. Two parallel stainless steel alignment rods that are also parallel to the γ-ray beam provide instrumental component alignment. The detectors are movable to allow sample changing and different collimator assemblies to be inserted into

[3] Eight transitions may be observed if the hyperfine field is weak, resulting in observation in the Paschen-Back region where $|m_I\rangle$ kets are not pure (singular) eigenstates.

the beam line, since a measurement typically requires the detectors to be placed as close as possible to the sample for maximum signal. Electronically, the spectrometer operation is relatively simple, and follows the general construction outlined in previous chapter. There are two separate nuclear channels that share one common drive (transducer) using an ELSCINT MFG-N-5 multifunction generator, which operates in constant acceleration mode at 4.5 Hz which is close to the mechanical transducer natural resonant frequency. This model is capable of several types of drive waveforms, including an idealized linearised sine mode, avoiding the need for mathematical correction. Such a drive motion requires a recoil-free (low rigidity and momentum) drive unit (transducer). In this work, the function generator is operated in constant acceleration mode yielding a linear velocity response with a triangular waveform. The transducer operates between ± 2.5 V, with a multi-channel analyser (MCA) group size of 1024 channels of 512 forward and 512 reverse. All electronic instrumentation are mounted in Mech-Tronics 150 series rack-mount instrument bins. Nuclear channel # 1 is operated from ORTEC based electronics and nuclear channel # 2 is operated from ELSCINT based electronics, with the former primarily used in research in this thesis. Both detectors are Reuter-Stokes RS-P3-1605-262 gas-proportional counters that contain krypton gas (97%) with CO_2 (3%) quencher at a total pressure of one atmosphere, with a 127 μm thick beryllium radiation entrance window in the stainless steel chassis (with internal aluminium lining). A beryllium window of this thickness yields 100% Mössbauer transmission. Krypton was originally chosen for optimization of spectral efficiency of the 14.41 keV line, since krypton exhibits an absorption edge at 14.32 eV. Such gas proportional counters have a designed life expectancy of typically ten years, and those employed in these studies are now 17 years old. Their excellent performance is attributed to the fact they are run at much lower voltages than standard operation (higher voltage corresponds to higher amplification). No iron-based components exist in the instrument γ-beam pathway; therefore any collimator, sample holders or housings are fabricated from lead or brass. For nuclear channel # 2, the detector is operated with a Mech-Tronics model 253 0-3 kV high voltage power supply operating at 1800 V. The detector signal is initially amplified with a Mech-Tronics model 401 F.E.T. based pre-amplifier and then further amplified with a Mech-Tronics model 514 spectroscopy amplifier operating at a 6.0×500 gain. Channel # 2 has an overall gain/voltage larger than that of channel # 1, which was previously established to best reproduce the ORTEC outputs. The amplifier output connects to an ELSCINT SCA-N-4 single channel analyser, which employs two electronic discriminators. In turn, this SCA connects to a DOS-based computer which contains an 8-bit ISA ORTEC model ACE MCS (MCA) that is controlled with the ORTEC multichannel scalar software package. A Cryo Industries model 110-165-SXA liquid-nitrogen-liquid-helium continuous flow cryostat assembly exists, however was not required for the room temperature studies in this thesis.

8.4. The goniometer assembly

In order to undertake single crystal measurements allowing determination of efg and msd tensors, construction of a suitable single-circle goniometer was required. Such a goniometer needs to provide different projections of the γ-beam on a regularly ordered single crystal. This can be achieved by mounting the single crystal at a

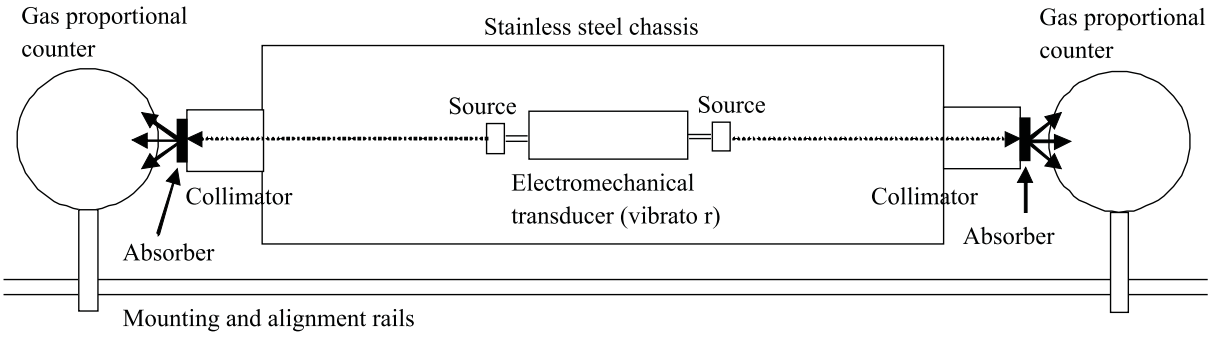

Figure 8.2.: Schematic overview of the dual Nuclear channel University of Canterbury Mössbauer spectrometer.

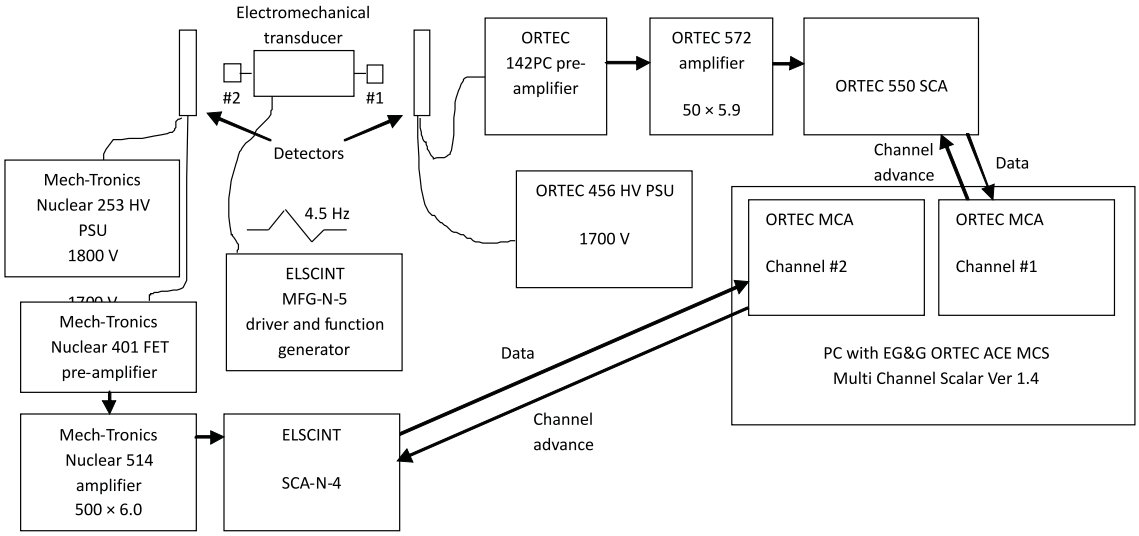

Figure 8.3.: Schematic overview of the University of Canterbury Mössbauer spectrometer electronic operation.

fixed angle with respect to the γ-beam and rotating the sample. By rotating the crystal through a 2π circular rotation, angular spectra can be accumulated that each contain different projections of the γ-beam on the msd and efg tensor principal values. This angle can vary between 0° and 90°. The angle of 0° is known as the perpendicular orientation where the rotation axis and γ-beam are coaxial, and as a consequence, no angular dependence will be observed since each orientation obtains no new projection of the γ-ray beam on the site tensors. The most general angle of 45° was arbitrary selected, therefore resulting in all recorded angular rotation spectra having the single crystal plane inclined at an angle of 45° with respect to the γ-beam. The designed goniometer was built in-house by the Department of Chemistry Mechanical Workshop and was constructed from iron-free high quality brass, and is shown in figures 8.4 and 8.5. The diameter of the inner bore was selected to match the polycrystalline collimator and diameter of the disc source. The total length (from source average position to the point where the γ-beam meets the crystal) was selected to minimize cosine smearing effects, since the single crystal absorbers have a finite diameter. Cosine smearing effects result in distortion and broadening of resonance lines and therefore need to be minimized as outlined by McCammon *et al.* [7]. Briefly,

the radiation emission angle, α, along the bore can be calculated by equation 8.21.

$$\alpha = \tan^{-1}(\frac{s}{2d}) \tag{8.21}$$

where s is the source diameter, and d is the separation to the sample or end of collimator. For a point source, α should typically be $\approx 10°$, and for a traditional disc source $\approx 5°$. The angle of 5° is a conservative estimate, and since the disc source in this work has $s = 4$ mm, then d was selected to be 23 mm.

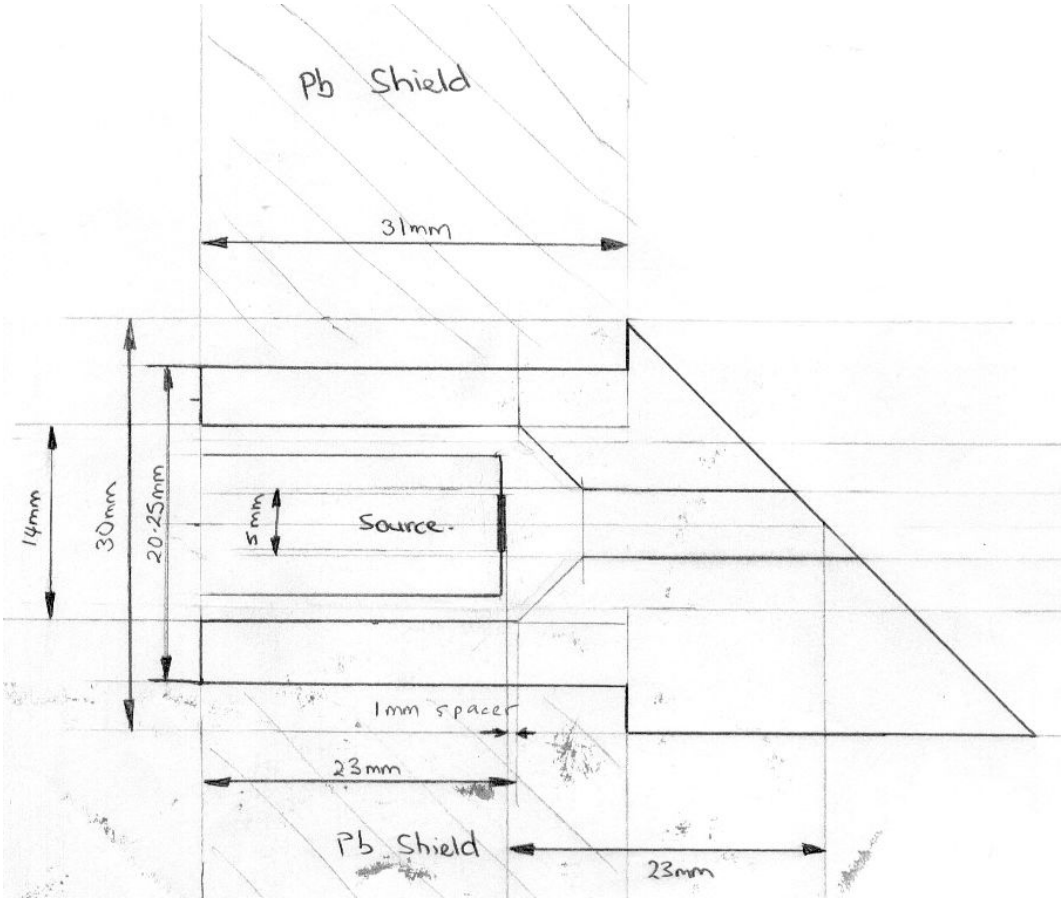

Figure 8.4.: Original design showing the dimensions of the single-circle goniometer assembly.

8.5. Drive linearity

It is usually assumed that a Mössbauer drive or electromechanical transducer has a sufficiency low rigidity to yield a physically linear velocity response waveform for the constant acceleration (triangular waveform) electrical drive. Any deviation typically occurs at the displacement extremes where the finite momentum of the drive yields a non-instantaneous response. Linearity should ideally be checked, since the studies in this thesis require accurate total and relative intensities, which could be altered by a non-linear drive response in part of the spectrum where resonance occurs. This was approximately checked by fitting an iron-foil spectrum over the

Figure 8.5.: Photograph of the goniometer assembly showing the rotating single-circle crystal mount.

velocity ranges of interest in experiments herein. Since the ranges were different for the two major studies reported later, two checks were made in the different velocity ranges, with both showing a four-line iron-foil magnetic calibration spectra, as schematically outlined in figure 8.6.

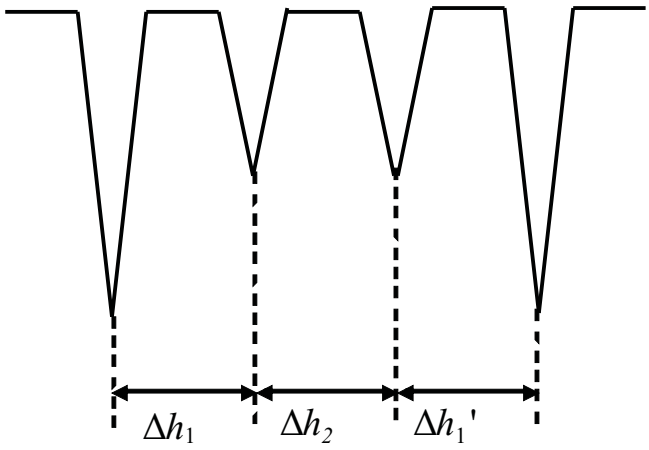

Figure 8.6.: Assignment of magnetic hyperfine splittings (with combined quadrupole splitting) in the ^{57}Fe-foil four-line Mössbauer spectrum.

The appropriate splittings were determined for the two cases, with those for ferrous ammonium sulphate hexahydrate (FAS) summarised in table 8.1. Briefly, three fits are made for each iron-foil calibration, the folded spectrum,[4] and the individual left and right halves. The latter two give indication of the positive or negative triangular wave response, and the former of the average response that corresponds to the experimental single crystal fits reported later. The high voltage drive velocities (arbitrary voltage units) are 0.5×100 and 0.7×100

[4]the folded spectrum arises from averaging both signal halves (forward and reverse or alternative known as left and right) of drive waveform.

Table 8.1.: Splitting parameters, in mm sec^{-1}, for the folded iron-foil calibration spectrum using the velocity ranges employed in the FAS single crystal studies.

Spectrum	Δh_1	Δh_2	$\Delta h_1'$
fold	2.2214±0.0023	1.6825±0.0022	2.2312±0.0023
reference[a]	2.2363	1.6794	2.2363

[a]Ref [8].

respectively for ferrous ammonium sulphate hexahydrate and ferrous chloride tetrahydrate.

Four comparisons need to be made: left and right splittings with respect to each other; left and right splittings with folded splittings; all measured splittings with the reference splittings; and the splitting errors (95% confidence interval) with respect to each of the three former comparisons. These three fits all show excellent agreement with reference splittings, therefore indicating the drive response to be linear. Note that for FAS, this calibration only collected 8.5×10^4 off-resonance counts owing to a weak source. Calibrations for the ferrous chloride tetrahydrate single crystal study, which employed a new source, gives slightly closer agreement with reference values.

8.5.1. MOSFUN

The majority of spectrum fittings in the course of this thesis were performed using the fitting program MOSFUN (MÖssbauer Spectra Fitting Program for UNiversal Theories), that was originally developed by E. W. Müller [9]. MOSFUN employs a Newton-Raphson type iterative non-linear least squares fitting procedure, and allows fits with Gaussian, Lorentzian, and Voigt line profiles. Both MOSFUN and another fitting program NORMOS [10] are capable of performing transmission integral corrections (outlined later) by numerical methods.

A "good" spectrum has a large number, i.e. 20,000 or more baseline (off-resonance) counts with clear peaks, and tails well incorporated within the maximum spectrum velocity. A given spectrum should optimize signal-to-noise and measurement should be undertaken until the standard deviation in the fitted parameters are smaller than any non-linearity in the transducer, that would be expected to show up as shoulders or bad Lorentzian line shape for non-overlapping spectral peaks. Measurements of a thin sample, containing the recommended ≈5 mg cm^{-2} in order to give narrow and well defined Lorentzian lines with a reasonable active source (≈ 5 mCi or greater), may take half a day to several days. The FAS single crystal spectra that are reported in a later chapter, each took between one to two weeks to record. High energy γ-ray radiation which necessarily accompanies the source transitions is the main source of background. While much of this is eliminated by the electronic window pulse discriminators in the spectrometer MCA, a small fraction still results in signal, and averages out for a large number of off-resonance counts. The natural background may be determined by using a Cu foil as the absorber that filters out all ^{57}Fe 14.4 keV Mössbauer radiation, while still allowing the high energy γ-rays (122 keV and 136 keV) to pass with intensities theoretically corrected with a mass absorption coefficient. The fitting parameter for a Mössbauer spectrum uses the modified chi-squared (χ^2) value (common in other

spectroscopies also), that considers the contribution from each channel to a resonance line, then each line to the overall spectrum. Fitting involves a non-linear least squares comparison of the experimental intensities with a trial fit. The parameters of the trial (half line widths, peak positions, peak intensities) are systematically optimized to minimize the value of χ^2 as given in equation 8.22 for n absorption lines. The resultant value is then normalized with respect to the number of degrees of freedom.

$$\chi^2 = 1 + \sum_{i=1}^{n} W_i (I_{i,obs} - I_{i,calc})^2 \tag{8.22}$$

where I represents each Lorentzian absorption line intensity from summation of each channels contribution, and W_i is the weighting factor of $\frac{1}{I_{obs}}$. The limit of perfect spectrum fitting is χ^2=1, and a general spectrum ideally has $\chi^2 < 1.5$. When overlapping spectral lines are present, the fit needs flexibility for peak superposition and knowledge of the expected number of superposition components that are known as sub-spectra.

Self-absorption and re-emission processes yield line broadening, since each nucleus has some small vibration motion, and therefore must be minimized. Line broadening causes a purely Lorentzian line shape to transform into a thermal Gaussian line shape. In such a situation, more comprehensive line shapes need to be fitted, such as a Voigt profile, which is a convolution of a Gaussian and a Lorentzian function. In order to avoid self-absorption line broadening, iron based samples ideally have a (thin absorber) concentration of 5 to 10 mg cm^{-2}, and no greater than 20 mg cm^{-2}. The magnitude of resonance, or intensity of a resonant absorption emission line, then depends on the effective thickness, t, as given in equation 8.23.

$$t = nf\sigma_\circ \tag{8.23}$$

where n is the number of resonant nuclei species per square centimetre, f is the recoilless fraction, and $\sigma_\circ$ is a nuclear cross-sectional constant.

8.5.2. Transmission corrections

When radiation is passed through a substance of finite thickness, attenuation of the radiation beam and/or various components of radiation polarization may occur. For the Mössbauer studies reported here, absorption intensity measurements are required that are dependent upon sample thickness. Intensities at the infinitesimally thin-limit are required, therefore corrections to experimental spectral fits need to be applied. Experimental measurement is a two sided coin - the absorber is required to have a finite thickness in order to obtain an absorption spectrum, yet cannot be too thick, requiring large corrections that introduce error. The attenuation of radiation by a substance can be approximated by the Beer-Lambert type expression given in equation 8.24.

$$I = I_\circ e^{-\left(\frac{\mu}{\rho}\right)\rho l} \tag{8.24}$$

where $I_\circ$ is the incident intensity, I is the intensity of the beam at distance of l into the substance, μ is the attenuation coefficient of the substance for the radiation of given energy, and ρ is the density. For a multi-

component substance, μ takes a linear-combination form. The parameter $\left(\frac{\mu}{\rho}\right)$ is known as the mass attenuation coefficient, and is analogous to the molar absorptivity in solution phase spectroscopy. These data are tabulated for a large range of materials and wavelengths [11].

The Mössbauer radiation emitted from the source is collimated, yet exists in polarizations described in terms of directions of the electric-field vector. Photons are boson particles with S=1, therefore have three components of spin, $M_S = -1, 0, 1$. Low symmetry space-group crystals can act as polarizing filters with net ordered electric and magnetic fields, with a finitely thick sample polarizing the radiation and altering the observed intensities - this can be described by a macroscopic efg tensor if known.

8.5.3. Transmission integral

Thickness corrections can be effected by a general transmission function, $T(v)$, where v is the calibrated Mössbauer velocity, as given in equation 8.25.

$$T(v) = \int_{-\infty}^{+\infty} S(E, v)A(E)dE \tag{8.25}$$

where $S(E, v)$ is a function describing the energy distribution of the Mössbauer source radiation (a Lorentzian function), and $A(E)$ is an absorber function which takes the dimensionless form of equation 8.26.

$$A(E) = e^{-\sigma(E_t)t} \tag{8.26}$$

where $\sigma(E_t)$ is the resonant absorber cross-section, and t is the effective thickness. This expression is obtained from generalization of equation 8.24 for the Mössbauer interaction. The total resonance dimensionless (counts) cross-section $\sigma(E)_t$ is composed of n Lorentzians functions and the summation is over all resonance lines, i, to give the total absorber cross-section in equation 8.27.

$$\sigma(E)_t = \sum_{i=1}^{n} W_i \frac{(\Gamma_0/2)^2}{(E - E_i)^2 + (\Gamma_0/2)^2} \tag{8.27}$$

where W_i is the probability of the transition, and E_i is the energy of the transition, i. In application, the integral in equation 8.25 is replaced by the summation given in equation 8.28.

$$T(j) = \sum_{i=1}^{m} S(i)A(j + i - 1)\Delta v \tag{8.28}$$

where j corresponds to the channel number equivalent to the source small velocity spread, Δv. This transmission integral allows an approximate correction to thickness and attenuation effects, and is applied in later chapters as a comparison to the thickness and polarization series expansion that are outlined in chapter 10.

8.6. Physical tensor properties of crystals

Crystals consist of a regular and rigid or frozen array of atoms, and as a consequence of solid-state ordering, a physical property may differ in different directions of observation. That is, a measurement observes the projection of the property on the direction of observation. The simplest example is electrical conductivity, that may take a continuous range of values depending on the measurement orientation, and fortunately there exist a finite number of independent directions and coefficients (c.f. reference Cartesian axis) that may be used to describe such properties. The physical tensors considered in this work are of the Cartesian symmetric type and can simply be considered as 3×3 matrices that abide by common matrix algebra laws. An isotropic tensor (sphere-like) has equal physical properties along all axes, whereas anisotropic (ellipsoid-type) tensors have unequal physical properties along two or more axes. The formalism of tensors in classical, relativistic and quantum mechanics can be found in the text of Byron and Fuller [12], and a very brief overview follows.

There are two types of crystal property tensors to differentiate. A microscopic tensor describes a property of an individual site, whereas a macroscopic tensor describes a bulk averaged property. Consider a crystal that contains more than one iron atom per unit cell. If these iron atoms are not symmetry-related, they exist in different crystallographic and electronic environments and would yield different Mössbauer hyperfine parameters (whether resolvable or not). In contrast, if these iron atoms are symmetry-related, they have the same crystallographic environment and contribute to the same Mössbauer hyperfine parameters (this work is concerned with the quadrupole doublet). In this case, the tensors describing physical properties will also be equivalent in magnitude but rotated in orientation. Mössbauer spectroscopy is ideally suited to the determination of efg and msd tensors due to its ultra-high resolution; however the Mössbauer radiation interaction measures only the macroscopic spectrum. When the macroscopic tensors are measured, detail is lost (for low symmetry sites) on the microscopic orientation since an average is observed, and there are usually many microscopic solutions that average to the same macroscopic result. This constitutes an ambiguity problem, and only exists when the site symmetry is lower than the host crystal point group symmetry. This problem is addressed in later chapters for the monoclinic case where a site in the crystallographic unit cell cannot have site symmetry higher than $\bar{1}$ for two different classical single crystal species.

In general, measurement and interpretation of tensor properties and their symmetries raises the need to consider four discrete physical and measurement symmetries:

1. bulk symmetry of the material (e.g. unit cell)
2. symmetry of external forces (e.g. application of perturbation magnetic field)
3. symmetry of the resulting change from interaction (e.g. orientation of the crystal with respect to probing radiation)
4. symmetry of the physical property with respect to the external force (e.g. symmetry of the physical property with respect to a perturbing magnetic field)

8.6.1. Definition of a tensor

The orthogonal transformation laws that apply to physical scalar or vector quantities that are given in equations 8.29 and 8.30 respectively, do not apply to tensor quantities. Consider the following two mathematical transformations for generalized mathematical descriptors:

$$\phi^{'} = \phi \tag{8.29}$$

which defines a scalar (zeroth rank tensor);

$$x_i^{'} = a_{ij} x_j \tag{8.30}$$

which defines a vector (first rank tensor), and a_{ij} are scalar parameters.

These two quantities are both different to the situation, where under an orthogonal transformation in three dimensions, the 3^N quantities, with tensor components, $T_{i_1,i_2,\ldots,i_N}$ (where $i = 1, 2, 3$ for a tensor of second rank), transform according to the condition in equation 8.31.

$$T^{'}_{i_1,i_2,\ldots,i_N} = a_{i_1,j_1} a_{i_2,j_2} \ldots a_{i_N,j_N} T_{j_1,j_2,\ldots,j_N} \tag{8.31}$$

with N summations implied. A tensor of second rank has nine T_{ij} components obeying the transformation law given in equation 8.32.

$$T^{'}_{ij} = a_{ik} a_{jl} T_{kl} \tag{8.32}$$

This work is concerned with tensors abiding to orthogonal transformations. The word tensor in general considers transformations under arbitrary coordinate frames, whose consideration is not required in these studies well and is above the level of mathematics outlined here - any tensor can be represented as a Cartesian tensor, but not any Cartesian tensor can be represented as a formal tensor, since the latter may fail to meet transformation laws in all coordinate reference frames. A monopole is described by a zeroth order tensor, a dipole by a first order tensor, and a quadrupole by a second-order symmetric tensor. In general, second rank tensors have symmetrical ($T_{ij} = T_{ji}$) and antisymmetrical ($T_{ij} = -T_{ji}$) types. For an antisymmetric tensor, the six off diagonal elements in pairs must have equal magnitudes and opposite signs, and the diagonal elements must be zero since $T_{ii} = -T_{ii}$. An antisymmetric tensor has only three independent quantities, which may be related by a pseudovector expression. These do not represent physical properties. The symmetrical tensor of second rank has six independent components: three diagonal; and three pairs of equal off diagonal. A second-rank tensor can be decomposed to, or constructed from consideration of the relationship between two interacting vector quantities, where the tensor can be represented in any selected coordinate system that can give a valid description for the vectors. The six scalars can be visualized as defining a quadric (ellipsoid) surface given in

equation 8.33.

$$Ax_1^2 + Bx_2^2 + Cx_3^2 + Dx_1x_2 + Ex_1x_3 + Fx_2x_3 = 1 \tag{8.33}$$

A symmetric tensor is then represented by the surface $T_{ij}x_ix_j = \pm 1$ with $\pm$ as the sign of the determinant. In effect, this expression describes an ellipsoid, and can also be expanded in spherical polar form (see later chapters). From herein, when the word tensor is used, this implies a symmetric Cartesian tensor of second rank. The coefficients A, B, C, D, E, F in equation 8.33 relate to the nine (although three are symmetry-related) direction cosines schematically shown in figure 8.7. Direction cosines describe the angular offset of pairs of axes within two coordinate reference frames with respect to each other. For example, in equation 8.34 the matrix element a_{11} defines the direction cosine of the angle between X and X′ in figure 8.7, while a_{21} defines the direction cosine between Y and X′.

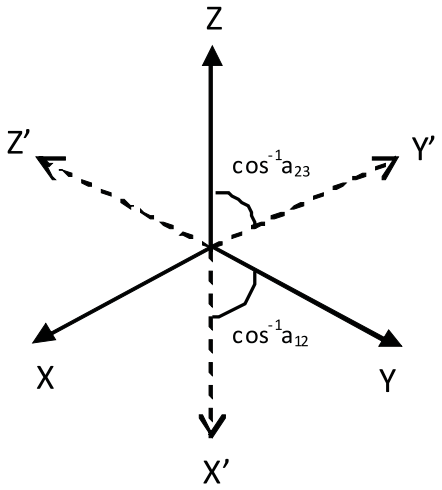

Figure 8.7.: Transformation of one orthogonal reference frame (unprimed) to another (primed), showing two direction cosines.

In figure 8.7 the primed and unprimed frames are related by a transformation matrix, given in equation 8.34 in matrix form.

$$\begin{bmatrix} X' \\ Y' \\ Z' \end{bmatrix} = \begin{bmatrix} a_{11} & a_{21} & a_{31} \\ a_{12} & a_{22} & a_{32} \\ a_{13} & a_{23} & a_{33} \end{bmatrix} \begin{bmatrix} X \\ Y \\ Z \end{bmatrix} \tag{8.34}$$

Equation 8.34 expressed in tensor notation is given in equation 8.35.

$$A_i' = \sum_j a_{ij}A_j = a_{ij}A_j \tag{8.35}$$

where generic $A = X, Y, Z$. This notation is know as the Einstein or index convention. The reverse transformation involves using the transpose of the direction cosines matrix. In any transformation of this type, two properties are of the tensor are invariant - the trace and the determinant. These two invariants are used throughout tensor application and interpretation.

Table 8.2.: Unit cell symmetry requirements for the seven crystal systems.

Crystal system	Symmetry requirements
triclinic	$a \neq b \neq c, \alpha \neq \beta \neq \gamma \neq 90°$
monoclinic	$a \neq b \neq c, \alpha = \gamma = 90° \neq \beta$
orthorhombic	$a \neq b \neq c, \alpha = \beta = \gamma = 90°$
rhombohedral	$a = b = c, \alpha = \beta = \gamma \neq 90°$
tetragonal	$a = b \neq c, \alpha = \beta = \gamma = 90°$
hexagonal	$a = b \neq c, \alpha = \beta = 90°, \gamma = 120°$
cubic	$a = b = c, \alpha = \beta = \gamma = 90°$

The formality of crystal symmetry effects on second-rank tensor properties is outlined in full in the well-known "bible" of Nye [13], and the so-called "understandable" interpretation of Lovett [14]. A brief introduction follows.

8.6.2. Crystal symmetry

The unit cell of a crystal is the regular repeating structural motif, and is represented by the axes of a three-dimensional parallelepiped. Convention selects the unit cell with edges, a, b, c, as small as possible, and angles α, β, γ, as close to 90° as possible, with corners necessarily located on crystallographic centres of inversion. Seven different parallelepiped possibilities exist, and are known as the seven crystal systems. These are outlined in table 8.2 and figure 8.8.

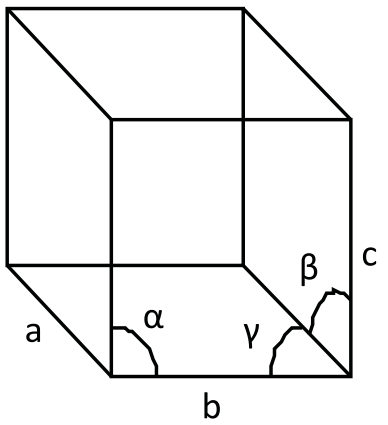

Figure 8.8.: Generalized parallelepiped describing a crystallographic unit cell. a, b, c are unit cell edge lengths, and α, β, γ are respective unit cell angles.

The density of a crystal, ρ, can be determined from equation 8.36.

$$\rho = \frac{MZ}{N_\circ V} \tag{8.36}$$

where M is the molecular mass of the unit cell asymmetric unit (smallest possible molecular configuration of the crystal species), Z is the number of asymmetric units per unit cell, $N_\circ$ is Avogadro's number, and V is the

unit cell volume in equation 8.37.

$$V = abc(1 - \cos^2\alpha - \cos^2\beta - \cos^2\gamma)^{\frac{1}{2}} \tag{8.37}$$

Single crystals have symmetry belonging to one of 32 crystal classes or crystallographic point groups. Combination of the crystallographic point groups with the crystalline transformation symmetry elements (glide plane/screw axis) permits 230 crystallographic space groups. Consideration of microscopic or site properties of atoms in a crystal requires only consideration of the 32 crystal classes, which are commonly referred to in Herman-Mauguin notation. When the point symmetry of a resonant site is lower than that of the host crystal, there can be more than one distinct orientation of that site in the unit cell. These are symmetry-related sites, and the restraints on the point symmetries needs to be outlined.

8.6.3. Neumann's Principle

Neumann's Principle provides limitations on the mathematical and symmetry descriptions of physical properties of crystals. This principle states: *the symmetry elements of any physical property of a crystal must include the symmetry elements of the crystal point group.* Any mathematical expression, spin-Hamiltonian, or tensor must also comply with this symmetry principle. This principle does not preclude the physical property containing symmetry elements that are not part of the point group, and may be purely co-incidental. A generalization of Neumann's Principle is known as Curie's Principle, that states: *a crystal under an external influence will exhibit only those symmetry elements that are common to the crystal without the influence and the influence without the crystal.*

8.6.4. Symmetry-related sites

All the tensor algebra required to relate symmetry-related sites is outlined by Weil *et al.* [15]. The tensors or parameter matrices describing symmetry-related sites, $\mathbf{Y}_n$, may be all generated from knowledge of one, $\mathbf{Y}$, by application of suitable similarity transformation in equation 8.38, where the rotation matrix, $\mathbf{R}_n$, conforms to the space group translational symmetries (point symmetry independent).

$$\mathbf{Y}_n = \mathbf{R}_n \cdot \mathbf{Y} \cdot \mathbf{R}_n^{-1} \tag{8.38}$$

The requirement that a physical property is described by a symmetric tensor means that any physical property *must* contain a center of inversion, such that the 32 crystallographic point groups may be reduced to the 11 Laue classes (centrosymmetric space groups). Consideration of Neumann's Principle allows calculation of the number of symmetry-related sites in a given Laue class, for a given site symmetry [16, 17]. The ambiguous case arises when two or more sites contribute to the same quadrupole doublet, and the Mössbauer measurement interacts in a way that observation yields macroscopic, or cell-averaged properties for symmetry-related sites [5]. This situation arises when the Laue class (point symmetry and center of inversion) of the site is lower than the Laue class of the host crystal. These conditions are outlined in table 8.3, giving the number of symmetry-related

sites for a known site and crystal point symmetry. In principle, in the absence of an internal magnetic field and magnetic hyperfine splitting, an external magnetic field can select individual transitions to resolve the low symmetry ambiguity by yielding distinct spectra for each site (almost certainly with the requirement of low temperatures) allowing a possible resolution of this problem [18]. Such a study would be very difficult, if not practically impossible, and to the author's knowledge has not been attempted successfully. This method as outlined [18], assumes an isotropic recoilless fraction, which is shown in later chapters to be invalid.

The ambiguous monoclinic case with two symmetry related sites can be visualized in terms of the general macroscopic intensity tensor as given in equation 8.39.

$$\left[\begin{array}{cc|c} P_{xx} & P_{xy} & 0 \\ P_{xy} & P_{yy} & 0 \\ \hline 0 & 0 & P_{zz} \end{array}\right] \tag{8.39}$$

where this block-diagonal (as indicated by the dividers) macroscopic tensor is diagonal with respect to the P_{zz} principal value, while the microscopic orientation and magnitudes of P_{xx} and P_{yy} principal values are not known with respect to the reference axis system, since the averaging procedure of the elements to zero loses the microscopic description.

8.7. MOSREF

The program MOSREF [16] was used to analyse Mössbauer single crystal data measured in this thesis. This program computes an "exact" ^{57}Fe Mössbauer spectrum by numerical methods from a Hamiltonian and parameter matrices in an arbitrary co-ordinate frame, as long as the site and crystal symmetry are known. The program can account for Goldanskii-Karyagan effects and magnetic hyperfine interactions. This program utilizes the efg intensity formalism of Zimmermann [5], and was originally tested to reproduce the sodium nitroprusside single crystal results of Grant *et al.* [19] which do not show the ambiguity problem. Application of this program can be two-fold. Firstly, calculation of thin crystal limit intensities from known efg and msd tensors, or secondly, refinement of best fit parameters of theory to experiment. Solution of microscopic quantities requires inclusion of the msd tensor. A small extension of this general program known as MOSPOW then allows calculation of powder intensities by averaging the computed single crystal intensities over a unit sphere. One published application of MOSREF to a new system was the study of a hedenbergite single crystal (not ambiguous), that was investigated using the milliprobe (point source) technique [20].

Tennant [16] has previously proposed that the simultaneous determination of efg and msd tensors can in principle provide a resolution of the monoclinic ambiguity problem. Such a resolution requires the msd tensor to be anisotropic and the total single crystal spectrum intensity (related to ratio of recoilless microscopic fraction projections) and the ratio of the quadrupole doublet lines (related to the ratio of the microscopic efg projections)

Table 8.3.: The number of symmetry-related sites for each crystal point group symmetry (horizontal) and special position site symmetry Laue class (vertical). This table is reproduced from (Rae 1969) and (Tennant 1992). Those in italics are situations where the site point group symmetry is lower than that of the Laue class but have only *one* site and are therefore not ambiguous in a Mössbauer experiment.

Crystal	Triclinic	Monoclinic	Orthorhombic	Tetragonal		Trigonal		Hexagonal		Cubic	
					422				622		
		2	222	4	4mm		32	6	6mm		432
	1	m	mm2	$\bar{4}$	$\bar{4}$2m	3	3m	$\bar{6}$	$\bar{6}$m2	23	$\bar{4}$3m
	$\bar{1}$	2/m	mmm	4/m	4/mmm	$\bar{3}$	$\bar{3}$m	6/m	6/mmm	m$\bar{3}$	m$\bar{3}$m
Site	(C_i)	(C_{2h})	(D_{2h})	(C_{4h})	(D_{4h})	(C_{3h})	(D_{3d})	(C_{6h})	(D_{6h})	(T_h)	(O_h)
$\bar{1}$	1	2	4	4	8	3	6	6	12	12	24
2/m		1	2	2	4		3	3	6	6	12
mmm			1		2				3	3	6
4/m				1	*1*						3
4/mmm					1						3
$\bar{3}$						1	*1*	*1*	*1*	4	4
$\bar{3}$m							1		*1*		4
6/m								1	*1*		
6/mmm									1		
m$\bar{3}$										1	*1*
m$\bar{3}$m											1

are anisotropic beyond experimental error. The difficulty with this procedure is measurement of the msd tensor, a process which has not been well established for Mössbauer spectroscopy. To obtain a microscopic tensor in the ambiguous case, MOSREF fits averaged microscopic or site parameters to agree with the macroscopic spectrum. Any refinement requires sufficient data to converge to a unique (determinate) solution, and therefore the measurements must contain at least one non-zero projection of all efg and msd principal directions. For refinement of theoretical parameters to agree with experimental data, initial trial parameters that are "sensible" are required.

One disclaimer needs to be noted. The way MOSREF is written means that a run will always result in an answer, which may or may not be correct. The iterative refinement procedure in MOSREF uses the well-known MINPACK subroutine (http://www.netlib.org/minpack/). Consider a multi-dimensional hyper-surface with many critical points as maxima, minima and saddle points. There exists presumably one global minimum and perhaps other local minima, with experimental data yielding best agreement (smallest root-mean-square-displacement or RMSD) with the global minimum. The trial parameters must therefore be close to the global minimum or convergence may occur to a local minimum that would represent a non-physical property. For this reason, considerable care must be taken to select good initial trial parameters, and monitor the effects of changes of trial parameters to the converged solution. Bad trial parameters can result in oscillations or divergences - all of which were observed by systematic trial-and-error estimates in studies in this thesis. The iterative procedure uses a non-linear least squares systematic Jacobian rotation matrix method that utilizes gradients to iteratively refine the parameters. Any parameters may be fixed in a given refinement providing more control of effects to individual or several tensor elements. Physical common-sense and interpretation of a resulting solution therefore needs to be applied to rationalize the "reality" (correctness) of a solution. For the studies in this thesis, accurate X-ray measurements were made, and several previous literature macroscopic parameter determinations existed to act as initial trial parameters. In general, any refinement should compare extrinsic parameters to converged solutions as a cross-check of reality. For determination of fundamental Mössbauer properties, the same fate is suffered as many analytical methods that weigh specificity and selectivity. X-ray is a general technique, whereas Mössbauer is selective in this work to ^{57}Fe, and when a technique becomes more selective, extrinsic parameters for comparison become fewer or more uncertain. In the refinements reported later, all studies involved systematically varying trial parameters, and where "sensible" parameters were used the fitting program converged to the same solution. When trial parameters were "non-sensible" i.e. dramatically different, and in most instances not physically sensible, divergence was observed. In all instances, convergence was to the same minimum, indicating a clean refinement hyper-surface.

The general procedure for efg and msd tensor refinement used in subsequent chapters is summarised in figure 8.9, and the relevant internal workings will be outlined in chapter 10. A full explanation of MOSREF and its procedures, including detailed examples of simulation and refinement cases are given elsewhere [16].

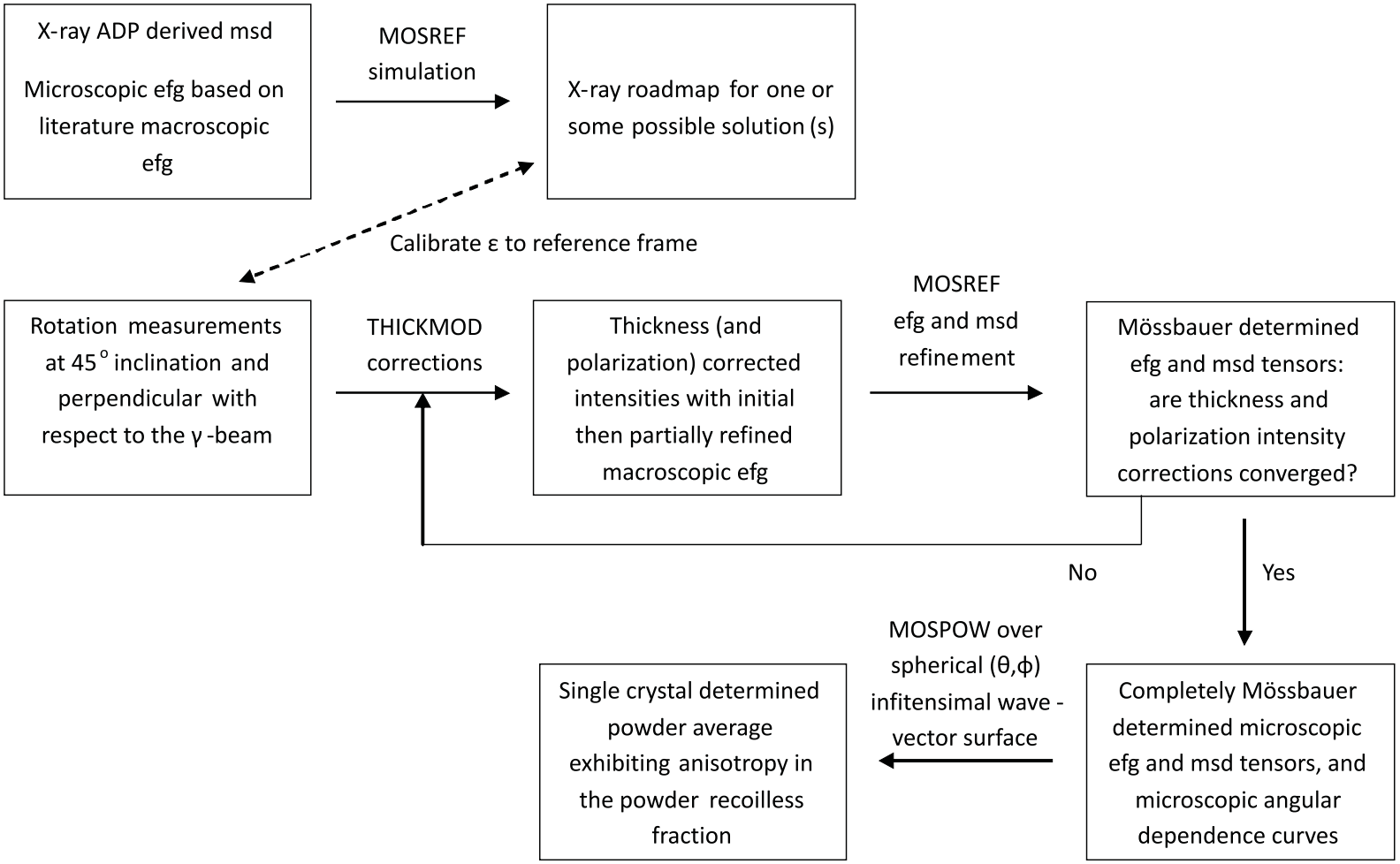

Figure 8.9.: Summary of the efg and msd tensor refinement procedure used in single crystal studies.

8.8. The intensity tensor

The efg has been traditionally represented by a Cartesian type tensor, although like some multivariate problems in integral calculus, the use of an alternative reference frame, e.g. spherical polar coordinates, can considerably simplify a very complex or otherwise analytically impossible task. The Mössbauer studies reported in this thesis use the intensity tensor formalism that was developed by Zimmermann [21,22], which considerably simplifies the internal workings of MOSREF and allows simple application of several invariant condition, to assist resolution of the ambiguity problem. This formalism will be briefly outlined.

The angular dependence of a quadrupole line intensity can be described by equation 8.40.

$$I = \sum_{pq} I_{pq} e_p e_q \tag{8.40}$$

where I_{pq} are the components of the intensity tensor, and $e_{p,q} = e_x, e_y, e_z$ are the direction cosines of the γ-beam relative to the coordinate reference frame, which in turn can be defined arbitrarily relative to the crystallographic axes. The direction cosines are usually expressed in spherical polar form, given in equation 8.41.

$$\begin{aligned} e_x &= \sin\theta\cos\phi \\ e_y &= \sin\theta\sin\phi \\ e_z &= \cos\theta \end{aligned} \tag{8.41}$$

The intensity tensor is a second rank symmetric tensor, whose elements are related to the traditional efg tensor by equation 8.42.

$$I_{pq} = \frac{1}{2}\delta_{pq} \pm \frac{eQ}{8|\Delta E_Q|} V_{pq} \tag{8.42}$$

where Q is the nuclear quadrupole moment, e is the elementary charge, ΔE_Q is the quadrupole splitting, V_{pq} is the traditional Cartesian efg tensor element, and the $\pm$ represents the sign of the quadrupole splitting, and δ_{pq} is the Dirac delta function, where $\delta_{pq} = 0$ or 1 for $p \neq q$ and $p = q$ respectively. When considering these components in the principal axis system, $e_{\hat{x}}, e_{\hat{y}}, e_{\hat{z}}$, the relation to efg elements, are given in equation 8.43.

$$\begin{aligned} I_{\hat{x}\hat{x}} &= \tfrac{1}{2} - sign(V_{\hat{z}\hat{z}})(1-\eta)/\left(8\sqrt{(1+\tfrac{1}{3}\eta^2)}\right) \\ I_{\hat{y}\hat{y}} &= \tfrac{1}{2} - sign(V_{\hat{z}\hat{z}})(1+\eta)/\left(8\sqrt{(1+\tfrac{1}{3}\eta^2)}\right) \\ I_{\hat{z}\hat{z}} &= \tfrac{1}{2} - sign(V_{\hat{z}\hat{z}})2/\left(8\sqrt{(1+\tfrac{1}{3}\eta^2)}\right) \end{aligned} \tag{8.43}$$

where η is the asymmetry parameter. Equation 8.43 imposes the tensor trace condition of the diagonal elements given in equation 8.44.

$$I_{xx} + I_{yy} + I_{zz} = \frac{3}{2} \tag{8.44}$$

It is useful to define a traceless intensity tensor, with elements P_{pq}, from equation 8.42, which is expressed in equation 8.45.

$$P_{pq} = I_{pq} - \frac{1}{2}\delta_{pq} \tag{8.45}$$

where δ_{pq} is the Dirac delta function.

This traceless intensity tensor is also proportion to the traditional efg tensor in three ways. Firstly, the principal axes system of the intensity tensor are equivalent to the principal axes system of the traditional efg tensor. Secondly, the asymmetry parameter takes exactly the same form in both conventions. Thirdly, the largest principal value of the intensity tensor has the same sign as the efg tensor. These conditions are of course only valid locally for the same (or symmetry-related) lattice sites. The intensity tensor by name inherently assumes that the Mössbauer measurement cannot determine which of several symmetry-related sites a γ-beam photon is emitted from, and therefore represents the superposition (macroscopic) efg intensity over all symmetry-related sites for an oriented single crystal. Generalizing to N sites, the macroscopic (superscript m) intensity tensor given in equation 8.45 takes the form given in equation 8.46.

$$P_{pq^m} = \frac{1}{N}\sum_{i=1}^{N} P_{pq} \tag{8.46}$$

Apart from the intensity trace invariance condition, a second invariance analogous to the square of the quadrupole splitting for the efg intensity tensor may also be defined, and is given in equation 8.47.

$$1 = 16P_{\hat{z}\hat{z}}^2(1 + \frac{1}{3}\eta^2) \tag{8.47}$$

When equation 8.47 is expanded for η in an arbitrary reference frame, which does not need to the principal axis system, the expression given in equation 8.48 can be obtained.

$$\frac{1}{16} = P_{zz}^2 + \frac{1}{3}(P_{xx} - P_{yy})^2 + \frac{4}{3}(P_{xy}^2 + P_{xz}^2 + P_{yz}^2) \tag{8.48}$$

The first analytical expression to describe the orientation and angular dependence of a single crystal quadrupole doublet was that of Zory [23], which is given in terms of relative line absorption probabilities, p_i, for $i = 1, 3$, and is given in equation 8.49 and 8.50 respectively. These expressions are formally only applicable to describe a macroscopic intensity tensor, or the case where there is one type of site, since Zory [23] neglected to consider the case of symmetry-related sites.

$$p_3(\theta, \phi) = 2R\left(4\left[\frac{3+\eta^2}{3}\right]^{\frac{1}{2}} + \left(3\cos^2\theta - 1 + \eta\sin^2\theta\cos 2\phi\right)\right) \tag{8.49}$$

$$p_1(\theta,\phi) = 2R\left(4\left[\frac{3+\eta^2}{3}\right]^{\frac{1}{2}} - \left(3\cos^2\theta - 1 + \eta\sin^2\theta\cos 2\phi\right)\right) \tag{8.50}$$

where $2R = \langle\frac{1}{2}||\hat{M}||\frac{3}{2}\rangle$ is the reduced magnetic dipole transition coefficient, and may be factored out when relative intensities are considered. When there is more than one symmetry-related site, intensities need to be summed over all n sites, as given in equation 8.51. This is the procedure that MOSREF internally (numerically) uses, where intensities are weighted by corresponding recoilless fractions, $f(\theta,\phi)$. Note that in application, MOSREF utilizes reduced ratios.

$$\frac{p_3}{p_1} = \frac{\sum_{i=1}^{n} p_3(\theta_i,\phi_i)f(\theta_i,\phi_i)}{\sum_{i=1}^{n} p_1(\theta_i,\phi_i)f(\theta_i,\phi_i)} \tag{8.51}$$

References

[1] G. Briet and E. P. Wigner. *Phys. Rev.*, 49:519, 1936.

[2] H. Spiering. *Mössbauer spectroscopy applied to inorganic chemistry*, volume 1, chapter Electric field gradient and quadrupole interaction, page 77. Plenum Press: New York, 1984.

[3] S. V. Kayagin. *Dokl. Akad. Nauk. SSSR*, 148:1102, 1963.

[4] J. M. Greneche and F. Varret. *J. Physique Lett.*, 43:L–223, 1982.

[5] R. Zimmermann. *Nucl. Instrum. Methods*, 128:537, 1975.

[6] H. D. Pfannes and U. Gonser. *Appl. Phys.*, 1:93, 1973.

[7] C. A. McCammon, V. Chaskar, and G. G. Richards. *Meas. Sci. Technol.*, 2:657, 1991.

[8] D. R. Lide, editor. *CRC Handbook of Chemistry and Physics*, volume 77. CRC Press, Cleveland, OH, 1996.

[9] E. W. Müller. *Mössbauer spectrum fitting program for universal theories.* Institut für anorganische Chemie und Analytische Chemie, Johannes Gutenberg Universtität, Mainz, 1980.

[10] R. N. Brand. *Program NORMOS.* Distributed by Wissenschaftliche Elektronik, GmbH, Germany, 1994.

[11] J. Stevens and V. E. Stevens. *Mössbauer Effect Data Index.* Plenum Publication Corporation: New York, 1976.

[12] F. W. Byron and R. W. Fuller. *Mathematics of Classical and Quantum Physics.* Dover Publications, 1992.

[13] J. F. Nye. *Physical Properties of Crystals.* Oxford University Press: London, 1957.

[14] D. R. Lovett. *Tensor Properties of Crystals.* IOP Publishing Ltd.: Bristol, 1989.

[15] J. A. Weil, T. Buch, and J. E. Clapp. *Adv. Magn. Reson.*, 6:183, 1973.

[16] W. C. Tennant. *J. Phys.: Condens. Matter*, 4:6993, 1992.

[17] D. A. Rae. *J Chem. Phys.*, 50:2672, 1969.

[18] T. C. Gibb. *J. Phys. C: Solid State Phys.*, 8:229, 1975.

[19] R. W. Grant, R. M. Housley, and U. Gonser. *Phys. Rev.*, 178:523, 1969.

[20] W. C. Tennant, C. A. McCammon, and R. Miletich. *Phys. Chem. Minerals*, 27:156, 2000.

[21] R. Zimmermann. *Nucl. Instrum. Methods*, 128:537, 1975.

[22] R. Zimmermann. *Advances in Mössbauer Spectroscopy*, pages 273–315. Elsevier, Amsterdam, 1983.

[23] P. Zory. *Phys. Rev. A*, 140:1401, 1965.

9. Isomorphism of Ferrous Chloride Tetrahydrate: X-ray and Mössbauer

This chapter describes the redetermination of the crystal structure of ferrous chloride tetrahydrate, $FeCl_2{\cdot}4H_2O$, as well as the serendipitous discovery and ensuing characterization of an unreported isomorph. This chapter is a reproduction of an article in submission:

James N Bull, Christopher M Fitchett, Robert G A R Maclagan, Ward T Robinson, and W Craighead Tennant, in submission to *Journal of Physics and Chemistry of Solids*

In the work described in this chapter, initial X-ray data collections were conducted under the guidance of Prof. Ward Robinson, and some subsequent short refinements and preparation of the crystallographic information file (cif) conducted by Dr. Chris Fitchett. Assoc. Prof. Robert Maclagan and Dr. Craig Tennant provided discussions on theoretical calculations and Mössbauer spectroscopy respectively.

Overview

An accurate redetermination of the structure of ferrous chloride tetrahydrate, $FeCl_2{\cdot}4H_2O$, is reported. In addition, a new and previously unreported isomorph, $Fe(H_2O)_6{\cdot}FeCl_4(H_2O)_2$, that is unstable in air is tentatively characterized by X-ray crystallography and confirmed by Mössbauer spectroscopy. The re-determined unit cell for $FeCl_2{\cdot}4H_2O$ has space group $P2_1/c$, with unit cell parameters: $a = 5.8765(3)$ Å, $b = 7.1100(3)$ Å, $c = 8.4892(5)$ Å, and $\beta = 111.096(1)^\circ$. The second isomorph, also space group $P2_1/c$, exhibits essentially the same cell dimensions, with one edge doubled, and contains two different Fe^{2+} species per unit cell, $[Fe(H_2O)_6]^{2+}$ and $[FeCl_4(H_2O)_2]^{2-}$. Upon atmospheric exposure, transformation to the $FeCl_2{\cdot}4H_2O$ isomorph occurs with decay following a sigmoidal profile in time. Density functional theory (DFT) calculations at the BP86, LC-BP86, B97D and wB97XD functionals and TZVP basis set are in accord with experimental observation, supporting an energetically favourable H_2O catalysed transformation.

9.1. Introduction

The need to re-determine the structure of $FeCl_2{\cdot}4H_2O$ (reported herein) arose from a requirement to have very precise atomic displacement parameters (ADPs) at 293 K that, via related Debye-Waller factors, could be utilized in single-crystal Mössbauer experiments and calculations. The Mössbauer single-crystal experiments in question involve attempted precise measurement of quadrupole intensity ratios leading to electric-field gradient (efg) elucidation, and total intensities leading to the elucidation of mean-squared displacements (msds) (related to Lamb-Mössbauer factors). The aim is to determine for monoclinic $FeCl_2{\cdot}4H_2O$ the microscopic efg and msd tensors - that is, the tensors for individual symmetry-related sites in the unit cell. Previous Mössbauer determinations have been restricted to measurement of a macroscopic efg tensor only, where two symmetry-related ferrous sites contribute to the same quadrupole doublet.

There have been three previously reported crystal structures of $FeCl_2{\cdot}4H_2O$ [1–3]. The first, by Penfold and Grigor [1], identified the monoclinic space group $P2_1/c$ with two discrete $FeCl_2{\cdot}4H_2O$ groups per unit cell. They identified the array of hydrogen bonding between a water of one octahedron and the chloride of a neighbouring octahedron to be the main group cohesion force. Meunier-Piret and Van Meerssche [2] reported a redetermination, relocating two oxygen atoms. El Saffar and Murty [4] reported NMR studies in an attempt to locate hydrogen atoms. Verbist *et al.* [3] then performed a neutron diffraction study again to locate hydrogen atom positions. They found that, by treating the two iron sites at (0,0,0) and $(0,\frac{1}{2},0)$ differently a better R factor was obtained. Structurally this involved the inversion of tilt angle on two *trans*- water molecules. Their final refinement was a weighted average of 80% identical and 20% inverted sites, yielding evidence of the lowering of space group symmetry from $P2_1/c$ to $P2_1$, which they attributed to result in a slightly better hydrogen bonding orientation.

A single crystal of suitable size was initially selected from a bottle labelled $FeCl_2{\cdot}4H_2O$, BDH Analar. The structure, also tentatively characterized herein, surprisingly turned out to be of a different isomorph, with molecular formula $Fe(H_2O)_6{\cdot}FeCl_4(H_2O)_2$, that is, with the same stoichiometry for the tetrahydrate compound, but with two quite distinct ferrous sites. Good single crystals of the tetrahydrate were found in the same bottle, and it was verified by Mössbauer spectroscopy that the bottle contained a mixture of the two crystalline forms. These experiments are reported also, together with the further unexpected result that the second form converted to the more familiar tetrahydrate over a period of 10-15 days following atmospheric exposure. Density functional theory calculations provide rationalization for the occurrence of such a transformation to occur.

9.2. Experimental

9.2.1. X-ray crystallography

Recrystallized ferrous chloride was prepared following the procedure of King [5], under concentrated hydrochloric acid conditions at 293 K with exposure to atmosphere. Crystals are pale blue-greenish in colour and hygroscopic.

Table 9.1.: Crystallographic experimental and refinement parameters for $FeCl_2{\cdot}4H_2O$. Errors reported in parentheses.

Crystallized from		HCl/H_2O
Empirical formula		$FeCl_2{\cdot}4H_2O$
Formula weight (g mol^{-1})		397.63
Crystal colour, habit		Platelet, pale green-blue
Crystal dimensions (mm)		0.11×0.35×0.40
Crystal temp. (K)		293(2)
Radiation, wavelength		Mo K_α (0.71073 Å)
Crystal system		Monoclinic
Space group		$P2_1/c$
Unit cell	a (Å)	5.8765(3)
parameters	b (Å)	7.1100(3)
	c (Å)	8.4892(5)
	α (°)	90.000
	β (°)	111.096(1)
	γ (°)	90.000
	V ($Å^3$)	330.92(2)
Density (g cm^{-3})		1.995
Z		2
μ (mm^{-1})		3.010
F(000)		200
θ_{min} / θ_{max}		3.72 / 29.99
Total reflections measured		5738
Symmetry-independent reflections		955 [R(int) = 0.0350]
Reflections used ($F_\circ > 4\sigma(F_\circ)$)		927
Parameters refined		34
R ($F_\circ > 4\sigma(F_\circ)$)		0.0151
wR ($F_\circ > 4\sigma(F_\circ)$)		0.0472
w *		$1/[\sigma^2(F_\circ) + 0.0452P^2 + 0.0P]$
S		1.421

* where $P = (F_\circ^2 + 2F_c^2) / 3$

Upon atmospheric exposure, crystallites readily oxidize over several days to a brown Fe^{3+}-containing slurry. Observation of suitable small crystallites for X-ray crystallography under a microscope revealed surface wetting over the period of minutes.

Crystallography was performed using a Bruker Apex II CCD area detector, with phi and omega scans, at room temperature, or 293(2) K. Relevant experimental and refinement parameters for $FeCl_2{\cdot}4H_2O$ are listed in table 9.1. The structures were solved by direct methods with the SHELXS program [6], and refinement on F^2 by least-squares procedures with the SHELXL-97 program [6]. Multi-scan absorption corrections were included for all atoms. Non-hydrogen atoms were refined with anisotropic displacement parameters, and hydrogen atoms with isotropic displacement parameters. Once refined, a final Fourier synthesis showed no evidence of significant residual electron density for either isomorph crystal structure.

9.2.2. Mössbauer spectroscopy

Mössbauer transmission spectra were collected on a PC-based ORTEC system with ELSCINT drive electronics operated in constant acceleration mode. A ^{57}Co/Rh source of nominal strength 5 mCi was used as the gamma source and iron foil as the velocity and isomer shift calibrant.

To study the disappearance of the $Fe(H_2O)_6{\cdot}FeCl_4(H_2O)_2$ isomorph, a thin powder was prepared that, following brief atmospheric exposure, was secured in a perspex capsule that was anticipated to be air tight owing to a good seal. A series of data sets were collected over 24 hour periods for 12 days at 293 K, with each data set containing approximately 1×10^5 off-resonance (background) counts. Each spectrum in the time series was fitted with three quadrupole doublets of Lorentzian line shape, with an additional single broad Lorentzian function included for the small Fe^{3+} signal. Isomer shifts, quadrupole splitting and line widths were all optimized in the fits. All spectra were fitted using the program MOSFUN [7], with all spectra attaining $\chi^2 < 1.28$ "goodness of fit" criteria. Fits showed that three quadrupole doublets yield significantly better χ^2 (improvement of $\Delta\chi^2 > 0.4$) than two quadrupole doublets. Characterization of the recrystallised sample collected approximately 5×10^5 off-resonance counts. Observation of the sealed sample after time-series data collection showed no apparent slurry formation, nor brown colouration. That is, the sample appeared identical at the beginning and the end of all data collection. Further, all Mössbauer fits reveal no oxidation to ferric over the period of analysis.

9.3. Results and Discussion

9.3.1. X-Ray crystallography

The structure of $FeCl_2{\cdot}4H_2O$, shown in figure 9.1, consists of discrete slightly distorted *trans*-octahedra, where the iron sites sit on centres of inversion and are symmetry-related with respect to the *b*-unique axis. The distortion feature is the presence of two slightly different Fe-O bond lengths, listed in table 9.2, where one Fe-O bond is 0.037 Å longer than the other. This is significantly different to the 0.50 Å difference determined by Penfold and Grigor [1], which was subsequently relocated [2]. The density functional theory calculations, to be outlined later, reveal both types of water molecules to be relatively weakly bound, with no appreciable difference between the two types. The 2+ charge on the iron atom polarizes the water molecules, promoting hydrogen bonding to neighbouring chlorine atoms. O-H...Cl^- hydrogen bonds act as the main cohesion force holding the octahedra together. Each water molecule forms one bond with the central iron atom, with each hydrogen atom involved in one hydrogen bond, and each chloride is involved in four hydrogen bonds. One octahedron is surrounded by ten others, where no two hydrogen bonds between adjacent octahedra are exactly equivalent. Following the hydrogen bonding schematics of Verbist *et al.* [3] the water molecules and hydrogen bond geometrical parameters are shown in figure 9.2, with values tabulated in table 9.3. The present relocation of the hydrogen atoms, giving a much better *R*-factor than the neutron diffraction study of Verbist *et al.* [3], reveals two water molecules per octahedra have a subtle tilt angle distortion of 34.4°, resulting in a better

Table 9.2.: Selected bond lengths and geometries for $FeCl_2{\cdot}4H_2O$ and $Fe(H_2O)_6{\cdot}FeCl_4(H_2O)_2$. Isolated gas-phase optimized BP86/TZVP bond lengths reported in parentheses. All bond lengths in Å, and bond angles in degrees.

Species	Bond	Length	Bonds	Angle
$FeCl_2{\cdot}4H_2O$	Fe1-O11	2.077(1) (2.162)	O11-Fe1-O12	90.26(5)
	Fe1-O12	2.114(2) (2.195)	O11-Fe1-Cl11	92.11(3)
	Fe1-Cl11	2.5266(3) (2.373)	O12-Fe1-Cl11	90.05(3)
$(FeCl_4(H_2O)_2)^{2-}$	Fe11-O11	2.12(3) (2.108)	Cl11-Fe1-Cl12	85.6(2)
	Fe11-Cl11	2.518(5) (2.451)	Cl11-Fe1-O11	88.9(6)
	Fe11-Cl12	2.525(6) (2.585)	Cl12-Fe1-O11	88.4(6)
$(Fe(H_2O)_6)^{2+}$	Fe21-O21	2.113(16) (2.141)	O21-Fe2-O22	88.9(2)
	Fe21-O22	2.050(12) (2.141)	O21-Fe2-O25	94.8(2)
	Fe21-O23	2.15(3) (2.151)	O24-Fe2-O25	93.8(2)

hydrogen bonding geometry and giving two octahedra in the unit cell. The un-tilted water molecules are essentially co-planar with the Cl-Fe-Cl plane.

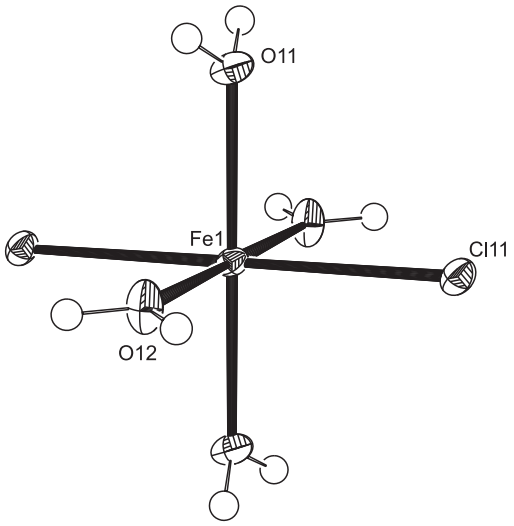

Figure 9.1.: Crystal structure of $FeCl_2.4H_2O$, showing the approximate 34° tilt angle on the O11 water molecule, and the O12 water molecule coplanar with the Fe-Cl bonds.

Refinement in the $P2_1$ space group, as indicated by the neutron diffraction study, with two subtly different iron sites from application of hydrogen atom dihedral angle restraints yields an crystallographic R factor increase of 0.003. As would be expected, the ADP principal values for two iron sites in the $P2_1$ refinement are essentially identical, and also essentially identical to the $P2_1/c$ refinement, and these differences, if real, would be indeterminate with Mössbauer spectroscopy. From the refinements here, it is concluded that there is no real evidence for $P2_1$ space group symmetry, although X-ray diffraction is not ideal for hydrogen atom location owing to weak diffraction signal from minimal electron density involved in bonds with hydrogen atoms. Neutron diffraction is well-suited for determination of hydrogen atom positions, however the reported structure refinement R factors are three times greater than those achieved here, and the determined hydrogen-bonding

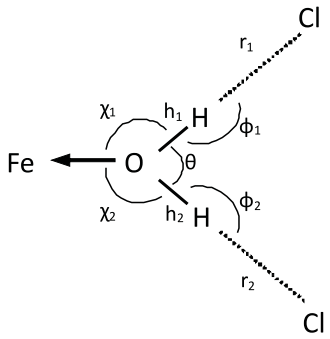

Figure 9.2.: Assignment of geometrical parameters for the hydrogen bonding arrangement in $FeCl_2{\cdot}4H_2O$.

Table 9.3.: Hydrogen bonding geometric parameters for $FeCl_2{\cdot}4H_2O$. Bond length and angles assignments shown in previous figure. Presentation follows the neutron diffractions study of Verbist *et al.* for comparison. All bond lengths in Å, and bond angles in degrees.

Fe-O	h_1	h_2	r_1	h_2	θ	ϕ_1	ϕ_2	χ_1	χ_2
Fe1-O11	0.767	0.823	2.402	2.358	111.1	163.6	159.2	120.1	118.7
Fe1-O12	0.803	0.792	2.423	2.424	97.2	178.2	177.9	132.0	130.6

parameters are still in qualitative agreement with those reported in the neutron diffraction study.

It should be noted that the previously reported $FeCl_2{\cdot}4H_2O$ crystal structures have not followed the convention of selecting the smallest unit cell edges and angles closest to orthogonal, as outlined in figure 3 and table 4. If this unit cell is reselected with an orthorhombic transformation to achieve this convention, then $c' = 8.4108(5)$ Å and $\beta = 109.441(1)°$. These may be determined with basic trigonometry outlined in equations 9.1 and 9.2.

$$(c')^2 = a^2 + c^2 - 2ac \cdot \cos(180 - \beta) \tag{9.1}$$

$$\beta' = 180 - \cos^{-1}\left(\frac{a^2 + (c')^2 - c^2}{2a(c')}\right) \tag{9.2}$$

Appropriate orthogonalized anisotropic displacement U_{ij} thermal parameters for the iron site at 293 ± 2 K, which are relevant to microscopic Mössbauer studies are reported in table 9.5.

As outlined in the introduction, the first X-ray data collection at 293(2) K was on a non-recrystallized BDH

Table 9.4.: Unit cell parameters for $FeCl_2{\cdot}4H_2O$.

Parameter	Ref [1]	Ref [2]	Ref [3]	This work
a / Å	5.91(3)	5.885(3)	5.885(3)	5.8765(3)
b / Å	7.17(3)	7.174(3)	7.180(6)	7.1100(3)
c / Å	8.44(4)	8.505(4)	8.514(4)	8.4892(5)
β / °	112.17(33)	111.11(5)	111.09(2)	111.096(1)

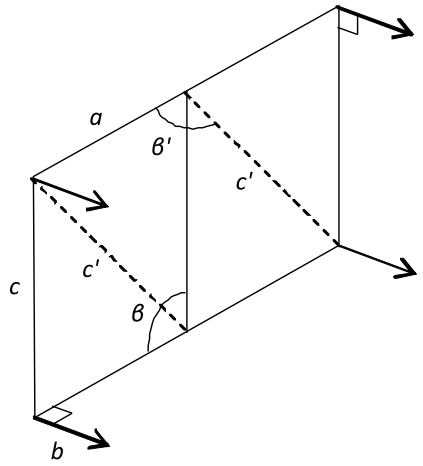

Figure 9.3.: $FeCl_2{\cdot}4H_2O$ unit cell selection, the current selection as unprimed/solid, and the alternative orthorhombic transformation as primed/dashed. The closeness of these parameters means that $c/a/c'$ almost form an isosceles triangle.

Table 9.5.: X-ray determined orthogonalized anisotropic U_{ij} for iron in $FeCl_2{\cdot}4H_2O$, in units $Å^2$ at 293 ± 2 K. Errors reported at one standard deviation.

Atom	U_{11}	U_{22}	U_{33}	U_{12}	U_{13}	U_{23}
Fe1	0.00906	0.01449	0.00937	0.001224	0.00052	0.00030
error	0.00019	0.00019	0.00019	0.000060	0.00013	0.00007

Analar crystallite. Refinement on the first half of the data collection (R=0.0516, $\theta_{min}/\theta_{max}$ = 3.86/25.46 with 435 symmetry independent reflections with $F_\circ > 4\sigma(F_\circ)$) revealed the structure to unexpectedly be an isomorph, $Fe(H_2O)_6{\cdot}FeCl_4(H_2O)_2$. Then, refinement on the complete data set yields a slightly better fit to the $FeCl_2{\cdot}4H_2O$ refinement reported above, and as will be outlined through Mössbauer spectroscopy measurements, it is not unreasonable that during the course of the room temperature data collection an isomorph transformation occurred. The crystallite did have a thin coating of a crystallographic hydrocarbon oil that may provide some atmospheric isolation after initial exposure. This tentative $Fe(H_2O)_6{\cdot}FeCl_4(H_2O)_2$ isomorph structure contains two discretely different octahedra in the asymmetric unit, namely $[Fe(H_2O)_6]^{2+}$ and $[FeCl_4(H_2O)_2]^{2-}$ as shown in figure 9.4. Combined, these yield the same stoichiometry as two $FeCl_2{\cdot}4H_2O$ octahedra. The tentative unit cell (a=11.749(4) Å, b=7.097(2) Å, c=8.487(3 Å), β=111.148(6)°), also of space group $P2_1/c$, shows very close parameters to that refined for $FeCl_2{\cdot}4H_2O$ except for the doubling of one unit cell edge. Although this refinement is based on a small number of reflections, bonding parameters for non-hydrogen atoms are sufficiently well determined for use in density functional theory calculations. These parameters are reported in table 9.2, and comparison of both $[Fe(H_2O)_6]^{2+}$ and $[FeCl_4(H_2O)_2]^{2-}$ octahedra with $FeCl_2{\cdot}4H_2O$ revealing only small to moderately small bonding deviations. Similar to $FeCl_2{\cdot}4H_2O$, these discrete octahedra show that each water and chloride is co-ordinated to one and only one iron atom. Although hydrogen atom positions are not well defined they show directionality towards nearest potential hydrogen-bonding neighbours. The refinement shows, and is also intuitive based on octahedral formulae and oxygen atom positions, that each chloride may hydrogen

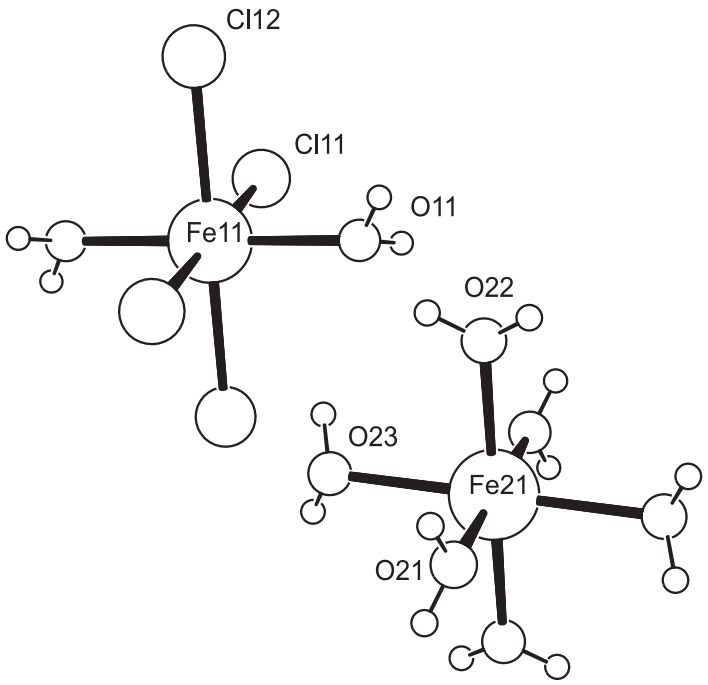

Figure 9.4.: Tentative crystal structure of $Fe(H_2O)_6{\cdot}FeCl_4(H_2O)_2$, supported by Mössbauer spectroscopy, showing two discretely different iron octahedra, $[FeCl_4(H_2O)_2]^{2-}$ (left) and $[Fe(H_2O)_6]^{2+}$ (right).

bond with two adjacent water molecules. The *trans-* water molecules in the $[FeCl_4(H_2O)_2]^{2-}$ octahedra show no chloride hydrogen bonding. The $[Fe(H_2O)_6]^{2+}$ octahedron reveals four water molecules in a square planar configuration that hydrogen bond with one chloride, while the two axial or *trans-* waters are directed in an orientation that bisects an adjacent Cl-Fe-Cl (*cis−*) angle, and therefore participate in two hydrogen bonds. Overall, this $Fe(H_2O)_6{\cdot}FeCl_4(H_2O)_2$ isomorph would appear to show considerably decreased hydrogen-bonding compared to the usual $FeCl_2{\cdot}4H_2O$ isomorph.

Comparison of the two isomorph structures in figures 9.1 (with translational symmetry operation) and 9.4 indicates that the transformation from one isomorph to the other would simply involve the exchange of both O11(+hydrogens) with Cl11′, where prime denotes action of translational symmetry elements to the next octahedron in figure 9.1. The DFT calculations reported later reveal, via calculated bond dissociation energies, that this ligand-swapping process, $\Delta H \approx 320$ kcal mol^{-1}, is an exothermic or favourable process. In this calculation the X-ray determined geometry is assumed and differences in hydrogen-bonding interactions are neglected.

This newly reported $Fe(H_2O)_6{\cdot}FeCl_4(H_2O)_2$ isomorph is believed not to be an artefact of a poor X-ray structural refinement, since its existence can be confirmed by Mössbauer spectroscopy. Mössbauer spectroscopy which primarily identifies first coordination shell influences on nuclear energy level quantization to ^{57}Fe only, is ideally suited to fingerprinting such species. A more comprehensive X-ray data set for the $Fe(H_2O)_6{\cdot}FeCl_4(H_2O)_2$ isomorph could not be obtained due to its rapid degradation, and inability to find or synthesise a new crystallite.

9.3.2. Mössbauer spectroscopy

Powder Mössbauer spectroscopy revealed that the $Fe(H_2O)_6{\cdot}FeCl_4(H_2O)_2$ isomorph gradually diminished in abundance over a period of some days, until eventually only a single quadrupole doublet corresponding to $FeCl_2{\cdot}4H_2O$ remained. For $FeCl_2{\cdot}4H_2O$ ($\chi^2 = 1.10$), at 293(2) K the isomer shift, δ, is determined to be 1.232(1) mm sec^{-1} and quadrupole splitting, $\Delta E_Q = 2.994(1)$ mm sec^{-1}. These are in excellent agreement with previously established values [8]. The $[FeCl_4(H_2O)_2]^{2-}$ has $\delta = 1.186(6)$ and $\Delta E_Q = 3.03(1)$ mm sec^{-1}, while $[Fe(H_2O)_6]^{2+}$ has these parameters slightly smaller at $\delta = 1.058(2)$ mm sec^{-1} and $\Delta E_Q = 2.329(3)$ mm sec^{-1}. These were unambiguously assigned by comparison with a series of ferrous chloride and aquo complexes [9].

The change in relative quadrupole doublet areas for each species over the thirteen-day decay period are shown in figure 9.5, normalized with respect to the day-one data set. Representative spectra of two such cases are shown in figure 6, and show the decay of one quadrupole doublet as the other increases for the same sample. It has been assumed that for a given Mössbauer-active species at constant temperature, the spectral peak intensity is directly proportional to abundance of resonant species giving rise to the signal. The $Fe(H_2O)_6{\cdot}FeCl_4(H_2O)_2$ isomorph follows a sigmoidal decay profile with time, and after the thirteen-day period from initial atmospheric exposure this signal had essentially disappeared. The relative intensity for the known $FeCl_2{\cdot}4H_2O$ isomorph appears to show a slow increase in intensity with time. Determining the signal intensity difference for a given day with respect to the normalization and subtracting twice this from the $FeCl_2{\cdot}4H_2O$ doublet intensity yields a linear trend in time, which remains at unit normalized intensity well within experimental error (centre line in figure 5). This provides strong evidence that the $Fe(H_2O)_6{\cdot}FeCl_4(H_2O)_2$ isomorph is in fact transforming into the well-known $FeCl_2{\cdot}4H_2O$ isomorph. The small, $\approx 0.04\%$ on-resonance signal arising from oxidized ferric species remained constant over this period, and was therefore not produced during the data collections. One minor caveat should be acknowledged. For a given spectrum, allowing the single quadrupole doublet area (widths) of the recrystallized $FeCl_2{\cdot}4H_2O$ to be independently optimized yielded a difference of $\approx 6.0\%$. This almost certainly arises from preferred crystallite orientations (texture effects) in packing, since $FeCl_2{\cdot}4H_2O$ crystallizes in flat plates, and is equally present in all temporal decay spectra, therefore not affecting the relative calculated intensities.

It is hard to believe that a purely solid state transformation is occurring. Rather, upon atmospheric exposure to adsorbed and/or absorbed moisture, the preferential solvation of the $Fe(H_2O)_6{\cdot}FeCl_4(H_2O)_2$ isomorph and then recrystallization as the $FeCl_2{\cdot}4H_2O$ isomorph could be a feasible transformation route. Another possible route could involve efflorescence where, upon exposure to the air or atmosphere, crystallites lose waters of crystallization, leaving a partially anhydrous form. For both processes, the adsorbed or released water may condense on the crystallite surface resulting in solvation and re-crystallization of the $Fe(H_2O)_6{\cdot}FeCl_4(H_2O)_2$ isomorph as the $FeCl_2{\cdot}4H_2O$ isomorph in a catalytic process. Both processes are catalytic since the isomorphs have the same stoichiometry, and the adsorbed water apparently causes interconversion of the entire bulk sample. Similar polymorphic processes have been observed in NH_4NO_2 particles with infra-red spectroscopy under varying humidity conditions [10]. The original cause or process of formation of the $Fe(H_2O)_6{\cdot}FeCl_4(H_2O)_2$

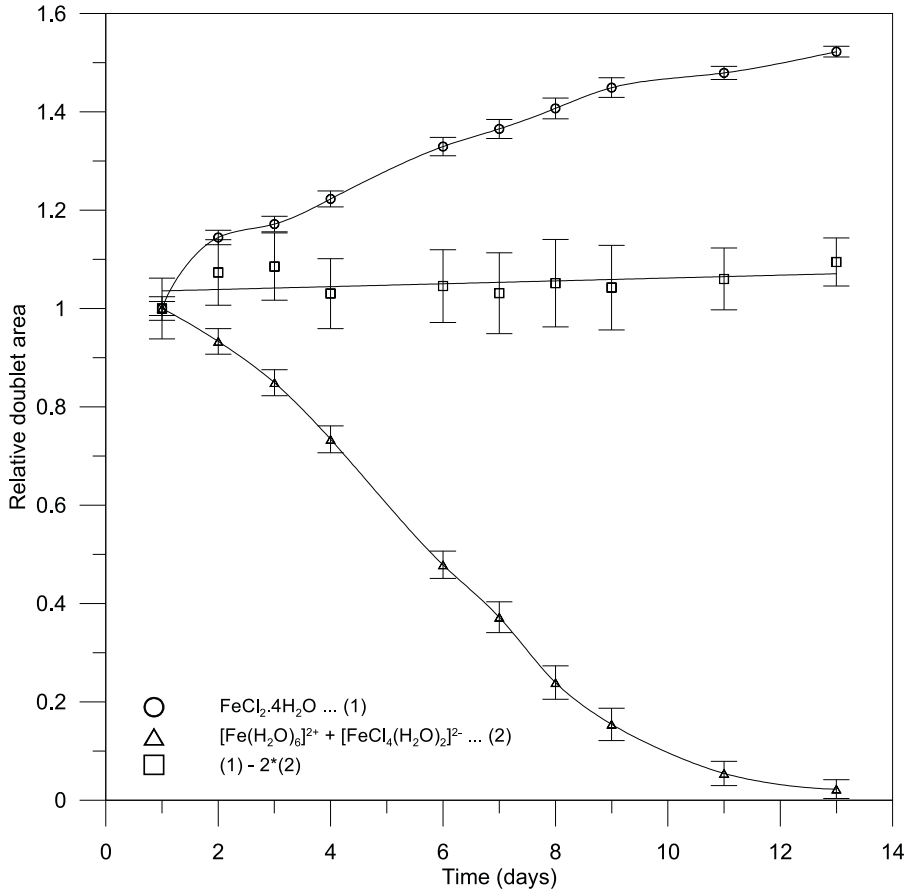

Figure 9.5.: Decay curve for sequential time-series Mössbauer spectra of $Fe(H_2O)_6{\cdot}FeCl_4(H_2O)_2$ in $FeCl_2{\cdot}\ 4H_2O$. Quadrupole doublet areas are normalized to $Fe(H_2O)_6{\cdot}FeCl_4(H_2O)_2$ intensity after day 1. Errors reported at 95% confidence intervals.

isomorph remains unknown. In either mechanism, the hygroscopic nature of the crystallites would ensure catalytic adsorbed water is present.

9.3.3. Density functional theory calculations

Although not formally organometallic with strong covalent bonding, $FeCl_2{\cdot}4H_2O$ is an 18 electron (S=2) complex and thus obeys the 18 electron octet rule. $[Fe(H_2O)_6]^{2+}$ and $[FeCl_4(H_2O)_2]^{2-}$ would be 16 electron and 20 electron complexes respectively, and hence anticipated to be less stable. In accord with Mössbauer spectra, each species contains Fe^{2+} in the high-spin $^5T_2$ configuration, with DFT calculations revealing the bound chlorides to have charges of approximately +0.6 or greater. The DFT $FeCl_2{\cdot}4H_2O$ chloride Mulliken charge is in excellent agreement with the CASSCF(6,11)/TZVP level of theory, where the active space includes 4s, 3d and 4d orbitals. To further investigate the stabilities of each isomorph, the relative energies were calculated using density functional theory at the BP86/TZVP, LC-BP86/TZVP, B97D/TZVP and wB97XD/TZVP levels of theory with the Gaussian computational package [11]. The first level of theory has shown good performance for geometries of a range of iron complexes including the dihalides [12, 13], and also hydrogen-bonding and

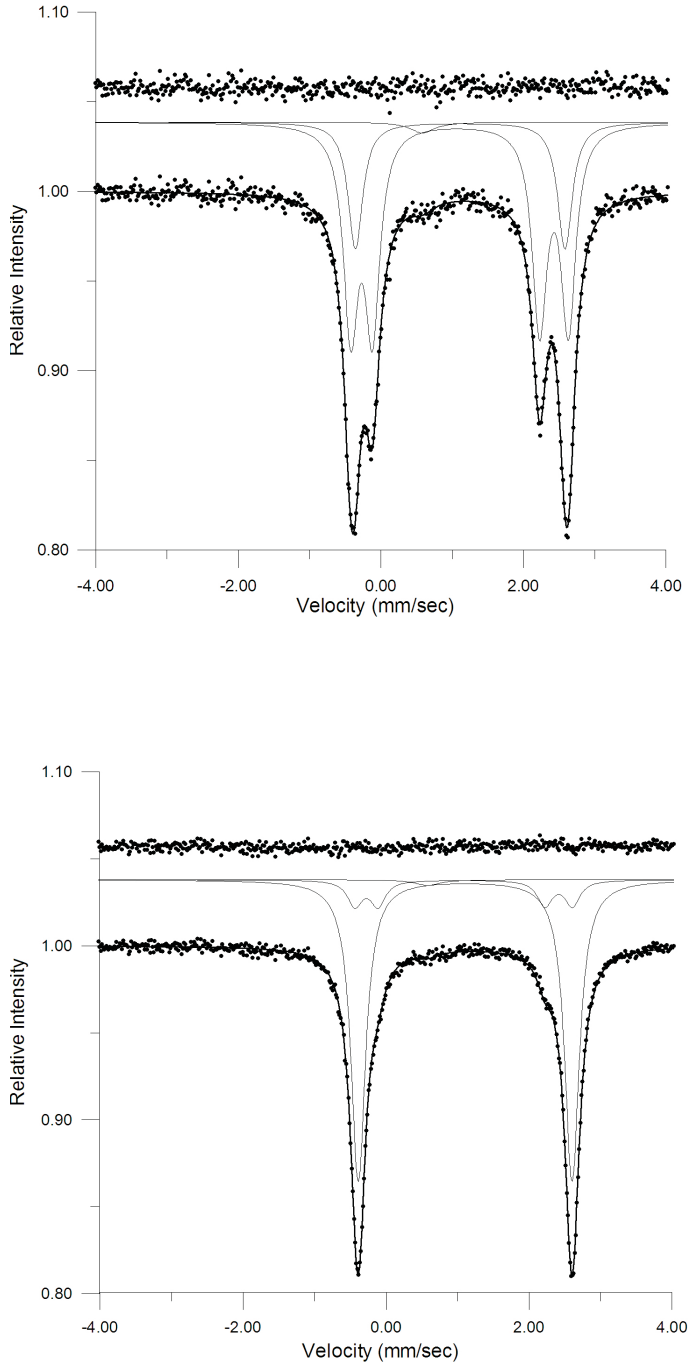

Figure 9.6.: Mössbauer spectra of $FeCl_2 \cdot 4H_2O$ (single quadrupole doublet) and $Fe(H_2O)_6 \cdot FeCl_4(H_2O)_2$ (two quadrupole doublets), showing the latter isomorph soon after atmosphere exposure (upper) and on day 11 after exposure (lower).

electrostatic interactions [14, 15]. It has also been applied to the determination of hydration enthalpies for a series of fourth row transition metal hexaaquo complexes, including $[Fe(H_2O)_6]^{2+}$, which show good agreement to experimental data [16]. The latter three functionals contain more recent re-parameterizations and include long-range dispersion corrections. Although DFT methods can treat hydrogen-bonding reasonably, they generally perform poorly for instantaneous long-range (London) dispersion interactions. As a consequence, development

of long-range correlation (LC-) schemes provides correction to GGA functionals [17]. The more recent B97D and the re-parameterized and re-optimized wB97XD functionals show good agreement (typically slightly underestimating with mean deviations up to 10 kcal mol^{-1}) with long-range CCSD(T)/CBS calculations and experimental data [18, 19]. Such calculations serve not to provide absolute quantities, but rather to identify qualitative reasons for isomorph energy differences.

Isolated gas-phase optimizations at the BP86/TZVP level of theory show different geometries to those (solid state) determined by X-ray, as outlined in table 9.2. The previously reported X-ray diffraction Fe-O bond length for $[Fe(H_2O)_6]^{2+}$ is 2.12 ± 0.02 Å [20], which is in excellent agreement with the optimized values at 2.141 Å. Allowing this complex to optimize from T_H to slightly lower energy D_{2H} point symmetry facilitates a Jahn-Teller stretching of two *trans-* waters. This effect has also been characterized elsewhere [21]. The optimized D_{2H} structure for $[FeCl_4(H_2O)_2]^{2-}$ shows the waters to be coplanar with the meridional Cl-Fe-Cl plane, resulting in two slightly different Fe-Cl bond lengths, whereas the crystal structure shows the water plane to bisect the facial Cl-Fe-Cl angle, with a slight tilt of the hydrogen atoms towards the chlorides. The $FeCl_2{\cdot}4H_2O$ optimization of D_{4H} point symmetry shows each water to be coplanar with the meridional Cl-Fe-Cl plane, in contrast to the crystal structure, with two slightly different Fe-O bond lengths. B97D/TZVP optimizations yield essentially no change to BP86/TZVP geometries. These calculations allow comparisons of unit cell energy differences, as outlined in table 9.6. For gas-phase optimized geometries at the BP86/TZVP level of theory, these data reveal reasonable variance (up to 30%) between DFT functionals, although agree that the $FeCl_2{\cdot}4H_2O$ isomorph is considerably more stable. Isomorph energy difference calculations at the X-ray determined geometries of respective species yields small stability energy variance (≈ 3%) between DFT functionals which are all systematically larger than respective geometrical optimized calculations, indicating the $FeCl_2{\cdot}4H_2O$ isomorph to be more stable at respective X-ray crystalline geometries.

Any isolated energy calculations omit the presence of the surrounding lattice perturbing both the energy and geometry. The $FeCl_2{\cdot}4H_2O$ crystal structure is well-known to have an intricate hydrogen-bonding environment that needs to be considered in relative isomorph solid-state energies. In addition, the $Fe(H_2O)_6{\cdot}FeCl_4(H_2O)_2$ isomorph would show electrostatic (ionic) interactions between octahedra that need to be accounted for. These effects can be approximated by the inclusion of several surrounding cell atoms, as a second co-ordination shell scaffold. This cell scaffold is selected by atoms included in a spherical volume surface centred on the iron site for the $FeCl_2{\cdot}4H_2O$ structure, and contains eight chloride anions, and eight water molecules. Two octahedra with scaffolds would then require 16 chloride anions and 16 water molecules. The $[Fe(H_2O)_6]^{2+}$ and $[FeCl_4(H_2O)_2]^{2-}$ scaffolds require different surrounding species, yet combined, are consistent with stoichiometry for the doubled $FeCl_2{\cdot}4H_2O$ isomorph scaffold. For $[Fe(H_2O)_6]^{2+}$, this scaffold contains ten chloride anions and six water molecules, giving a total charge of -8, consistent with the $FeCl_2{\cdot}4H_2O$ scaffold. Similarly, the $[FeCl_4(H_2O)_2]^{2-}$ scaffold contains six chloride anions and ten water molecules with an overall charge of -8. These scaffolds naturally select the adjacent species closest to the central complex, and would incorporate the complex counter-charge Coulombic interactions. Each scaffold has a spin multiplicity of 2S+1=1, and retains the spin state of the

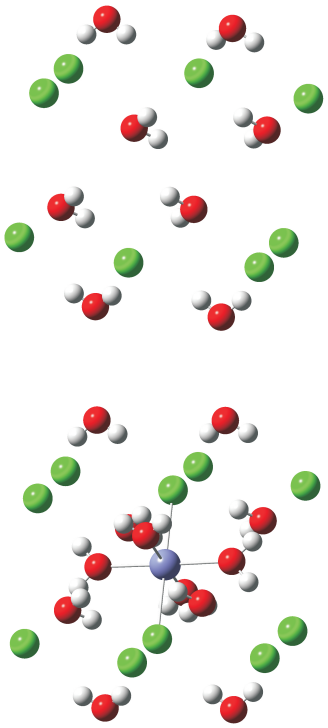

Figure 9.7.: $FeCl_2{\cdot}4H_2O$ scaffold (upper) and $FeCl_2{\cdot}4H_2O$ complex inserted into scaffold (lower), used in the density functional theory calculations to recover the major extent of inter-octahedron interactions.

inner complex. Representations of the $FeCl_2{\cdot}4H_2O$ scaffold and scaffold containing an $FeCl_2{\cdot}4H_2O$ octahedron are shown in figure 9.7. Geometrical optimizations on the $FeCl_2{\cdot}4H_2O$ complex and scaffold, where the scaffold water molecules are removed and chlorides are replaced by point-charges of either -1 or the Mulliken population charge on a bound chloride in the X-ray geometry isolated complex, do not show considerable geometrical change from the X-ray geometry. This indicates the employed level of theory gives good agreement with X-ray geometries, recovering the major extent of octahedra cohesion interactions. In addition, owing to the tentative hydrogen atom locations in the $Fe(H_2O)_6{\cdot}FeCl_4(H_2O)_2$ isomorph structure, several scaffold calculations where hydrogen positions (bond angles of $\approx$ 5-10°) were systematically varied, showed final isomorph calculated energy differences of several kcal mol^{-1}. Such small differences would be expected since these systematic variations change separations by only a fraction of the relatively long-range hydrogen-bond lengths. These scaffold energy differences are also reported in table 9.6.

The scaffold isomorph energy differences indicate that the $Fe(H_2O)_6{\cdot}FeCl_4(H_2O)_2$ isomorph becomes a further $\approx$ 50% less stable than the $FeCl_2{\cdot}4H_2O$ isomorph on inclusion of scaffold interactions, with all the DFT functionals employed in good agreement. This difference of $\approx$ 740 kcal mol^{-1} for the best case is surprisingly large, considering the lattice enthalpy for $FeCl_2(s) \rightarrow Fe^{2+}(g) + 2Cl^-(g)$ is $\approx$ 600 kcal mol^{-1} [22]. That the energy difference between X-ray structure with the scaffold is $\approx$ 250 kcal mol^{-1} lower energy than without the

Table 9.6.: Gas-phase optimized and X-ray diffraction relative isomorph energy differences in kcal mol^{-1}, with all calculations using the TZVP basis set. Energy (**E**) difference calculated as $2\mathbf{E}(FeCl_2{\cdot}4H_2O))$ $(\mathbf{E}([Fe(H_2O)_6]^{2+}) + \mathbf{E}([FeCl_4(H_2O)_2]^{2-})$, with a negative difference indicating the $FeCl_2{\cdot}4H_2O$ isomorph is more stable.

Level of theory	Gas-phase optimized	X-ray structure	X-ray + scaffold*
BP86	-454	-492	-747
LC-BP86	-320	-480	-737
B97D	-328	-483	-719
wB97XD	-418	-476	-726

*The scaffold for each species is described in the text.

scaffold indicates a much better hydrogen bonding environment in the $FeCl_2{\cdot}4H_2O$ isomorph. It is concluded that these data reveal that hydrogen bonding plays a very dominant role in cohesion of octahedra. It is therefore energetically (thermodynamically) favourable for the observed transformation to occur. The attractive ionic (Coulombic) effect of $[Fe(H_2O)_6]^{2+}$ and $[FeCl_4(H_2O)_2]^{2-}$ appears not to outweigh the poorer hydrogen bonding environment and energetically less stable species.

It is well-known that lattice energy relates to solubility, with two opposing effects (ignoring entropic effects): the endothermic lattice energy must be overcome to break the crystalline lattice apart; but this is offset by the exothermic hydration by coordination of water molecules. To explore the difference in stability of the two lattices and the potential for water catalyzed transformation, calculations on the non-geometrically optimized (diabatic) bond dissociation energies (BDE) for the complexes assuming the X-ray geometry were performed. These BDE are reported in table 9.7, with BP86 and B97D BDEs in close agreement. The gas-phase adiabatic ionic BDE for $FeCl_2$ has been experimentally determined at 12.8(5) eV [23] from electron impact appearance energies, which is comparable with the following calculated values: 9.1 eV (BP86); 9.6 eV (LC-BP86); 8.9 eV (B97D); 9.3 eV (wB97XD). The calculated adiabatic BP86/TZVP heterolytic BDE at 4.7 eV is in excellent accord with previous *ab intio* calculations and experiment at 5.3 eV [24]. Zero-point energy corrections are calculated to be < 0.01 eV, and therefore neglected. These calculations indicate the difficulties in properly treating large transition metal containing species, and while DFT typically may underestimate absolute quantities, relative quantities can be determined in reasonable accord. For $FeCl_2{\cdot}4H_2O$, the two different types of waters are considerably more weakly bound than the chloride, with chloride having about half the binding energy of that in gas-phase $FeCl_2$. The X-ray $[Fe(H_2O)_6]^{2+}$ species shows two major types of water, which have approximately four times the binding energy of that in $FeCl_2{\cdot}4H_2O$. The $[FeCl_4(H_2O)_2]^{2-}$ species appears to be relatively unstable to ligand dissociation, with waters essentially unbound, and removal of one chloride to be exothermic. Loss of one chloride, with a -0.72 Mulliken charge, would achieve charge-separation and a more ideal 18 electron configuration. Removal of the second *trans*- chloride from $[FeCl_3(H_2O)_2]^-$ then becomes endothermic at 1.48 eV, which would yield a 16 electron configuration. These data support the hypothesis of water assisted/catalysed transformation of the $Fe(H_2O)_6{\cdot}FeCl_4(H_2O)_2$ isomorph, where the exothermicity of chloride loss from $[FeCl_4(H_2O)_2]^{2-}$ is greater than the endothermicity of water loss from $[Fe(H_2O)_6]^{2+}$. This is sufficient to propagate transformation to an overall thermodynamically more stable product.

Table 9.7.: Diabatic X-ray geometry gas-phase bond dissociation energies (BDE) in units of eV, with all calculations using the TZVP basis set.

Species	Ligand dissociated	BP86	B97D
FeCl2·4H_2O	Cl^-	5.75	5.77
	H_2O	0.25, 0.34	0.34, 0.45
$(Fe(H_2O)_6)^{2+}$	H_2O	1.03, 1.22	1.15, 1.35
$(FeCl_4(H_2O)_2)^{2-}$	Cl^-	-1.97	-1.91
	H_2O	0.03	0.12
$(FeCl_3(H_2O)_2)^-$	*trans*- Cl^-	1.48	1.54

9.4. Conclusion

The crystal structure of $FeCl_2{\cdot}4H_2O$ has been redetermined to high-precision with assignment in space group $P2_1/c$, and confirmation that hydrogen atoms form an intricate hydrogen-bonding network binding discrete octahedra. A tentative structural determination of a newly characterized isomorph, $Fe(H_2O)_6{\cdot}FeCl_4(H_2O)_2$, which has been confirmed by Mössbauer spectroscopy, has also been reported. This species exhibits essentially identical unit cell parameters, with minimal ligand exchange between the two isomorphs. The newly reported isomorph appears to be unstable in air, and Mössbauer spectroscopy studies have characterized a decay from the $Fe(H_2O)_6{\cdot}FeCl_4(H_2O)_2$ isomorph to the common $FeCl_2{\cdot}4H_2O$ isomorph to occur spontaneously. Density functional theory calculations reveal that the $Fe(H_2O)_6{\cdot}FeCl_4(H_2O)_2$ isomorph has a considerably less favourable hydrogen-bonding environment, and isomorphic transformation is an energetically favourable process where, upon atmospheric exposure, adsorbed and/or absorbed water may catalyze the transformation.

References

[1] B. R. Penfold and J. A. Grigor. *Acta Cryst.*, 12:850, 1959.

[2] P. J. Meunier-Piret and M. Van Meerssche. *Acta Cryst. B*, 28:2329, 1972.

[3] J. J. Verbist, W. C. Hamilton, T. F. Koetzle, and M. S. Lechmann. *J. Chem. Phys.*, 56:3257, 1972.

[4] Z. M. El Saffar and C. R. K. Murty. *Acta Cryst.*, 15:285, 1962.

[5] A. King. *Inorganic Preparations: a systematic course of experiments.* Allen and Unwin: London, 1950.

[6] G. M. Sheldrick. *Acta. Cryst A*, 64:112, 2008.

[7] E. W. Müller. *Mössbauer spectrum fitting program for universal theories.* Institut für anorganische Chemie and Analytische Chemie, Johannes Gutenberg Universtität, Mainz, 1980.

[8] H. Spiering and H. Vogel. *Hyperfine Interact.*, 3:221, 1977.

[9] T. C. Gibb N. N. Greenwood. *Mössbauer Spectroscopy.* Chapman and Hill Ltd.: London, 1971.

[10] C. K. Chan H. B. Wu, M. N. Chan. *Aerosol. Sci. Tech.*, 41:581, 2007.

[11] M. J. Frisch, G. W. Trucks, H. B. Schlegel, G. E. Scuseria, M. A. Robb, J. R. Cheeseman, J. A. Montgomery, Jr., T. Vreven, K. N. Kudin, J. C. Burant, J. M. Millam, S. S. Iyengar, J. Tomasi, V. Barone, B. Mennucci, M. Cossi, G. Scalmani, N. Rega, G. A. Petersson, H. Nakatsuji, M. Hada, M. Ehara, K. Toyota, R. Fukuda, J. Hasegawa, M. Ishida, T. Nakajima, Y. Honda, O. Kitao, H. Nakai, M. Klene, X. Li, J. E. Knox, H. P. Hratchian, J. B. Cross, V. Bakken, C. Adamo, J. Jaramillo, R. Gomperts, R. E. Stratmann, O. Yazyev, A. J. Austin, R. Cammi, C. Pomelli, J. W. Ochterski, P. Y. Ayala, K. Morokuma, G. A. Voth, P. Salvador, J. J. Dannenberg, V. G. Zakrzewski, S. Dapprich, A. D. Daniels, M. C. Strain, O. Farkas, D. K. Malick, A. D. Rabuck, K. Raghavachari, J. B. Foresman, J. V. Ortiz, Q. Cui, A. G. Baboul, S. Clifford, J. Cioslowski, B. B. Stefanov, G. Liu, A. Liashenko, P. Piskorz, I. Komaromi, R. L. Martin, D. J. Fox, T. Keith, M. A. Al-Laham, C. Y. Peng, A. Nanayakkara, M. Challacombe, P. M. W. Gill, B. Johnson, W. Chen, M. W. Wong, C. Gonzalez, and J. A. Pople. Gaussian 03, Revision C.02. Gaussian, Inc., Wallingford, CT, 2004.

[12] M. Bühl and H. Kabrede. *J. Chem. Theory Comput.*, 2:1282, 2006.

[13] K. P. Jensen, B. O. Roos, and U. Ryde. *J. Chem. Phys.*, 126:014103, 2007.

[14] C. F. Guerra, F. M. Bickelhaupt, and E. J. Baerends. *Cryst. Growth Des.*, 2:239, 2002.

[15] H. Jacobsen. *Chem. Phys.*, 345:95, 2008.

[16] M. Uudsemaa and T. Tamm. *Chem. Phys. Lett.*, 400:54, 2004.

[17] H. Iikura, T. Tsuneda, T. Yanai, and K. Hirao. *J. Chem. Phys.*, 115:3540, 2001.

[18] J. Antony and S. Grimme. *Phys. Chem. Chem. Phys.*, 8:5287, 2006.

[19] J. Chai and M. Head-Gordon. *Phys. Chem. Chem. Phys.*, 10:6615, 2008.

[20] R. J. Deeth and N. Fey. *J. Comp. Chem.*, 25:1840, 2004.

[21] A. Fouqueau, S. Mer, M. E. Casida, L. M. L. Daku, A. Hauser, T. Mineva, and F. Neese. *J. Chem. Phys.*, 120:9473, 2004.

[22] D. R. Lide, editor. *CRC Handbook of Chemistry and Physics*, volume 77, chapter 10. CRC Press: Cleveland, OH, 1996.

[23] R. C. Schoonmaker and R. F. Porter. *J. Chem. Phys.*, 29:116, 1958.

[24] R. D. Bach, S. Shobe, and H. B. Schlegel C. J. Nagel. *J. Phys. Chem.*, 100:8770, 1996.

10. Ferrous Ammonium Sulphate Hexahydrate: a combined Mössbauer and X-ray single crystal study

This chapter describes the elucidation of the microscopic mean square displacement (msd) and electric-field-gradient (efg) tensors in a ferrous ammonium sulphate hexahydrate (FAS), $Fe(NH_4)_2(SO_4)_2{\cdot}6H_2O$, single crystal. This chapter is a heavily modified reproduction of a previously published article:

James N. Bull, Ward T. Robinson, W. Craighead Tennant, Hyperfine Interactions, 194 (2009) 347-366.

The contents of this chapter results from the work of a project under the informal supervision of Dr. Craig Tennant. The content follows the general outline and format of the above article and, of course, reaches the same conclusions, but is a complete reinterpretation of all data. Many additional discussions and other material is added to assist understanding to readers unfamiliar with this field. One nomenclature convention difference should be noted. In the original manuscript, when a symbol representing a vector (vector = first-order tensor) or tensor is used as an adjective it is in non-bold font, whereas when used as a noun, it is in bold font. For ease of understanding here, this convention has been dropped. Several minor omissions in the original publication are corrected in this chapter. The reader should keep in mind that this FAS study provided a complete data interpretation without any analytical function fitting, with all theoretical simulation and fitting by a numerical Hamiltonian to obtain sensible microscopic efg and msd tensors. Methods of macroscopic data averaging are discussed in the appendix to this chapter and chapter 12.

This study represents the first and longest of the Mössbauer studies that were undertaken, since the methodology and procedure required to tackle such a problem was developed. Using the methodology developed in this study, applications to subsequent systems were more straight forward. In contrast to the *ab initio* calculations outlined in previous chapters that in some instances took days even on 512 CPUs on the UCSC Blue Gene supercomputer, simulations in this chapter are sub-second, and were performed on the (ageing) University of Canterbury VAX (CANTVA) computer. The software employed has also been successfully ported the to the IA-32 architecture using the Intel FORTRAN compiler, allowing use on any 32-bit microcomputer.

FAS was originally selected since it represented the prototypical ambiguous monoclinic case, and this species

has seen many attempts at macroscopic efg determinations in the past, allowing comparisons with the MOSREF method.

Overview

This chapter investigates the electric-field gradient (efg) tensor for the Fe^{2+} ion sites in ferrous ammonium sulphate hexahydrate (FAS) single crystals at ambient temperature (293 K) from two different approaches that under ideal conditions should be nearly equivalent. Firstly, calculations are performed on the expected angular dependence of the thin-crystal-limit reduced intensity ratios and total intensities of the Mössbauer quadrupole doublet utilizing previous literature determined macroscopic intensity tensor data and X-ray determined atomic-displacement parameters (ADPs). The computer program employed, MOSREF, utilizes matrix diagonalization in an arbitrary reference frame to numerically calculate Mössbauer intensities for sites of any specified symmetry in crystals of any specified symmetry. In the second method, experimental measurements are made on a series of related Mössbauer spectra. Through extraction of Lamb-Mössbauer f-factors, characterization of a Mössbauer mean-square-displacement (msd) tensor is facilitated, which in turn can be related to the Fe^{2+} ADPs. From experimental measurement of the angular dependence of the reduced intensities (areas) which are corrected to the thin crystal limit, and the Mössbauer determined mean-square-displacement tensor, the microscopic electric-field-gradient tensors for the two symmetry-related Fe^{2+} sites in the unit cell are determined. This is achieved by using the refinement option in MOSREF, where both reduced intensities and total intensities are refined simultaneously. Successful determination of microscopic tensors relies upon anisotropy in the absorber recoilless fractions that are related to anisotropic Lamb-Mössbauer factors.

10.1. Introduction

Ferrous ammonium sulphate hexahydrate (FAS), $Fe(NH_4)_2(SO_4)_2{\cdot}6H_2O$, is a well-known Fe^{2+} high-spin inorganic species that is commonly referred to as Mohr salt. This species exhibits a single relatively large quadrupole splitting ($\Delta E_Q = 1.745$ mm sec^{-1}, this work) whose quadrupole doublet lines are well resolved, and shows no magnetic hyperfine structure at room temperature. Unlike many ferrous compounds that oxidise on atmospheric exposure to a ferric containing species, FAS is inert to atmospheric exposure and may be readily handled and studied. For these reasons it has represented a traditional Mössbauer case study since the early 1960's. To date, there have been at least six experimental single crystal Mössbauer studies with the objective of measuring the electric-field gradient (efg) tensor. The first is that of Ingalls *et al.* [1] at 4.2 K and 300 K, where it was concluded that apparently no symmetry relation existed between efg principal directions and the crystal structure, and the sign of the quadrupole splitting was positive. Ingalls [2] and Golding *et al.* [3] calculated a large temperature-dependent quadrupole splitting, ΔE_Q, for such ferrous compounds from consideration of the combined action of a uniaxial field with rhombohedral distortion and spin-orbit coupling interactions. For FAS, this temperature dependence has been experimentally measured to be ≈ 1 mm sec^{-1} between 4.2 K and 300 K [2]. Chandra and Puri [4] also reported 300 K single crystal electric-field gradient determinations in FAS and ferrous chloride heptahydrate using essentially the same method developed by Zory [5] for ferrous chloride tetrahydrate. Unfortunately, as first pointed out by Zimmermann [6], Chandra and Puri did not appreciate that for the case of Fe^{2+} occupying a site of $\bar{1}$ Laue symmetry in a monoclinic crystal, only a macroscopic efg is measurable; nor did they correct experimental intensities to the thin crystal limit. One can determine, at best, only a manifold of efg solutions which contains the microscopic efg tensors for the two symmetry-related sites in the monoclinic unit cell. Zimmermann and Doefler [7] and Zimmerman [8] later detailed the determination of this manifold of solutions for FAS, after correcting to the thin crystal limit, using a series expansion of the theoretical expression for the absorption area of Mössbauer lines [9], which was outlined by Houseley *et al.* [10] in their sodium nitroprusside (SNP) study. Interestingly, Zimmermann and Doefler [7] state the principal components of the intensity tensor (outlined later) at 4.2 K are within experimental error of those at 300 K (and also between 77 K and 300 K) and comment that they find essentially no temperature dependence of the intensity tensor. This would seemingly contradict the well-established (experimentally) temperature dependence of the quadrupole splitting. Later, Doerfler [11] performed 4.2 K single-crystal measurements under high magnetic field conditions determining the sign of the quadrupole splitting to be negative, in accord with a ligand-field model [12]. Gibb [13,14] initially assumed a positive sign of the quadrupole splitting based in twin-crystal polarized experiments, then later in polarized source experiments was unable to confidently determine the sign. He stated that his experiments, "give additional polarization data in the plane normal to the axis of observation", eluding to the potential for some microscopic characterization. Following this study, Spiering [15] remarked that "Even with polarized source experiments, one can determine the macroscopic intensity tensor (efg) only - not more". Both of the Gibb experiments attempted thickness and polarization corrections to approximate the thin crystal limit. All above determinations assumed an isotropic mean square displacement of the iron site, which is argued herein from experimental and theoretical simulation to be incorrect. Garg and

Puri [16] following the methodology of Zory report a macroscopic efg determination in related $Fe(KSO_4)_2{\cdot}4H_2O$ single crystals, claiming to determine a positive sign of the quadrupole splitting.

This chapter attempts to resolve the ambiguity of two symmetry-related Mössbauer sites that contribute to the same quadrupole doublet, and to give the most accurate characterization of the efg and msd tensors at 293 K. That is, since the two Fe^{2+} sites are symmetry equivalent by operation of space group translational symmetries in the unit cell, they are crystallographically equivalent and therefore undergo resonant absorption and emission with the same hyperfine parameters. It is believed that resolution of the ambiguous monoclinic case may be achieved by simultaneously measuring a series of related (rotation) spectra and extracting both total intensity and intensity ratios for the two lines of the quadrupole doublet. The total intensity of a resonant line is proportional to the number and efficiency of resonant nuclei. While the former remains constant for a given single crystal at any orientation, the latter does not, and can be represented by a Lamb-Mössbauer f-factor, which is in general anisotropic. This f-factor has some analogous properties to a Cartesian second-rank tensor that may be used to represent a crystal physical property, in that it has magnitudes along three orthogonal axes. Yet, some reservations exist (from discussions with Prof. Harmut Spiering) as to whether this can formally be represented in tensor form, although it was found in the refinements reported later that convergence to exactly the same solution is obtained using the so-called f-matrix or msd tensor. It was pointed out some time ago that measurement of the angular dependence of the macroscopic total intensity in principle allows determination of a microscopic msd tensor, and measurement of the macroscopic intensity ratios allows determination of an efg tensor. [17] The msd, like the efg, is described by a second-rank tensor that is a property of the site (i.e. microscopic) representing the expectation anisotropic nuclear displacement. In this work, the term msd is restricted to that arising from the Mössbauer interaction, but in principle is measurable by X-ray crystallography studies as electron-density-fitted atomic displacement parameters (ADPs). Further, the interaction of resonant absorption and emission from a Mössbauer process is termed a 'slow' process since there is some small excited state half-life (i.e. the Mössbauer nuclei is undergoing state changes during the measurement process), and is *different* to the 'fast' scattering process of X-ray measurements. The only experimental measurement comparing the msd tensors from the two techniques, was that of Housley *et al.* [10] using a SNP single-crystal. Their results indicated that the Mössbauer determination exceeded X-ray values by $\approx 50\%$, although the precision of ADPs from a crystal structure of that era is however, questionable. In general, the msd tensor is anisotropic and it has been pointed out earlier that intensity calculations involving an anisotropic msd tensor can, in favourable circumstances, resolve the microscopic ambiguity [18]. By "favourable" it is implied that the anisotropy in the msd is adequate - this can be approximated in advance from X-ray determined ADPs for Fe^{2+} providing that an X-ray structural determination of adequate precision is available.

There are other possible procedures for resolution of the ambiguous problem when two or more symmetry-related resonant sites contribute to the same quadrupole doublet. For example, if the magnetic hyperfine components can be resolved at low temperatures or in the presence of external magnetic fields then potentially symmetry-related magnetic hyperfine spectra could be observed for each site. In practice, such experiments

are difficult if not essentially impossible to carry out. Further, determination of precise angular dependence from line intensities from complex spectra, which almost certainly would have overlapping symmetry-related hyperfine multiples, would introduce a high degree of uncertainty.

The algebra for handling symmetry-related sites is well-known in EPR spectroscopy, where sites are related by 3×3 Euler rotation matrices. These matrices are one or more of the 24 rotation matrices of the point symmetry group O, and have been tabulated and discussed by Weil *et al.* [19] in detail. For FAS of monoclinic $P2_1/c$ unit cell symmetry, there exist two symmetry-related sites, which are related by a translational two-fold rotation (screw axis) about the unique (crystallographic b) axis.

This chapter will be ordered as follows. Firstly, calculations are reported on one example of the angular dependence of area ratios of the Fe^{2+} quadrupole doublet of FAS in the thin crystal limit. This simulation utilizes an X-ray determined msd tensor, and Mössbauer parameters (namely, macroscopic efg) from earlier polycrystalline and single crystal studies [1,8,13,14]. Secondly, the crystal orientation technique is outlined for the crystal under study. This involves rotation of the crystal on a single-circle goniometer inclined at a fixed angle (45° in these experiments) about an axis fixed with respect to the crystal; the γ-beam then traces out a right (circular) cone in the crystal. This technique has been described analytically by Weil *et al.* [19], and used by Spiering and Vogel [17] in their Mössbauer study of ferrous chloride tetrahydrate. Following this, the results of raw and thin-crystal-limit-corrected angular dependence measurements are reported. The measured intensities are interpreted in two different ways. Firstly the data are analysed by fitting program MOSFUN [20] using background-corrected dimensionless areas including thickness and polarization corrections utilizing a series expansion based on a theoretical expression for absorption area developed by Housley *et al.* [10] which was based on the theory of Bykov and Hein [9]. The Housley *et al.* [10] modification considers thickness and polarization corrections for the relatively simple case of a single-line unpolarized magnetic dipole source which is appropriate to these studies. Secondly, the data are analysed using the fitting program NORMOS [21], and again using background corrected-dimensionless area ratios and including the programs implementation for a finite-sum transmission-integral correction for thickness only.

10.2. Background theory

10.2.1. Crystallography and intensity-tensor relationships

FAS crystallizes in the monoclinic space group $P2_1/c$, which contains two crystallographically equivalent sites for Fe^{2+} per unit cell. Each has point-group symmetry 1 (Laue class $\bar{1}$) and the sites are symmetry-related by a rotation π with respect to the unique axis, b. FAS is commonly known as the mineral Mohrite in the picromerite group, named after the German analytical chemist Karl Friedrich Mohr [22]. In this group, the NH_4^+ and SO_4^{2-} are mutually eight-coordinate with the $Fe(H_2O)_6$ octahedra located in interstitial sites. As part of this work, a room temperature (293 ± 2 K) X-ray structure (Mo-K_α radiation) was determined on a small single crystal obtained by recrystallizing a small sample of "Analar" (≈ 99.9 % purity) material in MilliQ water, acidified to

Table 10.1.: Crystallographic data for $Fe(NH_4)_2(SO_4)_2{\cdot}6H_2O$.

Crystallized from	$H_2SO_4/(NH_4)_2SO_4$ solution
Empirical formula	$Fe(NH_4)_2(SO_4)_2{\cdot}6H_2O$
Formula weight (g mol^{-1})	262.93
Crystal colour, habit	pale blue-green, plate
Crystal temp. (K)	293(2)
Radiation, wavelength	Mo K_α, $\lambda = 0.70926$ Å
Crystal system	monoclinic
Space group	$P2_1/c$
a(Å)	6.2482(2)
b(Å)	12.5979(4)
c(Å)	9.2931(3)
$\alpha(^\circ)$	90.0
$\beta(^\circ)$	106.7870(10)
$\gamma(^\circ)$	90.0
V($Å^3$)	700.33
Density (g cm^{-3})	1.247
Z	2
$\mu(mm^{-1})$	1.247
F(000)	260.0
$\theta_{min}/\theta_{max}$	2.80/31.74
Total reflections measured	10824
Symmetry-independent reflections	2197
Reflections used ($F_\circ$ $4\sigma(F_\circ)$)	2073
Parameters refined	128
$R(F_\circ\ 4\sigma(F_\circ))$	0.0310
$wR(F_\circ\ 4\sigma(F_\circ))$	0.0853
w	$\frac{1}{\sigma^2(F_\circ)}$
S	4.707

$\approx$ 1 mol L^{-1} with sulphuric acid. Crystallography was performed using a Bruker Apex II CCD area detector with phi and omega scans. The structure was solved using direct methods with the SHELXS program [23] and refinement on F^2 by least-squares procedures with the SHELXL-97 program [24]. Non-hydrogen atoms were refined with anisotropic displacement parameters and hydrogen atoms with isotropic displacement parameters. Once refined, a final Fourier synthesis showed no evidence of significant residual electron density. As a guide in crystal structure refinement and analysis, the previous determination by Montgomery *et al.* [25] and more recent determination of Cotton *et al.* [26] was used. The refined structure is in excellent agreement with both previous low temperature studies. For space group $P2_1/c$ the determined cell parameters, in units of Å, were: $a = 6.2482(2)$; $b = 12.5979(4)$; $c = 9.2931(3)$; and $\beta = 106.787(1)^\circ$. The atomic displacement parameters (ADPs) at 293(2) K for Fe^{2+} referred to the crystal axis system were, in units of $Å^2$: $U_{11} = 0.01739(19)$; $U_{22} = 0.01706(16)$; $U_{33} = 0.01406(16)$; $U_{12} = -0.00094(12)$; $U_{13} = 0.00356(13)$; and $U_{23} = 0.00091(11)$. The crystallographic R factor was 3.10% for 2073 symmetry unique reflections. Crystal structure data collections and analyses were performed for FAS under the guidance of Prof. Ward T. Robinson. The parameters of the room temperature refinement are summarised in table 10.1.

Table 10.2.: Selected X-ray determined bonding parameters for FAS asymmetric unit with errors reported in parentheses. O1, O2 and O3 represent waters coordinated to the Fe^{2+} ion which sits on a crystallographic centre of symmetry.

Atoms	Bonding parameter
Fe-O1	2.1419(13) Å
Fe-O2	2.1419(13) Å
Fe-O3	2.1442(14) Å
Fe-N	4.834(2) Å
Fe-S	4.841(2) Å
O1-Fe-O2	89.23(6)°
O1-Fe-O3	89.03(6)°
O2-Fe-O3	89.03(6)°

The FAS structure reveals water co-ordination to be close to octahedral. Figures 10.1 and 10.2 show the asymmetric unit and spherical volumes enclosing a central octahedron, respectively. Relevant bonding parameters are listed in table 10.2.

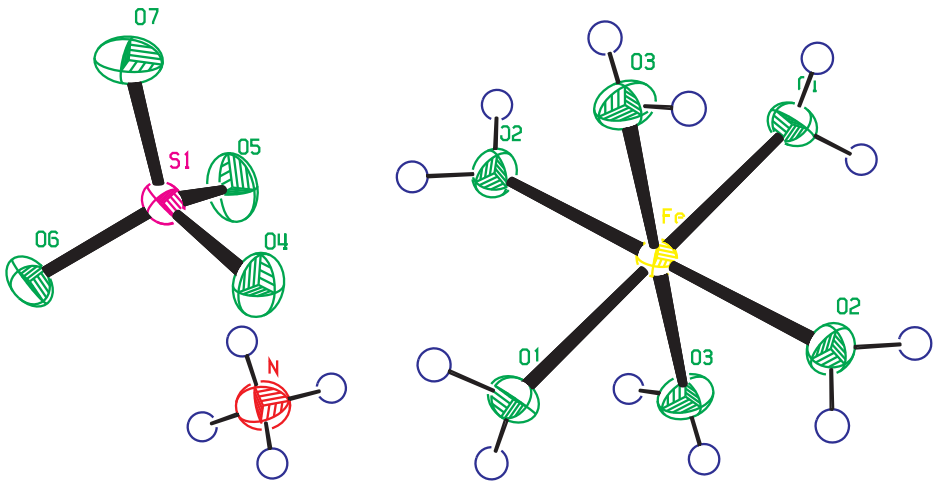

Figure 10.1.: FAS asymmetric unit (with Fe^{2+} octahedron completed) showing atom labelling. The $Fe(H_2O)_6^{2+}$ octahedra are slightly distorted from octahedral symmetry.

For the Mössbauer experiments and simulations/refinements reported here, the convention of Ingalls [2] and Zimmermann and Doerfler [7] is followed in choosing an orthogonal set of axes (x_0, y_0, z_0) related to the crystallographic orthogonal set, (x_f, y_f, z_f), which is shown in figure 10.3 (later). This study requires a set of orthogonalized ADPs, U_{ij}^C (in units of $Å^2 = 10^{-16}$ cm^2), for the Fe^{2+} site. These were obtained by two methods, firstly with the program ORTEP [27], or alternatively with the algebraic approach outlined by Trueblood *et al.* [28] utilizing the monoclinic data from the crystal structure. In the former case these are referred to as the principal values of the so-called probability covariance matrix. As a check, in the latter case for the choice of axis set, the orthogonalized matrix of anisotropic displacement parameters, $\mathbf{U}_C$, were obtained by application of equation 10.1.

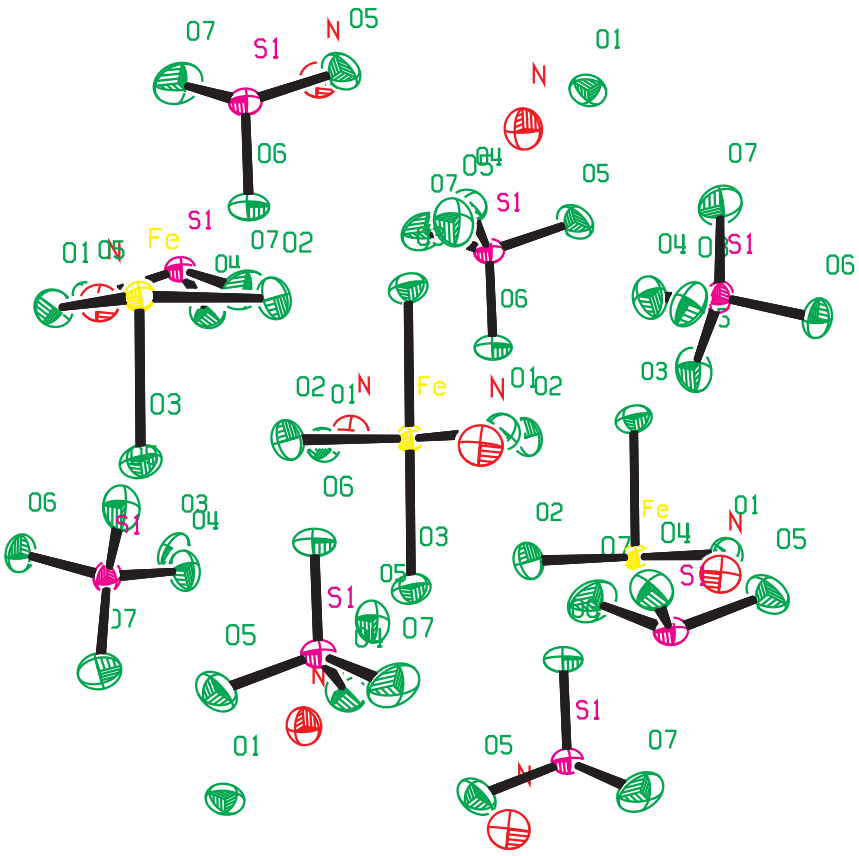

Figure 10.2.: FAS sphere of enclosure showing relative orientation of eight counter charge units to one central octahedron.

$$\mathbf{U}^C = \mathbf{AUA}^T \tag{10.1}$$

where $\mathbf{A}$ is the transformation rotation matrix from unit cell coordinates to Cartesian coordinates, and $\mathbf{A}^T$ the matrix transpose of $\mathbf{A}$. $\mathbf{U}$ is the corresponding atomic displacement matrix in the crystal-axis reference frame, which is given in equation 10.2.

$$\mathbf{U} = \begin{bmatrix} 0.01739 & -0.00094 & 0.00356 \\ -0.00094 & 0.01706 & 0.00091 \\ 0.00356 & 0.00091 & 0.01406 \end{bmatrix} \tag{10.2}$$

In general, the rotation matrix, $\mathbf{A}$, takes the form given in equation 10.3 and is defined in terms of fractional (direct), unit cell coordinates. Use of the identity $\sqrt{(1-\cos^2\beta)} = \sin\beta$ is applied in equation 10.3 upon simplification for the monoclinic case.

$$\mathbf{A} = \begin{bmatrix} a & b\cos\gamma & c\cos\beta \\ 0 & b\sin\gamma & c(\cos\alpha - \frac{\cos\beta\cos\gamma}{\sin\gamma}) \\ 0 & 0 & \frac{V}{ab\sin\gamma} \end{bmatrix} \tag{10.3}$$

where $V = \frac{1}{V^*} = abc\sqrt{1-\cos^2\alpha-\cos^2\beta-\cos^2\gamma+2\cos\alpha\cos\beta\cos\gamma}$, where $(^*)$ refers to reciprocal or inverse unit cell parameters. Substitution of $\alpha=\gamma=90^\circ$ for the monoclinic case yields equation 10.4.

$$\mathbf{A} = \begin{bmatrix} a & 0 & c\cos\beta \\ 0 & b & 0 \\ 0 & 0 & c\sin\beta \end{bmatrix} \begin{bmatrix} a^* & 0 & 0 \\ 0 & b^* & 0 \\ 0 & 0 & c^* \end{bmatrix} \tag{10.4}$$

where $a^* = \frac{1}{a\sin\beta}$, $b^* = \frac{1}{b}$, $c^* = \frac{1}{c\sin\beta}$. Matrix multiplication then yields equation 10.5 as the transformation matrix in the monoclinic case.

$$\mathbf{A} = \begin{bmatrix} \csc\beta & 0 & \cot\beta \\ 0 & 1 & 0 \\ 0 & 0 & 1 \end{bmatrix} \tag{10.5}$$

Application of equation 10.1 then yields, in units of Å^2, the orthogonalized Cartesian X-ray $\mathbf{U}^C$ matrix given in equation 10.6.

$$\mathbf{U}^C = \begin{bmatrix} 0.018010 & -0.001256 & -0.000523 \\ -0.001256 & 0.017060 & 0.000910 \\ -0.000523 & 0.000910 & 0.014060 \end{bmatrix} \tag{10.6}$$

The expectation or isotropic mean-squared displacement is given by $\langle U^2\rangle = \frac{1}{3}Tr(\mathbf{U}^C) = \frac{1}{3}(U^C_{11}+U^C_{22}+U^C_{33})$, from which the related temperature factor $B_{eq} = 8\pi^2\langle U^2\rangle$ may be obtained. The corresponding (X-ray) Debye-Waller factor, f', was then calculated by equation 10.7. In the anisotropic approximation, $\langle U^2\rangle$ is substituted by the square of the anisotropic $\mathbf{U}$ matrix, also known as the msd tensor. This parameter describes the attenuation of X-ray radiation in the scattering process, and is angularly dependent upon the wave-vector, $\mathbf{k}$. The analogous nuclear Lamb-Mössbauer factor is denoted f.

$$f' = e^{(-k^2\langle U^2\rangle)} \tag{10.7}$$

where, for the ^{57}Fe Lamb-Mössbauer factor, $k^2 = \dfrac{4\pi^2}{\lambda^2} = 53.3494\times10^{16}$ cm^2, with λ being the Mössbauer radiation wavelength. Equation 10.7 arises from consideration of the harmonic approximation in the Einstein or Debye model of the crystal, where essentially no difference between these models exists at room temperature. The elements of the X-ray derived msd tensor may be defined in terms of the dimensionless quantities, $\text{msd}_{ij} = k^2U_{ij}$, where the U_{ij} are displacements along the wave-vector $\mathbf{k}$, with the msd tensor given in equation 10.8.

$$\mathbf{msd}_f = \begin{bmatrix} 0.96075 & -0.06703 & -0.02790 \\ -0.06703 & 0.91014 & 0.04855 \\ -0.02790 & 0.04855 & 0.075009 \end{bmatrix} \tag{10.8}$$

Equations 10.6 and 10.8 are in the crystallographic Cartesian reference frame, (x_f, y_f, z_f), and for correspondence to the Mössbauer experiments, these need to be transformed into the laboratory choice of axes, (x_0, y_0, z_0). This

relationship is shown in figure 10.3, where for the choice of laboratory axes, $x_f \parallel x_0$, $y_f \parallel z_0$, $z_f \parallel y_0$.

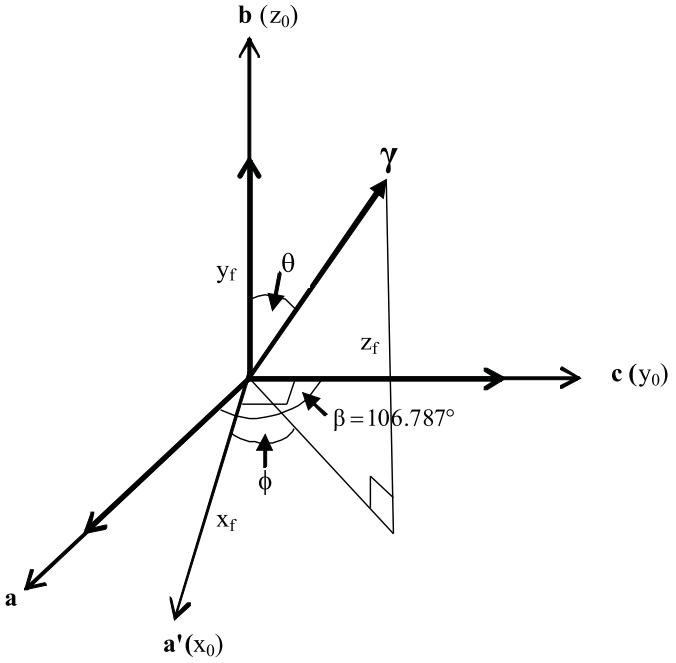

Figure 10.3.: Relationship between crystallographic Cartesian reference frame, (x_f, y_f, z_f), and the orthogonal laboratory reference frame, (x_0, y_0, z_0). **a**, **b**, and **c** are the crystallographic unit cell edges. Note that the beam traces out the surface of a cone when the crystal is rotated - the γ-beam is fixed which fixes the laboratory axis, it is the crystal that rotates.

To transform $\mathbf{msd}_f$ to $\mathbf{msd}_0$, a rotation of $\omega = 90°$ (clockwise) about x_f needs to be applied. The appropriate transformation matrix is given in equation 10.9.

$$\mathbf{R}_{0\leftarrow f} = \begin{bmatrix} 1 & 0 & 0 \\ 0 & \cos\omega & -\sin\omega \\ 0 & \sin\omega & \cos\omega \end{bmatrix} \tag{10.9}$$

Application to $\mathbf{msd}_f$ yields $\mathbf{msd}_0$, which is given in equation 10.10. From here on, $\mathbf{msd}_0$ will be denoted as msd.

$$\mathbf{msd}_0 = \begin{bmatrix} 0.96075 & 0.02790 & -0.06703 \\ 0.02790 & 0.75009 & -0.04855 \\ -0.06703 & -0.04855 & 0.09101 \end{bmatrix} \tag{10.10}$$

The X-ray anisotropic thermal ellipsoid represents an expectation or average displacement, where the principal

values represent the average displacement along respective principal vectors. It has been subsequently realized (outlined in a later chapter) that this X-ray msd was calculated using the wrong radiation k^2, meaning that all elements are incorrect by a constant factor. This is not serious considering all these elements are refined, and ultimately the same microscopic solutions are obtained.

With the X-ray derived msd, an initial microscopic efg tensor in the crystallographic axis system is also required. For simplicity, and following the requirements of the simulation/refinement program MOSREF, the intensity tensor formalism that was first introduced by Zimmermann [6] is utilized. In this formalism the spin-Hamiltonian for a nuclear quadrupole interaction referred to in an arbitrary coordinate frame is given in equation 10.11.

$$\hat{H} = \frac{eQ}{2I(2I+1)} \hat{I} \cdot \mathbf{V} \cdot \hat{I} \tag{10.11}$$

where e is the elementary charge, Q is the nuclear electric quadrupole moment, $I = \frac{3}{2}$ is the total nuclear spin for the first excited ^{57}Fe state, $\hat{I}$ is the nuclear spin operator, and $\mathbf{V}$ is the second-rank efg tensor, which like the msd tensor can be expressed as a 3×3 matrix. The principal axis system (PAS), which is denoted by subscripts with hats hereafter, is the orthogonal reference frame in which the axes are aligned with the principal directions - common in Euler rotations for the classical moment of inertia. Use of this formalism simplifies expressions and calculations. The expression for the quadrupole splitting in the PAS is given in equation 10.12.

$$\Delta E_Q = \frac{1}{2} eQ V_{\hat{z}\hat{z}} (1 - \frac{\eta^2}{3})^{\frac{1}{2}} \tag{10.12}$$

where e is the elementary charge, Q is the quadrupole moment for ^{57}Fe, and $V_{\hat{z}\hat{z}}$ is the largest efg principle value, and η is teh asymmetry parameter. In the Zimmermann [6] formalism, the traditional Cartesian efg elements, V_{pq}, are replaced with symmetric traceless intensity tensor elements, P_{qp}, that are proportional to the diagonal in the same PAS as $\mathbf{V}$. When referred to in the PAS, the asymmetry parameter, η, is given in equation 10.13.

$$\eta = \frac{P_{\hat{x}\hat{x}} - P_{\hat{y}\hat{y}}}{P_{\hat{z}\hat{z}}} \tag{10.13}$$

Two invariants now exist within the intensity tensor, given in equations 10.14 and 10.15.

$$P_{\hat{x}\hat{x}} + P_{\hat{y}\hat{y}} + P_{\hat{z}\hat{z}} = 0 \tag{10.14}$$

$$P_{\hat{x}\hat{x}}^2 + \frac{1}{3}(P_{\hat{x}\hat{x}} - P_{\hat{y}\hat{y}})^2 = \frac{1}{16} \tag{10.15}$$

Equation 10.14 states that in the PAS the intensity tensor is traceless, and equation 10.15 arises from consideration of the norm (length) of the intensity tensor in irreducible form (derivation and further information in [18]) and, when expressed in an arbitrary reference frame, takes the form given in equation 10.16.

$$P_{zz}^2 + \frac{1}{3}(P_{xx} - P_{yy})^2 + \frac{4}{3}(P_{xy}^2 + P_{xz}^2 + P_{yz}^2) = \frac{1}{16} \tag{10.16}$$

These two invariants together impose limitations (reduce degrees of freedom) on the number of refinement parameters and therefore dimensionality of the refinement hyper-surface. The program MOSREF therefore refines on four independent elements of the traceless efg tensor. No such limitations exist for the msd tensor, so a full refinement of efg and msd tensors therefore refines on ten independent parameters. In practice, two diagonal elements of the efg tensor are entered, with the third being given by invariance equation 10.14, but, arbitrarily, only one is iterated upon together with the three off-diagonal elements. Errors for each element are internally calculated by MOSREF using a variance-covariance matrix, and following the invariances outlined above, each diagonal efg tensor element is in turn iterated upon. Hereafter, the intensity tensor is simply referred to in text as the efg tensor.

For the initial trial efg tensor, the macroscopic intensity tensor experimentally obtained by Zimmermann [8] is considered, which is given in equation 10.20. Briefly, Zimmerman reports $I_{xx} = 0.691, I_{yy} = 0.273, I_{zz} = 0.536, \phi_\circ = 34.4°$, where $\phi_\circ$ takes its normal meaning as the projection of the efg tensor on the xy plane and referenced with respect to the x axis. The 2×2 rotation matrix, $R_{\phi M}$, describing this $\phi_\circ$ is given in equation 10.17.

$$\mathbf{R}_{\phi M} = \begin{bmatrix} \cos\phi_\circ & \sin\phi_\circ \\ -\sin\phi_\circ & \cos\phi_\circ \end{bmatrix} \tag{10.17}$$

Application to the Zimmerman xy-plane diagonal 2×2 matrix yields equation 10.18.

$$\mathbf{R}_{\phi_\circ} = \begin{bmatrix} 0.691\cos^2\phi_\circ 0.273\sin^2\phi_\circ & -0.418\cos\phi_\circ\sin\phi_\circ \\ -0.418\cos\phi_\circ\sin\phi_\circ & 0.691\cos^2\phi_\circ 0.273\sin^2\phi_\circ \end{bmatrix} \tag{10.18}$$

Evaluating for $\phi_\circ$ yields equation 10.19.

$$\mathbf{I}_M = \begin{bmatrix} 0.55758 & -0.19486 & I_{xz} \\ -0.19486 & -0.09358 & I_{yz} \\ I_{xz} & I_{yz} & 0.036 \end{bmatrix} \tag{10.19}$$

This intensity matrix has a trace of 1.5, therefore to convert into the traceless symmetric intensity tensor, 0.5 is subtracted from each diagonal element, giving the final literature macroscopic efg in equation 10.20.

$$\mathbf{P}_M = \begin{bmatrix} 0.0576 & -0.1948 & P_{xz} \\ & -0.0936 & P_{yz} \\ & & 0.0360 \end{bmatrix} \tag{10.20}$$

The ambiguity in the monoclinic case (where the iron atoms do not sit on a two-fold rotation axis) in effect means that P_{xz} and P_{yz} are indeterminate for the microscopic efg tensor. As outlined later, the sign of $P_{\hat{z}\hat{z}}$,

which is the largest magnitude eigenvalue of the efg tensor is taken as negative in 10.20. The indeterminate nature means that a manifold of solutions is possible, which is restrained by the boundary condition in equation 10.21. This boundary follows from application of equation 10.16 to $\mathbf{P}_M$.

$$P_{xz}^2 + P_{yz}^2 = 0.002222 \tag{10.21}$$

The simulations and refinements in this work require values for these indeterminate elements, while infinite combinations exist in the general symmetric case when $P_{xz} = P_{yz} = 0.033332$ is selected. This combination is selected, as seen later, for correspondence of macroscopic spectrum to experiment. The simulations of reduced and total intensities in the conical section that mimics the single-crystal experiment are described next using the X-ray derived msd tensor with this guess macroscopic efg tensor.

10.2.2. The goniometer assembly

FAS crystallizes from aqueous solution most commonly as flat plates containing the $(\bar{2}01)$ crystal plane. Single crystal data are collected by rotating the crystal about the perpendicular (normal) to this plane on a single-circle goniometer inclined at 45° to the direction of the γ-ray beam. The γ-beam then traces out a right-circular cone in the crystal, where the directions of measurement (laboratory rotation angles) lie on the surface of the cone; with a 2π rotation required to obtain a repeat spectrum. The formalism is now outlined for the calculation of spherical polar angles in the laboratory reference frame for both the "perpendicular" and 45° inclined measurements. For the latter, the coplanar "0" and "180" unit vectors, designated with respect to their arbitrary goniometer rotation angle ε, are used as generators to obtain the required parameters for any other laboratory measurement at 45° inclination.

An analytical expression for the rotation matrix that describes the link between the crystal axis rotation axis (perpendicular) and the laboratory rotation angle ε, is first required. A general discussion of such rotation matrices may be found in Golding and Tennant [29]. From figure 10.3, in spherical polar coordinates, the crystal system has the γ-beam projection considered on the $b \parallel z_o$ axis, where θ is the angle the γ-beam makes with $z_o||b$, and ϕ is the angle the γ-beam projection in the ac plane referenced anti-clockwise with respect to the $a^{'}||x_\circ$ axis. Then to rotate ϕ to ε, the lab rotation angle, a rotation about $z_\circ$ is required. The required rotation matrix, $\mathbf{R}_\phi$, is given in equation 10.22.

$$\mathbf{R}_\phi = \begin{bmatrix} \cos\phi & -\sin\phi & 0 \\ \sin\phi & \cos\phi & 0 \\ 0 & 0 & 1 \end{bmatrix} \tag{10.22}$$

Similarly, the projection of the azimuthal ϕ coordinate is considered with reference to the $a^{'} \parallel x_\circ$ axis, therefore to relate ε to the defined axis system, the rotation matrix $\mathbf{R}_\varepsilon$ is also required and given in equation 10.23. The similarity (orthogonal reference frame) transformation, $\mathbf{A} = \mathbf{R}_\phi \mathbf{R}_\varepsilon \mathbf{R}_\phi^{-1}$, was then evaluated.

$$\mathbf{R}_{\varepsilon} = \begin{bmatrix} 1 & 0 & 0 \\ 0 & \cos\varepsilon & \sin\varepsilon \\ 0 & -\sin\varepsilon & \cos\varepsilon \end{bmatrix} \tag{10.23}$$

This general analytical rotation matrix, $\mathbf{A}$, is given in equation 10.24. The trigonometry identities, $\sin^2 k + \cos^2 k = 1$, and $\sin 2k = 2\sin k \cos k$ were applied for simplification of A_{11}, A_{22}, and A_{12}/A_{21} elements respectively.

$$\mathbf{A} = \begin{bmatrix} 1-\sin^2\phi(1-\cos\varepsilon) & \frac{1}{2}\sin 2\phi(1-\cos\varepsilon) & -\sin\phi\sin\varepsilon \\ \frac{1}{2}\sin 2\phi(1-\cos\varepsilon) & 1-\cos^2\phi(1-\cos\varepsilon) & \cos\varepsilon\sin\varepsilon \\ \sin\phi & -\cos\phi\sin\varepsilon & \cos\varepsilon \end{bmatrix} \tag{10.24}$$

Next, the general spherical polar θ (polar) and ϕ (azimuthal) angles for the 45° γ-beam inclination on the cut *crystal plane* were considered. Determination is slightly complicated (compared to the FCL situation in the next chapter) since a non-trivial $(\bar{2}01)$ crystal plane is being considered. In effect, this requires two mathematical transformations to relate the crystalline plane to the laboratory axis and experiment. This plane is schematically shown in figure 10.4, with application of simple trigonometry yielding for the "perpendicular" orientation, $\theta = 90°$, $\phi = 136.995°$. A description of (θ, ϕ) determination for the $(\bar{2}01)$ crystal plane follows. Note that this ϕ represents a different azimuthal angle than the preceding paragraphs.

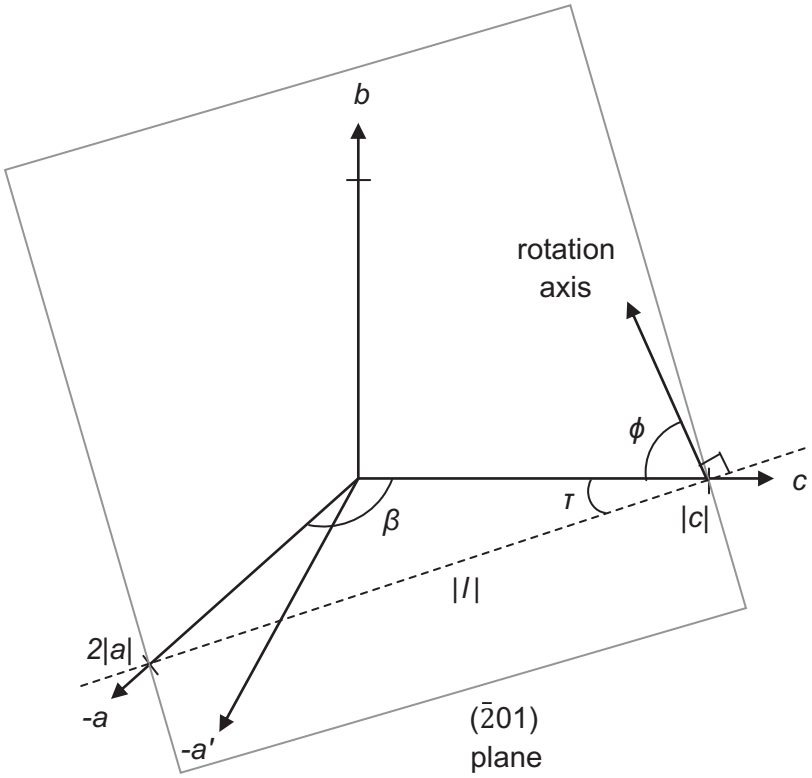

Figure 10.4.: Representation of the $(\bar{2}01)$ plane on the axis system in order to calculate ϕ.

When defining a crystallographic plane with Miller indices, the reciprocal (inverse) lattice is used. For a general (lmn) plane, the l, m, n integers denote planes orthogonal to the reciprocal lattice vector, or the planes that intercept unit cell axes at $\frac{a}{l}, \frac{b}{m}, \frac{c}{n}$ respectively. For the $(\bar{2}01)$ plane, the intercepts are at $\left(-\frac{1}{2}a, \infty, c\right)$ along the unit cell axes

For $l = -2, \frac{a}{-2} = \frac{1}{2}a$; $m = 0, \frac{b}{0} = \infty$; and $n = 1, \frac{c}{1} = c$. This generalization for angle ε follows the Gibb study [14], where the rotation axis was the perpendicular (normal) to the $(\bar{2}01)$ plane, in contrast to the 45° inclination here, although with the same rotation axis. This axis inclination results in the γ-beam tracing out the surface of a cone with its center as the $(\bar{2}01)$ normal or crystallographic b axis as shown in figure 10.5. This rotation axis is off-set from the crystallographic b axis by a small angle ξ. An accurate determination of the perpendicular orientation is crucial for tight non-linear dependent convergence since, in a general sense, is more independent than the ε rotation measurements. Considering figure 10.4, application of the cosine formula yields $|l|$=17.5921 Å, and then application of the sine formula yields τ=43.005°, which is the angle the $(\bar{2}01)$ plane makes with the crystallographic c axis. Therefore, $\phi = 90° - 43.005° = 46.995°$, or transposing to align with positive c, $\phi + 90° = 136.995°$.

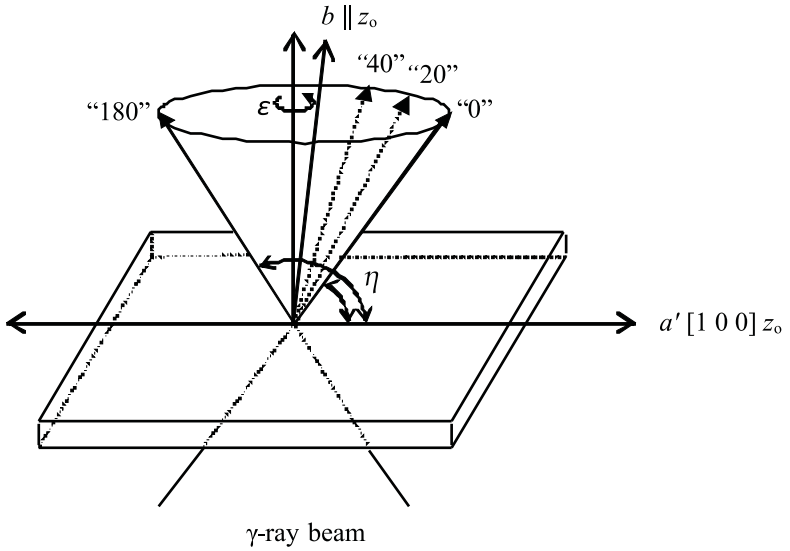

Figure 10.5.: Relationship between the laboratory (γ-ray beam direction), the crystal reference frame and the angular rotation of ε about the normal to the $(\bar{2}01)$ plane that is almost coaxial with $b||z_o$. For these experiments, $\eta = 45°$, and 90° for the "perpendicular" measurement.

The "0" vector is defined as an arbitrary unit vector that occurs on the surface of the cone for $\varepsilon = 0$. The angle between "0" and the crystal plane is $\eta = 45°$, and as shown in figure 10.6, ξ is the small angular offset of the crystal normal with $b||z_o$. This is calculated at $\xi = 46.995° - 45° = 1.995°$.

From figure 10.6, the vector "0" and its antisymmetric pair, "180" are given in equation 10.25. The set of vectors, denoted as "ε" and "$\varepsilon + 180°$" pairs, were calculated, where each such pair is bisected by the experimental rotation axis.

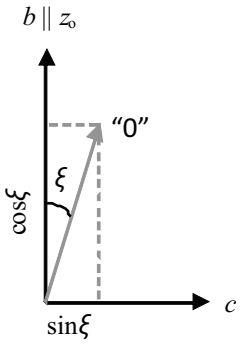

Figure 10.6.: Calculation of angle ξ for the 45° inclination projections of a unit vector on the γ-beam rotation cone.

$$\text{“0”} = \begin{bmatrix} -\cos\xi \\ \sin\xi \\ 0 \end{bmatrix} = \begin{bmatrix} -0.999394 \\ 0.034812 \\ 0 \end{bmatrix}, \text{“180”} = \begin{bmatrix} -\sin\xi \\ \cos\xi \\ 0 \end{bmatrix} = \begin{bmatrix} -0.034812 \\ 0.999394 \\ 0 \end{bmatrix} \tag{10.25}$$

With this “0” vector, application of the rotation matrix **A** then yields the general expression, **B**, for determination of the direction cosines of the γ-beam on the cone surface for any ε angle, as outlined in equation 10.26.

$$\mathbf{B} = \mathbf{A} \times \begin{bmatrix} -0.999394 \\ 0.034812 \\ 0 \end{bmatrix} = \begin{bmatrix} -0.999394 + 0.0482291(1 - \cos\varepsilon) \\ 0.517193(1 - \cos\varepsilon) - 0.034812 \\ \dfrac{-\sin\varepsilon}{\sqrt{2}} \end{bmatrix} \tag{10.26}$$

These vectors finally need to be projected onto the laboratory axis in order to obtain corresponding (θ, ϕ) polar and azimuthal angles. These are obtained by the Cartesian to spherical polar expressions, $\theta = \tan^{-1}\left(\dfrac{\sqrt{(x^2+y^2+z^2)}}{z}\right)$, and $\phi = \tan^{-1}\left(\dfrac{y}{x}\right)$. For the experimental ε angles, the corresponding (θ, ϕ) angles are calculated and tabulated in table 10.3, with respect to the laboratory reference frame.

10.2.3. Intensity calculations

The experimental quadrupole doublet relative line intensities are interpreted in terms of reduced intensities, $I^{(r)}$, which are defined in terms of equation 10.27.

$$I^{(r)} = \frac{I_l^0}{I_l^0 + I_u^0} \tag{10.27}$$

where I_u^0 and I_l^0 are the upper (higher velocity) and lower (lower velocity) line intensities at the thin-crystal limit (denoted by superscript zero), with $I^{(r)}$ calculated for each angle ε over the 2π angular rotation. In practice these line intensities are first experimental fitted areas, and following application of thickness and polarization corrections, the line intensities will be denoted as p_u^0 and p_l^0 respectively, and are also known as ”thicknesses”. Assuming the X-ray determined msd tensor in equation 10.10, and the macroscopic intensity

Table 10.3.: Polar (θ) and azimuthal (ϕ) angles for the rotating the general vector "0" about the laboratory rotation angle ε. All angles in degrees.

$\varepsilon \pm 0.5°$	θ	ϕ
0.0	90.0000	181.9950
20.0	103.9955	180.2142
40.0	117.0340	174.4487
60.0	127.7612	163.5601
80.0	134.1360	146.8461
100.0	134.1360	127.1439
120.0	127.7612	110.4299
140.0	117.0340	99.5413
160.0	103.9954	93.7758
180.0	90.0000	91.9950
200.0	76.0046	93.7758
220.0	62.9660	99.5413
240.0	52.2388	110.4299
260.0	45.8640	127.1439
280.0	45.8640	146.8461
300.0	52.2388	163.5601
320.0	62.9660	174.4487
340.0	76.0046	180.2148
360.0	90.0000	181.9950
perpendicular	90.0000	136.9950

tensor of Zimmermann [8] with substituted elements as given in equations 10.20 and 10.21, calculated reduced and total intensities are required. Again it is emphasised that the choice of $P_{xz} = P_{yz} = 0.033332$ represents *one* possible example, and symmetrical at that, from a manifold of solutions given by equation 10.21. As will be seen later, this choice is not completely arbitrary.

Calculated angular rotation intensities, or simulations are performed by mimicking the Mössbauer interaction. This involves the purely magnetic-dipole radiation (M=1) from a ^{57}Co source expressed in terms of the ket vectors given in equations 10.28 and 10.29 [10, 18, 30].

$$|1,+1\rangle\prime = \frac{1}{2}((1+\cos\theta)e^{-i\phi}|1,1\rangle + (1-\cos\theta)e^{i\phi}|1,-1\rangle + \sqrt{2}\sin\theta|1,0\rangle) \tag{10.28}$$

$$|1,-1\rangle\prime = \frac{1}{2}((1-\cos\theta)e^{-i\phi}|1,1\rangle + (1+\cos\theta)e^{i\phi}|1,-1\rangle - \sqrt{2}\sin\theta|1,0\rangle) \tag{10.29}$$

where $|1,1\rangle$, $|1,-1\rangle$ are the basis kets representing right-handed, left-handed circular polarized components. The intensities of the transitions between ground and excited states are calculated in accord with equations 10.28 and 10.29, and the principal directions of the two states using vector coupling and appropriate Clebsch-Gordan coefficients. The intensities of individual magnetic-hyperfine transitions are obtained as the elements of the 2×4 matrix **T** [18], defined in equation 10.30.

$$\mathbf{T} = |\mathbf{E}_g\mathbf{R}_R\mathbf{E}_e|^2 + |\mathbf{E}_g\mathbf{R}_L\mathbf{E}_e|^2 \tag{10.30}$$

In equation 10.30 $\mathbf{E}_g$ and $\mathbf{E}_e$ are the 2×2 and 4×4 principal direction matrices of the ground and excited states respectively, and the 2×4 arrays describing the intensity operators $\mathbf{R}_R$ and $\mathbf{R}_L$ are given in table 10.4, which are reproduced from Tennant [18]. These intensity operator matrices elements are products of terms of equations 10.28 and 10.29 and appropriate Clebsch-Gordan coefficients.

Table 10.4.: Elements of the 2×4 intensity-operator matrices $\mathbf{R}_R$ and $\mathbf{R}_L$. These are reproduced from tabulation in Tennant (1992). g and e refer to ground and excited states respectively, $I = \frac{1}{2}$ for the ground state and $I = \frac{3}{2}$ for the excited state.

$\mathbf{R}_R$	$\lvert\frac{3}{2}e-\frac{3}{2}\rangle$	$\lvert\frac{3}{2}e-\frac{1}{2}\rangle$	$\lvert\frac{3}{2}e+\frac{1}{2}\rangle$	$\lvert\frac{3}{2}e+\frac{3}{2}\rangle$
$\langle\frac{1}{2}g+\frac{1}{2}\rvert$	0	$\frac{1}{2\sqrt{3}}(1-\cos\theta)e^{i\phi}$	$\frac{1}{\sqrt{3}}\sin\theta$	$\frac{1}{2}(1+\cos\theta)e^{-i\phi}$
$\langle\frac{1}{2}g-\frac{1}{2}\rvert$	$\frac{1}{2}(1-\cos\theta)e^{i\phi}$	$\frac{1}{\sqrt{3}}\sin\theta$	$\frac{1}{2\sqrt{3}}(1+\cos\theta)e^{-i\phi}$	0
$\mathbf{R}_L$	$\lvert\frac{3}{2}e-\frac{3}{2}\rangle$	$\lvert\frac{3}{2}e-\frac{1}{2}\rangle$	$\lvert\frac{3}{2}e+\frac{1}{2}\rangle$	$\lvert\frac{3}{2}e+\frac{3}{2}\rangle$
$\langle\frac{1}{2}g+\frac{1}{2}\rvert$	0	$\frac{1}{2\sqrt{3}}(1+\cos\theta)e^{i\phi}$	$-\frac{1}{\sqrt{3}}\sin\theta$	$\frac{1}{2}(1-\cos\theta)e^{-i\phi}$
$\langle\frac{1}{2}g-\frac{1}{2}\rvert$	$\frac{1}{2}(1+\cos\theta)e^{i\phi}$	$-\frac{1}{\sqrt{3}}\sin\theta$	$\frac{1}{2\sqrt{3}}(1-\cos\theta)e^{-i\phi}$	0

These intensity calculations are effected by the program MOSREF [31], which utilizes exact matrix diagonalizations of the Hamiltonian given in equation 10.11 in arbitrary coordinates in addition to the intensity operator given in equation 10.30. The intensities of the two peaks of the quadrupole doublet are obtained by summation of the intensities of the appropriate hyperfine components T_{ij} of the matrix $\mathbf{T}$. The simulation angular parameters are selected to be identical to experiment, that is, calculations are performed over the range $0° \leq \varepsilon \leq 360°$ in 20° steps (i.e., for each (θ, ϕ) pair), and for each of the symmetry-related sites. Each calculated intensity is also modified by the respective Lamb-Mössbauer (of Debye-Waller for simulation) factor, $f' = e^{(-\langle U^2\rangle)}$. The expression used to calculate $\langle U^2\rangle$ for each crystal measurement was determined as follows. Consider the unit vector $\mathbf{k}$ (i.e. wave unit vector) on the msd tensor for each (θ, ϕ) pair. To convert general Cartesian to spherical polar coordinates the unit projection ket and bra are given in equation 10.31.

$$|k\rangle = \begin{bmatrix} \sin\theta\cos\phi \\ \sin\theta\sin\phi \\ \cos\theta \end{bmatrix}; \langle k| = \begin{bmatrix} \sin\theta\cos\phi & \sin\theta\sin\phi & \cos\theta \end{bmatrix} \tag{10.31}$$

The expectation value is simply given as $\langle U^2\rangle = \langle k|\mathbf{msd}_o|k\rangle$, and is expanded in equation 10.32.

$$\langle U^2\rangle = msd_{11}\sin^2\theta\cos^2\phi + msd_{22}\sin^2\theta\sin^2\phi + msd_{33}\cos^2\theta + msd_{12}\sin^2\theta\sin 2\phi + msd_{13}\sin 2\theta\cos\phi + msd_{23}\sin 2\theta\sin\phi \tag{10.32}$$

where the msd_{ij} are the elements of the msd tensor. Finally, by averaging over the two symmetry-related microscopic sites, the expected macroscopic (observable) spectrum is obtained. The results of the simulation is shown are figures 10.7 and 10.8, where referencing is made with respect to upper and lower lines respectively. The powder average is also shown, which averages all intensities over all single crystal orientations (since a polycrystalline powder sample contains all and ideally completely random orientation of crystallites). This is

achieved by averaging over all (θ, ϕ) pairs on a spherical surface, with vanishingly small increments of θ and ϕ, using the program MOSPOW, which is an extension of MOSREF. In these figures the powder average is not an average of the plotted intensity ratios since these single crystal simulations represent only the $(\bar{2}01)$ plane.

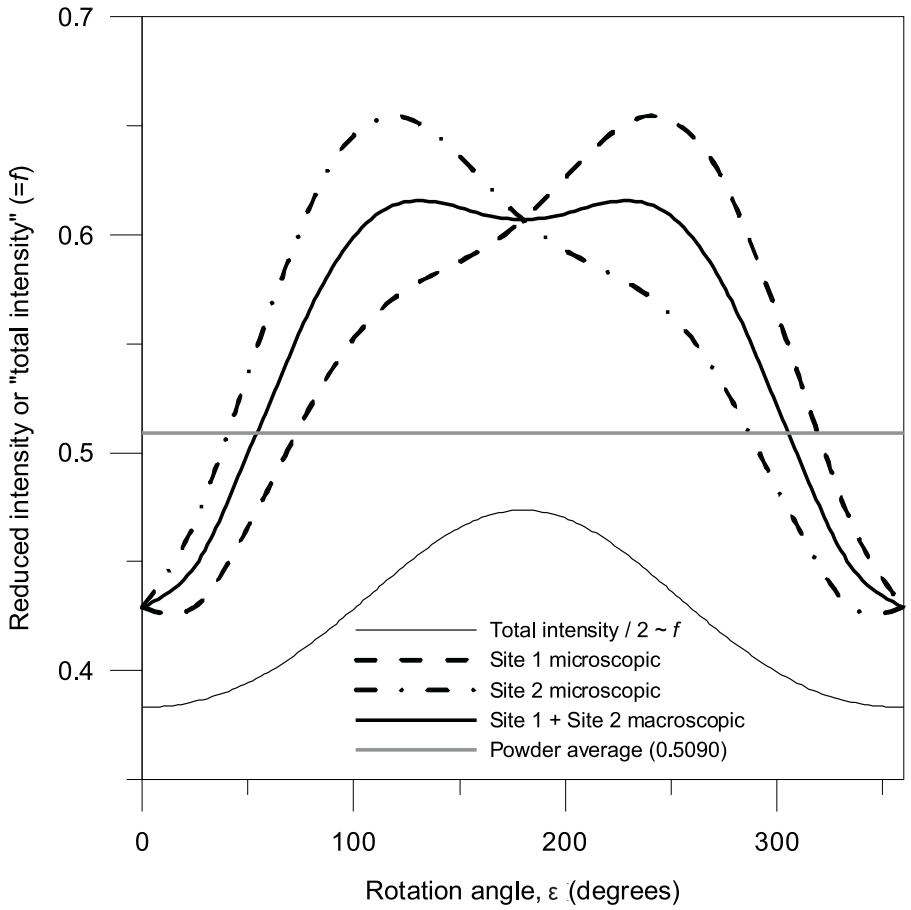

Figure 10.7.: Simulation of expected reduced intensity ratio, $I^{(r)}$, referenced with respect to the upper line, and total intensity as a function of laboratory rotation angle, ε. This is decomposed into contributions from site 1 and 2 respectively. The lower total intensity plots the expected observed average intensities of the two peaks.

The shape (curvature) of the simulation that arises entirely from X-ray msd and literature macroscopic efg tensor reproduces the angular dependences and approximate magnitudes of the experimental intensities (shown later). This would seemingly indicate that the parameters used in this simulation will be good initial starting parameters for refinement to experimental intensities. The dashed lines in figures 10.7 and 10.8 indicate the microscopic or site contributions to each efg tensor. The refinement procedures then reverse the simulation method; that is, MOSREF is used to obtain efg and msd tensors from an unbiased set of starting parameters using the experimentally measured reduced and total intensities as fixed boundary conditions. As a cross-check, without experimental intensities, the simulated reduced and total intensities were used as the refinement reduced and total intensities for five different refinements of efg and msd tensors. These are (with RMSD/iterations in parentheses):

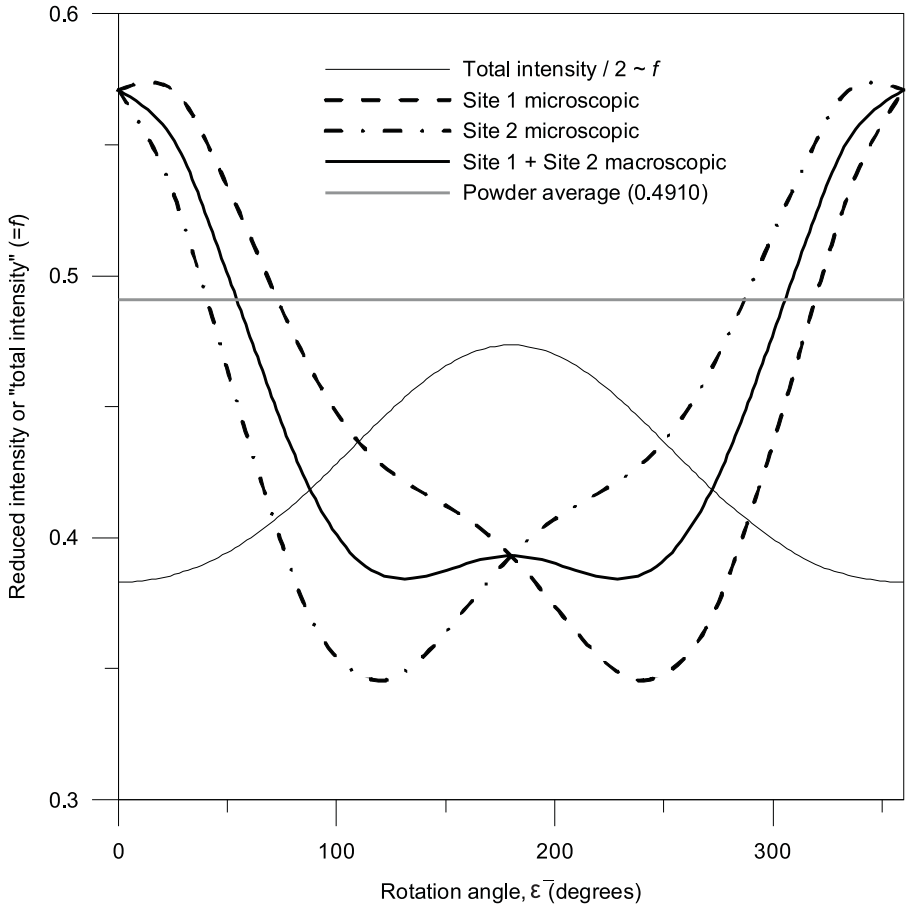

Figure 10.8.: Simulation of expected reduced intensity ratio, $I^{(r)}$, referenced with respect to the lower line, and total intensity as a function of laboratory rotation angle, ε. This is decomposed into contributions from site 1 and 2 respectively. The lower total intensity plots the expected observed average intensities of the two peaks.

1. Zimmerman macroscopic efg with the P_{xz} and P_{yz} set to zero, and diagonal identity msd tensor (0.00001/150);
2. Zimmerman macroscopic efg with only diagonal elements non-zero, and diagonal identity msd tensor (0.00001/479);
3. Tetragonal (trace 3/2) efg, and diagonal identity msd tensor (0.00001/329);
4. Tetragonal (trace 3/2) efg, and diagonal identity msd tensor with unrounded intensities to 4 d.p. (0.000124/352);
5. Tetragonal (trace 3/2) efg, and diagonal identity msd tensor with unrounded intensities to 3 d.p. $\approx$ experimental error (0.000271/419)

These refinements all show convergence to tensors resembling the original trial efg and msd, including determination of the P_{xz} and P_{yz} elements of both matrices. That convergence is obtained to the same result from near unit efg and unit msd tensors indicates the refinement hyper-surface is not immediately contaminated by non-global minima. Simulation refinement case 5 models data with approximately the same uncertainty as experimental intensities, and convergence is again to the same result, although in this case the

refinement root mean square displacement (RMSD) is an order of magnitude better than actual experimental data refinement. Finally, it needs to be stated that, in principle, the macroscopic intensity tensor is always obtainable experimentally with single crystals.

10.3. Experimental

All Mössbauer (transmission) measurements were carried out on a PC-based ORTEC system employing ELSCINT drive electronics operated in constant acceleration mode. A ^{57}Co/Rh source of nominal strength $\approx$ 1 mCi was used as the 14.4 keV γ-ray source, and iron foil used as the velocity and isomer shift calibrant. Large single crystals were grown in their natural habit as flat plates that contain the $(\bar{2}01)$ crystal plane, from an aqueous solution of recrystallised FAS, the solution being slightly acidified with sulphuric acid.[1] One single crystal surface was lightly polished and was then super glued to a perspex (plexiglass) disc of thickness $\approx$ 0.5 mm. The disc was mounted in a brass guide and the crystal hand polished using systematically finer-grained polishing paper with a silicone oil lubricant to a final thickness of 0.602 $\pm$ 0.001 mm. Crystal thickness was measured using a digital micrometer with 0.001 mm resolution on several points on the crystal surface. All measurements were in excellent agreement, indicating a uniform thickness over the crystal surface. It was then ascertained that the crystal was indeed single by observing good (sharp) extinctions at 90° intervals under a polarizing microscope. Crystal growth was monitored each day to ensure that visual twinning was not occurring. The doubly polished crystal and perspex disc were then located on the single circle goniometer mounted (on a brass collimator) at 45° to the γ-ray beam, as shown in figure 10.9. An annular Pb shield restricted the crystal portion exposed to γ-rays to a diameter of 9 mm, and ensured that all counts reaching the gas proportional detector had passed through the crystal. Spectra were collected around the full 2π angular range at 20.0 $\pm$ 0.5° intervals, with approximately 1.5×10^5 off-resonance counts accumulated in each case. Backgrounds due to accompanying high energy γ-rays (136 and 122 keV) at the observation channel were determined from the average of two measurements with Cu foils of thickness 0.25 and 0.27 mm; only one background determination is required since the crystal had, for all 45° measurements, the same thickness. One further measurement was made perpendicular to the crystal (i.e., γ-beam parallel to the conical rotation axis) and a separate background correction made. A blank perspex and super-glue measurement showed negligible attenuation of the γ-beam. A final smaller correction of $\approx$ 2.5% was made for the "dark" signal of the detector, which arises from stray radiation and bogus counts. This was measured by inserting a thick lead shield between an iron foil absorber and the detector, and that the spectrum shows no iron foil resonances and indicates no transmission. The dark count correction is small, but included since the source was quite weak; normally, with a stronger source such correction would be negligible. Two powder specimens were prepared from recrystallized FAS as follows: finely powdered FAS was pressed into two holders with thicknesses 0.25 mm and 0.5 mm respectively. Spectra were collected, subsequent to completion of the single-crystal experiments, with a new ^{57}Co/Rh source of nominal strength $\approx$ 5 mCi. Around 2×10^6 off-resonance counts were accumulated in each case.

[1] this took a long time!

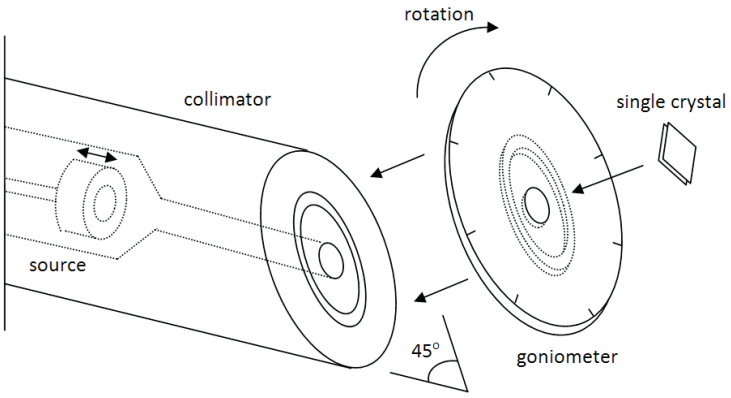

Figure 10.9.: Schematic of the mounting of a single-crystal on the single circle goniometer assembly with the rotation axis inclined at 45° with respect to the γ-beam.

All spectra were fitted with a two line quadrupole doublet of Lorentzian line shape, with intensities and line widths independently optimized using program MOSFUN [20]. No attempt was made to include line-shape modifications such as Voigt. In general, a Voigt type magnetic resonance line profile is a convolution of a Gaussian and Lorentzian function allowing for increased fit flexibility. It was assumed that since all $\chi^2 \approx 1$, and from the lack of unfitted area in the difference spectra shown in figure 10.10, that the spectra conform well to Lorentzian shapes. Three representative spectra are shown in figure 10.10. The spectra were also fitted, with the same assumptions, by program NORMOS [21] and fitting parameters were identical to those from MOSFUN. This program allowed, in addition, a transmission integral thickness correction. The intensities from these two fitting procedures are illustrated in figure 10.11. The corrections from the transmission integral compared to the truncated thickness correction expansion (see later) are, as expected, essentially identical.

10.4. Results and discussion

10.4.1. Theory and experiment intensities

From the simulations and experimental results presented in figures 10.7 and 10.11 respectively, it is clear that the experimental reduced intensities, and total intensities, expressed here in terms of $f^{'}$ numbers determined from equation 10.33 in the thin-crystal limit, are in good qualitative agreement in both functional shape and magnitude. That is, simulated intensties from the X-ray determined Debye-Waller factors yields a quite good approximation to experimental Mössbauer single crystal spectra. Total intensities at the thin crystal limit result from the sum of intensities of both quadrupole split lines, and hence both sites. This match was used to calibrate the rotation axis ε, since the relative alignment of the unit cell axes to the external crystal morphology is not known in advance. The simulations predict a center of symmetry in the plot, and the experimental measured angular dependences also reveal that a center of symmetry exists between corresponding pairs of quadrupole intensities within error. The experimental intensities are therefore averaged in pairs for $\varepsilon \neq 0°, 180°$. The final experimental-pair-averaged, background-corrected dimensionless areas (outlined later) for upper and lower lines

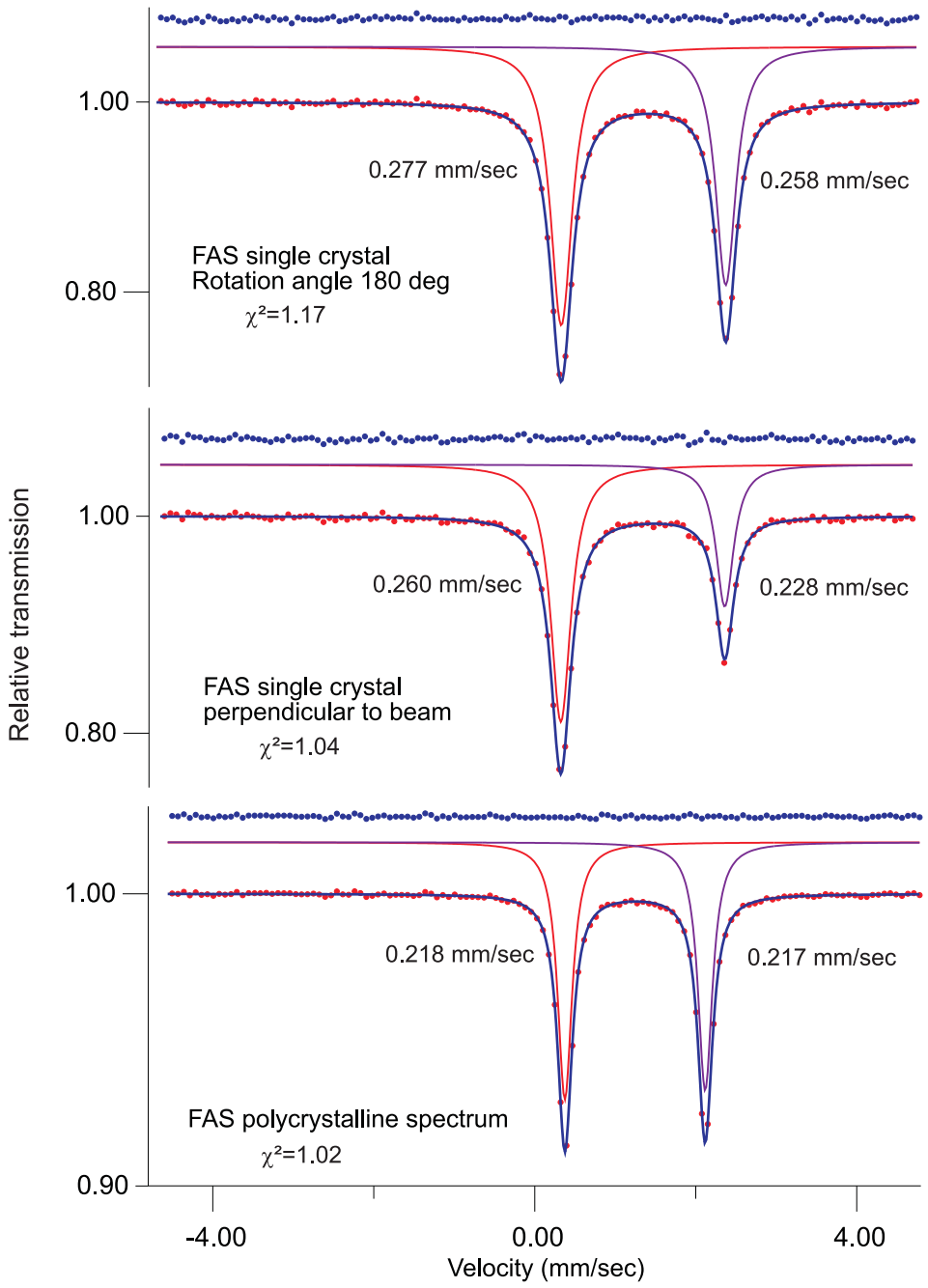

Figure 10.10.: Three representative spectra of FAS showing raw data, fitted quadrupole doublets and residual intensity for each. χ^2 fitting parameters and line widths (FWHM) are given for each.

are reported in table 10.5.

$$p_l^0 + p_u^0 = n_{Fe}\sigma_0 f \tag{10.33}$$

In equation 10.33, p_l^0 and p_u^0 refer to thickness or thickness and polarization corrected line intensities as background-corrected dimensionless areas, n_{Fe} is the number of resonant iron atoms per unit area, σ_0 is the resonant cross section per Mössbauer nucleus respectively, and f is the absorber recoilless fraction. For ^{57}Fe, σ_0

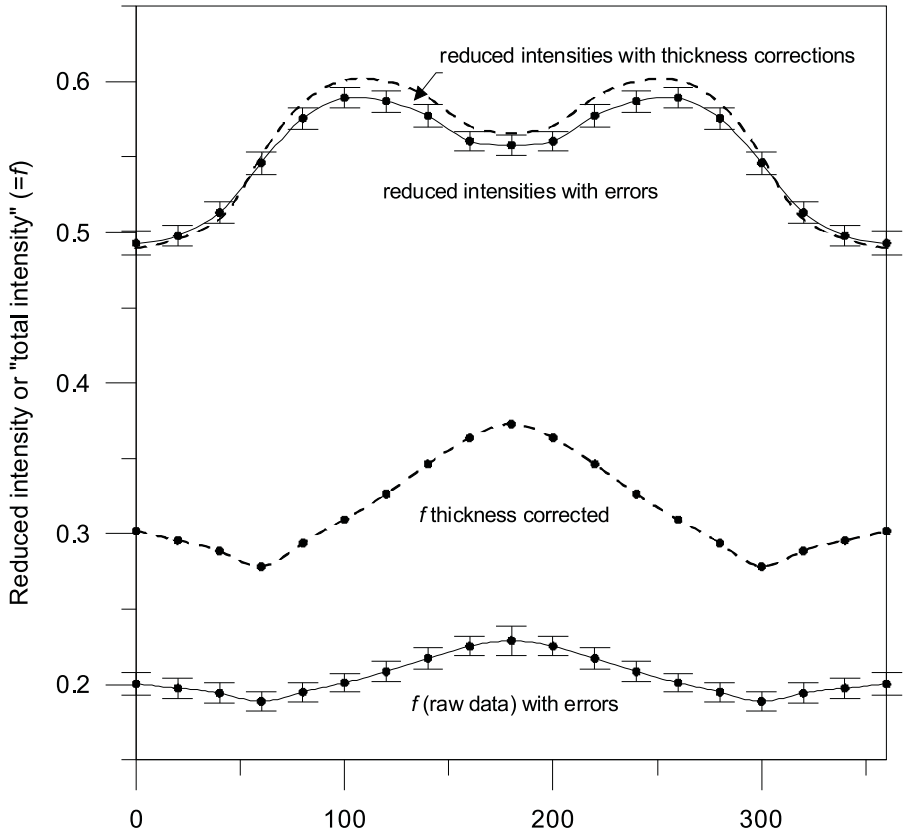

Figure 10.11.: Raw experimental and transmission integral corrected (program NORMOS) reduced intensity ratios, $I^{(r)}$ (upper two curves), and raw and thickness corrected total intensities (lower two lines) - see text for details.

has the value 255.75×10^{-20} cm^2 [32]. The observed full Lorentzian lower line widths at half maximum height (FWHM), with upper in parentheses, range from 0.254 ± 0.003 (0.253 ± 0.003) mm sec^{-1} for $\varepsilon = 0°$, to 0.276 ± 0.002 mm sec^{-1} (0.256 ± 0.003) for $\varepsilon = 180°$ (0.261 ± 0.003 mm sec^{-1} perpendicular). The experimental non-averaged and pair-averaged FWHM for both lines of the quadrupole doublet over all experimental laboratory rotation angles, ε, are shown in figure 10.12. This graph would indicate that changes in quadrupole line areas arise not only from dip changes, but also from line width changes, which would seemingly indicate a change in resonant cross-section for one of the hyperfine excited states.

Experimental f numbers were determined from the known composition and physical properties of the crystal, being the physical thickness and density (1.8644 g cm^{-3}). In the 45° orientation, the effective thickness is 0.851 mm, corresponding to 23.3878 mg cm^{-2} of total iron. The number of resonant nuclei per unit area is then $n_{Fe} = 0.054228 \times 10^{20}$ cm^{-2}, which yields $n_{Fe}\sigma_0 = 13.8687$. Similarly, for the perpendicular orientation, $n_{Fe}\sigma_0 = 9.8061$ (i.e. ratio of $\sqrt{2}$ difference to 45°). Application of equation 10.33 gives f_i, where i represents each single crystal measurement.

The simulation in figure 10.7 refers to the thin-crystal limit. Therefore, the experimental intensities shown

Table 10.5.: Experimentally determined, pair averaged background corrected dimensionless areas, p_0^l and p_0^u, that are used in subsequent data analysis. Orientation perp corresponds to single-crystal measurement perpendicular to the γ-beam. Experimental fitting errors are in the last one/two decimal figures.

Lab rotation angle, ε (degrees)	Lower line intensity	Upper line intensity
0	1.3687	1.4091
20	1.3638	1.3760
40	1.3824	1.3120
60	1.4296	1.1888
80	1.5559	1.1476
100	1.6429	1.1459
120	1.6969	1.1945
140	1.7401	1.2742
160	1.7515	1.3736
180	1.7720	1.4050
200	1.7515	1.3736
220	1.7401	1.2742
240	1.6969	1.1945
260	1.6429	1.1459
280	1.5559	1.1476
300	1.4296	1.1888
320	1.3824	1.3120
340	1.3638	1.3760
360	1.3687	1.4091
perp	1.5474	0.7461

in figure 10.11 must be corrected for thickness and polarization before meaningful refinements can be obtained from program MOSREF. That thickness and polarization corrections are important is easily demonstrated from examination of figure 10.11, which shows the change in total intensity with thickness (transmission integral) correction. It was found that the transmission integral and the iterative thickness procedure outlined later, give almost identical final thickness corrections. The lower two plots in figure 10.11 show thickness corrections to the total areas. In this instance, the areas are background-corrected dimensionless areas [10] (outlined later) obtained from the MOSFUN fittings. Grant *et al.* [10] have pointed out that a strictly correct thickness correction of an absorption line must also take into account the degree of polarization of the radiation. The procedures for obtaining simultaneous thickness and polarization corrections will now be outlined.

10.4.2. Thickness and polarization corrections

Following Housely *et al.* [10], Zimmermann [8], and the detailed derivations and example applications by Golding and Tennant [29], this expression is derived in terms of a polarization operator, σ, which is in turn defined in terms of elements of a macroscopic efg tensor and the same experimental ε rotation (θ, ϕ) γ-beam angles. The eigenvalues of this operator are denoted σ_1 and σ_2, and the "thicknesses", p, are effectively the cross-section at resonance. These parameters are related by equation 10.34.

$$p = \frac{(\sigma_1 + \sigma_2)}{2} \tag{10.34}$$

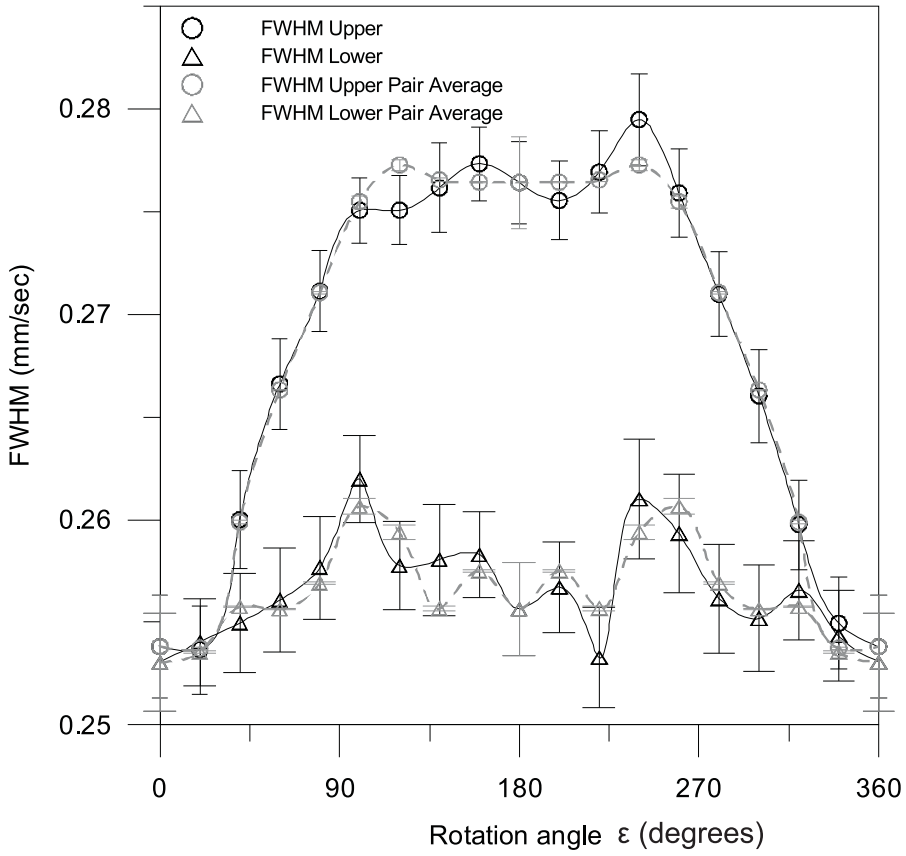

Figure 10.12.: Experimental raw and pair averaged full width at half maximum height (FWHM) line widths for the two-line quadrupole doublet. The upper line appears to reproduce the experimental intensity ratio pattern, whereas the lower line width appears relatively invariant to rotation angle.

The degree of polarization (a=0 if no polarization) is defined in equation 10.35.

$$a = \frac{(\sigma_1 - \sigma_2)}{(\sigma_1 + \sigma_2)} \tag{10.35}$$

The eigenvalues, σ_1 and σ_2, are in turn defined in terms of p and a in equation 10.36.

$$\begin{aligned} \sigma_1 &= p(1+a) \\ \sigma_2 &= p(1-a) \end{aligned} \tag{10.36}$$

Assuming that the γ-ray source is a single line unpolarized source (true for a disc type cubic-Rh matrix source), then the dimensionless absorption areas, S, are given [8, 10, 29] by the Bykov and Hein [9] expression in equation 10.37.

$$S(p,a) = \frac{\sigma_1}{2} e^{-\frac{\sigma_1}{2}} \left(I_0 \frac{\sigma_1}{2} + I_1 \frac{\sigma_1}{2} \right) + \frac{\sigma_2}{2} e^{-\frac{\sigma_2}{2}} \left(I_0 \frac{\sigma_2}{2} + I_1 \frac{\sigma_2}{2} \right) \tag{10.37}$$

where I_0 and I_1 are the modified Bessel functions of the first kind (with imaginary argument) of order 0 and 1 respectively. The I_0 expansion gives rise to odd powers of the series of p, whereas the expansion I_1 gives rise to even powers of the series of p. Expanding equation 10.37 with σ_i substitution yields equation 10.38. Application

of this expression requires this functions inverse, which is given in equation 10.39 [8, 10, 29].

$$\begin{aligned} S &= p - \tfrac{1}{4}(1-a^2)p^2 + \tfrac{1}{16}(1+3a^2)p^3 - \tfrac{5}{384}(1+6a^2+a^4)p^4 + \tfrac{7}{3072}(1+10a^2+5a^4)p^5 \\ &\quad -\tfrac{7}{20480}(1+15a^2+15a^4+a^6)p^6 + \tfrac{11}{245760}(1+21a^2+35a^4+7a^6)p^7 + ... \end{aligned} \tag{10.38}$$

$$\begin{aligned} p &= S + \tfrac{1}{4}(1+a^2)S^2 - \tfrac{1}{16}(1+a^2+2a^4)S^3 + \tfrac{5}{384}(1+a^4+6a^6)S^4 + \tfrac{1}{3072}(5-22a^2-47a^4-24a^6+168a^8)S^5 \\ &\quad +\tfrac{7}{30720}(-1-15a^2-35a^4-81a^6-80a^8+180a^{10})S^6 + \\ &\quad \tfrac{1}{737280}(-169-549a^2-635a^4-3087a^6-12496a^8-17640a^{10}+23760a^{12})S^7 + ... \end{aligned} \tag{10.39}$$

Equation 10.39 then expresses a thickness or intensity in terms of polarization operators, and orders of (raw experimental) dimensionless absorption areas. These equations are truncated at the terms of seventh degree, which is usually sufficient to obtain a convergent thickness correction. This convergence for the case of no polarization (a=0) is shown in figure 10.13 for three cases of upper line dimensionless areas. Polarization corrections are always smaller, and show similar convergence. Ideally these corrections are small since any relative error between datum points is magnified with large thickness and polarization corrections.

The correction was checked by substitution into equation 10.38. Several high-order terms for equation 10.38 are given in equation 10.40.

$$\begin{aligned} &+... - \tfrac{143}{27525120}(1+28a^2+70a^4+28a^6+a^8)p^8 + \tfrac{143}{264241152}(1+36a^2+126a^4+84a^6+9a^8)p^9 \\ &-\tfrac{283}{6794772480}(1+45a^2+210a^4+210a^6+45a^8+a^{10})p^{10} \end{aligned} \tag{10.40}$$

These procedures have been incorporated by Dr. Craig Tennant into an addition to MOSREF known as THICKMOD. The first step in refinement requires background-corrected dimensionless areas, p_α (where $\alpha = l, u$ and superscript 0 in the thickness and polarization corrected thin crystal limit), for both lines of the quadrupole doublet for each rotation angle ε, and the perpendicular orientation. The procedure of Grant *et al.* [33] is followed, where for a spectral peak of Lorentzian line shape, the background corrected dimensionless area were calculated by equation 10.41.

$$p_\alpha = \frac{\text{“}Dip\text{”} \times 2\Gamma}{0.7032 \times \text{“}Background\text{”}} \times \frac{1}{f_s \Gamma_s} \tag{10.41}$$

In this expression f_s is the source recoilless fraction (=0.7 according to manufacturer specifications), and Γ_s is the source natural line width (=0.097135 mm sec^{-1}). "*Dip*" corresponds to the spectral line intensity (in counts), and "*Background*" the fitted background over all spectra channels. Note that "*Dip*" $\times \Gamma$ is equivalent to the MOSFUN fitted peak intensity. As previously outlined in the experimental section, measurements with filters of Cu foils, which exhibit an absorption edge suitable for 14.4 keV attenuation, allow the average high energy γ-rays across all channels to be determined at 29.68%. Hence, the correction factor of 100 - 29.68 =

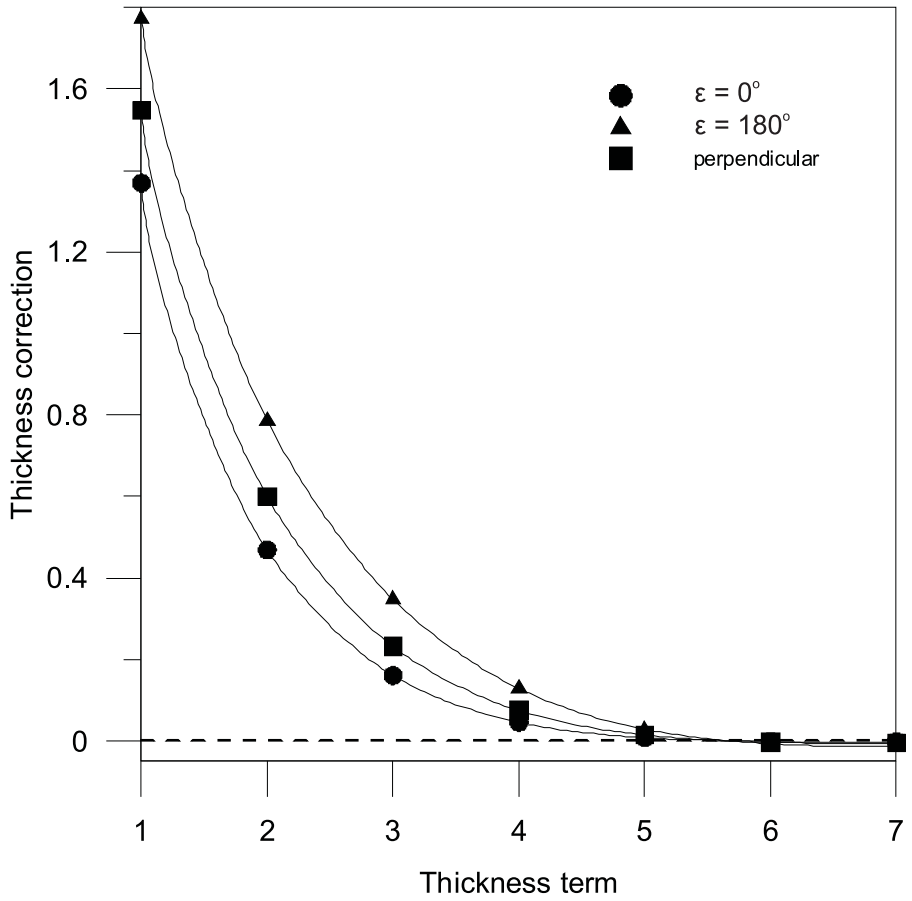

Figure 10.13.: Convergence of thickness corrections to the lower dimensionless areas for $\varepsilon = 0°, 180°$ and the perpendicular orientation.

70.32% (=0.7032) is applied to all dimensionless areas at the 45° inclination. This background correction is determined to be 38.73% for the thinner perpendicular orientation, yielding the correction factor of 100 - 38.73% = 61.27% (=0.6127). Such high-energy γ-beam backgrounds *necessarily* accompany the Mössbauer transition, with a thinner absorber allowing more 14.4 keV and high-energy transmission through the crystal per unit time.

Application of thickness and polarization corrections is an iterative process [8,10] since the refined macroscopic efg tensor is required for these corrections, and is not known in advance. Firstly, experimental background corrected dimensionless areas are calculated and corrected for thickness using equation 10.38 in the absence of polarization effects ($a = 0$), yielding thickness-corrected p_α. These p_α are then entered into MOSREF, where a refinement on the trial macroscopic efg tensor yields first estimates of the experimental macroscopic efg tensor. A second application of 10.38 allowing for polarization by use of this first iteration refined macroscopic efg gives thickness and polarization corrected $I^{(r)}$ and total intensities. The macroscopic efg tensor is calculated by averaging the two microscopic site efg tensors - since all elements are equivalent except the P_{xz} and P_{yz} which are of equal magnitude but opposite sign, the macroscopic efg tensor has these two elements at 0. These new tensors are entered into MOSREF with refinement now on both efg and msd tensors yielding an efg tensor corrected for the effects of the msd tensor. The msd-corrected macroscopic efg tensor is then used

Table 10.6.: Final fits for the efg (intensity tensor, **P**), and msd together with principal values and directions. Error estimates reported in parentheses. The asymmetry parameter η=0.564±0.039.

Y	Y_{ij}			k	Principal values, Y_k	Principal θ_k	directions[a] ϕ_k
P	-0.0003 (9)	-0.1766 (38)	-0.0032 (31)	1	-0.2377 (26)	76.2 (8)	53.5 (3)
		-0.0769 (9)	0.0986 (24)	2	0.0519 (24)	124.0 (1.2)	134.0 (0.5)
			0.0772 (9)	3	0.1859 (21)	37.4 (9)	162.2 (6)
msd	1.2075 (86)	0.0824 (41)	0.2080 (409)	1	1.4836 (209)	38.2 (2)	319.8 (4.7)
		1.0221 (91)	-0.2844 (330)	2	1.2212 (95)	79.7 (4.0)	36.4 (8.0)
			1.2136 (62)	3	0.7385 (124)	53.7 (1.9)	118.7 (12.3)

[a]Angle θ measured with respect to the b axis, and ϕ measured from a' towards c.

to obtain accurate thickness and polarization corrections, which are again used in MOSREF for the final refinement. Convergence on thickness and polarization corrections is reached by showing that the last iterations are essentially invariant since the macroscopic efg tensors are very similar - the thickness corrections are about 4-5× larger than polarization. In these iterative corrections, the same experimental background corrected dimensionless areas are always used as input, with just the macroscopic efg tensor updated in each cycle.

With the experimental intensities now corrected to the thin crystal limit, a final MOSREF refinement is carried out over the two symmetry-related sites. The corresponding efg or msd tensor for the second symmetry-related site, generically denoted $\mathbf{Y}_2$, is related to the first by equation 10.42 [18,19].

$$\begin{aligned} \mathbf{Y}_2 &= \mathbf{R}\mathbf{Y}_1\mathbf{R}^{-1} \\ \mathbf{R} &= \begin{bmatrix} -1 & 0 & 0 \\ 0 & -1 & 0 \\ 0 & 0 & 1 \end{bmatrix} \end{aligned} \tag{10.42}$$

The final efg and msd tensors for site 1 are tabulated, with uncertainty, in table 10.6. A plot of the final fits is shown in figure 10.14.

10.4.3. General discussion

The total of 22 FAS Mössbauer measurements (single-crystal and powder) yield the averaged quadrupole splitting of $\Delta E_Q = 1.774 \pm 0.004$ mm sec^{-1} and isomer shift, $\delta = 1.2458 \pm 0.0003$ mm sec^{-1}. As outlined in the chapter 8, the drive unit appears to be linear within experimental uncertainty for a four line iron foil spectrum. However, since the stability and linearity has not been ascertained to an accuracy lower than ≈ 0.001 mm sec^{-1}, these values should not be interpreted as more precise than three decimal places. In the single-crystal results given in table 10.6, the convention of Zimmermann [8] has been followed in taking the sign of $P_{\hat{z}\hat{z}}$ (or the quadrupole splitting) to be negative. Neither the present simulations nor experiments determine this sign, and such determinations are ideally performed experimentally using polarized, or magnetically perturbed low temperature measurements. This microscopic determination permits comparison of the asymmetry parameter, $\eta = 0.564 \pm 0.039$, to the values of 0.6-0.8 determined by Zimmermann [8] for the manifold of solutions from their macroscopic efg. The refined value here is in accord with the lower end of this previously determined range,

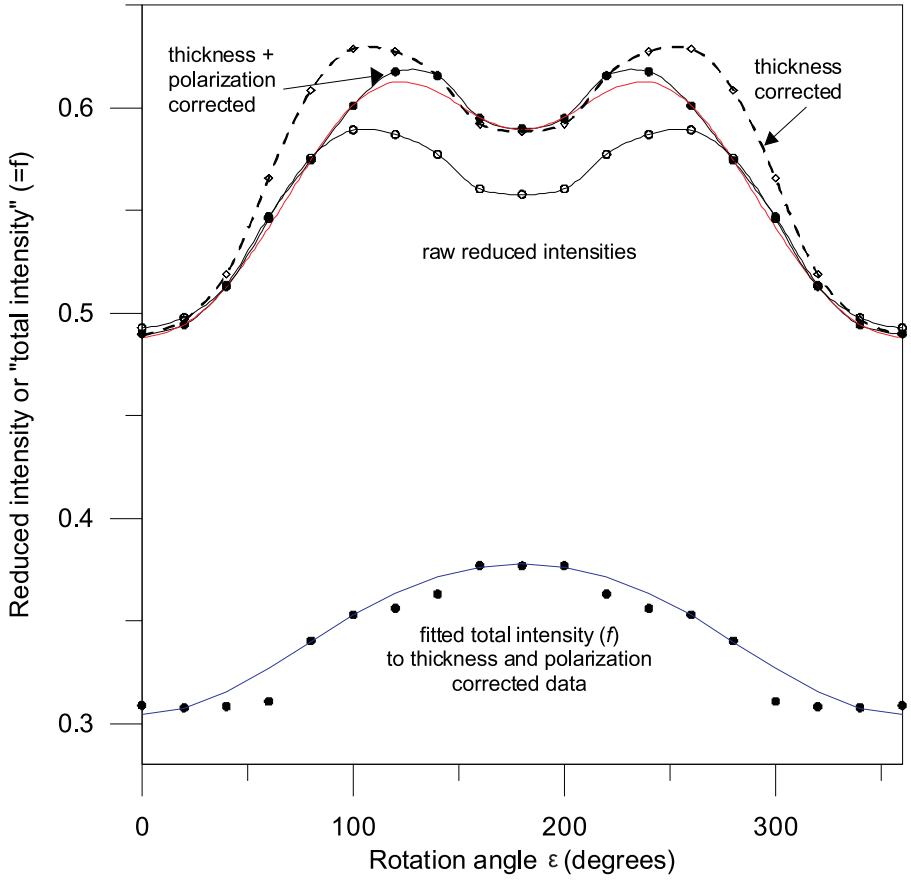

Figure 10.14.: Final fits to experimental intensities: raw in the upper data set; thickness corrected (dashed spline); thickness and polarization corrected (solid spline) points; and the final MOSREF fit to reduced intensities, $I^{(r)}$ in red. In the lower data set are the final MOSREF fit to thickness and polarization corrected total intensities, plotted as (1/2)×total intensity (=f) in blue.

although the previous determination assumed an isotropic approximation, which would not be valid according to these refinements.

The results in table 10.6 and figure 10.14 show that the efg and dimensionless msd tensors have been determined with reasonable precision, for *both* symmetry-related sites in the monoclinic unit cell. That this outcome is possible was first pointed out some years ago [18], and in part prompted development of the program MOSREF. The determining factor for resolution of the ambiguity was whether or not the msd, or equivalently, absorber anisotropic recoilless fractions, could be obtained for ^{57}Fe with sufficient precision to yield meaningful results. Examination of corresponding X-ray determined anisotropic displacement parameters (ADPs) indicate that indeed they could. However, with the exception of the pioneering study of SNP by Housley *et al.* [10], few attempts are reported at reliable Mössbauer determination of msd tensors. Concomitantly, there are few reliable comparisons able to be made between X-ray and Mössbauer determined parameters.

How meaningful are these results? The approximations made and several caveats need to be acknowledged. Firstly, the f values determined from the msd tensor assume the harmonic approximation, where changes

in phonon energy due to coupling between phonons via anharmonic terms in the vibrational Hamiltonian are neglected. Kolk [17] has shown how to calculate several higher order anharmonic terms, which may be parameterized and experimentally evaluated if measurements are sufficiently precise. It is not believed that these measurements, carried out with a weak source, warrant such a procedure. It needs to be noted that aside from the ambiguity arising from two symmetry-related sites in the unit cell, this study considered one of the simplest possible systems. The FAS crystal contains only one type of ferrous high-spin Mössbauer nucleus, with a large quadrupole splitting, yielding well-resolved lines. Further, the single crystal is not too thick (although nearing the high-end limit) yielding sufficiently narrow Mössbauer lines, which through the fitting criterion ($\chi^2 \approx 1$), conform well to Lorentzian line shapes. The curtailed expansion of thickness and polarization corrections is effectively a perturbation procedure, which is valid only under these circumstances. Lastly, a single line unpolarized ^{57}Co source was utilized that is almost purely magnetic dipole (M=1) in character, which greatly simplifies the intensity calculations which are the basis of the parameter fitting program MOSREF.

For a site of $\bar{1}$ symmetry, there is no formal requirement for *any* of the efg and msd tensor principal values to have coaxial principal directions, and analysis of table 10.6 reveals this to be the case; the angles between any two pairs exceed the combined errors. Nor are there any relations between principal directions and crystallographic axes. FAS does represent a difficult system in which to determine any such relations, since the iron octahedron is surrounded by counter ions that would be expected to alter both efg and msd tensor. Interestingly, the $\mathbf{P}_1$ principal direction and msd_2 principal directions are relatively close, however comparison with internuclear vectors from crystallographic data reveal that there is nothing structurally co-incident about this direction. To assist visualization, a two-dimensional projection of efg and msd tensor principal directions are shown in figure 10.15. Analysis of these projections reveals that the msd tensor has no principal directions that are directly co-incidental or coaxial with any one bonding parameter. One might anticipate that for a Mössbauer nucleus located in a low symmetry site no rigid correspondence would exist. The efg tensor does show the largest $\mathbf{P}_3$ principal direction to be close to co-incidental with one bonded H_2O ligand, and appears to point in an "average direction" between this H_2O and SO_4^{2-} counter anion group. Since the efg arises from charge distribution, such an "averaged" direction would be physically sensible. The other respective principal directions must then comply to Cartesian tensor orthogonality conditions. These refinements would therefore indicate that the near octahedral water coordination of the Fe^{2+} site does not solely in major part contribute to the efg tensor. Rather, the entire asymmetric unit needs to be considered, in accord with the conclusions of Gibb [13, 14].

In an "ambiguous" case, such as in the present study, the analysis using a MOSREF input of thin-crystal-limit reduced intensities and total thicknesses will always lead to a solution. But is this solution "correct"? The analysis and author's understanding would indicate that the solution is physically sound. However, there is one further measurement that was made to check that the individual site parameters are meaningful. As noted earlier, this involves experimentally measuring the powder-averaged reduced intensity and comparing this to the experimentally observed reduced intensity for the "thin" powder samples. Carrying out the averaging over all orientations using the refined efg tensor yields the value of 0.5057. By comparison, the fitted reduced areas

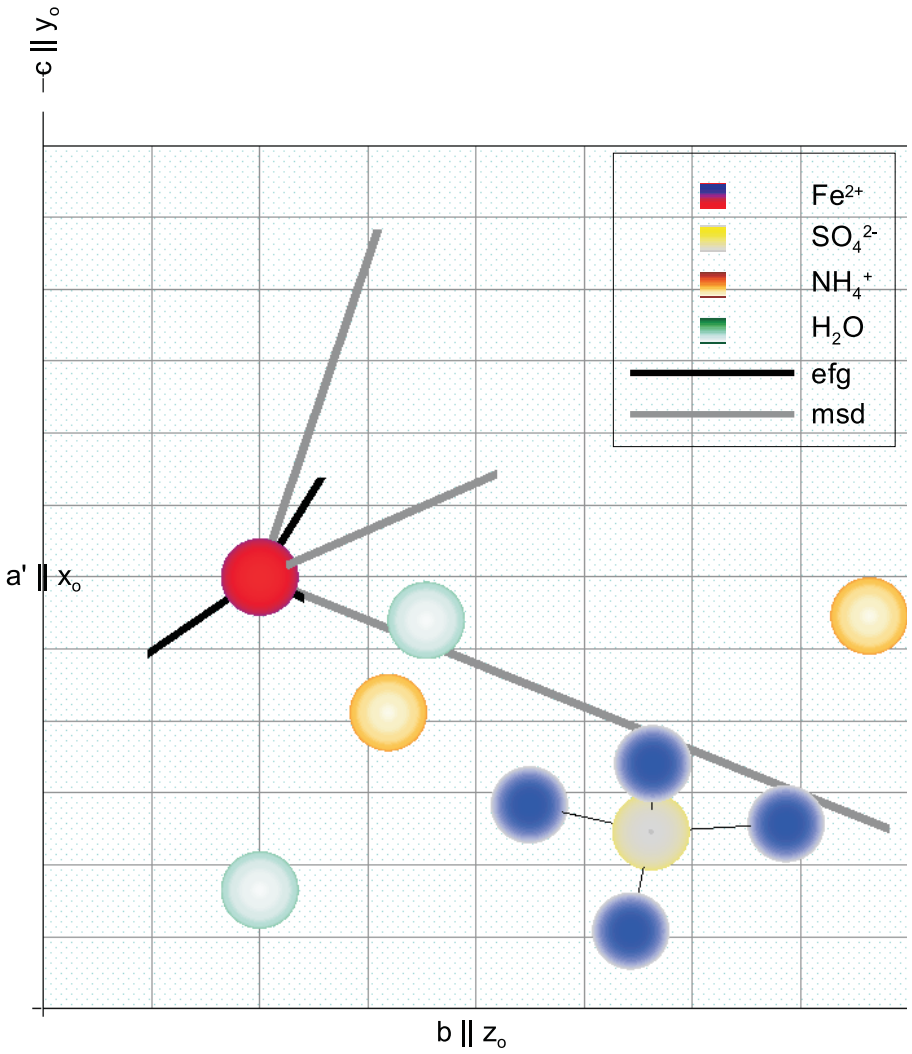

Figure 10.15.: Two-dimensional projection (down $a'||x_o$) of the relationship between site 1 efg (principal values $\times$ 10) and msd tensor principal directions for selection of one all-positive octant of unit cell contents.

for the powder sample perpendicular to the beam was 0.509 $\pm$ 0.005. This result is in agreement with both the X-ray simulated value and the single-crystal experimental refined value. Anisotropy in powder reduced areas can result from sources other than anisotropy in the absorber recoilless fractions (known as the Gol'danskii-Karyagan effect [34, 35]), namely, preferred crystallite orientations (texture) and/or differential relaxation periods in the two wings of the quadrupole doublet [36]. As a test for the former, the powder spectrum of the 0.25 mm thick FAS sample inclined at 45° to the γ-beam was measured, collecting some 1.8 $\times$ 10^6 off-resonance counts, which gave an area ratio of 0.504 $\pm$ 0.004. These data would indicate that even with a very finely powdered sample there is a problem with texture. In the case of uniaxial symmetry, a first-order quantitative estimate of the powder anisotropy may be obtained by simply orienting the powder absorber at $\cos(\frac{1}{\sqrt{3}}) = 54.7°$, the so-called NMR magic angle [37, 38]. The best that can be concluded is that a powder reduced area of approximately 0.504 is in reasonable agreement with the calculated value at 0.5057. A more complete discussion of texture effects in Mössbauer spectroscopy can be found elsewhere [37, 38]. Finally, the X-ray simulated value of 0.5091

is in not-so-good agreement. It is clear from these results that direct observation of anisotropy in the recoilless fractions in powder absorbers is far from simple, even though the anisotropy may be obtained relatively easily from single crystal studies.

A further check is the evaluation of the macroscopic efg tensor, $\mathbf{P}_M$, from averaging the refined microscopic (local) efg tensors, and is given in equation 10.43.

$$\mathbf{P}_M = \begin{bmatrix} -0.0003 & -0.1766 & 0 \\ -0.1766 & -0.0769 & 0 \\ 0 & 0 & 0.0772 \end{bmatrix} \tag{10.43}$$

The principal values of equation 10.43 are P_1=-0.219, P_2=0.142, and P_3=0.077. These may be compared with Zimmermann and Doerfler [7] and Zimmermann [8] values (from equation 10.20) at P_1=-0.227, P_2=0.191, P_3=0.036. In each case, P_3 is directed along the crystallographic unique b axis with respect to the coordinate system. P_2 lies in the plane perpendicular to b, making an angle of ϕ_M=-38.9° with a', where the corresponding Zimmerman-Doerfler angle is ϕ_M=-34.4°. This determination appears to be in good agreement, however it is noted that the efg tensor from [7] and [8] was obtained assuming an isotropic absorber recoilless fraction. The results of the current study would indicate this to be a relatively poor approximation, since if the recoilless fraction were isotropic then an isotropic (i.e. flat, and invariant to angular rotation) total intensity would have been observed. Experimentally, from figures 4 and 5, this is clearly not the case. It is not clear that neglect of anisotropy in the recoilless fraction could account for the differences in the macroscopic intensity tensors between the two experiments. A refinement on the determined macroscopic efg tensor with an averaged isotropic msd tensor and otherwise anisotropic data yields P_1=-0.244, P_2=0.170, P_3=0.074, which is in better agreement to the Zimmerman and Doerfler [7] determination, however with a fitting root mean square displacement (RMSD) over an order of magnitude worse. This would indicate the isotropic approximation to be poor.

Application of equation 10.7 and 10.32, yields the equivalent recoilless fractions corresponding to the principal values of the msd tensor, 1.4836, 1.2212, 0.7385, namely 0.227(3), 0.295(2), 0.478(8). These determinations represent the first time that anisotropic recoilless fractions have been determined for the ambiguous monoclinic case in single crystals. The isotropic recoilless fraction is obtained by averaging the msd principal values and application of equation 10.7, yielding the value of f_{iso} = 0.317(4), in good accord with the polycrystalline (powder) value of 0.27 experimentally determined by Gibb [14], for which the effects of texture are not known.

Our refined efg and msd tensors differ considerably from the microscopic trial values in equations 10.10 and 10.20 respectively. To ensure correct convergence, the elements were systematically altered in both combinations and entire tensors, and when physically sensible converged to the same solution. When not physically sensible (i.e. restriction on number of elements refined upon, and incorrect anisotropy), divergence was obtained without a solution. Had the msd tensor not been experimentally measured and refined by Mössbauer spectroscopy, but assumed to be that determined by X-ray, a rather different efg tensor is obtained, with η=0.73, and a root-mean-

square-displacement (RMSD) fitting over an order of magnitude poorer was obtained, although directionality in agreement with the Mössbauer refinements. The RMSD for the refinement final fit to experimental thickness and polarization corrected intensities is 0.0016 intensity units.

Finally, from the refined msd tensor, the expected $\mathbf{U}_{ij}$ atomic displacement matrix analogous to equation 10.6 was calculated by using the relationship $U_{ij} = (\frac{1}{k^2})msd_{ij}$ in the orthogonal crystal system (x_f, y_f, z_f). This is given in equation 10.44.

$$\mathbf{U}'_{ij} = \begin{bmatrix} 0.0226 & -0.0039 & 0.0015 \\ 0.0015 & 0.0227 & 0.0053 \\ 0.0039 & 0.0053 & 0.0192 \end{bmatrix} \tag{10.44}$$

The trace of this matrix differs from that of equation 10.6 by the constant factor of 1.316. It would be intuitive to expect the principal directions of the two matrices to be similar, yet the angle between the principal directions of the maximum eigenvalues is 7.9°, while the angles between other pairs are around 26°, again indicating substantial deviation (well beyond experimental error) from coaxiality.

10.5. Conclusions

This study is believed to yield for the first time an unambiguous solution to the "ambiguous" monoclinic case, in which the low symmetry Mössbauer nucleus does not sit on a twofold rotation axis. Indeed, it is the case that for space group $P2_1/c$ there exists no twofold rotation axis, and no site in the unit cell may have point-symmetry higher than $\bar{1}$ Laue class. It was however noted that this study represents a well-defined system with narrow, well-resolved lines that, experimentally, are close to Lorentzian line shape. In situations where there might exist more than one type of site, each with its symmetry-related partner(s), and possibly with overlapping lines, a more sophisticated approach than that used here would be required. In particular, the ability to simultaneously fit all angular-dependent spectra and to exactly treat the thickness and polarization problem would be highly desirable. Such a procedure is possible using the software developed by Spiering *et al.* [39], and there are tentative plans to adopt this program in the future. As a final note, the least well-determined experimental data in this study are the total intensities. This is attributed to the use of a weak source, and the relatively large thickness and polarization corrections from use of a thickish crystal. Further consideration of a better treatment of total intensities to improve quality, and therefore reduce errors, is considered in chapter 12.

References

[1] R. Ingalls, K. Ôno, and L. Chandler. *Phys. Rev.*, 172:296, 1968.

[2] R. Ingalls. *Phys. Rev. A*, 133:787, 1964.

[3] R. M. Golding, K. F. Mok, and J. F. Duncan. *Inorg. Chem.*, 5:774, 1966.

[4] K. Chandra and S. P. Puri. *Phys. Rev.*, 169:272, 1968.

[5] P. Zory. *Phys. Rev. A*, 140:1401, 1965.

[6] R. Zimmermann. *Nucl. Instrum. Methods*, 128:537, 1975.

[7] R. Zimmermann and R. Doerfler. 12:79, 1982.

[8] R. Zimmermann. *Advances in Mössbauer Spectroscopy*, pages 273–315. Elsevier, Amsterdam, 1983.

[9] G. A. Bykov and P. Z. Hein. *Sov. Phys. JETP*, 16:176, 1963.

[10] R. M. Housley, R. W. Grant, and U. Gonser. *Phys. Rev.*, 178:514, 1975.

[11] R. Doerfler. *Hyperfine Interact.*, 20:327, 1984.

[12] R. Doerfler. *J. Phys. C: Solid State Phys.*, 20:2533, 1987.

[13] T. C. Gibb. *J. Phys. C: Solid State Phys.*, 8:229, 1975.

[14] T. C. Gibb. *J. Phys. C: Solid State Phys.*, 7:1001, 1974.

[15] H. Spiering. Methodik und Anwendung der Mössbauer Absorptionspektroskopie am ^{57}Fe Habilitationsschrift. Technical report, Fachbereich Mathematik-Physik der Universität Erlangen-Nürnberg, 1978.

[16] V. K. Garg. *J. Inorg. Nucl. Chem.*, 35:2795, 1973.

[17] H. Spiering and H. Vogel. *Hyperfine Interact.*, 3:221, 1977.

[18] W. C. Tennant. *J. Phys.: Condens. Matter*, 4:6993, 1992.

[19] J. A. Weil, T. Buch, and J. E. Clapp. *Adv. Magn. Reson.*, 6:183, 1973.

[20] E. W. Müller. *Mössbauer spectrum fitting program for universal theories.* Institut für anorganische Chemie und Analytische Chemie, Johannes Gutenberg Universtität, Mainz, 1980.

[21] R. N. Brand. *Program NORMOS*. Distributed by Wissenschaftliche Elektronik, GmbH, Germany, 1994.

[22] Richard V. Gaines, H. Catherine W. Skinner, Eugene E. Foord, Brian Mason, and Abraham Rosenzweig. *Dana's New Mineralogy*. John Wiley and Sons Inc., 8 edition, 1997.

[23] G. M. Sheldrick. Shelx-97. Technical report, University of Göttingen, Germany, 1997.

[24] G. M. Sheldrick. *Acta. Cryst. A*, 64:112, 2008.

[25] H. Montgomery, R. V. Chastain, J. J. Natt, Am. M. Witkowska, and E. C. Lingafelter. *Acta. Cryst.*, 22:775, 1967.

[26] F. A. Cotton, L. M. Daniels, C. A. Murillo, and J. F. Quesada. *Inorg. Chem.*, 32:4861, 1993.

[27] C. K. Johnson. *A FORTRAN Thermal Ellipsoid Plot Program for Crystal Structure Illustrations*. Oak Ridge National Laboratory, Oak Ridge, Tennessee, USA, 1965.

[28] K. N. Trueblood, H. B. Bürgi, H. Burzlaff, J. D. Dunitz, C. M. Gramacciolo, H. H. Schulz, U. Shmueli, and S. C. Abrahams. *Acta. Cryst. A*, 52:770, 1996.

[29] R. M. Golding and W. C. Tennant. *Quantum Mechanics in Chemical Physics: An Exploration*. Common Ground Publishing, Melbourne, 2008.

[30] R. L. Collins and J. C. Travis. *Mössbauer Effect Methodology (edited by I. J. Gruverman)*, volume 3. Plenum, New York, 1967.

[31] W. C. Tennant, D. G. McGavin, and H. K. Patterson. Irl report no. 8. Technical report, New Zealand Institute for Industrial Research, 1992.

[32] P. Gütlich, R. Link, and A. Trautwein. *Mössbauer Spectroscopy and Transition Metal Chemistry, Table 7.1.* Springer, Berlin, 1978.

[33] R. W. Grant, R. M. Housley, and U. Gonser. *Phys. Rev.*, 178:523, 1969.

[34] V. I. Gol'danskii, E. F. Makarov, and V. V. Khrapov. *Phys. Lett.*, 3:344, 1963.

[35] S. V. Karyagin. *Sov. Phys. (Solid State)*, 5:1552, 1964.

[36] M. Blume. *Phys. Rev. Lett.*, 14:96, 1965.

[37] J. M. Greneche and F. Varret. *J. Physique Lett.*, 43:L–223, 1982.

[38] U. Gonser H. D. Pfannes. *Appl. Phys.*, 1:93, 1973.

[39] H. Spiering, L. Deak, and L. Bottyan. *Hyperfine Interact.*, 125:197, 2000.

11. Mössbauer and X-ray Single Crystal Study of Ferrous Chloride Tetrahydrate

This chapter describes the elucidation of the microscopic mean square displacement (msd) and electric-field gradient (efg) tensors in a ferrous chloride tetrahydrate, $FeCl_2{\cdot}4H_2O$, single crystal. This chapter contains the draft workings (with some additional content) of a manuscript planned for future publication:

James N. Bull, Christopher M. Fitchett, W. Craighead Tennant, in preparation for *Journal of Physics: Condensed Matter*

This chapter is started by acknowledging Prof. Peter Zory, Department of Electrical and Computer Engineering, University of Florida. As noted in the foregoing ferrous ammonium sulphate hexahydrate (FAS) study, the first Mössbauer study on elucidation of efg tenors from single crystal measurements was that of Zory (1965) [1]. During the course of the following ferrous chloride tetrahydrate (FCL) study, it was realised that the experimental measurements here involving one crystal cut resulted in an indeterminate solution (outlined in detail later). The experience or knowledge required to grow suitably large single crystals and then undertake different cuts was not available. Fortunately, the Zory study utilized Mössbauer measurements from seven different crystal cuts parallel to different planes, and incorporation of one of these measurements could resolve the problem here. An internet search revealed an active email address for Prof. Peter Zory, and through correspondence, an electronic copy of sections of Zory's 1964 thesis that contained the required details. In addition, a paper tape of Mössbauer multi-channel analyser counts was provided for the required crystal cut measurement. This was digitized and allowed a determinate microscopic solution to be found.

One unfortunate and unavoidable caveat with this study is the presence of a small ferric oxidation quadrupole doublet. It will been shown that this does not affect the interpretation, although ideally in hindsight, the crystal should have been polished and sealed under an inert (i.e. nitrogen or argon) and dry environment. No attempt was made to manufacture a new crystal since the crystal that was finally used in this study was the product of $\approx$ 2 years of slow trial and error at growing and polishing!

Overview

This chapter provides a simultaneous investigation of the electric-field gradient (efg) tensor and mean-square-displacement (msd) tensor for the Fe^{2+} ion in ferrous chloride tetrahydrate single crystals at 293 K. This system suffers from the ambiguous monoclinic problem, where previously it was thought that, at best, only a manifold of possible solutions could be obtained for the microscopic (local site) efg and msd tensors by Mössbauer spectroscopy, where two symmetry-related sites contribute to the same quadrupole doublet. Following the foregoing chapters study on ferrous ammonium sulphate (Bull *et al.*, Hyperfine Interact. 194 (2009) 347), simulations are initially performed to determine the expected macroscopic angular dependence of the two line quadrupole doublet utilizing earlier determined macroscopic intensity tensor data, and X-ray determined atomic displacement parameters. The simulation and refinement program, MOSREF, utilizes exact numerical matrix diagonalization in an arbitrary co-ordinate frame using the intensity tensor formalism to calculate Mössbauer intensities for any symmetry site in any crystal space group symmetry. Single crystal Mössbauer spectroscopy measurements are then reported in order to determine anisotropic Lamb-Mössbauer parameters that are proposed to facilitate resolution of the so-called ambiguous monoclinic problem. From the experimental reduced and total intensities corrected to the thin crystal limit, interpretation of the intensity ratios facilitated elucidation of the microscopic efg tensor, and total intensities facilitated elucidation of the msd for the two symmetry-related sites. This is achieved by refinement options of MOSREF, where the calculated microscopic intensities are averaged over the two symmetry-related sites to yield the macroscopic spectrum which is fitted to the experimental measurement. The successful determination requires sufficient anisotropy in the recoilless fractions, since in principle, the msd and efg tensors completely describe a single quadrupole doublet of a Mössbauer spectrum. A microscopic solution is reported that appears physically sound, and when averaged, reproduces other previously reported experimental parameters assuming the isotropic approximation. Further, these experiments and anisotropic refinements show the isotropic approximation assumed in all previous studies on this species to be invalid.

11.1. Introduction

Ferrous chloride tetrahydrate, $FeCl_2{\cdot}4H_2O$, denoted hereafter as FCL, is a well-known inorganic ferrous high-spin species that is hygroscopic and readily oxidized to ferric containing species under normal atmospheric conditions. There have been a number of previous studies that have reported the determination of the electric-field gradient (efg) tensor in FCL single-crystals by Mössbauer spectroscopy. The first, and most well-known, is that of Zory [1] who derived algebraic expressions for the intensity orientation dependence of a quadrupole doublet in the principal axis system of the efg tensor for the low symmetry case, where the asymmetry parameter, $\eta \neq 0$. He then utilized these equations to obtain the efg from seven different crystal cuts, including three orthogonal orientations of the laboratory axis system, $a' = c \times b, c, b$ of the monoclinic $P2_1/c$ space group of FCL. Based on this efg, Zory correctly inferred the sign of the quadrupole splitting as positive, and indicated the presence of anisotropy in the recoilless fraction, f.

Unfortunately, it was not recognized in Zory's study [1], as first pointed out by Zimmermann [2], that the efg obtained by Zory was in fact a macroscopic tensor arising from the composite quadrupole doublet of two symmetry-related Fe^{2+} sites in the monoclinic unit cell. Crystallographically, these two sites are related by a rotation π and translation about the crystallographic unique b axis. Zimmermann [2] determined the efg using the intensity tensor formalism in the principal axis system, where the boundary limits of a manifold of solutions were determined, from which one solution would correspond to the microscopic (local) site efg. The second site efg would be symmetry-related to the first. Both the Zory [1] and Zimmerman [2] studies assumed the "thin crystal approximation", where thickness and polarization effects to measured intensities were neglected by assuming the crystal was sufficiently thin. Gibb [3], using a polarized Mössbauer source, and Spiering and Vogel [4], redetermined the macroscopic efg for FCL, each attempting thickness and polarization corrections. The Spiering and Vogel [4] study used a single crystal essentially four times the thickness of Zory's cuts, and found the macroscopic efg in the thin crystal limit to be very similar to that derived from Zory's raw data [1]. The former of these two studies determined the principal axis of the efg tensor to be almost coaxial with the Fe-Cl bond, and the asymmetry parameter, $\eta = 0.40 \pm 0.15$, which was significantly larger than the Zory [1] or Zimmerman [2] values at $\eta \approx 0.1$ and $\eta = 0.25 \pm 0.15$ respectively. All of these previous studies assumed isotropic displacement and Lamb-Mössbauer (recoilless fraction) parameters. Gibb utilized a polarized source, allowing magnetically perturbed measurements, and determined e^2qQ (equivalent to $eP_{\hat{z}\hat{z}}Q$ in this paper) to be positive in agreement with Zory [1], and other temperature measurements of Grant *et al.* [5], Siebke *et al.* [6] and spectra below the Néel temperature by of Ono *et al.* [7]. Gibb [3] deduced the assumed isotropic recoilless fraction of 0.28 ± 0.02, which is in agreement with the previously reported powder value of 0.29 reported by Kerler and Neuwirth [8], which was used by Spiering and Vogel [4].

Several key outcomes from all the previous macroscopic efg studies need to be stated. Firstly, the sign of the quadrupole splitting was assumed or determined to be positive in all cases. Secondly, the largest macroscopic efg principal axis is approximately 40° to 45° inclined to the b-axis that would crystallographally bisect a Fe-Cl

and Fe-O bond, and also the smallest efg axis appears to be coaxial with the crystallographic c-axis, which crystallographically bisects two Fe-O bonds. For a site of such low symmetry there exists no formal requirement for any efg, msd or unit cell axes to be coaxial, which was shown to be the case in the foregoing chapters ferrous ammonium sulphate hexahydrate (FAS) study [9]. It could be expected that near symmetrical bonding interactions could result in approximate coaxiality of efg and msd tensors to unit cell or contents.

In the work reported herein, an attempt has been made to measure the mean-square-displacements (msds) of the Fe^{2+} directly from Mössbauer measurements, and therefore to obtain estimates of anisotropy in the related absorber recoilless fractions, assuming that such an anisotropy is measurable. These procedures have been applied in a recent study [9], to obtain values for both efg and msd tensors in FAS single-crystals, with the assumptions that generally the msd tensor will be anisotropic, and in *favourable* circumstances calculations involving an anisotropic msd can resolve the ambiguity problem from two symmetry-related sites contributing to the same quadrupole doublet [10]. By *favourable* circumstances it was implied that anisotropy is adequate, which is assumed since total intensity in the angular rotations reported herein show strong anisotropy, and good fit to an anisotropic msd tensor (or alternatively f fraction). Several caveats should however be outlined as follows. To obtain the msd tensor from Mössbauer measurements, good estimates of total intensities of the quadrupole doublet, expressed as dimensionless quantities, need to be obtained. As first indicated by Grant *et al.* [11] in their pioneering study on sodium nitroprusside, the msd is a symmetric second-rank tensor and usually many more orientation-dependent spectra are required for its determination than for the efg tensor. The measurements reported herein were restricted to a cone of orientations obtained by rotating a crystal about the perpendicular to the bc plane oriented at 45° to the γ-beam. The bc plane is the natural growth habit of FCL single crystals, which are readily doubly-polished parallel to this plane for Mössbauer experiments. This provides a large number of general orientations, yet as will be shown later, these intensities are still insufficient to fully describe the msd tensor, with some data from the original Zory [1] study required to yield a convergent refinement.

Nevertheless, following the foregoing chapters ferrous ammonium sulphate hexahydrate (FAS) study [9] (and in the foregoing chapter), the expected angular dependence of the intensity ratio and total intensities were simulated based on ADPs measured in this laboratory from a precise X-ray structure determination, and the macroscopic intensity tensor reported by Spiering and Vogel [4]. A number of simulations within the manifold of solutions were performed to assess how the solutions change the observed total and reduced intensities. One such set will be presented. This procedure is semi-qualitative, since to date, all measurements of Mössbauer-derived msd tensors show larger magnitude displacements, and do not necessarily have direct correspondence to X-ray derived parameters [9, 11]. For this reason care must be taken to ensure different guess parameters converge to the same solution. It was however observed that these predictions yield sufficiently good representation of observed reduced ratio and total intensities to confidently match experimental crystallographic orientations, in order to obtain first estimates of the msd tensor (and anisotropic recoilless fractions). Next, experimental intensities for the single crystal angular rotations are reported, and γ-beam corrections to the infinitely thin

crystal limit as first outlined by Housley *et al.* [12], further detailed by Zimmermann [13] and used by ourselves more recently [9] are performed. With these experimentally corrected intensities, MOSREF refinements are performed to determine a physically-sound unique microscopic efg and msd tensor solution. This is followed by an interpretation and comparison with previous macroscopic measurements.

11.2. Theoretical overview

11.2.1. Crystallography and intensity-tensor relationships

FCL crystallizes in the monoclinic space group $P2_1/c$ with two crystallographically equivalent Fe^{2+} sites per unit cell, with each exhibiting point-group symmetry 1 (Laue class $\bar{1}$) and the two being related by a rotation π about the crystallographic monoclinic unique axis, b. The crystal structure at 293(2) K has previously been established using recrystallized Analar FCL with Mo K_α radiation. Briefly, for space group $P2_1/c$, the unit cell parameters were, in units of Å: a=5.8765(3); b=7.1100(3); c=8.4892(5); and $\beta = 111.096(1)^\circ$. The crystallographic R factor was 1.51% for 927 reflections. Although neutron diffraction studies [14], with R factors three times those obtained for this work, had given indications of the two subtly different Fe^{2+} sites owing to tilt angle on two co-ordinated water molecules, such differences if real would be indeterminate in Mössbauer measurements.

The X-ray determined atomic displacement parameters (ADPs) in space group $P2_1/c$ for Fe^{2+}, in units of $Å^2$, and referred to in the crystal reference frame are: U_{11}=0.00945(19); U_{22}=0.01449(19); U_{33}=0.00937(19); U_{12}=0.00125(6); U_{13}=0.00386(13); and U_{23}=0.00030(7). These are expressed in matrix form in equation 11.1.

$$\mathbf{U} = \begin{bmatrix} 0.00945 & 0.00125 & 0.00386 \\ 0.00125 & 0.01449 & 0.00030 \\ 0.00386 & 0.00030 & 0.00937 \end{bmatrix} \tag{11.1}$$

For the experiments reported herein, the reference frame convention employed in earlier studies [1, 3, 4] has been selected in choosing an orthogonal set of axes (a', c, b)=$(c\times b, c, b)$, where a, b, and c are the crystallographic axes. The reference frames considered in this study are illustrated in figure 11.1.

The reported simulations and refinements require a set of orthogonalized displacement parameters, U_{ij} (in units of $Å^2 = 10^{-16}$ cm^2) referred to the laboratory axes (x_0, y_0, z_0)=$(c \times b, c, b)$. The above X-ray $\mathbf{U}$ matrix in equation 11.1 can be orthogonalized to matrix $\mathbf{U}^C$, with application of the non-orthogonal transformation given in equation 11.2.

$$\mathbf{U}^C = \mathbf{AUA}^T \tag{11.2}$$

where superscript 'T' indicates the matrix transpose of $\mathbf{A}$. Following Trueblood *et al.* [15], the transformation

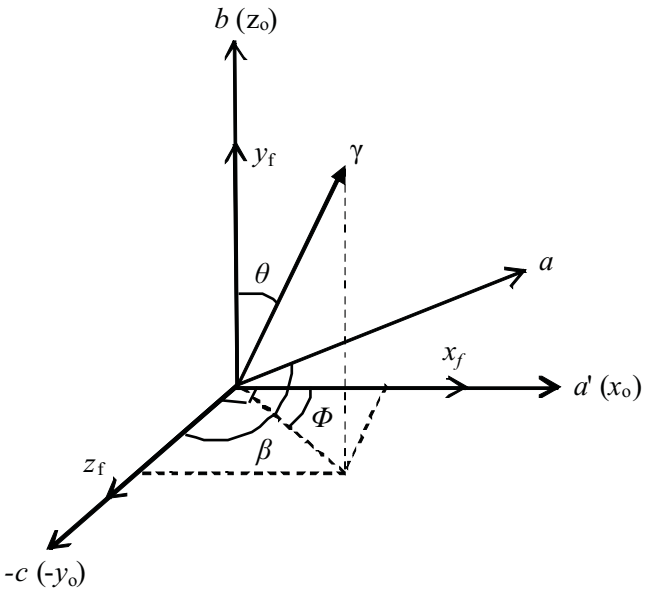

Figure 11.1.: The relationships between crystal unit cell edges (a, b, c), crystal Cartesian coordinates (x_f, y_f, z_f) and the orthogonal set (x_0, y_0, z_0) chosen as the "laboratory" set.

matrix **A** for the general monoclinic case is given in equation 11.3.

$$\mathbf{A} = \begin{bmatrix} a & 0 & c\cos\beta \\ 0 & b & 0 \\ 0 & 0 & c\sin\beta \end{bmatrix} \begin{bmatrix} a* & 0 & 0 \\ 0 & b* & 0 \\ 0 & 0 & c* \end{bmatrix} \tag{11.3}$$

where "*" denotes the reciprocal space unit cell parameter. The final orthogonalized $\mathbf{U}^C$ matrix is given in equation 11.4.

$$\mathbf{U}^C = \begin{bmatrix} 0.00906 & 0.00122 & 0.00052 \\ 0.00122 & 0.01449 & 0.00030 \\ 0.00052 & 0.00030 & 0.00937 \end{bmatrix} \tag{11.4}$$

The simulations also require the so-called mean square displacement (msd) tensor, whose dimensionless elements can be defined in terms U_{ij}^C by equation 11.5.

$$\mathbf{msd}_{ij} = k^2 U_{ij}^C \tag{11.5}$$

where for the X-ray Mo K_α radiation, $k^2 = \dfrac{4\pi^2}{\lambda^2} = 78.1605 \times 10^{16}$ cm^{-2}, with $\lambda = 0.7107$ Å being the wavelength of the (averaged fine-split) X-ray radiation, and U_{ij}^C are the displacements along wave vector **k**. The dimensionless msd tensor in the Cartesian crystal reference is then given in equation 11.6.

$$\mathbf{msd}_f = \begin{bmatrix} 0.70804 & 0.09567 & 0.04084 \\ 0.09567 & 1.13255 & 0.02345 \\ 0.04084 & 0.02345 & 0.73236 \end{bmatrix} \tag{11.6}$$

To transform $\mathbf{msd}_f$ into the laboratory reference frame, it can be see from figure 11.1 that a 90° clockwise rotation about the $a'||x_o$ axis is required. Application of this rotation then yields the final X-ray guess microscopic msd tensor given in equation 11.7.

$$\mathbf{msd}_0 = \begin{bmatrix} 0.70804 & -0.04084 & 0.09567 \\ -0.04084 & 0.73236 & -0.02345 \\ 0.09567 & -0.02345 & 1.13255 \end{bmatrix} \tag{11.7}$$

Hereafter, the $\mathbf{msd}_0$ tensor will be denoted simply as msd. Following Bull *et al.* [9], the orthogonalization given in equation 11.4 was identically reproduced by the so-called ORTEP [16] probability co-variance matrix. This is the completely X-ray determined microscopic msd tensor that, in principle, is analogous to the Mössbauer msd tensor that will be independently determined herein for FCL.

Within the Debye or Einstein models of a crystalline lattice, the nuclear Lamb-Mössbauer factor, f_i, for crystal orientation i, which is generally assumed to be anisotropic (although has always been taken as isotropic in previous studies), is the probability of a recoilless resonant absorption and emission process, and is related to the msd by equation 11.8. This is otherwise known as the recoilless fraction for a given orientation.

$$f_i = e^{-\langle r^2 \rangle_i} \tag{11.8}$$

where the scalar (expectation value) dimensionless displacement quantity, $\langle r^2 \rangle_i$, for each crystal orientation, i, is in turn described by spherical polar co-ordinate pairs (θ, ϕ), and is given in equation 11.9.

$$\langle r^2 \rangle_i = \langle (\sin\theta_i \cos\phi_i, \sin\theta_i \sin\phi_i, \cos\theta_i) | \mathbf{msd}_0 | \begin{pmatrix} \sin\theta_i \cos\phi_i \\ \sin\theta_i \sin\phi_i \\ \cos\theta_i \end{pmatrix} \rangle \tag{11.9}$$

In order to simulate and refine experimental data, an approximate microscopic efg tensor is required. Following the foregoing chapters studies on ferrous ammonium sulphate hexahydrate [9], the efg tensor will be expressed in the Zimmermann [2] intensity tensor formalism where, in addition to the requirements of zero trace, the invariant given in equation 11.10 holds in an arbitrary reference frame.

$$P_{zz}^2 + \frac{1}{3}(P_{xx} - P_{yy})^2 + \frac{4}{3}(P_{xy}^2 + P_{xz}^2 + P_{yz}^2) = \frac{1}{16} \tag{11.10}$$

For this microscopic efg tensor guess, the macroscopic efg of Spiering and Vogel [4] was adopted, which in the Zimmermann traceless formalism can be expressed in equation 11.11. Spiering and Vogel [4] used the (100)

plane and performed angular rotations with the rotation axis inclined at 20° to the γ-beam. The P_{xy} element is very small, and is not well determined at ≈ 0 within experimental error.

$$\mathbf{P}_M = \begin{bmatrix} -0.0755 & 0 & P_{xz} \\ 0 & 0.1470 & P_{yz} \\ P_{xz} & P_{yz} & -0.0715 \end{bmatrix} \tag{11.11}$$

From application of the invariant in equation 11.10, the manifold of solutions is determined to have the boundary condition $P_{xz}^2 + P_{yz}^2 = 0.030664$, representing the manifold of possible microscopic solutions. Hereafter, the microscopic intensity tensor will be denoted simply as efg in the text. Together with the X-ray determined msd tensor in equation 11.7, simulations will be considered in three limiting cases of this guess efg tensor:

1. $P_{xz} = 0$ when $P_{yz} = \pm 0.17511$
2. $P_{yz} = 0$ when $P_{xz} = \pm 0.17511$
3. $P_{xz} = P_{yz} = \pm 0.12382$

Briefly, these systematic simulations are performed since they produce some slight asymmetry in reduced intensity and total intensity curves. Experimentally, as will be seen later, this feature was also observed. By undertaking this series of simulations, information can be gained to characterize the subtle observed asymmetries, and ensure that there are not two or more different possible starting parameters that may yield sensible refinement solutions. These simulations are discussed in detail in a later section.

11.2.2. The goniometer assembly

FCL crystallizes most commonly as flat (100) plates that contain both the b and c crystallographic axes. In this work, Mössbauer single-crystal spectra were recorded by rotating the crystal about the perpendicular (the vector along unit cell edge a') to the bc plane on a single-circle goniometer inclined at $\eta = 45°$ to the γ-beam direction. The beam then traces out a right-circular cone in the crystal where the measured directions lie on the surface of the cone, with a full 360° rotation required to obtain a repeat spectrum. An analytical expression is required to relate laboratory and crystal Cartesian reference frames. This expressions is constructed from the product of the single crystal the rotation matrix, $\mathbf{R}_\varepsilon$, that describes the rotation about a' ($\theta = \frac{\pi}{2}, \phi = 0$), which is the normal to the (100) plane in the laboratory reference frame, and the general goniometer inclination vector with the rotation axis inclined at $\vartheta = 45°$ to a' that initially lies in the ac plane, with ($\theta = \frac{\pi}{4}, \phi = 0$). The resultant vector, $\mathbf{B}$, from rotating by angle ε is given in equation 11.12.

$$\mathbf{R}_\varepsilon \times \begin{bmatrix} \sin\vartheta \\ 0 \\ \cos\vartheta \end{bmatrix} = \begin{bmatrix} 1 & 0 & 0 \\ 0 & \cos\varepsilon & \sin\varepsilon \\ 0 & -\sin\varepsilon & \cos\varepsilon \end{bmatrix} \times \begin{bmatrix} \frac{1}{\sqrt{2}} \\ \frac{1}{\sqrt{2}}\sin\varepsilon \\ \frac{1}{\sqrt{2}}\cos\varepsilon \end{bmatrix} = \mathbf{B} \tag{11.12}$$

The vector $\mathbf{B}$ is therefore the general vector yielding direction cosines for the γ-beam parallel to the cone surface for any given rotation angle ε. Further, any rotation angle, ε, has a partner $\varepsilon + \pi$, where this pair of

angles is coplanar with the rotation axis, a'. This analytical expression is considerably simpler than that for the FAS [9] angular rotations, owing to that fact that FCL naturally crystallizes in a more fundamental (simple) plane. Appropriate simulation spherical polar (θ, ϕ) angles are given in table 11.1 for ε in 20° increments following experimental procedure.

Table 11.1.: Simulation polar (θ) and azimuthal (ϕ) angles for rotating the general γ-beam projection vector about the laboratory rotation angle ε, in the defined reference frame. All angles in degrees.

$\varepsilon \pm 0.5°$	θ	ϕ
0	45.0000	0.0000
20	48.3589	18.8817
40	57.2022	32.7324
60	69.2952	40.8934
80	82.9470	44.5615
100	97.0530	44.5615
120	110.7048	40.8934
140	122.7978	32.7324
160	131.6411	18.8817
180	135.0000	0.0000
200	131.6411	-18.8817
220	122.7978	-32.7324
240	110.7048	-40.8934
260	97.0530	-44.5615
280	82.9470	-44.5615
300	69.2952	-40.8934
320	57.2022	-32.7324
340	48.3589	-18.8817
360	45.0000	0.0000
perpendicular	90.0000	0.0000
Zory (010)	0.0000	0.0000

11.2.3. Intensity calculations

Since each site contributes to the same two line quadrupole doublet, following Bull *et al.* [9] and the requirements of the simulation and refinement program MOSREF [10], reduced intensities, $I^{(r)}$, which are defined in equation 11.13, are calculated. Reduced intensities are used in interpretation rather than the traditional intensity ratios that were employed in previous studies [1, 4], since the former can be used in an additive manner.

$$I^{(r)} = \frac{I_l^0}{I_l^0 + I_u^0} \tag{11.13}$$

where I_l^0 and I_u^0 are lower and upper line intensities respectively in the thin crystal limit, designated by superscript zero. These intensities are calculated for a single quadrupole doublet over a 2π angular range on the surface of a cone in the crystal, as traced out by the γ-beam shown in figure 11.2. Experimentally, these intensities are determined from fitted areas, which following thickness and polarization corrections, are termed "thicknesses", and denoted p_l^0 and p_r^0 respectively.

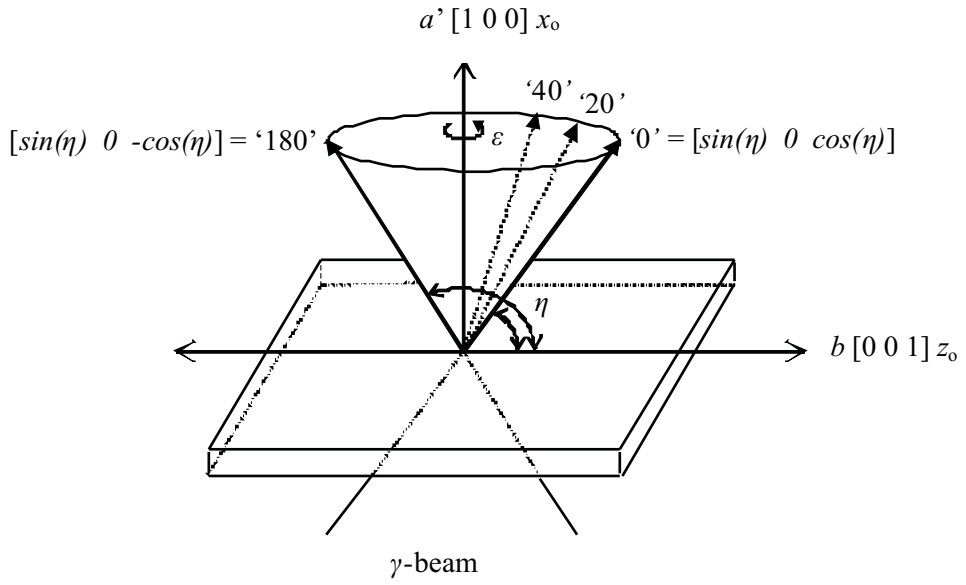

Figure 11.2.: Relationship between the laboratory and crystal reference frames, and the angular rotation by ε about $a'||x_o$. For the reported experiments, $\eta = 45°$, and 90° for the "perpendicular" measurement.

The refinement and simulation program MOSREF utilises exact numerical diagonalizations of the quadrupole doublet Hamiltonian matrix in an arbitrary reference frame. The total intensity in the FCL case results from the sum over two symmetry-related sites. In MOSREF the normalization over the eight possible hyperfine transitions between ground ($I = \frac{1}{2}$) and excited ($I = \frac{3}{2}$) states is to unity. Then the total intensity for n symmetry-related sites, for a given orientation, i, as determined from equations 11.8 and 11.9, is given in equation 11.14.

$$\begin{aligned} & f_i \times n \times 1 = f_i \times n \\ & \text{or} \\ & \frac{f_i \times n}{n} = f_i \text{ per site} \end{aligned} \tag{11.14}$$

The program MOSREF, internally uses microscopic parameters to calculate the required tensors for both sites, which are appropriately added or averaged to yield the observed macroscopic spectrum. This procedure is then used in reverse to fit an efg and msd tensor to experimental macroscopic data, using appropriate (θ, ϕ) direction cosines for each measurement of reduced and total intensities. In principle, the macroscopic efg tensor is always obtainable from single crystal measurements, and in the appendix to this chapter, an alternative (algebraic) method of determining a macroscopic efg from a minimal set of measurements is outlined.

The simulated angular dependence of the reduced and total intensities in the experimental crystal plane, assuming the guess X-ray msd tensor and Spiering and Vogel macroscopic efg tensor for the case that $P_{xz} = 0$, $P_{yz} = \pm 0.17511$, are shown in figure 11.3. The choice of off-diagonal elements are those that are similar to the final solution reported later, and those that reproduce the subtle but observable experimental total and reduced

intensity asymmetries also reported later.

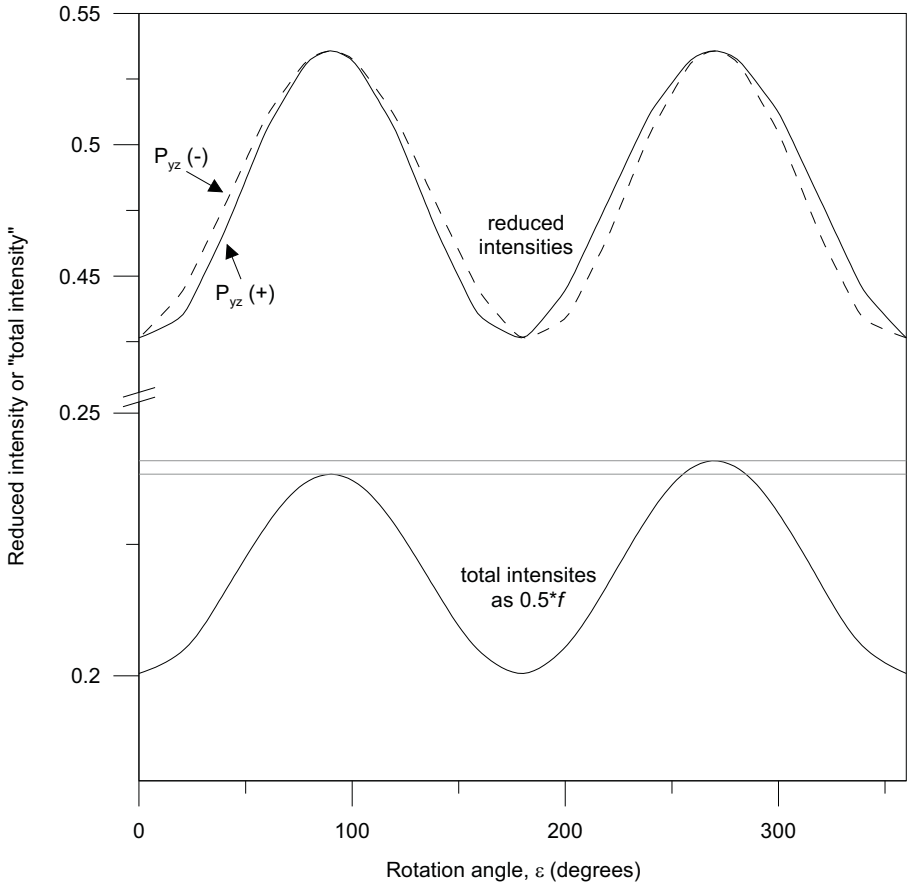

Figure 11.3.: Simulated averaged reduced and total intensities (as $0.5 \times f$) for both sites from Spiering and Vogel (1977) macroscopic efg tensor with $P_{xz} = 0, P_{yz} = \pm 0.1751$, and the X-ray determined msd tensor, plotted as a function of laboratory rotation angle, ε.

The functional form of calculated asymmetry for both total and reduced intensities is quite different from that calculated or experimentally observed in the foregoing chapters FAS study [9]. This difference is not unexpected, since these studies considered two quite different crystal cuts for the same space group. Briefly, the FAS study involved a single crystal rotation axis that was almost coaxial to the crystallographic b-axis, which in turn is the translational symmetry unique axis in the $P2_1/c$ space group. In contrast, for FCL, the b crystallographic axis lies in the plane of the crystal and is orthogonal to the rotation axis, and generally when there exists no formal requirement for coaxailty of principal directions of efg or msd tensor and unit cell axes, then different angular dependences would be expected.

11.3. Experimental

All Mössbauer (transmission) experiments were performed on a PC-based ORTEC multichannel scaling system together with ELSCINT drive electronics operated in constant acceleration mode. A ^{57}Co/Rh source of nominal strength 5 mCi was used as the γ-ray source, and a standard iron foil of thickness 12.7 μm as the velocity and isomer shift calibrant.

Large single crystals were grown by recrystallizing Analar FCL of $\approx$ 99.9% purity in MilliQ water that was acidified with concentrated hydrochloric acid. To minimize oxidation during preparation, solvent evaporation was performed in a sealed desiccator that was initially kept under slight vacuum, with concentrated sulphuric acid dehydrant. A large pentagonal shaped crystal of dimensions of approximate dimensions 6×4 mm was selected, and following washing with concentrated hydrochloric acid, was lightly polished on one surface. This polished face was then super-glued to a 0.5 mm thick perspex disc, which was mounted in a brass polishing guide, and hand polished to a final thickness of 0.138 $\pm$ 0.001 mm. A coating of araldite glue was then applied to cover the exposed crystal surface, providing a seal from atmospheric moisture and oxidizing conditions. A blank measurement of araldite glue applied to a similar perspex disc showed no resonant absorptions or sizeable γ-beam attenuation. The crystal was ascertained to be single by observation under a polarizing microscope which revealed sharp extinctions at 90° rotation intervals. The doubly polished crystal and mount was located on a single circle goniometer, which was mounted on the end of a brass collimator with the goniometer rotation axis making a $\eta = 45°$ angle with the γ-beam. Single crystal spectra were collected over the full 360° rotation at 20.0 $\pm$ 0.5° intervals. Background corrections due to high energy γ-rays were determined using 0.25 mm and 0.27 mm thick copper foils. The contribution of dark counts to the gas-proportional counters was negligible. Two different measurements were performed: the first at the perpendicular orientation with absorber thickness 0.138 mm; and the second for the 45° inclined rotations with a 0.195 mm effective thickness. All spectra at the 45° inclination accumulated approximately 1×10^6 off-resonance counts, and the perpendicular orientation accumulated 2×10^6 off-resonance counts. A fine polycrystalline powder was prepared by grinding a small sample of recrystallized FCL in a low viscosity polyphenyl ether oil, which was then weakly compressed into a perspex capsule giving a 0.5 mm absorber thickness. The oil was used in order to prevent rapid oxidization occurring on grinding, and the final spectra revealed no ferric oxidation, indicating reasonable atmospheric isolation. Spectra were recorded at both the perpendicular and the 45° inclined angle, collecting some 1×10^6 off-resonance counts in each case.

All single crystal spectra were fitted with two quadrupole doublets of Lorentzian line shape, and no attempts were made to include more general Voigt line shapes since all fits revealed good $\chi^2 \approx 1$ parameters and showed no systematic residual (unfitted) intensity. Fits were identical using the program MOSFUN [17] and NORMOS [18], with two representative spectra shown in figure 11.4. The fitted powder spectrum in the perpendicular orientation is shown in figure 11.5. As will be outlined later, these measurements did not contain sufficient projection of one principal direction of the msd, and was therefore indeterminate in the refinements.

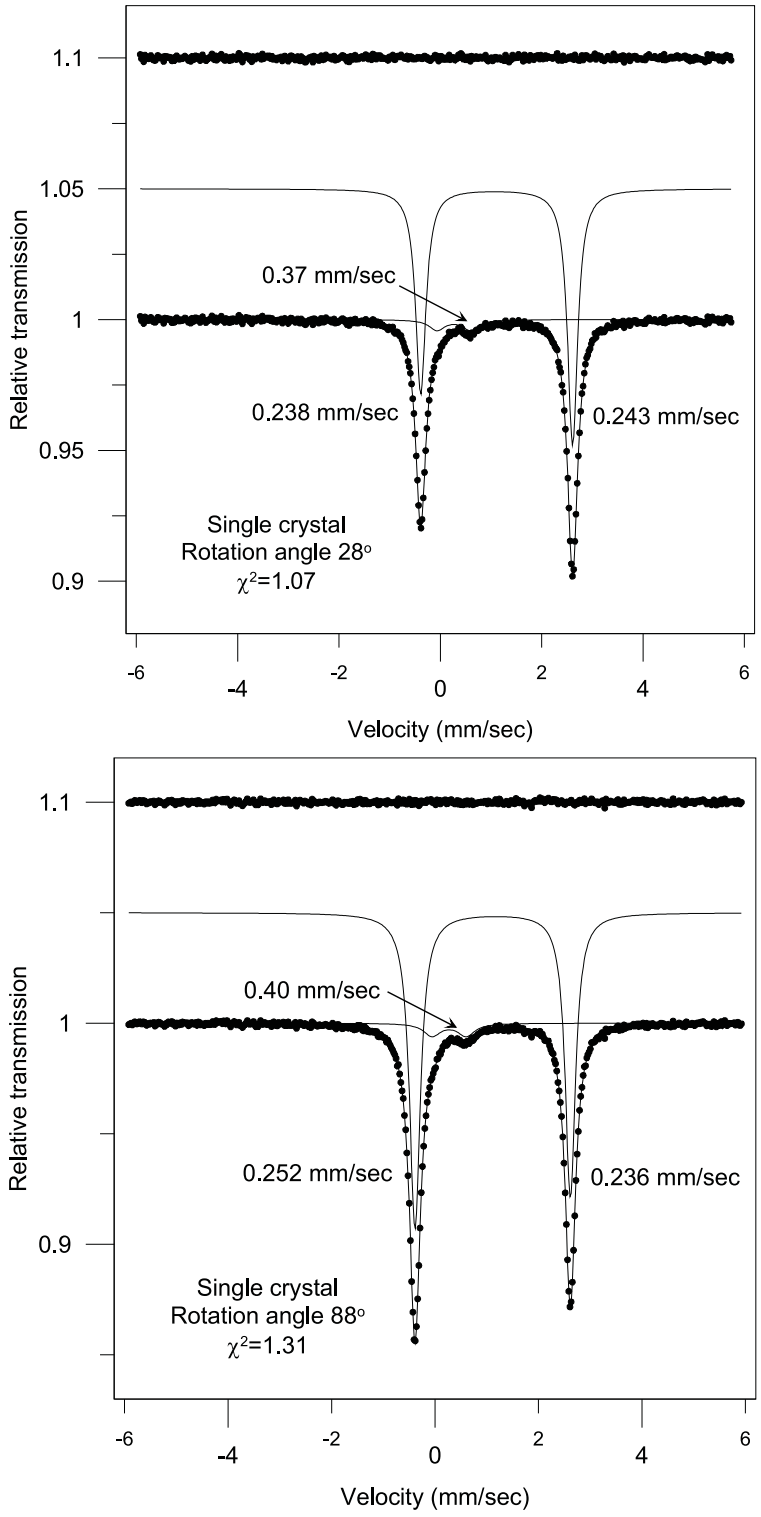

Figure 11.4.: Representative single crystal spectra for FCL showing for each the residual (unassigned) intensity, the doublet sub-spectra fit, and the final fit to raw data. χ^2 fitting parameters and the line widths (FWHM) are given for each. The lower χ^2 fit represents the "worst" fit for all angular rotations.

As a solution, the data for one measurement reported by Zory [1] was digitized and fitted, with the final fit shown in figure 11.6. This data was reportedly recorded at 300 K, using a 10 thou (0.254 mm) thick single

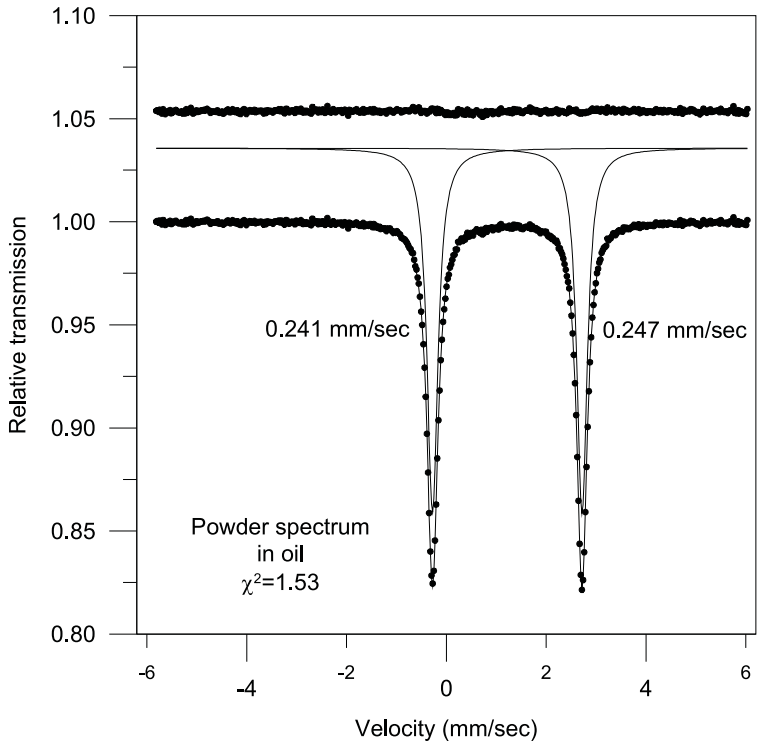

Figure 11.5.: Representative powder (polycrystalline) spectra for FCL showing for each the residual (unassigned) intensity, the doublet sub-spectra fit, and the final fit to raw data. χ^2 fitting parameters and the line widths (FWHM) are given for each.

crystal cut.

Unfortunately the single crystal preparation was not ideal, and one complication must be outlined. Due to the rapid oxidization of FCL, all spectra show some unavoidable ferric oxidation product. Presumably this occurred after polishing while the araldite coating was curing. This ferric quadrupole doublet was fitted using a symmetrical (i.e. angle independent) quadrupole doublet, where the ferric was assumed to be a randomly oriented powder present on the crystal surface. The intensity of the quadrupole doublet varies between approximately 6% to 12% of the total spectrum intensity, and to a good approximation is angle independent as shown in figure 11.7.

Several additional experimental measurements were made in order to minimize resonant aberration (and cosine smeared) effects of a γ-radiation penumbra that is schematically outlined in figure 11.8. These small errors occur since the aperture of the detector is larger than the aperture of the radiation collimator for close separations. The detector is required to be as close as possible to minimize distance attenuation. To check the significance of these effects, a lead shield fabricated from Analar quality material was constructed and mounted around the detector with a 6 mm diameter entrance and exit aperture. The incorporation of an exit aperture minimizes the potential for black-body resonances of initially unabsorbed or background radiation of any wavelength within the detector housing. In the perpendicular orientation, the center of the circular

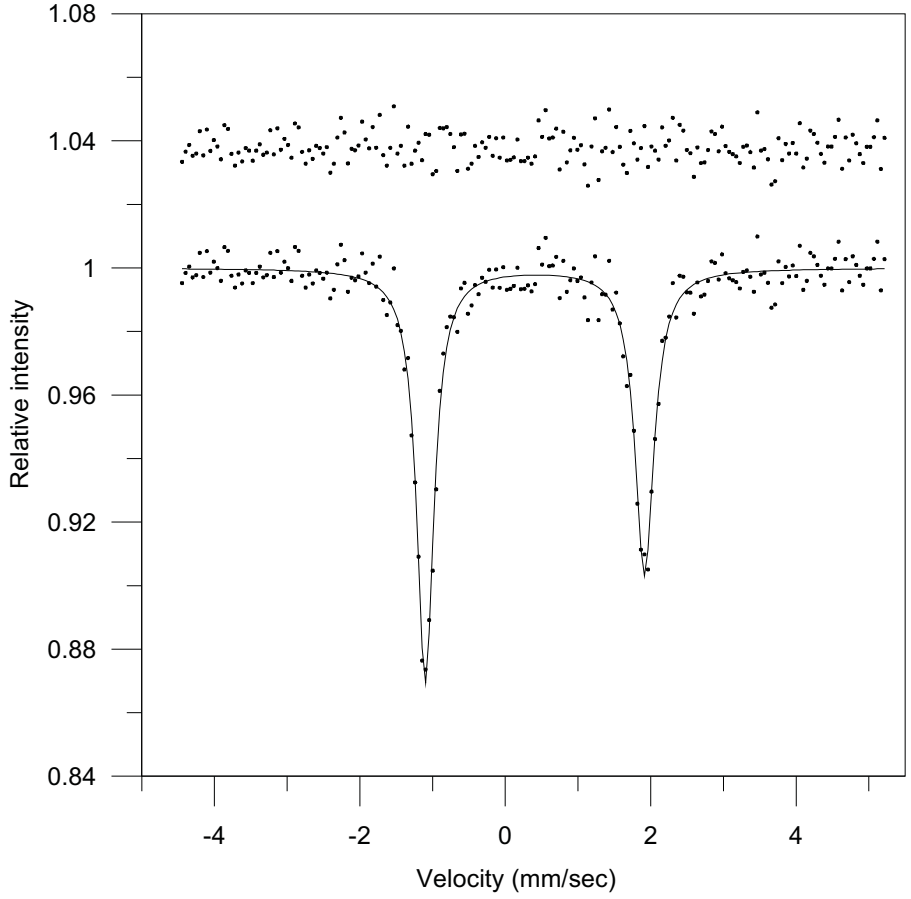

Figure 11.6.: Mössbauer spectrum for the (010) single crystal cut and measurement of FCL, fitted and linearised from the sinusoidal (harmonic) drive data of Zory (1965).

detector window is a few millimetres away from the sample, whereas in the 45° inclined angular rotations, the single crystal is mounted on a single-circle goniometer which increases the absorber-detector separation to approximately 20 mm. Two new measurements with background corrections were made. The first perpendicular orientation revealed reduced intensities to be in excellent agreement and well within the small experimental error, and in excellent accord with the hand fitted measurement of Zory. The second measurement with the crystal inclined at 45° for $\varepsilon = 28°$ again reveals reduced intensities within experimental error of those without the mask. As expected, total intensities were slightly affected, and the small scaling factor determined from several such measurements was applied to the angular rotation and perpendicular intensities.

The raw angular angular rotation data with experimental error is shown in figure 11.9. Error bars represent 95% confidence intervals, and importantly, the asymmetry in the so-called total intensity (or single crystal anisotropic recoilless fraction) curve amplitude well exceeds experimental error, providing direct evidence that the assumption of an isotropic total intensity (and Lamb-Mössbauer factor) would be incorrect. The magnitude of this anisotropy is considered sufficient to resolve the microscopic ambiguity.

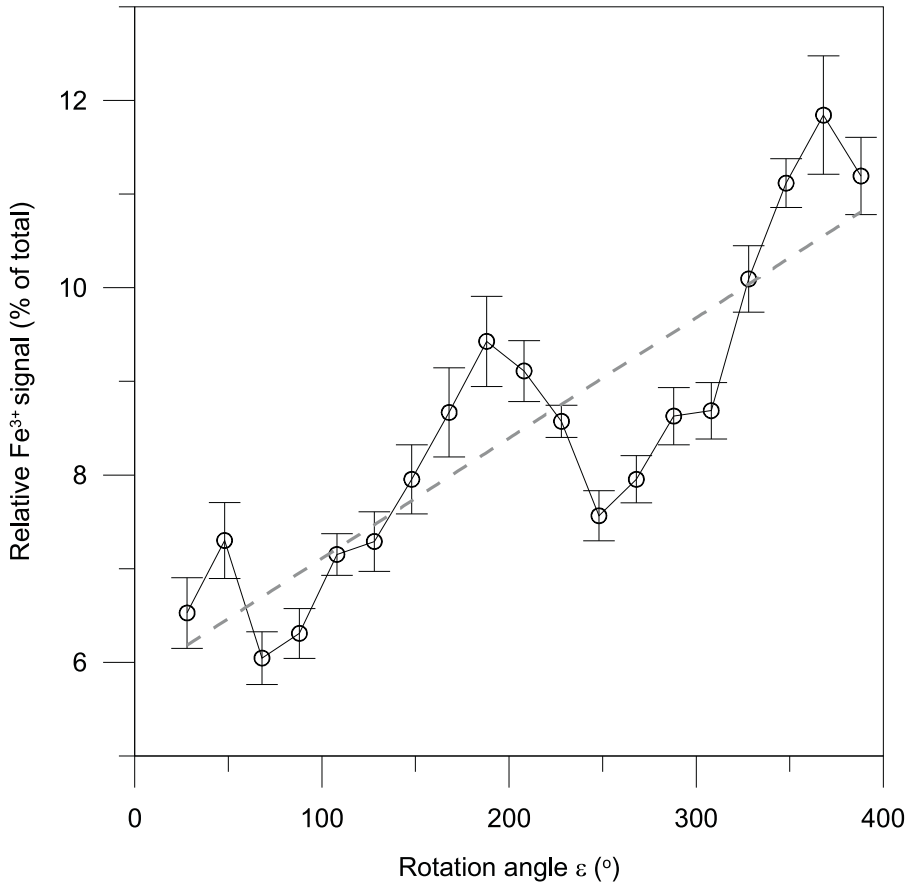

Figure 11.7.: Quadrupole doublet intensity of contaminant oxidization ferric (Fe^{3+}) species as percent of spectrum total intensity for each laboratory rotation angle, ε.

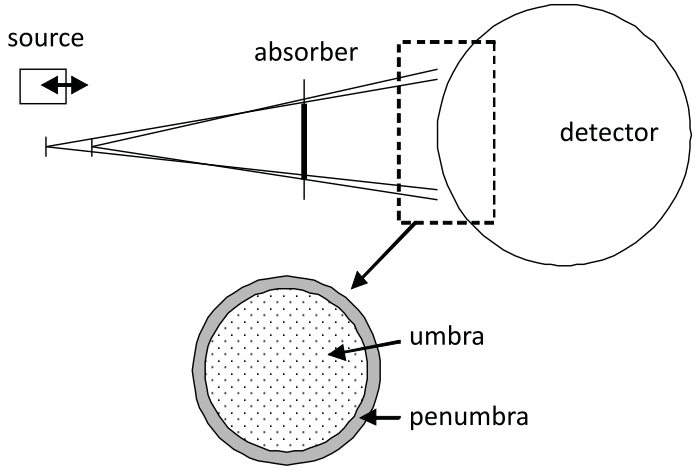

Figure 11.8.: Source, absorber, and detector arrangement with the detector window larger than the source collimation aperture allowing detection of the cosine smeared penumbra. The use of a 6 mm diameter Analar lead shield over the detector aperture eliminates this effect. This figure depicts the penumbra arising from a point source, where the penumbra effects increase for a traditional disc type source that has a finite diameter.

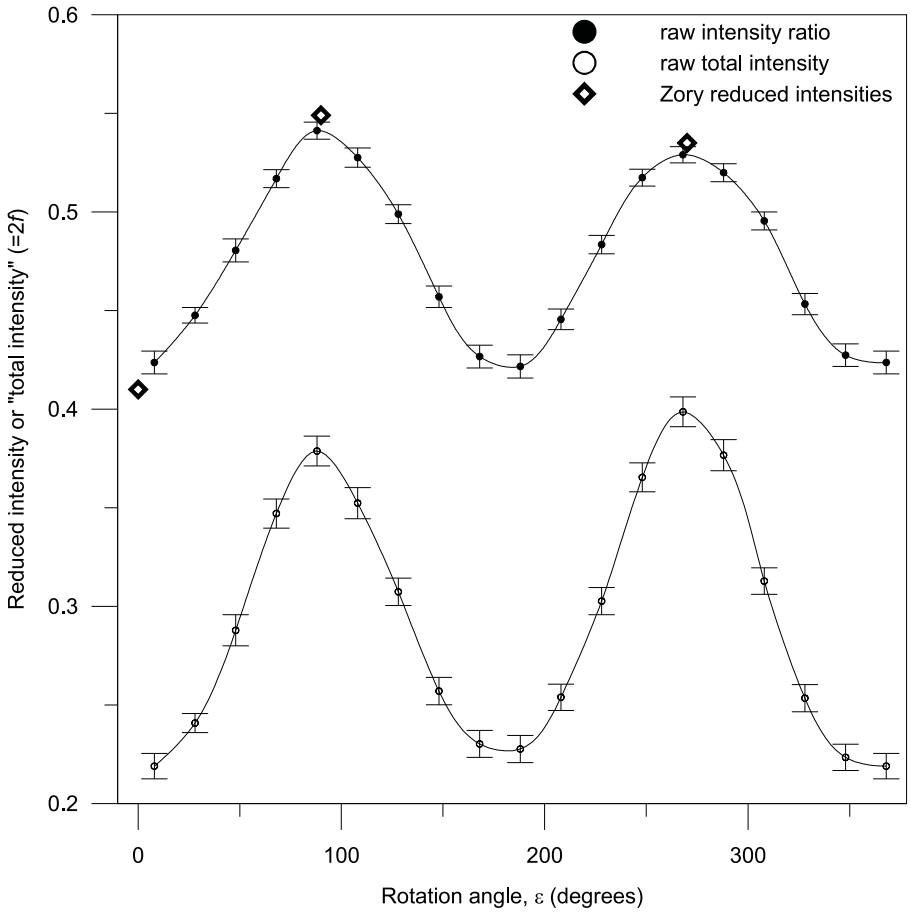

Figure 11.9.: Observed reduced intensities, $I^{(r)}$, in upper curve with error bars and the Zory (1965) measurements that fit on the angular rotation cone surface. Total intensities reported as $2f$.

11.4. Results and discussion

11.4.1. Preliminary discussion - comparison of simulated and experimental intensity curves

The functional forms of the experimental intensities shown in figure 11.9, and the simulated intensities shown in figure 11.3, are similar, and this correspondence was used to calibrate $\varepsilon = 0$ with the crystallographic $b||z_o$ axis, since the relation between the unit cell axes to the external crystal morphology was initially unknown. This calibration resulted in the shifting of arbitrary laboratory ε angles by a rotation angle of 28° so that maxima and minima coincide well, as determined by minimizing a non-linear least-squares regression coefficient. The resulting experimental spherical polar (θ, ϕ) angles that the γ-beam makes with respect to the laboratory axis system are tabulated in table 11.2.

The first step in the refinement procedure requires calculation of background-corrected dimensionless areas (denoted hereafter as dimensionless areas), p_α, for both lines of the quadrupole doublet in all orientations. Following Grant *et al.* [11] in the Lorentzian line shape approximation, dimensionless areas can be calculated

Table 11.2.: Experimental polar (θ) and azimuthal (ϕ) angles for the rotating the general γ-beam projection vector about the laboratory rotation angle ε. All angles in degrees.

$\varepsilon \pm 0.5°$	θ	ϕ
8	45.5549	7.9231
28	51.3664	25.1487
48	61.7612	36.6177
68	74.6398	42.8362
88	88.5859	44.9825
108	102.6214	43.5630
128	115.8068	38.2385
148	126.8456	27.9200
168	133.7612	11.7451
188	134.4451	-7.9231
208	128.6336	-25.1487
228	118.2388	-36.6177
248	105.3602	-42.8362
268	91.4141	-44.9825
288	77.3786	-43.5630
308	64.1932	-38.2385
328	53.1544	-27.9200
348	46.2388	-11.7451
perpendicular	90.0000	0.0000
Zory (010)	0.0000	0.0000

by equation 11.15.

$$p_\alpha = \frac{2D\delta}{Bbf_s\Gamma_s} \tag{11.15}$$

where subscript $\alpha = l, u$ indicating lower or upper line of the quadrupole doublet respectively. D is the quadrupole line intensity "dip", δ is the Lorentzian quadrupole half line width, b is the spectrum background off-resonance intensity count, f_s is the source recoilless fraction (= 0.75 according to manufacturer specifications), and Γ_s is the source natural line width (= 0.097135 mm sec^{-1}). The parameter B corresponds to the average background resulting from the necessarily accompanying high energy γ-rays. Values of B were determined using copper filters to be 91.37% for the 45° inclined measurements, and 75.84% for the perpendicular measurement.

Following Bull *et al.* [9], the reduced and total intensities as f or Lamb-Mössbauer factors for a given orientation, are related by the expression given in equation 11.16.

$$p_l^0 + p_u^0 = n_{Fe}\sigma_0 f \tag{11.16}$$

where n_{Fe} is the number of resonant iron atoms per unit area, and $\sigma_0 = 255.75 \times 10^{-20}$ cm^2 is the resonant cross section for absorption for ^{57}Fe nuclei. Equation 11.16 is necessarily defined in the thin crystal limit. In order to calculate the experimental f values, based on observed dimensionless areas, the factor $n_{Fe}\sigma_0$ needs to be applied to experimental data. This can be evaluated from the FCL density, $\rho = 1.93$ g cm^{-3}, and physical crystal cut thickness, T, by equation 11.17.

$$n_{Fe}\sigma_0 = \frac{\rho}{A_r(Fe)} n_A T \tag{11.17}$$

where A_r(Fe) is the atomic mass of iron, and n_A is Avagrado's number. When expressed in terms of a Mössbauer "thickness", $t = n_{Fe}\sigma_0$, in units of mass Fe per unit area, then $t = 7.482$ mg Fe cm^{-2} for measurement perpendicular to the beam, or 16.537 mg Fe cm^{-2} at the 45° inclination. The anisotropic Lamb-Mössbauer f values are then determined for each single crystal orientation. The final experimental dimensionless areas used in subsequent determinations are tabulated in table 11.3. Since details of the Zory [1] experiments were not fully outlined or characterized, it was initially assumed that background characteristics of his source were similar that employed here when determining dimensionless areas. These were then compared with a suitable refined simulation to obtain a correction factor relative to the perpendicular measurement (that was also measured by Zory), with an additional factor accounting for differences in the physical single crystal cut thicknesses.

Table 11.3.: Experimentally determined dimensionless areas, p_l and p_u, which are used in subsequent data analysis. Experimental fitting errors are inherent in the last two decimal figures.

Laboratory rotation angle, ε (degrees)	Upper line intensity	Lower line intensity
8	0.4139	0.5631
28	0.4809	0.5936
48	0.6171	0.6672
68	0.8004	0.7481
88	0.9146	0.7752
108	0.8293	0.7427
128	0.6842	0.6873
148	0.5241	0.6228
168	0.4383	0.5889
188	0.4283	0.5875
208	0.5048	0.6282
228	0.6528	0.6975
248	0.8434	0.7868
268	0.9409	0.8377
288	0.8737	0.8068
308	0.6914	0.7042
328	0.5126	0.6182
348	0.426	0.5709
perpendicular	0.4826	0.6180
Zory (010)	0.2028	0.2469

Equation 11.16 formally refers to the thin crystal limit. Practically it is difficult to handle large single crystals less than approximately 100 μm thickness, since they are very fragile and are easily fractured. Further, accurate thickness measurement becomes more difficult. Spectroscopically, thinner crystals have both advantages and disadvantages. The advantages are that the line widths of the two lines of the quadrupole doublet become narrower, and therefore resolution improves if the wings of the two lines overlap. The cost is the loss of spectral intensity from increased radiation transmission, that for a modest number of off-resonance counts would increase the fitted intensity errors.

Tensor refinement based on raw experimental data is formally not correct, since as first outlined by Grant *et al.* [11], the effects of both thickness and polarization effects to the γ-beam need to be considered for a finite thickness absorber. The original Zory [1] measurements with 0.254 mm absorbers assumed these to be approximate the thin crystal limit. As will be shown later, this assumption is reasonable. Thickness corrections are expected to increase exponentially from the thin crystal limit, and Spiering and Vogel [4] showed that such corrections were important for macroscopic efg tensor refinement on their 0.70 ± 0.03 mm thick single crystal cuts.

In contrast to the observation for FAS [9], the change in quadrupole doublet line intensities essentially arises from changes in observed intensity dip rather than changes in area resulting from changes in line widths. The full line widths at half maximum height (FWHM) are shown over the laboratory angular rotation for both upper and lower lines of the quadrupole doublet in figure 11.10.

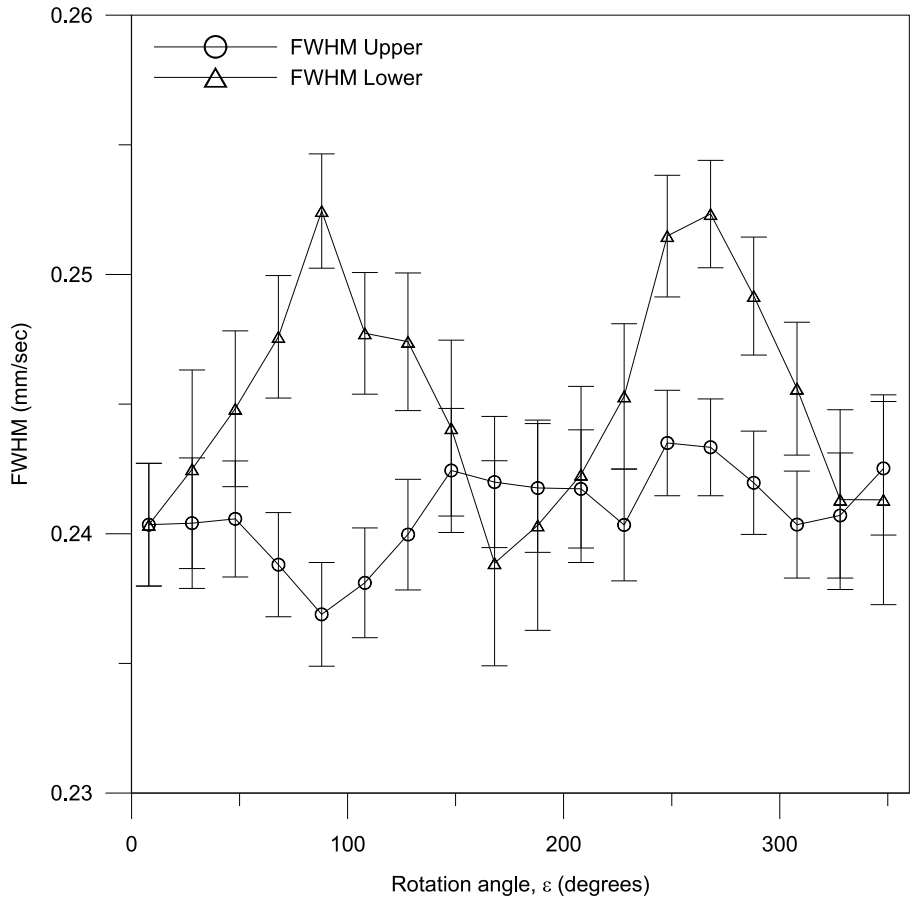

Figure 11.10.: Experimental full line widths at half maximum height (FWHM) with errors for the FCL two line quadrupole doublet. There is no apparent correlation between angular dependence of the FWHM and observed intensity ratios or total intensities within experimental error.

11.4.2. Thickness and polarization corrections

Thickness and polarization corrections to the experimentally determined dimensionless areas were made using the series expansion method first outlined by Housley *et al.* [12], and detailed by Zimmermann [13]. This method involves a Bessel function series expansion of the theoretical expression for the absorption area of a Mössbauer line first outlined by Bykov and Hein [19]. The first few terms in the appropriate expression for the area, S, in terms of thickness, p, and fractional degree of polarization, a, and its inverse are taken from Bull *et al.* [9] and given in equations 11.18 and 11.19.

$$S = p - \frac{1}{4}(1 - a^2)p^2 + \frac{1}{16}(1 + 3a^2)p^3 - \frac{5}{384}(1 + 6a^2 + a^4)p^4 + ... \tag{11.18}$$

$$p = S + \frac{1}{4}(1 + a^2)S^2 - \frac{1}{16}(1 + a^2 + 2a^4)S^3 + \frac{5}{384}(1 + a^4 + 6a^6)S^4 \tag{11.19}$$

Further terms may be found in Zimmerman [13] and Bull *et al.* [9]. The iterative correction procedure initially requires thickness-corrected data in the absence of polarization, using $a = 0$ in equation 11.19. As shown in figure 11.11, convergence of the series expansion was obtained with only four terms.

Since the three quantities: thickness correction; polarization correction; and the macroscopic efg tensor, are required for thickness and polarization corrections and are not known in advance, an iterative procedure is performed until convergence is achieved. The first step involves background corrected dimensionless areas corrected for thickness in the absence of polarization ($a = 0$) in equation 11.18, yielding thickness-corrected dimensionless areas. These thickness-corrected dimensionless areas are used in a MOSREF efg and msd tensor refinement to obtain a thickness-corrected macroscopic efg. This efg tensor is then used in a thickness and polarization correction to obtain first estimates at corrected dimensionless areas. A MOSREF refinement on these data then produces a slightly improved macroscopic efg tensor which in turn produces improved dimensionless areas. This procedure is repeated twice, with convergence in the fourth decimal place of dimensionless areas, which is an order of magnitude smaller than experimental errors in the dimensionless areas.

The final refinements are shown in figure 11.12 for the three different cases: raw experimental data; thickness-corrected data; and thickness and polarization corrected data. The final refined tensors for each of these three situations are given in table 11.4 and 11.5 for the case of the Zory (010) data weighted at 0.01 and 1.0 (full weighting) respectively. These refinements reveal that addition of the Zory (010) measurement is crucial in order to obtain convergence on the msd tensor, and will be discussed next.

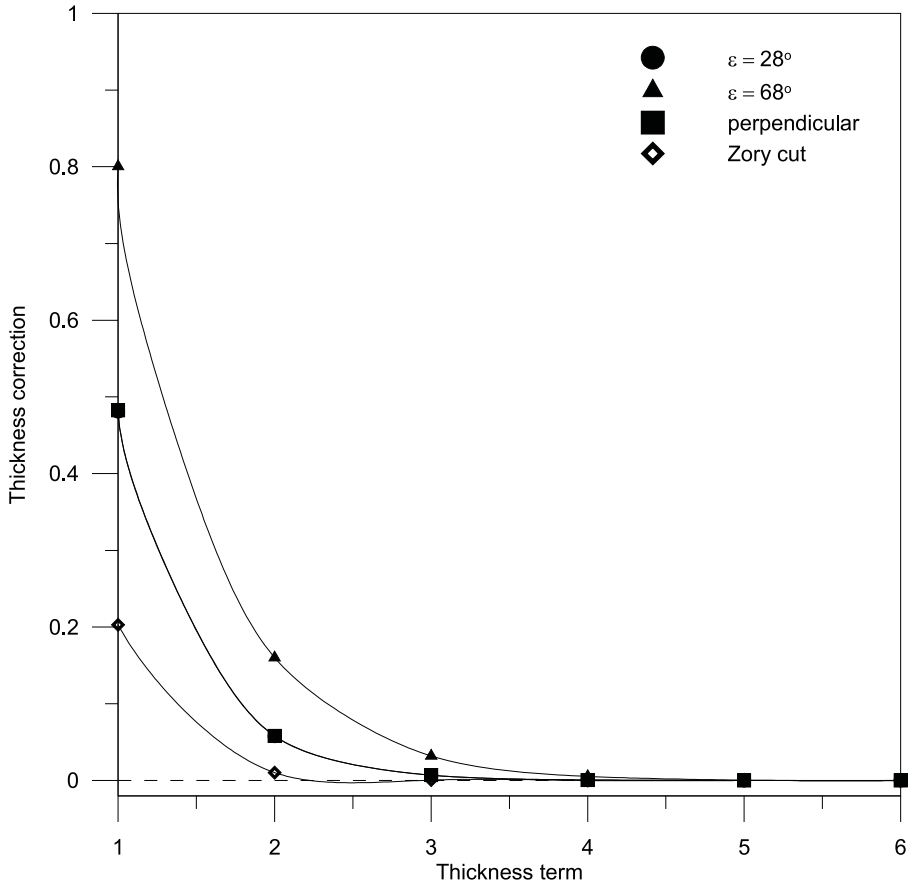

Figure 11.11.: Convergence of thickness corrections to the lower dimensionless areas for $\varepsilon = 28°, 68°$, the (100) perpendicular orientation, and the (010) Zory cut. The $\varepsilon = 28°$ and perpendicular corrections are essentially superimposed.

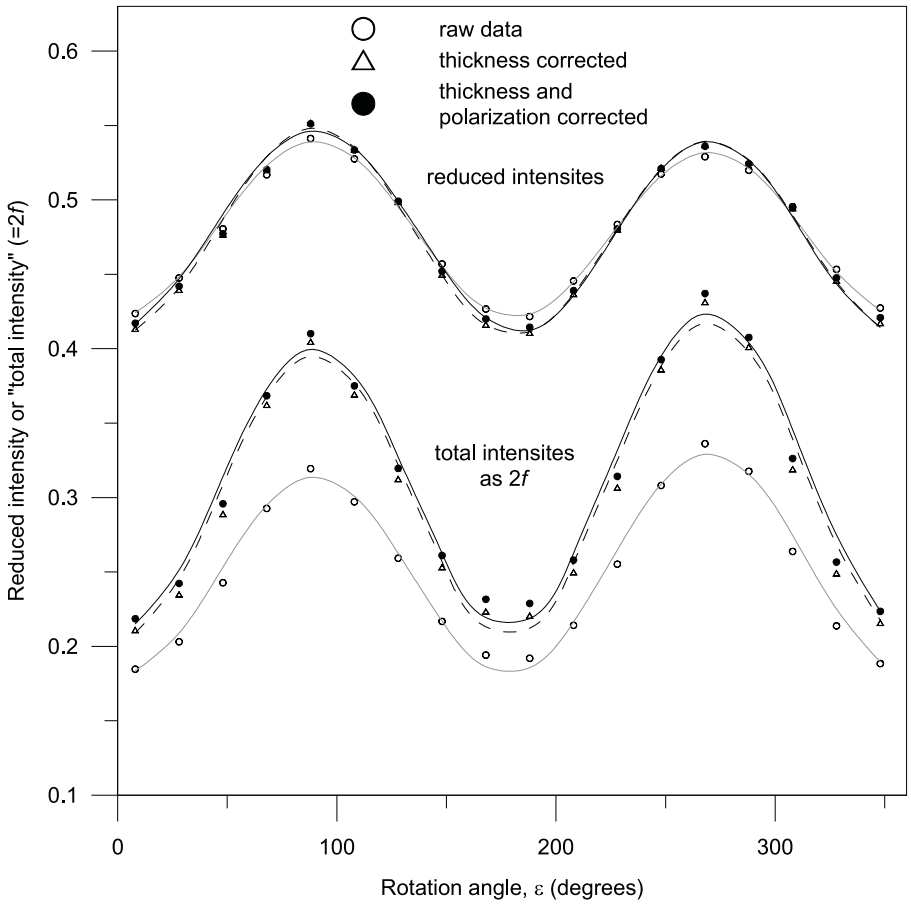

Figure 11.12.: Final macroscopic fitted reduced and total intensities for three cases: the raw experimental data; thickness-corrected data; and thickness and polarization corrected data.

Table 11.4.: Fits for the efg (intensity **P**) tensor, and msd tensor together with principal values and directions. Error estimates reported in parentheses. The Zory (010) orientation is weighted at 0.01. Three cases are considered: the raw experimental data; thickness corrected data; and thickness and polarization corrected data. The asymmetry parameter, $\eta = 0.303 \pm 0.060$ for the raw data refinements, $\eta = 0.244 \pm 0.062$ for thickness corrected data, and $\eta = 0.266 \pm 0.064$ for thickness and polarization corrected data.

Y	Y_{ij}			k	Principal values, Y_k	Principal θ_k	directions[a] ϕ_k
Raw data							
P (efg)	-0.0858 (69)	-0.0037 (24)	0.0000	1	-0.0858 (69)	91.4 (9)	359.9 (0.1)
		0.1569 (127)	-0.1684 (151)	2	-0.1605 (195)	152.0 (1.7)	87.2 (1.7)
			-0.0711 (58)	3	0.2463 (10)	62.1 (1.7)	270.6 (4)
msd	2.0095 (948)	0.0243 (46)	0.0000	1	1.6730 (680)	90.0	274.1 (4)
		1.6748 (685)	0.0000	2	2.0113 (953)	90.0	4.5 (4)
			3.0402 (2659)	3	3.0402 (2659)	0.0	0.0
Thickness corrected data							
P (efg)	-0.0935 (88)	-0.0044 (33)	0.0000	1	-0.0935 (88)	91.8 (1.3)	359.9 (0.1)
		0.1812 (170)	-0.1491 (187)	2	-0.1540 (230)	156.0 (2.4)	85.8 (2.7)
			-0.0877 (82)	3	0.2475 (23)	66.0 (2.4)	270.7 (5)
msd	1.8540 (1345)	0.0278 (62)	0.0000	1	1.3889 (831)	90.0	273.4 (4)
		1.3889 (853)	0.0000	2	1.8540 (1368)	90.0	3.4 (4)
			2.9948 (4212)	3	2.9948 (4212)	0.0	0.0
Thickness and polarization corrected data							
P (efg)	-0.0907 (86)	-0.0035 (33)	0.0000	1	-0.0907 (86)	91.4 (1.3)	0.0 (0.1)
		0.1762 (167)	-0.1535 (185)	2	-0.1564 (188)	155.2 (2.6)	86.9 (2.8)
			-0.0856 (81)	3	0.2471 (60)	65.2 (0.7)	270.6 (5)
msd	1.8155 (1327)	0.0297 (62)	0.0000	1	1.3887 (870)	90.0	274.0 (4)
		1.3908 (877)	0.0000	2	1.8176 (1334)	90.0	2.7 (4)
			2.9874 (4287)	3	2.9874 (4287)	0.0	0.0

[a] Angle θ measured with respect to the a' axis, and ϕ measured from c towards b

Table 11.5.: Final fits for the efg (intensity **P**) tensor, and msd tensor together with principal values and directions. Error estimates reported in parentheses. The Zory (010) orientation is weighted at 1.00 for tight msd convergence. Three cases are considered: the raw experimental data; thickness corrected data; and thickness and polarization corrected data. The asymmetry parameter, $\eta = 0.303 \pm 0.059$ for the raw data refinements, $\eta = 0.232 \pm 0.060$ for thickness corrected data, and $\eta = 0.266 \pm 0.067$ for thickness and polarization corrected data.

Y	Y_{ij}			k	Principal values, Y_k	Principal θ_k	directions[a] ϕ_k
Raw data							
P (efg)	-0.0874 (73)	-0.0036 (25)	0.0000	1	-0.0858 (57)	91.5 (1.0)	359.8 (0.1)
		0.1560 (130)	-0.1689 (153)	2	-0.1605 (210)	151.8 (1.7)	87.2 (1.7)
			-0.0687 (57)	3	0.2463 (7)	61.8 (1.7)	270.6 (4)
msd	2.1000 (207)	0.0245 (40)	0.0000	1	1.6134 (158)	90.0	272.9 (5)
		1.6147 (164)	0.0000	2	2.1012 (212)	90.0	2.9 (5)
			2.8212 (316)	3	2.8212 (316)	0.0	0.0
Thickness corrected data							
P (efg)	-0.0952 (92)	-0.0043 (34)	0.0000	1	-0.0952 (92)	88.1 (1.4)	359.9 (0.1)
		0.1800 (175)	-0.1501 (191)	2	-0.1526 (235)	155.6 (2.5)	85.7 (3.0)
			-0.0848 (82)	3	0.2478 (23)	65.7 (2.4)	270.7 (6)
msd	1.9375 (298)	0.0281 (65)	0.0000	1	1.3384 (201)	90.0	272.7 (6)
		1.9693 (208)	0.0000	2	1.9389 (304)	90.0	2.7 (6)
			2.7688 (495)	3	2.7688 (495)	0.0	0.0
Thickness and polarization corrected data							
P (efg)	-0.0907 (86)	-0.0045 (34)	0.0000	1	-0.0907 (88)	88.2 (2.4)	359.9 (0.1)
		0.1735 (169)	-0.1557 (187)	2	-0.1564 (235)	154.7 (2.4)	86.1 (2.6)
			-0.0829 (81)	3	0.2471 (14)	64.7 (2.3)	270.8 (6)
msd	1.9007 (287)	0.0300 (64)	0.0000	1	1.3371 (203)	90.0	274.0 (3)
		1.3387 (210)	0.0000	2	1.9023 (294)	90.0	4.0 (3)
			2.7515 (500)	3	2.7515 (500)	0.0	0.0

[a] Angle θ measured with respect to the a' axis, and ϕ measured from c towards b

Parameters are given arbitrarily for site 1 only. The corresponding tensors, $\mathbf{Y}_2$, for site 2 can be determined by application of equation 11.20.

$$\begin{aligned} \mathbf{Y}_2 &= \mathbf{R}\mathbf{Y}_1\mathbf{R}^{-1} \\ \mathbf{R} &= \begin{bmatrix} -1 & 0 & 0 \\ 0 & -1 & 0 \\ 0 & 0 & 1 \end{bmatrix} \end{aligned} \tag{11.20}$$

Errors were determined by diagonalizing both the refined microscopic tensors, and those with maximum errors added to each element. The difference between each respective principal value and principal direction is used as the error. This procedure would produce overestimates of actual errors. Finally, a plot showing the two calculated microscopic sub-spectra which average to yield the macroscopic observed spectrum is given in figure 11.13.

11.5. General discussion

In the course of these single crystal measurements the spectrum fits have determined the values of the isomer shift, δ, and quadrupole splitting, ΔE_Q, 19 times, from which the averaged values of δ = 1.224(1), and ΔE_Q = 3.011(3) are obtained. These room temperature determinations agree within the small experimental error with previously tabulated values [20]. The reported refinements assumed the sign of the quadrupole splitting (sign of $eQP_{\hat{z}\hat{z}}$) to be positive following all of the previous efg tensor studies outlined in the introduction. Note that these experiments and simulations do not directly determine the sign of the quadrupole splitting. The simulation presented previously was therefore chosen with $P_{xz} = 0$, for the reasons that the sign of $P_{\hat{z}\hat{z}}$ is positive, and the asymmetry parameter, $\eta < 0.5$. When $P_{xz} \approx P_{yz}$, then the sign of $P_{\hat{z}\hat{z}}$ would be negative. When $P_{xz} = 0$ and P_{yz} is changed between negative and positive, this effectively swaps site 1 and site 2 internal refinement parameters.

All of these refinements indicate the major source of uncertainty to arise from data related to the *b*-axis that was estimated from the Zory data, and from the perpendicular orientation measurement. Refinement without the Zory orientation yields considerably larger uncertainty in the msd_{zz} element and corresponding principal value, which in turn slightly alters the efg tensor, as seen by comparing the results in table 11.4 to those in table 11.5. The perpendicular orientation is also critical to determine well, since it is effectively used nine times (bisector of each $(\varepsilon, \varepsilon + \pi)$ such pair) in the refinement. Although the Zory measurements show significantly worse signal-to-noise ratio than those determined here, the refinements revealed that addition of this datum caused no significant change to any other refined tensor element when the indeterminate element was arbitrary fixed. Table 11.5 shows the final refinements using a full weighting of the Zory total intensity, to yield uncertainty at a quarter of that when this datum is not included. The uncertainty in the initial refinements, that essentially weighted out the Zory datum, incorporate refinements including the Zory datum.

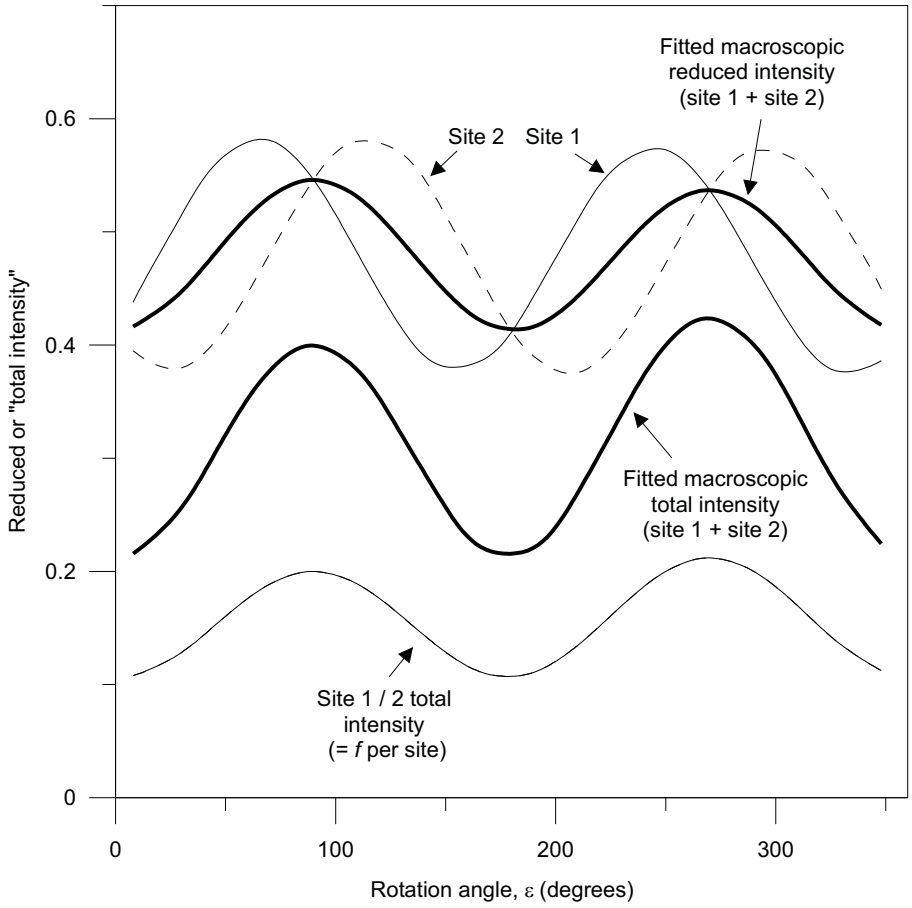

Figure 11.13.: Final thickness and polarization corrected macroscopic fitted spectrum showing respective microscopic site contributions to the reduced and total intensities. Site 1 and site 2 microscopic total intensities are superimposed.

The three sets of refinements, being raw data, thickness corrected data, and thickness and polarization corrected data, do not show large differences between final principal directions and principal values. All sets of refinements reveal asymmetry parameters to be almost within respective experimental error of any one. These correspondences would indicate that, in accord with rapid thickness and polarization convergence, the thin crystal approximation is reasonable in this case for raw experimental data. This would also be the case for the original study of Zory [1]. This is in contrast to the foregoing chapters FAS study [9], where FAS has a similar single crystal iron site density, but the single crystal cut had a physical crystal thickness several times that used here, with large thickness and polarization corrections required. In addition, the microscopic efg tensor and asymmetry parameter are essentially the same in all refinements considering the Zory datum weighted in or out. This indicates that the uncertainty in use of the Zory datum to obtain a determinate solution to the msd tensor does not substantially alter the microscopic efg solution.

The refined 293 K asymmetry parameters, that are given in table 11.5, are all in accord with the previous manifold of solutions ranging from, $\eta = 0.40 \pm 0.15$ determined by Gibb [3], to $\eta = 0.25 \pm 0.15$ determined by Zimmermann [2]. This is at variance with the approximated value at ≈ 0.1 by Zory [1]. The low temperature 4.2 K value has been reported at 0.30 ± 0.03 by Siebke *et al.* [6].

It is now required to assess if the refined efg and msd solutions are physically sensible. Several caveats need to be acknowledged. Firstly, the f factors were obtained from the msd tensor in the harmonic approximation, where changes in phonon energy due to coupling between crystalline quantized vibrational phonons are neglected. Addition of such corrections is possible using the expressions of Kolk [21]. However, the uncertainty in the reported measurements is expected to be considerably larger than such corrections. The present system represents one of the simplest possible cases of the monoclinic ambiguous problem, where only two symmetry-related sites contribute to the same quadrupole doublet and, even in the presence of small ferric oxidization, show relatively narrow line widths conforming well to Lorentzian line shapes with good fitting criteria ($\chi^2 \approx 1$). The refinement program, MOSREF, numerically calculates the spin-Hamiltonian assuming a single line, non-polarized magnetic dipole (M=1) source, which according to source manufacture specifications is correct. This criterion has not been independently assessed.

As a first check for correctness of the microscopic solution, where the thickness and polarization corrected refinement with the Zory measurement is assumed to be the "solution", MOSREF was used to calculate the observed intensity ratios for the five other (independent) reported Zory [1] cuts that were not used in these refinements. These data are reported in table 11.6. In all instances the calculated ratios are in good agreement, although this comparison makes two approximations. The first is that crystal thickness effects do not change intensity ratios significantly, since the Zory data was calculated for a thickness of 0.254 mm whereas the current determinations are corrected to the thin crystal approximation. As outlined, this approximation is believed to be reasonable. Secondly, the Zory data contained several orders of magnitude fewer off-resonance counts than the present measurements, and spectra were hand plotted without intensity (area) errors approximated.

Table 11.6.: Calculated intensity ratios of the other reported Zory (1965) crystal cuts that were not used in the current refinements.

θ°	ϕ°	Zory data at 300 K[a]	Calculated[b]
90	45	0.55	0.58
90	-45	0.55	0.59
90	90	0.45	0.45
45	90	0.47	0.46
45	0	0.37	0.33

[a]Ref [1]
[b]The calculated intensity ratios here assume the thin crystal limit, whereas the Zory data had single crystal cuts at 0.254 mm thickness.

Table 11.7.: Final fitted anisotropic Lamb-Mössbauer principle values for the Mössbauer determined msd tensor. Error estimates are reported in parentheses. Three cases are considered: the raw experimental data; thickness corrected data; and thickness and polarization corrected data.

k	raw data	thickness corrected	thickness and polarization corrected
1	0.199(2)	0.262(4)	0.263(4)
2	0.122(1)	0.144(2)	0.149(2)
3	0.060(1)	0.063(1)	0.064(1)
isotropic	0.127(1)	0.156(2)	0.159(2)
$2f_{iso}$	0.25	0.31	0.32

The Zory (010) spectrum was used in the current refinements was digitized and least-squares fitted. These comparisons would support a correct efg solution, with these other experimental ratios representing completely independent planes from any of the measurements used in the tensor refinements here.

The single crystal anisotropic recoilless fractions can be calculated from the msd tensor, and are reported in table 11.7. In addition, the isotropic recoilless fraction (isotropic Lamb-Mössbauer parameter), f_{iso}, is determined by averaging over the anisotropic f values. Multiplying the isotropic f case by a factor of two, which accounts for the two symmetry-related sites that contribute to the same quadrupole doublet, yields values in excellent accord with the previously reported experimental values at 0.28 ± 0.02 [3] and 0.29 [8], with the latter determined from a powder measurement. The best agreement is seen for the thickness and thickness and polarization corrected msd tensor data.

Comparison of the refined msd tensor with that determined from X-ray ADPs reveals the Mössbauer determined principal values to be, in this instance, on average $\approx 53\%$ larger than those determined by X-ray. This factor is in accord with the sodium nitroprusside study by Grant *et al.* [11]. The angles between respective principal directions have also been calculated and are: 169.7°; 75.5°; and 13.6°, and listed in order corresponding to increasing principal value. As expected with the small off-diagonal tensor elements, these angles show approximate coaxiality to unit cell axes considering respective errors, being close to 180°, 90°, and 0° respectively. This would again be in agreement with the type of coaxiality determined in the above sodium nitroprusside

study, and similar to FAS [9], where the largest principal value is approximately coaxial and the two smaller show some deviation. In these refinements, the largest msd principal value was restricted to be coaxial with the $x_o||a'$ axis since all refinements showed this to be the case within experimental error, and therefore constitutes an easy axis of recoil with a correspondingly small recoilless fraction. Crystallographically, as shown in figure 11.14, the a' and b axes are both oriented at a 45° angle with respect to a Cl-Fe-O bond, and one octahedra meridional plane is coplanar with the $a'b$ crystallographic plane. Therefore, the largest principal direction of the msd tensor does not directly point towards any bonding atom, rather symmetrically between atoms of different types. The smallest msd principal value lies orthogonal to this meridional plane, and is coaxial with a Fe-O bond, which in turn is coaxial with the $y_o||c$ axis. The intermediate msd principal value lies in the same meridonal plane as the largest principal value, and is coaxial with the $z_o||b$ axis. Intuitively for FCL, which exhibits ionic type bonding, it might have been expected that one msd principal direction would be coaxial with the Cl-Fe-Cl bonding vector from the presence of a reasonable symmetric Coulombic field, however, this appears not to be the case.

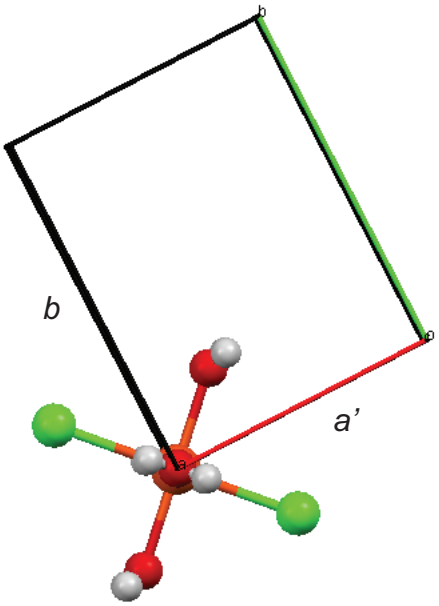

Figure 11.14.: Relative orientation of unit cell edges and unit cell contents. Normal to the plane of the page is the crystallographic c axis.

The microscopic efg tensor tabulated arbitrarily for site 1 reveals the smallest principal value to be directed along the crystallographic b axis within experimental error, which would be coaxial with the smallest msd principal direction and Fe-O vector outlined above. The intermediate and largest principal values therefore both essentially exist in the bc plane, making an angle of $\approx 30°$ from the b and c axes respectively. These two vectors trisect the oriented FCL asymmetric unit within $\approx 15°$.

There is no formal requirement for a site of $\bar{1}$ symmetry to have any efg or msd principal values with coaxial principal directions, although the correspondences outlined above are most likely not fortuitous. Rather, the

Table 11.8.: Comparison of the refined macroscopic intensity (efg) tensors with previously reported macroscopic determinations.

efg	P_{xx}	P_{yy}	P_{zz}	P_{xy}
raw[a]	-0.086(5)	0.175(9)	-0.071(4)	-0.004(2)
thickness[a]	-0.094(6)	0.181(12)	-0.088(6)	-0.004(2)
thickness and polarization[a]	-0.091(6)	0.176(18)	-0.086(6)	-0.004(2)
isotropic thickness and polarization[a]	-0.073	0.145	-0.072	-0.005
Zory[b] [1]	-0.071	0.146	-0.075	0.007
Zimmerman[c] [2]	-0.05(1)	0.11(1)	-0.06(1)	0
Spiering and Vogel[d] [4]	-0.076(1)	0.148(2)	-0.072(2)	0.005(9)

[a]This work.
[b]Using ellipsoid averaging expression (see appendix), in the absence or thickness and polarization corrections.
[c]Claimed elements to be essentially invariant over 77 K to 300 K range.
[d]Assuming an isotropic recoilless fraction, with large thickness and polarization corrections.

local crystal structure of each FCL octahedron may approximate to a higher point symmetry (almost D_{4H}) that would introduce approximate mirror planes and rotation axes. That is to say, the space group approximates to higher C2/m space group symmetry. The introduction of such symmetry elements would then remove the ambiguity problem.

Macroscopic efg tensors can be obtained by averaging the microscopic efg tensors in table 11.5 over the two symmetry-related sites, and are given and compared to the previous determinations in table 11.8. The macroscopic efg tensor is consistent with previous determinations, and shows the P_{xy} element to be essentially zero within error. When the thickness and polarization corrected refinement is repeated assuming an isotropic msd tensor with diagonal elements equal to the average of the msd principal values, at 1.9969 (and corresponding f equivalent to that used in literature isotropic studies), an RMSD fitting an order of magnitude larger than for the anisotropic refinement is obtained, and a macroscopic efg tensor well within error of the Spiering and Vogel [4] and Zory [1] macroscopic efg tensor was obtained. That is, the isotropic microscopic determination here, when averaged to yield a macroscopic quantity, is in excellent agreement with previous isotropic macroscopic determinations. That a significantly better refinement fit is found when using anisotropy in the recoilless fraction, provides strong evidence in support of inadequacies in the isotropic approximation. Therefore, in this case it is clear that neglect of anisotropy accounts for the difference between the anisotropic macroscopic tensor and respective literature isotropic approximated tensors. If the X-ray msd tensor (which is essentially coincidental with the refined msd tensor) is assumed rather than than simultaneously refining, a RMSD refinement two orders of magnitude poorer is obtained, with $\eta = 0.796$. This would not be a sensible solution, thus indicating a significant difference between the X-Ray and Mössbauer-determined msd tensors.

One further measurement was made to assess the correctness of individual site parameters. Following Bull *et al.* [9], this involves calculating the powder average reduced intensity ratio and comparison with the assumed "thin" experimentally determined intensity ratio. Assuming the microscopic efg and msd tensors, by averaging

the simulated reduced intensity ratio over a sphere described by all combinations of infinitesimally small (θ, ϕ) pairs, the following powder reduced intensity ratios are obtained: raw data efg/msd - 0.517; thickness corrected efg/msd - 0.524; thickness and polarization corrected efg/msd - 0.523. By comparison, the experimental value for both the powder samples mounted perpendicular and at a 45° inclination (that approximates the so-called magic angle [22]) to the γ-beam was 0.508 ± 0.005 with errors representing one standard deviation. Both spectra collected $\approx 1{\times}10^6$ off-resonance counts and show no apparent ferric oxidization. Fits allowing for an addition symmetrical quadrupole doublet for a ferric species does not change the experimental reduced intensity ratios within fitting uncertainty. The calculated single crystal data show agreement with experiment within two standard deviations, however, in general the simulated powder average in the anisotropy of the Lamb-Mössbauer factor (known as the Gol'danskii-Karagan effect [23, 24]) is larger than that experimentally determined. During the course of single crystal growing, it was noticed that all crystallites preferentially crystallize in flat plates containing the (100) plane, and showed a layered type structure, which would promote texture effects in the finely ground powder. It was assumed in preparation, that the polyphenyl ether oil matrix that was used in an attempt to prevent oxidization occurring, may actually assist in preventing some texture effects also. Another possible mode of anisotropy, which is usually neglected, is differential relaxation times of the two wings of the quadrupole doublet [25]. The calculated powder average based on X-ray determined msd is 0.504, which is not surprising considering that the msd tensor determined by X-ray is more isotropic than that determined by Mössbauer. In accord with the foregoing chapters FAS study [9], it can be concluded that measurement of the anisotropy in the recoilless fraction of a powder absorber is very difficult, whereas anisotropy can be relatively easily determined from single crystal Mössbauer spectroscopy.

11.6. Conclusion

This study on ferrous chloride tehrahydrate represents the first time for this species in which an unambiguous solution has been reported to the previously considered ambiguous monoclinic case, where the Fe^{2+} ions do not sit on a two-fold rotation axes, and the second time for the general monoclinic ambiguous case. The solution appears to reproduce independent literature experimental data, therefore indicating a physically sound description. It was found that the solution shows some characteristics of coaxaility for the efg and msd tensors, which might be expected considering the crystal structure consists of discrete octahedra that approximate to higher local point symmetry. Despite the presence of a small ferric quadrupole doublet, the observed, principal, ferrous doublet is resolved easily into two narrow lines that are close to pure Lorentzian line shape representing a relatively easy single crystal study. The largest source of uncertainty arises from the use of the Zory (010) intensities in the reported refinements, which could ideally be overcome by synthesizing a new crystal plane and measuring angular rotation intensity angular dependence. Angular dependence measurements over a full circle from two distinctly different fundamental planes would almost certainly reduce reported errors by an order of magnitude. Nevertheless, this study has experimentally shown distinct and resolvable anisotropy in the recoilless fraction as total intensities, indicating that an isotropic approximation to the recoilless fraction is

just that - an approximation.

11.7. Final comments

During the (many) attempts at crystal growing, it was noticed that large single crystals usually crystallized in two habits. The most common morphology was the pentagonal shape crystal containing the (100) plane that was utilized in the above study. The second morphology showed a needle type crystal, schematically shown figure 11.15, where the diagonal ends are slanted at an angle of $\approx \beta$ with respect to the long edges. A suitable single crystal of this second morphology was synthesised, and was cut parallel to the slanted face before several 45° inclined angular rotation spectra and a perpendicular spectrum were obtained. The final diamond-shape cut of approximate dimensions 5×4 mm was polished to a thickness of $\approx$ 250 μm, and was coated with a polyurethane lacquer. Unfortunately, this crystal has subsequently badly oxidized, and the nature of the crystal plane contained in the crystal cut was unable to be ascertained at the time. One could potentially attempt diffraction off one of the corners or oxidized face of the crystal to characterize the cut, although the lacquer, perspex and oxidation would significantly impede a certain assignment. Alternatively, it may be possible using the refined efg and msd tensors above, to simulate total and reduced intensities for likely planes, and then identify the closest match to experimental data. Then, assuming this assignment to be correct, incorporation of these additional intensities would potentially result in better refinements allowing the Zory datum to be excluded, and minimization of experimental error.

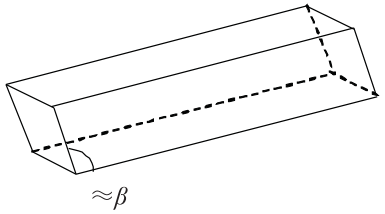

Figure 11.15.: Morphology of the second habit FCL single crystal. The cut was made parallel to the small slanted face, and unfortunately the crystal plane contained within this cut was unable to be determined.

11.8. Appendix

The ellipsoid equations

This appendix outlines a method of using an ellipsoid expansion in order to use simultaneous equations to solve for macroscopic efg tensor elements. Both the reported experimental measurements herein and the Zory data set are over-determined with respect to the macroscopic efg, in that several slightly different solutions can be obtained for the same elements depending on which intensities are used. By solving all possible combinations and averaging the results, the averaged macroscopic efg tensor can be obtained.

MOSREF utilizes a least squares matrix diagonalization procedure of experimental data that is believed to be precise and accurate. This procedure is numerical and therefore difficult to visualize. In this appendix, an alternative, but equivalent, procedure is outlined by using the property that a Cartesian symmetric second rank tensor can be expressed as an ellipsoid.

From Zimmerman [2], the experimental reduced intensity quantities $I^{(r)} = \frac{I^{(l)}}{(I^{(l)}+I^{(u)})}$ inherently contain details of the symmetric traceless efg (intensity) tensor. These quantities can be expressed in terms of equation 11.21.

$$I^{(r)} = \sum_{p,q=x,y,z} I_{pq} e_p e_q \tag{11.21}$$

where I_{pq} are components of an intensity tensor whose principal values, $I_{\hat{p}\hat{q}}$ are given in equation 11.22 [2].

$$\begin{aligned} I^{(r)}_{\hat{x}\hat{x}}(\mathbf{k}) &= \tfrac{1}{2} - sign(V_{\hat{z}\hat{z}})(1-\eta)/\left(8\sqrt{(1+\tfrac{1}{3}\eta^2)}\right) \\ I^{(r)}_{\hat{y}\hat{y}}(\mathbf{k}) &= \tfrac{1}{2} - sign(V_{\hat{z}\hat{z}})(1+\eta)/\left(8\sqrt{(1+\tfrac{1}{3}\eta^2)}\right) \\ I^{(r)}_{\hat{z}\hat{z}}(\mathbf{k}) &= \tfrac{1}{2} - sign(V_{\hat{z}\hat{z}})2/\left(8\sqrt{(1+\tfrac{1}{3}\eta^2)}\right) \end{aligned} \tag{11.22}$$

Equation 11.21 is simply a quadric polynomial equation of second degree, or visually represented as an ellipsoid. Following Weil *et al.* [26], this can be expressed explicitly in equation 11.23.

$$I^{(r)}(\mathbf{k}) = \sum_{i=x,y,z} \sum_{j=x,y,z} I_{ij} k_i k_j \tag{11.23}$$

If the unit wave vector, $\mathbf{k}$, is expressed in spherical polar coordinates, $\mathbf{k} = (\sin\theta\cos\phi, \sin\theta\sin\phi, \cos\theta)$, then equation 11.23 can be expanded to yield equation 11.24.

$$I^{(r)}(\mathbf{k}) = I_{xx}\sin^2\theta\cos^2\phi + I_{yy}\sin^2\theta\sin^2\phi + I_{zz}\cos^2\theta + I_{xy}\sin^2\theta\sin 2\phi + I_{xz}\sin 2\theta\cos\phi + I_{yz}\sin 2\theta\sin\phi \tag{11.24}$$

When $I^{(r)}(\mathbf{k})$ are measured for a small number of orientations (four or more) from two distinct crystal planes, then the coefficients I_{ij} can be evaluated and equated to efg matrix elements. Only four independent coefficients are obtainable since the averages of I_{xz} and I_{yz} over the two symmetry-related sites is zero in the monoclinic case with experimental macroscopic intensities.

The first reported single crystal $I^{(r)}(\mathbf{k})$ for FCL were by Zory [1] for seven different crystal orientations at 300 K. Zory used single crystals cut to a thickness of 0.254 mm, where each of which were mounted perpendicular to the γ-beam. Re-expressing the area ratios reported by Zory as reduced intensity ratios: $I^{(r)}(0,0) = 0.452$; $I^{(r)}(\frac{\pi}{2},0) = 0.446$; $I^{(r)}(\frac{\pi}{2},\frac{\pi}{2}) = 0.629$[1]; $I^{(r)}(\frac{\pi}{2},\frac{\pi}{4}) = 0.549$; $I^{(r)}(\frac{\pi}{2},\frac{-\pi}{2}) = 0.535$; $I^{(r)}(\frac{\pi}{4},\frac{\pi}{2}) = 0.535$; and $I^{(r)}(\frac{\pi}{4},0) = 0.410$. Application of equation 11.24 yields an over-determined set of simultaneous equations. Solving these sets for all possible combinations yields a unique I_{xy} and two values for each of I_{xx}, I_{yy}, I_{zz}.

[1] Average of four identical measurements

Averaging these diagonal elements and normalizing the trace, 1.507 to 1.5, as required by the intensity tensor relations in equation 11.22, allowed the macroscopic intensity tensor to be obtained in equation 11.25.

$$\mathbf{I}_{MZ} = \begin{bmatrix} 0.430 & 0.007 & I_{xz} \\ 0.007 & 0.645 & I_{yz} \\ I_{xz} & I_{yz} & 0.426 \end{bmatrix} \tag{11.25}$$

Adjusting $\mathbf{I}_M$ by subtracting 0.5 from the diagonal elements yields a traceless matrix, designated herein as the $\mathbf{P}$ matrix. Subscript M denotes a macroscopic entity, and Z denotes that derived from the Zory data. This is given in equation 11.26.

$$\mathbf{P}_{MZ} = \begin{bmatrix} -0.071 & 0.007 & I_{xz} \\ 0.007 & 0.145 & I_{yz} \\ I_{xz} & I_{yz} & -0.074 \end{bmatrix} \tag{11.26}$$

Application of the invariance condition given in equation 11.10, then gives the monoclinic ambiguous manifold relation that $P_{xz}^2 + P_{yz}^2 = 0.03114$.

A similar procedure may be applied to the angular rotation data determined in this work, however owing to a larger number of rotation measurements it is more convenient to consider groups of co-planar vectors. In the angular rotation measurements, the projection of the γ-beam for all sets of measurements can be located on the surface on a cone, and related by rotation angles ε and $\varepsilon + \pi$, where the rotation vectors, $\mathbf{a}'$ is the common bi-sector of all such pairs. By sum and difference substitution and simplification, each pair can be expressed as in equations 11.27 and 11.28.

$$I^{(r)}(\varepsilon) + I^{(r)}(\varepsilon + \pi) = 2\left(I^{(r)}(\mathbf{a}')\sin^2\theta\cos^2\phi + I_{yy}\sin^2\theta\sin^2\phi + I_{zz}\cos^2\theta\right) \tag{11.27}$$

$$I^{(r)}(\varepsilon) - I^{(r)}(\varepsilon + \pi) = 2\left(I_{xy}\sin^2\theta\sin 2\theta\right) \tag{11.28}$$

where $I^{(r)}(\mathbf{a}')$ is the reduced intensity for the perpendicular (bi-sector) orientation measurement. Application of equation 11.27 with the condition $I_{xx} + I_{yy} + I_{zz} = \frac{3}{2}$ and equation 11.28 to the intensities determined in this work yields ten sets of values for I_{xx}, I_{yy}, I_{zz} and I_{xy}. When averaged over these ten sets, the macroscopic intensity tensor is obtained, and is given in equation 11.29. Application of the trace condition yields the traceless intensity tensor that is given in equation 11.30.

$$\mathbf{I}_M = \begin{bmatrix} 0.4385 & 0.0024 & I_{xz} \\ 0.0024 & 0.0.1449 & I_{yz} \\ I_{xz} & I_{yz} & 0.4116 \end{bmatrix} \tag{11.29}$$

$$\mathbf{P}_M = \begin{bmatrix} -0.0615 & 0.0024 & I_{xz} \\ 0.0024 & 0.1449 & I_{yz} \\ I_{xz} & I_{yz} & -0.0834 \end{bmatrix} \tag{11.30}$$

where $P_{xz}^2 + P_{xz}^2 = 0.03115$ by application of the invariance condition given in equation 11.10. The excellent agreement between the experimental data in this work and that of Zory is not too surprising considering the crystals were of similar thickness: 0.254 mm for the Zory cuts, and 0.195 mm in the 45° angular rotation measurements here.

Finally, one feature of this method is that by averaging over many different measurements for determination of each macroscopic element, the error in the value of each element reduced. This procedure can also be used in reverse, for example, if each single crystal measurement contains reasonable error. By calculating an "averaged" macroscopic efg tensor, then the expected macroscopic spectrum can be calculated. In the following chapter, a method of averaging total intensity data will be outlined, since for both FAS [9] and FCL measurements, total intensities contribute the largest source of error in refinements.

References

[1] P. Zory. *Phys. Rev. A*, 140:1401, 1965.

[2] R. Zimmermann. *Nucl. Instrum. Methods*, 128:537, 1975.

[3] T. C. Gibb. *Chem. Phys.*, 7:449, 1975.

[4] H. Spiering and H. Vogel. *Hyperfine Interact.*, 3:221, 1977.

[5] R. W. Grant, H. Wiedersich, A. H. Muir Jr., U. Gonser, and W. N. Delgass. *J. Chem. Phys.*, 45:1015, 1966.

[6] W. Siebke, S. Hösl, H. Spiering, and G. Ritter. 5^{th} international conference on mössbauer spectroscopy. 1973.

[7] K. Ono, M. Shinohara, A. Ito, T. Fujite, and A. Ishigaki. *J. App. Phys.*, 39:1126, 1968.

[8] W. Kerler and W. Neuwirth. *Z. Phys.*, 167:176, 1962.

[9] J. N. Bull, W. T. Robinson, and W. C. Tennant. *Hyperfine Interact.*, 194:347, 2009.

[10] W. C. Tennant. *J. Phys.: Condens. Matter*, 4:6993, 1992.

[11] R. W. Grant, R. M. Housley, and U. Gonser. *Phys. Rev.*, 178:523, 1969.

[12] R. M. Housley, R. W. Grant, and U. Gonser. *Phys. Rev.*, 178:514, 1975.

[13] R. Zimmermann. *Advances in Mössbauer Spectroscopy*, pages 273–315. Elsevier, Amsterdam, 1983.

[14] T. F. Koetzle M. S. Lehmann J. J. Verbist, W. C. Hamilton. *J. Chem. Phys.*, 56:3257, 1972.

[15] K. N. Trueblood, H. B. Bürgi, H. Burzlaff, J. D. Dunitz, C. M. Gramacciolo, H. H. Schulz, U. Shmueli, and S. C. Abrahams. *Acta. Cryst. A*, 52:770, 1996.

[16] L. J. Farrugia. *J. Appl. Cryst.*, 30:565, 1997.

[17] E. W. Müller. *Mössbauer spectrum fitting program for universal theories.* Institut für anorganische Chemie und Analytische Chemie, Johannes Gutenberg Universtität, Mainz, 1980.

[18] R. N. Brand. *Program NORMOS.* Distributed by Wissenschaftliche Elektronik, GmbH, Germany, 1994.

[19] G. A. Bykov and P. Z. Hein. *Sov. Phys. JETP*, 16:176, 1963.

[20] T. C. Gibb N. N. Greenwood. *Mössbauer Spectroscopy.* Chapman and Hill Ltd.: London, 1971.

[21] B. Kolk: In: G. K. Horton and A. A. Maradudin (eds.). *Dynamical Properties of Solids*, volume 5. Elsevier, Amsterdam, 1984.

[22] J. M. Greneche and F. Varret. *J. Physique Lett.*, 43:L–223, 1982.

[23] V. I. Gol'danskii, E. F. Makarov, and V. V. Khrapov. *Phys. Lett.*, 3:344, 1963.

[24] S. V. Karyagin. *Sov. Phys. (Solid State)*, 5:1552, 1964.

[25] M. Blume. *Phys. Rev. Lett.*, 14:96, 1965.

[26] J. A. Weil, T. Buch, and J. E. Clapp. *Adv. Magn. Reson.*, 6:183, 1973.

12. Several additional Mössbauer investigations

This chapter outlines some details on further Mössbauer related studies that are ongoing. The contents may therefore be considered in terms of future work.

12.1. Ab Initio and DFT electric field gradients

Measurements to determine accurate electric-field gradient (efg) tensors with Mössbauer spectroscopy are difficult and time-consuming. The distribution of negative electrons about positive nuclei yields an electrostatic potential, V, that is characteristic of the compound and its geometry. The first derivative with respect to a spatial co-ordinate, q_i, is the electric field, and the second partial derivatives are the elements of the efg, V_{ij}, as given in equation 12.1.

$$V_{ij} = \frac{\partial^2 \mathbf{V}}{\partial q_i \partial q_j} \tag{12.1}$$

The efg is thus described by a symmetric Cartesian tensor of second-rank (3×3 matrix). Principal values (eigenvalues) are expressed in atomic units, where 1 a.u. = 9.717365×10^{21} Vm^{-2}. For a ^{57}Fe nucleus, the efg is non-zero when the charge density surrounding the nucleus is non-cubic in symmetry [1]. Convention describes the efg tensor in terms of the largest principal value, V_{zz}, and the axial asymmetry parameter, η, defined in equation 12.2.

$$\eta = \frac{V_{xx} - V_{yy}}{V_{zz}} \tag{12.2}$$

where by convention, $|V_{zz}| > |V_{yy}| \geq |V_{zz}|$, so that $0 \leq \eta \leq 1$ (i.e., $\eta = 0$ is isotropic for high-symmetry). The asymmetry parameter essentially describes the ellipticity of the efg tensor. In Mössbauer spectroscopy, the hyperfine coupling between the nuclear quadrupole moment, Q, for the first excited state with $I_e = \frac{3}{2}$ and the efg yields a quadrupole splitting, ΔE_Q, as given in equation 12.3.

$$\Delta E_Q = \frac{eQ}{2} V_{zz} \left(1 + \frac{\eta^2}{3}\right)^{\frac{1}{2}} \tag{12.3}$$

The efg at the iron nucleus therefore arises from the electron charge distribution (efg scales as r^{-3}), and may be considered from two sources: valence bonding electrons and spatial symmetries (major source); and second-coordination shell or lattice charges (minor source). The major contribution arises from charge anisotropy close to the nucleus. The $\left(1 + \frac{\eta^2}{3}\right)^{\frac{1}{2}}$ term in equation 12.3 is small, and only changes the quadrupole splitting

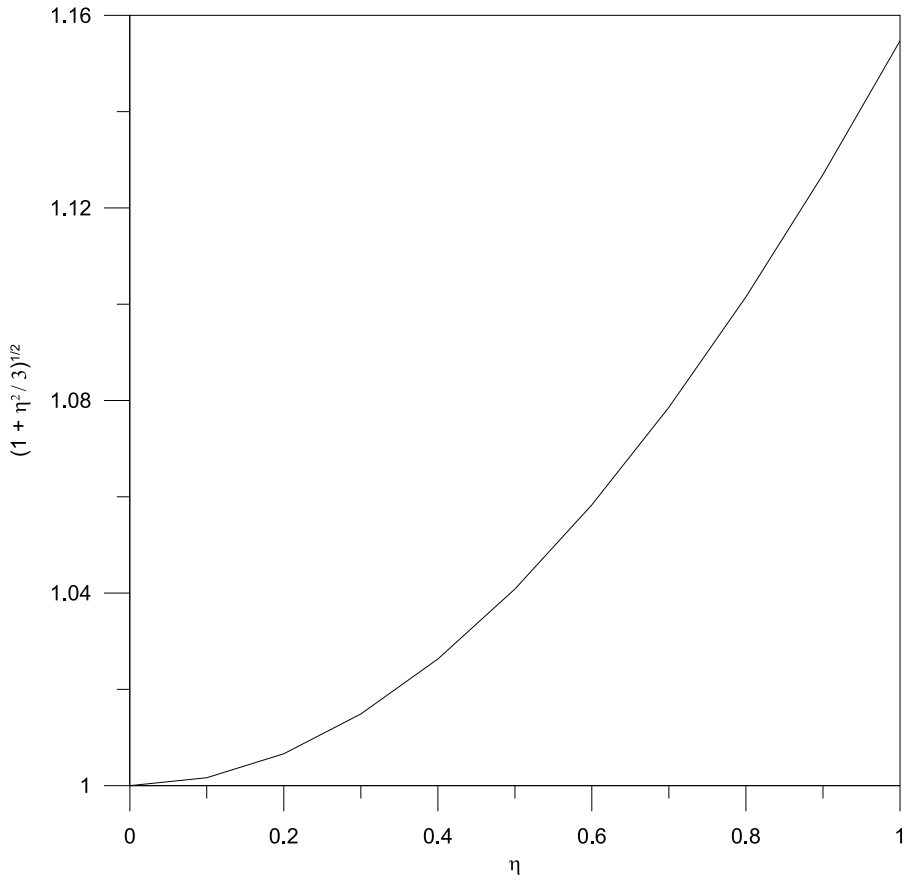

Figure 12.1.: Contribution of the $\left(1+\frac{\eta^2}{3}\right)^{\frac{1}{2}}$ term in the quadrupole splitting expression as a function of the asymmetry parameter, η.

typically by a few percent as shown in figure 12.1.

The determination of microscopic efg tensors at the ^{57}Fe nucleus in ferrous ammonium sulphate hexahydrate (FAS) or $Fe(NH_4)_2(SO_4)_2{\cdot}6H_2O$ [2], and ferrous chloride tetrahydrate (FCL) or $FeCl_2{\cdot}4H_2O$, in the previous chapters, which both crystallize in $P2_1/c$ space group, represent the first attempts at a solution to the so called "ambiguous" monoclinic case, where the symmetry-related sites do not sit on a C_2 (point symmetry) rotation axis. The refinements all yield excellent macroscopic accord between the calculated model intensities and the thin-crystal-limit experimental intensities. Systematic refinements in which input parameters are varied all show convergence to a unique solution, indicating a single global fit minimum. In principal, as a further check to the experiment, efg tensors (and sign of V_{zz}) should be able to be calculated using crystal field theory or more comprehensive molecular orbital *ab initio* and density functional theory methods [3, 4]. Unfortunately, transition metal containing species with degenerate and near degenerate states are well-known to be difficult to accurately describe in molecular orbital calculations, requiring suitably large basis sets with high level multi-reference type calculations. Further, *ab initio* or DFT calculations on three-dimensional crystalline or periodic systems ideally require consideration of lattice and packing such as with the program CRYSTAL [5]. Two initial caveats need to be outlined for any *ab initio* or DFT determinations. Firstly, it is well-known and experimentally

observed that quadrupole splitting (and necessarily efg) are very sensitive to subtle geometrical changes, and the quadrupole splitting often exhibits a temperature dependence [6, 7]. The experiments in the previous chapters were performed at 293(2) K, whereas calculations model 0 K conditions. Schwerdtfeger *et al.* [7] provides the most recent comparative *ab initio* and DFT study on the determination of the nuclear quadrupole moment, Q and efg tensor for $Fe(CO)_5$, $Fe(C_5H_5)_2$ (ferrocene), $FeCl_2$ and $FeBr_2$. These calculations considered gas-phase species at their optimized geometries. Efg calculations at X-ray geometries for each of the species considered yielded a considerable variation across various levels of theory, even when bonding parameters changed by magnitudes that in typical electronic structure calculations are usually negligible (i.e. 0.01 Å in bonding lengths). In agreement with other calculations on $Fe(CO)_5$, which employed several different DFT functionals [8], the Schwerdtfeger *et al.* [7] calculations revealed significant variance in calculated quadrupole splitting (and isotropic shielding parameters ≈ isomer shift), with the Becke half-and-half and a modified B3LYP functional including a higher fraction of Hartree-Fock exchange apparently performing best. The B3LYP functional with small double and triple zeta bases have also shown good linear correlation (R^2=0.975, ▽=1.04) for fourteen different low-spin d^6 organometallic quadrupole splittings, with η appearing to be less well determined [9]. These organometallic species are very large compared to FAS or FCL, and one would expect that crystal packing contributions would be significantly smaller, and therefore gas-phase calculations would give a reasonable approximation to the solid state. The B3LYP/cc-pVTZ level of theory has apparently performed very well for *p*-block chloride ^{27}Al values of Q, in close agreement with experiment [10]. DFT (hybrid and GGA) and multi-reference *ab initio* calculations on CuX diatomics (X=F, Cl, Br, I, H, Li) have shown poor general agreement, which for Cu was attributed to poor 3*d* orbital description when the species is polarized by electronegative ligands, and again indicated the extent of Hartree-Fock exchange (to functional) to be an important consideration [11]. The variances observed indicate that DFT methods may be erroneously fortuitous for many other transition metal compounds, and in general cannot be trusted. It is not surprising that calculations on the efg tensors in large Cd-complexes indicated that the metal ion needs to be described by a large basis set while the basis set can progressively become smaller for atoms further out of the co-ordination shell [12]. Finally, the development of meta-GGA (Laplacian-dependent generalized gradient approximation) type functionals appears to make a step towards an accurate calculation of transition metal hyperfine parameters [13].

To make matters more difficult, it appears that the value of Q (^{57}Fe Mössbauer transition nuclear quadrupole moment) is only tentatively known. The "2008 recommended value" of 160 mb [4, 14] is essentially based on theoretical DFT type calculations, and accurate experimental determinations are unavailable.[1] These calculations involve use of the linearised-augmented-plane-wave band structure method (GGA type DFT) [4,15] where experimental quadrupole splittings are related in a linear extrapolation with calculated efg tensors for a large number of small iron species by equation 12.3. Although individual efg tensors obtained are usually in not so good agreement with experiment, by extrapolating for a large number of calculated values it is argued that errors cancel. In addition, there are insufficient experimentally determined efg tensors of sufficient precision to extrapolate for Q. This procedure assumes errors are not systematically above or below experiment, which is

[1] 1 b (barn) = 1×10^{-20} m^2.

hard to assess since Q is not known in advance. The calculated values do show a varying degree of scatter, but in major part agree well with this extrapolation, yielding $Q = 170 \pm 20$ mb with the error determined by fitting confidence intervals.

A study is proposed that involves the calculation of efg tensors for both ferrous chloride tetrahydrate and ferrous ammonium sulphate, near 0 K, in an attempt to find accord with the previously reported experimental efg tensors at 293 K. The literature studies that have just been outlined were all performed some years ago, and with the rapid developments of computing power and computational methods, one may investigate the efg tensors at higher levels of theory than previously undertaken. The proposed comparison would be four-fold in parameters: unit cell contents; basis set; electron correlation/exchange-correlation functional; reference wave function (single or multi). Relativistic corrections for second, and third row species have been shown not to be important for efg tensor determinations of this type [7]. Single crystallographic unit and also scaffold geometries can initially be determined from the X-ray crystal structures, and then central octahedra can be (partially) optimized while surrounding (scaffold) species remain stationary.

12.1.1. Proposed computational method

The latest Gaussian 09 [16] and GAMESS-US [17] packages incorporate a wide range of modern meta-GGA DFT functionals that have varying degrees (up to complete) and parametrizations of Hartree-Fock exchange. Further, it could be feasible to perform multi-reference *ab initio* calculations on these species, where traditional single-reference methods perform poorly.

As a start, three hybrid basis sets are considered, denoted GEN1, GEN2 and GEN3, and are outlined in table 12.1.

Table 12.1.: Hybrid basis sets used for *ab initio* and DFT determination of electric field gradient tensors.

Species	GEN1	GEN2	GEN3
Fe	cc-pVQZ	cc-pVQZ	cc-pVQZ
Coordinated ligand atoms	TZV	cc-pVTZ	cc-pVQZ
Non-coordinated ligand atoms	TZV	cc-pVDZ	cc-pVQZ

The GEN1 to GEN3 basis sets provide an increasingly comprehensive description of the environment surrounding the Fe^{2+} nucleus. Comparison of efg tensors (whether accurate or not) between these basis set descriptions will, in part, indicate if the description of the efg tensor has converged with basis set description. The TZV basis set of Ahlrichs *et al.* [18], would most likely require further polarization, which could be initially achieved by addition of two d-type polarization functions and one f-type polarization function to second-row or heavier atoms. Treatment of iron with effective or model core potential basis sets would not be suitable [19].

Table 12.2.: Preliminary principal values in a.u. of efg tensors from DFT geometrical optimization calculations on the ferrous chloride tetrahydrate efg tensor at 0K, using the GEN2 basis set. Values should be multiplied by ≈ 0.1029 for correspondence to the single crystal results in this thesis.

Functional	V_{zz}	V_{yy}	V_{xx}	η
B3LYP	2.316	-1.953	-0.363	0.69
BMK	2.581	-1.826	-0.755	0.41
M06	0.898	-0.487	-0.410	0.09
M06-2X	2.225	-1.676	-0.549	0.51
M06-HF	2.481	-1.731	-0.751	0.39
BP86	0.892	-0.477	-0.416	0.07
TPSS	2.205	-1.949	-0.255	0.77
TPSSh	2.244	-1.928	-0.316	0.72
expt	2.401(14)	-1.609(242)	0.933(91)	0.266(67)

The isomorph studies in chapter 9 showed that the FCL crystal structure has an intricate array of hydrogen-bonding interactions that act as the main cohesion force holding octahedra together. Mulliken population analysis shows the chloride ligands carry essentially a negative charge, hence a scaffold should be constructed around one FCL octahedra that incorporates immediate neighbouring species. The scaffold constructed for the previous DFT calculations on hydrogen bonding interactions should be suitable. For FAS, the asymmetric unit contains one ammonium ion and one sulphate anion. Analysis of the FAS crystal structure, shows that hydrogen bonding interactions are significantly smaller compared with FCL, with Coulombic type ionic bonding constituting the main cohesion forces between octahedra (and counter-ions). Analogous to FCL, the scaffold should include the central water octahedron, the four counter anions and some fragments from neighbouring octahedra. Ideally, the scaffolds should be systematically constructed and species added until convergence of the calculated efg tensor is found, assuming an accurate computational method is known. This is a very involved procedure that would probably take many months of calculation time to establish.

Initial multi-configurational calculations could employ CASSCF(6,6) and CASSCF(6,11) active spaces that correspond to 4s, 3d and 3s, 3d, 4d active orbitals respectively. Current *ab intio* packages limit density matrix formation, which is used to compute the efg tensor, to only certain electron correlation methods such as MR-CISD. Therefore, other computational packages such as MOLPRO [20] may be required.

Some preliminary results of various DFT methods employing the GEN2 basis for FCL gas-phase optimizations are given in table 12.2.

These calculations show considerable variation in both V_{zz} and η. Best agreement with the experimental values of V_{zz}=2.401(14) a.u., and η=0.266(67) is found with the M06-HF functional, which includes 100% Hartree-Fock exchange [21]. It could be anticipated that low temperature measurements would alter these values only slightly (≈ 4%), since the quadrupole splitting changes from 2.98 mm sec^{-1} to 3.10 mm sec^{-1} between room temperature and 0.15 K [22]. These tentative calculations would also support the GEN2 basis

set as yielding a reasonable description.

In order to test suitability of the constructed basis sets, geometrical optimization parameters were considered for the $^5\Delta_g$ linear ground state $FeCl_2$ bond length, since this is well determined experimentally in the gas-phase at 2.128 ± 0.007 Å [23]. This bond length can change considerably depending on the extent of polarization altering the interaction between Cl 3p and Fe 3d orbitals, which in turn alters the extent of π bonding and hence bond length. Such considerations would be critical to consider for accurate efg tensor determinations. Preliminary results reveal the GEN3 basis set (largest considered here) to be sufficient to reproduce this bond length for multi-reference type and DFT calculations. Further, the high symmetry of the $FeCl_2$ species means that $\eta \approx 0$, and with a well-known quadrupole splitting of 1.201 mm sec^{-1} at 4.2 K [22], then this species can also be used to determine a suitable level of theory.

12.1.2. A proposed alternative method for determination of Q

With the shortfalls of DFT methods to determine efg tensors, and the computational complexity of reasonable CASSCF reference calculations including sufficient dynamical electron correlation, one should also consider a ligand-field (or even point charge crystal field) theory approach. Often more simplistic ligand field theory approaches can outperform high level *ab initio* or DFT methods for calculation of molecular properties such as efg tensors in situations where degeneracy and many closely separated electronic states exist [24–26]. Such a model may also be used to determine a value of Q by fitting to experimental measurements. Ferrous high spin compounds usually exhibit a strong temperature dependent quadrupole splitting, and the mathematics to describe this dependence have been well established by Golding [6, 27]. Assuming a Boltzmann temperature distribution over electronic states, the ferrous high-spin expectation nuclear quadrupole interaction is given in equation 12.4.

$$\langle E_Q \rangle = \frac{\sum_n \langle E_Q \rangle_n e^{-E_n/kT}}{\sum_n e^{-E_n/kT}} \tag{12.4}$$

where k is the Boltzmann constant, T is the temperature in Kelvin, and $\langle E_Q \rangle_n$ is the expectation nuclear quadrupole interaction for the electronic state of energy, E_n. These eigenvalues can be calculated assuming suitable wave functions (crystal field theory point charge, or more comprehensive) with the quadrupole Hamiltonian, $\hat{H}$, given in equation 12.5. Crystal field theory wave functions for the ^{57}Fe Mössbauer states and transitions are given in Golding [27].

$$\hat{H} = \frac{e^2 Q \langle r^{-3} \rangle}{7I(2I-1)} \sum_i \left((\hat{l}_i \cdot \hat{I})^2 + \frac{1}{2}(\hat{l}_i \cdot \hat{I}) - 2I(I+1) \right) \tag{12.5}$$

where $\hat{l}_i$ and $\hat{I}$ are electron and nuclear orbital and spin angular momentum operators respectively. Assuming the crystal field wave functions, with summation over the fifteen possible M_I states, $\langle E_Q \rangle$ can be expressed in equation 12.6.

$$\langle E_Q \rangle = \frac{e^2 Q \langle r^{-3} \rangle}{7I(2I-1)} \frac{\sum_{n=1}^{6} 2C_n e^{-a_n \zeta / kT} + \sum_{n=7}^{9} C_n e^{-a_n \zeta / kT}}{\sum_{n=1}^{6} 2e^{-a_n \zeta / kT} + \sum_{n=7}^{9} e^{-a_n \zeta / kT}} \left(3M_I^2 - I(I+1)\right) \tag{12.6}$$

Values of the coefficients C_n and a_n can be calculated from an expression involving the ratio of $\frac{\Delta}{\zeta}$, where Δ is the free $^5T_2$ Fe^{2+} octahedral crystal field splitting parameter, and ζ is the spin-orbit coupling constant [27]. When considering the ^{57}Fe Mössbauer transition between nuclear states $|\pm\frac{3}{2}\rangle$ and $|\pm\frac{1}{2}\rangle$, equation 12.6 simplifies to yield the quadrupole splitting expression, ΔE_Q, given in equation 12.7.

$$\Delta E_Q = \frac{2}{7} e^2 Q \langle r^{-3} \rangle \frac{\sum_{n=1}^{6} 2C_n e^{-a_n \zeta / kT} + \sum_{n=7}^{9} C_n e^{a_n \zeta / kT}}{\sum_{n=1}^{6} 2e^{-a_n \zeta / kT} + \sum_{n=7}^{9} e^{-a_n \zeta / kT}} \left(3M_I^2 - I(I+1)\right) \tag{12.7}$$

This expression contains a reasonable description of the temperature dependence of the quadrupole splitting. By experimentally measuring the temperature dependence of a quadrupole splitting for a given species, or taking previously measured literature data that is abundant for a wide range of Mössbauer active species, then the expression in 12.7 could be non-linear least squares fitted. In these fits there are several physical constants, where $\langle r^{-3} \rangle$ is the expectation radius function that has been determined for the Fe^{2+} $^5T_2$ configuration at 5.08861 a.u. by Hartree-Fock calculations [28]. The parameter ζ is the spin-orbit coupling constant, which has been experimentally measured at $\lambda = \frac{\pm\zeta}{2S}$ = -94 to -109 cm^{-1} [29,30] corresponding to a value of $\zeta \approx 420$ cm^{-1}, and calculated at λ = -115 cm^{-1} by Hartree-Fock theory [28].[2] These parameters are all assumed in the free atom approximation, and when fitted, would yield a value of Q. By applying this procedure for several different species, an estimate of Q could be obtained that could very well outperform DFT calculations. This procedure does allow one to gauge the suitability of the model by comparing fitted ζ with spectroscopic measurements for each respective compound. If unsuitable, the model could be improved with a more comprehensive ligand-field theory approach. In general, any model should always be able to reproduce other (well known or experimentally measured) related physical parameters to that of interest. Yet, the efg tensor studies of Dufek *et al.* [15] or Schwerdtfeger *et al.* [7], on first inspections show no detailed comparison or reference to other studies where this has been performed with their methods.

12.2. Experimental measurement of anisotropy in the recoilless fraction

In a wave mechanics picture, an atom contains electrons distributed in a well defined region of space, which may scatter incident electromagnetic radiation. For any given relative scattering orientation, the spatial arrangement of electrons contributes different waves with corresponding amplitudes and phases. The total atomic scattering factor (or amplitude), f_0, from this scattering interaction depends upon the averaged electron arrangement, and takes the general (elastic) one-dimensional form of equation 12.8.

$$f_0 = \int U(r), r, \theta, \lambda dr \tag{12.8}$$

[2]The $\pm$ when describing the spin-orbital coupling constant describes the relative orientation of sub-level splitting in the applied spin-orbit interaction, where + corresponds to a less than half filled *d*-orbital shell, and - corresponds to a more than half filled *d*-orbital shell.

where $U(r)$ is the electron distribution potential function for separation r, θ represents a relative scattering angle, and λ is the incident wavelength. In X-ray crystallography, the molecular structure factor involves superposition of atomic scattering factors of each atom in the unit cell with estimation of phases. Equation 12.8 assumes, apart from a small zero-point energy contribution, a stationary origin (nucleus), which is not the case for a real crystalline material at any temperature. Nuclei bound in crystals have an expectation position fixed in space by a complex combination of intermolecular forces which changes as a function of temperature. In effect, this reduces the scattering factor relative to an atom at rest. Assuming harmonic scattering with an isotropic temperature effect in one dimension, the thermal atomic scattering factor, f_X, otherwise known as the Debye-Waller factor, is given in equation 12.9 [31].

$$f_X = f_0 e^{-8\pi^2 \langle U^2 \rangle \frac{\sin^2 \theta}{\lambda^2}} \tag{12.9}$$

where $\langle U^2 \rangle$ ($=\langle r^2 \rangle$ in one dimension) is the isotropic mean-square-atomic-displacement parameter (ADP) that inherently incorporates temperature dependence. The $\sin^2 \theta$ angular dependence of this equation is easily derived by considering the projection of wave vector $\mathbf{k}$ on general tensor $\mathbf{U}$. A detailed discussion of thermal vibrations in crystals can be found in the text of Willis and Pyror [32]. In three-dimensional space, the ADP is represented by a 3×3 symmetric Cartesian tensor, $\mathbf{U}$, with elements denoted U_{ij}, which abides by the transformation properties of a 3×3 symmetric matrix. The more correct anisotropic thermal displacement has an ellipsoid type thermal displacement, with the 3×3 symmetric Cartesian tensor inherently containing orthogonal principal directions (maximum displacement directions) and principal values (maximum displacement amplitudes).

Expressions correcting for anharmonic effects (i.e. with cubic and higher order terms) to an anisotropic ADP are complex and their contribution almost certainly beyond the accuracy of the X-ray Mo K_α (or analogous Mössbauer herein) measurements [33]. In X-ray, the anisotropic $\mathbf{U}$ tensor is determined by refinement of electron probability densities for each atom, and the nucleus is assumed to be at the ellipsoid centre. Based on equation 12.9, in hindsight, the original FAS estimated X-ray determined msd tensor should have been calculated for Mo K_α radiation, nevertheless convergence was to the same result. The correction factor of $k^2(\text{Mo})/k^2(\text{Fe}) = 1.465$ would still not account for principal value differences. The corrected X-ray determined msd tensor is given in equation 12.10.

$$\mathbf{msd}_0 = \begin{bmatrix} 1.4077 & 0.0409 & -0.0982 \\ 0.0409 & 1.0990 & -0.0711 \\ -0.0982 & -0.07113 & 1.3335 \end{bmatrix} \tag{12.10}$$

In Mössbauer, the analogous Lamb-Mössbauer factor, f_M, is defined as the probability of a recoil-free resonant absorption and emission, with $0 \leq f_M \leq 1$. This is analogous to the Debye-Waller factor in X-ray crystallography, apart from that in Mössbauer spectroscopy, the vibrating nucleus is simultaneously

experiencing resonant absorption and emission. These differences are theoretically outlined by Trammell [34], and Lipkin [35], in an entertaining historical account of the early history of the Lamb-Mössbauer factor. It would be anticipated that the Lamb-Mössbauer angular dependence would be a function of $\cos^2\theta$ (i.e. with a $\frac{\pi}{2}$ phase offset to Debye-Waller situation) in equation 12.9, since in X-ray scattering, the maximum occurs for a large displacement, whereas for Mössbauer, the probability is minimum for a large displacement. The question arises, does a change in nuclear state change (to any appreciable extent) the thermal vibration? Intuitively, although the nuclear volume changes slightly, this would have negligible bonding effects and therefore minimal vibrational consequences. In Mössbauer spectroscopy, the Lamb-Mössbauer factor is determined to be analogous to the Debye-Waller factor, since the elastic scattering of X-rays without lattice excitation is considered to be equivalent. Interestingly, the physics required to understand the Mössbauer effect was published by Lamb [36] long before the discovery of the effect, when Mössbauers Nobel-Prize winning experiments provided the first experimental evidence that was interpreted in terms of Lamb's theory. The derivation of equation 12.11 for a one-dimensional type rotation with f_0 intuitively at unity in the Mössbauer case, was first achieved by Shapiro [37], who considered the classical theory of radiation and assumed a Lorentzian function arising from the nuclear cross-section. Detailed derivations considering the simple Einstein model or Deybe model of the crystal can be found in Danon [38] or Frauenfelder [39]. Further, it is noted that equation 12.11 is equivalent to a quantum model derivation by Van Hove [40]. Kolk [41] outlines some further anharmonic terms that could potentially be parameterized, if such effects were significant.

$$f_M = e^{\frac{-8\pi^2}{\lambda^2}\langle msd\rangle \sin^2\theta} \tag{12.11}$$

The expectation value $\langle msd\rangle$ for a general msd tensor in the anisotropic situation can be evaluated according to equation 12.12 for a known spherical polar (θ, ϕ) pair in the tensor principal axis reference frame.

$$\langle msd\rangle = \left(msd_{xx}\cos^2\phi + msd_{yy}\sin^2\phi\right)\sin^2\theta + msd_{zz}\cos^2\theta \tag{12.12}$$

where msd_{qq} are principal values of the msd tensor.

In contrast to X-ray results, the Mössbauer measurements reported in the previous chapters directly measure nuclear displacement rather than expectation atomic (electron density) displacement. The Mössbauer studies considered rotation of a single-crystal, about a laboratory angle ε, where the γ-beam sweeps out the surface of a cone in one dimension, with the laboratory rotation axis as the principal axis of the cone. This situation may be described by equation 12.11 where $\theta = \varepsilon$. Therefore, using the functional form of equation 12.11, the general expression given in equation 12.13 is fitted the macroscopic FAS thickness and polarization corrected angular rotation data.

$$f = Ae^{\left(-\sin^2\left(\frac{1}{2}\varepsilon\right)\right)} + B \tag{12.13}$$

where A and B are fitted variables that absorb the other parameters in equation 12.11. To assess the applicability of this expression, this function was first fitted to the original FAS simulation based on X-ray determined msd tensor and found that within 95% confidence intervals, this expression exactly fitted the simulated data. That is, this function reproduces the angular dependence of the fully numerical Hamiltonian procedure by MOSREF. This fitting procedure in effect provides a method of averaging, which in turn would yield better refinement parameters with substantially less error.

In equation 12.13, the factor of $\frac{1}{2}$ effectively halves the periodicity of the sinusoidal function. For a symmetric Cartesian tensor, with a one-dimensional angular rotation, one would intuitively expect a single period. This factor can be rationalized by considering the crystal cut and the microscopic contributions to observed macrosocopic intensity, as shown in figure 12.2, where averaging the contributing microscopic (site) phase offsets yields approximately 180 deg.

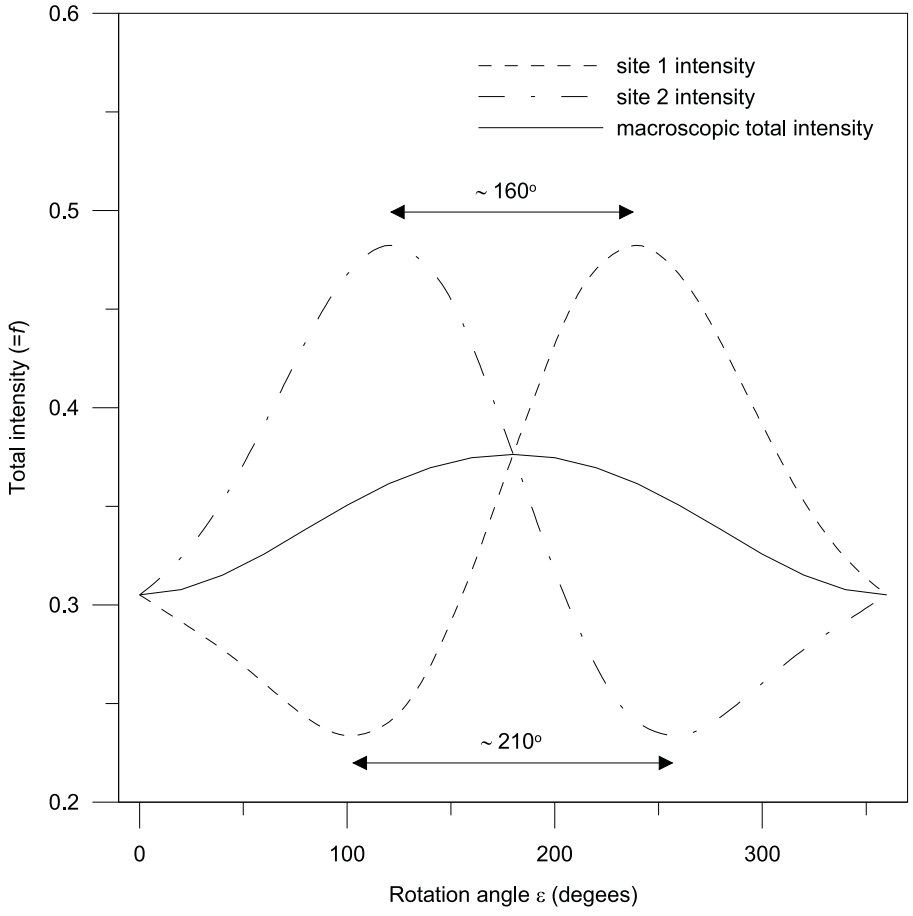

Figure 12.2.: Microscopic contributions in FAS of each of the two symmetry-related sites to the final macroscopic MOSREF fitted total intensity ($= f$).

The $(\bar{2}01)$ crystal cut involves the crystallographic unique b-axis to be offset by the small angle of $\xi \approx 1.9°$ from being co-axial with the crystal plane normal or goniometer rotation axis. Considering the error in the

reported rotation angles is estimated at $\approx \pm 0.5°$, the difference between these two measurements would be close to the small angular offset. In turn, this provides rationale for the apparent centre of symmetry existing in the observed angular rotation intensities. Application of this averaging procedure to the FAS total intensity yields a RMSD decrease by 0.001 intensity units, where each total intensity can be assumed at unit weighting, rather than hand optimizing weighting coefficients for each spectra by systematically weighting out the datum points that show poor fits to the model. The averaged MOSREF refined total intensities essentially overlap with the initial fitting function, as shown in figure 12.3.

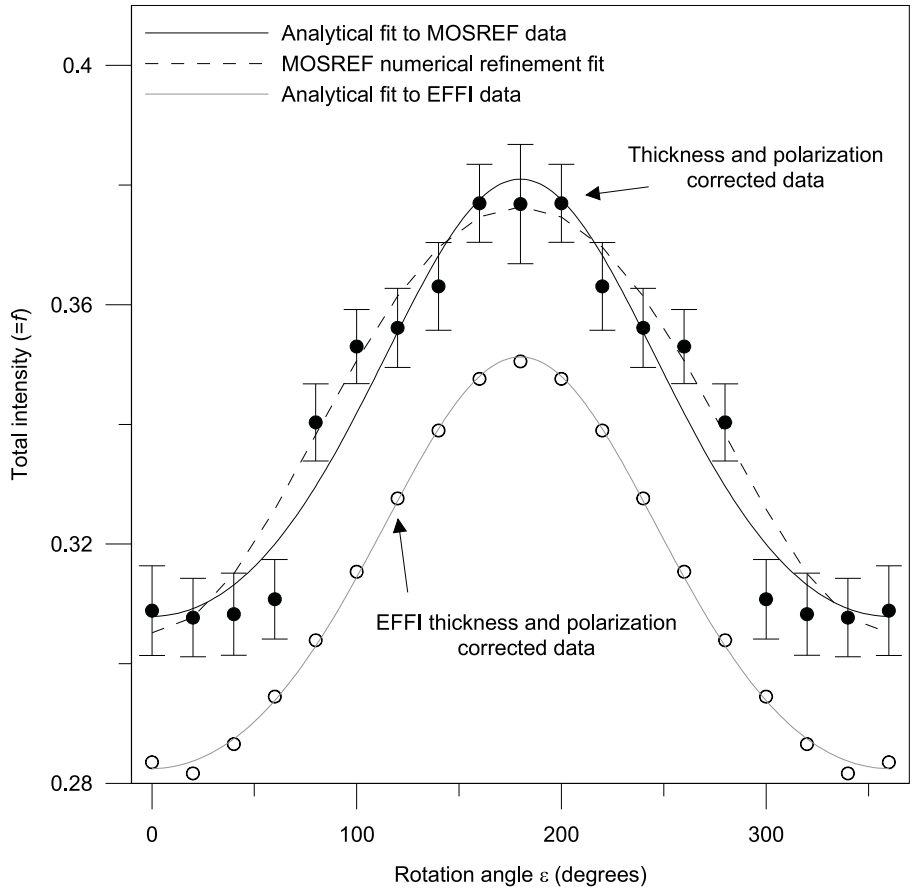

Figure 12.3.: Application of the analytical total intensity (Lamb-Mössbauer) fitting expression to FAS thickness and polarization intensities ($R^2 = 0.944$), and the simultaneous fitted and refined total intensities by program EFFI ($R^2 = 0.998$) - scaled to differentiate from the data. The MOSREF numerical fit with arbitrary weightings is also shown. When the MOSREF refinement utilizes the analytical fitted intensities, the refinement curve is essentially superimposed on the initial analytical fit.

It is more important to analytically fit the total intensities since any error in the relative total intensity between two lines of the quadrupole doublet, or two angular rotation spectra approximately cancels when intensity ratios are calculated. The analytically fitted thickness and polarization corrected refinement shows small differences to the tensor elements and diagonalizations reported in the FAS chapter, however in most cases, these are within reported errors. A full description is not outlined here since new experiments are currently being undertaken to repeat the measurements of the FAS spectra with a new thinner crystal and a higher-activity source, giving a five

to six fold off-resonance count increase. Also shown in figure 12.3 is application of the analytical fitting function to the exactly treated thickness and polarization intensities for FAS from program EFFI [42], where all fits, parameters and weightings in refinements are optimized simultaneously (obtained from personal communication with Prof. Harmut Spiering). The almost perfect fit again supports its application for averaging. Application of EFFI has not been considered here since the program outputs are in German, and the source code is difficult to compile on modern Linux distributions.

This fitting procedure can also be applied to FCL, where the angular rotation total intensities show a much smoother raw trend. The fitting is slightly more complicated than employing the function given in equation 12.13, since this would yield a symmetrical total intensity fit. Experimentally, a small asymmetry between two two angular rotation total intensity peaks was observed. This asymmetry can be traced back to the small non-zero off-diagonal element in the refined msd tensor. In turn, the double peak intensity pattern can again be traced back to the physical orientation of the crystal, where the crystallographic unique b-axis is now in the plane of the crystal, which in this instance is orthogonal to the goniometer rotation axis. The required fitting function therefore contains a trigonometric weighting function applied to two symmetrical functions taking the form of equation 12.13. This fitting function is given in equation 12.14.

$$f = \left(Ae^{-\sin^2\varepsilon} + B\right)\left(\frac{1}{2}\sin\varepsilon + \frac{1}{2}\right) + \left(Ce^{-\sin^2\varepsilon} + D\right)\left(\frac{1}{2}\sin(\varepsilon - 180) + \frac{1}{2}\right) \tag{12.14}$$

where a non-linear least squares fitting optimizes the four parameters A, B, C, and D. The fit to experimental thickness and polarization corrected intensities is shown in figure 12.4, and reduces the refinement RMSD by approximately 0.001 intensity units. The previously refined efg and msd tensors are essentially invariant to the analytically fitted and averaged total intensities.

These developments still shed no light on the fact that the Mössbauer determined msd tensors appear different in both principal values, and for FAS, in principal directions to those determined by X-ray. These fits do prove that the isotropic assumption is invalid and provides a physical interpretation, consistent with the fundamental properties of the Mössbauer effect, with the apparent experimental single crystal anisotropy in the recoilless fraction.

12.3. Almandine garnet

The studies on FAS and FCL were originally motivated by a similar point-source (milliprobe) study of a very small (sub 1 mm^2) almandine garnet crystal performed in part by Dr. Craig Tennant at the Bayerisches Geoinstitut, University of Bayreuth, Germany. Briefly, almandine has the general formula $Fe_3Al_2(SiO_4)_4$ with the cubic space group $Ia\bar{3}d$ [43]. Such minerals are naturally formed under certain geological conditions, and are mined for jewellery in areas of Alaska, Canada and the Czech Republic. Synthetic growth of large single crystals is generally difficult [44]. Unfortunately, natural isomorphic replacement of Fe^{2+} with Mg^{2+} yields a series of different stoichiometric compositions, which are not easily differentiated based on external colour and

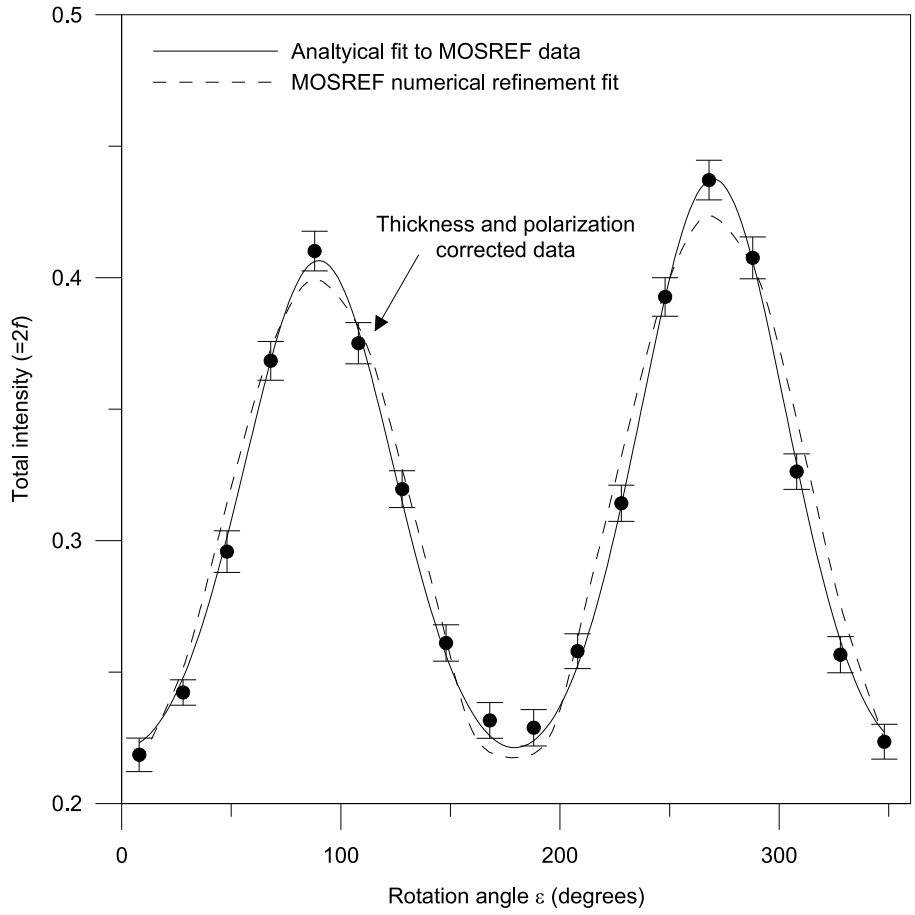

Figure 12.4.: Application of the analytical total intensity (Lamb-Mössbauer) fitting expression to FCL thickness and polarization corrected intensities ($R^2 = 0.997$).

morphology. The majority of high quality crystals are sold for jewellery purposes, and if one wishes to purchase one for Fe^{2+}-related Mössbauer studies, analysis has to be undertaken to ensure the pure almandine form is obtained with no isomorphic replacement. For an ideal almandine, the Fe^{2+} ions sit on crystallographic special positions conforming to octahedral (orthorhombic) coordination with 222 or Laue class mmm (D_{2h}) point symmetry, with six symmetry-related sites per unit cell, and each site contributing to the same quadrupole doublet. It is intuitive that for a cubic crystal, anisotropies will be smaller owing to higher symmetrical constraints. The Mössbauer spectrum shows one quadrupole doublet, with Lorentzian wings showing small overlap. The nature of the point source employed in the milliprobe study yielded large line widths, large error in the angular rotation asymmetry intensity ratios that naturally exhibit small asymmetry, and unfortunately resulted in poor fits to simulation/refinement.

During the course of this thesis, Dr. Craig Tennant while holidaying in Alaska in 2008, visited a garnet mine where he purchased several promising looking crystals. One of these which conformed to a regular dodecahedron was selected for study following the successful studies and goniometer assembly constructed from the work in this thesis. By tentative interpretation of the external morphology (consideration of three

and four point apices) of a highly symmetrical space group crystal, a face was selected that was thought to be suitable. Using a diamond toothed saw, a slice was cut and super glued to a perspex disc. This crystal was hand polished over several afternoons using the brass guide as described in FAS and FCL chapters, to a physical thickness of 252±9 μm. In contrast to FAS or FCL, which took only several hours of careful polishing, the garnet crystal was considerable harder (and showed a crystal structure similar to diamond!), where hand polishing took several afternoons. Analysis under the polarizing microscope showed sharp extinctions every 90°, indicating the crystal to be single, however close inspection of the slice and cut faces showed several fracture lines. Transmission electron microscope analysis by the Department of Electrical Energineering on a small bulk crystal face showed stoichiometry consistent with almandine. Crystallography on a ground powder sample revealed unit cell parameters in agreement with those previously published for a claimed pure almandine sample. A n X-ray florescence analysis revealed a composition consistent with a relatively pure and suitable almandine. With this crystal cut, and (at the time) the newly implemented 5 mCi nominal strength Mössbauer source, angular rotation spectra were obtained at the 45° rotation axis inclination. Each spectrum collected just over 1×10^6 off-resonance counts, corresponding to a five-fold increase on that collected for the first FAS study in this thesis. The collection of an increased number of counts showed considerable reduction of the experimental error which is important for almandine since observed intensity ratios show much smaller variance over rotation than FAS or FCL cases. Fits of angle-dependent spectra reveals this data to have considerably narrower line widths than those obtained in the milliprobe study. It was also determined that the Lorentzian line function was a rather poor approximation (not uncommon for silicate minerals [45]), where the residual showed unfitted intensity near the quadrupole doublet maxima, with χ^2=1.94 for the arbitrary angle of $\varepsilon = 0°$. Application of a Voigt profile gave considerable reduction of this residual and the better $\chi^2 = 1.37$. Intensities corrected with a transmission integral, and fitted to a Voigt profile then yielded $\chi^2 = 1.21$, with no apparent residual intensity. These fits reveal narrow lines and considerably reduced error compared to the original milliprobe study, and should be sufficient to obtain accurate intensity ratios required for efg tensor refinement. That thickness corrections for good fits are important could be expected since almandine garnet has a higher density than FAS or FCL, and therefore a higher mass absorption coefficient.

Interestingly, a polycrystalline powder spectrum, which should be free of texture effects from preferred crystallite orientations, reveals a slight asymmetric quadrupole area ratio of ≈ 0.5091 at room temperature in accord with previous studies [44]. After angular rotation spectra collection, Prof. Ward Robinson and Dr. Chris Fitchett performed X-ray diffraction off one face to determine that unfortunately this crystal cut contained a plane that was $\approx 18°$ off the ideal (100) plane that was initially targeted. Simulations performed by Dr. Craig Tennant revealed that this particular cut was not ideal for measurement of a large reduced intensity asymmetry. The appropriate (100) cut would give an asymmetry of approximately three times that of the cut obtained here. As a solution, the crystal was packaged and sent to the Bayerisches Geoinstitut, University of Bayreuth, where accurate crystal cutting and polishing to 200±1 μm was performed. This new cut was returned glued to the surface of a glass slide. Glass cannot be used in Mössbauer experiments owing to very large attenuation effects (high mass absorption coefficients), therefore the crystal needed to be removed and fixed to a perspex disc. The particular glue used (CrystalBond) could be dissolved in acetone, or thermally cleaved at ≈ 100°C. Crystals of

this thickness are ultra-sensitive to fracturing and it would be too risky to dissolve the glue and then reattach to a perspex disc (which would dissolve in acetone also). The obvious procedure would be to first fix a perspex disc (super glue) to the exposed crystal surface, and then to cleave the surface fixed to the glass, since super glue is resistant to cleavage at $\approx 100°$C. Unfortunately (and very ironically for a Chemistry Department!), there was no hotplate available at the time with accurate temperature control available, therefore one was constructed. This involved cannibalizing a third year lab thermocouple assembly, where the thermocouple was wrapped with some high-temperature electrical thread tape in order to proved electrical insulation, and fixed into a hole drilled into large flat aluminium plate, which was mounted on a hot plate with a rough temperature dial. A standard mercury thermometer in contact with the hot plate showed excellent control in agreement with the thermocouple digital readout, and selection of temperatures over the ranges required. Following the proposed procedure, removal was painless and angular rotation spectra of this new crystal cut were collected. Total intensities, as expected for a site of cubic symmetry, were experimentally invariant to laboratory rotation angle. This data awaits future refinement and interpretation, and hopefully will show the generalization of the method employed for FAS and FCL for two microscopic symmetry-related sites to six, although in the absence of the ambiguous monoclinic problem.

12.4. Ferrous ammonium sulphate hexahydrate

Following publication of the FAS single crystal study, and completion of data collection for FCL and the almandine garnet crystals, the Mössbauer source was still reasonably active so it was decided that a new FAS crystal should be synthesised and new measurements undertaken to reduce experimental error. In addition, simultaneous spectra fittings are planned using the program EFFI [42], in collaboration with Prof. Harmut Spiering. A new crystal was synthesised and polished to a physical thickness of 222±6 μm (0.354 μm at the 45° inclination) in the same $(\bar{2}01)$ plane. The first data collection revealed this much thinner crystal to collect approximately four to five times as many off-resonance counts in half the collection time as the original FAS study. The thinner crystal will also have significantly smaller thickness and polarization corrections to apply, although at a trade-off of background since the γ-beam on average experiences fewer resonant nuclei in its path. The new angular rotation intensities collected in December 2009 and early January 2010, with a non-calibrated laboratory rotation angle, are shown in figure 12.5.

It is clear from figure 12.5 that the errors in the total intensities are significantly reduced, where the magnitude of anisotropy in the total intensity curve is several times that of the individual datum errors bars. Application of the analytical function for the total intensity yields the arbitrary laboratory rotation angle offset from the laboratory rotation angle, ε, at 211.61° as determined by a non-linear least squares regression. This fit is expected to improve when further datum points become available on both sides of the maximum - currently the curve is only fitting to two data points on the left side of the maximum, and the fit will most likely improve on addition of more data.

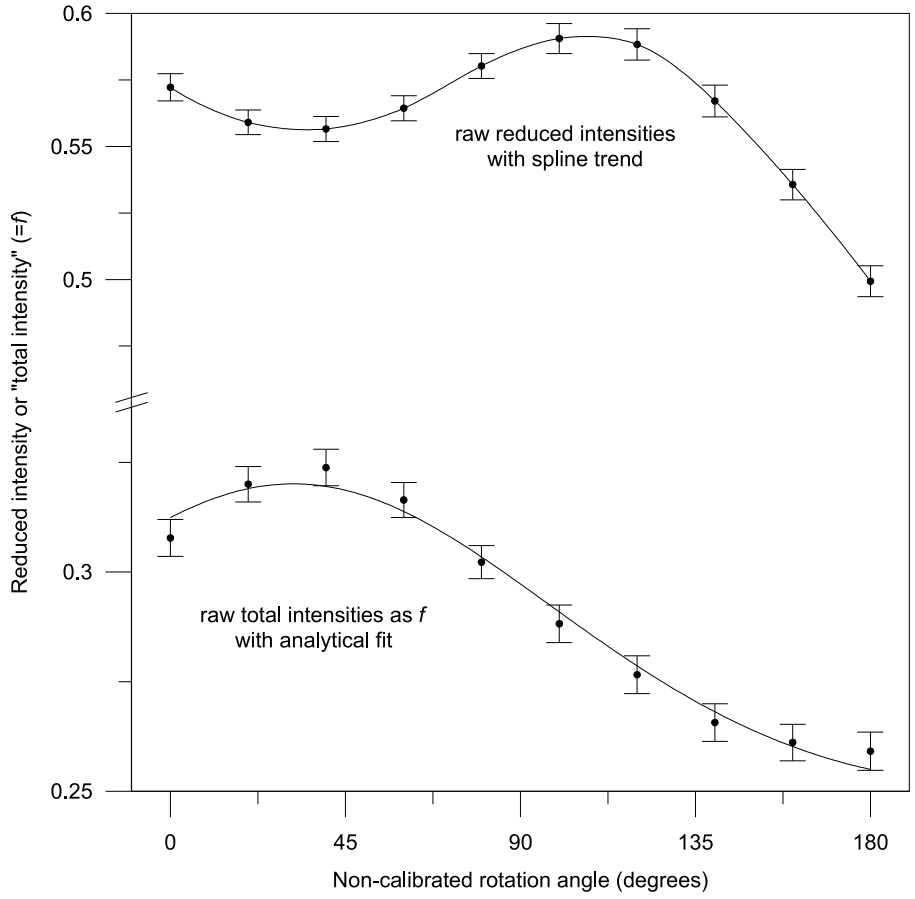

Figure 12.5.: Raw (not thickness and polarization corrected) reduced and total intensities ($= f$) for the new FAS angular rotation measurements. The total intensity shows the analytical function fit, with $R^2 = 0.985$ - more data points are required on both sides of the maximum for an accurate fit.

References

[1] E. N. Kaufmann and R. J. Vianden. *Rev. Mod. Phys.*, 51:161, 1979.

[2] J. N. Bull, W. T. Robinson, and W. C. Tennant. *Hyperfine Interact.*, 194:347, 2009.

[3] S. Cottenier, V. Vanhoof, D. Torumba, V. Bellini, M. Cakmak, and M. Rots. *Hyperfine Interact.*, 158:9, 2004.

[4] P. Blaha, K. Schwarz, W. Faber, and J. Luitz. *Hyperfine Interact.*, 126:389, 2000.

[5] R. Orlando, R. Dovesi, P. Ugliengo, C. Roetti, and V. R. Saunders. *Int. J. Inorg. Mat.*, 1:147, 1999.

[6] R. M. Golding, K. F. Mok, and J. F. Duncan. *Inorg. Chem.*, 5:774, 1966.

[7] P. Schwerdtfeger, T. Söhnel, M. Pernpointner, J. K. Laerdahl, and F. E. Wagner. *J. Chem. Phys.*, 115:5913, 2001.

[8] N. Godbout, R. Havlin, R. Salzmann, P. G. Debrunner, and E. Oldfield. *J. Phys. Chem. A*, 102:2342, 1998.

[9] R. H. Havlin, N. Gobout, R. Salzmann, M. Wojdelski, W. Arnold, C. E. Schulz, and E. Oldfield. *J. Am. Chem. Soc.*, 120:3144, 1998.

[10] G. J. Mains, E. A. Nantsis, and W. R. Carper. *J. Phys. Chem. A*, 105:4371, 2001.

[11] R. Bast and P. Schwerdtfeger. *J. Chem. Phys.*, 119:5988, 2003.

[12] L. Hemmingsen and U. Ryde. *J. Phys. Chem.*, 100:4803, 1996.

[13] A. V. Arbuznikov, M. Kaupp, V. G. Malkin, R. Reviakine, and O. L. Malkina. *Phys. Chem. Chem. Phys.*, 4:5467, 2002.

[14] P. Pyykkö. *Mol. Phys.*, 106:1965, 2008.

[15] P. Dufek, P. Blaha, and K. Schwarz. *Phys. Rev. Lett.*, 75:3545, 1995.

[16] M. J. Frisch, G. W. Trucks, H. B. Schlegel, G. E. Scuseria, M. A. Robb, J. R. Cheeseman, G. Scalmani, V. Barone, B. Mennucci, G. A. Petersson, H. Nakatsuji, M. Caricato, X. Li, H. P. Hratchian, A. F. Izmaylov, J. Bloino, G. Zheng, J. L. Sonnenberg, M. Hada, M. Ehara, K. Toyota, R. Fukuda, J. Hasegawa, M. Ishida, T. Nakajima, Y. Honda, O. Kitao, H. Nakai, T. Vreven, J. A. Montgomery, Jr., J. E. Peralta, F. Ogliaro, M. Bearpark, J. J. Heyd, E. Brothers, K. N. Kudin, V. N. Staroverov, R. Kobayashi, J. Normand,

K. Raghavachari, A. Rendell, J. C. Burant, S. S. Iyengar, J. Tomasi, M. Cossi, N. Rega, J. M. Millam, M. Klene, J. E. Knox, J. B. Cross, V. Bakken, C. Adamo, J. Jaramillo, R. Gomperts, R. E. Stratmann, O. Yazyev, A. J. Austin, R. Cammi, C. Pomelli, J. W. Ochterski, R. L. Martin, K. Morokuma, V. G. Zakrzewski, G. A. Voth, P. Salvador, J. J. Dannenberg, S. Dapprich, A. D. Daniels, O. Farkas, J. B. Foresman, J. V. Ortiz, J. Cioslowski, and D. J. Fox. Gaussian 09, Revision A.1. Gaussian, Inc., Wallingford, CT, 2004.

[17] M. W. Schmidt, K. K. Baldridge, J. A. Boatz, S. T. Elbert, M. S. Gordon, J. H. Jensen, S. Kosecki, N. Matsunaga, K. A. Nguyen, S. J. Su, T. L. Windus, M. Dupuis, and J. A. Montgomery. *J, Comput. Chem.*, 14:1347, 1993.

[18] A. Schäfer, C. Huber, and R. Ahlrichs. *J. Chem. Phys.*, 100:5829, 1994.

[19] M. Dolg. Effective core potentials. In *Modern Methods and Algorithms of Quantum Chemistry*, volume 3, page 507. John von Neumann Institute for Computing: Jülich, 2000.

[20] H. J. Werner, P. J. Knowles, R. Lindh, F. R. Manby, M. Schütz, P. Celani, T. Korona, A. Mitrushenkov, G. Rauhut, T. B. Adler, R. D. Amos, A. Bernhardsson, A. Berning, D. L. Cooper, M. J. O. Deegan, A. J. Dobbyn, F. Eckert, E. Goll, C. Hampel, G. Hetzer, T. Hrenar, G. Knizia, C. Köppl, Y. Liu, A. W. Lloyd, R. A. Mata, A. J. May, S. J. McNicholas, W. Meyer, M. E. Mura, A. Nicklass, P. Palmieri, K. Pfl"uger, R. Pitzer, M. Reiher, U. Schumann, H. Stoll, A. J. Stone, R. Tarroni, T. Thorsteinsson, M.Wang, and A. Wolf. *MOLPRO - version 2009.1, a package of ab initio programs,*. see http://www.molpro.net, 2009.

[21] Y. Zhao and D. G. Truhlar. *J. Phys. Chem. A*, 110:13130, 2006.

[22] T. C. Gibb N. N. Greenwood. *Mössbauer Spectroscopy*. Chapman and Hill Ltd.: London, 1971.

[23] M. Hargittai, N. Y. Subbotina, M. Kolonits, and A. G. Gershikov. *J. Chem. Phys.*, 94:7278, 1991.

[24] M. T. Hutchings. *Solid state physics: advances in research and applications*, volume 16, chapter Point-Charge Calculations of Energy Levels of Magnetic Ions in Crystalline Electric Fields, page 227. Academic Press Inc.: New York, 1964.

[25] A. Hudson and H. J. Whitfield. *Mol. Phys.*, 12:165, 1967.

[26] K. N. Woods, A. M. Khasanov, and J. G. Stevens. *Hyperfine Interact.*, 188:127, 2009.

[27] R. M. Golding. *Applied Wave Mechanics*. Van Nostrand Company: London, 1969.

[28] S. Fraga, K. M. S. Saxena, and J. Karwowski. *Handbook of Atomic Data*. Elsevier: Amsterdam, 2 edition, 1979.

[29] M. Blume and R. E. Watson. *Proc. Roy. Soc. A*, 271:565, 1963.

[30] J. S. Griffith. *The theory of transition-metal ions*. Cambridge University Press: London, 1961.

[31] K. N. Trueblood, H. B. Bürgi, H. Burzlaff, J. D. Dunitz, C. M. Gramacciolo, H. H. Schulz, U. Shmueli, and S. C. Abrahams. *Acta. Cryst. A*, 52:770, 1996.

[32] B. T. M. Willis and A. W. Pryor. *Thermal Vibrations in Crystallography.* Cambridge University Press:London, 1975.

[33] K. N. Pathak and B. Deo. *Physica*, 35:167, 1967.

[34] G. T. Trammell. *Phys. Rev.*, 126:1045, 1962.

[35] H. J. Lipkin. *Hyperfine Interact.*, 72:3, 1992.

[36] Jr. W. E. Lamb. *Phys. Rev.*, 55:190, 1939.

[37] F. L. Shapiro. *Usp. Fiz. Nauk.*, 72:68, 1960.

[38] J. Danon. *Lectures on the Mössbauer Effect.* Gordon and Breach, Science Publishers, Inc.: New York, 1968.

[39] H. Frauenfelder. *The Mössbauer Effect (Frontiers in Physics).* W. A. Benjamin, Inc.:New York, 1963.

[40] L. van Hove. *Phys. Rev.*, 95:249, 1954.

[41] B. Kolk: In: G. K. Horton and A. A. Maradudin (eds.). *Dynamical Properties of Solids*, volume 5. Elsevier, Amsterdam, 1984.

[42] H. Spiering, L. Deak, and L. Bottyan. *Hyperfine Interact.*, 125:197, 2000.

[43] S. S. Hafner G. Amthauer, H. Annersten. *Zeitschrift für Kristallographie*, 143:14, 1976.

[44] C. A. Geiger and K. Jiang W. Lottermoser G. Amthauer Th. Armbruster, G. A. Lager. *Phys. Chem. Minerals*, 12:121, 1992.

[45] D. G. Rancourt. *Phys. Chem. Minerals*, 21:244, 1994.

Appendix - From a Child's Toy to a Nobel Prize: Mössbauer Spectroscopy

Part of the requirements for a Ph.D. in Chemistry at the University of Canterbury is the presentation of a second year review seminar. Following this seminar, the author was invited to submit a written article to a New Zealand education journal. ChemEd NZ required that the article be understandable by undergraduates and be of a length of $\approx$ 4000 to 6000 words to summarise the fundamentals and applications of the chosen study. This chapter is an amended reproduction of that published article:

From a child's toy to a Nobel prize: Mössbauer Spectroscopy, James N. Bull, ChemEd NZ, 116 (2009) 11-19

Overview

The year 2008 marked the 50^{th} anniversary of the discovery, by German Ph.D. student Ruldolf Mössbauer, of recoilless absorption and emission of γ-ray quanta from nuclei bound in solids. He was awarded a Nobel Prize in Physics in 1961, within three years of his experiments, and represents one of the youngest recipients in the prize's history. The Mössbauer effect, which probes nuclear energy levels to characterize electronic structure has enjoyed remarkable success in pure and applied research in fields as diverse as archaeology, industry, the Mars environment and biology. This chapter provides a brief overview of the technique, and then outlines its contributions to some more exotic studies and applications.

BOX 1 - Resonance

Resonance is the tendency for two systems to become synchronized and oscillate with maximum amplitude. The simplest example is synchronization (motion) of a tuning fork with a persons ear drum (absorber), where sound pulses or beats of maximum amplitude are heard corresponding to resonant frequencies. Atomic resonance fluorescence (absorption and emission at the same wavelength) is fundamental to the understanding of atomic spectroscopy. This was first proposed by Lord Rayleigh in the 19^{th} century, and first observed in 1904 by Wood in the optical fluorescence of atomic sodium vapour [1]. For the case of sodium vapour, the small electronic transition energy and long excited state lifetime yields broad absorption and emission lines, which at room temperature have more than sufficient thermal motion to overlap and achieve resonance. This situation is shown in the upper diagram of figure 12.6.

Nuclei, like bound electrons, also have quantized energy levels. For the isotopes of interest in the Mössbauer effect, these nuclear transitions have energies in the $\approx$ 10-100 keV range, and usually involve the ground nuclear state. Photons have momentum given by $p = \frac{h}{\lambda}$, where h is Plank's constant and λ is the radiation wavelength, and this momentum results in any atomic or nuclear transition giving rise to recoil kinetic energy proportional to the square of the photon (transition) energy and inverse of the mass of the recoiling particle. That is, by conservation laws, a small portion of the photon energy is channelled into recoil energy of the emitter. The squared energy dependence results in gases undergoing high-energy (i.e. keV) nuclear transitions to be off-resonance, so nuclear resonant fluorescence is usually not observed. This situation is shown in the lower diagram of figure 12.6.

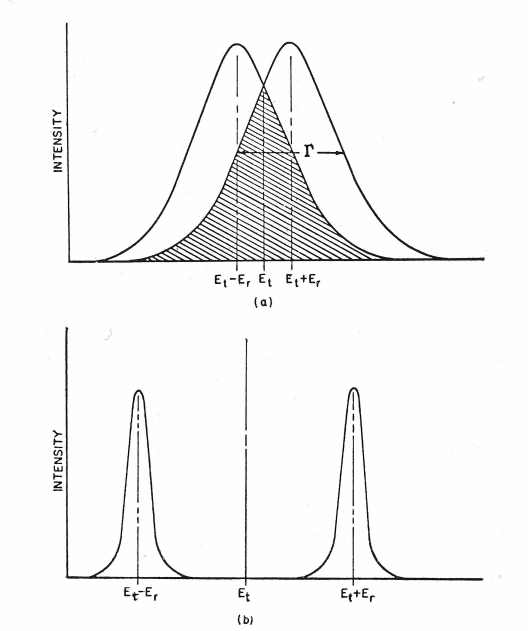

Figure 12.6.: Resonant (upper) and non-resonant (lower) absorption-emission process. E_t is the transition energy and E_r the recoil energy.

BOX 2 - Doppler effect

The Doppler effect is a source and absorber phenomenon, where the relative motion of the source and/or absorber adjusts the observed frequency of emitted sound or radiation. By changing the motion of either source or absorber (source in Mössbauer spectroscopy), the energy of an emitted photon can be slightly modified. Subtle hyperfine (nucleus + electron) interactions by the electronic environment of a Mössbauer-active nucleus correspond to a Doppler velocity energy shift of a few mm sec^{-1}, and therefore could potentially be resolved by application of the Doppler effect. These hyperfine spectral features give rise to a characteristic "fingerprint" for a given Mössbauer active compound. Mössbauer spectroscopy is one of the highest resolution spectroscopic techniques available. The crucial requirement for the Mössbauer effect is that the nucleus is contained in a solid, where the active nuclei are rigidly bound so that the recoil energy is taken up by the crystal as a whole rather than the individual atom that is experiencing the transition. For a typical macroscopic size crystallite, the mass is essentially infinite relative to that of the individual atom, meaning that the recoil energy is zero. Under these conditions, the transition profile moves from the non-resonant case (see lower diagram in figure 12.6) to the resonant case (see upper diagram in figure 12.6).

12.5. Historical development

The discovery of the Mössbauer effect was one that rapidly captured global interest, since the power of the technique could solve old problems with unprecedented resolution [2, 3]. Its discoverer, Rudolf Mössbauer (figure 12.7) was born in 1929 and completed a Masters degree at the Technical University in Munich, studying β^-/γ-ray scattering from ^{191}Os decay. He continued study with a Ph.D. at the Max Plank Institute for Medical Research in Heidelberg, where he essentially worked independently of his supervisor, Prof. Meier-Leibnitz, and received his doctorate in 1959 at age 29.

Figure 12.7.: Rudolf Ludwig Mössbauer at the time of winning the 1961 Nobel Prize in Physics. (Image from http://www.nobelprize.org/).

Mössbauer's Ph.D. involved scattering type experiments from ^{191}Ir $\longleftarrow^{191}$Pt decay with accompanying 129 keV γ-ray radiation which was passed through a ^{191}Ir foil scatterer. His supervisor, Prof. Meir-Leibnitz, had proposed that with a temperature decrease, the absorption and emission resonance lines would sharpen and the γ-ray intensity transmitted though the foil scatterer would increase. Experiments with temperatures above ambient showed little effect, but Mössbauer observed that a *decrease* in temperature resulted in an *increase* in resonant absorption and thus *decrease* in transmitted intensity. Mössbauer inferred that he was observing the resonant recoil-free absorption and emission of γ-ray quanta from the ^{191}Ir nuclei bound in the solid crystalline lattice, publishing his work in 1958 [4]. After completing his Ph.D., Mössbauer suddenly realised he "hadn't performed the main experiment", and immediately returned to his laboratory from a subsequent research position. By changing the source energy (or related wavelength) subtly by use of the Doppler Effect (see box 2), Mössbauer proposed that he could observe the resonance absorption lines in the ^{191}Ir foil absorber. But how could the source be physically modulated with a highly repetitive motion? By removing the rotating cam from a childs toy, he mounted the source in a lead block, and could vary the radiation source aperture location about its tangential circular motion to select a Doppler shifted energy, shown in 12.8. Liquid nitrogen frost caused the rotating cam to freeze, but wrapping the Dewar in tissue paper provided sufficient insulation to

give trouble-free motion. These experiments were performed as quickly as possible since proofs of Mössbauer's Ph.D. papers had already been sent to his competitor, P. B. Moon, for review. Moon [5], in 1950 had observed vapour-phase γ-ray nuclear fluorescence with ^{198}Hg atoms and a Hg lamp, by observing an intensity decrease (or cross-section increase) by a factor of 10^4 with application of a Doppler velocity of 670 ms^{-1} to offset recoil. Mössbauer hoped that Moon did not realise the implication of the Doppler Effect for his solid-state experiments. Fortunately, Moon did not, and the results of Mössbauer's experiment were published in a less well-known journal *Naturwissenschaften* [6], especially selected to avoid attention. His results showed a line width of $\approx$ 3 mm sec^{-1}, or resolution of 2.8×10^{10} which is nearing the natural line width limit for the radiocouple. His plan did not work: this publication received 270 requests for reprints in the first week after printing in 1959. Later in that year, Mössbauer attended a Colloquium in Germany where he passed on a reprint that was sent to prominent physicists at Caltech (California Institute of Technology). They recognized the importance of the work and offered him a research position overnight which he promptly accepted. The phenomenon of recoil-free γ-ray absorption and emission from nuclei bound in solids, later to be known as the Mössbauer effect, had been discovered and documented in the scientific community.

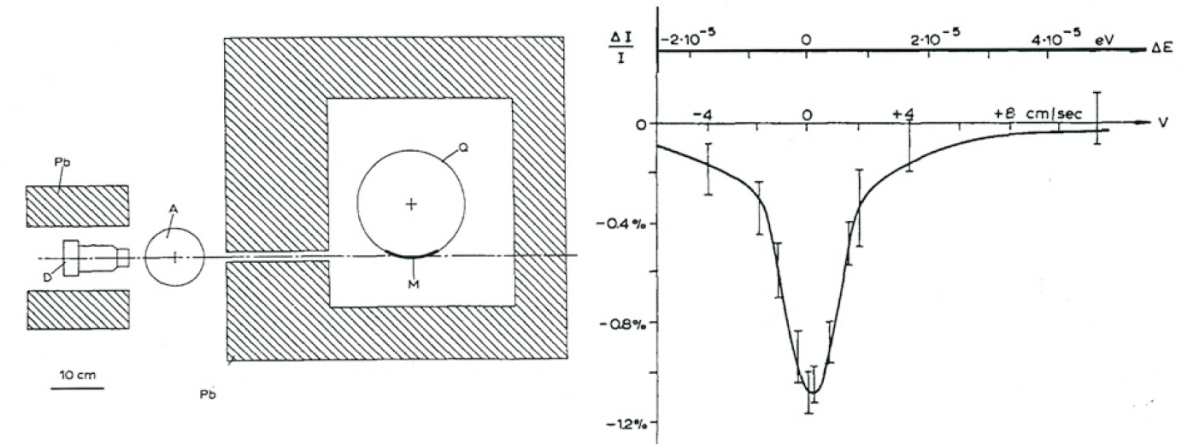

Figure 12.8.: The first Mössbauer experimental arrangement utilizing a rotating cam from a child's mechanical toy to achieve Doppler motion (left), and the first Mössbauer spectrum of ^{191}Ir foil (right). In this figure, D is the detector, A is the ^{191}Ir foil absorber, Q is the rotating cam with source M housed in a Pb block. The spectrum plots Doppler shifted velocity, v, or energy, ΔE, against the normalized resonance intensity absorbance, $\frac{I}{\Delta I}$ (Images taken from the 1961 Nobel lecture)

The large scale adoption of the resulting spectroscopy and applications led to Mössbauer receiving the Nobel Prize in Physics in 1961, just three years after his Ph.D. was completed and crucial experiments were published. Mössbauer remains one of the youngest scientists ever to receive the Nobel Prize [7]. An unanswered question for many years was how had Mössbauer obtained his radioactive source? Germany at the time had no fission reactors for radioisotope synthesis and refinement, and therefore any radioactive samples would have to be sourced from Harwell in England. In a recent publication [8], Mössbauer described how he had originally applied several times to legally import the required material, however the post-war military government restricted communications

with the British, who denied his requests. By writing directly to a woman with appropriate connection, he was able to import the required source illegally. Had Mössbauer not chosen this course of action, he would not have been able to perform his research that led to the award of the 1961 Nobel Prize. It is also known that Mössbauer had thought of observing the effect with ^{57}Fe but could not obtain the necessary ^{57}Co source [9].

12.6. The Mössbauer effect

The Mössbauer effect is the nuclear resonant absorption and emission of γ-ray quanta from nuclei which are bound in crystalline or metallic solid-state lattices. So-called hyperfine interactions, which result from extra-nuclear electrons interacting with the nucleus, result in energy shifting and splitting of the Mössbauer resonant transition energies. Measurement of these interactions therefore allows elucidation of the electronic environment (i.e. chemical structure) surrounding the Mössbauer active nucleus. A Mössbauer spectrum involves use of the Doppler Effect (see box 2) to vary the incident γ-ray energy slightly to achieve resonance (see box 1), which is recorded as spectral peaks. These hyperfine interactions are very small and prior, to Mössbauer's discovery had been thought impossible to observe, owing to the ultra-high resolution requirement. The technique has a theoretical resolution of up to 1 part in 10^{12}.

Mössbauer was fortunate that he had a sufficient mathematics (carried out on a slide rule) and physics knowledge to interpret his experimental results to identify a Lamb-Mössbauer f-factor, the probability that an absorption-emission event is truly recoil free. For an ^{57}Fe nucleus at room temperature, $f \sim 0.7$. Other Mössbauer active isotopes usually require at least liquid nitrogen or lower temperatures to obtain non-zero f-factors.

12.7. Hyperfine interactions

There are three principal hyperfine interactions of interest in a Mössbauer spectrum. These are (a) the isomer shift, (b) the quadrupole splitting, and (c) the magnetic hyperfine splitting or the nuclear Zeeman effect. The latter two interactions lift degeneracy and cause splitting in the spectrum. To observe and resolve these subtle hyperfine interactions, the radiation line width needs to be narrower than the interaction magnitudes. The limit of a spectral line width is governed by the Heisenberg Uncertainty Principle, and for many isotopes with non-metastable excited states, the magnitude of the hyperfine splitting or shift can be orders of magnitude smaller than the natural line width limit. This condition limits the applicability of most isotopes, meaning that although over 100 Mössbauer active nuclides are known, Mössbauer spectroscopy is in major part applied to ^{57}Fe.

The isomer shift gives an indication of the total electron density at the Mössbauer nucleus, resulting from a nuclear electric monopole interaction. Because a nucleus is not a point charge but has some small volume, there is a small but finite probability density of locating a 1s or 2s electron inside the nucleus. Other higher order angular momentum orbitals, e.g. p, d, have radial nodes precluding nuclear penetration. The nucleus volume

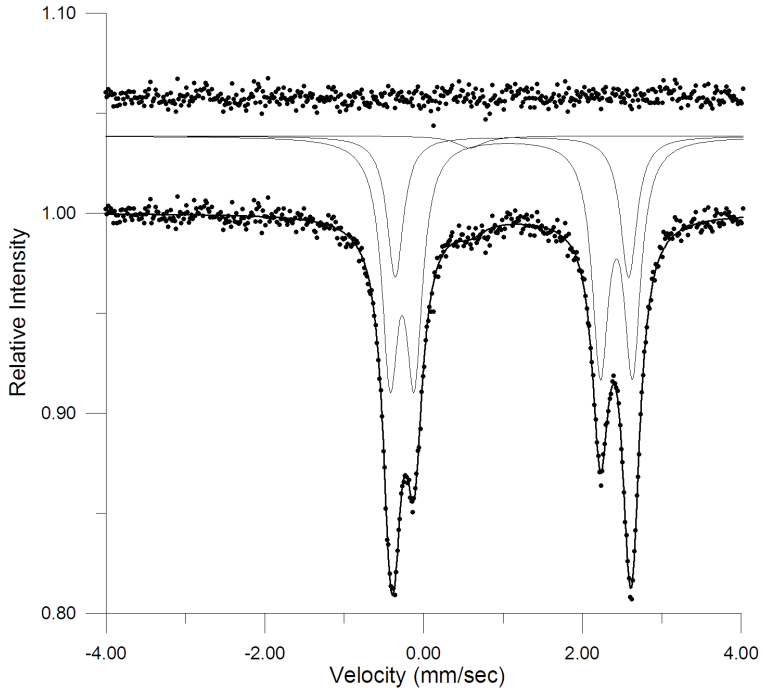

Figure 12.9.: A typical Mössbauer spectrum showing three isomer-shifted quadrupole split doublets for three different iron species in a polycrystalline (powder) sample.

varies between ground and excited states, which in effect, changes the centre of gravity of a spectrum relative to a reference species. In any inorganic compound, it is the valence orbitals (mainly 3d for iron) which are involved in bonding. These orbitals have radial density which penetrates the inner shell orbitals allowing screening and penetration of valence electronic effects to percolate down to the core orbitals. The most important use of isomer shift is the identification of oxidation state and spin state.

Nuclear electric dipoles are forbidden by nuclear symmetry; however, a nuclear electric quadrupole may exist. Electrons are charged particles and their spatial orbital localization gives rise to a local electric field, which in turn yields an electric-field gradient (efg) at the nucleus. The nuclear spin magnetic moment may then couple to the efg under certain electronic and symmetry conditions. A non-zero efg at the Mössbauer nucleus yields a quadrupole splitting, which is shown in the spectrum given in figure 12.9. For the nuclear spin state $I = \frac{3}{2}$ (excited state ^{57}Fe), two levels retaining m_I degeneracy exist. When the ligands or counter anions associated with the ^{57}Fe nucleus are changed or the symmetry is distorted from high symmetry, the different resulting electronic environment gives rise to a non-symmetrical efg and thus quadrupole splitting. In general, a non-zero efg at the nucleus has two different sources: the major valence contribution from valence electrons; and a smaller lattice contribution from charges and molecular orbitals further out in the lattice.

The third interaction results from interaction between the nuclear spin magnetic moment and the hyperfine magnetic field, yielding nuclear Zeeman splitting. This completely removes m_I degeneracy into $2I + 1$ levels, or four levels for the $I = \frac{3}{2}$ excited state, and two levels for the $I = \frac{1}{2}$ ground state of ^{57}Fe. The splitting between

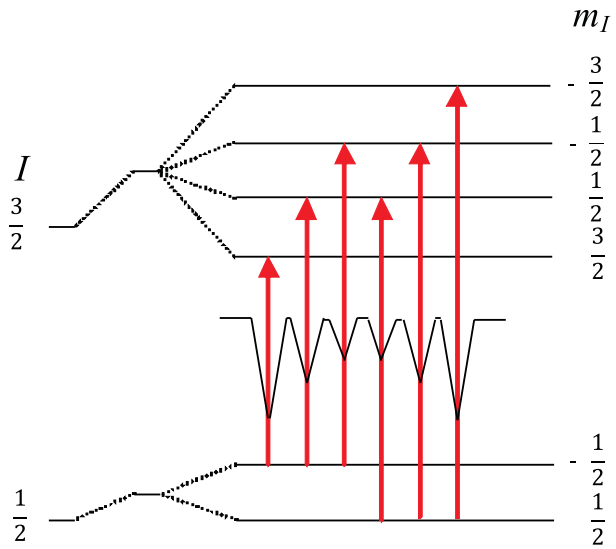

Figure 12.10.: The six observable isomer shifted magnetic hyperfine Mössbauer lines for ^{57}Fe. This situation depicts a typical iron foil spectrum showing a 3:2:1:1:2:3 intensity pattern.

each adjacent m_I level is uniform in the absence of a quadrupole splitting interaction and is proportional to the hyperfine field magnitude, which is used as a characteristic fingerprint of a magnetic iron-based mineral. Between the four excited state and two ground state hyperfine levels, eight transitions are possible, with six observed by magnetic dipole selection rules ($\Delta m_I = 0, \pm 1$) as shown in figure 12.10. Most paramagnetic inorganic complexes do not show magnetic structure in their Mössbauer spectrum, as electronic spins flip too rapidly and average the hyperfine field to zero or they are too magnetically dilute. Low temperature studies may identify characteristic temperatures of the appearance of a magnetic spectrum in ferromagnetic (Curie temperature) and anti-ferromagnetic (Néel temperature) compounds. The quadrupole splitting from a powder absorber almost always shows symmetrical intensities, and magnetic splittings show a 3:2:1:1:2:3 intensity pattern under normal conditions. Single crystal intensities are more complex and depend upon measurement orientation, although in principle can be relatively easily calculated with quantum mechanics. The use of polarized sources can select or remove various transitions.

One area of Mössbauer investigations is the study of magnetic ordering in solids, where magnetic domains can exist for magnetically concentrated samples. Such magnetic properties are very common in soils, clays and iron-based minerals. There are four types of magnetic ordering that can be studied: ferromagnetic coupling (parallel spins); antiferromagnetic coupling (antiparallel spins); ferrimagnetism coupling (generalization of antiferromagnetic coupling for different magnetic moment magnitudes); and canted antiferromagnetic coupling (with spins canted with respect to each other). Superparamagnetism is another important magnetic effect, commonly observed in concentrated iron oxides, hydroxides, and oxyhydroxides. This process occurs for small particles where each constitutes an individual magnetic domain. At sufficiently low temperatures, these particles may become co-operatively magnetically orientated (ordered). Measurement of magnetic properties and the magnetic behaviour onset temperature, allows determination of average particle size. Superparamagnetic

behaviour is characteristic for different minerals, and onset temperatures can typically occur over room temperature ranges.

The procedure of spectrum fitting is similar to that used in X-ray crystallography (or in fact most spectroscopic techniques), where some knowledge of the system is required in advance (i.e. number and symmetry of spectrum lines). One feature of Mössbauer spectroscopy is that if better signal-to-noise is required, the spectrum is left to collect longer. A typical spectrum may take hours to days to collect. The data is then transferred as raw intensities (counts) to a fitting program where the fitted peak positions, intensities, and line widths are refined (optimized) with a non-linear least squares fitting procedure.

Iron (^{57}Fe), with transition energy, $E_\gamma = 14.4$ keV, is by far the most common Mössbauer isotope and used in around 95% of all Mössbauer research. Iron is the sixth most abundant element on Earth (stable nuclear decay product) and the third most abundant cationic forming element, with three common accessible oxidation states, Fe^0, Fe^{2+} and Fe^{3+}. Iron exhibits rich inorganic transition metal chemistry with isomer shifts, quadrupole splittings and magnetic hyperfine structure relating to bonding (electronic) effects primarily involving electronic 3d orbitals. For a free ^{57}Fe nucleus, the recoil energy is 2×10^{-3} eV, which is several orders of magnitude larger than the natural line width of 4.6×10^{-9} eV, completely precluding isolated nuclear resonance. ^{57}Fe only has a 2.18% natural abundance, and for iron dilute systems (e.g. biological enzymes or proteins) enrichment or isotopic preparation can be carried out in order to achieve acceptable signals. ^{119}Sn is the second most commonly studied Mössbauer isotope, with a larger $E_\gamma = 23.8$ keV, broader lines and low temperatures required to give reasonable f-factors, the conditions are not nearly as ideal compared to ^{57}Fe. Further, since tin is not a transition metal, any efg primarily arises from 5p orbital imbalances, and therefore spectra are less informative about bonding.

12.8. Instrumentation

The instrumentation involved in a typical transmission Mössbauer spectrometer is relatively simple and outlined in figure 12.11. An instrument incorporates a source, a vibrator/transducer providing Doppler motion, an absorber or sample, and a detector. The Doppler Effect is employed to slightly modify the emitted radiation energy to achieve a resonant absorption condition with the sample nuclei. A spectrum thus measures the absorbance-velocity dependence of a sample. The transducer ideally provides longitudinal linear Doppler motion in the mm sec^{-1} range, corresponding to the magnitude of the hyperfine interactions (1 mm sec^{-1} = 4.808×10^{-8} eV in 14.4 keV ^{57}Fe). It is far more practical to modulate the source than the sample in transmission geometry, as the sample could be a fragile crystal or powder which may have preferred crystallite packing orientations. The most common transducers are usually of the electromechanical type, such as loud-speakers or solenoids. The common features of any transducer drive are that the response of the drive needs to be uniform and rapid, have a highly repetitive motion, and be highly robust. When resonance is achieved by the source motion for a given absorber sample, the radiation is absorbed and re-emitted in an isotropic fashion, thus decreasing the detector count rate for that velocity. A spectrometer is usually mounted on a vibration-damped platform to

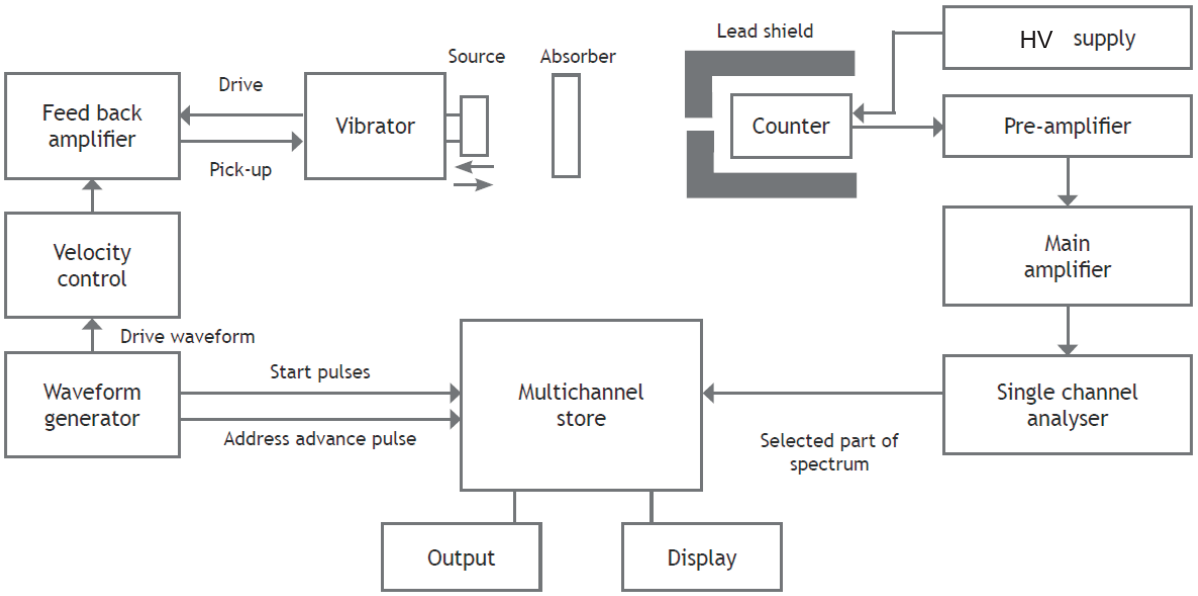

Figure 12.11.: Block diagram of a typical transmission Mössbauer spectrometer instrumental arrangement. The single channel analyser and multichannel store constitute a multichannel analyser (MCA).

avoid building and other external vibrations that may affect the transducer.

A Mössbauer source emits monochromatic radiation analogous to a hollow cathode lamp in atomic absorption studies, except involving nuclear transitions. The radiation is required to be monochromatic to the extreme, that is, nearing the natural line widths for dilute low activity sources. For ^{57}Fe the radioactive source or parent isotope is ^{57}Co. ^{57}Co decays by electron capture to an excited ^{57}Fe state with a 91% probability of decay to the Mössbauer active excited state as shown in figure 12.12. Since radiosources decay, they are made on request: for ^{57}Fe by cyclotron deuteron or proton irradiation of ^{56}Fe foil, with the product ^{57}Co chemically separated. This ^{57}Co is then electroplated and annealed with an inert Rh cubic matrix. With a half-life of 270 days, a source typically lasts approximately two years. Synchrotron sources have been used for rapid and time-resolved determinations, although they typically exhibit 2-3× the natural line width [10], therefore are not suitable for high-resolution analysis. ^{119m}Sn, which is a long-lived meta-stable excited state, is the parent isotope used for a tin Mössbauer source, and is synthesised by neutron bombardment of ^{118}Sn. The bombardment usually forms ^{119}Sb which then rapidly decays within days (38 hour half-life) to ^{119m}Sn, which in turn has a half-life of 250 days.

The absorber or sample may be of two different forms: a single crystal; or a polycrystalline powder. Good samples require a suitable so-called “absorber thickness” which maximizes the signal-to-noise ratio while keeping line widths as narrow as possible. In polycrystalline samples, crystallite morphology can result in preferred crystallite packing orientations that may adversely change spectral intensities. This effect can be avoided by diluting powders in a cubic non-absorbing matrix such as KBr or glucose.

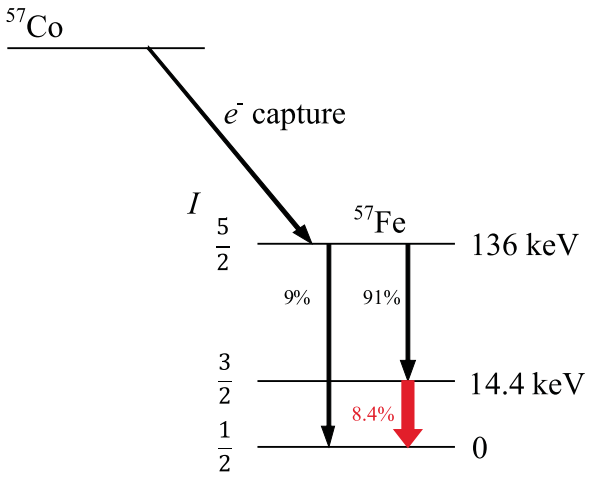

Figure 12.12.: Nuclear transitions that occur in a ^{57}Fe $\leftarrow^{57}$ Co Mössbauer source. The ^{57}Fe 14.4 keV line is the ^{57}Fe Mössbauer active transition.

There are three types of detectors and amplifiers for the detection of the transmitted radiation: scintillation counters ($E_\gamma > 40$ keV) that use a NaI or similar crystal scintillator in conjunction with the photoelectric effect and a photomultiplier; a gas proportional counter ($E_\gamma < 40$ keV) utilizing Compton scattering and accelerating electrodes; and more recently, Si/Ge solid state detectors, which provide the best signal-to-noise ratios.

In spectrometer operation, each Doppler velocity is divided into a small finite range (e.g. 512 iterations) using a multi-channel analyser (MCA) that records each Doppler velocity transmission intensity in a different memory location, and typically scans at $\approx$ 30 Hz. The MCA necessarily requires synchronization with the source motion, so that each memory location corresponds to a small linear velocity range. The monochromator may be considered to provide electronic windows (discriminators) in the MCA.

Mössbauer emission spectroscopy involves preparing the sample to contain the radioisotope, which is then used as the source, with Doppler modulation applied to a single line absorber. Such procedures are commonly employed for heterogeneous catalysis studies [11,12]. Another possible measurement geometry is backscattering. This orientation usually involves a thick sample, e.g. a rock (surface), where the source is placed close to the sample and the re-emitted 14.4 keV radiation which contains the Mössbauer spectrum is detected. The backscattering technique facilitates depth-based studies into the first 20 μm of a sample. The detection of conversion electrons that are produced by γ-ray emission knocking out inner-shell electrons with energy proportional to the binding energy and the emission energy, can be measured that also contain the Mössbauer spectrum. This method is known as conversion electron Mössbauer spectroscopy (CEMS) and operates for to depths of up to 1 μm.

12.9. Applications

The interdisciplinary nature of the Mössbauer effect has enabled the solution of many problems, some outlined in the following sections, with otherwise unchallenged spectroscopic resolution [13]. The technique is exclusively selective for the isotope under study, and may detect small or trace concentrations in complex environments, which may be highly ambiguous and/or poorly resolved with other techniques. Several exotic applications are now outlined.

12.9.1. General Relativity

The Mössbauer effect has been credited with providing the first classical experimental test of the theory of general relativity; testing the principle of equivalence. This principle states: "in a local region, one cannot distinguish between the effects of a uniform gravitational field and effects that would be found in a reference frame accelerating relative to an inertial reference frame, at the rate of and in a direction opposite to the acceleration of objects considered to be in free fall". The experiment, known as the Pound-Rebka experiment, was carried out in 1960 at the Jefferson Physical Laboratory, Harvard University in a 22.5 m elevator shaft and showed that the presence of a gravitational field can red-shift or blue-shift a photon [14, 15]. By mounting a ^{57}Co source at the top/bottom with a very thin ^{57}Fe-enriched foil absorber, and placing a gas-proportional counter at the bottom/top (see figure 12.13), slight gravitational shifting was observed. Both red- and blue-shifted experiments were performed; where red-shifting drops photons from top to bottom and vice versa for blue-shifting. The experimental results showed a slight isomer shift consistent with the predictions of General Relativity. Several higher resolution experiments followed. Previous to this experiment, all evidence pointing towards the correctness of the general theory of relativity was based on observations, where there was not complete control over all variables.

12.9.2. Archaeology

The non-destructive nature of backscattering and CEMS variants has led to extensive applications in the study of archaeological, clay and ceramic samples [16]. Pottery clays typically contain different iron oxides. These generally show subtly different phases, including several silicate and oxide phases, which vary with firing conditions and kiln baking regimes. Specifically, ratios of Fe^{2+} to Fe^{3+} depend on temperature, extent of reducing conditions, and baking time. Metallic iron and bronze (containing ^{119}Sn) artefacts and their corrosion products have also been studied. Examples include iron and ancient steel-based metalwork such as swords and tools, where the study of the various phases has provided knowledge of ancient heating and cooling phase processes, and has characterized their corrosion layers, indicating burial conditions and redox or humic processes. Some more recent examples include analysis of pigments and inks, facilitating potential identification of fakes and forgeries. The use of X-ray diffraction on old inks, manuscripts and their degradation products is usually difficult as beams can miss the ink line, or they contain badly crystallized components that cannot be identified - Mössbauer spectroscopy does not suffer from these problems. Old paints were traditionally made from natural

Figure 12.13.: A test of general relativity - the end of the flight path at the bottom (basement) of the elevator shaft in the Jefferson Tower at Harvard University as part of the Pound-Rebka experiment. This photograph shows helium filled mylar tubing with a single line foil absorber and detector.

products, many of which were iron oxide based, and therefore may be easily identified or fingerprinted based on magnetic or composite hyperfine structure. Since different paints were used in different eras and by different artists, identification of the paints can detect fakes and forgeries non-destructively. Mössbauer methods are usually employed in cases when various paints only differ very slightly and other analysis methods fail to differentiate them.

12.9.3. Planet Mars

One of the more recent applications of Mössbauer spectroscopy has involved the study of geological samples on the surface of planet Mars [17]. In the 1970s, the NASA Voyager spacecraft missions took the first well-known photographs of the highly oxidized red surface of Mars, showing red dust, soil and rock which are all well mixed by global wind cycles. The red surface colouration is attributed to iron-based compounds, with the surface having a composition of 13-18% iron by weight. Mössbauer spectroscopy has been used to identify various iron-bearing minerals and to infer ancient mineral and geological processes by analogy with those known on Earth [18–20]. Further, Mössbauer data can potentially make a serious contribution to the important questions: “Is there water on Mars?”; and “Is there life on Mars?”. On Earth, iron is critical for life and is found throughout biotic proteins. Life on Earth has been proposed to possibly originate at deep sea hydrothermal vents, where iron in its various oxidation states can act as a terminal electron acceptor or donor, facilitating respiration. The distribution of iron oxide and hydroxide minerals is also important to the sustainability of life. In 2004,

NASA successfully landed two Mars Exploration Rovers (Spirit and Opportunity) on the surface of Mars, with each rover having an extendable arm that holds a miniature Mössbauer spectrometer, as shown in figure 12.14. These spectrometers were required to be mechanically simple, have reliable electronics and mechanical components, to be shielded from intense UV and cosmic radiation, and to be sufficiently robust to survive the huge diurnal temperature variations in addition to the rover's landing/rough surface driving vibrations. These palm-sized spectrometers were nicknamed MIMOS II for MInaturised MOssbauer Spectrometer [21]. A spectrum is recorded by pressing a sensor head against the sample of interest until contact conformation by a contact plate, and collecting backscattered counts over the rovers night cycle. The backscattering geometry is ideal since it does not require any sample preparation, and a permanent magnet located on the robot's main body allowed collection of magnetic airborne aerosols and dust particles. The minerals magnetite, olivine and ferric oxide as magnetically trapped aerosols have been identified. A typical spectrum results from a ≈ 1.5 cm^2 irradiated area, and usually contains more than one compound, since most rock samples are covered in dust, resulting in complex and overlapping spectrum lines. Nevertheless, careful studies allow components to be resolved, and simultaneous 14.4 keV, 6.4 keV and CEMS channels provide depth-based measurements [22]. Although the rovers were initially designed for a 90-day life (from January 2004) on the Mars surface, they are still functioning and have collected over 150 Mössbauer data sets, identifying and characterizing many minerals [23]. For example, on 13 December 2004 Spirit took a spectrum of a rock denoted 'Clovis', identifying goethite, that contains hydroxyl anions of crystallization. This mineral can form by three known mechanisms, with only one in the absence of water. A second example was the discovery of jarosite on 3^{rd} February 2004. Jarosite contains on average 2%, but up to 10% water by weight as hydroxyl anions, and forms under acid-sulphuric conditions [24]. Its discovery provided some of the first mineralogical evidence for aqueous-type processes in the early history of Mars. Spherules of hematite (or 'blueberries'), which are known to form under aqueous conditions on Earth, have also been characterized in Martian soil [25, 26]. Moreover, some recent time-delayed photographs by the Mars Phoenix mission have shown the presence of some ice-water in scraped soil sections, and the following successful identification of water with TGA-MS (thermal gravimetric analysis with mass spectrometry characterization) techniques yielded confirmatory evidence of aqueous processes in the history of Mars.

12.10. Automotive sheet steel industry

Although Mössbauer spectroscopy is not usually employed as a routine tool in industry, the automotive sheet steel industry in the United States of America provides an example of an industrial application [27]. Galvannealing is a processes used for corrosion resistance in the automotive manufacturing industry, where rolls of thin steel sheet metal are passed through a zinc bath and then through ovens of typically 100 m length in order to bake the zinc coating. This procedure typically occurs at a rate of 3 ms^{-1} with an oven temperature of traditionally 650-700°C. Of the four different zinc-sheet metal phases that may form: gamma; gamma-1; delta; and zeta, delta has ideal properties and zeta has poor properties. The ideal delta phase galvanised sheet steel is easy to mould into car shapes and gives good spot welding properties. The galvanised layer has a

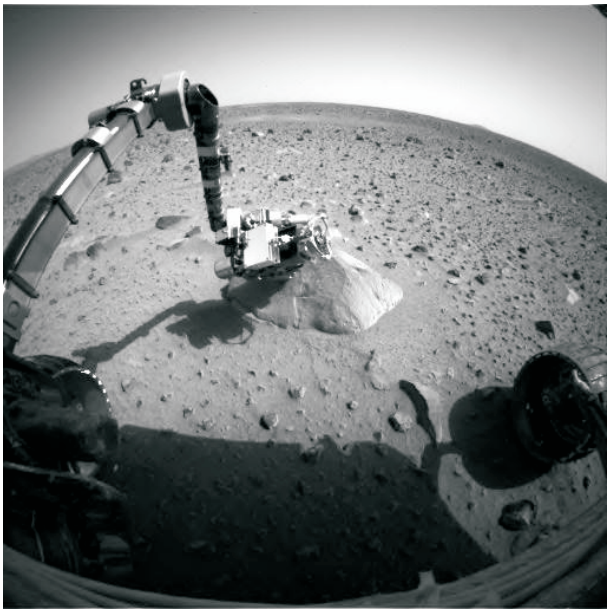

Figure 12.14.: One of the Mars Exploration Rovers extending its Mössbauer spectrometer to contact with a rock sample. (Image from http://nssdc.gsfc.nasa.gov/).

thickness of typically 3 μm for a >200 μm thick sheet. X-ray diffraction or electron microscopy techniques are unable to systematically differentiate between these phases, whereas Mössbauer spectroscopy is well suited to detecting the subtle differences. Application of Mössbauer spectroscopy has resulted in systematic time and temperature based studies in order to tune the manufacture conditions as well as quality-control analysis, where backscattering and CEMS processes can provide depth based information for optimizing the ideal protective layer thickness. Such studies have resulted in the baking temperature being reduced to 540°C, and speed of baking increased to 25 ms^{-1}, resulting in a 5× increase in production rate with the unfavourable zeta phase completely absent under these conditions. Mössbauer spectroscopy remains the only reliable technique to monitor Fe-Zn phase composition in galvanized steel.

12.10.1. Biochemistry

Literature categorizing has estimated that approximately 70% of all Mössbauer studies are biochemistry related, with biological applications generally be divided into porphyrin and non-porphyrin based studies. Iron is abundant in natural enzymes and proteins, and usually constitutes the active site for biological processes, such as in haemoglobin. Biochemists often face the challenge to obtain suitable crystals for characterization with X-ray crystallography. However, for Mössbauer, perfect crystals are not required, since a solution may be frozen to the solid-state and measurements undertaken - as long as the recoil is taken up by the crystalline lattice as a whole. Such studies are usually carried out in water, with a cooling regime applied to reduce or prevent expansion and any structural damage upon crystallization. Biochemical Mössbauer studies may include effects such as spin-crossover (e.g., cytochromes of low spin Fe^{3+}), valence delocalization and relaxation or magnetic

effects, with spectra often being pH dependent. As an example, consider both haemoglobin and myoglobin, each of which contain five nitrogen donor atoms at each active site, with the former protein containing four active sites. Mössbauer spectroscopy is well suited to studying the subtle interactions resulting from different ligand bonding and consequential structural and electronic effects, where in this instance, the efg arises entirely from the ligand interaction. Both of these proteins reversibly bind oxygen, and it has been clearly observed that the deoxy- form exhibits a high-spin Fe^{2+} (diamagnetic) state with a slightly out-of-porphyrin-plane iron atom owing to the axial ligand co-ordination [28]. Upon oxygen binding, low-temperature studies reveal that a spin-crossover occurs, yielding a low-spin-coupled Fe^{3+} state. Quadrupole splittings indicate that oxygen is bound in a bent (non-linear) geometry. Other π-ligands, for example NO and CO, also show the large quadrupole splitting characteristic of this type of bonding. Haemoglobin exposed to CO_2 yields a spectrum that is similar to blood in a nitrogen atmosphere, indicating either that no CO_2 binding occurs, or that it does not electronically interact with the iron centre to any appreciable extent. Mössbauer spectroscopy has facilitated significant steps in the understanding of biological systems.

12.11. Mössbauer spectroscopy in New Zealand

The first Mössbauer research in New Zealand was undertaken by Prof. James Duncan at Victoria University of Wellington. It was then subsequently through collaboration with the Chemistry Division of DSIR and the Physical and Engineering Laboratories of DSIR, that the first modern spectrometer was constructed in 1965 [29], a follow-up to pioneering the two other major spectroscopic techniques of the 1960s in New Zealand: NMR (1961); and EPR (mid 1960s). The DSIR spectrometer contained a 400-channel RIDL multichannel analyzer which was donated by the United States Air Force since this type of scientific research was considered of "strategic importance" at the time. All spectra were initially hand plotted, with eventual implementation of a paper tape plotter. The transducer consisted of two loud speakers that were vertically aligned, with the radioactive source mounted from one speaker on a metal rod. The first speaker provided the drive motion and the second acted as a pickup loop providing a feedback circuit. This transducer produced well-behaved simple harmonic motion that was algebraically linearised following data collection, however slow drift of the sine wave function generator with respect to the MCA required calendar-date calibration. Subsequent upgrades in the 1970s saw implementation of an ORTEC 1024 channel MCA in addition to a new transducer drive, eliminating the previous shortfalls. The DSIR ORTEC MCA and other later ELSCINT drive electronics are still in use in the Chemistry Department at the University of Canterbury, and were employed for the Mössbauer studies described in this thesis.

Mössbauer research in the Department of Chemistry, University of Canterbury, has been focused around fundamental single crystal studies. When a crystallographic unit cell contains more than one symmetry-related iron site and the spectrum exhibits a single quadrupole doublet (e.g. high spin Fe^{2+}), then each iron site contains its own microscopic (site) efg tensor. These average to give an overall macroscopic efg tensor and the same quadrupole doublet. Efg tensors must necessarily be determined by single crystal measurements,

where anisotropy of the quadrupole doublet occurs in accord with anisotropy of the recoilless fraction and related mean-square-displacement (msd) tensor. Figure 12.15 shows the arrangement for one such single crystal experiment.

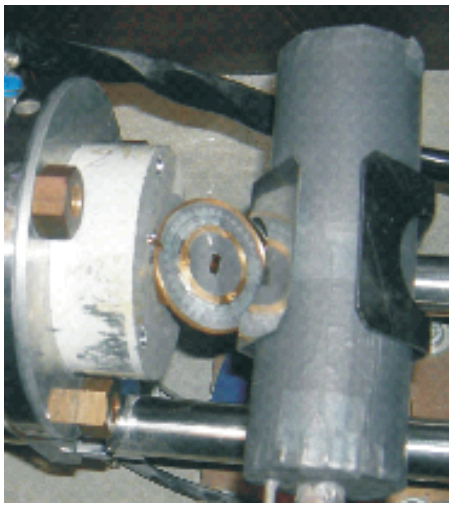

Figure 12.15.: The Mössbauer spectrometer at the University of Canterbury with a $Fe(NH_4)_2(SO_4)_2{\cdot}6H_2O$ (ferrous ammonium sulphate hexahydrate) single crystal located on a single circle goniometer assembly that is in turn mounted at 45° relative to the γ-beam. This assembly provides angular measurements allowing determination of microscopic tensor quantities.

Recently, measurements have been undertaken to resolve microscopic contributions to both efg and msd tensors for the "ambiguous" monoclinic case where the Fe^{2+} sites do not sit on a C_2 axis. The related Lamb-Mössbauer f-factor and msd tensors that were determined at room temperature completely from Mössbauer measurements have been found to be different but comparable with those derived from X-ray diffraction (Debye-Waller) measurements [30].

References

[1] J. Adetunhi and A. T. Dronsfield. *Edu. Chem.*, 39:97, 2002.

[2] U. Gonser and C. Schneider. *Mössbauer Spectroscopy Applied to Inorganic Chemistry*, volume 3. Plenum Press, 1984.

[3] H. J. Lipkin. *Hyperfine Interact.*, 72:3, 1992.

[4] R. L. Mössbauer. *Zeitschrift fur Physik A Hadrons and Nuclei*, 151:124, 1958.

[5] P. B. Moon. *Proc. Phys. Soc. (London)*, 64:76, 1951.

[6] R. L. Mössbauer. *Naturwissenschaften*, 45:538, 1958.

[7] R. L. Mössbauer. *Nobel Prize Lecture*, 1961.

[8] R. L. Mössbauer. *Hyperfine Interact.*, 126:1, 2000.

[9] S. S. Hanna, J. Heberle, C. Littlejohn, G. J. Perlow, R. S. Preston, and D. H. Vincent. *Phys. Rev. Lett.*, (1):28, 1960.

[10] E. E. Alp, W. Sturhahn, and T. Toellner. *Nuclear Instrum. Meth. Phys. Res. B*, 97:526, 1995.

[11] J. M. Millet. *Adv. Cata.*, 51:306, 2007.

[12] H. Topsoe, B. S. Clausen, and S. Morup. *Hyperfine Interact.*, 27:231, 1986.

[13] T. C. Gibb. *Hyperfine Interact.*, 13:45, 1983.

[14] R. V. Pound and Jr. G. A. Rebka. *Phys. Rev. Lett.*, 3:439, 1959.

[15] R. V. Pound and Jr. G. A. Rebka. *Phys. Rev. Lett.*, 7:337, 1960.

[16] F. E. Wagner and A. Kyek. *Hyperfine Interact.*, 154:5, 2004.

[17] T. J. Wdowiak, G. Klingelhöfer, M. L. Wade, and J. I. Nunez. *Geophys. Res.*, 108:38, 2003.

[18] C. Schröser, B. Bailey, G. Klingelhöfer, and H. Staudigel. *Plan. Space Sci.*, 54:1622, 2006.

[19] C. Schröser, G. Klingelhöfer, B. Bailey, and H. Staudigel. *Hyperfine Interact.*, 116:567, 2005.

[20] W. Goetz, P. Bertelsen, C. S. Binau, H. P. Gunnlaugsson, S. F. Hviid, K. M. Kinch, D. E. Madsen, M. B. Madsen, M. Olsen, R. Gellert, G. Klingelhöfer, D. W. Ming, R. V. Morris, R. Rieder, D. S. Rodionov, Jr P. A. de Souza, C. Schröder, S. W. Squyres, T. Wdowiak, and A. Yen. *Nature*, 436:62, 2005.

[21] G. Klingelhöfer. *Hyperfine Interact.*, 158:117, 2004.

[22] D. G. Agresti, M. D. Dyar, and M. W. Schaefer. *Hyperfine Interact.*, 167:845, 2006.

[23] G. Klingelhöfer, R. V. Morris, Jr. P. A. De Souza, D. Rodionov, and C. Schröder. *Hyperfine Interact.*, 170:169, 2006.

[24] G. Klingelhöfer, R. V. Morris, B. Bernhardt, C. Schröder, D. S. Rodionov, Jr. P. A. de Souza, A. Yen, R. Gellert, E. N. Evlanov, B. Zubkov, J. Foh, U. Bonnes, E. Kankeleit, P. Gutlich, D. W. Ming, F. Renz, T. Wdowiak, S. W. Squyres, and R. E. Arvidson. *Science*, 306:1740, 2004.

[25] A. S. Yen, R. Gellert, C. Schröder, R. V. Morris, III J. F. Bell, A. T. Knudson, B. C. Clark, D. W. Ming, J. A. Crisp, R. E. Arvidson, D. Blaney, J. Brückner, P. R. Christensen, D. J. Des Marais, Jr P. A. de Souza, T. E. Economou, A. Ghosh, B. C. Hahn, K. E. Herkenhoff, L. A. Haskin, J. A. Hurowitz, B. L. Joliff, J. R. Johnson, G. Klingelhöfer, M. Bo Madsen, S. M. McLennan, H. Y. McSween, L. Richter, R. Rieder, D. Rodionov, L. Soderblom, S. W. Squyres, N. J. Tosca, A. Wang, M. Wyatt, and J. Zipfel. *Nature*, 436:49, 2005.

[26] F. J. Berry. *Hyperfine Interact.*, 144:381, 2002.

[27] D.C. Cook. *ICAME*, 2001:1, 2001.

[28] U. Gonser. *Mössbauer Spectroscopy II: The Exotic Side of the Effect (Topics in Current Physics)*, volume 2. Springer, 1981.

[29] H. J. Whitfield. *N.N. Jl Sci.*, 9:782, 1966.

[30] J. N. Bull, W. T. Robinson, and W. C. Tennant. *Hyperfine Interact.*, 194:347, 2009.